Academic Affairs Excellence Awards

Application Form

Name: Arash Bodaghee

Rank: Associate Professor

Department: Chemistry, Physics and Astronomy

Award applying for:
(Check one)

	Excellence in Teaching Award*
	Excellence in Online Teaching Award*
X	Excellence in Scholarship & Creative Endeavors Award*
	Excellence in University Service*
	Excellence in Scholarship of Teaching & Learning Award*
	Department/Program Excellence Award^
	Irene Rose Community Service Award^
	Laurie Hendrickson McMillian Faculty Award^

*college selection required before being forwarded to university

^university awards

College nominees' final applications received by Center for Teaching and Learning (ctl@gcsu.edu) by March 1.

Please insert the required documentation in the pages below for the award category you have noted above. Detailed information associated with each award is available online at the Center for Teaching and Learning website.

GEORGIA COLLEGE.

GEORGIA'S PUBLIC LIBERAL ARTS UNIVERSITY

College of Arts and Sciences

Department of Chemistry, Physics and Astronomy
Campus Box 82
Milledgeville, Georgia 31061-0490
Phone 478-445-5769
Fax 478-445-1092

To:
Dean Eric Tenbus

Letter of Nomination for the Excellence in Scholarship and Creative Endeavors Award

I would like nominate **Arash Bodaghee,** Associate Professor of physics in the Department of Chemistry, Physics and Astronomy, for the Georgia College Excellence in Scholarship and Creative Endeavors Award.

Having served on the faculty research awards committee for 5 years (from fall 2009 to spring 2014), I can honestly say that Dr. Bodaghee's work would have easily placed him among the winners, if not the top award, in each of those years.

His publications in 2020-2021 include a first author paper in the *Astrophysical Journal*, by far the top journal in astrophysics. This would be roughly equivalent to publication in Nature or Science in the biological sciences and, in and of itself, would be sufficient for tenure at many R1 institutions. In addition, he is the co-author of three more papers published in the *Astrophysical Journal*, two in *Astronomy & Astrophysics* (another top international journal in the field), one in *Monthly Notices of the Royal Astronomical Society* (the top international journal from the UK), and one in *New Astronomy Reviews*. These journals are international in scope and read by all serious academic astronomers and astrophysicists world-wide.

Publication in these international peer-reviewed journals is very competitive and difficult. Doing so several times in a single year is quite unusual.

I am in strong support for Dr. Bodaghee's consideration for this Excellence in Scholarship Award in 2021.

Ralph H France III

Professor of Physics
Georgia College
Dept. of Chemistry, Physics & Astronomy

Milledgeville • Macon • Warner Robins

Georgia College, the state's designated public liberal arts university, combines the educational experience expected at esteemed private liberal arts colleges with the affordability of public higher education.

Department of Chemistry, Physics and Astronomy
College of Arts and Sciences
Campus Box 82
Milledgeville, Georgia 31061-0490
Phone (478) 445-3512
Fax (478) 445-1092
donovan.domingue@gcsu.edu

Friday, February 18, 2022

To Excellence in Scholarship Award Committee Members:

Please consider this letter of nomination for **Arash Bodaghee,** Associate Professor in the Department of Chemistry, Physics and Astronomy. This nomination is in recognition of his success in publication of his astrophysical research for the years 2020-2021.

During the term under consideration, Dr. Bodaghee has demonstrated a strong commitment to contributing to his academic field of research as well as including students in the process in order to foster an environment of productive undergraduate research. In 2021-2022, Dr. Bodaghee was able to contribute as author or co-author to 9 publications (8 currently published) to top tier journals in astrophysics for the U.S., U.K. and the E.U. These articles add to the body of knowledge in high energy astrophysics of x-ray binary stars, cataclysmic variable stars and black holes along with valuable characterizations of the x-ray and gamma ray emitting sky. This volume of contributions far exceeds the typical scholarship productivity of members of our department and I argue it is worthy of university wide recognition.

I draw your attention to the first-authored work published in the Astrophysical Journal in Oct. 2021 which includes 4 Georgia College undergraduates on the author list. I commend this accomplishment for highlighting our students and the work they are capable of. A second publication from Feb. 2020 includes another Georgia College undergraduate author that contributed to research involving the Hubble Space Telescope.

It is my opinion that Dr. Bodaghee's accomplishments in publication and scholarship in astrophysics and his successful involvement of 5 undergraduates in this two year term of research deserve the strongest consideration for the university level Excellence in Scholarship Award.

Sincerely,

Donovan Domingue, PhD
Professor of Physics and Astronomy
Interim Department Chair
Department of Chemistry, Physics and Astronomy
GEORGIA COLLEGE

Department of Chemistry, Physics and Astronomy
College of Arts and Sciences
Campus Box 82
Milledgeville, Georgia 31061-0490
Phone (478) 445-5769
Fax (478) 445-1092

GEORGIA
COLLEGE
GEORGIA'S PUBLIC LIBERAL ARTS UNIVERSITY

February 21, 2022

To Whom This May Concern

It is my pleasure to write this letter of recommendation for Dr Arash Bodaghee. I have worked with Dr Bodaghee for several years as both his supervisor and colleague. He has proven to be an excellent teacher and academic. In the classroom Dr Bodaghee is always prepared with lectures that are clear, interesting and right on schedule with course objectives. Dr Bodaghee has five publications in 2021. Any one of these publications would be sufficient to warrant a scholarship award, but to have five in one year at GCSU is truly outstanding. This quality and quantity of research is only realized in research universities and brings very positive national recognition to GCSU. This would be a fantastic for any professor, but in addition he has performed this cutting edge work with the involvement of undergraduates. His work has covered his summer salary, and provided a stipend for a summer research student.

Students are always interested in joining his research group, and all his students recognize the value of participating in undergraduate research with Dr Bodaghee. In addition, while performing this great research he has also found time for outreach. He has been actively involved in setting up public viewing opportunities at the Pohl Observatory. I highly recommend Dr Bodaghee for the Excellence in Scholarship and Creative Endeavors award. If you need any further information from me please contact me at your convenience.

Sincerely,

Dr K.C. McGill
Chair of GCSU Chemistry, Physics and Astronomy Department
ken.mcgill@gcsu.edu

Milledgeville • Macon • Warner Robins
Georgia College & State University, established in 1889, is Georgia's Public Liberal Arts University.
University System of Georgia

Department of Chemistry, Physics and Astronomy
College of Arts and Sciences
Campus Box 82
Milledgeville, Georgia 31061-0490
Phone (478) 445-5769
Fax (478) 445-1092

February 21, 2022

Dear Members of the Excellence in Scholarship & Creative Endeavors Award Committee,

I am writing this letter of support on behalf of Dr. Arash Bodaghee as part of his portfolio for the Excellence in Scholarship & Creative Endeavors Award - 2022. I had the pleasure of working alongside with Dr. Bodaghee since I joined Georgia College in Spring 2016. Since Dr. Bodaghee's portfolio provides ample examples of the impact of his research including creating the most accurate map of high-mass X-ray binaries ever made (https://frontpage.gcsu.edu/node/8425), I will focus more on the impact of his research on our students.

First of all, being a recognized astronomer in the field of High-Energy Astrophysics, Dr. Bodaghee attracts students to our physics program which strengthens our program. Most importantly his research helps to retain the best students at Georgia College as most of our physics majors come to Georgia College with the intention to transfer to Georgia Tech. One recent example I can think of is Cody Cox. Cody Cox is Dr. Bodagee's Physics Scholar. I am coordinating Physics Scholars program and have taught Cody several courses including three upper level courses. Students like Cody are living testimonies to the impact of highly engaged research experiences Dr. Bodaghee offers to our students. His national and international collaborations further provide opportunities for our students to work on collaborative research. This not only helps Dr. Bodaghee to strengthen his research portfolio but helps our students immensely. Dr. Bodaghee regularly sends his research students to conferences including National Conference on Undergraduate Research and American Astronomical Society Annual Meeting. Most importantly he trains his students well before they attend the respective conferences. Publishing on highly reputed journals with undergraduate co-authors speaks volumes of the impact of Dr. Bodaghee's research on our students.

I believe Dr. Bodaghee and his research is an asset to Georgia College and brings significant recognition to our program and college. The impact of his research to the field of High-Energy Astrophysics and most importantly for our students warrants the recognition of Excellence in Scholarship & Creative Endeavors Award – 2022.

Thank you.
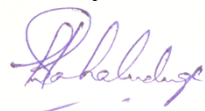
Hasitha Mahabaduge, PhD
Associate Professor of Physics
Georgia College & State University
Office: 478-445-8633
hasitha.mahabaduge@gcsu.edu

Publications in peer-reviewed journals (names in bold denote a GCSU affiliation)

1. "*Exploring the MeV Sky with a combined coded mask and Compton telescope: the Galactic Explorer with a Coded aperture mask COmpton telescope (GECCO)*"
E. Orlando, E. Bottacini, E. Moiseev, **A. Bodaghee**, W. Collmar, T. Ensslin, I.V. Moskalenko, M. Negro, S. Profumo, M.G. Baring, A. Bolotnikov, N. Cannady, G.A. Carini, S. Digel, I. Grenier, A.K. Harding, D. Hartmann, S. Herrmann, M. Kerr, R. Krivonos, P. Laurent, F. Longo, A. Morselli, M. Sasaki, P. Shawhan, G. Skinner, L.D. Smith, F.W. Stecker, A. Strong, S. Sturner, D.J. Thompson, J.A. Tomsick, Z. Wadiasingh, R.S. Woolf, E. Yates, A. Zoglauer,
Journal of High-Energy Astrophysics, submitted, (Dec. 2021)
https://ui.adsabs.harvard.edu/abs/2021arXiv211207190O
Description: This "white paper" was submitted in response to NASA's Astronomy 2020 Decadal Report. We propose a new space telescope that will bridge the gap in energies between X-rays and gamma-rays that is poorly covered by current observatories. If it is selected for continuation by NASA, this would represent a 10–30 year mission.

2. "*Evidence for low kick velocities among high-mass X-ray binaries in the Small Magellanic Cloud from the spatial correlation function*"
A. Bodaghee, V. Antoniou, A. Zezas, J.A. Tomsick, **R. Agnew**, **B. Jackson**,
Z. Jordan, **E. Frechette**, A.E. Hornschemeier, J. Rodriguez,
The Astrophysical Journal, Vol. 919, id. 81, 10 pp. (Oct. 2021)
https://ui.adsabs.harvard.edu/abs/2021ApJ...919...81B
Description: Four undergraduate students from GCSU helped me generated the first ever so-called spatial correlation function for the Small Magellanic Cloud (SMC) which is a nearby satellite galaxy of the Milky Way. This allowed us to perform a statistical comparison between two groups of objects: in our case, accreting neutron stars and massive star-forming complexes. Our results show that these groups in the SMC are moving apart less quickly than their equivalent populations in the Milky Way. Currently, an undergraduate student from GCSU (Cody Cox) is assisting with a revision of my Milky Way analysis from 2012. We were featured on FrontPage:
https://frontpage.gcsu.edu/node/8425 (Aug. 23, 2021)

3. "*15 years of Galactic surveys and hard X-ray background measurements*"
R.A. Krivonos, A.J. Bird, E.M. Churazov, J.A. Tomsick, A. Bazzano, V. Beckmann, G. Bélanger, **A. Bodaghee**, S. Chaty, E. Kuulkers, A.A. Lutovinov, A. Malizia, N. Masetti, I.A. Mereminskiy, R. Sunyaev, S.S. Tsygankov, P. Ubertini, C. Winkler,
New Astronomy Reviews, Vol. 92, id. 101612, (June 2021)
https://ui.adsabs.harvard.edu/abs/2021NewAR..9201612K
Description: This work reviews the current status from surveying observations of the Milky Way's diverse population of X-ray emitting objects, as well as what they can tell us about the observed background radiation in different directions of the galaxy.

4. "*Chandra, NuSTAR, and optical observations of the cataclysmic variables IGR J17528–2022 and IGR J20063+3641"*

J. Hare, J.P. Halpern, J.A. Tomsick, J.R. Thorstensen, **A. Bodaghee**, M. Clavel, R. Krivonos, K. Mori,
The Astrophysical Journal, Vol. 914, id. 85, 10 pp. (June 2021)
https://ui.adsabs.harvard.edu/abs/2021ApJ...914...85H
Description: Two previously-unclassified objects were observed with the Chandra and NuSTAR space telescopes enabling us to identify them as cataclysmic variables (i.e., a white dwarf paired with a normal star). For one of the objects, we found the spin period of the white dwarf and the orbital period of the system for the first time.

5. "*Using Chandra localizations and Gaia distances and proper motions to classify hard X-ray sources discovered by INTEGRAL*"
J.A. Tomsick, B.M. Coughenour, J. Hare, R. Krivonos, **A. Bodaghee**, S. Chaty, M. Clavel, F.M. Fornasini, J. Rodriguez, A.W. Shaw,
The Astrophysical Journal, Vol. 914, id. 48, 14 pp. (June 2021)
https://ui.adsabs.harvard.edu/abs/2021ApJ...914...48T
Description: Using data from the Chandra, Gaia, and INTEGRAL space telescopes, we were able to identify 4 previously-unclassified objects as cataclysmic variables (i.e., a white dwarf paired with a normal star), another as a candidate high-mass X-ray binary (i.e., a neutron star or a black hole paired with a massive star), and 2 others as active galactic nuclei (i.e., a supermassive black hole at the center of a distant galaxy).

6. "*X-ray spectral and flux variability of the microquasar GRS 1758-258 on timescales from weeks to years*"
M. Hirsch, K. Pottschmidt, D.M. Smith, **A. Bodaghee**, M. Cadolle Bel, V. Grinberg, N. Hell, F. Krauß, I. Kreykenbohm, A. Lohfink, M.A. Nowak, B.H. Rodrigues, R. Soria, J.A. Tomsick, J. Wilms,
Astronomy & Astrophysics, Vol. 636, id. 51, 12 pp. (Apr. 2020)
https://ui.adsabs.harvard.edu/abs/2020A%26A...636A..51H
Description: Twelve years of monitoring observations by the RXTE space telescope are presented for an accreting black hole. The source went through a few state transitions allowing us to follow the intensity of its emission as a function of energy (i.e., hardness-intensity diagram).

7. "*Evolution of MAXI J1631-479 during the January 2019 outburst observed by INTEGRAL/IBIS*"
M. Fiocchi, F. Onori, A. Bazzano, A.J. Bird, **A. Bodaghee**, P.A. Charles, V.A. Lepingwell, A. Malizia, N. Masetti, L. Natalucci, P. Ubertini,
Monthly Notices of the Royal Astronomical Society, Vol. 492, Issue 3, p. 3657 (Mar. 2020)
https://ui.adsabs.harvard.edu/abs/2020MNRAS.492.3657F
Description: A new X-ray source, first discovered by the MAXI space telescope, was observed during its outburst by the INTEGRAL space telescope. From this observation, we detected several state transitions which are typical of accreting black holes.

8. "*The stellar and wind parameters of six prototypical HMXBs and their evolutionary status*"
R. Hainich, L.M. Oskinova, J.-M. Torrejón, F. Fuerst, **A. Bodaghee**, T. Shenar, A.A.C. Sander, H. Todt, **K. Spetzer**, W.-R. Hamann,
Astronomy & Astrophysics, Vol. 634, id. 49, 38 pp. (Feb. 2020)

https://ui.adsabs.harvard.edu/abs/2020A%26A...634A..49H

Description: Six high-mass X-ray binaries (HMXBs) were observed for the first time with the Hubble space telescope. Parameters of the stellar wind derived from these observations were used to constrain models of stellar atmospheres. While this project was led by astronomers at the University of Potsdam, an undergraduate Physics Scholar at GCSU, Ms. Keri Spetzer, and I received external funding (Caltech) to do research during 2014. Our analysis of data from Hubble and from the Swift X-ray telescope represented the preliminary work of this publication. We were featured twice on Frontpage: the first instance is no longer accessible (Dec. 2, 2014)
https://frontpage.gcsu.edu/node/4446 (Mar. 3, 2020)

9. "*Chandra observations of high-energy X-ray sources discovered by INTEGRAL*"
J.A. Tomsick, **A. Bodaghee**, S. Chaty, M. Clavel, F.M. Fornasini, J. Hare, R. Krivonos, F. Rahoui, J. Rodriguez,
The Astrophysical Journal, Vol. 889, id. 53, 13 pp. (Jan. 2020)
https://ui.adsabs.harvard.edu/abs/2020ApJ...889...53T
Description: Using the Chandra space telescope, we observed 15 unidentified X-ray sources enabling more precise coordinates, which allowed us to classify the majority of them as either nearby cataclysmic variables or distant active galactic nuclei. This is part of an ongoing campaign to use Chandra to help characterize sources discovered with the INTEGRAL space telescope.

NB: *The Astrophysical Journal* is the world's preeminent journal for peer-reviewed articles devoted solely to astrophysics. It is published by IOP Sciences for the American Astronomical Society. The equivalent for the European Union is *Astronomy & Astrophysics* which is published by EDP Sciences for the European Southern Observatory. The equivalent for the United Kingdom is *Monthly Notices of the Royal Astronomical Society* which is published by Oxford University Press for the Royal Astronomical Society. *New Astronomy Reviews* is an international peer-reviewed journal of astronomy published by Elsevier Press.

Publications that were not peer-reviewed

"*INTEGRAL/GPS detections of a new outburst from 4U 1630–47 and XTE J1701–407*"
F. Onori, V. A. et al.,
Astronomer's Telegram, 13564, (Mar. 2020) https://www.astronomerstelegram.org/?read=13564

"*INTEGRAL GPS detects renewed activity from IGR J18483–0311 and GRS 1915+105*"
V.A. Lepingwell, et al.,
Astronomer's Telegram, 13676, (Apr. 2020) https://www.astronomerstelegram.org/?read=13676

"*INTEGRAL detection of 2S 1553-542*"
V.A. Lepingwell, et al.,
Astronomer's Telegram, 14335, (Jan. 2021) https://www.astronomerstelegram.org/?read=14335

"*INTEGRAL hard X-ray detection of a new outburst from GX339-4*"
V. Sguera, et al.,
Astronomer's Telegram, 14354, (Jan. 2021) https://www.astronomerstelegram.org/?read=14354

Excellence in Scholarship & Creative Endeavors Award   (Section 4: Reflective Statement)
Dr. Arash Bodaghee, Associate Professor of Physics & Astronomy

In our classrooms, aspiring scientists are introduced to the physical laws that govern nature. In our laboratories, these scientists experience how that mathematical framework is applied to explain our observations. Fortunately, as an astronomer, my laboratory is the Universe itself which naturally attracts a steady flow of stellar students.

The last time I was awarded this prize (2016), my reflection statement emphasized the work that students were doing on two promising lines of research that were not yet published, and so were not yet eligible: one involved the first ever Hubble space telescope observations of a class of objects called High-Mass X-ray Binaries (HMXBs) where a neutron star or a black hole is paired with a massive star; and the other involved the statistical analysis of HMXBs hosted by a nearby satellite galaxy of the Milky Way called the Small Magellanic Cloud (SMC). Both of these studies are now published in top-ranking peer-reviewed journals with five students as co-authors.

Keri Spetzer, a math and physics major, worked with me in 2014–2015 funded in part through a grant from the Space Telescope Science Institute (via Caltech). Keri and I did the preliminary analysis of the Hubble and Swift telescope data. In February 2020, Keri and I became co-authors of the article published by Hainich et al. (2020) in Astronomy & Astrophysics. We were featured on FrontPage twice (Dec. 2, 2014, and Mar. 3, 2020).

Zachary Jordan, Eric Frechette, Brenton Jackson, and Ryan Agnew, all physics majors, assisted me during 2014–2017 by rewriting my statistical analysis code in a language that allows us to perform large numbers of calculations more efficiently. In October 2021, we published an article that describes how our statistical technique, when applied to the HMXBs of the SMC, can reveal important clues about the life cycle of massive stars, e.g., how old these objects are and how fast they move, and how these parameters are influenced by the chemical conditions of their host galaxy. Those four students are co-authors of Bodaghee et al. (2021) in the Astrophysical Journal, whose author list also includes senior research scientists and professors from Harvard, UC Berkeley, and NASA, as well as international collaborators.

For the past year, a physics major named Cody Cox has taken our statistical analysis code and applied it to HMXBs in the Milky Way. To do this, Cody wrote a script that scours the NASA archives to collect the relevant data that we need like coordinates and distances to HMXBs. The script outputs a Wikipedia page listing the parameters of all known HMXBs (FrontPage: Aug. 23, 2021). This Wiki page is a valuable tool for the astrophysics community, so Cody will present a poster at the March 2022 meeting of the High-Energy Astrophysics Division of the American Astronomical Society in Pittsburgh, PA.

The best part of teaching through research at Georgia College is the ability to interact with these extraordinary students; first in the classroom, then in the laboratory. There is the additional pride of seeing Georgia College students listed in the author list among scientists from prestigious research institutions. While we are a public liberal arts university, it's clear that these students are playing in the "big leagues" of research and are already making a lasting impact on the field.

Exploring the MeV Sky with a Combined Coded Mask and Compton Telescope: The Galactic Explorer with a Coded Aperture Mask Compton Telescope (GECCO)

Elena Orlando[a,b], Eugenio Bottacini[c,d], Alexander Moiseev[e,f,g], Arash Bodaghee[h], Werner Collmar[i], Torsten Enßlin[j], Igor V. Moskalenko[b], Michela Negro[e,f,g], Stefano Profumo[k], Matthew G. Baring[l], Aleksey Bolotnikov[m], Nicholas Cannady[e,f,g], Gabriella A. Carini[m], Seth Digel[n], Isabelle A. Grenier[o], Alice K. Harding[p], Dieter Hartmann[q], Sven Herrmann[m], Matthew Kerr[w], Roman Krivonos[r], Philippe Laurent[s], Francesco Longo[a], Aldo Morselli[t], Makoto Sasaki[e,f,g], Peter Shawhan[e], Gerry Skinner[u], Lucas D. Smith[e,f,g], Floyd W. Stecker[f], Andrew Strong[i], Steven Sturner[e,f,g], David J. Thompson[f], John A. Tomsick[v], Zorawar Wadiasingh[e,f,g], Richard S. Woolf[w], Eric Yates[e], Andreas Zoglauer[v]

[a]University of Trieste and INFN, Trieste, via Valerio 2, I-34127 Trieste, Italy
[b]Hansen Experimental Physics Laboratory and Kavli Institute for Particle Astrophysics and Cosmology, Stanford University, Stanford, CA 94305, USA
[c]Dipartimento di Fisica e Astronomia G. Galilei, Univeristà di Padova, Padova, Italy
[d]Eureka Scientific, 2452 Delmer Street Suite 100, Oakland, CA 94602-3017, USA
[e]University of Maryland, Baltimore County, Baltimore, MD 21250, USA
[f]NASA Goddard Space Flight Center, Greenbelt, MD 20771, USA
[g]Center for Research and Exploration in Space Science and Technology, NASA/GSFC, Greenbelt, MD 20771, USA
[h]Dept. of Chemistry, Physics and Astronomy, Georgia College and State University, Milledgeville, GA 31061, USA
[i]Max-Planck-Institut für extraterrestrische Physik, Postfach 1312, 85741 Garching, Germany
[j]Max Planck Institute for Astrophysics, Karl-Schwarzschild-Str. 1, 85748 Garching, Germany
[k]Department of Physics, University of California, Santa Cruz, and Santa Cruz Institute for Particle Physics, 1156 High Street, Santa Cruz, CA 95064, USA
[l]Rice University, Houston, TX 77005, USA
[m]Brookhaven National Laboratory, Upton, NY11973,USA
[n]SLAC, 2575 Sand Hill Road, Menlo Park, CA 94025
[o]Université de Paris and Université Paris Saclay, CEA, CNRS, AIM, F-91190 Gif-sur-Yvette, France
[p]Los Alamos National Laboratory, Los Alamos, NM 87545
[q]Department of Physics and Astronomy, Clemson University, Clemson, SC 29634-0978, USA
[r]Space Research Institute (IKI), Profsoyuznaya 84/32, Moscow 117997, Russia
[s]CEA/DRF/IRFU/DAP, CEA Saclay, 91191 Gif sur Yvette Cedex, France
[t]INFN Roma Tor Vergata
[u]Honorary Research Fellow, School of Physics and Astronomy, University of Birmingham, UK
[v]Space Sciences Laboratory, University of California, Berkeley, CA 94720-7450, USA
[w]Space Science Division, U.S. Naval Research Laboratory, Washington, DC 20375, USA

Abstract

The sky at MeV energies is currently poorly explored. Here we present an innovative mission concept and we outline the scientific motivation for combining a coded mask and a Compton telescope.

The Galactic Explorer with a Coded Aperture Mask Compton Telescope (GECCO) is a novel concept for a next-generation telescope covering hard X-ray and soft gamma-ray energies. The potential and importance of this approach that will bridge the observational gap in the MeV energy range are presented. With the unprecedented angular resolution of the coded mask telescope combined with the sensitive Compton telescope, a mission such as GECCO will finally disentangle the discrete sources from the truly diffuse emission, unveiling the origin of the gamma-ray Galactic center excess and the Fermi Bubbles, and uncovering properties of low-energy cosmic rays, and their propagation in the Galaxy. Individual Galactic and extragalactic sources will be detected, which will also allow studies of source populations. Nuclear and annihilation lines will be spatially and spectrally resolved from the continuum emission and from sources, addressing the role of low-energy cosmic rays in star formation and galaxy evolution, the origin of the 511 keV positron line, fundamental physics, and the chemical enrichment in the Galaxy. It will also detect explosive transient gamma-ray sources, which will enable identifying and studying the astrophysical objects that produce gravitational waves and neutrinos in a multi-messenger context. A GECCO mission will provide essential contributions to the areas "New Messengers and New Physics" and "Unveiling the Drivers of Galaxy Growth" emphasized in the Decadal Report on Astronomy and Astrophysics 2020.

Keywords: X-Rays, Gamma Rays, Galactic Sources, Extragalactic sources, Low-Energy Cosmic Rays, Diffuse Emissions, Galactic Center, Fermi Bubbles, Gamma-Ray Bursts, 511 keV line, gamma-ray lines, dark matter

1. Introduction

At hard X-ray energies the sky has been observed by the coded mask instruments on board the INTErnational Gamma-Ray Astrophysics Laboratory (INTEGRAL) [52] for more than 15 years. On the contrary the sky at MeV energies currently remains poorly explored. Indeed, since the era of the Imaging Compton Telescope (COMPTEL) [37] on board the Compton Gamma Ray Observatory, operating from 1991 to 2000, the sky above a few MeV has been almost unexplored. As a consequence, at MeV energies there is a huge observational gap between X-rays and gamma rays. Many MeV Compton missions have been proposed in recent years (e.g., MEGA [6], GRIPS [19], AMEGO [22], AMEGO-X [17], e-Astrogam [12], but none has been definitively planned to operate, except for COSI [45, 46] that has been selected to fly in 2025. The science drivers of the cited proposed missions span Galactic sources, extragalactic objects, transients, dark matter, cosmic rays (CRs), diffuse continuum emission, and nucleosynthesis of elements.

The aim of this work is to outline the scientific opportunities for studies in the MeV energy range with the mission concept for a mid-size Galactic Explorer with a Coded Aperture Mask Compton Telescope (GECCO) or with a GECCO-like mission. A GECCO mission has the potential to answer open questions and will have great discovery potential. Among the most recently recognized science drivers, sensitive observations of the sky at MeV energies with unprecedented high resolution can open a new window to understand complicated regions such as the Galactic center, the origin of the Fermi Bubbles, the origin of the 511 keV line, possible Galactic winds, the mechanisms of propagation for low-energy cosmic rays, their sources and their role in Galactic evolution. It can also support multimessenger astrophysics by observing transients.

We briefly introduce the GECCO mission in Section 2, while in the following sections we discuss the possible analysis methods to disentangle the sources from the diffuse emission. Then, we present the specific topics that a GECCO mission will be able to address: the separation between sources and truly diffuse emission that will allow us to finally shed light on the Galactic center gamma-ray excess, the dark matter, the Fermi Bubbles, and the 511 keV line. The potential for study of large-scale diffuse interstellar emission with the related CRs and nucleosynthesis lines will be presented. Finally, what can be learned about classes of Galactic and extragalactic sources will be briefly discussed, together with the multimessenger connection between gamma-ray bursts and gravitational waves, and between neutrinos and cosmic rays.

2. GECCO instrument description

GECCO [23] is a innovative combination of a Compton telescope with a coded aperture mask to provide sensitive high-accuracy measurements of cosmic photons in the 50 keV to 10 MeV energy range. A rendering is shown in Fig. 1. The Compton telescope measures the detected photon energy and reconstructs a cone, or an event circle, of its arrival direction by analysis of the event pattern in the CdZnTe Imaging calorimeter (IC), as illustrated in Fig. 2. A classic example of such a space-borne telescope was COMPTEL onboard NASA's Compton Gamma-Ray Observatory (CGRO), which operated in orbit from 1991 to 2000, providing fundamental astrophysical results [37]. Usually, a Compton telescope consists of two separate detectors, with the first photon interaction occurring in the "upper" one, and the second in the "lower" one, as in COMPTEL cited above. For the correct event reconstruction, it is necessary to identify a sequence or order of interactions. This can be achieved by using the time-delay between the two interactions, requiring a certain minimum spacing between the detectors, which reduces the instrument aperture and detection efficiency. In GECCO approach, both interactions occur in one finely segmented IC with high 3D position resolution. The GECCO Compton telescope provides a per-photon angular resolution of a few degrees and $1 - 2\%$ energy resolution, with a large 60 x 60 degree field-of-view, and it measures diffuse gamma-radiation.

The angular resolution of a Compton telescope has an intrinsic limit of an order of one degree (depending on the scattering material and incident photon energy) due to Doppler broadening of the incident photon direction induced by the velocity of the electron where the Compton scattering occurred. Utilization of a coded aperture mask technique allows the instrument to reach arcmin and better resolution. In this technique an array of opaque and transparent elements, called a coded aperture mask, is placed in the instrument aperture. Incident photon flux creates a shadowgram of the mask in the detector, and the incident photon flux direction is reconstructed by cross-correlating of the shadowgram and the mask pattern [161, 120]. The angular resolution of such a system is approximately equal to the ratio of the mask element size to the distance between the mask and the detector.

In GECCO, the mask mode with its excellent angular resolution of ~arcmin but relatively small field-of-view of 4 x 4 degrees provides a good complement to the measurements made by a Compton telescope (Fig. 3). The performance of a coded mask instrument, in particular its signal-to-noise ratio, can be strongly impacted by backgrounds of all natures. For GECCO the impact is reduced by protecting the instrument aperture by a thick radiation-absorbing shield.

The angular resolution for a coded mask instrument can potentially be as good as desired, depending on the distance between the coded mask and the focal plane detector. This distance is constrained by available space, usually limited by the launcher shroud dimensions. An attractive option to increase the distance between the mask and the detector is to deploy the coded mask after reaching orbit. However, in this configuration the instrument aperture will be exposed to side-entering background radiation, which deteriorates performance. GECCO has a coded mask deployable to 20 meters and reduces the problem of side-entering background by selecting the events whose Compton-reconstructed direction points to the coded mask lo-

Email addresses: orlandele@gmail.com (Elena Orlando),
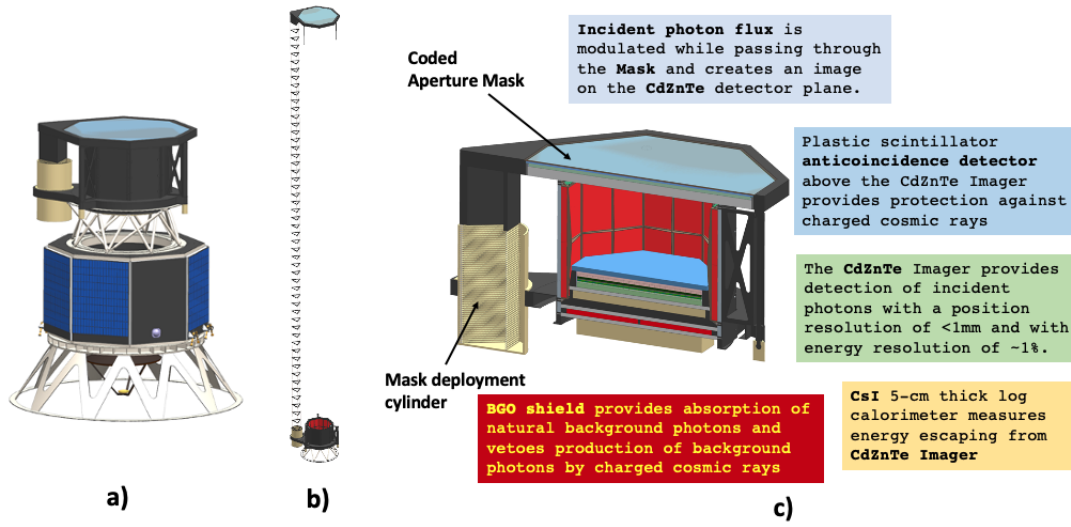eugenio.bottacini@unipd.it (Eugenio Bottacini)

Figure 1: GECCO conceptual design: a) GECCO with Mask in stowed position and notional spacecraft bus, b) GECCO with Mask in deployed position, c) GECCO, cutaway

cation. This is a unique feature of GECCO, which greatly improves its angular resolution while maintaining a high signal-to-noise ratio.
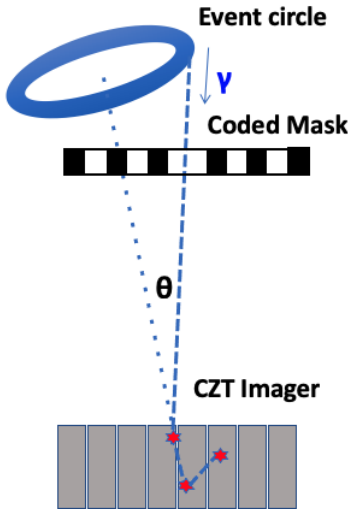

Figure 2: Diagram of photon detection by the CZT Imaging Calorimeter. Red stars show the points of photon interactions in the detector.

The expected performance of GECCO is the following: 50 keV−10 MeV energy range, with energy resolution of $< 1\%$ from $0.5-5$ MeV. In the mask mode the angular resolution is ~1 arcmin with $3°-4°$ field-of-view, while in the Compton mode the angular resolution is $3°-5°$ with $60°$ field-of-view. The sensitivity is expected to be $10^{-5}-10^{-6}$ MeV cm^{-2}s^{-1} over the en-

tire energy range.

In operation, GECCO will be able to make either scanning observations, e.g., of the Galactic plane, or pointed observations, e.g., of the Galactic center or to follow up bright transient events.
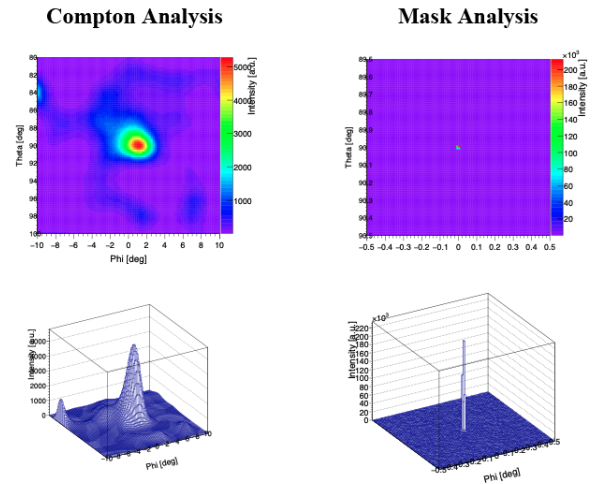

Figure 3: Left - Point source detection with Compton analysis (field-of-view ~ $60°$), right - the same source detected with Coded Aperture imaging with field-of-view $4°$

2.1. GECCO components

GECCO is octagonal with a medium diagonal of 92cm (Fig. 1). Such a shape provides better operation of the coded mask instrument when compared to a rectangular shape. GECCO has five main subsystems:: the IC is a key detector of GECCO, providing detection of incident photons with a 3D position resolution of < 1 mm and with energy resolution of $\sim 1\%$. It has

3

a modular structure and is based on the Virtual Frisch-grid drift CdZnTe bars approach [162]. The CsI log calorimeter (LC), situated below the IC, detects energy leaking from the Imager and measures the position of that energy deposition. It is especially important to catch escaping 511 keV annihilation photons. The LC is built from 20 - 30 cm long CsI(Tl) logs with a 1.5 cm × 1.5 cm cross section, viewed from both sides by SiPMs, a design largely inherited from Fermi-LAT. The sum of the signals from both ends provides the energy measure, and their ratio gives the centroid for the energy deposition in the log. The LC has for layers of logs, with orthogonal alignment on alternate layers. The 5-mm thick plastic scintillator antico-incidence detector (ACD) is positioned on the top of the IC to veto charged cosmic rays from triggering the instrument, which are 3-4 orders of magnitude more abundant than photons. It is read out by SiPMs from its edges. The stack of IC, LC and ACD is surrounded on all 8 sides and on the bottom by a 4-cm thick BGO scintillator shield. This shield absorbs the majority of side-entering photons, especially from the bright Earth limb, and also creates a veto signal for side-entering charged cosmic rays. Additionally, the BGO panels serve as a powerful gamma-ray burst (GRB) detector with a few degrees accuracy for GRB localization. The Coded Aperture Mask (CAM), covered on top by a 5-mm thick plastic scintillator detector with SiPM read-outs, sits directly on top of the BGO octagon. The CAM is equipped with a Canister-deployed Coilable Mast, which allows the CAM to be deployed to any selected distance up to 20 meters from the instrument and can be retracted back when needed. GECCO is triggered by the IC with adjustable thresholds as low as 20 keV, with included veto signals from the ACD and BGO shields. The BGO panels can also be read out separately to detect GRBs.

3. Point sources and diffuse: coded-mask vs Compton

3.1. Coded-mask mode and the INTEGRAL heritage

For coded-mask imaging systems an astrophysical source illuminates the coded mask that casts a shadowgram onto the pixel detector. Ideally, this shadowgram is unique allowing for the reconstruction of the incidence direction of each source on the sky. This implies two fundamental requirements for coded-mask telescopes: 1) the geometric arrangement of the mask must be such that for different incidence directions the shadowgram can be uniquely identified; 2) the detector plane must be position-sensitive to actually be able to register a shadowgram. Such an imaging technology has been successfully used by instruments on board the GRANAT, BeppoSAX, INTEGRAL, and Swift missions. Basic introductions to this imaging technique can be found in [120] and in [123]. Unlike in a conventional imaging systems, in which the recorded image is readily apparent due to the photon counts in the pixel detector, in coded-mask systems the sky image S is encoded through the mask M (a matrix of opaque and transparent elements to the radiation) in the pixel detector D. Very importantly the latter contains also an unmodulated background term B, which is due to the large collecting area. Since this latter term largely

affects the noise, it enters the determination of the detection significance (signal-to-noise ratio) of astrophysical sources for background-dominated instruments. For a more precise matrix notation:

$$D = M \circledast S + B \qquad (1)$$

where the convolution ($\circledast$) of two generic matrices X and Y can be written as:

$$(X \circledast Y)_{i,j} = \sum_k \sum_l X_{k,l} \, Y_{(i+k),(j+l)} \qquad (2)$$

To reconstruct the sky image S′ a decoding function G is needed such that:

$$S' = G \circledast D = G \circledast (M \circledast S) + G \circledast B \qquad (3)$$

Ideally, for a perfect imaging system S′ = S. Therefore, according to the equation above the decoding function G must be such that (G $\circledast$ M) = δ-function and simultaneously (G $\circledast$ B) $\simeq$ 0, which in actual practice is difficult to achieve [122]. To improve the deconvolution results, very accurate ground-based and in-flight background modeling is needed. The in-flight background modeling will be an important task for a GECCO mission.

Crucial to the performance of a coded-mask imaging system is the significance at which an astrophysical source can be detected above the background. Given that roughly half of the incident photons from astrophysical sources are blocked by the mask, the detection of sources is in any case more difficult than without the mask. Yet, the actors at play are rather well defined. Thus, the significance depends on the decoding (shown above), on the open fraction ρ of the mask pattern, on the astrophysical background B and the detector background b, on the intensity of the source S_1 (that is being considered for detection), and on the remaining number n of astrophysical sources S_i in the field of view as they illuminate the detector plane. The flux contribution of these sources acts as a background term for the source S_1 which is to be detected. Therefore, it is important to account for the contribution of these sources, especially in crowded sky areas (e.g. Galactic plane) where several sources can be found in the detector's field of view. These sources can also be variable. The contribution by these sources to the to the overall background can be accounted for by iteratively subtracting the modeled shadowgram of each source $S_{i \neq 1}$ in the field of view, which is cast onto the detector as shown for Swift/BAT and INTEGRAL/IBIS [119]. This allows also to naturally account for the variability of the sources when mosaicking observations for monitoring or survey purposes. The signal-to-noise ratio $\frac{S}{N}$ for a source with a δ-function PSF is given by [121]:

$$\frac{S}{N} = \frac{S_1}{\sqrt{\frac{S_1 + b}{\rho} + \mathcal{B}}} \qquad (4)$$

where

$$\mathcal{B} = \frac{B + \sum_{i \neq 1}^{n} S_i + b}{1 - \rho} \qquad (5)$$

4

3.2. Compton mode and the COMPTEL heritage

The Compton telescope COMPTEL (1991-2000) on CGRO was the first and up to now the only Compton telescope in space. It covered the energy range 0.75 to 30 MeV, a region hardly explored in astrophysics. Because no successor is in space yet, the COMPTEL data are still the main astrophysical resources in this MeV gamma-ray range.

3.2.1. Instrument and data analysis

COMPTEL was a double Compton-scatter telescope without event tracking (Fig. 4). It consisted of two layers of detectors, in which an incident gamma-ray was first Compton-scattered in a detector of the upper detector array (D1) and – in the positive case – then was absorbed in a detector module of the lower detector array (D2). In order to reduce background, COMPTEL had 1) an anti-coincidence shield, triggering on charged particles, 2) a time–of–flight (ToF) measurement between D1 and D2 and 3) pulse-shape discrimination (PSD) on the event triggers in D1, thereby discriminating between photons and particles. COMPTEL was sensitive to photons at soft MeV energies, i.e. 0.75 – 30 MeV, with an energy-dependent energy and angular resolution of 5 - 8 % (FWHM) and 1.7° – 4.4° (FWHM), respectively. It had a large field of view of ~1 sr and could detect gamma-ray sources with a positional accuracy of 1°–2°, depending on source flux [137]. COMPTEL, being a "first-generation" instrument, suffered from a high instrumental background. At an altitude of ~450 km CGRO and its instruments were exposed to a continuous bombardment by cosmic rays as well as to geomagnetically trapped particles along its near-Earth orbit, which - despite the applied background reduction techniques - generated via various channels on the whole CGRO satellite as well as inside and around COMPTEL a multitude of secondary particles and gamma-ray photons mimicking proper celestial MeV photons. These instrumental background photons outnumbered by far the astrophysical celestial photons, leading to low detection significances of MeV gamma-ray sources, and in turn to the high sensitivity limits of COMPTEL. The COMPTEL data analysis is usually done in a so-called three-dimensional data space, consisting of the scattered photon directions as x, y coordinates with the calculated scatter angle as z coordinate. These three quantities define a cone-shape point-source response in such a data space. Analyses and imaging methods, e.g. maximum entropy and maximum likelihood, had been developed in order to analyze such a data space with respect to source parameters (detection significances, fluxes, flux errors) and the generation of sky images. The analyses were carried out in individual energy bands, mainly the four standard bands (0.75–1, 1–3, 3–10, 10–30 MeV). Due to instrumental background constraints as well as mission constraints, revised, i.e. new standard, energy bands are preferably applied recently: 0.9–1.7. 1.7–4.3, 4.3–9.0, 9.0–30 MeV [142]. In order to use the ToF and PSD measurements for background reduction, optimized event selections for ToF and PSD were generated by maximizing for each energy interval the detection significance of the Crab, the strongest
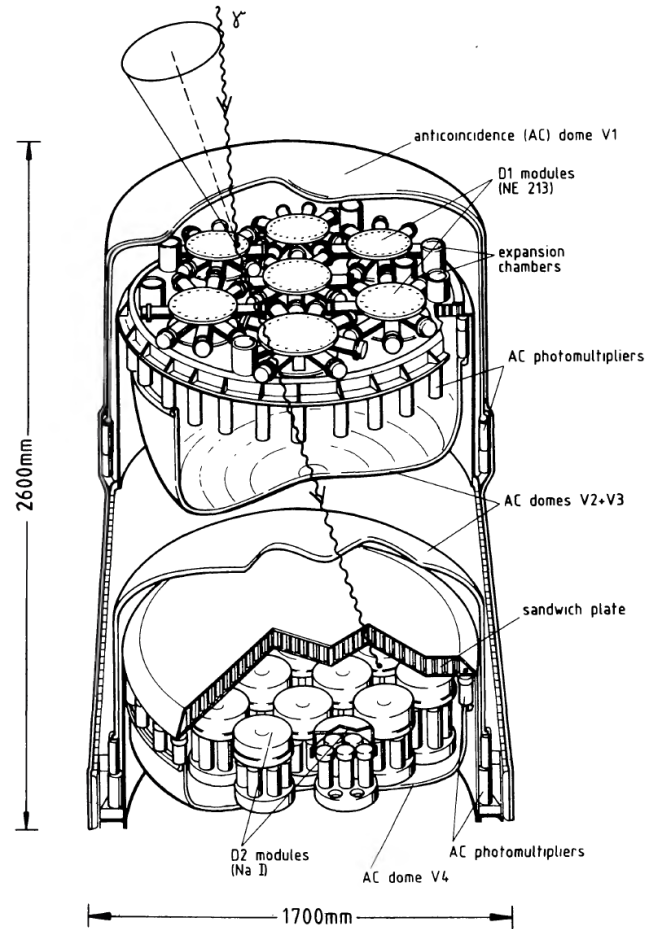

Figure 4: A sketch of the COMPTEL instrument (from [137]), showing the two layers of detectors as well as the detection principle of a photon in Compton mode.

COMPTEL MeV source, throughout the ToF and PSD parameter space. Point-source responses were generated accordingly.

3.2.2. Imaging

Imaging is challenging because only the scattered photon direction and energy deposit in D1, D2 are measured, so incoming photon directions are just constrained to circles on the sky via the Compton scattering formula; in fact these are annuli due to the measurement uncertainties. One method used with success is maximum entropy imaging (MEM) which is in fact well suited for such problems where image and data space are quite separate [141]. Another imaging method used in the COMPTEL data analysis is the maximum-likelihood method (MLM) [135], which is usually applied to derive source parameters like detection significances, fluxes and fluxe errors by a combined model fit of a background model and various source and/or diffuse emission models. While the MEM approach, generating intensity maps, is superior in the overall imaging of the MeV sky, the MLM approach, generating flux and significance maps, is superior in the quantitative analysis of point sources. Recently the MEM approach was updated for 1) modern methods

of a fast convolution-on-the-sphere and 2) the HEALPix[1] [136] all-sky equal-area pixelization concept in order to generate all-sky images much faster and with finer angular resolution [142]. An example of a recent all-sky all-mission map in the 9-30 MeV band is shown in Fig. 5.
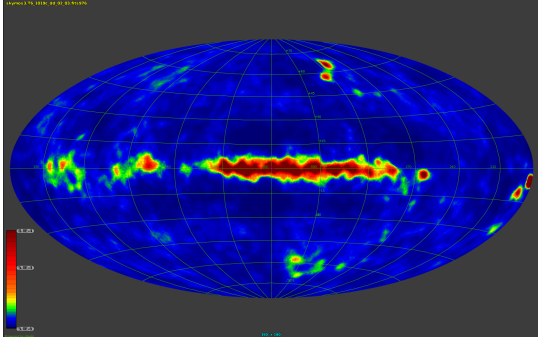

Figure 5: COMPTEL all-sky all-mission intensity map in the 9-30 MeV range, using the updated maximum-entropy method. Evidence for several Galactic and extragalactic point sources as well as Galactic diffuse emission is clearly visible.

3.2.3. COMPTEL science heritage

COMPTEL opened the soft MeV gamma-ray band (0.75-30 MeV) as a new astronomical window, thereby bridging the gap between hard X-rays and medium energy gamma-rays (>100 MeV). The first COMPTEL source catalog [138], mainly a summary of published results of the first 5.5 years of the mission, reports 32 sources ($> 3\sigma$) of various types, such as AGN, spin-down pulsars, gamma-ray binaries, gamma-ray line sources and extended emission regions. AGN, in particular blazars, are the majority of the COMPTEL point sources. Recent analyses, using data of the full COMPTEL mission and the newest analysis techniques, enlarge this number of point sources by typically a factor of 1.5 [134].

The Galactic diffuse emission in the COMPTEL band was studied as well [140, 139], resulting for the inner galaxy in a spectrum which is dominated below 10 MeV by inverse-Compton emission and above 10 MeV by a combination of inverse-Compton and bremsstrahlung emission.

3.3. Separating point sources from diffuse emission

The separation of point sources from diffuse emission is a common problem in astronomical imaging, and a large number of approaches have been developed to deal with it [88, 89, 90, 91]. Due to the sophysticated instrument response of GECCO it is worth thinking through this problem from the very beginning. We will see that this leads naturally to information field theory (IFT) [92, 93, 94], a probabilistic description of the problem involving field-like quantities. A good part of the existing approaches can then be understood as different (approximate)

solutions to the sky brightness field inference problem, based on a number of differing prior assumptions.

We start this discussion with generic considerations about the separation of point sources from diffuse emission, before we discuss GECCO-specific particularities.

3.3.1. Generic considerations

The diffuse gamma ray flux is dominated by the emission from the Milky Way. Thanks to our position within the Galaxy, the flux reaches us from all directions, but with a clear preference for directions in the Galactic plane. Point sources can in principle appear at any sky location and in nearly any intensity. The separation of the point source and diffuse flux sky contributions therefore requires the reconstruction of two sky images, one for each of these components. Let us call them p and q, respectively, so that the total sky flux $f = (f_x)_{x \in sky}$ as a function of the sky position x is $f_x = p_x + q_x$.

Even with a perfect instrument, which would map the sky brightness completely, noiselessly, and with arbitrary resolution, the separation of one observed sky brightness distribution into two is an challenging task, as each of those could explain the full data. The separation is nevertheless meaningful, as the idealized concepts of point sources and diffuse emission capture coarsely relevant physical concepts. Point sources are very localized compact objects and diffuse emission results from interstellar processes.

In order to achieve such a separation the concepts of point sources and diffuse emission have to be used as discriminating criteria. Doing so may require a probabilistic or Bayesian perspective on the problem, as this provides a natural framework for incorporating prior knowledge. In this section we describe this approach.

A description of the measurement process in terms of a likelihood $\mathcal{P}(d|f)$ is necessary, incorporating the signal response consisting of point-spread and energy dispersion functions as well as the Poisson statistics of the shot noise. Here, d denotes the data. In addition to this, priors for the sky brightness distributions of the two components $\mathcal{P}(p)$ and $\mathcal{P}(q)$ are required as well. These should encode our knowledge of the sky before measurement, but only in a generic way, so as not to determine our scientific results beyond the introduction of the two components mentioned above.

For the point source sky, a model as described below might be considered. As point sources could be anywhere, and these are largely uncorrelated (despite some preference to appear in the Galactic plane for Galactic sources) a pixelized sky map with a sufficiently high resolution should represent the point source sky, with a potential point source at each pixel location, and their fluxes being a priori uncorrelated with each other. The absence of a point source would then simply be represented by a vanishing flux at the corresponding location. With p_x being the point source flux at pixel x, the prior for the point source sky would be separable into individual single point source flux priors $\mathcal{P}(p_x)$,

$$\mathcal{P}(p) = \prod_{x \in sky} \mathcal{P}(p_x). \tag{6}$$

As a priori no location should be singled out, $\mathcal{P}(p_x)$ is to be taken the same for all locations and encodes the point source brightness distribution function. This function is either postulated, e.g. a power law with high and low brightness cut offs, or better, inferred together with the point sources. For the latter option, hyper-priors that encode natural assumptions on $\mathcal{P}(p_x)$ have to be formulated, for example that it is a strictly positive, preferentially smooth function, with a preference for power-law like slopes. All this can easily done within the language of IFT. This point source prior, a power-law-like falling brightness function $\mathcal{P}(p_x)$ for high flux values p_x, can be regarded as a sparseness enforcing prior, as it will prefer that some flux within a resolution element of the instrument is represented by a single bright source over the possibility of an ensemble of dim sources, which share the observed flux in similar parts.[2]

For the diffuse emission prior, a number of plausible assumptions are possible. Here, a minimalist choice should be discussed. Diffuse emission is characterized by exhibiting a more or less smooth sky brightness distribution $q = (q)_{x \in \text{sky}}$. This means that the sky flux does in general not change erratically from one location to the next, as the point source sky flux does, but that it is spatially correlated. It can, however, vary largely from one area to the next, with brightness differences by orders of magnitude, but always being positive. A minimalist model (or maximum entropy model) incorporating these assumptions is that of a log-normal model, in which a Gaussian process determines the log-brightness of the diffuse sky $s = (s_x)_{x \in \text{sky}} := (\ln q_x)_{x \in \text{sky}}$, with

$$\mathcal{P}(s) = \mathcal{N}(s|\bar{s}, S) = \frac{1}{\sqrt{2\pi S}} \exp\left(\frac{1}{2}(s - \bar{s})^\dagger S^{-1}(s - \bar{s})\right) \quad (7)$$

where $\bar{s}$ is the average log-sky brightness and $S = (S_{xy})_{x,y \in \text{sky}}$ the two-point correlation structure of s. As both are unknown a priori, they might be inferred as well. This is possible, if we restore to the a priori assumption that no location on the sky is singled out and therefore $S_{xy} = C_s(x - y)$ should be a function only of the distance between x and y. Then we seek only a one dimensional function $C_s(r)$ and this can be easily done with the instruments of IFT.

This prior for diffuse flux can be regarded as a generalization for many Tikhonov regularization schemes, which are based on quadratic functionals of the regularized quantity, here s. It does not, however, enclose so called *Maximum entropy priors*, as these can be shown to be separable w.r.t. the sky position, i.e. to be of the structure of our point source prior (Eq. 6), just with a very peculiar assumed luminosity function [102, B.6]. Furthermore, we note that the assumption of Gaussianity is not necessarily the only possible one.

The (Gaussian process or other) prior for s specifies $P(q) = P(s=\ln q) \|\partial s/\partial q\|$ and these or similar assumptions specify the

full Bayesian model, as the probability for all sky components and data realizations can now be specified,

$$\mathcal{P}(d, p, q) = \mathcal{P}(d|f = p + q) \mathcal{P}(p) \mathcal{P}(q). \quad (8)$$

From this, the posterior probability

$$\mathcal{P}(p, q|d) = \frac{\mathcal{P}(d, p, q)}{\mathcal{P}(d)} \quad (9)$$

allows us to make statements about the most probable sky flux distributions (the maximum a postiori estimator), their posteriori means and uncertainty dispersion. The numerical infrastructure to perform these calculations at least approximately is already in place [95, 96, 97] and has been used to develop a point source separating imaging algorithm incorporating the above described priors [98]. This was even extended into the spectral domain [99], and successfully applied to data [100, 101].

3.3.2. GECCO specific considerations

The particularities of the GECCO instrument enter the above discussion via the likelihood function $\mathcal{P}(d|f)$. This is key to inferring the possible locations from which an observed photon might have come. GECCO offers two constraints on this, one via the Compton measurement and one via the coded mask. Both restrict the sky area for possible photon origins, and the more they do so, individually or jointly, the better the imaging and the separation of point sources from diffuse flux will be.

The implementation of the likelihood may require some technical developments as well. The reason for this is that the data space is six dimensional, with two photon interaction points and two energy depositions. The instrument response function is therefore a mapping from a three dimensional emission field (as a function of sky position and photon energy) into a six dimensional data space. Fast implementations of this mapping, as well as its adjoint operation, the back-projection of data space locations to possible signal space locations an observed photon could have originated from, will be required for high-performance, high-resolution imaging. These will probably be based on machine learning technologies, and exploratory studies in this direction are under way.

4. Science drivers for a GECCO mission

4.1. Interstellar Emission and cosmic rays

The gamma-ray interstellar emission is produced by interactions of Galactic CRs with gas and photons as CRs propagate from their sources throughout the Galaxy. Observations to date by the Fermi LAT, INTEGRAL, and COMPTEL underline some discrepancies with present interstellar models, leaving open questions on the large-scale distribution of CR sources, on CR transport mechanisms in the Galaxy, and on their density and spectral variation over the Galaxy (see e.g. [1, 29, 38, 20, 13] and reference therein). Moreover, Galactic CRs with energies below a few GeV/nucleon and their associated gamma-ray emission are barely addressed with present telescopes. These low-energy CRs contain the majority of the

---

[2]The reason for this is that with a power-law-like single source flux prior, the decrease in prior probability by brightening a pixel by some factor can be compensated by making a dim pixel within the same resolution element dimmer by the same factor. The total flux within the resolution element, however, increases by this operation. Thus, explaining the observed flux in a resolution element with only a single pixel strongly excited is preferred, leading to the mentioned sparseness enforcement.

energy density of the CRs. They are the main source of ionization, which affects star formation, and they provide pressure gradients to support large-scale outflows and Galactic winds, which affect the evolution of the Galaxy. A GECCO mission will assess for the first time this low-energy CR population. In particular, for the first time it will provide observations of CR electrons and positrons distributions across the Galaxy, allowing separate determination of CR leptons from hadrons. This is possible thanks to the capability of observing the inverse Compton emission component, which is related to CR electors and the Galactic photons. These data together with observations of the large-scale synchrotron emission will also permit the Galactic magnetic field distribution to be assessed. A GECCO mission will also provide the first nuclear spectroscopic observation of the low-energy CRs, allowing the study for the first time of spectra, composition, and distribution of low-energy CR nuclei across the Galaxy. The focus of this section is the large-scale continuum emission and the de-excitation nuclear lines.

The science case in this section clearly aligns with the Decadal Report on Astronomy and Astrophysics 2020 (Astro2020) [11] priority area "Unveiling the Drivers of Galaxy Growth" because a GECCO mission will be able to finally revolutionize our understanding of the relation between CR, their ionization of gas, and the magnetic field that impact the formation of stars and the evolution of galaxies.

4.1.1. Continuum emission

The large-scale continuum interstellar emission in gamma rays is produced by CRs interacting with the interstellar medium, interstellar photons, and the CMB, the cosmic microwave background. The hadronic gas-related pion-decay emission is the major interstellar component at GeV energies, while below 100 MeV most of the emission comes from inverse-Compton scattering and from Bremsstrahlung due to CR electrons [29, 39]. Observations of the large-scale Galactic gamma-ray interstellar emission from 50 keV to 10 MeV provide insights on CR sources, electron spectra, density, distribution, propagation properties, and the CR interplay with the magnetic field across the Galaxy. Indeed, below 10 MeV the continuum interstellar gamma rays are almost totally produced by low-energy CRs inverse-Compton scattering on Galactic photons (infrared, optical, and the CMB) [29, 34].

A recent work [29] has compared the expected interstellar emission by inverse Compton with data of the diffuse emission at X-ray and soft gamma-ray energies. Details on the inverse Compton interstellar models for that work are as follows. Propagation parameters were defined in such a way that the modeled local interstellar CR spectra and abundances reproduced the latest precise CR measurements by AMS02 [5] and Voyager I [10] after propagation. CR electrons and secondary positrons were also constrained by local gamma-ray data and especially by synchrotron data in radio and microwaves (note that the same CR electrons and positron that generate the inverse Compton emission also produce interstellar synchrotron emission by spiralling in the Galactic magnetic field).

The CR propagation was calculated with the GALPROP

code[3] [e.g. 26, 25, 42, 21] accounting for the recent extension of the code to synchrotron emission and 3D models of the magnetic field [40, 30] (for the effect of the 3D model of the magnetic field on the inverse Compton spatial distribution see [27]). Details on the data in [29] are as follows. Data were taken by INTEGRAL [52] with its coded-mask telescope SPI, the SPectrometer for INTEGRAL [51]. A detailed study by [8] provided spectral data of the Galactic diffuse emission for energies between ~80 keV and ~2 MeV from 2003 to 2009 for the inner Galaxy region. For the same sky region intensity data at somewhat higher energies (1–30 MeV) were provided by [43] from COMPTEL in three energy bands: 1 – 3 MeV, 3 – 10 MeV, and 10 – 30 MeV. SPI and COMPTEL data were both cleaned by subtracting the sources [43, 8]. The conclusion of [29] was that the best model described above underestimates the X-ray emission in the inner Galaxy. The same authors suggest that SPI and COMPTEL diffuse data in the inner Galaxy region may be affected by contamination from unresolved sources (due to the well-known limited sensitivity and angular resolution of the instruments). Such a possible contaminating source population in the SPI and COMPTEL energy band could be the soft gamma-ray pulsars that were found to have hard power-law spectra in the hard X-ray band and reach maximum luminosity typically in the MeV range [16].

A GECCO mission will be able to detect these potential sources and definitively disentangle the true diffuse emission from possible unresolved sources. This will also enable study of low-energy CRs that are thought to be a fundamental component of the interstellar medium, but whose composition, distribution, and flux are poorly known. Observations at soft gamma-ray energies and below would shed light on the large-scale distribution of CR sources, on CR transport mechanisms in the Galaxy, and on their density and spectral variation over the Galaxy (see e.g. [38, 28]). Observations at soft-gamma rays would also provide information about the interplay of low-energy CRs with Galactic winds and on the role of low-energy CRs on Galaxy evolution. The connection between low-energy CRs below a few GeV/nuc and galaxy evolution has started to be investigated only recently and is still poorly understood (e.g. [14, 32, 31, 15, 18, 36, 33]). Even more specifically, a GECCO mission for the first time will allow observations of the emissions from CR electrons clearly separated by the emission from CR nuclei. It will reveal the spatial and spectral distributions of the inverse Compton emission in the Galaxy [29], important for disentangling emission not only from unresolved sources (e.g. [41]), but also from the extragalactic diffuse gamma-ray background (e.g. [3]), or from potential signals of dark matter annihilation (e.g. [4]), which have distributions similar to the inverse Compton component. Such observations also allow inferences about the distribution of CR electrons, which best sample CR inhomogeneity, because they are affected by energy losses more strongly than nuclei, and they remain much closer to their sources. Moreover, observations of gamma rays below 10 MeV produced by the same electrons that produce

---

[3]http://galprop.stanford.edu/

synchrotron emission in radio and microwaves provide firmer constraints on Galactic magnetic fields (see e.g. [30, 29, 27]).

4.1.2. De-excitation nuclear lines

Gamma-ray lines in the 0.1 - 10 MeV range are produced by nuclear collisions of CRs with interstellar matter [9]. Their detection allows study of the spectra, composition, and distribution of CR nuclei below the kinetic energy threshold for production of neutral pions (~300 MeV for p+p collisions). The most intense lines are expected to be from the de-excitation of the first nuclear levels in ^{12}C, ^{16}O, ^{20}Ne, ^{24}Mg, ^{28}Si, and ^{56}Fe [35]. The total nuclear line emission is also composed of broad lines produced by interaction of CR heavy ions with the H and He nuclei of the interstellar gas, and of thousands of weaker lines [9]. The gamma-ray spectrum is predicted to have a characteristic bump in the range 3 - 10 MeV, which is produced by several strong lines of ^{12}C and ^{16}O. Simulated gamma-ray line spectra of an individual nearby superbubble is reported in [44, 7]. The spectrum is comprises narrow and broad ^{12}C and ^{16}O lines, the observation of which would constrain low energy CR composition. More details can be found in [9].

4.2. Nucleosynthesis lines

The sites believed to produce radioisotopes observable as gamma-ray line emission are novae, core-collapse Supernovae (SN), SN type Ia, Wolf-Rayet stars, and asymptotic giant branch stars. Nuclear emission lines from isotopes in massive and exploding stars, such as ^{44}Ti, ^{26}Al, and ^{60}Fe, allow a probe of nucleosynthesis and chemical evolution of the Galaxy. While the above-cited radioisotopes with relatively long lifetimes produce diffuse emission that provides insights on stellar nucleosynthesis and also on the Galactic interstellar medium, the radioisotopes with shorter lifetimes, such as ^7Be, ^{56}Ni, ^{58}Ni, provide information about the explosion and the early evolution of the remnant.

The all-sky COMPTEL map showed the gamma-ray emission produced by the radioactive decay of ^{26}Al [48] to be concentrated along the plane, tracing regions with massive young stars throughout the Milky Way. More recently [47], the Doppler shifts of the gamma-ray energy caused by the Galactic rotation has been observed with INTEGRAL/SPI, which depends on the location of the source region within the Galaxy, and, hence can enable a census of massive stars in the Galaxy. Moreover, being produced in the innermost ejecta of core-collapse supernovae, ^{44}Ti provides a direct probe of the supernova engine. Most numerical simulations of stellar core-collapse explosions require spatial asymmetry, which has been observed in Cassiopeia A with NuSTAR [49] thanks to the detailed image of ^{44}Ti line at around 70 keV. This provides strong evidence for the development of low-mode convective instabilities in core-collapse SNe. Even more recently, an asymmetric explosion has been revealed with the detection of the ^{44}Ti gamma-ray emission line from SN1987A with NuSTAR [50].

Other nucleosynthesis lines in the energy range of a GECCO mission are: ^{56}Ni and ^{57}Co.

A GECCO telescope will allow mapping of radioactive material in SN remnants, resolving the Galactic chemical evolution and sites of nucleosynthesis of elements.

4.3. Understanding the Galactic center gamma-ray excess

The Galactic center (GC), a favorite target for telescopes across the whole electromagnetic spectrum, provides guaranteed exciting scientific return. The GC harbors the SMBH with mass of $4 \times 10^6 M_\odot$ and dense populations of all types of objects including binary and multiple systems, while its relative proximity allows many such objects to be resolved. The two huge Fermi Bubbles, each 10 kpc across, presumably emanating from the GC to the North and to the South of the Galactic plane were discovered by Fermi-LAT in gamma rays [64, 65], and are also visible in X-rays by eRosita [66], testifying that this is a multi-wavelength phenomenon (for more details see Section 4.5). The high-energy processes that involve particle acceleration and interactions reveal themselves through generation of non-thermal emission observed from radio- to gamma rays. The GC is also bright in an enigmatic positron annihilation emission that includes 511 keV line and three-photon continuum emission [67].

Recent observations of the GC with Fermi-LAT reveal an excess in the energy range around 10 GeV [63, 68]. The analysis made using different techniques indicates that the excess is spatially extended and concentrated around the GC. The NFW template fitted with other templates built using a GALPROP-based diffuse emission model effectively flattens the residuals leaving a burning question about the origin of the excess open.

Two main interpretations of the excess relate its nature to the unresolved sources that may be abundant in the inner Galaxy [59] or to emission due to DM annihilation [60]. Both interpretations are supported with valid arguments that have to be tested with further observations. In particular, the DM interpretation is supported by observations of the excess in CR antiprotons and with observations of the extended 400 kpc-across the gamma ray halo around the Andromeda galaxy (M31) [61]. In both cases the excesses are observed in the same energy range [62] giving strong support to the DM scenario. Meanwhile, the conventional astrophysical interpretation in terms of the weak unresolved gamma ray sources is supported with the logN-logS plots [57, 58].

Addressing this question will require high-resolution observations in the MeV-GeV energy range. However, the currently operating Fermi-LAT instrument has very limited capabilities below ~500 MeV with angular resolution becoming as bad as a few degrees below 100 MeV. X-ray telescopes have the angular resolution at arcsec scale; however, their operating energy is too far below the MeV scale to provide relevant information. The sources that are observed with X-ray telescopes and the processes of generation of X-ray emission may and likely are very different from those in the MeV scale. That diminishes their capabilities to resolve this issue.

It becomes clear that addressing this outstanding question requires a brand new instrument. This instrument should be targeting the MeV range and yet have angular resolution an order of magnitude better than current instruments.

4.4. Searches for dark matter and new physics

A GECCO telescope will offer unprecedented opportunities in the search for dark matter and new physics [103, 104]. Specifically, "light" dark matter, in the GeV or sub-GeV mass range, has come to the forefront in the present era that has been dubbed one of the "waning of the WIMP" [69]. The pair-annihilation or the decay of such light dark matter particles, resulting in MeV gamma rays from a number of targets, most notably the center of the Galaxy, nearby galaxies such as M31, and nearby dwarf satellites of the Milky Way, would have escaped detection with previous telescopes, but would be detectable by a GECCO telescope.

[103] studied in detail the potential of GECCO to discover a signal of dark matter annihilation or decay, using the state-of-the-art code Hazma for the calculation of the gamma-ray spectrum from simplified dark matter models matched via chiral perturbation theory onto final-state hadrons [105] (see also [54]). The key findings of [103] are that:

1. The Galactic center is the most promising target for searches for dark matter annihilation, followed by M31 and by local dSph such as Draco;

2. Considering individual final states, a GECCO mission will improve over current constraints from Fermi-LAT, EGRET and COMPTEL by over 4 orders of magnitude for dark matter annihilating to e^+e^- and by 3-4 for annihilation into $\gamma\gamma$ or $\mu^+\mu^-$ (see fig. 1 in [103]);

3. For dark matter decay, the largest gains will be made for e^+e^- and $\gamma\gamma$, again via observations of the Galactic center;

4. Considering a specific simplified model, [103] finds that for light scalar mediators (lighter than the dark matter mass) a GECCO mission will probe thermal relic dark matter in a very wide range of masses, from 0.5 MeV up to a GeV, improving by up to 4 orders of magnitude current constraints;

5. For a vector mediator, similarly, a GECCO mission will outperform current constraints by several orders of magnitude, especially in the sub-MeV dark matter mass range.

[104] additionally studied opportunities for constraining or discovering light primordial black holes that are currently in the process of evaporating via the mechanism of Hawking radiation. Interestingly, the expression for the approximate black hole lifetime τ as a function of the hole's mass M,

$$\tau(M) \simeq 200\tau_U \left(\frac{M}{10^{15}\,\text{g}}\right)^3 \simeq 200\tau_U \left(\frac{10\,\text{MeV}}{T_H}\right)^3, \qquad (10)$$

where τ_U is the age of the universe, and T_H the Hawking temperature of the hole, points to temperatures at evaporation at most as large as 10 MeV. Of course more energetic particles can also be radiated via thermal fluctuations, but it is clear that the expected detectable gamma-ray emission falls squarely within GECCO observing capabilities. [104] presented an accurate evaluation of the expected gamma-ray spectra from light black hole evaporation, and showed that a GECCO mission will enable the possible discovery of light primordial black holes as massive as 10^{18} g as dark matter candidates, significantly extending current constraints, by up to 1-2 orders of magnitude in mass.

4.5. The Fermi Bubbles

The Fermi Bubbles (FB) are a pair of Galactic-scale structures extending, almost symmetrically, above and below the Galactic plane. Discovered in 2010 by [106] in a search for a gamma-ray counterpart to the WMAP[4] haze (see e.g. [108]), the FB were deeply studied in 2014 by [107] who performed detailed spectral and morphological analysis for |b| > 10°: both bubbles are elliptical, extending 55° North-South and 45° East-West in diameter; they appear to have a vertical axis (perpendicular to the Galactic plane) roughly intercepting the GC; they have an almost uniform intensity, a quite hard spectrum well described by a log parabola or a power-law with exponential cutoff; their gamma-ray luminosity between 100 and 500 MeV was estimated to be $L\gamma = (3.5 - 6.8) \times 10^{37}$ erg/s and leptonic inverse Compton or hadronic (plus inverse Compton from secondary leptons) models can explain the data well. Leptonic scenarios can also explain the microwave haze observations, but hadronic scenarios do not suffer from radiative losses and can thus maintain high-energy particles even if operating on much longer timescales (although particle confinement on Gyr timescales is challenging). Assuming a jet-like FB formation from the GC, the FB expansion velocity should be greater than 20,000 km/s in order to have a bubble formation time greater than the cooling time of TeV electrons (assuming both inverse Compton and synchrotron losses in a 5 μG Galactic magnetic field); this corresponds to electron acceleration time scales of roughly 500 kyr [107]. A 2019 study of the low-latitude region of the FB [109] found greater intensities than the FB at high latitudes with a spectrum compatible with a single power law between 10 GeV and 1 TeV and, more interestingly, a centroid shifted to the west of the GC. The latter observation disfavors models attributing the origin of the FB to past AGN-like activities of the super-massive black hole in the center of our Galaxy.

Observing a soft gamma-ray counterpart of the FB would favor a leptonic scenario in which a low-energy CR electron population produces gamma rays below ~10 MeV through inverse Compton scattering on the interstellar radiation field. On the contrary, an absence of such a counterpart would favor an origin in hadronic processes for the FB in which the main process of gamma-ray production is pion decay (completely subdominant below 100 MeV with respect to inverse Compton and bremsstrahlung). Additionally, the unique capability of a GECCO mission to resolve point-like sources along the Galactic plane will help disentangle the emission from such sources and the FB low-latitude emission, providing useful insights about the origin of these large-scale features.

Recently eROSITA [110] detected a new gigantic bubble-like feature in the Southern hemisphere of our Galaxy [111], complementary to a Northern hemisphere feature already known

---

[4]Wilkinson Microwave Anisotropy Probe: https://map.gsfc.nasa.gov.

from X-ray and radio observations[5]. The eROSITA bubbles (eRB) are morphologically almost spherical, extending $\approx 80°$ in diameter, and they are not obviously symmetric if considering a vertical axis passing through GC. The measured intensity between 0.6 and 1 keV is not uniform, with a total luminosity (assuming a hot X-ray-emitting plasma) of $L_X \approx 10^{39}$ erg/s, and a measured average surface brightness of $(2 - 4) \times 10^{-15}$erg/cm^2/s/arcmin^2 (assuming an emission from hot plasma with temperature kT=0.3 keV) that decreases with Galactic latitude. In [111], assuming a Mach number of the shock of 1.5, the authors estimate a characteristic expansion time to the present size of around 20 Myr ($\approx$ 40 times the FB expansion timescales for leptonic scenarios).

[111] suggests a connection between the eRB and FB, in which the latter are driving the expansion of the former and they are both associated with the same energy release in the GC region. In this scenario the FB outflow piles up and heats the surrounding interstellar gas and the outer eRB boundary represents the termination shock of this heating wave. The pressure between the FB and eRB surfaces is constant and the total thermal energies at the two boundaries reflect their volumes (hotter plasma at the outer eRB boundary). However, although some morphological similarities exist, the connection between the eRB and the FB (and even their association to the GC itself) is not straightforward. More dedicated studies and new observations are needed to better investigate the physical relation (if any) between the FB and the eRB. Continuum observations of gamma rays between hundreds of keV and tens of MeV could be crucial to unveil the origins of the FB [116] and possible connections between FB and eRB.

From our perspective, it is not yet known whether such gigantic bubbles are truly of galactic scales originating in the GC or if they are smaller, closer features. The Andromeda galaxy (M31) is a barred spiral galaxy like our Milky Way, and the two also share similar virial masses and reasonably similar formation stories: Andromeda is approximately a twin of the Milky Way. Observations of Andromeda provide a different perspective on our own Galaxy. For this reason, the gamma-ray observation of giant bubble-like structures extending above and below Andromeda's plane [117] is an extremely interesting piece of information, pointing toward truly galactic-scale interpretation of the FB. Recently [118] provided a gamma-ray imaging of M31 which gives the visual impression of bubble-like structures, limited however by the relatively poor angular resolution of the LAT at the observed energies. Outstanding spatial resolution capabilities, achievable in coded-mask mode, of a GECCO mission could also provide a soft-gamma-ray picture of our twin galaxy, providing again very valuable hints about the origin of the FB.

4.6. The 511 keV line

A 511 keV line emission from positron-electron pair annihilation in the central regions of the Milky Way was discovered

by balloon-borne experiments as early as 1975 (see e.g. [70]). Further observations with space telescopes, specifically OSSE on the Compton Gamma-Ray Observatory [71] and, more recently, the SPI spectrometer [72, 73] and the IBIS imager on board INTEGRAL [74] have significantly sharpened the observational picture of the 511 keV line. The line intensity is, overall, around 10^{-3} photons cm^{-2} s^{-1}, originating from a 10° region around the Galactic Center.

New physics explanations for the 511 keV emission are constrained by observations both at higher and lower energies, indicating, for instance, that the mass of a putative dark matter candidate whose annihilation could produce the observed line is bounded from above at around 3 MeV [77, 78]. Absent large-scale magnetic fields [79], any astrophysical source of the 511 keV line emission should additionally lie within approximately 250 pc of the annihilation sites [80], thus implying that the source distribution should quite closely resemble the actual signal distribution in the sky [81, 80].

While the nature of such astrophysical sources continues to be debated, the morphology and a lower-limit on the number of sources rules out a single source (e.g. Sgr A* [82]) or a single injection event, such as a gamma-ray burst or a hypernova in the Galactic Center [83]. The signal sources must therefore be associated with a population of sources that could, or not, be resolved as individual point sources (a possibility somewhat constrained by prior observations [84]). Source classes that have been considered include massive stars, pulsars, including millisecond pulsars, core-collapse supernovae and SNe Ia, Wolf-Rayet stars, and low-mass X-ray binaries (LMXB), especially microquasars [85, 86]. In many instances, these astrophysical objects are also found much closer to the solar system than in the Galactic Center region.

The angular resolution and point-source sensitivity of a GECCO telescope make the instrument ideally suited to enable differentiation between multiple point sources and a genuinely diffuse origin for the 511 keV emission, as expected from dark matter annihilation or other exotic scenarios. Specifically, if one source class dominated the positron emission, a GECCO mission could detect nearby members of that source class. [103] specifically showed that GECCO sensitivity should enable the detection of any positron source responsible for a significant fraction of the 511 keV signal closer than 4 kpc.

Additional information on the nature of the origin of the 511 keV signal from the Galactic Center will be provided by observations of nearby systems such as the Andromeda galaxy (M31), the Triangulum galaxy (M33), nearby clusters such as Fornax and Coma, and nearby satellite dwarf galaxies such as Draco and Ursa Minor [87]. Using as a crude estimate of the predicted 511 keV signal a simple mass to distance-squared ratio, [103] finds that the 511 keV signal from M31 should be detectable by a GECCO mission, as should the signal from the nearby dSph Fornax and (although marginally) the Coma cluster. [103] predicts that M33, and local dSph should not be bright enough at 511 keV to be detectable by GECCO. Integral/SPI already searched for a 511 keV line from Andromeda (M31), reporting an upper limit to the flux of 1×10^{-4} cm^{-2} s^{-1} [86]. Certain types of new physics explanations such as dark matter

---

[5]The Northern hemisphere feature is associated with the North Polar Spur observed in X-rays [112] and Loop I observed in radio [113].

decay would follow a similar scaling, while others would have a more complicated, model-specific dependence.

4.7. Sources and source populations

Current available observations in the MeV domain have an angular resolution of several degrees. This rather large angular resolution is due to the changing nature of the photon-matter interaction used to detect the astrophysical radiation. Indeed, while at several tens of MeV pair production dominates, at lower energies at a few MeV Compton scatting is the primary interaction process, which was used by COMPTEL. Inevitably also GECCO pure Compton mode is affected by the large angular resolution. However, the coded-mask mode allows a GECCO mission to reach a superb, for this energy domain, angular resolution of ~1 arcmin. The ability to separate the flux contribution of single sources at the arcmin level also allows precise spectroscopy. This feature helps in identifying newly detected sources in a basically unexplored energy range. In fact, while COMPTEL sources are mostly associated and/or identified through variability of exceptionally bright sources, GECCO newly detected sources can be positionally and spectroscopically identified through the contiguous energy bands of the Fermi-LAT and the well known keV sky. Here we summarize the most significant and interesting source populations, both extragalactic and Galactic that can be observed by a GECCO mission.

4.7.1. Extragalactic source populations

The high-energy cosmic diffuse background radiation is a useful tool to constrain the population of astrophysical sources that are responsible for it. This background radiation at MeV energies has been measured by COMPTEL in a study by [125], who accurately accounted for the instrumental effects. This measurement ties in well with the measurement of the diffuse X-ray background by several instruments [e.g. 130] and the diffuse gamma-ray background measured by the Fermi-LAT [124]. The extrapolation of the latter to lower energies and the extrapolation of the former to higher energies, require a hard MeV component, which has been measured by COMPTEL. A major contribution to the low energy part between a few hundreds of keV and a few MeV comes from blazars that are efficiently detected in hard X-ray (>15 keV) due to their rather hard spectra. Among the most interesting of such sources detected at hard X-rays are the extreme synchrotron BL Lac objects [e.g. 128] and the high-redshift blazars [e.g. 119]. High-redshift blazars, especially Flat Spectrum Radio Quasars, are important as they are known to host supermassive black holes of the order of 10^9 M$_\odot$ [131]. The existence of such massive black holes in the early universe is relevant for scenarios in which they are formed by accretion or by merger-driven evolution. In contrast, the extreme synchrotron BL Lac objects carry information about the composition of the jet. The very high-energy spectral energy distribution (SED) can be explained as due to a hadronic component in the jet [e.g. 129], which can account for a significant fraction of the neutrino emission. The contribution to the diffuse high-energy hard component measured by

COMPTEL calls for candidates different from blazars. While DM can contribute to it as discussed in section 6, also point sources different from blazars are good candidates. An intriguing class of sources are star-forming galaxies (SFG). SFG are rich in CR that undergo hadronic interactions with the interstellar medium. This process led to the detection of some SFG in the GeV band [126]. However, the exact contribution to the diffuse background remains unsettled [133]. The excellent sensitivity and angular resolution of a GECCO mission allows for detecting and pinpointing these sources, thereby accounting for their contribution to the diffuse background radiation. A further contributing class of sources to the high-end of the MeV diffuse emission are radio galaxies [132], which have been detected in this energy range.

4.7.2. Galactic source populations

The Milky Way and similar galaxies host a rich diversity of objects capable of radiating in the MeV range. Many of these objects involve a neutron star (NS) or a black hole (BH) which represent the densest forms of matter in the Universe and are the final stage in the lives of massive stars.

Around a NS, gamma-rays can be generated by thermonuclear reactions of material on the hot surface (bursters) or by extraction of magnetic or rotational energy from the NS (magnetars and pulsars, respectively). There are 239 pulsars listed in the fourth Fermi-LAT catalog [143]. Since a GECCO mission samples the energy band below LAT's limit of 50 MeV, it will not only expand the population of young pulsars whose emission is expected to peak in the MeV range [144], it will also fill in the gaps in the spectra of pulsars between the X-ray and gamma-ray bands.

Around a NS or a BH, gamma-rays can result from the accretion of charged particles accelerated in the strong gravitational and electromagnetic fields of so-called X-ray binaries (XRBs). There are around 400 known XRBs in our Galaxy [145, 146, 147]. Cyclotron lines have been found in the range of 10–100 keV for 35 XRBs [148], but some XRBs could host magnetars [$B \gtrsim 10^{14}$ G, 149] that would push these lines, as well as their harmonics, to hundreds of keV where they can be seen by a GECCO mission.

If the NS or BH features a jet, the X-ray photons (and UV photons from the donor star) can interact with particles in the jet causing them to be upscattered via inverse Compton to GeV energies [e.g., 150, and references therein]. Thus far, GeV emission has been detected from a dozen so-called gamma-ray binaries. Most of them have a NS as the accretor while a few have a BH: the only thing they appear to have in common is that they all have a high-mass star as the donor. Their emission is expected to peak in the MeV band, which means that a GECCO mission will connect the X-ray continuum with that from the GeV band. This connection can then be used to disentangle conflicts between leptonic and hadronic emission models. In the same way, a GECCO mission will extend the tail in the hard state of BH-XRBs into the MeV domain. Photons originating from the base of the accretion column are expected to be polarized [e.g., 151] which GECCO is conveniently built to detect.

Before a massive star turns into a NS or a BH, it goes through a supernova (SN) phase where stellar material accelerated by the sudden collapse of the core emits gamma-rays at specific energies that reveal the star's chemical composition (Section 4.2). Prior to the SN stage, many of these massive stars are bound gravitationally to another massive star. The shock region where the stellar winds collide can also give rise to gamma-ray emission in these colliding-wind binaries [CWBs: e.g., 152, and references therein]. In the MeV range, a GECCO mission will link the keV to GeV continuum from CWBs such as eta Car [153] and allow us to dissociate the contributions from leptonic (inverse Compton) and hadronic (pion decay) acceleration mechanisms.

For these reasons, when a GECCO telescope observes the Milky Way's MeV-emitting populations, it will show us different stages in the life cycle of massive stars. Once both stars have collapsed into a NS or a BH, and when the pair eventually merges into a single object, the merger produces gravitational waves detectable by the LIGO and Virgo observatories. Though such signals have been extragalactic in origin so far, predictions for the merger rate depend on knowing how many members from each of the populations above are hosted by galaxies like ours [154].

4.8. Multimessenger and multifrequency Synergies

Given the transient and variable origin of multimessanger and multifrequency astrophysical sources, the fraction of the sky being monitored at any given time is a major asset for a space mission. In its Compton observing mode a GECCO mission will cover a large fraction of the sky of 60° × 60° in zenithal direction allowing to keep watch over flaring phenomena like blazars and transient phenomena like Gamma-Ray Bursts (GRBs). Also, GECCO BGO shielding, specifically designed for background rejection with its octagonal structure of large-size detectors of ∼3000 cm^2, will have the additional ability to locate the prompt emission of GRBs within a few degrees similar to INTEGRAL [160]. The prompt emission by merging neutron stars can be effectively observed in GECCO energy band ∼keV–MeV. They reveal themselves as short GRBs as well as kilonovae. Such events also provide gravitational wave (GW) signals allowing a GECCO mission to tie in with multimessanger and multiwavength observations. Amid the prompt-emission detection, the telescope can repoint within a few minutes depending on the slewing angle, allowing for locating the source within better than 1 arcmin precision. It will also act as an alert system for follow-up observations. The study of neutron star mergers provides insights into relativistic jets and particle physics. Neutron stars might also be involved in the emission of very short GRBs when transitioning to strange quark stars [156]. While this intriguing hypothesis is still an open question, it enables studies related to fundamental physics of matter. In a multifrequency approach, GECCO large field of view allows for the coverage of the little explored MeV range of flaring sources. Such sources can be galactic or extragalactic in origin. Among the extragalactic sources blazars represent a major discovery space. Indeed, a tentative ∼ 3σ association of a high-energy neutrino detected by IceCube with a flaring blazar [155] has revived the lepto-hadronic emission scenario for these sources, which would favor the neutrino production in the jet. The energy band of ∼keV–MeV carries the signature to constrain the content of the jet [e.g. 158, 159, 157]. The multimessenger science case addressed by a GECCO mission clearly aligns with the Decadal Report on Astronomy and Astrophysics 2020 (Astro2020) [11] priority area "New Messengers and New Physics".

5. Conclusions

In this work we demonstrate the importance of a mission like GECCO at hard X-rays and soft gamma rays that will finally cover the huge observational gap between X-rays and gamma rays. The new mission concept of combining the high-resolution of the coded mask with the high sensitivity of the Compton telescope will allow to clearly distinguish and detect point sources from truly diffuse emission even in very dense regions of the sky. With such an instrument we can finally assess complicated regions such as the Galactic center with its supermassive black hole. Observations with a GECCO telescope will also shed light on the origin of the Fermi Bubbles, on the origin of the 511 keV line, on the nucleosynthesis of elements and the chemical evolution of the Galaxy, on the dynamics of Galactic winds, on the mechanisms of transport in the low-energy CRs, and eventually on the role of low-energy CRs on the Galaxy evolution and star formation. Moreover, the possibility of resolving sources at gamma-ray energies will also enable us to answer open questions regarding Galactic diffuse emissions and cosmic rays. In more detail, observations of the diffuse inverse Compton component of the interstellar emission will allow determination of the spatial distribution of low-energy CR electrons, their sources, their propagation and acceleration, and their relation to the interstellar medium. As a consequence, a GECCO mission will also enable indirect detection searches for dark matter and searches for new physics [e.g. 2] and extragalactic studies [e.g. 3]. Thanks to the power of a GECCO mission to resolve otherwise confused point sources from the diffuse emission and to its unprecedented sensitivity a GECCO mission will also enable studies of single extragalactic and Galactic sources and of populations of sources allowing discoveries of new astrophysical phenomena whose spectra peak in a poorly explored gamma-ray range. With the BGO detector a GECCO mission will also detect transients such as GRBs and will enable improved multimessenger astrophysics.

The science cases for a GECCO mission address the priority area "New Messengers and New Physic" and the priority area "Unveiling the Drivers of Galaxy Growth" emphasized in the Decadal Report on Astronomy and Astrophysics 2020 (Astro2020) [11].

Authors'contribution

References

[1] Abdo, A. A., Ackermann, M., Ajello, M., et al. 2009, Physical Review Letters, 103, 251101

[2] Ackermann, M., Ajello, M., Albert, A., et al. 2017, ApJ, 840, 43

[3] Ackermann, M., Ajello, M., Albert, A., et al. 2015, ApJ, 799, 86

[4] Ackermann, M., Ajello, M., Albert, A., et al. 2017, ApJ, 840, 43

[5] Aguilar, M., Alberti, G., Alpat, B., et al. 2013, Physical Review Letters, 110, 141102

[6] Andritschke, R., Zoglauer, A., Kanbach, G., et al. 2005, Experimental Astronomy, 20, 395. doi:10.1007/s10686-006-9040-7

[7] Benhabiles-Mezhoud, H., Kiener, J., Tatischeff, V., & Strong, A. W. 2013, ApJ, 763, 98. Erratum: ApJ, 766, 139

[8] Bouchet, L., Strong, A. W., Porter, T. A., et al. 2011, ApJ, 739, 29

[9] Bykov, A. M. 2014, Astronomy Astrophysics Reviews 22, 77

[10] Cummings, A. C., Stone, E. C., Heikkila, B. C., et al. 2016, ApJ, 831, 18

[11] No author 2021, Pathways to Discovery in Astronomy and Astrophysics for the 2020s, Consenses Study Report. Washington, DC: The National Academies Press, 2021.

[12] de Angelis, A., Tatischeff, V., Grenier, I. A., et al. 2018, Journal of High Energy Astrophysics, 19, 1. doi:10.1016/j.jheap.2018.07.001

[13] Drury, L. O. & Strong, A. W. 2017, A&A, 597, A117

[14] Enßlin, T. A., Pfrommer, C., Springel, V., & Jubelgas, M. 2007, A&A, 473, 41

[15] Hanasz, M., Otmianowska-Mazur, K., Kowal, G., & Lesch, H. 2009, A&A, 498, 335

[16] Kuiper, L., & Hermsen, W. 2015, MNRAS, 449, 3827

[17] Fleischhack, H. 2021, Proceedings of 37th International Cosmic Ray Conference PoS(ICRC2021), doi: 10.22323/1.395.0649

[18] Giacinti, G., Kachelrieß, M., & Semikoz, D. V. 2012, Physical Review Letters, 108, 261101

[19] Greiner, J., Iyudin, A., Kanbach, G., et al. 2009, Experimental Astronomy, 23, 91. doi:10.1007/s10686-008-9102-0

[20] Grenier, I. A., Black, J. H., & Strong, A. W. 2015, Annual Review of Astronomy and Astrophysics, 53, 199

[21] Jóhannesson, G., Porter, T. A., & Moskalenko, I. V. 2018, ApJ, 856, 45. doi:10.3847/1538-4357/aab26e

[22] McEnery, J., van der Horst, A., Dominguez, A., et al. 2019, Astro2020: Decadal Survey on Astronomy and Astrophysics, APC white papers, no. 245; Bulletin of the American Astronomical Society, Vol. 51, Issue 7, id. 245

[23] Moiseev, A.A., for the GECCO Collaboration, Proceedings of the 37th ICRC, Berlin, 2021, PoS(ICRC2021)648, DOI:10.22323/1.395.0648

[24] Moiseev, A. 2019, 36th International Cosmic Ray Conference (ICRC2019), 36, 585

[25] Moskalenko, I. V., Jóhannesson, G., Orlando, E., et al. 2015, 34th International Cosmic Ray Conference (ICRC2015), 34, 492

[26] Moskalenko, I. V., & Strong, A. W. 2000, ApJ, 528, 357

[27] Orlando, E. 2019, PhRvD, 99, 043007. doi:10.1103/PhysRevD.99.043007

[28] Orlando, E., Grenier, I., Tatischeff, V., et al. 2019, BAAS 51, 151

[29] Orlando, E. 2018, MNRAS, 475, 2724

[30] Orlando, E., & Strong, A. 2013, MNRAS, 436, 2127

[31] Padovani, M., Galli, D., & Glassgold, A. E. 2009, A&A, 501, 619

[32] Persic, M., & Rephaeli, Y. 2010, MNRAS, 403, 1569

[33] Pfrommer, C., Pakmor, R., Schaal, K., Simpson, C. M., & Springel, V. 2017, MNRAS, 465, 4500

[34] Porter, T. A., Moskalenko, I. V., Strong, A. W., Orlando, E., & Bouchet, L. 2008, ApJ, 682, 400

[35] Ramaty, R., Kozlovsky, B., & Lingenfelter, R. E. 1979, ApJS, 40, 487

[36] Recchia, S., Blasi, P., & Morlino, G. 2016, MNRAS, 462, L88

[37] Schoenfelder, V., Aarts, H., Bennett, K., et al. 1993, ApJS, 86, 657

[38] Strong, A. W., Moskalenko, I. V., & Ptuskin, V. S. 2007, Annual Review of Nuclear and Particle Science, 57, 285

[39] Strong, A. W. 2011, Cosmic Rays for Particle and Astroparticle Physics, 473-481, doi:10.1142/9789814329033_0059

[40] Strong, A. W., Orlando, E., & Jaffe, T. R. 2011, A&A, 534, A54

[41] Strong, A. W. 2007, Ap&SS, 309, 35

[42] Strong, A. W., Moskalenko, I. V., Reimer, O., Digel, S., & Diehl, R. 2004, A&A, 422, L47

[43] Strong, A. W., Bloemen, H., Diehl, R., Hermsen, W., & Schönfelder, V. 1999, Astrophysical Letters and Communications, 39, 209

[44] Tatischeff, V., & Kiener, J. 2004, New Astronomy Reviews, 48, 99

[45] Tomsick, J., Zoglauer, A., Sleator, C., et al. 2019, Bulletin of the American Astronomical Society

[46] Zoglauer, A., Siegert, T., Lowell, A., et al. 2021, arXiv:2102.13158

[47] Diehl, R., Halloin, H., Kretschmer, K., et al. 2006, Nature, 439, 45. doi:10.1038/nature04364

[48] Plüschke, S., Kretschmer, K., Diehl, R., et al. 2001, Exploring the Gamma-Ray Universe, 459, 91

[49] Grefenstette, B. W., Harrison, F. A., Boggs, S. E., et al. 2014, Nature, 506, 339. doi:10.1038/nature12997

[50] Boggs, S. E., Harrison, F. A., Miyasaka, H., et al. 2015, Science, 348, 670. doi:10.1126/science.aaa2259

[51] Vedrenne, G., Roques, J.-P., Schönfelder, V., et al. 2003, A&A, 411, L63

[52] Winkler, C., Courvoisier, T. J.-L., Di Cocco, G., et al. 2003, A&A, 411, L1

[53] A. Coogan, L. Morrison and S. Profumo, JCAP 01, 056 (2020) doi:10.1088/1475-7516/2020/01/056 [arXiv:1907.11846 [hep-ph]]

[54] A. Coogan, L. Morrison and S. Profumo, [arXiv:2104.06168 [hep-ph]].

[55] A. Coogan, A. Moiseev, L. Morrison and S. Profumo, [arXiv:2101.10370 [astro-ph.HE]].

[56] A. Coogan, L. Morrison and S. Profumo, Phys. Rev. Lett. 126, no.17, 171101 (2021) doi:10.1103/PhysRevLett.126.171101 [arXiv:2010.04797 [astro-ph.CO]].

[57] Brandt, Timothy D. and Kocsis, Bence, ApJ 812 (2015) 15.

[58] Hong, JaeSub and Mori, Kaya and Hailey, Charles J. et al., ApJ 825 (2016) 132.

[59] Chang, L. J. and Mishra-Sharma, Siddharth and Lisanti, Mariangela and Buschmann, Malte and Rodd, Nicholas L. and Safdi, Benjamin R., Phys. Rev. D 101 (2020) 023014

[60] Karwin, Christopher and Murgia, Simona and Tait, Tim M. P. and Porter, Troy A. and Tanedo, Philip, PhRvD 95 (2017) 103005.

[61] Karwin, Christopher M. and Murgia, Simona and Campbell, Sheldon and Moskalenko, Igor V., ApJ 880 (2019) 95.

[62] Karwin, Christopher M. and Murgia, Simona and Moskalenko, Igor V. and Fillingham, Sean P. and Burns, Anne-Katherine and Fieg, Max, PhRvD 103 (2021) 023027.

[63] Hooper, Dan and Goodenough, Lisa, Physics Letters B 697 (2011) 412

[64] Su, Meng and Slatyer, Tracy R. and Finkbeiner, Douglas P., ApJ 724 (2010) 1044.

[65] Ackermann, M. and Albert, A. and Atwood, W. B. and et al., ApJ 793 (2014) 64.

[66] Predehl, P. and Sunyaev, R. A. and Becker, W. et al.Nature 588 (2020) 227.

[67] Churazov, Eugene and Bouchet, Laurent and Jean, Pierre and et al., New

Astronomy Reviews 90 (2020) 101548.

[68] Ajello, M. and Albert, A. and Atwood, W. B. and et al., ApJ 819 (2016) 44.

[69] G. Arcadi, M. Dutra, P. Ghosh, M. Lindner, Y. Mambrini, M. Pierre, S. Profumo and F. S. Queiroz, Eur. Phys. J. C 78, no.3, 203 (2018) doi:10.1140/epjc/s10052-018-5662-y [arXiv:1703.07364 [hep-ph]].

[70] R.C. Haymes, G.D. Walraven, C.A. Meegan, R.D. Hall, F.T. Djuth and D.H. Shelton, Astrophysical Journal 201 (1975) 593.

[71] J. Skibo, W. Johnson, J. Kurfess, R. Kinzer, G. Jung, J. Grove et al., astro-ph/9704207].

[72] G. Weidenspointner et al., Nature 451 (2008) 159.

[73] P. Jean, J. Knödlseder, V. Lonjou, M. Allain, J.P. Roques, G.K. Skinner et al., Astronomy and Astrophysics 407 (2003) L55

[74] G. De Cesare, A. Bazzano, F. Capitanio, M. Del Santo, V. Lonjou, L. Natalucci et al., Adv. Space Res. 38 (2006) 1457

[75] P. Sizun, M. Cassé and S. Schanne, Physical Review D 74 (2006) 063514

[76] P. Sizun, M. Cassé, S. Schanne and B. Cordier, in The Obscured Universe. Proceedings of the VI INTEGRAL Workshop, vol. 622 of ESA Special Publication, p. 61, Jan., 2007

[77] F.A. Agaronyan and A.M. Atoyan, Soviet Astronomy Letters 7 (1981) 395.

[78] J.F. Beacom and H. Yüksel, Physical Review Letters 97 (2006) 071102.

[79] N. Prantzos, Astronomy and Astrophysics 449 (2006) 869.

[80] P. Jean, J. Knödlseder, W. Gillard, N. Guessoum, K. Ferrière, A. Marcowith et al., Astronomy and Astrophysics 445 (2006) 579.

[81] E. Churazov, R. Sunyaev, S. Sazonov, M. Revnivtsev and D. Varshalovich, Monthly Notices of the Royal Astronomical Society 357 (2005) 1377.

[82] R.E. Lingenfelter and R. Ramaty, in "The Galactic Center", G.R. Riegler and R.D. Blandford, eds., vol. 83 of American Institute of Physics Conference Series, pp. 148–159, May, 1982.

[83] R.E. Lingenfelter and G.J. Hueter, in "High Energy Transients in Astro-Physics", S.E. Woosley, ed., vol. 115 of American Institute of Physics Conference Series, pp. 558–567, May, 1984.

[84] J. Knödlseder, P. Jean, V. Lonjou, G. Weidenspointner, N. Guessoum, W. Gillard et al., Astronomy and Astrophysics 441 (2005) 513.

[85] T. Siegert, R. Diehl, G. Khachatryan, M.G. Krause, F. Guglielmetti, J. Greiner et al., Astron. Astrophys. 586 (2016) A84.

[86] R.M. Bandyopadhyay, J. Silk, J.E. Taylor and T.J. Maccarone, Mon. Not. Roy. Astron. Soc. 392 (2009) 1115.

[87] J. Wolf, G.D. Martinez, J.S. Bullock, M. Kaplinghat, M. Geha, R.R. Munoz et al. Mon. Not. Roy. Astron. Soc. 406 (2010) 1220.

[88] Bertin, E., Arnouts, S., 1996, A&A suplement series, 117, 2, 393–404,

[89] Stetson, P., 1987, Publications of the Astronomical Society of the Pacific, 99, 613, 191

[90] Guglielmetti, F., Fischer, R., Dose, V., 2009, Monthly Notices of the Royal Astronomical Society, 396, 1, 165–190

[91] Popowicz, A., Smolka, B., 2015, Monthly Notices of the Royal Astronomical Societym 452, 1, 809–823

[92] Enßlin, T. A. 2019, Annalen der Physik, 531, 1800127. doi:10.1002/andp.201800127

[93] Enßlin, T. 2013, Bayesian Inference and Maximum Entropy Methods in Science and Engineering: 32nd International Workshop on Bayesian Inference and Maximum Entropy Methods in Science and Engineering, 1553, 184. doi:10.1063/1.4819999

[94] Enßlin, T. A., Frommert, M., & Kitaura, F. S. 2009, PhRvD, 80, 105005. doi:10.1103/PhysRevD.80.105005

[95] Selig, M., Bell, M. R., Junklewitz, H., et al. 2013, A&A, 554, A26. doi:10.1051/0004-6361/201321236

[96] Steininger, Theo and Dixit, Jait and Frank Philipp, et al. 2019, Annalen der Physik, 531, 3, publisher Wiley Online Library

[97] Arras, Philipp and Baltac, Mihai and Ensslin, Torsten A , et al. 2019, ascl, 1903

[98] Selig, M. & Enßlin, T. A. 2015, A&A, 574, A74. doi:10.1051/0004-6361/201323006

[99] Pumpe, D., Reinecke, M., & Enßlin, T. A. 2018, A&A, 619, A119. doi:10.1051/0004-6361/201832781

[100] Selig, M., Vacca, V., Oppermann, N., et al. 2015, A&A, 581, A126. doi:10.1051/0004-6361/201425172

[101] Selig, Marco and Vacca, Valentina and Oppermann, Niels and Enßlin, Torsten 2015 *Imaging the Fermi γ-ray sky*

[102] Junklewitz, H. and Bell, M. R. and Selig, M. and Enßlin, T. A. 2016 A&A, 586, A76. doi:10.1051/0004-6361/201323094

[103] Coogan, A., Moiseev, A., Morrison, L., et al. 2021, arXiv:2101.10370

[104] Coogan, A., Morrison, L., & Profumo, S. 2020, Phys. Rev. Lett. 126, no.17, 171101

[105] Coogan, A., Morrison, L., & Profumo, S. 2020, JCAP, 2020, 056. doi:10.1088/1475-7516/2020/01/056

[106] Dobler, G., et al., The Astrophysical Journal, Vol. 717, 825 (2010)

[107] Ackermann et al. (LAT Collab.) The Astrophysical Journal, Vol. 793, 1 (2014)

[108] Su, M., & Finkbeiner, D. P. 2012, The Astrophysical Journal, Vol. 753, 61

[109] Herold, L. & Malyshev D. Astron. Astrophys. 625, A110 (2019)

[110] Merloni, A. et al. Preprint at https://arxiv.org/abs/1209.3114 (2012).

[111] Predehl, P., et al. Nature 588, 227–231 (2020).

[112] Egger, R. & Aschenbach, B., Astron Astrophys. 294, L25–L28 (1995).

[113] Berkhuijsen, E. M. Astron. Astrophys. 14, 359–386 (1971).

[114] Ade, P. A. R., Aghanim, N., Arnaud, M., et al. Astron Astrophys. 554, A139 (2013)

[115] Gruber, D. E. et al. The Astrophysical Journal, Vol. 520, 124-129 (1999)

[116] Negro, M. et al. Submitted to The Astrophysical Journal (Nov. 2021), Preprint available: arXiv:2111.10362

[117] M. S. Pshirkov, V. V. Vasiliev, K. A. Postnov Monthly Notices of the Royal Astronomical Society: Letters, Vol. 459, 1, (2016)

[118] Arnold, C. & Calore, F. Preprint: arXiv:2102.06447 [astro-ph.HE]

[119] Bottacini, E., Ajello, M., & Greiner, J. 2012, ApJS, 201, 34. doi:10.1088/0067-0049/201/2/34

[120] Caroli, E., Stephen, J. B., Di Cocco, G., et al. 1987, Space Sci. Rev., 45, 349. doi:10.1007/BF00171998

[121] in 't Zand, J. J. M., Heise, J., & Jager, R. 1994, A&A, 288, 665

[122] Skinner, G. K. & Ponman, T. J. 1994, MNRAS, 267, 518. doi:10.1093/mnras/267.3.518

[123] Skinner, G. K. 1995, Experimental Astronomy, 6, 1. doi:10.1007/BF00419252

[124] Ackermann, M., Ajello, M., Albert, A., et al. 2015, ApJ, 799, 86. doi:10.1088/0004-637X/799/1/86

[125] Weidenspointner, G., Varendorff, M., Kappadath, S. C., et al. 2000, The Fifth Compton Symposium, 510, 467. doi:10.1063/1.1307024

[126] Abdollahi, S., Acero, F., Ackermann, M., et al. 2020, ApJS, 247, 33. doi:10.3847/1538-4365/ab6bcb

[127] Bottacini, E., Ajello, M., Greiner, J., et al. 2010, A&A, 509, A69. doi:10.1051/0004-6361/200913260

[128] Costamante, L., Ghisellini, G., Giommi, P., et al. 2001, A&A, 371, 512. doi:10.1051/0004-6361/20010412

[129] Cerruti, M., Zech, A., Boisson, C., et al. 2015, MNRAS, 448, 910. doi:10.1093/mnras/stu2691

[130] Faucher-Giguère, C.-A. 2020, MNRAS, 493, 1614. doi:10.1093/mnras/staa302god

[131] Ghisellini, G., Della Ceca, R., Volonteri, M., et al. 2010, MNRAS, 405, 387. doi:10.1111/j.1365-2966.2010.16449.x

[132] Inoue, Y. 2011, ApJ, 733, 66. doi:10.1088/0004-637X/733/1/66

[133] Owen, E. R., Lee, K.-G., & Kong, A. K. H. 2021, MNRAS, 506, 52. doi:10.1093/mnras/stab1707

[134] Collmar, W., et al., 2022, in preparation

[135] de Boer H., Bennett K., Bloemen H., et al., 1992, in Data Analysis in Astronomy IV, eds. V. Di Gesù, L. Scarsi, R. Buccheri, et al., (New York: plenum Press), p. 241

[136] Górski, K. M., Hivon, E., Banday, A. J., et al. 2005, ApJ, 622, 759. doi:10.1086/427976

[137] Schönfelder, V., Aarts, H., Bennett, K., et al., 1993, ApJS, 86, 657

[138] Schönfelder, V., Bennett, K., Blom, J.J., et al., 2000, A&AS, 143, 145

[139] Strong, A., Bloemen, H., Diehl, R., et al., 1999, Astrophys. Lett. Comm., 39, 677, arXiv:astro-ph/9811211

[140] Strong, A., Diehl, R., Schönfelder, V., et al., 1997, AIP Conference Proceedings, 410, 1198

[141] Strong, A., 1995, Experimental Astronomy, 6, 97

[142] Strong, A. & Collmar, W., 2019, Memorie della Socieata Astronomica Italiana, v.90, 297

[143] Abdollahi, S., Acero, F., Ackermann, M., et al. 2020, ApJS, 247, 33. doi:10.3847/1538-4365/ab6bcb

[144] Kuiper, L. & Hermsen, W. 2015, MNRAS, 449, 3827.

15

doi:10.1093/mnras/stv426

[145] Liu, Q. Z., van Paradijs, J., & van den Heuvel, E. P. J. 2001, A&A, 368, 1021. doi:10.1051/0004-6361:20010075

[146] Liu, Q. Z., van Paradijs, J., & van den Heuvel, E. P. J. 2006, A&A, 455, 1165. doi:10.1051/0004-6361:20064987

[147] Kretschmar, P., Fürst, F., Sidoli, L., et al. 2019, New Astronomy Reviews, 86, 101546. doi:10.1016/j.newar.2020.101546

[148] Staubert, R., Trümper, J., Kendziorra, E., et al. 2019, A&A, 622, A61. doi:10.1051/0004-6361/201834479

[149] Bozzo, E., Falanga, M., & Stella, L. 2008, ApJ, 683, 1031. doi:10.1086/589990

[150] Bosch-Ramon, V. & Khangulyan, D. 2009, International Journal of Modern Physics D, 18, 347. doi:10.1142/S0218271809014601

[151] Laurent, P., Rodriguez, J., Wilms, J., et al. 2011, Science, 332, 438. doi:10.1126/science.1200848

[152] Pittard, J. M., Vila, G. S., & Romero, G. E. 2020, MNRAS, 495, 2205. doi:10.1093/mnras/staa1099

[153] Hamaguchi, K., Corcoran, M. F., Pittard, J. M., et al. 2018, Nature Astronomy, 2, 731. doi:10.1038/s41550-018-0505-1

[154] Abbott, R., Abbott, T. D., Abraham, S., et al. 2021, ApJL, 913, L7. doi:10.3847/2041-8213/abe949

[155] IceCube Collaboration, Aartsen, M. G., Ackermann, M., et al. 2018, Science, 361, 147. doi:10.1126/science.aat2890

[156] Alcock, C., Farhi, E., & Olinto, A. 1986, ApJ, 310, 261. doi:10.1086/164679

[157] Bottacini, E., Böttcher, M., Pian, E., et al. 2016, ApJ, 832, 17. doi:10.3847/0004-637X/832/1/17

[158] Gao, S., Fedynitch, A., Winter, W., et al. 2019, Nature Astronomy, 3, 88. doi:10.1038/s41550-018-0610-1

[159] Reimer, A., Böttcher, M., & Buson, S. 2019, ApJ, 881, 46. doi:10.3847/1538-4357/ab2bff

[160] von Kienlin, A., Arend, N., & Lichti, G. G. 2001, Gamma-ray Bursts in the Afterglow Era, 427. doi:10.1007/10853853_118

[161] G.K. Skinner, 1984, Nuclear Instruments and Methods in Physics Research, 221, 33

[162] A.E. Bolotnikov et al., 2020, Nuclear Instruments and Methods, A954, 161036

CrossMark

Evidence for Low Kick Velocities among High-mass X-Ray Binaries in the Small Magellanic Cloud from the Spatial Correlation Function

Arash Bodaghee[1] , Vallia Antoniou[2,3,4] , Andreas Zezas[5] , John A. Tomsick[6] , Zachary Jordan[1], Brenton Jackson[1],
Ryan Agnew[1], Eric Frechette[1], Ann E. Hornschemeier[7,8], and Jérôme Rodriguez[9]

[1] Dept. of Chemistry, Physics and Astronomy, Georgia College and State University, Milledgeville, GA 31061, USA
[2] Dept. of Physics and Astronomy, Texas Tech University, Lubbock, TX 79409, USA
[3] Smithsonian Astrophysical Observatory, Cambridge, MA 02138, USA
[4] Harvard-Smithsonian Center for Astrophysics, Cambridge, MA 02138, USA
[5] Dept. of Physics, University of Crete, GR-71003 Heraklion, Greece
[6] Space Sciences Laboratory, University of California, Berkeley, CA 94720, USA
[7] NASA Goddard Space Flight Center, Greenbelt, MD 20771, USA
[8] Dept. of Physics and Astronomy, Johns Hopkins University, Baltimore, MD 21218, USA
[9] Lab. AIM, CEA/CNRS/Université Paris-Saclay, Université de Paris, CEA-Saclay F-91191 Gif-sur-Yvette, France

Abstract

We present the two-point cross-correlation function between high-mass X-ray binaries (HMXBs) in the Small Magellanic Cloud (SMC) and their likely birthplaces (OB associations: OBAs). This function compares the spatial correlation between the observed HMXB and OBA populations against mock catalogs in which the members are distributed randomly across the sky. A significant correlation ($\sim15\sigma$) is found for the HMXB and OBA populations when compared with a randomized catalog in which the OBAs are distributed uniformly over the SMC. A less significant correlation (4σ) is found for a randomized catalog of OBAs built with a bootstrap method. However, no significant correlation is detected when the randomized catalogs assume the form of a Gaussian ellipsoid or a distribution that reflects the star formation history from 40 Myr ago. Based on their observed distributions and assuming a range of migration timescales, we infer that the average value of the kick velocity inherited by an HMXB during the formation of its compact object is 2–34 km s^{-1}. This is considerably less than the value obtained for their counterparts in the Milky Way hinting that the galactic environment affecting stellar evolution plays a role in setting the average kick velocity of HMXBs.

1. Introduction

A high-mass X-ray binary (HMXB) is a system in which a compact object (usually a neutron star, sometimes a black hole) accretes wind material shed by a massive ($M \gtrsim 10\,M_\odot$) stellar companion. According to the mass−age relation for high-mass stars (Schaller et al. 1992), around 10 Myr is thought to elapse between stellar birth and supernova. This implies that HMXBs are young systems that do not have enough time to migrate far away from their birthplaces, i.e., OB associations (OBAs), which are loose collections of young, massive O-type and B-type stars. Thus, the observed locations of HMXBs serve to trace recently active sites of massive star formation in a galaxy (e.g., Grimm et al. 2002).

In a previous study, we assessed the degree of spatial correlation between the HMXB and OBA populations in the Milky Way (Bodaghee et al. 2012) by building the two-point spatial cross-correlation function (Peebles 1980; Landy & Szalay 1993). We found that the spatial distributions of the two populations were closely related, as expected. More importantly, we were able to use this correlation to derive average distances or durations for the HMXBs as they migrated away from their birthplaces over the past few million years. The migration is thought to be due to a combination of effects including recoil due to anisotropic mass loss from the primary to the secondary (Blaauw 1961), dynamical ejection and cluster outflows (Poveda et al. 1967; Pflamm-Altenburg &

Kroupa 2010), or natal kicks. In fact, this natal kick could allow the HMXB to reach a significant velocity if the supernova event that created the neutron star is asymmetrical (Shklovskii 1970). An example of an asymmetric supernova was seen by NuSTAR in SN1987A situated in the Large Magellanic Cloud (Boggs et al. 2015), although this object did not ultimately lead to an HMXB. The energy available for kicks depends on a number of factors internal to the system such as the mass ratio of the binary, magnetic fields, etc., but also on external factors, such as the metallicity, that affect the entire population.

Unfortunately, cases in which an HMXB can be linked back to its parent OBA, and its velocity measured, are rare and only possible for relatively nearby systems in the Milky Way (e.g., Mirabel et al. 2004). Thus, a statistical approach applied to these populations offers a way to estimate the average kick velocity of the sample and how much this value depends on the galactic environment in which these systems reside.

At a distance of 61 kpc (Hilditch et al. 2005), the Small Magellanic Cloud (SMC) is an irregular dwarf galaxy with a relatively large and active population of HMXBs (e.g., Liu et al. 2005) that are bright, easy to resolve, and with low intervening extinction (Zaritsky et al. 2002) and photoelectric absorption (Kalberla et al. 2005). The SMC underwent chemical and stellar evolutionary processes that led to disparities in its HMXB population compared with those of the Milky Way (e.g., Clark et al. 1978; Majid et al. 2004;
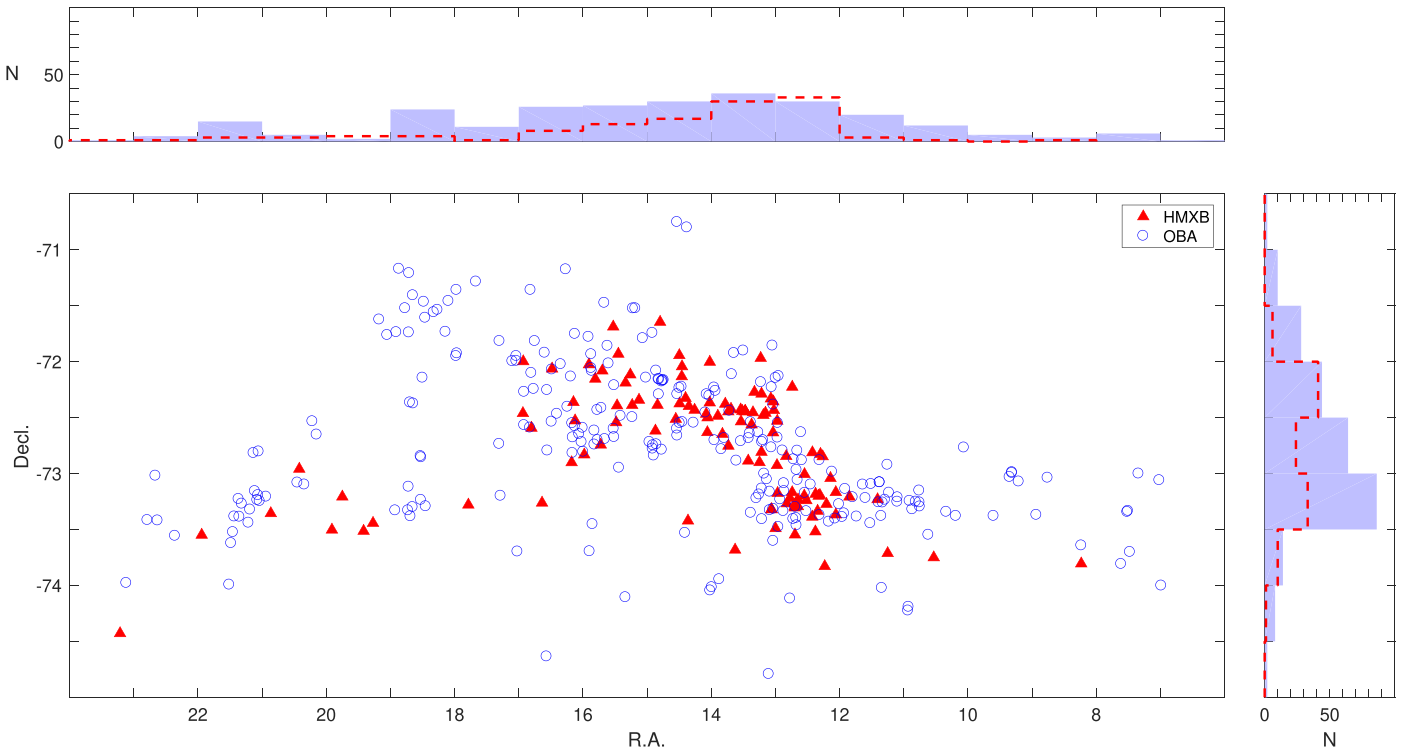
Figure 1. Spatial distributions are presented for objects belonging to the Small Magellanic Cloud that are considered in this study. High-mass X-ray binaries are shown as red triangles (115 HMXBs from Haberl & Sturm 2016), while the locations of known OB associations are represented by blue circles (283 OBAs from Bica et al. 2008). The histograms present the number of HMXBs (dashed red line) and observed OBAs (blue shaded region) over J2000.0 equatorial coordinates in degrees.

Dray 2006; Lehmer et al. 2010; Linden et al. 2010; Mineo et al. 2012; Fragos et al. 2013; Fornasini et al. 2020). The primary difference is that stars in the SMC feature a lower average metallicity than stars in our Galaxy (Luck et al. 1998; Antoniou & Zezas 2016). Another difference is that nearly all HMXBs in the SMC host Balmer emission line stars (so-called BEXBs; Coe et al. 2005; Antoniou et al. 2009; Haberl & Sturm 2016), while only two host supergiant OB stars (so-called SGXBs; Maravelias et al. 2014).

In the Milky Way, BEXBs are also the dominant subclass, but the percentage of SGXBs is an order of magnitude greater and continues to increase as new SGXBs are discovered (Walter et al. 2015, and references therein). This enhancement of HMXBs in the SMC (and BEXBs in particular) is attributed to a lower galactic metallicity (e.g., Linden et al. 2010; Kaaret et al. 2011; Basu-Zych et al. 2016) and a prolific episode of new star formation 40 Myr ago (Dray 2006; Antoniou et al. 2010). Remarkably, there are no confirmed HMXBs with black holes in the SMC, likely due to the preponderance of BEXBs (Zhang et al. 2004). The SMC offers a homogeneous population of HXMBs that can be compared with an HMXB population in the Milky Way that evolved under a different star formation history.

The goal of the present work is to generate the two-point spatial correlation function for the HMXB and OBA populations in the SMC, as was done previously for these populations in the Milky Way. Section 2 presents the source populations and the analysis methods including the generation of randomized source distributions. In Section 3, the main results are discussed and then summarized.

2. Data and Analysis Methods

2.1. Observed and Randomized Catalogs

Beginning with the list of 148 HMXB candidates in the catalog of Haberl & Sturm (2016), we exclude 27 objects whose HMXB classification is in doubt according to the catalog's authors. Of the remaining 121 confirmed or likely HMXBs, 6 objects are rejected due to being in the Magellanic Bridge. The range of R.A. for the final list of 115 HMXBs considered in this study is 6–24°. Within that range of R.A., there are 283 OBAs from the catalog of Bica et al. (2008), which will be referred to as the "observed OBA catalog."

Figure 1 presents the observed populations of HMXBs and OBAs as they are distributed within the boundaries of the sky region considered in this study. By eye, it is apparent that these populations are clustered together in space, as expected. The significance of any spatial clustering can be found by constructing the spatial correlation function. Essentially, this function takes the spatial distribution of the HMXB population and determines which provides a better match: the observed OBA catalog, or a mock OBA catalog in which the members are distributed randomly.

Four different mock catalogs were created, each containing 10^5 members whose sky coordinates were randomly generated according to some distribution function or resampling method. They are referred to as the "randomized OBA catalogs":

1. Homogeneous: the OBAs are placed randomly under the assumption of a uniform surface density.
2. Elliptical: an elliptical function is fit to the observed OBA catalog and parameters (center and foci; lengths and angles of the major and minor axes) corresponding to the 90% containment region are extracted. Then, we
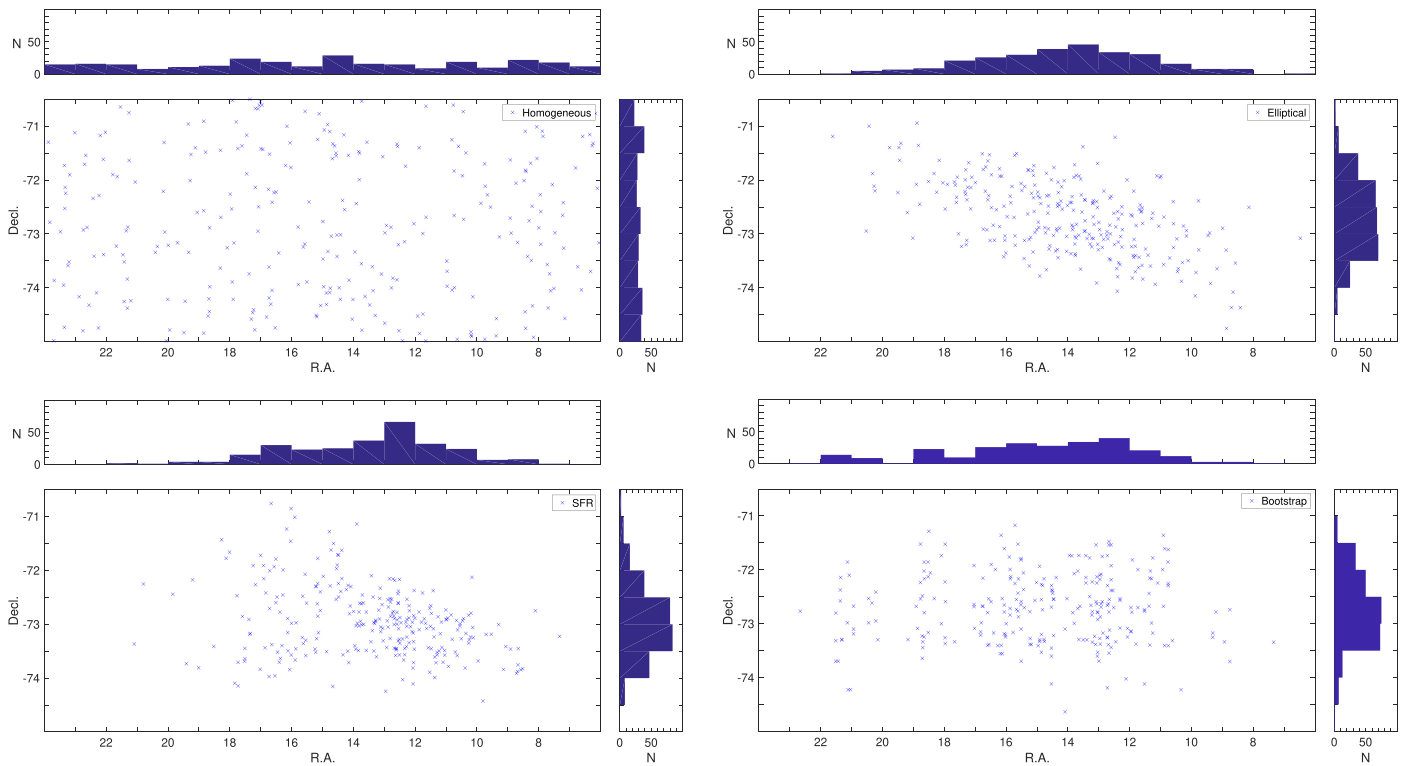
Figure 2. Example subsets of the four randomized OBA catalogs used in this work. Each of the main panels presents the same sky area as shown in Figure 1. Blue crosses represent 283 objects drawn at random (out of 10^5 members) from each randomized OBA catalog; clockwise from the upper left are Homogeneous, Elliptical, Bootstrap, and SFR.

randomly distribute OBAs across this ellipse according to a Gaussian profile; that is, the number of objects peaks at the ellipse's center and gradually decreases outward.

3. SFR: the OBAs are randomly placed with a surface density weighted to the star formation rate (SFR) of each region for the epoch corresponding to 40 Myr ago (Rubele et al. 2018), which Antoniou et al. (2010) cite as being the era from which the observed batch of HMXBs likely originates. We also used the SFR map of Harris & Zaritsky (2004), dividing the sky grid in the same way as these authors, then randomly placing OBAs according to the SFR for that epoch, and we found no significant differences in the results that are presented later.

4. Bootstrap: unlike the other randomized catalogs, where source coordinates were created based on an external constraint (e.g., mimicking the overall shape of the observed population), bootstrap sampling produces a randomized OBA catalog using only values found in the observed OBA catalog. New source coordinate pairs are generated by randomly assembling the R.A. value of one observed OBA with the decl. value of another. The same coordinate value, and even the same coordinate pair, may appear multiple times in the final catalog, while others might not appear at all. Bootstrap resampling, which is frequently used in spatial correlation studies of extragalactic surveys (e.g., Gilli et al. 2005; Meneux et al. 2009; Krumpe et al. 2010), serves as a comparison to the methods above where we assume a specific morphology for the population.

Examples of the four randomized OBA catalogs are shown in Figure 2. Figure 3 and Table 1 compare the range of

distances separating an HMXB and the nearest OBA belonging to the observed and randomized catalogs.

2.2. The Spatial Correlation Function ξ

Consider a member of Population 1 located in a volume element δV_1. The probability δP of finding a neighbor from Population 2 in a volume element δV_2 separated by a distance r is given by:

$$\delta P = n_1 n_2 [1 + \xi(r)] \delta V_1 \delta V_2$$

where the number densities of each population are listed as n_1 and n_2, and where $\xi(r)$ is the spatial (or two-point) correlation function. If $\xi = 0$, then the equation yields a uniform probability, and so the spatial correlation function essentially describes the probability in excess of Poisson. Peebles (1980) provide the following estimator for ξ:

$$\xi(r) = \frac{D_1 D_2}{D_1 R_2} - 1.$$

The subscripts (1) and (2) will refer to HMXBs and OBAs, respectively. A member drawn from an observed catalog is designated D for data, while a member of a population drawn from a randomized catalog is labeled R. When two letters are combined, it signifies the normalized number of pairs of such type within a given volume element. In other words, $D_1 D_2 \equiv n^2 N_{D_1 D_2}(r)$ represents the number of pairs combining an observed HMXB with an observed OBA within a volume element of radius r, while $D_1 R_2 \equiv n N_{D_1 R_2}(r)$ signifies the number of pairs combining an observed HMXB with an OBA from a randomized catalog. The ratio of random to observed data points is given by $n \equiv n_R / n_D$.
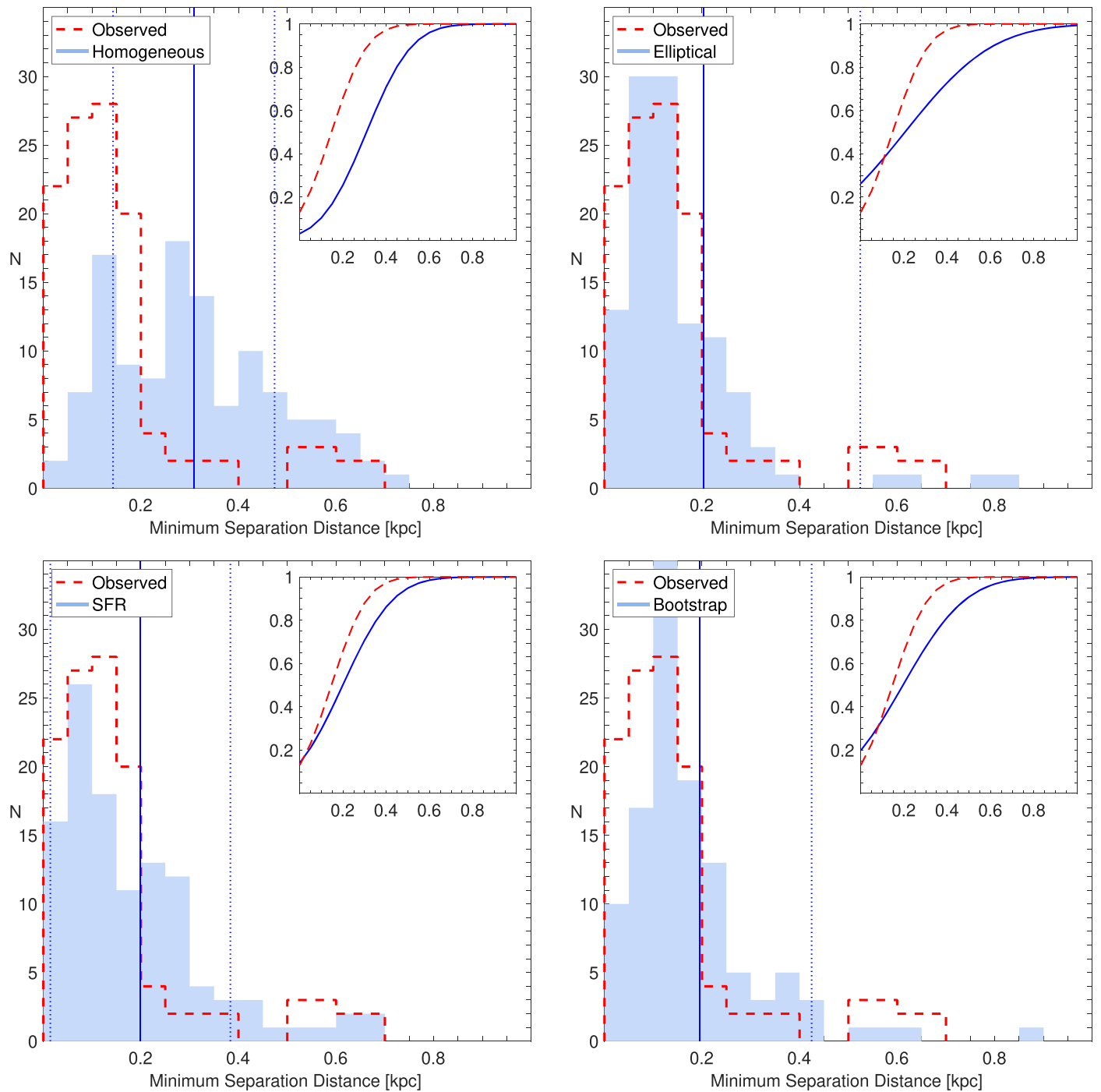
Figure 3. Distribution of distances between an HMXB and its nearest OBA drawn from either the observed catalog (dashed red line) or from a randomized catalog (blue shaded region). Clockwise from the upper left, the panels show the four randomized OBA catalogs: Homogeneous, Elliptical, Bootstrap, and SFR. The vertical solid and dotted lines indicate the mean and standard deviation from a Gaussian fit to the distribution. The inset panels feature the same data over the same x-axis but plotted as cumulative distribution functions.

Since we do not have reliable distance measurements for these objects, we assume that they are all located at the average SMC distance of 61 kpc. This means that distances between members of the populations, and any relative motion, are only considered along the direction tangent to our line of sight. So instead of volume elements, we use surface elements for spatial binning.

Around each HMXB, we draw 30 concentric annuli where each spatial bin has radial boundaries corresponding to $[r - dr/2, r + dr/2)$, and where dr is the spatial bin size of $0°.5$. This

angular scale corresponds to a physical distance of around 500 pc at the SMC distance. Different sizes were attempted for the spatial bins ($0°.3$, $0°.5$, and $1°.0$), but we settled on $0°.5$ since it was wide enough to permit enough counting statistics while also encompassing the average migration distance of 65 pc that was found by Coe (2005) for HMXBs in the SMC. Within each spatial bin, we count the number of OBAs drawn from the observed catalog ($D_1 D_2$) while keeping a tally of the members drawn from a randomized OBA catalog ($D_1 R_2$).

Table 1
Separation Distances (kpc) between HMXBs and OBAs

OBA Catalog		Mean Distance	Minimum Distance[a]
Observed	Total	3.62 ± 0.97	0.15 (0.13)
	Bar	2.56 ± 0.49	0.12 (0.09)
	Wing	6.40 ± 1.16	0.46 (0.18)
Randomized	Homogeneous	5.40 ± 0.64	0.31 (0.17)
	Elliptical	3.34 ± 1.20	0.20 (0.32)
	SFR	3.49 ± 1.30	0.20 (0.18)
	Bootstrap	3.34 ± 1.05	0.19 (0.23)

Note.
[a] This corresponds to the mean and standard deviation from a Gaussian fit to the histograms in Figure 3.

Table 2
First Five Eigenvalues of the Correlation Matrix of ξ

	Homogeneous	Elliptical	SFR	Bootstrap
λ_1	17.1570	21.1065	21.9915	18.7840
λ_2	6.6233	4.4770	4.1303	5.7872
λ_3	2.4948	1.4395	1.4877	1.5210
λ_4	1.3956	0.7997	0.4570	1.0844
λ_5	0.5331	0.3335	0.2356	0.4458

Counting in this manner for all HMXBs, we generate ξ in each spatial bin out to 15 kpc. To account for any unexpected spatial clustering or voids within the randomized catalog itself, we repeat the process $N = 10^4$ times (trials), where in each trial we select a new subset of OBAs from the randomized catalog. Each trial assumes an equal number of randomized OBAs as observed OBAs occupying equal sky areas, so $n = 1$ in the estimator. We thus obtain a mean value of ξ for each distance r from a given HMXB.

Essentially, if a given spatial bin contains as many D_1D_2 pairs as D_1R_2 pairs, then $\xi = 0$ for that radius, which means that the neighbor of a given HMXB is equally as likely to be drawn from the observed OBA catalog as it is from the randomized OBA catalog. However, if ξ is significantly greater than 0, which will be referred to as a "clustering signal," then OBAs near a given HMXB are more likely to be members of the observed (as opposed to the randomized) OBA catalog.

Landy & Szalay (1993) propose an alternate estimator of the spatial correlation function:

$$\xi(r) = (D_1D_2 - D_1R_2 - D_2R_1 + R_1R_2)\frac{1}{R_1R_2}.$$

In this function, the number counts within each spatial bin are also considered for HMXBs that are randomly distributed in the same manner as the OBAs. These terms appear as $D_2R_1 \equiv nN_{D_2R_1}(r)$ and $R_1R_2 \equiv N_{R_1R_2}(r)$. This accounts for any effects caused by the choice of survey boundaries or incompleteness in the observed populations. After ensuring the consistency of the results for both the Peebles (1980) and Landy & Szalay (1993) estimators of ξ, we elect to use the latter, whose variance is expected to be closer to Poissonian.

2.3. Error Analysis

Studies of the correlation function applied to cosmological surveys show that the uncertainty associated with one spatial bin of the survey is interdependent on the other bins (e.g., Ling et al. 1986; Bernstein 1994; Meneux et al. 2009; Norberg et al. 2009, and references therein). Furthermore, these authors show that the choice of randomization method will affect the uncertainty on ξ, whether internal methods are employed (e.g., the Bootstrap catalog), or whether external estimates are used (e.g., the Elliptical and SFR catalogs).

Errors calculated with internal methods can account for systematic biases, e.g., detection limits of the telescope, and observation strategies. Such biases are not accounted for in external methods where we make assumptions about the

underlying physical processes that created the distribution. That said, internal estimates can be hindered by the limited size of the original data set. Variances from bootstrapping can be larger by a factor of 2 or more compared with those of Poisson statistics, but they appropriately describe the correlation function at small distance scales, especially when oversampling (e.g., Norberg et al. 2009). Since our data are interdependent, including across spatial bins, we employ moving-block bootstrapping where overlapping blocks of varying length are resampled to create the Bootstrap catalog (Kunsch 1989; Loh 2008).

Therefore, additional tests are performed in order to better ascertain the uncertainty on ξ. For each randomization method, we determine the average ξ for each of the 30 spatial bins over all 10^4 trials. Then, we generate the 30×30 covariance matrix C whose elements are:

$$C_{ij} = \frac{1}{N-1}\sum_{k=1}^{N}(\xi_i^k - \bar{\xi}_i)(\xi_j^k - \bar{\xi}_j)$$

where $\bar{\xi}$ is the mean:

$$\bar{\xi}_i = \frac{1}{N}\sum_{k=1}^{N}\xi_i^k$$

and where ξ_i^k denotes the value of ξ in spatial bin i for trial k. Standard deviations on ξ are collected directly from the square root of the diagonal elements of the covariance matrix.

The correlation matrix R permits a direct check of the dependence of each of the 30 spatial bins on the other. Each element of the correlation matrix can be constructed according to:

$$R_{ij} = \frac{C_{ij}}{\sqrt{C_{ii}C_{jj}}}.$$

The elements of R, when given in terms of their absolute values, decrease gradually from 1 (full correlation) to 0 (no correlation) when moving away from the diagonal along the same row or column. As discussed in the next section, there remains significant bin-to-bin correlation off diagonal at distance scales of 5–15 kpc. We are interested primarily with clustering at small distance scales (i.e., within about 1 kpc), so this will not affect our conclusions.

Eigenvalues are gathered from each correlation matrix, and the first five components (of 30) are listed in Table 2. While the sum of the eigenvalues equals the dimension as expected, it is clear that the primary eigenvalue, and to a lesser extent the next four components, dominate the correlation matrix made with each randomization method.

As an additional test, we introduce perturbations to the data by moving each HMXB in either a random direction or toward the nearest OBA, and recalculate ξ in the normal manner. We show later that ξ remains stable to small-scale perturbations to
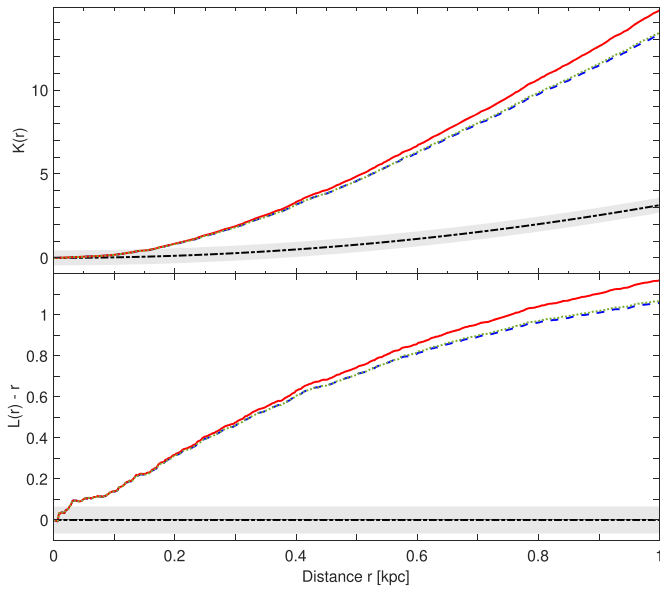
Figure 4. Ripley's K function (upper panel) and its associated L function (lower panel) are illustrated for cross-pair distances between observed HMXBs and OBAs, with isotropic (dashed blue curve), translational (solid red curve), and border (dotted green curve) corrections applied. The dotted–dashed curve refers to the Poisson expectation of πr^2 with the shaded region indicating the range of 10^3 simulations.

the data on the order of a few hundreds of parsecs of physical distance.

Finally, we applied Ripley's K (cross-)function to the observed HMXB and OBA catalogs (e.g., Feigelson & Babu 2012):

$$K_{12}(r) = (n_1 n_2 A)^{-1} \sum_i \sum_j w(1_i, 2_j) I(d_{1_i, 2_j} < r).$$

As before, the labels 1 and 2 refer to HMXBs and OBAs, respectively, with their number densities given by n_1 and n_2 in the survey area A. The term $d_{1_i, 2_j}$ is the distance between the ith HMXB and the jth OBA. The indicator function I has a value of 1 if this distance is within a circle of radius r and 0 otherwise. To include edge corrections, the term $w(1_i, 2_j)$ represents the fraction of this circle's circumference that resides within A. If the HMXB and OBA populations are spatially independent, then we would expect $K_{12}(r) = \pi r^2$. An alternate form is the L (cross-)function:

$$L_{12}(r) = \sqrt{\frac{K_{12}(r)}{\pi}}.$$

When the distance r is subtracted from it, the L function conveniently reduces to 0 under spatial independence. Both functions show significant departure from the values expected for complete spatial randomness (Figure 4). This strongly suggests spatial clustering between the HMXB and OBA populations for pair counts in circular areas whose radii are greater than about 0.1–0.2 kpc.

Unless specified otherwise, results in this work are cited at 90% confidence.

3. Results and Discussion

3.1. Spatial Clustering

Figure 5 presents the spatial correlation function ξ as a function of the distance r from a given HMXB, for each of the

four randomized OBA catalogs. In all four cases, ξ was consistent with 0 at large distances from a given HMXB ($r \gtrsim 5$ kpc). This is expected since sky regions far from a given HMXB should contain equivalent numbers of OBAs drawn from the observed catalog as from the randomized catalog.

As one approaches a given HMXB ($r \lesssim 5$ kpc), ξ deviates significantly from 0 when the randomized OBA catalog follows a homogeneous distribution (upper left panel of Figure 5). The spatial correlation function is significantly greater than 0 for distances up to 3 kpc, with a peak of 15σ for distances less than 0.5 kpc from a given HMXB. The Homogeneous catalog has a distribution that is Poissonian by design, so this means there is an overabundance of observed OBAs in close proximity to an HMXB.

In other words, the observed OBA catalog offers a better match to the HMXBs than would be expected from a random distribution. This is evidence of spatial clustering, which reinforces the link between OBAs and HMXBs. This clustering was previously established for smaller samples in the SMC by, e.g., Coe (2005) and Antoniou et al. (2010), based on the minimum separations between individual members of the observed populations as shown in Figure 3 and Table 1. However, this is the first time that the clustering is confirmed with the spatial correlation function and it does not require us to assume that a given HMXB is linked with the nearest OBA.

Randomizing the OBA catalog to follow an Elliptical distribution yields an ξ that remains consistent with 0 for all distances from a given HMXB, with an insignificant (2σ) uptick at the shortest distances (upper right panel of Figure 5). Since the spatial correlation function does not find significant clustering at any distance scale, this suggests that the Elliptical OBA catalog is a good approximation of the observed distribution of OBAs. This is not surprising given that this model's parameters were based on a fit to the observed OBA catalog.

When the randomization profile is based on mimicking the SFR of the SMC, the ξ that results has values that are consistent with 0 for all distances from a given HMXB, with a low significance (3σ) deviation from 0 in the first spatial bin (lower left panel of Figure 5). As with the Elliptical catalog, the overall shape of the SFR catalog appears to be a suitable proxy for that of the observed OBA catalog. These results imply that the actual locations of the randomized OBAs in the SFR catalog do not matter as much as does the overall shape of the distribution. Members of the SFR catalog could change their coordinates, which they do change multiple times over all the trials, but as long as they are placed according to a number density that is proportional to the star formation rate, then the spatial correlation function cannot tell the difference between the SFR catalog and the observed OBA catalog. Taken together, this suggests that places where massive stars are forming today, i.e., what we call the observed OBA catalog, are essentially the same as the regions of the SMC that featured a peak outburst of star formation 40 Myr ago (Antoniou et al. 2010; Antoniou & Zezas 2016).

The Bootstrap catalog generates an ξ function with a small, but significant (4σ), clustering signal in the first spatial bin (lower right panel of Figure 5). The clustering signal remains above 3σ in the first bin even if the variance is increased by 50%.

In summary, there is a strong spatial link between observed HMXBs and observed OBAs as attested by the ξ made with the
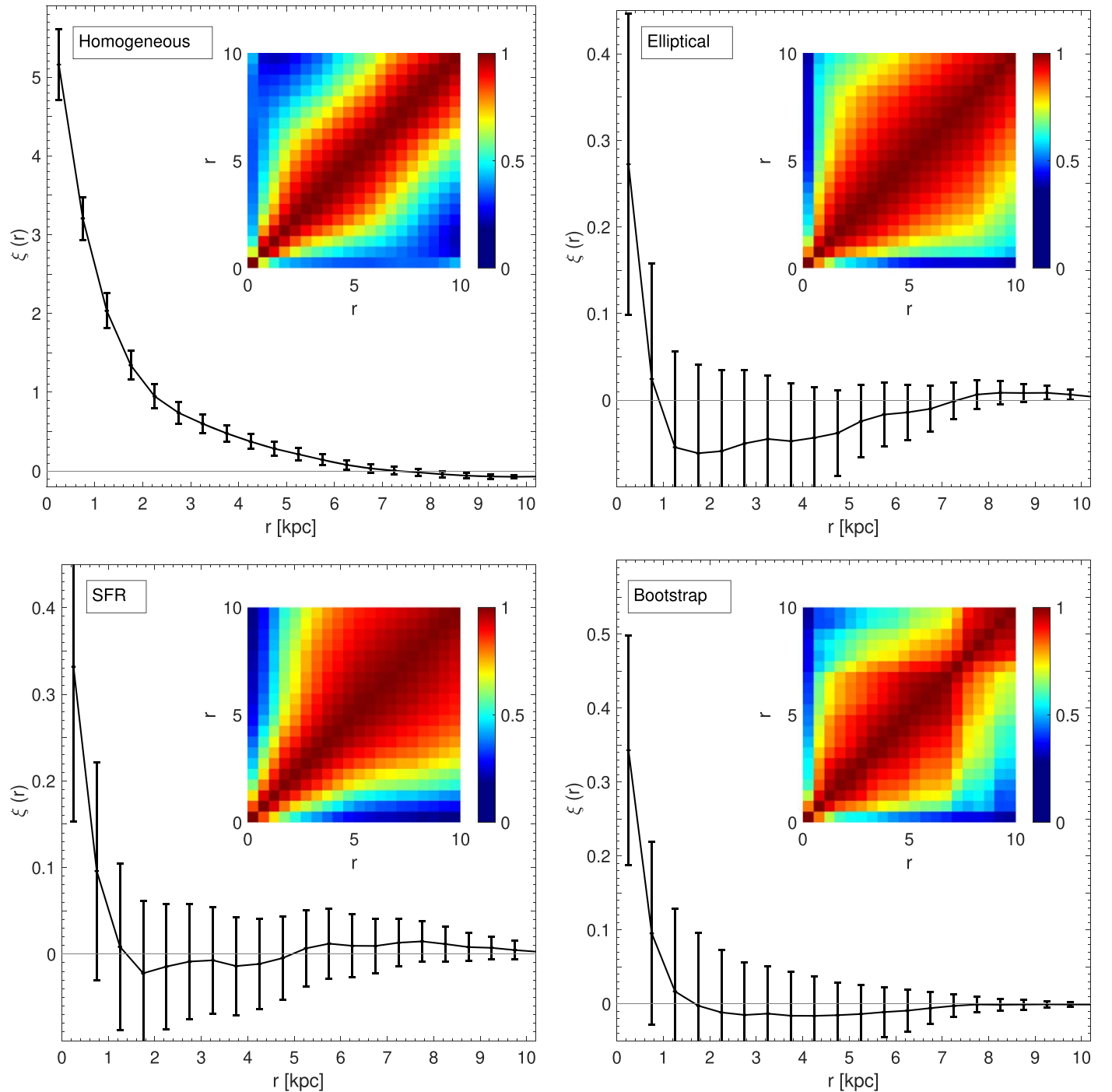
Figure 5. Spatial correlation functions ξ derived by comparing HMXBs to the observed OBA population and to one of four randomized OBA catalogs, where, clockwise from the upper left, the panels show distributions corresponding to Homogeneous, Elliptical, Bootstrap, and SFR. The inset in each panel shows the correlation matrix for ξ whose eigenvalues are listed in Table 2.

Homogeneous catalog, and it is of low significance compared with the Bootstrap catalog, and possibly with the SFR Catalog. The spatial correlation functions made with the Elliptical and SFR catalogs do not show any significant clustering, which is not surprising given that these catalogs are based on fitting the observed OBA distribution in some way.

Clustering between the observed HMXB and OBA populations takes on three visible forms: it can be pair-wise whereby an HMXB is found within a few tens or, at most, a few hundred parsecs from a neighboring OBA (this is the case for a subset of

the HMXBs); it can be group-wise whereby a small group of HMXBs is found within a few kiloparsecs of a group of OBAs; and it can be global meaning that the overall morphologies of the populations are compatible. Using the Homogeneous catalog, the spatial correlation function shows evidence of pair-wise and group-wise clustering with the signal remaining significant to 2–3 kpc. With the Elliptical and SFR catalogs, there is global compatibility, and even some group-wise clustering, but there does not appear to be enough pair-wise clustering to produce a significant signal. If the clustering

Figure 6. Values for the spatial correlation function ξ (with 3σ error bars) as a function of the migration timescale for small distances from an HMXB ($r \leqslant 0.5$ kpc). Each HMXB was moved in a random direction at some velocity (crosses, triangles, and circles denote 5, 20, and 35 km s^{-1}, respectively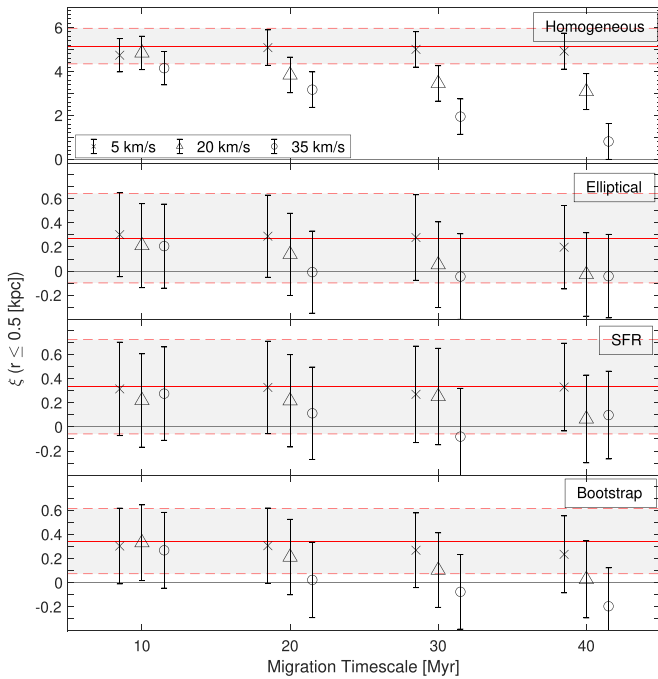) during timescales of 10, 20, 30, and 40 Myr. The original, unperturbed data ($v = 0$ km s^{-1}) is shown as a solid red line, while the dashed red lines represent 3σ confidence levels (shaded in gray to denote the boundaries).

Figure 7. Same as Figure 6, but in this case, each HMXB is moved in the direction of its nearest OBA.

signal found with the Bootstrap catalog is real, then it could suggest some pair-wise clustering in addition to some group-wise clustering and global similarity.

To test the degree to which the pair-wise and group-wise clustering influence the correlation, each HMXB was displaced in a random direction assuming some velocity (5, 20, and 35 km s^{-1}) and some timescale (10, 20, 30, and 40 Myr). Averaging ξ over all trials leads to the results shown in Figure 6. Only ξ from the closest region around a given HMXB is shown ($r \leqslant 0.5$ kpc). The figure illustrates the stability of the spatial correlation function's values (indicated by the horizontal dashed lines showing the 3σ confidence boundaries) to small perturbations of the data (represented by the symbols). In nearly all cases, the perturbed and unperturbed ξ values were statistically consistent with each other. The only exceptions were for high velocities ($v = 20$ or 35 km s^{-1}) and long timescales ($t = 30$ and 40 Myr) where the significance of the clustering signal decreases for the Homogeneous catalog. Essentially, these perturbations broaden the HMXB distribution on the sky. This enhanced scatter makes the HMXB distribution more similar to the Homogeneous catalog, which leads to a decrease in the value of ξ.

In an alternate test, we moved each HMXB toward its nearest OBA under the same assumptions of velocity and timescale as before, and generated ξ in the usual way over multiple trials. By moving the observed populations closer together, the clustering significance is expected to increase if pair-wise clustering dominates over group-wise or global clustering. However, the clustering signal did not change in a significant way for any randomized catalog (Figure 7). Taken with the result of the previous test, where the HMXBs were moved around randomly, this suggests that the spatial
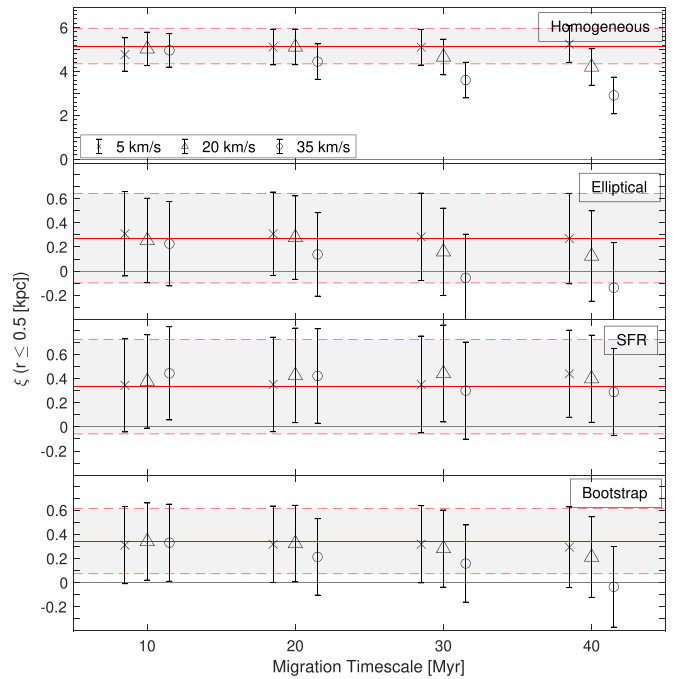
correlation function gets its significance mostly from group-wise and global clustering, with pair-wise clustering being a less important factor.

Structurally, the SMC can be divided into two regions: the Bar, which hosts the majority of the dwarf galaxy's massive stars and HMXBs, and the Wing, which roughly corresponds to the sky area in Figure 1 having R. A. $\gtrsim 18°$ and decl. $\lesssim -72°.5$ (see also Rubele et al. 2018). Oey et al. (2018) showed that objects in these regions can be distinguished kinematically with the Wing moving away from the Bar and toward the LMC at ~ 64 km s^{-1}. The clustering signal remains at a significance of 16σ and 4σ for the Homogeneous and Bootstrap catalogs, respectively, when the correlation function is limited to the 106 HMXBs in the Bar. The correlation function applied only to the 9 HMXBs in the Wing generates error bars that are too large to draw meaningful conclusions. In the Bar, the average minimum distance between an HMXB and an OBA is 120 ± 90 pc, which is a factor 2–4 less than in the Wing (450 ± 180 pc).

3.2. Constraints on Kick Velocities

The main reason to study the spatial clustering of HMXB and OBA populations is to determine the magnitude of the natal kick of the HMXB as it moves away from its birthplace. Migration of this magnitude is not observable on human timescales, so we do not know which OBA is the birthplace of each HMXB, and it is not necessarily the closest one on the sky. However, knowing how clustered the two populations are can tell us the typical migration distance. If we have an idea of how old these objects are, we can use this distance to determine a kick velocity. Gravitational ejection, cluster outflows, recoil due to anisotropic mass transfer, and asymmetric supernovae can impart velocity to a young HMXB displacing it from its parent cluster (Blaauw 1961; Poveda et al. 1967; Shklovskii 1970; Pflamm-Altenburg & Kroupa 2010).

Based on a Gaussian fit to the distance distributions (Figure 3 and Table 1), we find that the distance separating

an HMXB from the nearest observed OBA is 150 pc, on average, with a 90% confidence upper limit of 300 pc. These minimum distances are even smaller in the Bar (120 ± 90 pc). Twenty percent of the HMXBs in the sample have a minimum distance below 50 pc, with the smallest values on the order of 10 pc. This sets a lower limit on the migration distance. These values are consistent with that of Coe (2005), who found 65 pc from a sample of 17 HMXBs.

Among these minimum distances, the highest values are in the range of 500–700 pc. We can compare this with the value given by the spatial correlation function, which is designated by the largest radius for which ξ remains significantly greater than 0. Using the Homogeneous catalog, the clustering signal is significant out to a distance of 2–3 kpc from a given HMXB, which is equivalent to $\sim$2–3° on the sky. This represents an unrealistically large value for a typical migration distance. When using the Bootstrap catalog, the clustering signal is significant in the first bin only, which suggests a maximum migration distance of $\sim$500 pc, consistent with the value from the distance distribution. This sets an upper limit on the migration distance, and so the range of distances separating an HMXB from a neighboring OBA is $\sim$10–700 pc with a mean of 150 pc.

Around 40 Myr ago, the SMC underwent a particularly intense episode of star formation which produced dozens of massive stellar binaries per Myr and per arcmin squared (Dray 2006; Antoniou et al. 2010). Depending on the initial masses of the stellar binary, another 5–20 Myr are needed for the system to evolve into an HMXB that kicks itself out of its OBA (Savonije & van den Heuvel 1977; Belczynski et al. 2008). This sets theoretical lower and upper bounds on the migration timescale of 20–35 Myr.

These timescales lead to kick velocities of 2–34 km s^{-1} over the range of minimum distances found here. Since this is purely the transverse velocity component, the true velocity could be twice as large, on average. This agrees with estimates of the kick velocity in HMXBs from the SMC found by Coe (2005), Antoniou et al. (2009, 2010), and Oey et al. (2018) with smaller samples, and it is consistent with the prediction of 15 ± 6 km s^{-1} for BEXBs given by van den Heuvel et al. (2000). It also agrees with the mean transverse velocity of 11.3 ± 6.7 km s^{-1} that was found for 13 Galactic BEXBs in the Hipparcos catalog (Chevalier & Ilovaisky 1998). Binary systems that survive the supernova phase to later remain bound as an HMXB tend to have low velocities that are attributable to natal kicks, whereas large migration velocities are acquired from the gravitational potential energy of the cluster. The average velocity that we find is lower than expected from cluster ejection where simulations show velocities over 80 km s^{-1} with rare cases reaching several hundred km s^{-1} (Perets & Šubr 2012).

More than half of the HMXBs in the SMC have a kick velocity that is significantly less than that of their counterparts in the Milky Way, where the average velocity was found to be 100 ± 50 km s^{-1} at 90% confidence (Bodaghee et al. 2012). Accepting at face value the maximum migration distance of 2–3 kpc from the clustering signal of the Homogeneous catalog, this returns kick velocities of 50–150 km s^{-1} that are in line with velocities of HMXBs in the Milky Way. Yet these would be the most extreme cases and are not representative of the majority.

It is possible to derive kick values that are more consistent with those of the Milky Way if one considers the average HMXB lifetime to be much lower (e.g., at 10 Myr). A factor of 4 reduction in average lifetime corresponds to a factor of 4 increase in the kick velocity, and so the average kick velocity of HMXBs in the SMC will be consistent (within the errors) with those of the Milky Way only if the HMXBs are $\lesssim$10 Myr old. However, this would be too short a timescale for stellar evolution models and it is not consistent with the expectation that the majority of these systems are by-products of that starburst episode from 40 Myr ago.

Thus, we find that HMXBs in the SMC are migrating less quickly than those of the Milky Way. In our Galaxy, the known HMXB population is nearly evenly split between the classes of BEXBs and SGXBs (Walter et al. 2015; Kretschmar et al. 2019). In the SMC, the HMXB population is almost exclusively composed of BEXBs (113/115). van den Heuvel et al. (2000) showed that BEXBs have kick velocities that are around 3 times lower than those of SGXBs, though there was no notable difference in how these classes were clustered with OBAs in the Milky Way (Bodaghee et al. 2012). Using this velocity factor under a hypothetical scenario in which the SMC population is evenly split between BEXBs and SGXBs, then only the fastest systems in the SMC (70 km s^{-1}) would overlap with the lower bound of the Milky Way population. So some other effect must be responsible for constraining the average velocity of HMXBs in the SMC.

It is known that the lower average metallicity of stars in the SMC led to a preponderance of BEXBs over SGXBs, particularly those with low kick velocities (e.g., Linden et al. 2009, 2010; Antoniou et al. 2010; Kaaret et al. 2011; Basu-Zych et al. 2016). At lower metallicity, a higher fraction of electron-capture supernovae is expected, and this disproportionately generates BEXBs having low values for the kick velocity ($\lesssim$50 km s^{-1}). This effect, cited by Antoniou & Zezas (2016) to explain the lower velocities in the SMC compared with the LMC, is still present with 43 additional HMXBs in this work. In a recent study (Oey et al. 2018), 15 SMC HMXBs showed relatively little dispersion in their mean velocity of 17 km s^{-1} compared with noncompact binary systems, which suggests the former are the product of less energetic supernova kicks.

An alternative explanation for the low average kick value is that some of the HMXBs in the SMC harbor black holes whose formation via direct collapse failed to produce a natal kick (Belczynski 2020). As of this study, no black hole has ever been confirmed among the HMXBs in the SMC. Assuming that the nonpulsating HMXBs in the SMC all host black holes, they would constitute a minority of the population, so this process has a small or negligible impact on the average kick that we measure for the whole population.

4. Summary and Conclusions

In this study, we generated the first two-point cross-correlation function between HMXBs and OBAs belonging to the SMC. In order to assess the spatial distributions of these related populations, we built comparison catalogs in which the systems were distributed in a random fashion. Four catalogs with randomized distributions were considered: a homogeneous one, a Gaussian ellipsoid, a distribution that mimics the recent star formation history of this galaxy, and a bootstrap resampling.

The spatial distributions of the HMXB and OBA populations were found to be significantly correlated when compared with a randomized catalog in which the systems are spread homogeneously across the field (15σ), or when following bootstrap resampling (4σ). This reinforces the link expected between the observed HMXB and OBA populations. However, no correlation was seen when the randomized catalogs assume the Elliptical and SFR distributions. This is not surprising since these catalogs were made by fitting some characteristic of the observed population.

Our results indicate that in the SMC, an HMXB inherits an average natal kick velocity of 2–34 km s^{-1}, which is consistent with values cited in the literature. This is considerably less than the average kick velocity of HMXBs in the LMC and Milky Way. One factor driving this discrepancy is that BEXBs, which inherit smaller average kick velocities than do SGXBs, are far more common among the HMXBs in the SMC. This is due to the lower average metallicity in the SMC, which favors the creation of BEXBs over SGXBs. This lower average metallicity also contributes to the discrepancy by leading to a higher probability of electron-capture supernovae, which produce less energetic kicks. Thus, the galactic environment plays a role in setting the natal kick, which is then perceived as smaller migration velocities in the observed HMXB population.

ORCID iDs

Arash Bodaghee https://orcid.org/0000-0002-7315-3732
Vallia Antoniou https://orcid.org/0000-0001-7539-1593
Andreas Zezas https://orcid.org/0000-0001-8952-676X
John A. Tomsick https://orcid.org/0000-0001-5506-9855
Jérôme Rodriguez https://orcid.org/0000-0002-4151-4468

References

Antoniou, V., & Zezas, A. 2016, MNRAS, 459, 528
Antoniou, V., Zezas, A., Hatzidimitriou, D., & Kalogera, V. 2010, ApJL, 716, L140
Antoniou, V., Zezas, A., Hatzidimitriou, D., & McDowell, J. C. 2009, ApJ, 697, 1695
Basu-Zych, A. R., Lehmer, B., Fragos, T., et al. 2016, ApJ, 818, 140
Belczynski, K. 2020, ApJL, 905, L15
Belczynski, K., Kalogera, V., Rasio, F. A., et al. 2008, ApJS, 174, 223
Bernstein, G. M. 1994, ApJ, 424, 569
Bica, E., Bonatto, C., Dutra, C. M., & Santos, J. F. C. 2008, MNRAS, 389, 678
Blaauw, A. 1961, BAN, 15, 265
Bodaghee, A., Tomsick, J. A., Rodriguez, J., & James, J. B. 2012, ApJ, 744, 108
Boggs, S. E., Harrison, F. A., Miyasaka, H., et al. 2015, Sci, 348, 670
Chevalier, C., & Ilovaisky, S. A. 1998, A&A, 330, 201
Clark, G., Doxsey, R., Li, F., Jernigan, J. G., & van Paradijs, J. 1978, ApJL, 221, L37
Coe, M. J. 2005, MNRAS, 358, 1379
Coe, M. J., Edge, W. R. T., Galache, J. L., & McBride, V. A. 2005, MNRAS, 356, 502
Dray, L. M. 2006, MNRAS, 370, 2079
Feigelson, E. D., & Babu, G. J. 2012, Modern Statistical Methods for Astronomy (Cambridge: Cambridge Univ. Press)
Fornasini, F. M., Civano, F., & Suh, H. 2020, MNRAS, 495, 771
Fragos, T., Lehmer, B., Tremmel, M., et al. 2013, ApJ, 764, 41
Gilli, R., Daddi, E., Zamorani, G., et al. 2005, A&A, 430, 811
Grimm, H.-J., Gilfanov, M., & Sunyaev, R. 2002, A&A, 391, 923
Haberl, F., & Sturm, R. 2016, A&A, 586, A81
Harris, J., & Zaritsky, D. 2004, AJ, 127, 1531
Hilditch, R. W., Howarth, I. D., & Harries, T. J. 2005, MNRAS, 357, 304
Kaaret, P., Schmitt, J., & Gorski, M. 2011, ApJ, 741, 10
Kalberla, P. M. W., Burton, W. B., Hartmann, D., et al. 2005, A&A, 440, 775
Kretschmar, P., Fürst, F., Sidoli, L., et al. 2019, NewAR, 86, 101546
Krumpe, M., Miyaji, T., & Coil, A. L. 2010, ApJ, 713, 558
Kunsch, H. R. 1989, AnSta, 17, 1217
Landy, S. D., & Szalay, A. S. 1993, ApJ, 412, 64
Lehmer, B. D., Alexander, D. M., Bauer, F. E., et al. 2010, ApJ, 724, 559
Linden, T., Kalogera, V., Sepinsky, J. F., et al. 2010, ApJ, 725, 1984
Linden, T., Sepinsky, J. F., Kalogera, V., & Belczynski, K. 2009, ApJ, 699, 1573
Ling, E. N., Frenk, C. S., & Barrow, J. D. 1986, MNRAS, 223, 21P
Liu, Q. Z., van Paradijs, J., & van den Heuvel, E. P. J. 2005, A&A, 442, 1135
Loh, J. M. 2008, ApJ, 681, 726
Luck, R. E., Moffett, T. J., Barnes, Thomas, G., & Gieren, W. P., I. 1998, AJ, 115, 605
Majid, W. A., Lamb, R. C., & Macomb, D. J. 2004, ApJ, 609, 133
Maravelias, G., Zezas, A., Antoniou, V., & Hatzidimitriou, D. 2014, MNRAS, 438, 2005
Meneux, B., Guzzo, L., de la Torre, S., et al. 2009, A&A, 505, 463
Mineo, S., Gilfanov, M., & Sunyaev, R. 2012, MNRAS, 419, 2095
Mirabel, I. F., Rodrigues, I., & Liu, Q. Z. 2004, A&A, 422, L29
Norberg, P., Baugh, C. M., Gaztañaga, E., & Croton, D. J. 2009, MNRAS, 396, 19
Oey, M. S., Dorigo Jones, J., Castro, N., et al. 2018, ApJL, 867, L8
Peebles, P. J. E. 1980, The Large-scale Structure of the Universe (Princeton, NJ: Princeton Univ. Press), 435
Perets, H. B., & Šubr, L. 2012, ApJ, 751, 133
Pflamm-Altenburg, J., & Kroupa, P. 2010, MNRAS, 404, 1564
Poveda, A., Ruiz, J., & Allen, C. 1967, BOTT, 4, 86
Rubele, S., Pastorelli, G., Girardi, L., et al. 2018, MNRAS, 478, 5017
Savonije, G. J., & van den Heuvel, E. P. J. 1977, ApJL, 214, L19
Schaller, G., Schaerer, D., Meynet, G., & Maeder, A. 1992, A&AS, 96, 269
Shklovskii, I. S. 1970, SvA, 13, 562
van den Heuvel, E. P. J., Portegies Zwart, S. F., Bhattacharya, D., & Kaper, L. 2000, A&A, 364, 563
Walter, R., Lutovinov, A. A., Bozzo, E., & Tsygankov, S. S. 2015, A&ARv, 23, 2
Zaritsky, D., Harris, J., Thompson, I. B., Grebel, E. K., & Massey, P. 2002, AJ, 123, 855
Zhang, F., Li, X. D., & Wang, Z. R. 2004, ApJ, 603, 663

15 years of galactic surveys and hard X-ray background measurements

Roman A. Krivonos [a,*], Antony J. Bird [b], Eugene M. Churazov [a,c], John A. Tomsick [d], Angela Bazzano [e], Volker Beckmann [f], Guillaume Bélanger [g], Arash Bodaghee [h], Sylvain Chaty [i,j], Erik Kuulkers [k], Alexander Lutovinov [a], Angela Malizia [l], Nicola Masetti [l,m], Ilya A. Mereminskiy [a], Rashid Sunyaev [a,c], Sergey S. Tsygankov [n,a], Pietro Ubertini [e], Christoph Winkler [k]

[a] Space Research Institute (IKI), Profsoyuznaya 84/32, Moscow 117997, Russia
[b] School of Physics and Astronomy, University of Southampton, SO17 1BJ, UK
[c] Max-Planck-Institut für Astrophysik (MPA), Karl-Schwarzschild-Strasse 1, Garching 85741, Germany
[d] Space Sciences Laboratory, 7 Gauss Way, University of California, Berkeley, CA 94720-7450, USA
[e] INAF - Istituto di Astrofisica e Planetologia Spaziali, Via Fosso del Cavaliere 100, Roma, I-00133, Italy
[f] Ministère de l'Enseignement supérieur, de la Recherche et de l'Innovation, 1 rue Descartes, 75005 Paris, France
[g] European Space Astronomy Centre - ESA/ESAC, Villanueva de la Cañada, Madrid, Spain
[h] Georgia College & State University, CBX 82, Milledgeville, GA 31061, USA
[i] AIM, CEA, CNRS, Université Paris-Saclay, Université de Paris, F-91191 Gif-sur-Yvette, France
[j] Université de Paris, CNRS, Astroparticule et Cosmologie, F-75006 Paris, France
[k] ESA-ESTEC, Research and Scientific Support Dept., Keplerlaan 1, 2201 AZ, Noordwijk, The Netherlands
[l] INAF - Osservatorio di Astrofisica e Scienza dello Spazio, via Piero Gobetti 101, I-40129, Bologna, Italy
[m] Departamento de Ciencias Físicas, Universidad Andrés Bello, Fernández Concha 700, Las Condes, Santiago, Chile
[n] Department of Physics and Astronomy, FI-20014 University of Turku, Finland

ARTICLE INFO

ABSTRACT

The *INTEGRAL* hard X-ray surveys have proven to be of fundamental importance. *INTEGRAL* has mapped the Galactic plane with its large field of view and excellent sensitivity. Such hard X-ray snapshots of the whole Milky Way on a time scale of a year are beyond the capabilities of past and current narrow-FOV grazing incidence X-ray telescopes. By expanding the *INTEGRAL* X-ray survey into shorter timescales, a productive search for transient X-ray emitters was made possible. In more than fifteen years of operation, the *INTEGRAL* observatory has given us a sharper view of the hard X-ray sky, and provided the triggers for many follow-up campaigns from radio frequencies to gamma-rays. In addition to conducting a census of hard X-ray sources across the entire sky, *INTEGRAL* has carried out, through Earth occultation manoeuvres, unique observations of the large-scale cosmic X-ray background, which will without question be included in the annals of X-ray astronomy as one of the mission's most salient contribution to our understanding of the hard X-ray sky.

1. Introduction

A wide variety of astrophysical phenomena cannot be sufficiently well investigated via observations of individual sources, but requires instead a systematic approach based on large statistical samples. The last few decades of X-ray astronomy have provided us with great opportunities for studies of the populations of compact X-ray sources (white dwarfs, neutron stars, black holes) in our Galaxy and beyond, with the use of new long-lasting facilities.

Two powerful and currently active hard X-ray missions, ESA's *IN-TEGRAL* observatory (Winkler et al., 2003a) and NASA's Neil Gehrels Swift Observatory (Gehrels et al., 2004) are performing some of the deepest and widest serendipitous X-ray surveys ever undertaken at

energies $E > 20$ keV. In contrast to *Swift*, with a nearly uniform all-sky survey, which is especially useful for studies of active galactic nuclei (AGN; Tueller et al., 2010; Cusumano et al., 2010; Ajello et al., 2012; Baumgartner et al., 2013; Oh et al., 2018), the *INTEGRAL* observatory provides a sky survey with exposures that are deeper in the Galactic plane (GP) and Galactic Centre (GC) regions and with higher angular resolution, which is essential in these crowded regions. It allowed to study in depth different populations of galactic binary systems, such as low- and high-mass X-ray binaries, cataclysmic variables, symbiotic systems, etc. (see, e.g., Revnivtsev et al., 2008; Bodaghee et al., 2012; Lutovinov et al., 2005a, 2013b; Kretschmar et al., 2019). This makes the *Swift* and *INTEGRAL* surveys complementary to each

---

* Corresponding author.
  E-mail address: krivonos@cosmos.ru (R.A. Krivonos).

other. In this review we concentrate on the valuable contribution of the *INTEGRAL* observatory to the surveying of the hard X-ray sky over the last 15 years.

The *INTEGRAL* observatory, selected as the M2 mission within ESA's Horizon 2000 program, has been successfully operating in orbit since its launch in 2002. Due to the high sensitivity and relatively good angular resolution of its instruments, in particular the coded-mask telescope IBIS (Ubertini et al., 2003), surveying the sky in hard X-rays is one of the mission primary goals.

2. *INTEGRAL* hard X-ray surveys

2.1. Observations before INTEGRAL

Since the beginning of X-ray astronomy many X-ray surveys have been successfully carried out with the aim of both discovering new types of X-ray emitters and to investigate the nature of the Cosmic X-ray Background. A brief review of the hard X-ray surveys before the *INTEGRAL* era is presented hereafter. A more detailed overview of the Hard X-ray/Soft gamma-ray experiments and missions can be found in Cavallari and Frontera (2017).

Markert et al. (1979) described observations of the cosmic X-ray sky performed by the MIT 1–40 keV X-ray detectors on the OSO 7 satellite between 1971 October and 1973 May. The authors made intensity determinations or upper limits for 3rd Uhuru (Giacconi et al., 1974) and OSO 7 (Markert et al., 1976, 1977) catalogued sources in different energy bands, including the 15–40 keV range.

Uhuru, also known as the Small Astronomical Satellite 1 (SAS-1) provided the first comprehensive and uniform all sky survey with a sensitivity of 10^{-3} the Crab intensity. Forman et al. (1978) presented the list of detected 339 X-ray sources with measured 2–6 keV intensities. The major classes of identified objects included binary stellar systems, supernova remnants, Seyfert galaxies and clusters of galaxies.

The first ever attempt to survey the sky at high energies (26–1200 keV) was performed in 1974–1979 with the Sky Survey Instrument on *Ariel V* (Coe et al., 1982), which provided the first galactic Log*N*-Log*S* relation above 100 keV.

Skinner et al. (1987b) reported observations of the Galactic Centre made with a coded mask X-ray telescope flown on the Spacelab 2 mission, providing the first images of the GC in high-energy X-rays up to 30 keV.

In the hard X-ray range (2.8–30 keV), an all-sky survey was conducted with the BeppoSAX Wide Field Camera (WFC; Jager et al., 1997). The WFC discovered 21 transients in the GC region and more than 50 transient and recurrent sources along the Galactic plane.

Levine et al. (1984) presented the first systematic study of X-ray sources at high X-ray energies (13–180 keV) over the whole sky. This all-sky survey was based on data obtained with the UCSD/MIT Hard X-ray and Low-Energy Gamma-Ray Instrument A4 on board the HEAO 1 satellite from August 1977 until January 1979. The survey catalogue contains 72 sources at a flux sensitivity of $\sim$10–15 mCrab.

The Galactic Centre region was observed with the TTM/COMIS coded mask imaging spectrometer on the Kvant module of the MIR orbital station in 1989 (Syunyaev et al., 1991b; Sunyaev et al., 1991). Several observations of Galactic sources were performed, deriving the hard X-ray component of their emission (Sunyaev et al., 1988; Syunyaev et al., 1989, 1991a; Borkous et al., 1997; Kaniovsky et al., 1997). Sunyaev et al. (1989) presented the hard X-ray (2–30 keV) observations of the Large Magellanic Cloud (LMC) performed in 1988–1989 with the TTM/COMIS instrument, reporting the results of monitoring and spectral observations of LMC X–1, LMC X–2, LMC X–3, LMC X–4 and PSR 0540-693. Emelyanov et al. (2000) assembled a catalogue of 67 X-ray sources observed by the TTM/COMIS telescope in 1988–1998 at a confidence level higher than 4σ.

In 1990–1992 more than 400 sky fields were observed with the ART-P coded-mask telescope aboard the *GRANAT* observatory in the 2.5–60 keV energy band (Sunyaev et al., 1990). ART-P provided a good 5′ FWHM angular resolution within $3.4° \times 3.6°$ field of view (FOV), which made it especially useful for studying the crowded field of the GC. Pavlinsky et al. (1994) reported a detection of 12 point X-ray sources during a $\sim$5° × 5° survey of the GC with the sensitivity of $\sim$1 mCrab in the 3–17 keV energy range.

At higher energies, in the period of 1990–1998 the SIGMA telescope on board *GRANAT* observed more that one quarter of the sky with the sensitivity better than 100 mCrab (Revnivtsev et al., 2004a). The SIGMA telescope (Paul et al., 1991), designed in a coded-mask paradigm, allowed to reconstruct first images of the hard X-ray sky in the energy band 35–1300 keV with an angular resolution of $\sim$15′. During its operation time the SIGMA telescope detected 37 hard X-ray sources in the 40–100 keV energy band (Revnivtsev et al., 2004a).

2.2. INTEGRAL performance for surveys

The IBIS telescope (Ubertini et al., 2003) is the most suitable for the imaging surveys in the hard X-ray band among the major instruments on board *INTEGRAL*. This instrument provides the best combination of field of view, sensitivity and angular resolution needed to conduct a wide-angle survey of the sky in a reasonable amount of time. This was optimized with the scientific goal to regularly monitor a large fraction of the Galactic plane and to discover most of the expected transient sources, whose existence was anticipated by X-ray missions like *BeppoSAX* and *RXTE*, operating at lower energies and/or coarser spatial resolutions in the '90. The low-energy detector layer, ISGRI (INTEGRAL Soft Gamma Ray Imager; Lebrun et al., 2003) is made of a pixelated 128×128 CdTe solid-state detector that views the sky through a coded aperture mask. IBIS generates images of the sky with a 12′ FWHM resolution over a $28° \times 28°$ field of view in the working energy range 15–1000 keV.

The IBIS telescope is designed in a coded-aperture imaging paradigm. The sky is projected onto the detector plane through the transparent and opaque elements of the mask mounted above the detector plane. The sky reconstruction is based on the deconvolution of the detector image with the known mask pattern (see Fenimore and Cannon, 1981; Skinner et al., 1987a). The standard IBIS/ISGRI analysis is presented in the paper by Goldwurm et al. (2003).

Thanks to the coded-aperture design, the IBIS telescope incorporates a very large fully-coded FOV of 9°×9° (all source radiation is modulated by the mask) and partially-coded FOV of $28° \times 28°$ (only a fraction of source flux is modulated by the mask). In addition to that, the "dithering" pattern around the nominal target position, a controlled and systematic spacecraft dithering manoeuvres introduced in order to minimize systematic effects due to spatial and temporal background variations in the spectrometer's (SPI) detectors, results in an even larger sky coverage. The combination of the standard 5×5 dithering grid and numerous *INTEGRAL* pointings, via the approved Guest Observer Program at the Galactic X-ray sources makes the effective latitude coverage of the Galactic plane $|b| < 17.5°$ (Krivonos et al., 2012). As a result, *INTEGRAL* can conduct time-resolved mapping of the Galactic plane on the time-scale of a year. This leads to the unique possibility of taking snapshots of the whole Milky Way in hard X-rays, which is not possible with narrow-FOV grazing X-ray telescopes.

The energy response of the IBIS telescope at hard X-rays ($E > 20$ keV) opens another possibility: to detect highly obscured objects. This makes the *INTEGRAL*/IBIS survey of the Galaxy unbiased against line-of-sight (or intrinsic to the source) attenuation of X-ray photons. Going to even higher energies, the ISGRI detector of *INTEGRAL*/IBIS can provide a census of Galactic hard X-ray emitters at energies above 100 keV (Bazzano et al., 2006; Krivonos et al., 2015).
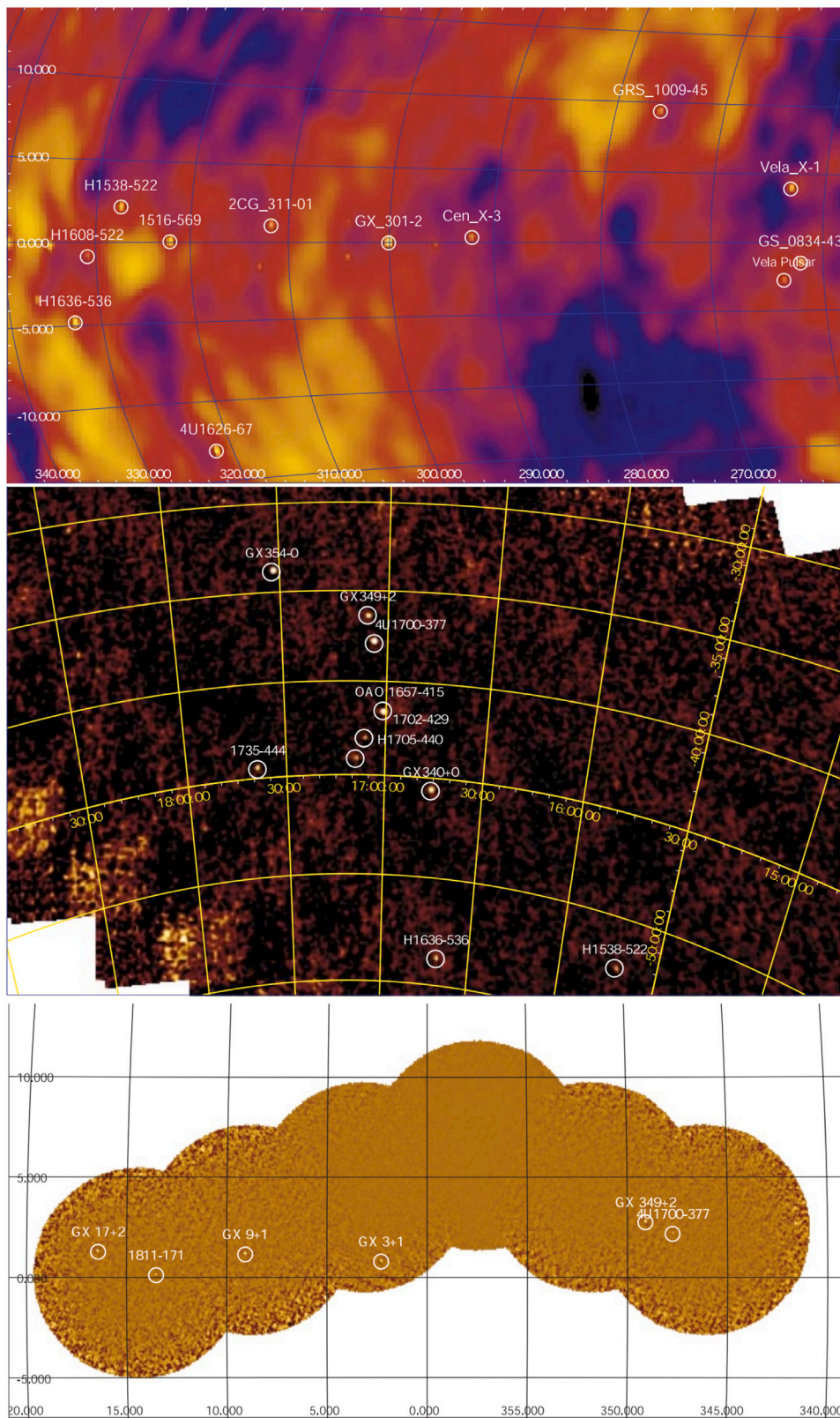
Fig. 1. Typical observational strategy of the *INTEGRAL* GPS scans (filled symbols). The fully coded fields of view (FCFOV, SPI: 16°, IBIS: 9°×9°, JEM-X: 5°), and some known high energy targets are shown for illustration.
Source: Adopted from Winkler et al. (2003b).

2.3. Brief overview of INTEGRAL surveys

During the first years of operations, *INTEGRAL* conducted its so-called Core Programme (CP), i.e., a set of guaranteed observations dedicated to frequent monitoring of the Galactic plane in order to detect transient sources, and to perform time resolved mapping of the Galactic plane (Winkler, 2001). The CP consisted of a deep exposure of the central Galactic radian (GCDE: Galactic Centre Deep Exposure), regular scans of the Galactic plane (GPS: Galactic Plane Scan, Fig. 1) and pointed observations. This program resulted in a first deep survey of the Galactic plane (Winkler et al., 2003b), which listed 100 known X-ray emitters and 10 new X-ray sources have been detected with IBIS/ISGRI for the first time. Fig. 2 shows the first *INTEGRAL* wide-angle Galactic sky maps obtained during the GPS scans with SPI, IBIS/ISGRI, and JEM-X. During the first year of observations, *INTEGRAL* demonstrated its strength in discovering new transient sources. 10 new sources were found over a period of about 4 months, giving a discovery rate of more than 2 per month.

Deep surveys of the Galactic centre region (Revnivtsev et al., 2004b), made within the Russian quota time, were a valuable addition to the *INTEGRAL* CP and demonstrated the excellent capabilities of the *INTEGRAL* telescopes to construct sensitive sky maps. In total, 60 sources with a flux higher than 1.5 mCrab were detected, including 2 sources detected at energies above 20 keV for the first time.

Soon after, the *INTEGRAL* hard X-ray cartography of the Galactic plane has been extended by deep observations of the Sagittarius spiral arm (Molkov et al., 2004), a region very rich of young massive stars and remnants of their evolution. This part of the Milky Way contains the brightest well-known microquasar GRS 1915+105 (Hannikainen et al., 2003), the peculiar object SS433 (Cherepashchuk et al., 2003), soft gamma-ray repeaters, supernova remnants, about dozen of persistent and transient X-ray bursters (e.g. 4U 1915-05, Ser X-1, Aql X-1), and X-ray pulsars. As a result of the *INTEGRAL* Sagittarius arm survey, Molkov et al. (2004) reported the significant detection of 28 X-ray sources with a flux level above 1.4 mCrab, including three previously unknown X-ray emitters.

Next step in the deep surveys of galactic spiral arms was made in 2005 with observations of the Galactic plane region in Crux (Revnivtsev et al., 2006). In total it detected 47 hard X-ray sources, with 15 of them being new ones. Among the identified sources there were 12 active galactic nuclei, and 11 and 6 galactic binary systems with high-mass and low-mass optical companions, respectively.

In February 2005 the program of monitoring the source activity in the Galactic bulge region started.[1] Kuulkers et al. (2007) presented a detailed study of a homogeneous (hard) X-ray sample of 76 sources in the Galactic bulge region, based on the first 1.5 years of the program.

The authors showed that almost all the sources in the Galactic bulge are variable. Additionally, 6 new hard X-ray sources were discovered.

Also, den Hartog et al. (2006) presented results based on 1.6 Ms *INTEGRAL* observations of the Cassiopeia region. The analysis of the IBIS/ISGRI data resulted in detection of 11 sources at energies above 20 keV, including 3 new hard X-ray sources.

The discovery of hard X-ray emission from the anomalous X-ray pulsar 4U 0142+61 up to 150 keV demonstrated the unique capabilities of the IBIS/ISGRI imager.

Thanks to the continuing observations and, consequently, rapidly growing exposure, Bird et al. (2004) released a first systematic survey of hard X-ray sources detected with the IBIS telescope, based on 5 Ms of total exposure time. This initial survey has revealed the presence of ∼120 sources detected with the unprecedented sensitivity of ∼1 mCrab in the energy range 20–100 keV. The survey contains also 28 objects of unknown nature.

A sequence of IBIS/ISGRI survey catalogues has been released at regular basis as more data have become available. The second *INTEGRAL*/IBIS/ISGRI catalogue (Bird et al., 2006) used a greatly increased data set of 10 Ms to unveil a soft gamma-ray sky comprising 209 sources, again with a substantial component (25%) of new and unidentified sources.

In the meantime the first sensitive survey of the central part of the Galaxy was performed at very high energy gamma-rays (E > 100 GeV) with the *High Energy Stereoscopic System* (HESS, Aharonian et al., 2005). This survey revealed a new population of previously unknown sources emitting at very high energies. At least two had no known radio or X-ray counterpart. One year later the extended HESS survey of the Galaxy (±30° in longitude and ±3° in latitude) confirmed the detection of 14 galactic sources (Aharonian et al., 2006). Most of them had no known radio or X-ray counterpart and were hypothesized to be representative of a new class of dark nucleonic cosmic sources. In fact, high energy gamma-rays with energies $E > 10^{11}$ eV were, and actually are, the best proof of non-thermal processes in the universe and provide a direct in-site view of matter–radiation interaction at energies by far greater than producible in human-made accelerators. *INTEGRAL* survey results were a powerful tool to immediately investigate the nature of this new type of galactic cosmic accelerator (Ubertini, 2005) thanks to the unprecedented *INTEGRAL*/IBIS angular resolution and Point Source Location Capability of about 1-2 arcminute between 15 keV and a few MeV. Furthermore, *INTEGRAL* had already performed deep observations of almost all HESS detected sources: the new INTEGRAL source IGR J18135−1751 was identified as the soft gamma-ray counterpart of HESS J1813−178 (Ubertini et al., 2005) and AX J1838.0−0655 as the X/gamma-ray counterpart of HESS J1837−069 (Malizia et al., 2005), as shown in Fig. 3. It was immediately obvious that most of the common *INTEGRAL/HESS* sources identified belonged to SNR and Pulsar Wind Nebulae.

With the aim to provide a prompt release of the *INTEGRAL* hard X-ray survey information to the community, Bird et al. (2007) released a third *INTEGRAL* survey that covers > 70% of the sky with an exposure of at least 10 ks. This "all-sky" survey, based on more than 40 Ms of *INTEGRAL* exposure, comprises more than 400 high-energy sources detected in the energy range 17–100 keV, including both transients and faint persistent objects revealed on time-averaged maps.

Using alternative IBIS/ISGRI sky reconstruction software, Krivonos et al. (2007) released the first *INTEGRAL*/IBIS/ISGRI survey with all-sky coverage. The catalogue of detected sources includes 403 objects, 316 of which exceed a 5σ detection threshold on the time-averaged map of the sky, with the rest detected in various subsamples of exposures. Since this was the first all-sky survey in hard X-ray energy band with unprecedented sensitivity (a factor of 10 deeper than the extragalactic part of the HEAO 1 A-4 source catalogue, Levine et al., 1984), the statistical properties of extragalactic X-ray source population (mainly AGNs) have been significantly improved. In particular, using 68 AGNs detected by *INTEGRAL*, Krivonos et al. (2007) presented evidence of a

---

[1] http://isdc.unige.ch/Science/BULGE/.

Fig. 2. Examples of Galactic sky maps obtained during the GPS observations. *Top panel*: SPI significance 20–40 keV sky map in galactic coordinates (December 2002–March 2003). *Middle panel*: 15–30 keV IBIS/ISGRI skymap in equatorial J2000 coordinates (12 March 2003). *Bottom panel*: 3–15 keV JEM-X sky map close to the Galactic Centre (24 March 2003).
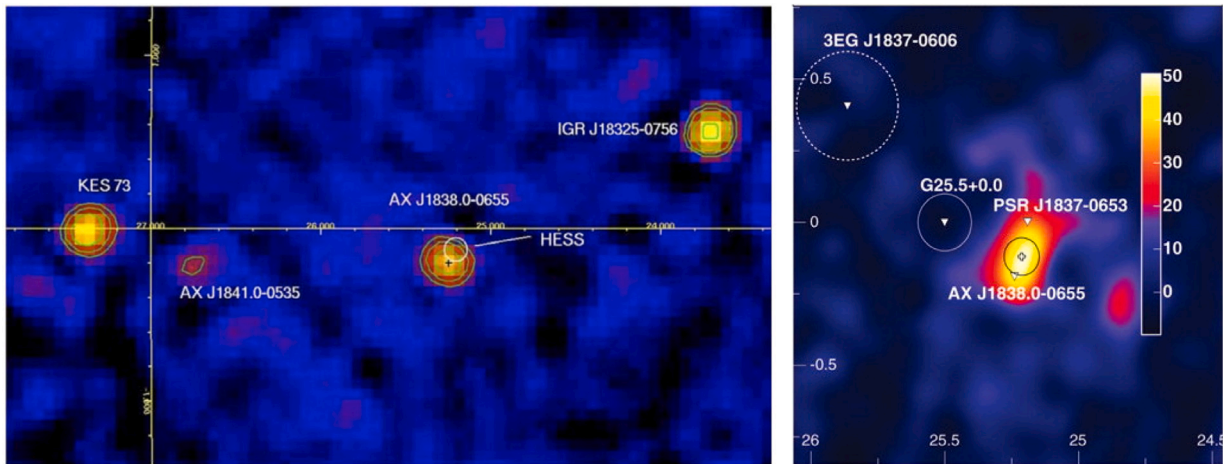*Source:* Adopted from Winkler et al. (2003b).

Fig. 3. *Left:* The IBIS 20–300 keV sky region map containing AX J1838.0−0655 as well as the position and extension of HESS J1837−069 (white circle) and the position determined by the *Einstein* telescope (black cross). Figure adapted from Ubertini (2005) and Malizia et al. (2005). *Right panel:* The emission region of HESS J1837-069 overlapped to the ASCA source AX J1838.0−0655 error box. Note that even if the two sources were positionally coincident, the TeV emission was suggestive of an extended object, confirmed at a later stage. Figure adapted from Aharonian et al. (2005).
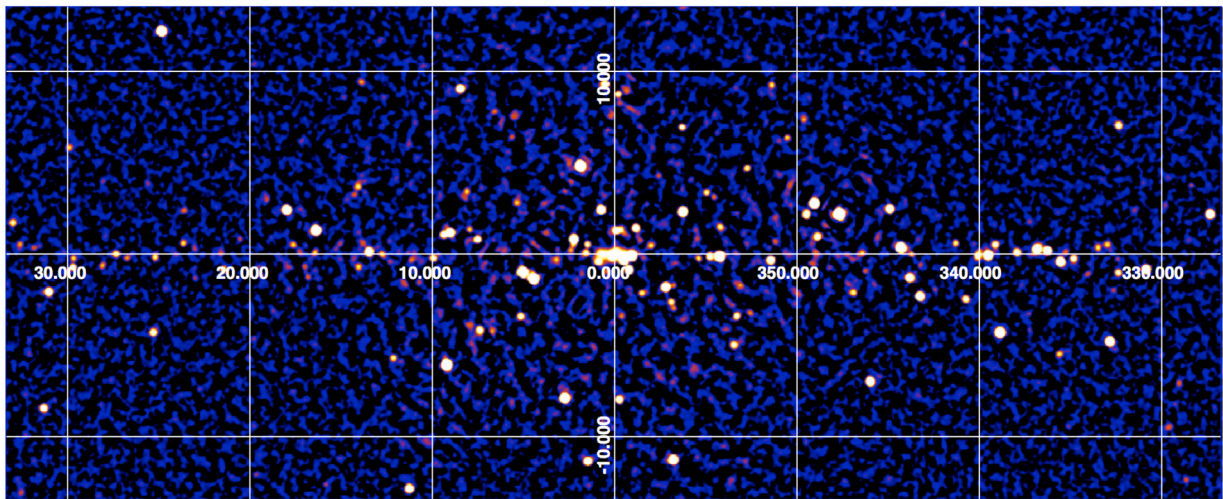
Fig. 4. Map of the central part of the Galaxy obtained with IBIS/ISGRI in the 17–60 keV energy band using the improved sky reconstruction method (Krivonos et al., 2010a). The total exposure is about 20 Ms in the region of the Galactic centre. To highlight background fluctuations, the image is shown in significance with a squared root colour map ranging from 0 to 25. As a consequence of the chosen colour scheme, the apparent diameters of the source images partially scale as the X-ray brightness of the sources. (For interpretation of the references to colour in this figure legend, the reader is referred to the web version of this article.)
Source: Figure adapted from Krivonos et al. (2010a).

strong inhomogeneity in the spatial distribution of nearby (<70 Mpc) AGNs, which reflects the large-scale structure in the local Universe. This finding has been later confirmed and significantly improved with ∼6 times larger AGN sample detected in *Swift*/BAT all-sky survey by Ajello et al. (2012).

In the following years, *INTEGRAL* continued to accumulate exposure time within the Galactic plane. However, the growing exposure time was not reflected by a corresponding increase in survey sensitivity, since the observations are strongly affected by the systematics related to the crowded field of the Galactic centre. Krivonos et al. (2010a) developed an improved method of sky image reconstruction for the IBIS telescope, which allowed them to significantly suppress the systematic noise in the deep images of the Galactic centre (see Fig. 4), and practically remove non-statistical noise from the high-latitude sky images. This improved method of sky reconstruction was used by Krivonos et al. (2010b) to conduct the most sensitive survey of the Milky Way above 20 keV at that time. The minimal detectable flux with a 5σ detection level reached the value of 3.7×10^{-12} erg s^{-1} cm^{-2}, which corresponds to ∼0.26 mCrab in the 17–60 keV energy band. The catalogue of detected sources includes 521 objects, 449 of which exceed a 5σ detection threshold on the time-averaged map of the sky, and 53 were detected in different periods of observations. Among the identified sources, 262 are Galactic and 221 are of extragalactic origin.

Bird et al. (2010) presented the fourth soft gamma-ray source catalogue obtained with IBIS/ISGRI based on 70 Ms of high-quality observations performed during the first five and a half years of the Core Program and public observations. The catalogue includes a substantially increased coverage of extragalactic fields, and comprises more than 700 high-energy sources detected in 17–100 keV energy range. The authors performed careful analysis of IBIS data using the latest official OSA software[2] and source detection techniques. Particular care has been taken to optimize the detection of the transient sources that are common to find both transients and faint persistent objects that can only be revealed with longer exposure times.
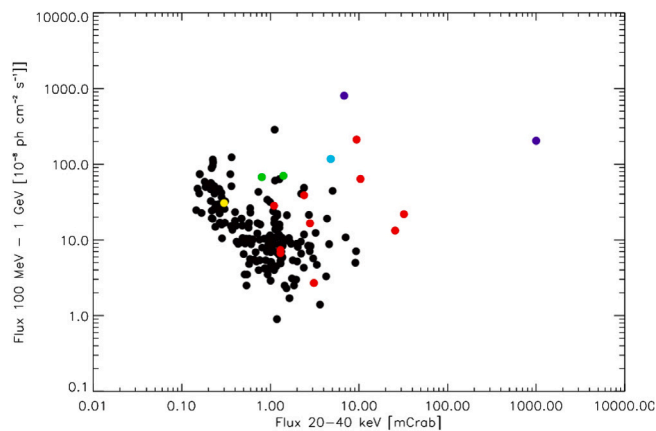
Fig. 5. Gamma-ray flux (100 MeV–1 GeV) of each *Fermi*/LAT source as a function of the corresponding 20–40 keV IBIS/ISGRI flux. The coloured points refer to the IBIS detections, specifically red points are blazars, dark blue are pulsars, green are HMXBs, yellow is Eta Carinae and finally light blue is IGR J17459–2902. The black points refer to IBIS non-detections (2σ upper limit). (For interpretation of the references to colour in this figure legend, the reader is referred to the web version of this article.)
Source: Figure adapted from Ubertini et al. (2009).

Six years later, Bird et al. (2016) reported an all-sky catalogue of soft gamma-ray sources based on IBIS observations during the first 1000 orbits of *INTEGRAL*. This legacy-level survey contains all good-quality data acquired from the launch in 2002, up to the end of 2010 and contains 110 Ms of scientific public observations, with a concentrated coverage on the Galactic Plane and extragalactic deep exposures. The catalogue includes 939 sources above a 4.5σ significance threshold detected in the 17–100 keV energy band. The list of previously undiscovered soft gamma-ray emitters contains 120 sources. Substantial efforts have been taken to detect transient sources on different time scales as described in Section 2.4.

In June 2008 the *Fermi Gamma-ray Space Telescope* was successfully launched and soon after the first high energy catalogue was published. Ubertini et al. (2009) reported the result of the cross correlation between the 4th *INTEGRAL*/IBIS soft gamma-ray catalogue Bird et al. (2010), in the range 20–100 keV, and the *Fermi*/LAT bright source list of objects emitting in the 100 MeV–100 GeV range. Surprisingly, the main result was that only a minuscule part of the 720 sources detected by INTEGRAL were present among the 205 *Fermi*/LAT sources (Fig. 5). This result was not expected due to the mCrab *INTEGRAL* sensitivity and the *Fermi* breakthrough at MeV–GeV energies. Most of the *Fermi*/LAT gamma-ray sources present in the 4th INTEGRAL/IBIS catalogue were optically identified as AGNs (10) complemented by 2 isolated pulsars (Crab and Vela) and 2 High Mass X-ray Binaries (HMXB, LS I +61°303 and LS5039). Two more possible associations were found: one is 0FGL J1045.6–5937, possibly the counterpart at high energy of the massive colliding wind binary system Eta Carinae, discovered to be a soft gamma-ray emitter. For the remaining 189 *Fermi*/LAT sources no *INTEGRAL* counterparts were found.

This initial (unbiased) cross-correlation between low and high energy gamma-ray sources showed that MeV/GeV *Fermi* sources were usually not associated with IBIS/ISGRI sources in the range 20–100 keV. The handful of objects common to both surveys comprised only Flat Spectrum Radio Quasars (FSRQ) and BL Lac objects, but no X-ray Binaries, with the exception of the two microquasars mentioned. Also absent were the AXP, which were known to be strong emitters in the keV–MeV range with a total energy rising in νF_ν and no cut-off detected in their spectra up to a few hundreds of keV (Kuiper and Hermsen, 2009), implying some kind of switch-off mechanism in the MeV regime. Similarly, SGR and Magnetars, detected even in quiescence mode by IBIS/ISGRI (Rea et al., 2009) and among the brightest sources of the hard X-ray sky when flaring (Kouveliotou et al., 1999; Götz et al., 2006;

Israel et al., 2008) were not detected in the high energy gamma-ray range.

As mentioned earlier, most of the observing time of *INTEGRAL* is dedicated to Galactic source population studies, making possible the deepest Galactic survey in hard X-rays ever compiled. Using sky reconstruction algorithms especially developed for the high quality imaging of IBIS/ISGRI data (Krivonos et al., 2010a), Krivonos et al. (2012) published an *INTEGRAL* Galactic plane survey based on nine years of observations, from December 2002 to January 2011. As seen from the range of the used spacecraft revolutions 26–1013, the time span of this survey is similar to that covered by 1000-orbits survey by Bird et al. (2016). Krivonos et al. (2012) presented sky images, sensitivity maps, and catalogues of detected sources in different energy bands (17–60, 17–35, and 35–80 keV) within the Galactic plane ($|b| <$ 17.5°). Using the extended data set, Krivonos et al. (2017) reported on a catalogue of new hard X-ray source candidates based on the sky maps comprising 14 years of data acquired with the IBIS telescope within the Galactic Plane ($|b| < 17.5°$). The catalogue includes in total 72 hard X-ray sources detected at $S/N > 4.7\sigma$ and not known to previous INTEGRAL surveys.

Most of the *INTEGRAL* surveys have been conducted in the 17–100 keV regime where the IBIS/ISGRI sensitivity is optimal in search for point sources. However, energy response of ISGRI detector allows to effectively detect photons at even higher energies, as seen from many studies of bright X-ray sources of different nature (see e.g., Lutovinov et al., 2012b; Revnivtsev et al., 2014; Natalucci et al., 2015; Churazov et al., 2015; Kajava et al., 2016; Lubiński et al., 2016; De Falco et al., 2017). The first systematic study of X-ray emitters detected with IBIS/ISGRI in soft gamma-ray band 100–150 keV has been conducted by Bazzano et al. (2006) based on the Core Program and public open-time observations up to 2005 April. The catalogue includes 49 sources detected in the 100–150 keV band, of which 14 are also seen in the 150–300 keV range. The source types in 100–150 keV band are dominated by Galactic low and high mass X-ray binary systems, and also include active galaxies (10). Among the binary systems that are detected above 150 keV, more than 50% are associated with black hole candidates. Bazzano et al. (2006) constructed the first 100–150 keV Galactic and extragalactic Log$N$-Log$S$ relation, predicting at $E > 100$ keV around 200 Galactic sources and almost 350 active galaxies at a flux above 1 mCrab.

Ten years later, using significantly increased exposure time, Krivonos et al. (2015) published an *INTEGRAL* all-sky survey at energies above 100 keV. The catalogue of detected sources includes 132 objects, which significantly increases the high-energy source sample compared to the work of Bazzano et al. (2006). The whole sky map of all the detected sources in the survey, discriminated in four basic source classes, is shown in Fig. 6. The survey is dominated by 97 hard X-ray sources of Galactic origin (mainly Low-Mass X-ray Binaries – LMXBs and HMXBs, 83 in total) in comparison with the extragalactic source population, represented by 35 AGNs. Compared to Bazzano et al. (2006), the Log$N$-Log$S$ was extended down to fainter fluxes by a factor of 1.4 and has a steeper slope.

INTEGRAL regular observations of the Galactic plane make it possible to address non-standard questions: for instance, Tsygankov et al. (2016) performed the deepest systematic search for the nuclear de-excitation lines of titanium-44 (^{44}Ti) at 67.9 and 78.4 keV, as a tracer of core-collapse supernova explosions in the Galaxy. The peak sensitivity of this ^{44}Ti survey reached an unprecedented level of 4.8×10^{-6} ph cm^{-2} s^{-1} that improved the sensitivity of the survey done by Compton Gamma-Ray Observatory/COMPTEL (Iyudin et al., 1999) by a factor of ~5. As a result, constraining upper limits for all sources from the catalogue of Galactic supernova remnants (SNR; Green, 2014) were derived. These upper limits can be used to estimate the exposure needed to detect ^{44}Ti emission from any known SNR using existing and prospective X- and gamma-ray telescopes.
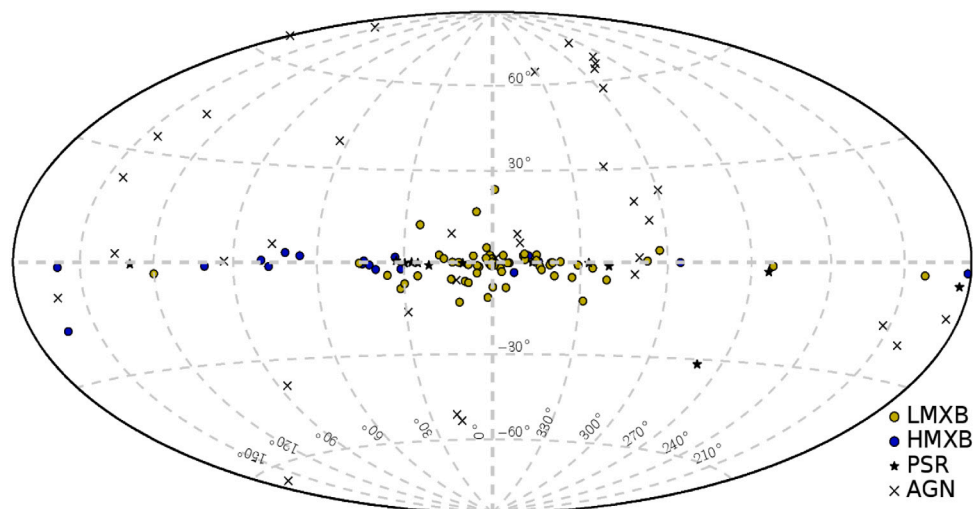
Fig. 6. All-sky map showing the four basic X-ray source types detected in the 100–150 keV survey by Krivonos et al. (2015): 65 LMXBs, 19 HMXBs, 13 PSRs (mostly in the Galactic plane) and 35 AGNs.
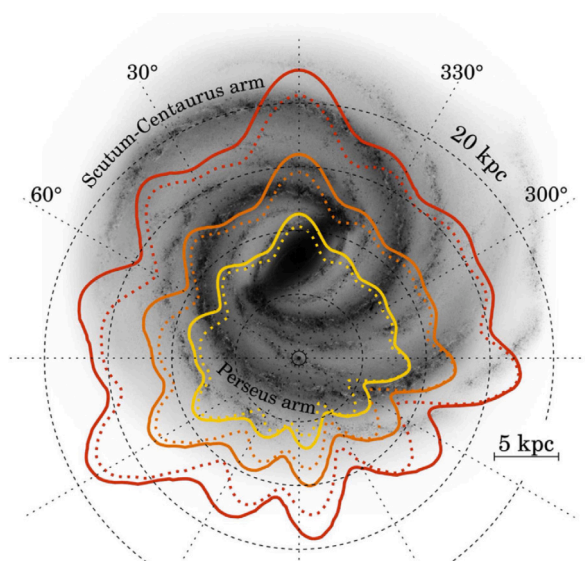*Source:* Adapted from Krivonos et al. (2015).

Fig. 7. Face-on view of the Galaxy shown along with the distance range at which an X-ray source of a given luminosity L_{HX} (or more) can be detected according to the 17–60 keV sensitivity of the 14-year *INTEGRAL* survey (solid lines, Krivonos et al., 2017), compared to the 9-year Galactic plane survey (dotted lines, Krivonos et al., 2012). Red, orange and yellow contours correspond to $L_{HX} = 2 \times 10^{35}$, 10^{35} and 5×10^{34} erg s^{-1}, respectively. (For interpretation of the references to colour in this figure legend, the reader is referred to the web version of this article.)
Source: The background image is a sketch of the Galaxy adapted from Churchwell et al. (2009).

Thanks to large observational campaigns of the extragalactic sky, *INTEGRAL* accumulated a number of deep fields at high Galactic latitudes. The first *INTEGRAL* extragalactic survey was conducted in the direction towards the Coma cluster of galaxies by Krivonos et al. (2005), who detected 12 serendipitous sources with statistical significance > 4σ and extended the extragalactic source counts in the 20–50 keV energy band down to a limiting flux of ∼1 mCrab. This is more than a factor of 10 improvement in sensitivity compared to the previous hard X-ray results in this energy band obtained with the HEAO 1 A-4 instrument. As a significant step forward, Beckmann et al. (2006) compiled a complete extragalactic sample based on a ∼25,000 deg² sky coverage down to a limiting flux of 3×10^{-11} erg s^{-1} cm^{-2} in 20–40 keV. The sample of 38 AGNs was used to construct Log$N$-Log$S$ and to

produce the first luminosity function of AGNs in the 20–40 keV energy range. The census of nearby AGNs and their statistical properties was later extended by Sazonov et al. (2007b) using a representative sample of 127 AGN from Krivonos et al. (2007). Later on, Paltani et al. (2008) presented an analysis of a deep hard X-ray survey of the 3C 273/Coma region with sky coverage of about 2500 deg², resulting in a list of 34 candidate sources detected in the mosaic with a significance σ > 5. Another extragalactic field, that of the LMC, was scrutinized during the large observational campaign aimed at detecting the emission lines from the decay of ^{44}Ti in the remnant of SN1987A (Grebenev et al., 2012). The catalogue of sources in the LMC region was published by Grebenev et al. (2013) and consisted of 21 sources, 4 of which were detected in hard X-rays for the first time. Later, a number of deep extragalactic fields, including M81, LMC and 3C 273/Coma, were studied in Mereminskiy et al. (2016), who detected 147 sources at $S/N > 4\sigma$, including 37 sources observed in hard X-rays for the first time.

The SPI spectrometer with its comparably large field of view provides the opportunity to expand the energy range of the *INTEGRAL* surveys up to a few MeV. Based on only the first year's data, Bouchet et al. (2005) detected 63 sources at energies below 100 keV and four above 300 keV. The main contribution made by SPI was done in studies of the diffuse emission of the Galaxy, which are beyond the scope of the current review (see review by Diehl, 2014). However, the positron annihilation line at 511 keV may have not only diffuse origin but can also originate from the very vicinity of compact objects. A systematic search for outbursts in the narrow positron annihilation line on various time scales based on the *INTEGRAL*/SPI data was performed by Tsygankov and Churazov (2010). As a result, upper limits on the rate of outbursts with a given duration and flux in different parts of the sky were provided.

The two JEM-X telescopes on-board *INTEGRAL* have a smaller (partially coded) field of view (10° in diameter) compared to the IBIS/ISGRI partially coded FOV of 28° × 28°, which restricted their ability to conduct wide-angle surveys; however, Grebenev and Mereminskiy (2015) released an X-ray survey of the GC region based on ∼10 years of observations (2003–2013).

Table 1 summarizes the *INTEGRAL* surveys conducted with IBIS/ISGRI, JEM-X, and SPI, listing important survey characteristics such as limiting flux, sky coverage, total number of detected sources and completeness. Since this table is sorted by year of publication, one can see how sensitivity improves with time, resulting in the growing number of detected sources. It is not trivial to count all hard X-ray

sources discovered with *INTEGRAL* in different surveys by different research groups; however, as seen in Table 1, the total number of new IGR sources can easily reach several hundreds of objects, which demonstrates great impact of *INTEGRAL* in surveying the hard X-ray sky.

The on-going survey of the Galactic plane with *INTEGRAL* provides a continuous improvement in sensitivity, which makes it possible to probe deeper into the Galaxy. Fig. 7 shows a face-on schematic view of the Milky Way and the distances at which *INTEGRAL* can observe a hard X-ray source of a given luminosity L_{HX}. One can notice that *INTEGRAL* can detect all sources with the luminosity $L_{HX} > 2 \times 10^{35}$ erg s^{-1} at the far end of the Galaxy in the direction towards the Galactic Centre; the distance range for the luminosity $L_{HX} > 2 \times 10^{35}$ erg s^{-1} covers most of the Galactic stellar mass; and the Galactic central bar is fully reachable at luminosities $L_{HX} > 5 \times 10^{34}$ erg s^{-1} (Krivonos et al., 2017).

2.4. Time domain

The deep sensitivity of modern hard X-ray surveys is largely achieved by stacking large numbers of relatively short exposures taken for the same fields over many years. In the case of IBIS, observations are divided into short pointings, or *science windows* of typically 2000 s, separated by short slews during which the instrument pointing direction changes by a few degrees. Each science window can be considered an independent measurement of the flux from all points in the field of view for that pointing.

The final outcome of this stacking approach is essentially used to derive the weighted mean of many 2000 s of measurements of source flux taken over a time period in excess of a decade. The weighted mean is used because the measurement quality is non-uniform, being affected by several factors such as exposure time, changing position of the source in the field of view, and the presence of other bright sources in the field. For a *persistent* emitter, the weighted mean of the flux, and the error on that weighted mean, is an excellent estimator of the mean flux and how significantly the mean flux is non-zero; this is the detection significance usually quoted in survey catalogues. In other words, in the assumption that the source is persistent, the significance tells us how confident we can be that we detect a non-zero flux from a given sky position. But this assumption fails for variable or transient sources.

In order to optimize transient source detection, sources must be searched for on different timescales. This may be done with the construction of multiple maps covering different time periods, or directly on light curves of known (or suspected) sources. Inevitably, biases are introduced when we search for emission on a specific set of timescales, as we must make the problem tractable.

The first IBIS survey (Bird et al., 2004) employed a straightforward stacking analysis, but from the second catalogue (Bird et al., 2006) onward, which analysed ~18 months of data, it was realized that source searches on additional time intervals would be needed to optimize the detection of sources that only emitted on shorter timescales. Consequently, maps were constructed and searched not only for the full archive, but also for each revolution (satellite orbit, ~3 days) and for the periods covering the Galactic Centre Deep Exposure (GCDE) core program (~1 month each). In the third catalogue (Bird et al., 2007) the GCDE mosaics were replaced by a broader category of *revolution sequences* covering any observing period where the telescope performed a deep exposure on a single field. During the third catalogue construction, it was noticed that sources detected in previous catalogues were becoming difficult to detect, and strategies were developed to deal with the increasing baseline of the dataset. The problem is illustrated by the detection of the gamma-ray burst GRB041219A, one of the brightest sources ever detected by INTEGRAL. A strong detection of GRB041219A in the specific science window reduces rapidly as the observation window lengthens, and if more than ~5 revolutions of data
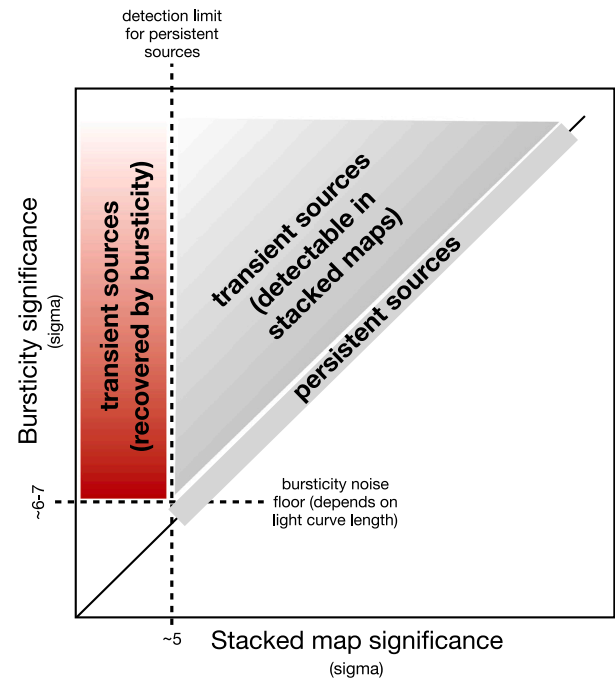

Fig. 8. Source recovery by bursticity (explanation in the text).

are stacked, the source is no longer detectable. The 4th catalogue (Bird et al., 2010) introduced *bursticity* analysis, a sliding-window analysis that sought to detect sources on whatever timescale optimized their detection significance. Most recently, the bursticity method was refined for the catalogue of 1000 orbits (Bird et al., 2016) which had a dataset spanning 8 years of satellite operations, and yet searches were performed for transient emission on timescales down to 0.5 days.

Fig. 8 illustrates how the bursticity method aids the recovery of transient sources in long datasets, plotting the outburst significance against the significance derived from the full light curve. Persistent sources fall along the line of $y = x$ (the diagonal dashed white line), but many sources sit above $y = x$ indicating that their significance can be enhanced in a more limited time period. Sources that fall below the global significance threshold (the vertical red line) but above a burst detection threshold (horizontal dashed white line) can be recovered into the catalogue. The level of the burst detection threshold is determined experimentally — see below.

Bursticity searches, as currently implemented, are still somewhat biased because in order to improve the speed of the algorithm not all window sizes are tested and the stride (the speed with which the window passes along the light curve) is quite large. This means that not all possible windows are tested, although the assumption is made that the significance is only slowly degraded by using a non-optimal window, and only the very faintest outbursts will be missed in this way.

Of more concern is that bursticity is testing a very large number of non-independent windows, since the stride is typically ~10% of the window length. This makes an analytical determination of the false alarm probability, or the burst detection threshold, difficult. Furthermore, the burst detection threshold depends both on the length and the time structure of the light curve. For the longest light curves (IBIS sources in the Galactic Plane) more than 100,000 window tests are performed during a search. In practice, monte-carlo simulations of a flux-randomized light curve with realistic temporal structure are used to establish confidence limits. Such tests are really only valid for light curves containing pure white noise, so any long-term source variability affects the determination of the burst detection threshold. Furthermore, the detection threshold actually increases with greater exposure as the number of trials increases, which is counter to normal expectations for persistent sources.

Table 1
The list of the *INTEGRAL* surveys.

Paper by	*INTEGRAL* telescope	ΔE [keV]	Sensitivity [mCrab (σ)]	Sky coverage	Total number of sources	IGR sources[c]	Completeness[d]
Winkler et al. (2003b)	IBIS/ISGRI	15–40	36[a] (5σ)		110	10	
	SPI	20–40	62[a] (5σ)		33	3	
	JEM-X	5–20	20[a] (5σ)		50		
Revnivtsev et al. (2004b)	IBIS/ISGRI	18–60	1–2	~900 deg^2	60	5	10/60
Molkov et al. (2004)	IBIS/ISGRI	18–60	1.4	35° × 40°	28	7	7/28
Bird et al. (2004)	IBIS/ISGRI	20–100	~1		120	5	28/120
Krivonos et al. (2005)	IBIS/ISGRI	20–50	~1 (4σ)	40° × 40°	13	5	5/13
Revnivtsev et al. (2006)	IBIS/ISGRI	17–60	0.8–1 (5σ)	50° × 50°	46	20	13/46
Bouchet et al. (2005)	SPI	20–150		100° × 50°	63	8	
Bird et al. (2006)	IBIS/ISGRI	20–100	~1	~50%	209	56	~75%
Bazzano et al. (2006)	IBIS/ISGRI	100–150	~2 (4σ)	~50%	49		100%
Bird et al. (2007)	IBIS/ISGRI	17–100	~1	~70%	421	167	~75%
Krivonos et al. (2007)	IBIS/ISGRI	17–60	~1	100%	403	137	48/403
Kuulkers et al. (2007)	IBIS/ISGRI	20–60,	1[b] (3σ)		76	18	
		60–150	3[b] (3σ)		76	18	
	JEM-X	3–10,			18		
		10–25			18		
Paltani et al. (2008)	IBIS/ISGRI	20–60	0.5 (5σ)	2500 deg^2	34	34	~100%
Krivonos et al. (2010b)	IBIS/ISGRI	17–60	0.26 (5σ)	100%	521	212	38/521
Bird et al. (2010)	IBIS/ISGRI	17–100	< 1	100%	723	378	~70%
Krivonos et al. (2012)	IBIS/ISGRI	17–80	~0.2 (4.7σ)	$|b|$ < 17.5°	402	180	~92%
Grebenev et al. (2013)	IBIS/ISGRI	20–60	~0.5 (4.5σ)	640 deg^2	21	4	90%
	JEM-X	3–20	~0.5 (5σ)	~100 deg^2	10	0	100%
Krivonos et al. (2015)	IBIS/ISGRI	100–150	~2 (4σ)	100%	132		100%
Grebenev and Mereminskiy (2015)	JEM-X	5–25		$|l, b|$ < 20°	105	24	
Bird et al. (2016)	IBIS/ISGRI	17–100	< 1	100%	939	~560	
Tsygankov et al. (2016)	IBIS/ISGRI	64.6–82.2	~0.7 (4.7σ)	$|b|$ < 17.5°	1		
Mereminskiy et al. (2016)	IBIS/ISGRI	17–60	~0.18 (4σ)	4900 deg^2	147	37	25/147
Krivonos et al. (2017)	IBIS/ISGRI	17–60	~0.15 (4.7σ)	$|b|$ < 17.5°	72	72	46/72

[a]Average sensitivity per one GPS scan.

[b]Average sensitivity per season.

[c]The total number of IGR sources discovered with *INTEGRAL* in a given survey or previous works.

[d]The completeness column describes the fraction of sources with known nature, if specified with percentile. The numbers shown as a fraction represent the number of unclassified sources with respect to the total number of sources detected.

3. Follow-up campaigns of INTEGRAL surveys

Multiwavelength followup of serendipitously detected X-ray sources is crucial to understand the properties of the objects observed, resulting in large imaging campaigns from radio frequencies to gamma-rays for specific areas of the sky. INTEGRAL provides input for many follow-up X-ray and optical campaigns.

3.1. Soft X-ray campaigns

While the *INTEGRAL* surveys have been very successful at finding sources of high-energy emission, for new or previously poorly studied IGR sources, follow-up observations are necessary to obtain classifications. *INTEGRAL*'s few arcminute positions typically do not allow for the identification of optical or near-IR counterparts, especially in the crowded Galactic Plane, but follow-up X-ray observations reduce the error circles to the subarcsecond level (with the *Chandra X-ray Observatory*) or the few arcsecond level (with *XMM-Newton* or the *Neil Gehrels Swift Observatory*), allowing for the correct counterpart to be found. In addition to localizations, soft X-ray spectra provide important diagnostics for classifying sources, including the spectral slope in the 1–10 keV bandpass and the column density. Finally, for some IGR sources, the angular resolution in the soft X-rays has led to the discovery of extended emission.

Early in the *INTEGRAL* mission, it was realized that many IGR sources were being found in the spiral arm regions of the Galaxy, and this led to the discovery of many HMXBs. The first IGR source, IGR J16318–4848, constitutes an excellent example where follow-up *XMM* observations provided important information. While the *XMM* spectrum showed an extremely high column density $N_\mathrm{H} > 10^{24}$ cm^{-2}, the localization of the source indicated a match with a bright near-IR ($K_s = 7$) star, which proved that a large amount of material was obscuring the X-ray source (Matt and Guainazzi, 2003; Walter et al., 2003). Spectroscopy of the near-IR source showed that it is a B[e]-type supergiant (Filliatre and Chaty, 2004), surrounded by an inner cavity and an outer very large disk of gas and dust heated by this hot star, similar to Herbig Ae/Be stars, the compact object likely orbiting close to the rim separating the cavity from the disk (Chaty and Rahoui, 2012). The existence of this disk was confirmed by the detection of flat-topped iron lines originating from a spherically symmetric disk wind, using broad-band spectroscopy with the ESO/VLT X-Shooter instrument (Fortin et al., 2020). A stellar atmosphere and wind modelling, with the PoWR code, of the optical to mid-IR spectral energy distribution of this source — adding mid-infrared *Spitzer* and *Herschel* data to these X-Shooter observations, showed that the central star likely has an helium-enhanced atmosphere, due to an intense stellar wind shedding part of its hydrogen envelope (Fortin et al., 2020).

A new class of obscured HMXBs had thus been discovered. IGR J16318–4848, with a likely long orbital period of ~80 days (Iyer and Paul, 2017), is in the Norma spiral arm region of the Galaxy, and further soft X-ray observations uncovered more HMXBs in this region. Although we still do not know the nature of the compact object in IGR J16318–4848, IGR J16320–4751 was found to be an HMXB with a slowly rotating (1300 s period) neutron star using *XMM* observations (Lutovinov et al., 2005b; García et al., 2018). Additional IGR HMXBs were uncovered in the Norma region as well as other part of the Galaxy, using *Chandra* localizations and information about the optical or near-IR counterpart (Tomsick et al., 2006, 2008, 2009, 2012a, 2016, 2020). Other identifications made use of the *Neil Gehrels Swift Observatory* (e.g. Rodriguez et al., 2008, 2009b,a), and *XMM-Newton* observations provided spectral and timing information about a large number of IGR HMXBs (Walter et al., 2006; Halpern et al., 2014).

In addition to HMXBs, other large groups of IGR sources are Cataclysmic Variables (CVs) and Low-Mass X-ray Binaries (LMXBs, see

e.g. Fortin et al., 2018; Lutovinov et al., 2020), Active Galactic Nuclei (AGN, see e.g. Tomsick et al., 2015), and pulsars or Pulsar Wind Nebulae (PWNe). In some cases, localizations by *Swift* provide identifications (see e.g., Landi et al., 2017, and references therein). CVs are often nearby with bright optical counterparts (Landi et al., 2009a), and AGN usually have IR or radio counterparts (Landi et al., 2009b). For PWNe, extended X-ray emission is present, and IGR J11014–6103 provides a dramatic example (Tomsick et al., 2012b).

While soft X-rays have been a critical component to classifying IGR sources, firm classifications most often require optical or near-IR spectroscopy, which is discussed in the following.

3.2. Optical and near-infrared spectroscopy of IGR sources

With the publication of the 1st *INTEGRAL*/IBIS survey (Bird et al., 2004) it was realized that about one third of the catalogued hard X-ray sources had no identified nature or had too poor information on their characteristics. This percentage of unidentified or poorly known objects kept nearly constant in the subsequent issues of the all-sky *INTEGRAL*/IBIS surveys (see Bird et al., 2010, for details). Therefore, the need for a multiwavelength approach to pinpoint the nature of these objects, and ultimately the spectroscopic study of their optical and/or near-infrared (NIR) counterparts was apparent. Indeed, this technique allows the identification of the nature of the newly-discovered *INTEGRAL* sources and the characterization thereof by exploring their spectral features (mainly emission lines, which generally herald high-energy activity in cosmic sources) and overall continuum, thus permitting the determination of the main physical parameters for these sources, such as distance, luminosity and chemical composition among others.

However, the first, straightforward attempts to unravel the nature of these emitters involved searching the online multiwavelength repositories, such as SIMBAD,[3] for known conspicuous (i.e., line-emitting) optical objects within the IBIS error circle of unidentified *INTEGRAL* sources: a paradigmatic example of the application of this technique was the case of IGR J12349–6433 (=RT Cru), for which a symbiotic star nature was first suggested by Masetti et al. (2005) on the basis of the localization of this peculiar optical source inside the hard X-ray positional uncertainty and of its published optical characteristics (Cieslinski et al., 1994): the identification was then confirmed with the detection of soft X-rays (Tueller et al., 2005) from this optical object.

Notwithstanding, the X-ray follow-up approach outlined in the previous subsection, of course, allows a better knowledge of the position of hard X-ray sources by reducing their error circles from a few arcminutes down to some arcseconds or less, thus reducing the search area in the sky by a factor of up to 10^5. Indeed, Stephen et al. (2006) showed a low (<2%) chance coincidence probability between the positions of *INTEGRAL* detections and those of softer X-ray sources within the hard X-ray error circle; similar figures are found using radio surveys (e.g., Maiorano et al., 2011). This approach largely helps pinpointing the actual optical, as well as NIR, counterpart of the object responsible for the hard X-ray emission detected with *INTEGRAL*, which can then be studied through optical/NIR spectroscopy (see Fig. 9 for a sketch; for details, see Chaty et al., 2008; Zurita Heras and Chaty, 2008; Butler et al., 2009; Coleiro et al., 2013; Fortin et al., 2018; Masetti et al., 2013; Bikmaev et al., 2006, 2008; Burenin et al., 2008, 2009; Lutovinov et al., 2012a, 2013a; Özbey Arabacı et al., 2012; Karasev et al., 2018, 2020, and references therein), and also through mid-IR observations (Rahoui et al., 2008).

Fifteen years of optical and NIR spectroscopic follow-up studies of unidentified *INTEGRAL* sources performed by several groups worldwide led to a host of identifications: to the best of our knowledge, 265 such objects had their nature identified or better described through optical/NIR spectroscopy, with the following percentage breakdown: 58%

AGNs, 28% Galactic X-ray binaries (3/4 of them identified as HMXBs), 13% CVs and about 1% active stars. We notice that, if one takes into account the NIR spectroscopic identifications only, the overwhelming majority of sources is made of HMXBs (~90%), with just about 10% of AGNs (Coleiro et al., 2013; Fortin et al., 2018) and references therein. A large fraction of the INTEGRAL AGN have been characterized in terms of optical and X-ray properties by Malizia et al. (2016), as demonstrated in the all-sky map in Fig. 10.

The above figures can be compared to e.g. the identified *INTEGRAL* sources in the first IBIS catalogue Bird et al. (2004) grouped into the same broad classes: this gives AGN, X-ray binary and CV percentages of 4%, 64% (with LMXBs being more than twice in number than HMXBs) and 3% and no active stars, respectively. Thus, the contribution of *INTEGRAL* to the advancement of our knowledge of the hard X-ray sky, combined with the optical/NIR followup of the unidentified sources in its surveys, has been multifold, namely: (1) it allowed the exploration of the extragalactic sky through the so-called 'Zone of Avoidance' along the Galactic Plane, where the attenuation induced by dust and gas is not an hindrance for high-energy detectors; (2) similarly, it enhanced our knowledge on HMXBs by increasing the source statistics; (3) it allowed the detection of a significant number of (mostly magnetic) hard X-ray emitting CVs, which was unexpected (but not unprecedented in hindsight, see, e.g., recent review of Lutovinov et al., 2020, and references therein).

Although in-depth presentations will be given in other contributions within this group of reviews, we would like to conclude this section by focusing on a few issues raised thanks to the optical/NIR follow-up of *INTEGRAL* sources: these considerations are connected with the points listed above and, according to us, deserve to be mentioned.

First, it is stressed (Masetti et al., 2012) that the use of medium-sized and large telescopes (above 4 metres in diameter) allows the study of the faint end of the distribution of putative optical counterparts of the extragalactic share of these high-energy sources. Indeed, a Kolmogorov–Smirnov test showed that the probability that the redshift distributions of the newly-identified hard X-ray AGNs and of the ones already classified in the *INTEGRAL* surveys are the same is less than 0.001; that is, the former ones are drawn from a different distribution of more distant objects. Therefore, the deeper *INTEGRAL* observations available with the latest surveys allow one to explore the hard X-ray emitting sources in the far universe, at an average distance ~5 times larger than that of the average of such type of objects known up to now.

Then, we remark that this identification program in hard/soft X-rays plus optical surprisingly boosted the number of magnetic CVs, suggesting this subclass as an important member of Galactic X-ray sources: these systematic studies, according to the review of de Martino et al. (2020), allowed increasing the sample the magnetic CV subclass by a factor of two, permitting extensive and dedicated explorations on specific cases, on these objects as a group, as well as comparative studies as a function of the magnetic field strength of the white dwarf accretor.

Finally, we briefly mention that the combination of the information extracted from the *INTEGRAL* surveys and the optical follow-up work allowed the discovery and/or the characterization of a number of new classes of Galactic X-ray binaries, such as Supergiant Fast X-ray Transients (Sguera et al., 2005; Negueruela et al., 2006), Transitional Millisecond X-ray Pulsars (e.g., de Martino et al., 2013; Bassa et al., 2014) and Symbiotic X-ray Binaries (e.g., Masetti et al., 2007; Smith et al., 2012).

The timely multiwavelength exploration of the *INTEGRAL* sources remaining to be identified and classified is thus of high importance.
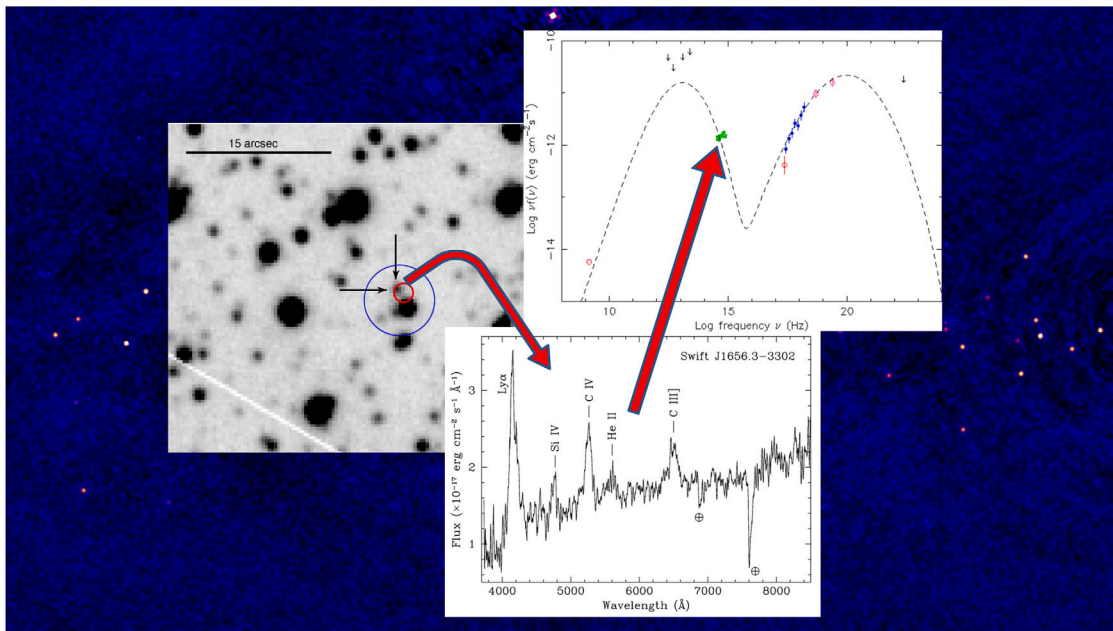
---

[3] http://simbad.u-strasbg.fr.

Fig. 9. Graphic representation of the followup process described in Section 3.2, going from the accurate positioning through soft X-ray observations, to the optical spectroscopy allowing the identification of the nature and main features of the source, and ending with its multiwavelength characterization thanks to the building of a spectral energy distribution for the object.
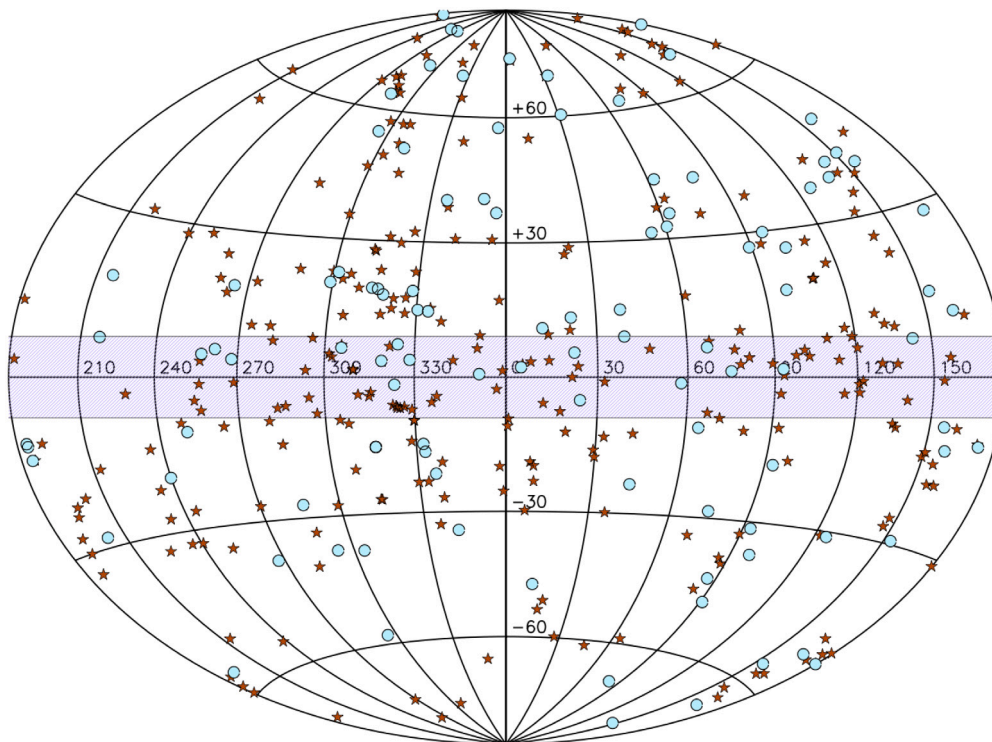*Source:* (adapted from Masetti et al., 2008).

Fig. 10. AGNs detected by INTEGRAL/IBIS surveys (Malizia et al., 2016). The stars represent the 107 new active galaxies studied in Malizia et al. (2016) and first reported in the INTEGRAL/IBIS survey (Bird et al., 2016). The circles show AGNs detected in previous INTEGRAL/IBIS surveys.
Source: Adapted from Malizia et al. (2016).

4. Total CXB spectrum measurements by *INTEGRAL* in the 4–200 keV band

INTEGRAL/IBIS (Ubertini et al., 2003) together with Swift/BAT (Barthelmy et al., 2005), having both good sensitivity and wide-field sky coverage, allowed to make a significant progress in the study of the high energy domain in the last decay. In particular they have provided a great improvement in our knowledge of the extragalactic sky by detecting more than 1000 (mostly local) AGN at high energies. In Fig. 10 all the AGN detected by *INTEGRAL*/IBIS until 2016, and consequently classified and spectrally characterized, have been plotted (Malizia et al., 2016). The high energy band (20–200 keV) is extremely important
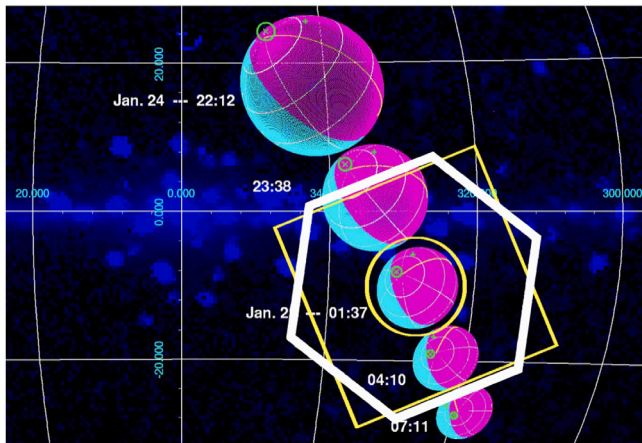
Fig. 11. Illustration of the *INTEGRAL* Earth observing mode in 2006 (see Churazov et al., 2007, for the original version of this figure). FOVs of JEM-X, IBIS and SPI are schematically shown with a circle, a box and an hexagon respectively superposed on to the RXTE 3–20 keV slew map in Galactic coordinates. In the course of this observation the pointing direction of the telescopes remains the same, while the Earth moves across the instruments FOVs. The day side of the Earth is shown by cyan colour. As the distance from the Earth increases during this portion of the 3-day INTEGRAL orbit, the angular size of the Earth disk decreases and the solid angle of the obscured CXB goes down.

for the study of the extragalactic sky and in particular for AGN; it is also the most appropriate for population and survey studies, since it is almost unbiased against obscuration, a severe bias which affects surveys at other frequencies. The great improvement achieved in this field thanks to the *INTEGRAL* surveys has been extensively discussed in the dedicated review on INTEGRAL view of AGN by Malizia et al. in this special issue. Here we want to stress the importance of the survey work for the determination of the Cosmic X-ray Background (CXB).

As described above, in the deepest extra-galactic fields *INTEGRAL* can reliably detect sources at the limiting 20–60 keV flux $\sim$few 10^{-12} erg s^{-1} cm^{-2} (e.g. Mereminskiy et al., 2016). At this sensitivity level only a small fraction ($\sim$ few %) of the total CXB in this energy band is resolved (Krivonos et al., 2007). Detection of fainter objects comprising the bulk of the CXB requires a prohibitively long exposure time. This stems from the intrinsic limitation of coded mask telescopes, when photons from a single source are distributed across the entire detector. At the same time, coded mask telescopes often have large FOVs and the total count rate associated with the CXB can be large. Therefore, the detector spectra of the telescopes on-board INTEGRAL contain information on the total flux from all resolved and unresolved (no matter how faint they are) sources within the FOV.

Separating the contribution of the CXB from the particle background in the detector spectra is a non-trivial exercise. One (difficult) route is to build a comprehensive model of the detector non-astrophysical background, which usually dominates the count rate, so that this model can be subtracted from recorded spectra. Another possibility is to modulate the astrophysical flux so that it can be singled out from the particle background. Here we discuss the results of total CXB flux measurements by *INTEGRAL* using the latter possibility.

The modulation of the CXB flux has already been employed in early space X-ray experiments. In particular the HEAO-1 observatory used a movable 5 cm thick CsI crystal to partly block the instrument field of view and to modulate the CXB signal (Kinzer et al., 1997; Gruber et al., 1999). For *INTEGRAL*, the problem of modulation was solved by "placing" the Earth into the telescopes FOVs (Churazov et al., 2007; Türler et al., 2010). The same technique was also used by Frontera et al. (2007) for the BeppoSAX mission and by Ajello et al. (2008) for the data of the Burst Alert Telescope (BAT) aboard the Swift spacecraft.

INTEGRAL was launched onto a 3-day elongated orbit with a perigee of $\sim$6 000 km and an apogee of $\sim$150 000 km. The orbit crosses the Earth

radiation belts at the distance of $\sim$50 000 km, so that useful observations are possible at larger distances. During *INTEGRAL* observations of the Earth in 2006, the satellite was kept in a controlled 3-axis stabilization with telescopes' axes starting at a point where the Earth was predicted to be some 6 h after the perigee passage (see Fig. 11). Four such observations were performed in 2006, each lasting about 30 ks ($\sim$8 h). When the Earth was close to the telescopes' pointing direction, the radius of the Earth disk was $\sim$5.4°, i.e. the CXB signal from some 90 sq.deg. was subtended. In terms of the flux near 30 keV, such solid angle corresponds to $\sim$200 mCrab, i.e. a very significant modulation. Moreover, as the distance from the Earth changes and the Earth moves through the FOV, the modulation amplitude can be readily predicted and, therefore, used to separate it from other contaminating signals.

Apart from the genuine CXB signal, modulated by the obscuration by the Earth disk, there is a number of other variable components that have to be accounted for. Namely:

- Individual compact X-ray sources (mostly in the Galaxy) which induce sharp edges in the recorder light-curves when the disk edge goes over them.
- Unresolved foreground emission of the Galactic Ridge.
- Emission of the Earth atmosphere due to scattering of the CXB photons (Churazov et al., 2008) and induced by cosmic rays impinging the atmosphere (Sazonov et al., 2007a).
- Earth Auroral emission that was strong and variable in several *INTEGRAL* observations.
- Variability of the intrinsic detector background.

Individual compact X-ray sources are relatively easy to deal with, as long as they are not variable. Their spectra can be measured using a portion of the observation when they are not obscured by the Earth disk. Their modulation pattern can be described as a simple mask function (either 0 or 1 at any moment) set by their position with respect to the Earth disk (see Fig. 12).

The Galactic Ridge emission is more difficult to account properly due to its diffuse nature. The portions of the data when the Earth disk was moving over the bright regions of the Ridge can be either ignored (Churazov et al., 2007), or a spatial model of the Ridge can be used (Türler et al., 2010).

The idea of having the Earth shadowing the CXB is based on the assumption that its disk is dark in X-rays. This is only partly true, since the CXB photons can be partly reflected by the Earth atmosphere, while cosmic rays can generate secondary gamma-radiation. The CXB radiation reflected by the atmosphere (Fig. 13) can be straightforwardly calculated (Churazov et al., 2008), although it depends on the CXB spectrum itself. Fortunately, the albedo, i.e. the ratio of the reflected and the incident spectra is weakly sensitive to the shape of the incident spectrum in the relevant energy band, implying that the reflected component can be readily evaluated if the albedo is calculated using reasonable guess on the CXB shape.

Cosmic rays, in particular protons impinging the Earth atmosphere, undergo a series of hadronic interactions and electromagnetic cascades to induce a glow of the atmosphere in hard X-rays. Examples of expected spectra from the Monte Carlo simulations (Sazonov et al., 2007a) based on the GEANT4 software package (Agostinelli et al., 2003) are shown in Fig. 14.

Finally, the emission of the Earth Aurora can be bright and highly variable. Currently, there are no good recipes for properly modelling the contribution of the Aurora. Therefore all observations severely affected by the Aurora were excluded from the analysis. For instance, among four 30 ks *INTEGRAL* observations of the Earth done in 2006, two have signatures of the Aurora emission.

With all the components mentioned above, the spectrum observed by the *INTEGRAL* instruments $S(E, T)$ at any given moment can be represented as
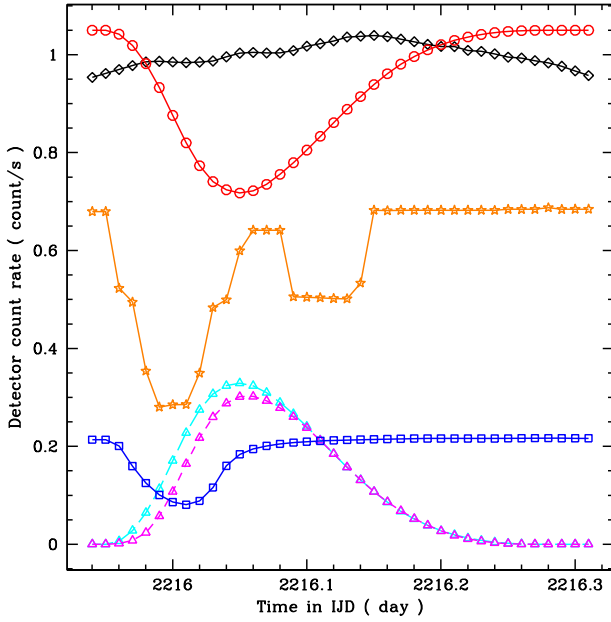
$$S(E, t) = B(E, t)+$$

Fig. 12. Model lightcurves of each component for a ∼2 keV wide energy channel centred at ∼27 keV during the first *INTEGRAL* observation of the Earth. The drop of the detector count rate due to the shadowing of the CXB is shown with red circles. The other components are the effective contribution of the point sources (orange stars), the GRXE (blue squares), the Earth CXB reflection (cyan triangles, long-dashed), the CR-induced emission (magenta triangles, short-dashed), and the estimated instrumental background (black diamonds). (For interpretation of the references to colour in this figure legend, the reader is referred to the web version of this article.)
Source: Adapted from Türler et al. (2010).
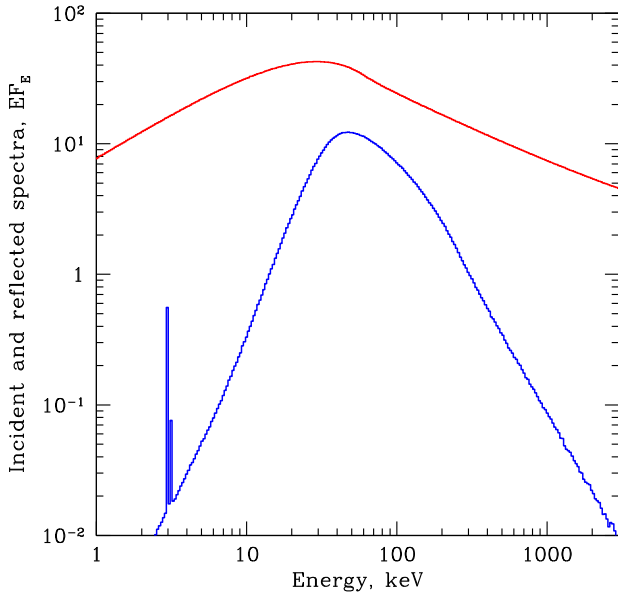
Fig. 13. The CXB spectrum (top) and the spectrum reflected by the Earth atmosphere (bottom). The reflected spectrum was integrated over all angles. The features in the reflected spectrum near 3 keV are the fluorescent lines of Argon.
Source: Adapted from Churazov et al. (2008).

$$CXB(E) - CXB(E) \times \Omega(t) \times [1 - A(E)] +$$
$$CR(E) \times \Omega(t) +$$
$$\Sigma_i I_i(E, \alpha, \delta) \times M(\alpha, \delta, t), \tag{1}$$

where $B(E, t)$ is the intrinsic background; $CXB(E)$ is the spectrum of the CXB, $\Omega(t)$ is the solid angle subtended by the Earth disk, A is the
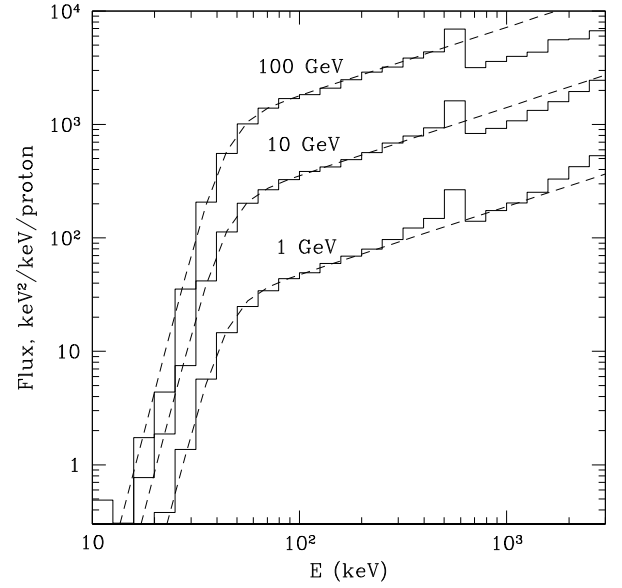
Fig. 14. Examples of simulated spectra (solid lines) of atmospheric emission produced by cosmic protons of given energy: $E_p = 1$, 10 and 100 GeV. It can be seen that in the photon energy range 25–300 keV the shape of the emergent spectrum is almost invariant (the dashed lines).
Source: Adapted from Sazonov et al. (2007a).

Earth albedo for the CXB-like spectrum (Fig. 13), $CR(E)$ is the particle-induced emission of the Earth atmosphere (Fig. 14), $I_i(E, \alpha, \delta)$ is the spectrum of individual bright source located at coordinates (α, δ) and $M(\alpha, \delta, t)$ is the time dependent mask due to the Earth occultation of the source position.

The examples of the light curves predicted for the ISGRI/IBIS instrument in a narrow energy band near 27 keV are shown in Fig. 12. As is clear from this Figure and also from Eq. (1), the CXB obscuration, the CXB and CR albedos share the same time dependence associated with $\Omega(t)$. Therefore, these components have to be modelled simultaneously using the information about their spectral shapes (see Figs. 13 and 14).

Actual light curves for all three instruments on board the *INTEGRAL* are shown in Fig. 15. It is clear that the detector light curves are indeed modulated and the time variations are consistent with expectations (red curves). Repeating the analysis in many different bands and measuring the amplitude of the modulation allows the reconstruction of the CXB spectrum (see Churazov et al., 2007; Türler et al., 2010, for details of the analysis).

The derived CXB spectrum is shown in Fig. 16 along with the data from other experiments, including HEAO1 A4 in the 100–300 keV band (Gruber et al., 1999) and *Swift*/BAT in the 14–195 keV band (Ajello et al., 2008). The obtained normalization of CXB spectrum is ∼10% higher than suggested by Gruber et al. (1999) and consistent with recent CXB measurement performed with the *NuSTAR* telescope in 3–20 keV band (Krivonos et al., 2020). The observed CXB spectrum is well described by the standard population synthesis model of AGNs, including the fraction of Compton-thick AGNs and the reflection strengths from the accretion disk and torus based on the luminosity- and redshift-dependent unified scheme (Ueda et al., 2014).

5. Conclusions

One of the many areas where the *INTEGRAL* observatory provides a significant scientific outcome to the astrophysical community is surveying the sky at energies above 20 keV. *INTEGRAL* surveys of the Galactic Plane and extragalactic fields triggered a large number of new studies and observational campaigns in other wavelengths.
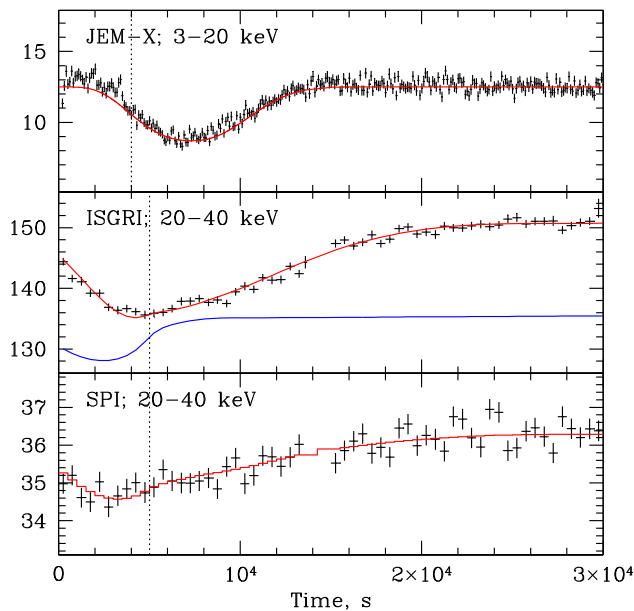
Fig. 15. The light curves (crosses) of JEM-X, IBIS/ISGRI and SPI instruments in units of counts per second. The red curves show the model light curve that includes the shadowing by the Earth disk. In the middle panel the blue curve shows schematically (with arbitrary normalization) the time dependence of the Galactic Ridge emission, modulated by the Earth occultation. In order to avoid contamination of the CXB measurements due to Galactic plane contribution, the first few ksec of data (on the left of the dotted vertical lines) were dropped from the analysis. Note that for JEM-X a less strict cut was applied since its field of view is smaller than that of the other instruments. (For interpretation of the references to colour in this figure legend, the reader is referred to the web version of this article.)
Source: Adapted from Churazov et al. (2007).
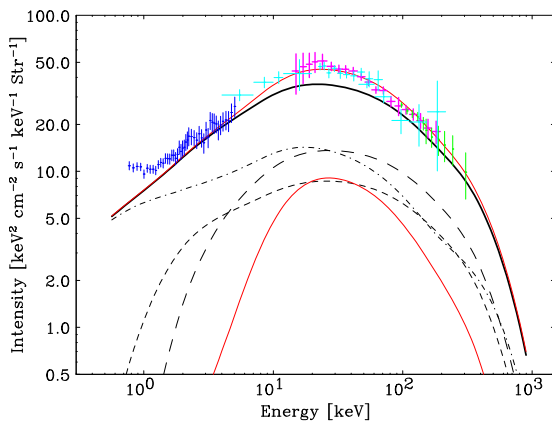
Fig. 16. Cosmic X-ray Background (CXB) spectrum calculated from AGN population synthesis models (upper solid curve, red; Ueda et al., 2014) compared with the observed data by different X-ray missions (Ajello et al., 2008). Middle solid curve (black): the integrated spectrum of Compton-thin AGNs (log NH < 24). Lower solid curve (red): that of Compton-thick AGNs (log NH= 24–26). Long-dashed curve (black): that of AGNs with log NH= 23–24. Short-dashed curve (black): that of AGNs with log NH= 22–23. Dot-dashed curve (black): that of AGNs with log NH<22. Data points in the 0.8–5 keV (blue), 4–215 keV (cyan), 14–195 keV (magenta), and 100–300 keV (green) bands refer to the CXB spectra observed with ASCA/SIS (Gendreau et al., 1995), *INTEGRAL* (Churazov et al., 2007), Swift/BAT (Ajello et al., 2008), and HEAO A4 (Gruber et al., 1999), respectively. (For interpretation of the references to colour in this figure legend, the reader is referred to the web version of this article.)
Source: Adapted from Ueda et al. (2014).

Thanks to its coded-aperture design, the IBIS telescope, the main instrument for *INTEGRAL* hard X-ray surveys, incorporates a very large fully-coded FOV of 28°×28°, which allows to conduct cartography of the

sky in reasonable time. In particular, *INTEGRAL* is able to take hard X-ray snapshots of the whole Milky Way over a time scale of a year, which is far from the capabilities of narrow-FOV grazing X-ray telescopes.

Apart from providing the census of hard X-ray emitters over the whole sky, *INTEGRAL* conducted a unique observation of the large-scale cosmic X-ray background via Earth-occultation manoeuvre, which will undoubtedly be included in the legacy of the *INTEGRAL* observatory.

List of abbreviations

List of definitions of abbreviations used in the paper.
FOV: Field of View;
AGN: Active Galactic Nuclei;
HMXB: High Mass X-ray Binary;
LMXB: Low Mass X-ray Binary;
CV: Cataclysmic Variable;
PSR: Pulsar;
PWN: Pulsar Wind Nebula;
CXB: Cosmic X-ray Background;
GRXE: Galactic Ridge X-ray Emission;
PoWR: the Potsdam Wolf–Rayet Models.

Acknowledgements

References

Agostinelli, S., Allison, J., Amako, K., Apostolakis, J., Araujo, H., Arce, P., Asai, M., Axen, D., Banerjee, S., Barrand, G., Behner, F., Bellagamba, L., Boudreau, J., Broglia, L., Brunengo, A., Burkhardt, H., Chauvie, S., Chuma, J., Chytracek, R., Cooperman, G., Cosmo, G., Degtyarenko, P., Dell'Acqua, A., Depaola, G., Dietrich, D., Enami, R., Feliciello, A., Ferguson, C., Fesefeldt, H., Folger, G., Foppiano, F., Forti, A., Garelli, S., Giani, S., Giannitrapani, R., Gibin, D., Cadenas, J.G., González, I., Abril, G.G., Greeniaus, G., Greiner, W., Grichine, V., Grossheim, A., Guatelli, S., Gumplinger, P., Hamatsu, R., Hashimoto, K., Hasui, H., Heikkinen, A., Howard, A., Ivanchenko, V., Johnson, A., Jones, F., Kallenbach, J., Kanaya, N., Kawabata, M., Kawabata, Y., Kawaguti, M., Kelner, S., Kent, P., Kimura, A., Kodama, T., Kokoulin, R., Kossov, M., Kurashige, H., Lamanna, E., Lampén, T., Lara, V., Lefebure, V., Lei, F., Liendl, M., Lockman, W., Longo, F., Magni, S., Maire, M., Medernach, E., Minamimoto, K., de Freitas, P.M., Morita, Y., Murakami, K., Nagamatu, M., Nartallo, R., Nieminen, P., Nishimura, T., Ohtsubo, K., Okamura, M., O'Neale, S., Oohata, Y., Paech, K., Perl, J., Pfeiffer, A., Pia, M., Ranjard, F., Rybin, A., Sadilov, S., Salvo, E.D., Santin, G., Sasaki, T., Savvas, N., Sawada, Y., Scherer, S., Sei, S., Sirotenko, V., Smith, D., Starkov, N., Stoecker, H., Sulkimo, J., Takahata, M., Tanaka, S., Tcherniaev, E., Tehrani, E.S., Tropeano, M., Truscott, P., Uno, H., Urban, L., Urban, P., Verderi, M., Walkden, A., Wander, W., Weber, H., Wellisch, J., Wenaus, T., Williams, D., Wright, D., Yamada, T., Yoshida, H., Zschiesche, D., 2003. Geant4—a simulation toolkit. Nucl. Instrum. Methods Phys. Res. A 506 (3), 250–303. http://dx.doi.org/10.1016/S0168-9002(03)01368-8, URL: http://www.sciencedirect.com/science/article/pii/S0168900203013688.

Aharonian, F., Akhperjanian, A.G., Aye, K.M., Bazer-Bachi, A.R., Beilicke, M., Benbow, W., Berge, D., Berghaus, P., Bernlöhr, K., Boisson, C., Bolz, O., Borgmeier, C., Braun, I., Breitling, F., Brown, A.M., Gordo, J.B., Chadwick, P.M., Chounet, L.M., Cornils, R., Costamante, L., Degrange, B., Djannati-Ataï, A., Drury, L.O., Dubus, G., Ergin, T., Espigat, P., Feinstein, F., Fleury, P., Fontaine, G., Funk, S., Gallant, Y.A., Giebels, B., Gillessen, S., Goret, P., Hadjichristidis, C., Hauser, M., Heinzelmann, G.,

Henri, G., Hermann, G., Hinton, J.A., Hofmann, W., Holleran, M., Horns, D., de Jager, O.C., Jung, I., Khélifi, B., Komin, N., Konopelko, A., Latham, I.J., Le Gallou, R., Lemière, A., Lemoine, M., Leroy, N., Lohse, T., Marcowith, A., Masterson, C., McComb, T.J.L., de Naurois, M., Nolan, S.J., Noutsos, A., Orford, K.J., Osborne, J.L., Ouchrif, M., Panter, M., Pelletier, G., Pita, S., Pühlhofer, G., Punch, M., Raubenheimer, B.C., Raue, M., Raux, J., Rayner, S.M., Redondo, I., Reimer, A., Reimer, O., Ripken, J., Rob, L., Rolland, L., Rowell, G., Sahakian, V., Saugé, L., Schlenker, S., Schlickeiser, R., Schuster, C., Schwanke, U., Siewert, M., Sol, H., Steenkamp, R., Stegmann, C., Tavernet, J.P., Terrier, R., Théoret, C.G., Tluczykont, M., van der Walt, D.J., Vasileiadis, G., Venter, C., Vincent, P., Visser, B., Völk, H.J., Wagner, S.J., 2005. A new population of very high energy gamma-ray sources in the milky way. Science 307 (5717), 1938–1942. http://dx.doi.org/10.1126/science.1108643, arXiv:astro-ph/0504380.

Aharonian, F., Akhperjanian, A.G., Bazer-Bachi, A.R., Beilicke, M., Benbow, W., Berge, D., Bernlöhr, K., Boisson, C., Bolz, O., Borrel, V., Braun, I., Breitling, F., Brown, A.M., Chadwick, P.M., Chounet, L.M., Cornils, R., Costamante, L., Degrange, B., Dickinson, H.J., Djannati-Ataï, A., Drury, L.O., Dubus, G., Emmanoulopoulos, D., Espigat, P., Feinstein, F., Fontaine, G., Fuchs, Y., Funk, S., Gallant, Y.A., Giebels, B., Gillessen, S., Glicenstein, J.F., Goret, P., Hadjichristidis, C., Hauser, M., Heinzelmann, G., Henri, G., Hermann, G., Hinton, J.A., Hofmann, W., Holleran, M., Horns, D., Jacholkowska, A., de Jager, O.C., Khélifi, B., Komin, N., Konopelko, A., Latham, I.J., Le Gallou, R., Lemière, A., Lemoine-Goumard, M., Leroy, N., Lohse, T., Martin, J.M., Martineau-Huynh, O., Marcowith, A., Masterson, C., McComb, T.J.L., de Naurois, M., Nolan, S.J., Noutsos, A., Orford, K.J., Osborne, J.L., Ouchrif, M., Panter, M., Pelletier, G., Pita, S., Pühlhofer, G., Punch, M., Raubenheimer, B.C., Raue, M., Raux, J., Rayner, S.M., Reimer, A., Reimer, O., Ripken, J., Rob, L., Rolland, L., Rowell, G., Sahakian, V., Saugé, L., Schlenker, S., Schlickeiser, R., Schuster, C., Schwanke, U., Siewert, M., Sol, H., Spangler, D., Steenkamp, R., Stegmann, C., Tavernet, J.P., Terrier, R., Théoret, C.G., Tluczykont, M., Vasileiadis, G., Venter, C., Vincent, P., Völk, H.J., Wagner, S.J., 2006. The H.E.S.S. Survey of the inner galaxy in very high energy gamma rays. Astrophys. J. 636 (2), 777–797. http://dx.doi.org/10.1086/498013, arXiv:astro-ph/0510397.

Ajello, M., Alexander, D.M., Greiner, J., Madejski, G.M., Gehrels, N., Burlon, D., 2012. The 60 month all-sky burst alert telescope survey of active galactic nucleus and the anisotropy of nearby AGNs. Astrophys. J. 749 (1), 21. http://dx.doi.org/10.1088/0004-637X/749/1/21, arXiv:1202.3137.

Ajello, M., Greiner, J., Sato, G., Willis, D.R., Kanbach, G., Strong, A.W., Diehl, R., Hasinger, G., Gehrels, N., Markwardt, C.B., Tueller, J., 2008. Cosmic X-ray background and earth albedo spectra with swift BAT. Astrophys. J. 689 (2), 666–677. http://dx.doi.org/10.1086/592595, arXiv:0808.3377.

Barthelmy, S.D., Barbier, L.M., Cummings, J.R., Fenimore, E.E., Gehrels, N., Hullinger, D., Krimm, H.A., Markwardt, C.B., Palmer, D.M., Parsons, A., Sato, G., Suzuki, M., Takahashi, T., Tashiro, M., Tueller, J., 2005. The burst alert telescope (BAT) on the SWIFT midex mission. Space Sci. Rev. 120 (3–4), 143–164. http://dx.doi.org/10.1007/s11214-005-5096-3, arXiv:astro-ph/0507410.

Bassa, C.G., Patruno, A., Hessels, J.W.T., Keane, E.F., Monard, B., Mahony, E.K., Bogdanov, S., Corbel, S., Edwards, P.G., Archibald, A.M., Janssen, G.H., Stappers, B.W., Tendulkar, S., 2014. A state change in the low-mass X-ray binary XSS J12270-4859. Mon. Not. R. Astron. Soc. 441 (2), 1825–1830. http://dx.doi.org/10.1093/mnras/stu708, arXiv:1402.0765.

Baumgartner, W.H., Tueller, J., Markwardt, C.B., Skinner, G.K., Barthelmy, S., Mushotzky, R.F., Evans, P.A., Gehrels, N., 2013. The 70 month swift-BAT all-sky hard X-ray survey. Astrophys. J. Suppl. 207 (2), 19. http://dx.doi.org/10.1088/0067-0049/207/2/19, arXiv:1212.3336.

Bazzano, A., Stephen, J.B., Fiocchi, M., Bird, A.J., Bassani, L., Dean, A.J., Malizia, A., Ubertini, P., Lebrun, F., Walter, R., Winkler, C., 2006. INTEGRAL IBIS census of the sky beyond 100 keV. Astrophys. J. 649 (1), L9–L12. http://dx.doi.org/10.1086/508171, arXiv:astro-ph/0608164.

Beckmann, V., Soldi, S., Shrader, C.R., Gehrels, N., Produit, N., 2006. The hard X-ray 20-40 keV AGN luminosity function. Astrophys. J. 652 (1), 126–135. http://dx.doi.org/10.1086/507510, arXiv:astro-ph/0606687.

Bikmaev, I.F., Burenin, R.A., Revnivtsev, M.G., Sazonov, S.Y., Sunyaev, R.A., Pavlinsky, M.N., Sakhibullin, N.A., 2008. Optical identifications of five INTEGRAL hard X-ray sources in the galactic plane. Astron. Lett. 34 (10), 653–663. http://dx.doi.org/10.1134/S1063773708100010, arXiv:0810.2018.

Bikmaev, I.F., Revnivtsev, M.G., Burenin, R.A., Sunyaev, R.A., 2006. XSS J00564+4548 and IGR J00234+6141: New cataclysmic variables from the RXTE and INTEGRAL all-sky surveys. Astron. Lett. 32 (9), 588–593. http://dx.doi.org/10.1134/S1063773706090039, arXiv:astro-ph/0603715.

Bird, A.J., Barlow, E.J., Bassani, L., Bazzano, A., Bélanger, G., Bodaghee, A., Capitanio, F., Dean, A.J., Fiocchi, M., Hill, A.B., Lebrun, F., Malizia, A., Mas-Hesse, J.M., Molina, M., Moran, L., Renaud, M., Sguera, V., Shaw, S.E., Stephen, J.B., Terrier, R., Ubertini, P., Walter, R., Willis, D.R., Winkler, C., 2006. The second IBIS/ISGRI soft gamma-ray survey catalog. Astrophys. J. 636, 765–776. http://dx.doi.org/10.1086/498090.

Bird, A.J., Barlow, E.J., Bassani, L., Bazzano, A., Bodaghee, A., Capitanio, F., Cocchi, M., Del Santo, M., Dean, A.J., Hill, A.B., Lebrun, F., Malaguti, G., Malizia, A., Much, R., Shaw, S.E., Stephen, J.B., Terrier, R., Ubertini, P., Walter, R., 2004. The first IBIS/ISGRI soft gamma-ray galactic plane survey catalog. Astrophys. J. 607, L33–L37. http://dx.doi.org/10.1086/421772.

Bird, A.J., Bazzano, A., Bassani, L., Capitanio, F., Fiocchi, M., Hill, A.B., Malizia, A., McBride, V.A., Scaringi, S., Sguera, V., Stephen, J.B., Ubertini, P., Dean, A.J., Lebrun, F., Terrier, R., Renaud, M., Mattana, F., Götz, D., Rodriguez, J., Belanger, G., Walter, R., Winkler, C., 2010. The fourth IBIS/ISGRI soft gamma-ray survey catalog. Astrophys. J. Suppl. 186, 1–9. http://dx.doi.org/10.1088/0067-0049/186/1/1, arXiv:0910.1704.

Bird, A.J., Bazzano, A., Malizia, A., Fiocchi, M., Sguera, V., Bassani, L., Hill, A.B., Ubertini, P., Winkler, C., 2016. The IBIS soft gamma-ray sky after 1000 integral orbits. Astrophys. J. Suppl. 223, 15. http://dx.doi.org/10.3847/0067-0049/223/1/15, arXiv:1601.06074.

Bird, A.J., Malizia, A., Bazzano, A., Barlow, E.J., Bassani, L., Hill, A.B., Bélanger, G., Capitanio, F., Clark, D.J., Dean, A.J., Fiocchi, M., Götz, D., Lebrun, F., Molina, M., Produit, N., Renaud, M., Sguera, V., Stephen, J.B., Terrier, R., Ubertini, P., Walter, R., Winkler, C., Zurita, J., 2007. The third IBIS/ISGRI soft gamma-ray survey catalog. Astrophys. J. Suppl. 170, 175–186. http://dx.doi.org/10.1086/513148, arXiv:astro-ph/0611493.

Bodaghee, A., Tomsick, J.A., Rodriguez, J., James, J.B., 2012. Clustering between high-mass X-ray binaries and OB associations in the milky way. Astrophys. J. 744 (2), 108. http://dx.doi.org/10.1088/0004-637X/744/2/108, arXiv:1109.3466.

Borkous, V.V., Kaniovsky, A.S., Sunyaev, R.A., Efremov, V.V., Kendziorra, A., Kretschmar, P., Kunz, M., Maisack, M., Staubert, R., Englhauser, J., Pietsch, W., Reppin, C., Truemper, J., 1997. Hard X-ray observations of the bursting pulsar GRO J1744-28 by HEXE onboard MIR-KVANT. In: Winkler, C., Courvoisier, T.J.L., Durouchoux, P. (Eds.), The Transparent Universe. In: ESA Special Publication, 382, p. 299.

Bouchet, L., Roques, J.P., Mandrou, P., Strong, A., Diehl, R., Lebrun, F., Terrier, R., 2005. INTEGRAL SPI observation of the galactic central radian: Contribution of discrete sources and implication for the diffuse emission. Astrophys. J. 635 (2), 1103–1115. http://dx.doi.org/10.1086/497419, arXiv:astro-ph/0510084.

Burenin, R.A., Bikmaev, I.F., Revnivtsev, M.G., Tomsick, J.A., Sazonov, S.Y., Pavlinsky, M.N., Sunyaev, R.A., 2009. Optical identification of the hard X-ray source IGR J18257-0707. Astron. Lett. 35 (2), 71–74. http://dx.doi.org/10.1134/S1063773709020017, arXiv:0810.2512.

Burenin, R.A., Mescheryakov, A.V., Revnivtsev, M.G., Sazonov, S.Y., Bikmaev, I.F., Pavlinsky, M.N., Sunyaev, R.A., 2008. New active galactic nuclei among the INTEGRAL and SWIFT X-ray sources. Astron. Lett. 34 (6), 367–374. http://dx.doi.org/10.1134/S1063773708060017, arXiv:0802.1791.

Butler, S.C., Tomsick, J.A., Chaty, S., Heras, J.A.Z., Rodriguez, J., Walter, R., Kaaret, P., Kalemci, E., Özbey, M., 2009. Identifications of five INTEGRAL sources via optical spectroscopy. Astrophys. J. 698, 502–508. http://dx.doi.org/10.1088/0004-637X/698/1/502, arXiv:0903.1302.

Cavallari, E., Frontera, F., 2017. Hard X-ray/soft gamma-ray experiments and missions: Overview and prospects. Space Sci. Rev. 212 (1–2), 429–518. http://dx.doi.org/10.1007/s11214-017-0426-9, arXiv:1709.10414.

Chaty, S., Rahoui, F., 2012. Broadband ESO/VISIR-Spitzer infrared spectroscopy of the obscured supergiant X-ray binary IGR J16318-4848. Astrophys. J. 751 (2), 150. http://dx.doi.org/10.1088/0004-637X/751/2/150, arXiv:1205.2225.

Chaty, S., Rahoui, F., Foellmi, C., Tomsick, J.A., Rodriguez, J., Walter, R., 2008. Multi-wavelength observations of galactic hard X-ray sources discovered by INTEGRAL. I. The nature of the companion star. Astronom. Astrophys. 484 (3), 783–800. http://dx.doi.org/10.1051/0004-6361:20078768, arXiv:0802.1774.

Cherepashchuk, A.M., Sunyaev, R.A., Seifina, E.V., Panchenko, I.E., Molkov, S.V., Postnov, K.A., 2003. INTEGRAL observations of SS433, a supercritically accreting microquasar with hard spectrum. Astronom. Astrophys. 411, L441–L445. http://dx.doi.org/10.1051/0004-6361:20031323, arXiv:astro-ph/0309140.

Churazov, E., Sazonov, S., Sunyaev, R., Revnivtsev, M., 2008. Earth X-ray albedo for cosmic X-ray background radiation in the 1-1000 keV band. Mon. Not. R. Astron. Soc. 385 (2), 719–727. http://dx.doi.org/10.1111/j.1365-2966.2008.12918.x.

Churazov, E., Sunyaev, R., Isern, J., Bikmaev, I., Bravo, E., Chugai, N., Grebenev, S., Jean, P., Knödlseder, J., Lebrun, F., Kuulkers, E., 2015. Gamma-rays from type ia supernova SN2014J. Astrophys. J. 812, 62. http://dx.doi.org/10.1088/0004-637X/812/1/62, arXiv:1502.00255.

Churazov, E., Sunyaev, R., Revnivtsev, M., Sazonov, S., Molkov, S., Grebenev, S., Winkler, C., Parmar, A., Bazzano, A., Falanga, M., Gros, A., Lebrun, F., Natalucci, L., Ubertini, P., Roques, J.-P., Bouchet, L., Jourdain, E., Knödlseder, J., Diehl, R., Budtz-Jorgensen, C., Brandt, S., Lund, N., Westergaard, N.J., Neronov, A., Türler, M., Chernyakova, M., Walter, R., Produit, N., Mowlavi, N., Mas-Hesse, J.M., Domingo, A., Gehrels, N., Kuulkers, E., Kretschmar, P., Schmidt, M., 2007. INTEGRAL observations of the cosmic X-ray background in the 5-100 keV range via occultation by the Earth. Astronom. Astrophys. 467, 529–540. http://dx.doi.org/10.1051/0004-6361:20066230, arXiv:astro-ph/0608250.

Churchwell, E., Babler, B.L., Meade, M.R., Whitney, B.A., Benjamin, R., Indebetouw, R., Cyganowski, C., Robitaille, T.P., Povich, M., Watson, C., Bracker, S., 2009. The Spitzer/GLIMPSE surveys: A new view of the milky way. Publ. Astron. Soc. Pac. 121 (877), 213. http://dx.doi.org/10.1086/597811.

Cieslinski, D., Elizalde, F., Steiner, J.E., 1994. Observations of suspected symbiotic stars. Astron. Astrophys. Suppl. Ser. 106, 243–251.

Coe, M.J., Carpenter, G.F., Engel, A.R., Quenby, J.J., 1982. Journal of high energy X-ray observations from the Ariel V satellite. Mon. Not. R. Astron. Soc. 200, 385–390. http://dx.doi.org/10.1093/mnras/200.2.385.

Coleiro, A., Chaty, S., Zurita Heras, J.A., Rahoui, F., Tomsick, J.A., 2013. Infrared identification of high-mass X-ray binaries discovered by INTEGRAL. Astronom. Astrophys. 560, A108. http://dx.doi.org/10.1051/0004-6361/201322382, arXiv:1310.0451.

Courvoisier, T.J.L., Walter, R., Beckmann, V., Dean, A.J., Dubath, P., Hudec, R., Kretschmar, P., Mereghetti, S., Montmerle, T., Mowlavi, N., Paltani, S., Preite Martinez, A., Produit, N., Staubert, R., Strong, A.W., Swings, J.P., Westergaard, N.J., White, N., Winkler, C., Zdziarski, A.A., 2003. The INTEGRAL science data centre (ISDC). Astronom. Astrophys. 411, L53–L57. http://dx.doi.org/10.1051/0004-6361:20031172, arXiv:astro-ph/0308047.

Cusumano, G., La Parola, V., Segreto, A., Ferrigno, C., Maselli, A., Sbarufatti, B., Romano, P., Chincarini, G., Giommi, P., Masetti, N., Moretti, A., Parisi, P., Tagliaferri, G., 2010. The palermo swift-BAT hard X-ray catalogue. III. Results after 54 months of sky survey. Astronom. Astrophys. 524, A64. http://dx.doi.org/10.1051/0004-6361/201015249, arXiv:1009.0522.

De Falco, V., Kuiper, L., Bozzo, E., Ferrigno, C., Poutanen, J., Stella, L., Falanga, M., 2017. The transitional millisecond pulsar IGR J18245-2452 during its 2013 outburst at X-rays and soft gamma-rays. Astronom. Astrophys. 603, A16. http://dx.doi.org/10.1051/0004-6361/201730600, arXiv:1704.04181.

de Martino, D., Belloni, T., Falanga, M., Papitto, A., Motta, S., Pellizzoni, A., Evangelista, Y., Piano, G., Masetti, N., Bonnet-Bidaud, J.M., Mouchet, M., Mukai, K., Possenti, A., 2013. X-ray follow-ups of XSS J12270-4859: a low-mass X-ray binary with gamma-ray Fermi-LAT association. Astronom. Astrophys. 550, A89. http://dx.doi.org/10.1051/0004-6361/201220393, arXiv:1212.1615.

de Martino, D., Bernardini, F., Mukai, K., Falanga, M., Masetti, N., 2020. Hard X-ray cataclysmic variables. Adv. Space Res. 66 (5), 1209–1225. http://dx.doi.org/10.1016/j.asr.2019.09.006, arXiv:1909.06306.

den Hartog, P.R., Hermsen, W., Kuiper, L., Vink, J., in't Zand, J.J.M., Collmar, W., 2006. INTEGRAL survey of the cassiopeia region in hard X rays. Astronom. Astrophys. 451 (2), 587–602. http://dx.doi.org/10.1051/0004-6361:20054711, arXiv:astro-ph/0601644.

Diehl, R., 2014. Cosmic gamma-ray spectroscopy. Astron. Rev. 9 (3), 1–54. http://dx.doi.org/10.1080/21672857.2014.11519736.

Emelyanov, A.N., Aleksandrovich, N.L., Sunyaev, R.A., 2000. A catalog of X-ray sources as observed by the TTM/COMIS telescope onboard the Mir-Kvant observatory in 1988-1998. Astron. Lett. 26, 297–308. http://dx.doi.org/10.1134/1.20394.

Fenimore, E., Cannon, T.M., 1981. Uniformly redundant arrays: digital reconstruction methods. Appl. Opt. 20 (10), 1858–1864. http://dx.doi.org/10.1364/AO.20.001858, URL: http://ao.osa.org/abstract.cfm?URI=ao-20-10-1858.

Filliatre, P., Chaty, S., 2004. The optical/near-infrared counterpart of the INTEGRAL obscured source IGR J16318-4848: An sgB[e] in a high-mass X-ray binary? Astrophys. J. 616 (1), 469–484. http://dx.doi.org/10.1086/424869, arXiv:astro-ph/0408407.

Forman, W., Jones, C., Cominsky, L., Julien, P., Murray, S., Peters, G., Tananbaum, H., Giacconi, R., 1978. The fourth uhuru catalog of X-ray sources. Astrophys. J. Suppl. 38, 357–412. http://dx.doi.org/10.1086/190561.

Fortin, F., Chaty, S., Coleiro, A., Tomsick, J.A., Nitschelm, C.H.R., 2018. Spectroscopic identification of INTEGRAL high-energy sources with VLT/ISAAC. Astronom. Astrophys. 618, A150. http://dx.doi.org/10.1051/0004-6361/201731265, arXiv:1808.09816.

Fortin, F., Chaty, S., Sander, A., 2020. Optical and infrared study of the obscured B[e] supergiant high-mass X-ray binary IGR J16318-4848. Astrophys. J. 894 (2), 86. http://dx.doi.org/10.3847/1538-4357/ab881c, arXiv:2004.04997.

Frontera, F., Orlandini, M., Landi, R., Comastri, A., Fiore, F., Setti, G., Amati, L., Costa, E., Masetti, N., Palazzi, E., 2007. The cosmic X-ray background and the population of the most heavily obscured AGNs. Astrophys. J. 666 (1), 86–95. http://dx.doi.org/10.1086/519985, arXiv:astro-ph/0611228.

García, F., Fogantini, F.A., Chaty, S., Combi, J.A., 2018. Spectral evolution of the supergiant HMXB IGR J16320-4751 along its orbit using XMM-Newton. Astronom. Astrophys. 618, A61. http://dx.doi.org/10.1051/0004-6361/201833365, arXiv:1810.01910.

Gehrels, N., Chincarini, G., Giommi, P., Mason, K.O., Nousek, J.A., Wells, A.A., White, N.E., Barthelmy, S.D., Burrows, D.N., Cominsky, L.R., Hurley, K.C., Marshall, F.E., Mészáros, P., Roming, P.W.A., Angelini, L., Barbier, L.M., Belloni, T., Campana, S., Caraveo, P.A., Chester, M.M., Citterio, O., Cline, T.L., Cropper, M.S., Cummings, J.R., Dean, A.J., Feigelson, E.D., Fenimore, E.E., Frail, D.A., Fruchter, A.S., Garmire, G.P., Gendreau, K., Ghisellini, G., Greiner, J., Hill, J.E., Hunsberger, S.D., Krimm, H.A., Kulkarni, S.R., Kumar, P., Lebrun, F., Lloyd-Ronning, N.M., Markwardt, C.B., Mattson, B.J., Mushotzky, R.F., Norris, J.P., Osborne, J., Paczynski, B., Palmer, D.M., Park, H.S., Parsons, A.M., Paul, J., Rees, M.J., Reynolds, C.S., Rhoads, J.E., Sasseen, T.P., Schaefer, B.E., Short, A.T., Smale, A.P., Smith, I.A., Stella, L., Tagliaferri, G., Takahashi, T., Tashiro, M., Townsley, L.K., Tueller, J., Turner, M.J.L., Vietri, M., Voges, W., Ward, M.J., Willingale, R., Zerbi, F.M., Zhang, W.W., 2004. The swift gamma-ray burst mission. Astrophys. J. 611 (2), 1005–1020. http://dx.doi.org/10.1086/422091, arXiv:astro-ph/0405233.

Gendreau, K.C., Mushotzky, R., Fabian, A.C., Holt, S.S., Kii, T., Serlemitsos, P.J., Ogasaka, Y., Tanaka, Y., Bautz, M.W., Fukazawa, Y., Ishisaki, Y., Kohmura, Y., Makishima, K., Tashiro, M., Tsusaka, Y., Kunieda, H., Ricker, G.R., Vanderspek, R.K., 1995. ASCA observations of the spectrum of the X-ray background. Publ. Astron. Soc. Japan 47, L5–L9.

Giacconi, R., Murray, S., Gursky, H., Kellogg, E., Schreier, E., Matilsky, T., Koch, D., Tananbaum, H., 1974. The third UHURU catalog of X-ray sources. Astrophys. J. Suppl. 27, 37. http://dx.doi.org/10.1086/190288.

Goldwurm, A., David, P., Foschini, L., Gros, A., Laurent, P., Sauvageon, A., Bird, A.J., Lerusse, L., Produit, N., 2003. The INTEGRAL/IBIS scientific data analysis. Astronom. Astrophys. 411, L223–L229. http://dx.doi.org/10.1051/0004-6361:20031395, arXiv:astro-ph/0311172.

Götz, D., Mereghetti, S., Molkov, S., Hurley, K., Mirabel, I.F., Sunyaev, R., Weidenspointner, G., Brand t, S., del Santo, M., Feroci, M., Göğüş, E., von Kienlin, A., van der Klis, M., Kouveliotou, C., Lund, N., Pizzichini, G., Ubertini, P., Winkler, C., Woods, P.M., 2006. Two years of INTEGRAL monitoring of the soft gamma-ray repeater SGR 1806-20: from quiescence to frenzy. Astronom. Astrophys. 445 (1), 313–321. http://dx.doi.org/10.1051/0004-6361:20053648, arXiv:astro-ph/0508615.

Grebenev, S.A., Lutovinov, A.A., Tsygankov, S.S., Mereminskiy, I.A., 2013. Deep hard X-ray survey of the large magellanic cloud. Mon. Not. R. Astron. Soc. 428, 50–57. http://dx.doi.org/10.1093/mnras/sts008, arXiv:1207.1750.

Grebenev, S.A., Lutovinov, A.A., Tsygankov, S.S., Winkler, C., 2012. Hard-X-ray emission lines from the decay of ^{44}Ti in the remnant of supernova 1987A. Nature 490 (7420), 373–375. http://dx.doi.org/10.1038/nature11473, arXiv:1211.2656.

Grebenev, S.A., Mereminskiy, I.A., 2015. JEM-X/INTEGRAL X-ray survey of the galactic center region. Astron. Lett. 41, 765–784. http://dx.doi.org/10.1134/S1063773715120038.

Green, D.A., 2014. A catalogue of 294 Galactic supernova remnants. Bull. Astron. Soc. India 42 (2), 47–58. arXiv:1409.0637.

Gruber, D.E., Matteson, J.L., Peterson, L.E., Jung, G.V., 1999. The spectrum of diffuse cosmic hard X-rays measured with HEAO 1. Astrophys. J. 520 (1), 124–129. http://dx.doi.org/10.1086/307450, arXiv:astro-ph/9903492.

Halpern, J.P., Tomsick, J.A., Gotthelf, E.V., Camilo, F., Ng, C.Y., Bodaghee, A., Rodriguez, J., Chaty, S., Rahoui, F., 2014. Discovery of X-ray pulsations from the INTEGRAL source IGR J11014-6103. Astrophys. J. 795 (2), L27. http://dx.doi.org/10.1088/2041-8205/795/2/L27, arXiv:1410.2332.

Hannikainen, D.C., Vilhu, O., Rodriguez, J., Brand t, S., Westergaard, N.J., Lund, N., Mocœur, I., Durouchoux, P., Belloni, T., Castro-Tirado, A., Charles, P.A., Dean, A.J., Fender, R.P., Feroci, M., Hakala, P., Hunstead, R.W., Kaiser, C.R., King, A., Mirabel, I.F., Pooley, G.G., Poutanen, J., Wu, K., Zdziarski, A.A., 2003. First INTEGRAL observations of GRS 1915+105. Astronom. Astrophys. 411, L415–L419. http://dx.doi.org/10.1051/0004-6361:20031444, arXiv:astro-ph/0309532.

Israel, G.L., Romano, P., Mangano, V., Dall'Osso, S., Chincarini, G., Stella, L., Campana, S., Belloni, T., Tagliaferri, G., Blustin, A.J., Sakamoto, T., Hurley, K., Zane, S., Moretti, A., Palmer, D., Guidorzi, C., Burrows, D.N., Gehrels, N., Krimm, H.A., 2008. A swift gaze into the 2006 March 29 burst forest of SGR 1900+14. Astrophys. J. 685 (2), 1114–1128. http://dx.doi.org/10.1086/590486, arXiv:0805.3919.

Iyer, N., Paul, B., 2017. Orbital variations in intensity and spectral properties of the highly obscured sgHMXB IGR J16318-4848. Mon. Not. R. Astron. Soc. 471, 355–363. http://dx.doi.org/10.1093/mnras/stx1575, arXiv:1706.07199.

Iyudin, A.F., Schönfelder, V., Bennett, K., Bloemen, H., Diehl, R., Hermsen, W., Knödlseder, J., Lichti, G.G., Oberlack, U., Ryan, J., Strong, A.W., Winkler, C., 1999. COMPTEL all-sky survey in ^{44}Ti line emission. Astrophys. Lett. Commun. 38, 383.

Jager, R., Mels, W.A., Brinkman, A.C., Galama, M.Y., Goulooze, H., Heise, J., Lowes, P., Muller, J.M., Naber, A., Rook, A., Schuurhof, R., Schuurmans, J.J., Wiersma, G., 1997. The wide field cameras onboard the BeppoSAX X-ray astronomy satellite. Astron. Astrophys. Suppl. Ser. 125, 557–572. http://dx.doi.org/10.1051/aas:1997243.

Kajava, J.J.E., Veledina, A., Tsygankov, S., Neustroev, V., 2016. The origin of seed photons for comptonization in the black hole binary swift J1753.5-0127. Astronom. Astrophys. 591, A66. http://dx.doi.org/10.1051/0004-6361/201527939, arXiv:1603.08796.

Kaniovsky, A.S., Arefiev, V.A., Aleksandrovich, N.L., Borkous, V.V., Borozdin, K.N., Efremov, V.V., Sunyaev, R.A., Kendziorra, E., Kretschmar, P., Kunz, M., Maisack, M., Staubert, R., Doebereiner, S., Englhauser, J., Pietsch, W., Reppin, C., Truemper, J., Skinner, G.K., Willmore, A.P., Brinkman, A.C., Heise, J., Jager, R., 1997. Three hard X-ray transients: GRO J0422+32, GRS 1716-24, GRS 1009-45. Broad band observations by Roentgen-MIR-KVANT observatory. Adv. Space Res. 19 (1), 29–34. http://dx.doi.org/10.1016/S0273-1177(97)00033-1.

Karasev, D.I., Lutovinov, A.A., Tkachenko, A.Y., Khorunzhev, G.A., Krivonos, R.A., Medvedev, P.S., Pavlinsky, M.N., Burenin, R.A., Eselevich, M.V., 2018. Optical identification of X-ray sources from the 14-year INTEGRAL all-sky survey. Astron. Lett. 44 (8–9), 522–540. http://dx.doi.org/10.1134/S1063773718090037, arXiv:1809.02949.

Karasev, D.I., Sazonov, S.Y., Tkachenko, A.Y., Khorunzhev, G.A., Krivonos, R.A., Medvedev, P.S., Zaznobin, I.A., Mereminskiy, I.A., Burenin, R.A., Pavlinsky, M.N., Eselevich, M.V., 2020. Optical identification of four hard X-ray sources from the INTEGRAL sky surveys. Astron. Lett. 45 (12), 836–846. http://dx.doi.org/10.1134/S1063773719120028, arXiv:2003.07199.

Kinzer, R.L., Jung, G.V., Gruber, D.E., Matteson, J.L., Peterson, L.E., 1997. Diffuse cosmic gamma radiation measured by HEAO 1. Astrophys. J. 475 (1), 361–372. http://dx.doi.org/10.1086/303507.

Kouveliotou, C., Strohmayer, T., Hurley, K., van Paradijs, J., Finger, M.H., Dieters, S., Woods, P., Thompson, C., Duncan, R.C., 1999. Discovery of a magnetar associated with the soft gamma repeater SGR 1900+14. Astrophys. J. 510 (2), L115–L118. http://dx.doi.org/10.1086/311813, arXiv:astro-ph/9809140.

Kretschmar, P., Fürst, F., Sidoli, L., Bozzo, E., Alfonso-Garzón, J., Bodaghee, A., Chaty, S., Chernyakova, M., Ferrigno, C., Manousakis, A., Negueruela, I., Postnov, K., Paizis, A., Reig, P., Rodes-Roca, J.J., Tsygankov, S., Bird, A.J., Bissinger né Kühnel, M., Blay, P., Caballero, I., Coe, M.J., Domingo, A., Doroshenko, V., Ducci, L., Falanga, M., Grebenev, S.A., Grinberg, V., Hemphill, P., Kreykenbohm, I., Kreykenbohm né Fritz, S., Li, J., Lutovinov, A.A., Martínez-Núñez, S., Mas-Hesse, J.M., Masetti, N., McBride, V.A., Neronov, A., Pottschmidt, K., Rodriguez, J., Romano, P., Rothschild, R.E., Santangelo, A., Sguera, V., Staubert, R., Tomsick, J.A., Torrejón, J.M., Torres, D.F., Walter, R., Wilms, J., Wilson-Hodge, C.A., Zhang, S., 2019. Advances in understanding high-mass X-ray binaries with INTEGRALand future directions. New Astron. Rev. 86, 101546. http://dx.doi.org/10.1016/j.newar.2020.101546.

Krivonos, R., Revnivtsev, M., Lutovinov, A., Sazonov, S., Churazov, E., Sunyaev, R., 2007. INTEGRAL/IBIS all-sky survey in hard X-rays. Astronom. Astrophys. 475, 775–784. http://dx.doi.org/10.1051/0004-6361:20077191, arXiv:astro-ph/0701836.

Krivonos, R., Revnivtsev, M., Tsygankov, S., Sazonov, S., Vikhlinin, A., Pavlinsky, M., Churazov, E., Sunyaev, R., 2010a. INTEGRAL/IBIS 7-year all-sky hard X-ray survey. I. Image reconstruction. Astronom. Astrophys. 519, A107. http://dx.doi.org/10.1051/0004-6361/200913814, arXiv:1006.2463.

Krivonos, R., Tsygankov, S., Lutovinov, A., Revnivtsev, M., Churazov, E., Sunyaev, R., 2012. INTEGRAL/IBIS nine-year galactic hard X-ray survey. Astronom. Astrophys. 545, A27. http://dx.doi.org/10.1051/0004-6361/201219617, arXiv:1205.3941.

Krivonos, R., Tsygankov, S., Lutovinov, A., Revnivtsev, M., Churazov, E., Sunyaev, R., 2015. INTEGRAL 11-year hard X-ray survey above 100 keV. Mon. Not. R. Astron. Soc. 448, 3766–3774. http://dx.doi.org/10.1093/mnras/stv150, arXiv:1412.1051.

Krivonos, R.A., Tsygankov, S.S., Mereminskiy, I.A., Lutovinov, A.A., Sazonov, S.Y., Sunyaev, R.A., 2017. New hard X-ray sources discovered in the ongoing INTEGRAL galactic plane survey after 14 yr of observations. Mon. Not. R. Astron. Soc. 470, 512–516. http://dx.doi.org/10.1093/mnras/stx1276, arXiv:1704.03364.

Krivonos, R., Tsygankov, S., Revnivtsev, M., Grebenev, S., Churazov, E., Sunyaev, R., 2010b. INTEGRAL/IBIS 7-year all-sky hard X-ray survey. II. Catalog of sources. Astronom. Astrophys. 523, A61. http://dx.doi.org/10.1051/0004-6361/201014935, arXiv:1006.4437.

Krivonos, R., Vikhlinin, A., Churazov, E., Lutovinov, A., Molkov, S., Sunyaev, R., 2005. Extragalactic source counts in the 20-50 keV energy band from the deep observation of the coma region by INTEGRAL IBIS. Astrophys. J. 625, 89–94. http://dx.doi.org/10.1086/429657, arXiv:astro-ph/0409093.

Krivonos, R., Wik, D., Grefenstette, B., Madsen, K., Perez, K., Rossland, S., Sazonov, S., Zoglauer, A., 2020. NuSTAR measurement of the cosmic X-ray background in the 3-20 keV energy band. arXiv e-prints, arXiv:2011.11469.

Kuiper, L., Hermsen, W., 2009. High-energy characteristics of the schizophrenic pulsar PSR J1846-0258 in Kes 75. Multi-year RXTE and INTEGRAL observations crossing the magnetar-like outburst. Astronom. Astrophys. 501 (3), 1031–1046. http://dx.doi.org/10.1051/0004-6361/200811580, arXiv:0904.4376.

Kuulkers, E., Shaw, S., Paizis, A., Chenevez, J., Brandt, S., Courvoisier, T.-L., Domingo, A., Ebisawa, K., Kretschmar, P., Markwardt, C., Mowlavi, N., Oosterbroek, T., Orr, A., Rísquez, D., Sanchez-Fernandez, C., Wijnands, R., 2007. The INTEGRAL Galactic bulge monitoring program: the first 1.5 years. Astronom. Astrophys. 466 (1), 595–618. http://dx.doi.org/10.1051/0004-6361:20066651, arXiv:astro-ph/0701244.

Landi, R., Bassani, L., Bazzano, A., Bird, A.J., Fiocchi, M., Malizia, A., Panessa, F., Sguera, V., Ubertini, P., 2017. Investigating the X-ray counterparts to unidentified sources in the 1000-orbit INTEGRAL/IBIS catalogue. Mon. Not. R. Astron. Soc. 470 (1), 1107–1120. http://dx.doi.org/10.1093/mnras/stx908, arXiv:1704.03872.

Landi, R., Bassani, L., Dean, A.J., Bird, A.J., Fiocchi, M., Bazzano, A., Nousek, J.A., Osborne, J.P., 2009a. INTEGRAL/IBIS and swift/XRT observations of hard cataclysmic variables. Mon. Not. R. Astron. Soc. 392 (2), 630–640. http://dx.doi.org/10.1111/j.1365-2966.2008.14086.x, arXiv:0810.1844.

Landi, R., Stephen, J.B., Masetti, N., Grupe, D., Capitanio, F., Bird, A.J., Dean, A.J., Fiocchi, M., Gehrels, N., 2009b. The AGN nature of three INTEGRAL sources: IGR J18249-3243, IGR J19443+2117, and IGR J22292+6647. Astronom. Astrophys. 493 (3), 893–898. http://dx.doi.org/10.1051/0004-6361:200810503, arXiv:0811.2318.

Lebrun, F., Leray, J.P., Lavocat, P., Crétolle, J., Arquès, M., Blondel, C., Bonnin, C., Bouère, A., Cara, C., Chaleil, T., Daly, F., Desages, F., Dzitko, H., Horeau, B., Laurent, P., Limousin, O., Mathy, F., Mauguen, V., Meignier, F., Molinié, F., Poindron, E., Rouger, M., Sauvageon, A., Tourrette, T., 2003. ISGRI: The INTEGRAL soft gamma-ray imager. Astronom. Astrophys. 411, L141–L148. http://dx.doi.org/10.1051/0004-6361:20031367, arXiv:astro-ph/0310362.

Levine, A.M., Lang, F.L., Lewin, W.H.G., Primini, F.A., Dobson, C.A., Doty, J.P., Hoffman, J.A., Howe, S.K., Scheepmaker, A., Wheaton, W.A., Matteson, J.L., Baity, W.A., Gruber, D.E., Knight, F.K., Nolan, P.L., Pelling, R.M., Rothschild, R.E., Peterson, L.E., 1984. The HEAO1 A-4 catalog of high-energy X-ray sources. Astrophys. J. Suppl. 54, 581–617. http://dx.doi.org/10.1086/190944.

Lubiński, P., Beckmann, V., Gibaud, L., Paltani, S., Papadakis, I.E., Ricci, C., Soldi, S., Türler, M., Walter, R., Zdziarski, A.A., 2016. A comprehensive analysis of the hard X-ray spectra of bright seyfert galaxies. Mon. Not. R. Astron. Soc. 458, 2454–2475. http://dx.doi.org/10.1093/mnras/stw454, arXiv:1602.08402.

Lutovinov, A.A., Burenin, R.A., Revnivtsev, M.G., Bikmaev, I.F., 2012a. Optical identification of six hard X-ray sources from the INTEGRAL and SWIFT all-sky surveys. Astron. Lett. 38 (1), 1–11. http://dx.doi.org/10.1134/S1063773712010045.

Lutovinov, A.A., Mironov, A.I., Burenin, R.A., Revnivtsev, M.G., Tsygankov, S.S., Pavlinsky, M.N., Korobtsev, I.V., Eselevich, M.V., 2013a. Identification of four X-ray sources from the INTEGRAL and swift catalogs. Astron. Lett. 39 (8), 513–522. http://dx.doi.org/10.1134/S1063773713080069, arXiv:1307.2761.

Lutovinov, A., Revnivtsev, M., Gilfanov, M., Shtykovskiy, P., Molkov, S., Sunyaev, R., 2005a. INTEGRAL insight into the inner parts of the Galaxy. High mass X-ray binaries. Astronom. Astrophys. 444 (3), 821–829. http://dx.doi.org/10.1051/0004-6361:20042392, arXiv:astro-ph/0411550.

Lutovinov, A.A., Revnivtsev, M.G., Tsygankov, S.S., Krivonos, R.A., 2013b. Population of persistent high-mass X-ray binaries in the Milky Way. Mon. Not. R. Astron. Soc. 431 (1), 327–341. http://dx.doi.org/10.1093/mnras/stt168, arXiv:1302.0728.

Lutovinov, A., Rodriguez, J., Revnivtsev, M., Shtykovskiy, P., 2005b. Discovery of X-ray pulsations from IGR J16320-4751 = AX J1631.9-4752. Astronom. Astrophys. 433 (2), L41–L44. http://dx.doi.org/10.1051/0004-6361:200500092, arXiv:astro-ph/0411547.

Lutovinov, A., Suleimanov, V., Manuel Luna, G.J., Sazonov, S., Martino, D.d., Ducci, L., Doroshenko, V., Falanga, M., 2020. INTEGRAL view on cataclysmic variables and symbiotic binaries. New Astron. Rev. 91, 101547. http://dx.doi.org/10.1016/j.newar.2020.101547, arXiv:2008.10665.

Lutovinov, A., Tsygankov, S., Chernyakova, M., 2012b. Strong outburst activity of the X-ray pulsar X Persei during 2001-2011. Mon. Not. R. Astron. Soc. 423 (2), 1978–1984. http://dx.doi.org/10.1111/j.1365-2966.2012.21036.x, arXiv:1204.0483.

Maiorano, E., Landi, R., Stephen, J.B., Bassani, L., Masetti, N., Parisi, P., Palazzi, E., Parma, P., Bird, A.J., Bazzano, A., Ubertini, P., Jiménez-Bailón, E., Chavushyan, V., Galaz, G., Minniti, D., Morelli, L., 2011. Searching for active galactic nuclei among unidentified INTEGRAL sources. Mon. Not. R. Astron. Soc. 416 (1), 531–540. http://dx.doi.org/10.1111/j.1365-2966.2011.19065.x, arXiv:1105.3089.

Malizia, A., Bassani, L., Stephen, J.B., Bazzano, A., Ubertini, P., Bird, A.J., Dean, A.J., Sguera, V., Renaud, M., Walter, R., Gianotti, F., 2005. The INTEGRAL/IBIS source AX J1838.0-0655: A soft X-ray-to-TeV γ-ray broadband emitter. Astrophys. J. 630 (2), L157–L160. http://dx.doi.org/10.1086/491653, arXiv:astro-ph/0507660.

Malizia, A., Landi, R., Molina, M., Bassani, L., Bazzano, A., Bird, A.J., Ubertini, P., 2016. The INTEGRAL/IBIS AGN catalogue: an update. Mon. Not. R. Astron. Soc. 460 (1), 19–29. http://dx.doi.org/10.1093/mnras/stw972, arXiv:1604.06303.

Markert, T.H., Canizares, C.R., Clark, G.W., Hearn, D.R., Li, F.K., Sprott, G.F., Winkler, P.F., 1977. Observations of galactic X-ray sources by OSO-7. Astrophys. J. 218, 801–814. http://dx.doi.org/10.1086/155737.

Markert, T.H., Canizares, C.R., Clark, G.W., Li, F.K., Northridge, P.L., Sprott, G.F., Wargo, G.F., 1976. OSO-7 observations of high galactic latitude X-ray sources. Astrophys. J. 206, 265–272. http://dx.doi.org/10.1086/154381.

Markert, T.H., Winkler, P.F., Laird, F.N., Clark, G.W., Hearn, D.R., Sprott, G.F., Li, F.K., Bradt, H.V., Lewin, W.H.G., Schnopper, H.W., 1979. The MIT/OSO 7 catalog of X-ray sources: intensities, spectra, and long-term variability. Astrophys. J. Suppl. 39, 573–632. http://dx.doi.org/10.1086/190587.

Masetti, N., Bassani, L., Bird, A.J., Bazzano, A., 2005. Igr J12349-6434 = RT Cru ? Astronom.'s Telegr. 528, 1.

Masetti, N., Landi, R., Pretorius, M.L., Sguera, V., Bird, A.J., Perri, M., Charles, P.A., Kennea, J.A., Malizia, A., Ubertini, P., 2007. IGR J16194-2810: a new symbiotic X-ray binary. Astronom. Astrophys. 470 (1), 331–337. http://dx.doi.org/10.1051/0004-6361:20077509, arXiv:0704.3682.

Masetti, N., Mason, E., Landi, R., Giommi, P., Bassani, L., Malizia, A., Bird, A.J., Bazzano, A., Dean, A.J., Gehrels, N., Palazzi, E., Ubertini, P., 2008. High-redshift blazar identification for Swift J1656.3-3302. Astronom. Astrophys. 480 (3), 715–721. http://dx.doi.org/10.1051/0004-6361:20078901, arXiv:0801.2976.

Masetti, N., Parisi, P., Jiménez-Bailón, E., Palazzi, E., Chavushyan, V., Bassani, L., Bazzano, A., Bird, A.J., Dean, A.J., Galaz, G., Landi, R., Malizia, A., Minniti, D., Morelli, L., Schiavone, F., Stephen, J.B., Ubertini, P., 2012. Unveiling the nature of INTEGRAL objects through optical spectroscopy. IX. Twenty two more identifications, and a glance into the far hard X-ray Universe. Astronom. Astrophys. 538, A123. http://dx.doi.org/10.1051/0004-6361/201118559, arXiv:1201.1906.

Masetti, N., Parisi, P., Palazzi, E., Jiménez-Bailón, E., Chavushyan, V., McBride, V., Rojas, A.F., Steward, L., Bassani, L., Bazzano, A., Bird, A.J., Charles, P.A., Galaz, G., Landi, R., Malizia, A., Mason, E., Minniti, D., Morelli, L., Schiavone, F., Stephen, J.B., Ubertini, P., 2013. Unveiling the nature of INTEGRAL objects through optical spectroscopy. X. A new multi-year, multi-observatory campaign. Astronom. Astrophys. 556, A120. http://dx.doi.org/10.1051/0004-6361/201322026, arXiv:1307.2898.

Matt, G., Guainazzi, M., 2003. The properties of the absorbing and line-emitting material in IGR J16318 - 4848. Mon. Not. R. Astron. Soc. 341 (3), L13–L17. http://dx.doi.org/10.1046/j.1365-8711.2003.06658.x, arXiv:astro-ph/0303626.

Mereminskiy, I.A., Krivonos, R.A., Lutovinov, A.A., Sazonov, S.Y., Revnivtsev, M.G., Sunyaev, R.A., 2016. INTEGRAL/IBIS deep extragalactic survey: M81, LMC and 3C 273/Coma fields. Mon. Not. R. Astron. Soc. 459, 140–150. http://dx.doi.org/10.1093/mnras/stw613, arXiv:1602.00463.

Molkov, S.V., Cherepashchuk, A.M., Lutovinov, A.A., Revnivtsev, M.G., Postnov, K.A., Sunyaev, R.A., 2004. A hard X-ray survey of the sagittarius arm tangent with the IBIS telescope of the INTEGRAL observatory: A catalog of sources. Astron. Lett. 30, 534–539. http://dx.doi.org/10.1134/1.1784495, arXiv:astro-ph/0402416.

Natalucci, L., Fiocchi, M., Bazzano, A., Ubertini, P., Roques, J.-P., Jourdain, E., 2015. High energy spectral evolution of V404 Cygni during the 2015 June outburst as observed by INTEGRAL. Astrophys. J. 813, L21. http://dx.doi.org/10.1088/2041-8205/813/1/L21, arXiv:1510.03197.

Negueruela, I., Smith, D.M., Reig, P., Chaty, S., Torrejón, J.M., 2006. Supergiant fast X-ray transients: A new class of high mass X-ray binaries unveiled by INTEGRAL. In: Wilson, A. (Ed.), The X-Ray Universe 2005. In: ESA Special Publication, vol. 604, p. 165, arXiv:astro-ph/0511088.

Oh, K., Koss, M., Markwardt, C.B., Schawinski, K., Baumgartner, W.H., Barthelmy, S.D., Cenko, S.B., Gehrels, N., Mushotzky, R., Petulante, A., Ricci, C., Lien, A., Trakhtenbrot, B., 2018. The 105-month swift-BAT all-sky hard X-ray survey. Astrophys. J. Suppl. 235 (1), 4. http://dx.doi.org/10.3847/1538-4365/aaa7fd, arXiv:1801.01882.

Özbey Arabacı, M., Kalemci, E., Tomsick, J.A., Halpern, J., Bodaghee, A., Chaty, S., Rodriguez, J., Rahoui, F., 2012. Investigating the optical counterpart candidates of four INTEGRAL sources localized with Chandra. Astrophys. J. 761 (1), 4. http://dx.doi.org/10.1088/0004-637X/761/1/4, arXiv:1210.4789.

Paltani, S., Walter, R., McHardy, I.M., Dwelly, T., Steiner, C., Courvoisier, T.J.L., 2008. A deep INTEGRAL hard X-ray survey of the 3c 273/Coma region. Astronom. Astrophys. 485, 707–718. http://dx.doi.org/10.1051/0004-6361:200809450, arXiv:0805.0537.

Paul, J., Mandrou, P., Ballet, J., Cantin, M., Chabaud, J.P., Cordier, B., Ehanno, M., Goldwurm, A., Lambert, A., Landé, J., Laurent, P., Lebrun, F., Leray, J.P., Ména, B., Niel, M., Roques, J.P., Rouaix, G., Salotti, L., Souleille, P., Vedrenne, G., 1991. SIGMA: The hard X-ray and soft gamma-ray telescope on board the GRANAT space observatory. Adv. Space Res. 11 (8), 289–302. http://dx.doi.org/10.1016/0273-1177(91)90181-I.

Pavlinsky, M.N., Grebenev, S.A., Sunyaev, R.A., 1994. X-ray images of the galactic center obtained with art-P/granat: Discovery of new sources, variability of persistent sources, and localization of X-ray bursters. Astrophys. J. 425, 110. http://dx.doi.org/10.1086/173967.

Rahoui, F., Chaty, S., Lagage, P.-O., Pantin, E., 2008. The most obscured high-energy sources of the Galaxy brought to light by optical/infrared observations. Astron. Astrophys. 484, 801.

Rea, N., Israel, G.L., Turolla, R., Esposito, P., Mereghetti, S., Götz, D., Zane, S., Tiengo, A., Hurley, K., Feroci, M., Still, M., Yershov, V., Winkler, C., Perna, R., Bernardini, F., Ubertini, P., Stella, L., Campana, S., van der Klis, M., Woods, P., 2009. The first outburst of the new magnetar candidate SGR0501+4516. Mon. Not. R. Astron. Soc. 396 (4), 2419–2432. http://dx.doi.org/10.1111/j.1365-2966.2009.14920.x, arXiv:0904.2413.

Revnivtsev, M., Lutovinov, A., Churazov, E., Sazonov, S., Gilfanov, M., Grebenev, S., Sunyaev, R., 2008. Low-mass X-ray binaries in the bulge of the Milky Way. Astronom. Astrophys. 491 (1), 209–217. http://dx.doi.org/10.1051/0004-6361:200810115, arXiv:0805.0259.

Revnivtsev, M.G., Sazonov, S.Y., Molkov, S.V., Lutovinov, A.A., Churazov, E.M., Sunyaev, R.A., 2006. Hard X-ray survey of the Galactic plane region in Crux: A catalog of sources. Astron. Lett. 32 (3), 145–148. http://dx.doi.org/10.1134/S1063773706030017, arXiv:astro-ph/0508155.

Revnivtsev, M.G., Sunyaev, R.A., Gilfanov, M.R., Churazov, E.M., Goldwurm, A., Paul, J., Mandrou, P., Roques, J.P., 2004a. A hard X-ray sky survey with the SIGMA telescope of the GRANAT observatory. Astron. Lett. 30, 527–533. http://dx.doi.org/10.1134/1.1784494, arXiv:astro-ph/0403481.

Revnivtsev, M.G., Sunyaev, R.A., Varshalovich, D.A., Zheleznyakov, V.V., Cherepashchuk, A.M., Lutovinov, A.A., Churazov, E.M., Grebenev, S.A., Gilfanov, M.R., 2004b. A hard X-ray survey of the galactic-center region with the IBIS telescope of the INTEGRAL observatory: A catalog of sources. Astron. Lett. 30, 382–389. http://dx.doi.org/10.1134/1.1764884, arXiv:astro-ph/0402027.

Revnivtsev, M.G., Tsygankov, S.S., Churazov, E.M., Krivonos, R.A., 2014. Hard X-ray emission of Sco X-1. Mon. Not. R. Astron. Soc. 445 (2), 1205–1212. http://dx.doi.org/10.1093/mnras/stu1831, arXiv:1409.1679.

Rodriguez, J., Tomsick, J.A., Bodaghee, A., Zurita Heras, J.A., Chaty, S., Paizis, A., Corbel, S., 2009a. The nature of the X-ray binary <ASTROBJ>IGR J19294+1816</ASTROBJ> from INTEGRAL, RXTE, and Swift observations. Astronom. Astrophys. 508 (2), 889–894. http://dx.doi.org/10.1051/0004-6361/200912739, arXiv:0910.2799.

Rodriguez, J., Tomsick, J.A., Chaty, S., 2008. Swift follow-up observations of INTEGRAL sources of unknown nature. Astronom. Astrophys. 482, 731–737. http://dx.doi.org/10.1051/0004-6361:20079208, arXiv:0712.1005.

Rodriguez, J., Tomsick, J.A., Chaty, S., 2009b. Swift follow-up observations of 17 INTEGRAL sources of uncertain or unknown nature. Astronom. Astrophys. 494 (1), 417–428. http://dx.doi.org/10.1051/0004-6361:200810773, arXiv:0811.4707.

Sazonov, S., Churazov, E., Sunyaev, R., Revnivtsev, M., 2007a. Hard X-ray emission of the Earth's atmosphere: Monte Carlo simulations. Mon. Not. R. Astron. Soc. 377 (4), 1726–1736. http://dx.doi.org/10.1111/j.1365-2966.2007.11746.x, arXiv:astro-ph/0608253.

Sazonov, S., Revnivtsev, M., Krivonos, R., Churazov, E., Sunyaev, R., 2007b. Hard X-ray luminosity function and absorption distribution of nearby AGN: INTEGRAL all-sky survey. Astron. Astrophys. 462 (1), 57–66. http://dx.doi.org/10.1051/0004-6361:20066277, arXiv:astro-ph/0608418.

Sguera, V., Barlow, E.J., Bird, A.J., Clark, D.J., Dean, A.J., Hill, A.B., Moran, L., Shaw, S.E., Willis, D.R., Bazzano, A., Ubertini, P., Malizia, A., 2005. INTEGRAL observations of recurrent fast X-ray transient sources. Astronom. Astrophys. 444 (1), 221–231. http://dx.doi.org/10.1051/0004-6361:20053103, arXiv:astro-ph/0509018.

Skinner, G.K., Ponman, T.J., Hammersley, A.P., Eyles, C.J., 1987a. Techniques for the analysis of data from coded mask X-ray telescopes. Astrophys. Space Sci. 136 (2), 337–349. http://dx.doi.org/10.1007/BF00642125.

Skinner, G.K., Willmore, A.P., Eyles, C.J., Bertram, D., Church, M.J., 1987b. Hard X-ray images of the galactic centre. Nature 330 (6148), 544–547. http://dx.doi.org/10.1038/330544a0.

Smith, D.M., Markwardt, C.B., Swank, J.H., Negueruela, I., 2012. Fast X-ray transients towards the Galactic bulge with the rossi X-ray timing explorer. Mon. Not. R. Astron. Soc. 422 (3), 2661–2674. http://dx.doi.org/10.1111/j.1365-2966.2012.20836.x, arXiv:1202.6434.

Stephen, J.B., Bassani, L., Malizia, A., Bazzano, A., Ubertini, P., Bird, A.J., Dean, A.J., Lebrun, F., Walter, R., 2006. Using the ROSAT catalogues to find counterparts for the second IBIS/ISGRI survey sources. Astronom. Astrophys. 445 (3), 869–873. http://dx.doi.org/10.1051/0004-6361:20053958, arXiv:astro-ph/0509620.

Sunyaev, R.A., Babichenko, S.I., Goganov, D.A., Tabaldyev, S.R., Iamburenko, N.S., 1990. X-ray telescopes ART-P and ART-S for the granat project. Adv. Space Res. 10 (2), 233–237. http://dx.doi.org/10.1016/0273-1177(90)90147-R.

Sunyaev, R., Borozdin, K., Gilfanov, M., et al., 1991. "MIR - KVANT" observations of extremely hard X-ray source 1E 1740.7-2942. Pisma v Astronomicheskii Zhurnal 17, 126.

Sunyaev, R., Churazov, E., Gilfanov, M.R., Yamburenko, V.L.N., Skinner, G.K., Patterson, T.G., Willmore, A.P., Emam, O., Brinkman, A.C., Heise, J., Int-Zand, J.J.M., Jager, R., 1989. X-Ray observations of the large magellanic cloud field by the TTM instrument on board the KVANT module - 1988NOV - 1989JUN. In: Hunt, J., Battrick, B. (Eds.), Two Topics in X-Ray Astronomy, Volume 1: X Ray Binaries. Volume 2: AGN and the X Ray Background. In: ESA Special Publication, vol. 1, p. 633.

Sunyaev, R.A., Lapshov, I.Y., Grebenev, S.A., Efremov, V.V., Kaniovsky, A.S., Stepanov, D.K., Yunin, S.N., Gavrilova, N.S., Loznikov, V.M., Prudkoglyad, A.V., Rodin, V.G., Babushkina, O.P., Kiselev, S.V., Kuznetsov, A.V., Melioransky, A.S., Melioransky, A.S., Smith, A., Parmar, A., Pietch, W., Doebereiner, S., Englhauser, J., Reppin, C., Truemper, J., Voges, W., Kendziorra, E., Maisack, M., Mony, B., Staubert, R., 1988. Detection of hard component in the X-ray spectrum of X-ray nova in Vulpecula. Preliminary results from KVANT module. Pisma v Astronomicheskii Zhurnal 14, 771–786.

Syunyaev, R.A., Arefev, V.A., Borozdin, K.N., Gilfanov, M.R., Efremov, V.V., Kaniovskii, A.S., Churazov, E.M., Kendziorra, E., Mony, B., Kretschmar, P., Maisack, M., Staubert, R., Dobereiner, S., Englhauser, J., Pietsch, W., Reppin, C., Trumper, J., Skinner, G.K., Nottingham, M.R., Pan, H., Willmore, A.P., 1991a. Broadband X-ray spectra of black-hole candidates X-ray pulsars and low-mass binary X-ray systems - KVANT module results. Sov. Astron. Lett. 17, 409.

Syunyaev, R., Borozdin, K., Gilfanov, M., Efremov, V., Kaniovskii, A., Churazov, E., Skinner, G.K., Al-Emam, O., Patterson, T.G., Willmore, A.P., Brinkman, A.C., Heise, J., Int-Zand, J.J.M., Jager, R., Voges, W., Pietsch, W., Doebereiner, S., Engelhauser, J., Trumper, J., Reppin, C., Kendziorra, E., Mony, B., Maisack, M., Staubert, R., 1991b. Anomalously hard spectrum from the source 1E:1740.7-294 - Data from the rontgen observatory on the KVANT module. Sov. Astron. Lett. 17, 54.

Syunyaev, R.A., Kaniovskii, A.S., Efremov, V.V., Grebenev, S.A., Kuznetsov, A.V., Loznikov, V.M., Melioranskii, A.S., Engelhauser, J., Dobereiner, S., Pietsch, W., Reppin, C., Trumper, J., Kendziorra, E., Maisack, M., Mony, B., Staubert, R., 1989. Hard X-ray decline of supernova 1987A in 1988 - the MIR / KVANT data. Sov. Astron. Lett. 15, 125.

Tomsick, J.A., Bodaghee, A., Chaty, S., Clavel, M., Fornasini, F.M., Hare, J., Krivonos, R., Rahoui, F., Rodriguez, J., 2020. Chandra observations of high-energy X-ray sources discovered by INTEGRAL. Astrophys. J. 889 (1), 53. http://dx.doi.org/10.3847/1538-4357/ab5fd2, arXiv:1912.03315.

Tomsick, J.A., Bodaghee, A., Chaty, S., Rodriguez, J., Rahoui, F., Halpern, J., Kalemci, E., Özbey Arabaci, M., 2012a. Localizing INTEGRAL sources with Chandra: X-ray and multi-wavelength identifications and energy spectra. Astrophys. J. 754 (2), 145. http://dx.doi.org/10.1088/0004-637X/754/2/145, arXiv:1206.1071.

Tomsick, J.A., Bodaghee, A., Rodriguez, J., Chaty, S., Camilo, F., Fornasini, F., Rahoui, F., 2012b. Is IGR J11014-6103 a pulsar with the highest known kick velocity? Astrophys. J. 750 (2), L39. http://dx.doi.org/10.1088/2041-8205/750/2/L39, arXiv:1204.2836.

Tomsick, J.A., Chaty, S., Rodriguez, J., Foschini, L., Walter, R., Kaaret, P., 2006. Identifications of four INTEGRAL sources in the galactic plane via Chandra localizations. Astrophys. J. 647 (2), 1309–1322. http://dx.doi.org/10.1086/505595, arXiv:astro-ph/0603810.

Tomsick, J.A., Chaty, S., Rodriguez, J., Walter, R., Kaaret, P., 2008. Chandra localizations and spectra of INTEGRAL sources in the galactic plane. Astrophys. J. 685 (2), 1143–1156. http://dx.doi.org/10.1086/591040, arXiv:0807.2278.

Tomsick, J.A., Chaty, S., Rodriguez, J., Walter, R., Kaaret, P., 2009. Chandra localizations and spectra of integral sources in the galactic plane: The cycle 9 sample. Astrophys. J. 701 (1), 811–823. http://dx.doi.org/10.1088/0004-637X/701/1/811, arXiv:0906.2577.

Tomsick, J.A., Krivonos, R., Rahoui, F., Ajello, M., Rodriguez, J., Barrière, N., Bodaghee, A., Chaty, S., 2015. Chandra identification of two AGN discovered by INTEGRAL. Mon. R. Astron. Soc. 449, 597–604. http://dx.doi.org/10.1093/mnras/stv325, arXiv:1502.05054.

Tomsick, J.A., Krivonos, R., Wang, Q., Bodaghee, A., Chaty, S., Rahoui, F., Rodriguez, J., Fornasini, F.M., 2016. Chandra observations of eight sources discovered by INTEGRAL. Astrophys. J. 816 (1), 38. http://dx.doi.org/10.3847/0004-637X/816/1/38, arXiv:1512.00044.

Tsygankov, S.S., Churazov, E.M., 2010. Search for outbursts in the narrow 511-keV line from compact sources based on INTEGRAL data. Astron. Lett. 36 (4), 237–247. http://dx.doi.org/10.1134/S106377371004002X, arXiv:1003.1413.

Tsygankov, S.S., Krivonos, R.A., Lutovinov, A.A., Revnivtsev, M.G., Churazov, E.M., Sunyaev, R.A., Grebenev, S.A., 2016. Galactic survey of ^{44}Ti sources with the IBIS telescope onboard INTEGRAL. Mon. Not. R. Astron. Soc. 458, 3411–3419. http://dx.doi.org/10.1093/mnras/stw549, arXiv:1603.01264.

Tueller, J., Baumgartner, W.H., Markwardt, C.B., Skinner, G.K., Mushotzky, R.F., Ajello, M., Barthelmy, S., Beardmore, A., Brandt, W.N., Burrows, D., Chincarini, G., Campana, S., Cummings, J., Cusumano, G., Evans, P., Fenimore, E., Gehrels, N., Godet, O., Grupe, D., Holland, S., Kennea, J., Krimm, H.A., Koss, M., Moretti, A., Mukai, K., Osborne, J.P., Okajima, T., Pagani, C., Page, K., Palmer, D., Parsons, A., Schneider, D.P., Sakamoto, T., Sambruna, R., Sato, G., Stamatikos, M., Stroh, M., Ukwata, T., Winter, L., 2010. The 22 month swift-BAT all-sky hard X-ray survey. Astrophys. J. Suppl. 186 (2), 378–405. http://dx.doi.org/10.1088/0067-0049/186/2/378, arXiv:0903.3037.

Tueller, J., Gehrels, N., Mushotzky, R.F., Markwardt, C.B., Kennea, J.A., Burrows, D.N., Mukai, K., Sokoloski, J., 2005. Swift confirms identification of RT Cru as the IGR J12349-6434 hard x-ray source. Astronom.'s Telegr. 591, 1.

Türler, M., Chernyakova, M., Courvoisier, T.J.-L., Lubiński, P., Neronov, A., Produit, N., Walter, R., 2010. INTEGRAL hard X-ray spectra of the cosmic X-ray background and Galactic ridge emission. Astronom. Astrophys. 512, A49. http://dx.doi.org/10.1051/0004-6361/200913072, arXiv:1001.2110.

Ubertini, P., 2005. The INTEGRAL HESS/MAGIC connection: A new class of cosmic high energy accelerators from keV to TeV. Exp. Astron. 20 (1–3), 75–83. http://dx.doi.org/10.1007/s10686-006-9057-y, arXiv:astro-ph/0605228.

Ubertini, P., Bassani, L., Malizia, A., Bazzano, A., Bird, A.J., Dean, A.J., De Rosa, A., Lebrun, F., Moran, L., Renaud, M., Stephen, J.B., Terrier, R., Walter, R., 2005. INTEGRAL IGR J18135-1751 = HESS J1813-178: A new cosmic high-energy accelerator from keV to TeV energies. Astrophys. J. 629 (2), L109–L112. http://dx.doi.org/10.1086/447766, arXiv:astro-ph/0505191.

Ubertini, P., Lebrun, F., Di Cocco, G., Bazzano, A., Bird, A.J., Broenstad, K., Goldwurm, A., La Rosa, G., Labanti, C., Laurent, P., Mirabel, I.F., Quadrini, E.M., Ramsey, B., Reglero, V., Sabau, L., Sacco, B., Staubert, R., Vigroux, L., Weisskopf, M.C., Zdziarski, A.A., 2003. IBIS: The imager on-board INTEGRAL. Astron. Astrophys. 411, L131–L139. http://dx.doi.org/10.1051/0004-6361:20031224.

Ubertini, P., Sguera, V., Stephen, J.B., Bassani, L., Bazzano, A., Bird, A.J., 2009. The Fermi/LAT sky as seen by INTEGRAL/IBIS. Astrophys. J. 706 (1), L7–L11. http://dx.doi.org/10.1088/0004-637X/706/1/L7, arXiv:0910.1738.

Ueda, Y., Akiyama, M., Hasinger, G., Miyaji, T., Watson, M.G., 2014. Toward the standard population synthesis model of the X-ray background: Evolution of X-ray luminosity and absorption functions of active galactic nuclei including compton-thick populations. Astrophys. J. 786 (2), 104. http://dx.doi.org/10.1088/0004-637X/786/2/104, arXiv:1402.1836.

Walter, R., Rodriguez, J., Foschini, L., de Plaa, J., Corbel, S., Courvoisier, T.J.L., den Hartog, P.R., Lebrun, F., Parmar, A.N., Tomsick, J.A., Ubertini, P., 2003. INTEGRAL discovery of a bright highly obscured galactic X-ray binary source IGR J16318-4848. Astronom. Astrophys. 411, L427–L432. http://dx.doi.org/10.1051/0004-6361:20031369, arXiv:astro-ph/0309536.

Walter, R., Zurita Heras, J., Bassani, L., Bazzano, A., Bodaghee, A., Dean, A., Dubath, P., Parmar, A.N., Renaud, M., Ubertini, P., 2006. XMM-Newton And INTEGRAL observations of new absorbed supergiant high-mass X-ray binaries. Astronom. Astrophys. 453 (1), 133–143. http://dx.doi.org/10.1051/0004-6361:20053719.

Winkler, C., 2001. The INTEGRAL core observing programme. In: Gimenez, A., Reglero, V., Winkler, C. (Eds.), Exploring the Gamma-Ray Universe. In: ESA Special Publication, vol. 459, pp. 471–478, arXiv:astro-ph/0102007.

Winkler, C., Courvoisier, T.J.L., Di Cocco, G., Gehrels, N., Giménez, A., Grebenev, S., Hermsen, W., Mas-Hesse, J.M., Lebrun, F., Lund, N., Palumbo, G.G.C., Paul, J., Roques, J.P., Schnopper, H., Schönfelder, V., Sunyaev, R., Teegarden, B., Ubertini, P., Vedrenne, G., Dean, A.J., 2003a. The INTEGRAL mission. Astronom. Astrophys. 411, L1–L6. http://dx.doi.org/10.1051/0004-6361:20031288.

Winkler, C., Gehrels, N., Schönfelder, V., Roques, J.P., Strong, A.W., Wunderer, C., Ubertini, P., Lebrun, F., Bazzano, A., Del Santo, M., Lund, N., Westergaard, N.J., Beckmann, V., Kretschmar, P., Mereghetti, S., 2003b. First results from the INTEGRAL galactic plane scans. Astronom. Astrophys. 411, L349–L355. http://dx.doi.org/10.1051/0004-6361:20031325, arXiv:astro-ph/0307220.

Zurita Heras, J.A., Chaty, S., 2008. INTEGRAL, XMM-Newton and ESO/NTT identification of AX J1749.1-2733: an obscured and probably distant be/X-ray binary. Astronom. Astrophys. 489, 657–667. http://dx.doi.org/10.1051/0004-6361:20079097, arXiv:0801.3803.

Roman Krivonos has been working in the field of X-ray astronomy including all aspects of experiments: instrumentation, observation, and data interpretation since 2001, when he came to the High Energy Astrophysics Department of the Space Research Institute (IKI), Moscow. He graduated with a degree in Nuclear Physics from the National Research Nuclear University MEPHI (Moscow Engineering Physics Institute) in 2003. From the beginning of the *INTEGRAL* mission he worked on the *IBIS* data analysis, in particular on the hard X-ray surveys and accretion processes in the Galactic X-ray binaries and nearby supermassive black holes. Roman obtained a Ph.D. in 2007 from IKI with a thesis on the X-ray background observed at large angular scales: the Galactic Ridge X-ray Emission and Cosmic X-ray Background. In 2008, Roman continued to work with the *INTEGRAL* data as a Postdoctoral researcher at Max Planck Institute for Astrophysics, Garching, Germany. He has served in the Target Allocation Committee of *INTEGRAL* in 2007–2015. In 2012, Roman accepted an Assistant Project Scientist Position in the Space Sciences Laboratory at the University of California (USA), where he got involved with *NuSTAR* – the first focussing hard X-ray satellite in orbit, as part of the science team during the primary phase of the mission. Roman returned back to IKI in 2015, where he continues to work on data from *INTEGRAL*, *NuSTAR* and other X-ray telescopes, in particular, he takes an active part in the work of the *Spectrum-Roentgen-Gamma* project launched in 2019. By the end of 2020, the list of peer-reviewed publications by Roman, or with his active participation, contains more than 180 refereed papers, cited more than 3000 times in the scientific literature (H-index 25).

Chandra, NuSTAR, and Optical Observations of the Cataclysmic Variables IGR J17528-2022 and IGR J20063+3641

Jeremy Hare[1,9] , Jules P. Halpern[2] , John A. Tomsick[3] , John R. Thorstensen[4] , Arash Bodaghee[5] , Maïca Clavel[6] ,
Roman Krivonos[7] , and Kaya Mori[8]

[1] NASA Goddard Space Flight Center, Greenbelt, MD 20771, USA; jeremy.hare@nasa.gov
[2] Department of Astronomy, Columbia University, 550 West 120th Street, New York, NY 10027, USA
[3] Space Sciences Laboratory, 7 Gauss Way, University of California, Berkeley, CA 94720, USA
[4] Department of Physics and Astronomy, Dartmouth College, Hanover NH 03755, USA
[5] Department of Chemistry, Physics and Astronomy, Georgia College and State University, Milledgeville, GA 31061, USA
[6] Univ. Grenoble Alpes, CNRS, IPAG, F-38000 Grenoble, France
[7] Space Research Institute of the Russian Academy of Sciences (IKI), Moscow, 117997, Russia
[8] Columbia Astrophysics Laboratory, Columbia University, New York, NY 10027, USA
Received 2020 September 15; revised 2021 April 20; accepted 2021 April 20; published 2021 June 17

Abstract

We report on Chandra, NuSTAR, and MDM observations of two International Gamma-ray Astrophysics Laboratory (INTEGRAL) sources, namely IGR J17528−2022 and IGR J20063+3641. IGR J17528−2022 is an unidentified INTEGRAL source, while IGR J20063+3641 was recently identified as a magnetic cataclysmic variable (mCV) by Halpern et al. The Chandra observation of IGR J17528−2022 has allowed us to locate the optical counterpart to the source and to obtain its optical spectrum, which shows a strong Hα emission line. The optical spectrum and flickering observed in the optical time-series photometry in combination with the X-ray spectrum, which is well fit by an absorbed partially covered thermal bremsstrahlung model, suggest that this source is a strong mCV candidate. The X-ray observations of IGR J20063+3641 reveal a clear modulation with a period of 172.46 ± 0.01 s, which we attribute to the white dwarf spin period. Additional MDM spectroscopy of the source has also allowed for a clear determination of the orbital period at 0.731 ± 0.015 days. The X-ray spectrum of this source is also well fit by an absorbed partially covered thermal bremsstrahlung model. The X-ray spectrum, spin periodicity, and orbital periodicity allow this source to be further classified as an intermediate polar.

Unified Astronomy Thesaurus concepts: Cataclysmic variable stars (203); X-ray binary stars (1811); X-ray sources (1822)

1. Introduction

The International Gamma-ray Astrophysics Laboratory (INTEGRAL; Winkler et al. 2003) has played a pivotal role in uncovering the relatively faint end ($F_X \gtrsim 10^{-11}$ erg cm^{-2} s^{-1}) of the Galactic hard X-ray source population (see, e.g., Bird et al. 2016; Tomsick et al. 2016; Krivonos et al. 2017; Lutovinov et al. 2020). While INTEGRAL has uncovered many new sources, a large fraction of them still remain unidentified due to their large positional uncertainties ($\sim 1'$–$4'$), making it difficult to confidently locate their longer-wavelength counterparts. Therefore, we have been carrying out a Nuclear Spectroscopic Telescope Array (NuSTAR) legacy survey to uncover the nature of a number of hard Galactic X-ray sources discovered by INTEGRAL (see, e.g., Clavel et al. 2016, 2019; Hare et al. 2019 for recent results). NuSTAR's hard X-ray sensitivity allows one to more reliably characterize the unidentified source's hard X-ray spectrum. Chandra observations have also been obtained for several sources and, with its superb angular resolution, allows one to confidently locate the hard X-ray source's optical/NIR counterpart, which then can be followed up with optical/NIR spectroscopy.

Galactic INTEGRAL sources belong to a variety of different source classes, including isolated pulsars and their wind nebulae, high- and low-mass X-ray binaries hosting either a black hole or neutron star, and supernova remnants. However, among the most numerous Galactic source types uncovered by INTEGRAL are

cataclysmic variables (CVs; see, e.g., Bird et al. 2016), which consist of a white dwarf (WD) that accretes material via Roche-lobe overflow from a late-type main-sequence companion. CVs typically have orbital periods (P_{orb}) of ~ 1–10 hr (Mukai 2017) and are often characterized as being either magnetic (mCVs) or non-magnetic based on the magnetic field strength of the WD (i.e., having $B_{WD} \gtrsim 1$ MG or $B_{WD} \lesssim 1$ MG for mCVs or non-magnetic CVs, respectively). The mCVs, which are most commonly detected at hard X-ray energies (see, e.g., Barlow et al. 2006; Mukai 2017; de Martino et al. 2020), can be further subdivided into polars and intermediate polars (IPs) depending on the strength of the WD's magnetic field, having $B_{WD} \approx 10$–230 MG or $B_{WD} \approx 1$–10 MG, for polars and IPs, respectively (Chanmugam et al. 1990; Burwitz et al. 1997; Ferrario et al. 2015), and its effects on the accretion flow. In polars, the WD has a strong enough magnetic field to channel a large fraction of the accretion flow onto its magnetic poles, thus preventing the formation of an accretion disk. As a result of the strong magnetic field of the WD locking on to the companion, the WDs in these systems are typically found to have spin periods (P_{spin}) equal to the orbital period of the system. On the other hand, IPs contain WDs with intermediate-strength magnetic fields, which allow for the formation of an accretion disk that is truncated by the WD's magnetosphere from where the accreted material is channeled onto the WD's magnetic poles. These systems typically have WD spin periods of 10 s to a few 1000 s with $P_{spin} < P_{orb}$ (see, e.g., Figure 4 in de Martino et al. 2020).

---
[9] NASA Postdoctoral Program Fellow.

The hard X-ray emission from mCVs is thought to be produced by thermal bremsstrahlung emission from the shocked material in the accretion column above the surface of the WD. This material exhibits a multitude of temperatures, but typically has a peak temperature of tens of keV (Mukai et al. 2015; Bernardini et al. 2017). X-ray emission from this multi-temperature thermal plasma can also excite Fe on the WD surface/pre-shock accretion flow or in the post-shock accretion flow for neutral and ionized species, respectively, leading to strong Fe line features at 6.4 keV (neutral), 6.7 keV (He-like), and 6.97 keV (H-like; see, e.g., Ezuka & Ishida 1999; Wu et al. 2001; Hellier & Mukai 2004).

IGR J17528−2022 and IGR J20063+3641 (J17528 and J20063 hereafter, respectively) are two INTEGRAL sources that were part of our NuSTAR legacy survey. J17528 was first discovered by the Swift-BAT at the ∼12σ level and was reported in the fourth Palermo Swift-BAT catalog (i.e., 4PBC J1752.6-2020; Cusumano et al. 2014). The source was subsequently detected by INTEGRAL at the 6.7σ level and reported in the catalog of Krivonos et al. (2017). In both catalogs, the source was designated as unidentified, but was observed and detected at soft X-ray energies by Swift-XRT. However, the positional accuracy of Swift-XRT did not afford a unique optical/NIR counterpart to the source, so it remained unclassified.

J20063 was reported in the 70 month Swift-BAT catalog, having a detection significance of ∼8.7σ (i.e., Swift J2006.4 +3645; Baumgartner et al. 2013; Oh et al. 2018) and a soft X-ray Swift-XRT counterpart. Krivonos et al. (2017) also reported the detection of this source by INTEGRAL at the 9.1σ level. During the time of the NuSTAR and Chandra observing campaign reported here, Halpern et al. (2018) identified the optical counterpart of the XRT source and obtained spectra that showed Balmer emission lines, and a He II λ4686 line that had a comparable strength to the Hβ line. They classified J20063 as a nova-like variable, or possibly a magnetic CV, at a distance of ∼1–4 kpc. A lower limit of 0.25 d was placed on the spectroscopic period of the system, with the strongest candidates at 0.421 days and 0.733 days. Time-series photometry showed a peak in the power spectrum at 172 s, which the authors (mistakenly, it turns out; see Section 3) attributed to a multiple of their 43 s sampling period.

Here we report on NuSTAR and Chandra observations of J17528 and J20063. The precise X-ray localization of J17528 has also allowed us to identify the source's optical counterpart and to obtain its optical spectrum and optical time-series photometry, which are also presented here. Additionally, new optical spectra of J20063 resolve the ambiguity of its orbital period. The paper layout is as follows: in Section 2 we discuss the observations and data reduction, in Section 3 we discuss our timing and spectral analyses, and in Section 4 we discuss where these sources lie in the broader X-ray-emitting CV population (i.e., polars versus IPs). We summarize our findings in Section 5.

2. X-ray Observations and Data Reduction

2.1. Chandra

J17528 and J20063 were observed with the Chandra Advanced CCD Imaging Spectrometer (ACIS; Garmire et al. 2003) on 2018 April 27 (MJD 58236.0; ObsID 20199) and 2018 February 25 (MJD 58174.9; ObsID 20198), respectively. Both sources were observed by the back-illuminated ACIS-S3

chip operated in timed exposure mode and the data were telemetered using the "faint" mode. The sources were observed using a 1/8 sub-array in order to reduce the frame time to 0.4 s so that the pile-up remained <2% throughout the observations. J17528 was observed for 4.6 ks, while J20063 was observed for 4.51 ks. The Chandra data analysis reported here was performed using the Chandra Interactive Analysis of Observations (CIAO) software version 4.11 and the 4.8.3 version of the Calibration Database (CALDB). Prior to analysis, both event files were reprocessed with the CIAO tool `chandra_repro`.

The CIAO task `wavdetect` was run on the 0.5–8 keV band image to identify all sources detected by Chandra in these two observations. In the field of J17528 only one point source was significantly detected (i.e., >3σ) at the location R.A. = 268°.205423, decl. = −20°.404359, having a statistical positional uncertainty of 0″.12 (estimated using Equation (12) from Kim et al. 2007). Similarly, only one point source was significantly detected in the field of J20063 at the location R.A. = 301°.593318, decl. = +36°.695425, with a statistical positional uncertainty of 0″.12 estimated in the same way as above. Unfortunately, since no additional sources are detected in either field, we are unable to correct for any systematic offset in the absolute astrometry. Therefore, we account for this uncertainty by adopting Chandra's 90% overall astrometric uncertainty of 0″.8[10], which we convert to the 95% uncertainty by multiplying by 2.0/1.7. We then add the statistical and systematic positional uncertainties together in quadrature and find a 2σ positional uncertainty of 0″.95 for each source.

The Chandra energy spectra and barycentered event arrival times (corrected to the solar system barycenter using the CIAO tool `axbary` prior to extraction) for these sources were extracted from a 2″ radius circular region[11] centered on each source's `wavdetect` position. The background spectra were extracted from source-free annuli (5″ < r < 20″) also centered on each source's position. The energy spectrum of J17528 contained 316 net counts, while the energy spectrum of J20063 contained 395 net counts. We binned both spectra to have a signal-to-noise ratio of at least five per energy bin. Unless otherwise noted, all uncertainties in this paper are reported at the 1σ level.

2.2. NuSTAR

J17528 was observed by NuSTAR (Harrison et al. 2013) on 2018 May 9 (MJD 58247.6; ObsID 30401004002) for ∼43 ks, while J20063 was observed by NuSTAR on 2018 March 23 (MJD 58200.1; ObsID 30401003002) for ∼36 ks. Both data sets were reduced using the NuSTAR Data Analysis Software (NuSTARDAS) version 1.8.0 with CALDB version 20190410. The data sets were also both filtered for the increase in background flares caused by NuSTAR's passage through the South Atlantic Anomaly by using the options `saacalc = 2`, `saamode = optimized`, for both sources, and with `tentacle = no` for J17528 and `tentacle = yes` for J20063, reducing the exposure times to ∼42 ks and ∼35 ks, respectively.

The NuSTAR energy spectra and barycentered event arrival times (corrected to the solar system barycenter using the `barycorr` tool) for each source were extracted from a circular
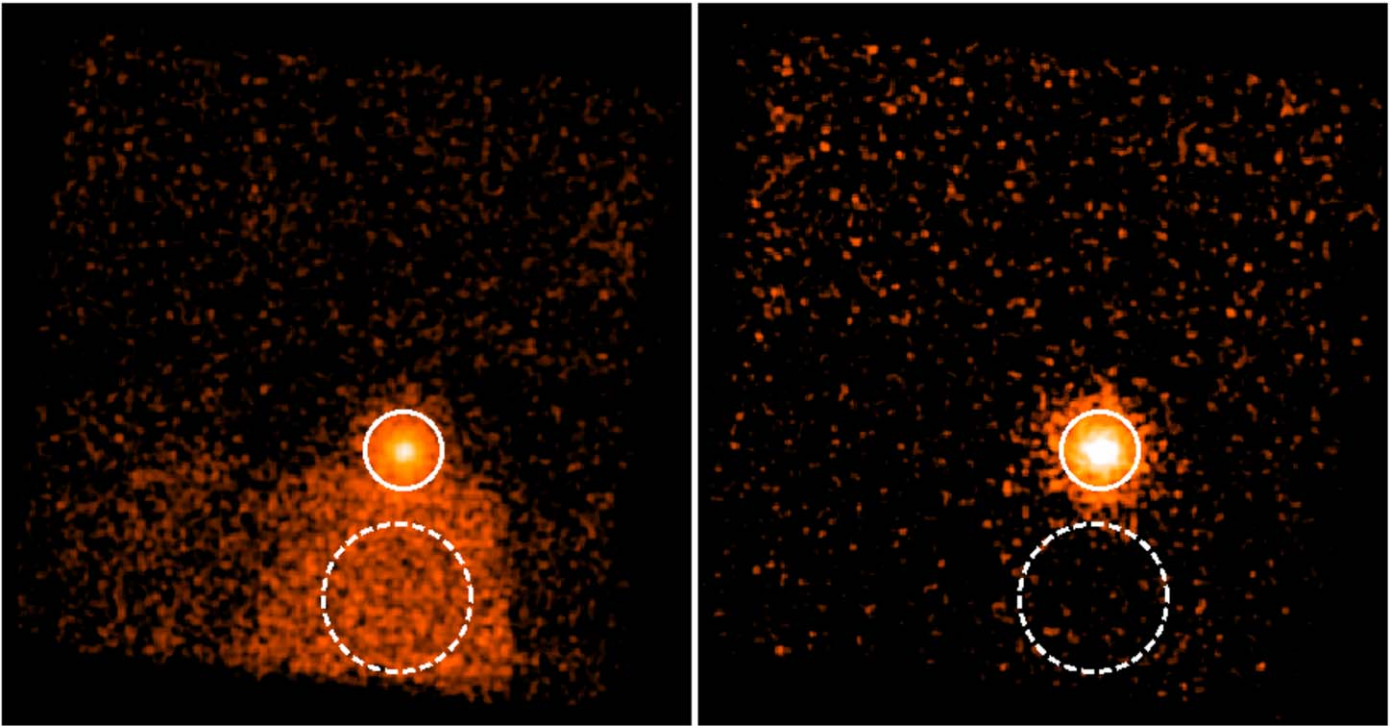

Figure 1. Left: NuSTAR FPMA 3–79 keV image of J20063. Strong absorbed stray light (likely from Cyg X-1; see Section 2.2) overlaps the source. The solid and dashed white circles show the source and background extraction regions for the source's energy spectra and light curves. Right: same image as on the left but filtered to contain only the 3–20 keV energy range. The strong absorbed stray light is effectively filtered out using this energy cut.

aperture ($r = 70''$ and $r = 50''$, for J17528 and J20063, respectively) centered on the source. The background energy spectra for J17528 were extracted from a source-free circular region ($r \approx 2'$) placed on the same detector chip as the source. The observation of J20063 suffered from strong absorbed stray light in the Focal Plane Module A (FPMA) detector, likely from Cygnus X-1 which is located $\sim2°\!\!.2$ away from J20063. Fortunately, this absorbed stray light is only strongly observed above 20 keV (see Figure 1 and Section 4.2 in Madsen et al. 2017 for more details). Additionally, the FPMB detector also suffered from normal stray light. To account for the absorbed and standard stray light, we extracted the background energy spectra for J20063 from a circular region ($r \approx 1'\!\!.6$) placed on the regions containing the stray light, but still on the same detector chip as the source (see Figure 1). Due to the absorbed stray light, and the fact that the source becomes background dominated above ~20 keV, we limit our NuSTAR analysis of J20063 to the 3–20 keV energy range. The NuSTAR spectra for both sources were grouped to have a signal-to-noise ratio of at least five per energy bin. J17528 has no spectral energy bins with a signal-to-noise ratio >5 above 30 keV, so the spectrum does not extend beyond this energy (note that the the FPMB spectrum only extends up to ~25 keV).

2.3. Swift-BAT

We use Swift-BAT data to extend the energy range coverage for J20063 due to the absorbed stray light in NuSTAR (see Section 2.2). The spectrum, covering the 14–195 keV energy range, were taken from the Swift-BAT 105-month Hard X-ray Survey[12] (Oh et al. 2018). However, the source becomes background dominated above ~100 keV so we limit our Swift-BAT analysis to the 14–100 keV energy range.

----

[12] https://swift.gsfc.nasa.gov/results/bs105mon/

3. Results

3.1. X-ray Timing

The barycenter-corrected event lists from both Chandra and NuSTAR were used to search for orbital and spin periodicity using the Z_1^2 test (Buccheri et al. 1983). The false alarm probability (FAP) for the maximum Z_1^2 value found in each periodogram is calculated by multiplying $e^{(-Z_{1,\mathrm{max}}^2/2)}$ by the number of trials, while the 1σ uncertainties are given by the frequency where the periodogram has decreased to $Z_{1,\mathrm{max}}^2 - 1$. Additionally, to search for non-periodic variability, we constructed light curves with varying time bin sizes (i.e., 250 s, 500 s, 1 ks) for both the Chandra and NuSTAR barycenter-corrected event lists. We then fit a constant to these light curves to assess the significance of any variability. The light curves were constructed using the Stingray python package (Huppenkothen et al. 2019) by removing 300 s from the beginning and end of each good time interval (GTI) to minimize possible effects from an increased background that may appear near the borders of GTIs (see, e.g., Section 5 in Bachetti et al. 2015). The Chandra light curves were made using the 0.5–8 keV energy band. For NuSTAR, we used the 3–30 keV energy band for J17528, while for J20063 we only use the 3–20 keV band due to the absorbed and standard stray light dominating above 20 keV (see Section 2.2).

Neither the Chandra nor the NuSTAR light curves of J17528 displayed any significant variability, with the highest variability significance being detected in the 500 s binned 3−30 keV NuSTAR light curves at the $\sim2.3\sigma$ level. The Z_1^2 test was run on the Chandra event list in the frequency range between $\nu \approx 3.9 \times 10^{-4}$−0.16 Hz using $\sim$16,000 equally spaced frequencies. The maximum $Z_1^2 = 19.92$ at a frequency of 0.142 Hz (7.03 s) corresponds to a FAP of 74%. The Z_1^2 test
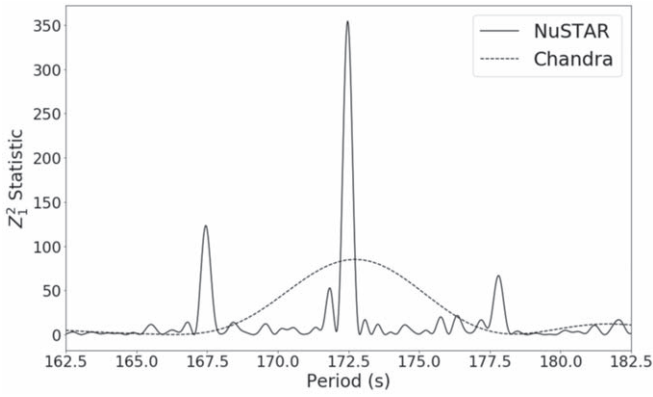
Figure 2. Results of the Z_1^2 test for J20063. A strong periodic signal is detected in the NuSTAR and Chandra data of the source at a period $P_{\rm spin} \approx 172.5$ s.

Figure 3. NuSTAR FPMA+FPMB pulse profile, folded at the $P_{\rm spin} = 172.46$ s period, of J20063 in the 3–20 keV energy range.

was also used to search the 3–30 keV NuSTAR event list in the frequency range $\nu \approx 4.7 \times 10^{-5}-1$ Hz over $\sim 10^5$ equally spaced frequencies. The largest $Z_1^2 = 29.04$ occurs at a frequency of 0.653 Hz ($P = 1.53$ s) and has a FAP of 5%. Therefore, we conclude that no significant spin/orbital periodicity is detected in this source and that it is not variable on $\sim 0.25-1$ ks timescales.

J20063 also shows no indications of variability in the Chandra or NuSTAR light curves on timescales $\geqslant 250$ s. The highest variability significance was detected in the 500 s binned NuSTAR light curve at the 1.5σ level and the 250 s Chandra light curve at the $\sim 2.1\sigma$ level. We also ran the Z_1^2 test on the Chandra event list over $\sim 16,000$ equally spaced frequency bins spanning the frequency range between $\nu \approx 4.0 \times 10^{-4}-0.16$ Hz. Interestingly, a strong signal is detected in the Chandra periodogram at a frequency of $(5.79 \pm 0.01) \times 10^{-3}$ Hz ($P = 172.7 \pm 0.4$ s) with a maximum $Z_1^2 = 85.1$, corresponding to a FAP of 5×10^{-15} (see Figure 2). We attribute this short period to the spin of the WD. We calculated the pulsed fraction of J20063 by taking the number of counts at the peak spin phase, subtracting off the number of counts at the minimum spin phase, and then dividing by the sum of these two numbers. For Chandra the background contribution is negligible, and we find a pulsed fraction of $60 \pm 8\%$ in the 0.5–8 keV energy range.

A strong Z_1^2 peak is also detected in the NuSTAR data at a frequency of $(5.7983 \pm 0.0004) \times 10^{-3}$ Hz ($P_{\rm spin} = 172.46 \pm 0.01$ s) with a maximum $Z_1^2 = 361.4$ (see Figure 2). The 3–20 keV NuSTAR FPMA+B pulse profile, folded on the 172.46 s period, is shown in Figure 3. The background contribution in NuSTAR is significant. Therefore, we calculate the pulsed fraction in the same way as above but subtract the phase-averaged background from the maximum and minimum number of counts. We find a pulsed fraction of $54 \pm 5\%$ in the 3–20 keV energy band. We also calculate a pulsed fraction of $57 \pm 7\%$ in the 3–10 keV band and $51 \pm 8\%$ in the 10–20 keV band.

3.2. X-ray Spectra

3.2.1. Non-reflection Fits

For the spectral analyses of both IGR sources, we simultaneously fit the Chandra and NuSTAR spectra in the 0.5–8 keV and 3–30 keV energy ranges for J17528, and 0.5–8 keV and 3–20 keV energy ranges for J20063, respectively. For J20063, we also simultaneously fit the 14–100 keV Swift-BAT data. In all fits discussed below, a multiplicative
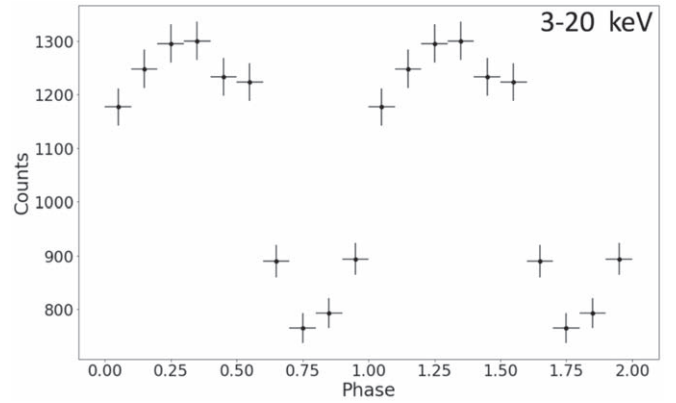
constant is used to account for possible calibration differences between the instruments. All energy spectra in this paper were fit using XSPEC version 12.10.1 (Arnaud 1996). Additionally, we used the Tuebingen–Boulder interstellar medium absorption model (tbabs) with the solar abundances of Wilms et al. (2000) in our fits. We note that the Galactic absorbing column densities are $N_H = 4.3 \times 10^{21}$ cm^{-2} and $N_H = 9.7 \times 10^{21}$ cm^{-2} in the directions of J17528 and J20063, respectively (HI4PI Collaboration et al. 2016).

The spectra for J17528 were first fitted with an absorbed power-law model. The fitted model has a hard photon index of $\Gamma = 0.91 \pm 0.03$ and relatively large absorbing column density, $N_H = 4.0_{-0.7}^{+0.9} \times 10^{22}$ cm^{-2}. However, the quality of the fit is poor ($\chi^2/\nu = 393/252$), showing large residuals around the Fe line complex at 6.4 keV and evidence for a spectral cutoff above ~ 20 keV. Therefore, we switch the continuum model to an absorbed thermal bremsstrahlung model (i.e., bremss in Xspec; Kellogg et al. 1975), but the fitted model has an unconstrained temperature, large residuals at soft X-ray energies, and provides a poor fit to the data ($\chi^2/\nu = 450/257$). To overcome the large residuals at soft energies, we add partial covering absorber to the model. This model provides the best fit to the continuum having a reduced chi-squared $\chi^2/\nu = 287/250$. Finally, we add a Gaussian to the model to account for the neutral Fe Kα line at 6.4 keV, leading to a reduced chi-squared $\chi^2/\nu = 252/248$ or, in other words, a $\Delta\chi^2 = 35$ for two fewer degrees of freedom. For clarity, the final model is const×tbabs×pcfabs×(bremss +Gauss), which is hereafter referred to as Model 1. The best-fit parameters for Model 1 are shown in Table 1 while the residuals to this model are shown in Figure 4(c).

J20063 was previously identified as a CV (Halpern et al. 2018), so we start with Model 1 (defined above) to fit its spectrum. Fitting the spectrum with a single Gaussian leads to a large line width ($\sigma_{\rm line} = 0.49_{-0.11}^{+0.13}$ keV), which is larger than those typically observed in CVs (Hellier & Mukai 2004). To check for contributions from H-like and He-like Fe, we also fit a Gaussian allowing the line center to be a free parameter. In this case, the line center shifts to ≈ 6.5 keV and the line width drops to ≈ 350 eV (but is still consistent within the 1σ uncertainty of the line width found when the Gaussian was fixed at 6.4 keV). The addition of a second Gaussian does not statistically significantly improve the quality of the fit, nor does it significantly alter the neutral Fe line width. Thus, we use a single Gaussian in the model for simplicity, as the data are not of high enough quality to constrain the contributions from
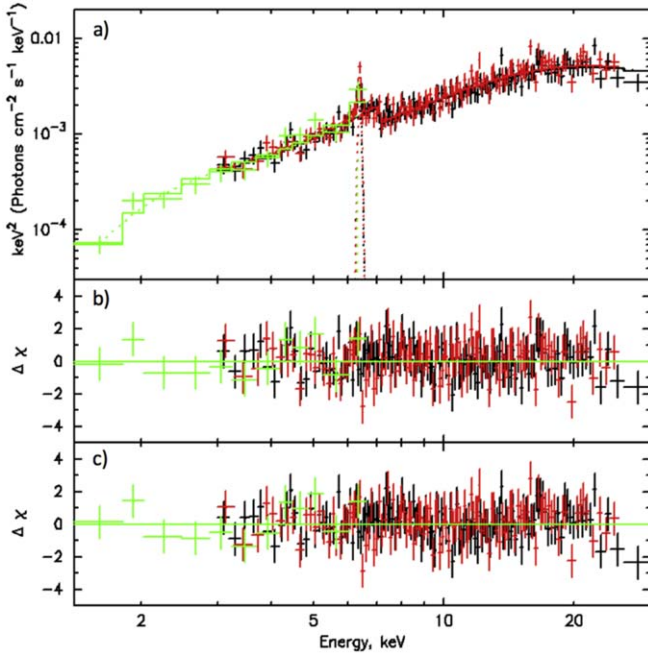
Figure 4. Chandra (green; 0.5–8 keV) and NuSTAR FPMA (black; 3–30.0 keV) and FPMB (red; $3 \simeq 25.0$ keV) spectra for J17528 with the best-fit Model 4 (panel a) and residuals (panel b). Panel c shows the residuals from the best-fit Model 1.

Table 1
Best-fit Parameters Derived from Model 1 and Model 4 for J17528

| Model Component	Parameter	Unit	Model 1	Model 4
const	FPMB/FPMA	⋯	1.04 ± 0.02	1.04 ± 0.02
	CXO/FPMA	⋯	1.02 ± 0.08	1.04 ± 0.08
tbabs	N_H	10^{22} cm^{-2}	3.4 ± 0.5	3.2 ± 0.5
pcfabs	N_H	10^{22} cm^{-2}	121 ± 15	90 ± 14
	Covering fraction	⋯	0.72 ± 0.03	0.66 ± 0.03
Gaussian	E	keV	6.4[a]	6.4[a]
	σ	keV	$0.10^{+0.07}_{-0.09}$	$0.049^{+0.088}_{-0.046}$
	N	10^{-5} ph cm^{-2} s^{-1}	$2.1^{+0.5}_{-0.4}$	$1.4^{+0.4}_{-0.3}$
Equivalent width		eV	252^{+57}_{-50}	202^{+56}_{-43}
reflect	$\Omega/2\pi$	⋯	⋯	1.0[a]
	A	⋯	⋯	1.0[a]
	A_{Fe}	⋯	⋯	1.0[a]
	$\cos i$	-	⋯	>0.72
bremss	kT	keV	40^{+13}_{-8}	25^{+4}_{-3}
	N	10^{-3}	1.8 ± 0.2	1.3 ± 0.1
Observed flux	$0.5 - 79.0$ keV	10^{-11} erg cm^{-2} s^{-1}	$1.65^{+0.15}_{-0.12}$	1.36 ± 0.07
χ^2/d.o.f.			252/248	241/247

Note.
[a] Fixed value.
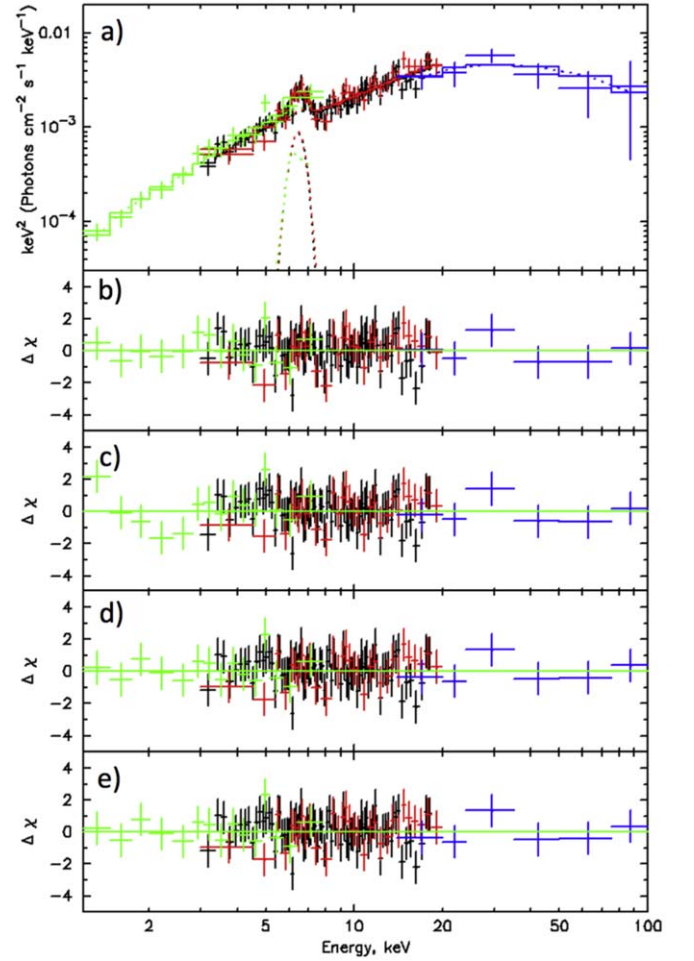
Figure 5. (a) Chandra (green; 0.5–8 keV), NuSTAR FPMA (black; 3–20.0 keV) and FPMB (red; 3–20.0 keV), and Swift-BAT (blue; 14–100 keV) spectra for J20063 with the best-fit Model 4. (b) Residuals for the best-fit Model 4. (c) Residuals for the best-fit Model 1. Systematic residuals are apparent in the 1–3 keV energy range. (d) Residuals for the best-fit Model 2. (e) Residuals for the best-fit Model 3.

ionized Fe lines, but note that there is likely some contribution from ionized Fe which is affecting the single-line parameters.

While Model 1 adequately fits the data, there are still systematic residuals at soft X-ray energies (see Figure 5c). Therefore, we considered two additional models to account for these residuals. For the first model, we simply added an additional bremsstrahlung component to Model 1 (i.e., const×tbabs×pcfabs× (bremss+bremss+Gauss); hereafter referred to as Model 2). This model was used since the emitting plasma in CVs often has a multi-temperature structure (Mukai 2017). For the second model, we added a blackbody component to Model 1 (i.e., const×tbabs×pcfabs×(bremss+bbodyrad+Gauss); hereafter referred to as Model 3) to account for these residuals. These models further improve the fits by $\Delta\chi^2 = 12$ and 11, respectively for two fewer degrees of freedom and reduce the systematic residuals at low energies. An F-test gives a statistical significance of $\sim 3\sigma$ for the additional bremsstrahlung or blackbody component. For Model 2, we find that the additional bremsstrahlung component has a low temperature of 170^{+40}_{-30} eV, which is similar to but larger than the fitted blackbody temperature of 122^{+24}_{-21} eV. The best-fit parameters for these models are shown in Table 2 and the residuals for the fitted spectra are shown in Figures 5(d, e). We also added a second Gaussian to these model

Table 2
Best-fit parameters Derived from Models 1, 2, 3, and 4 for J20063

Model Component	Parameter	Unit	Model 1	Model 2	Model 3	Model 4
const	FPMB/FPMA	⋯	1.04 ± 0.04	1.04 ± 0.04	1.04 ± 0.04	1.04 ± 0.04
	CXO/FPMA	⋯	1.06 ± 0.08	$1.14^{+0.09}_{-0.08}$	$1.14^{+0.09}_{-0.08}$	$1.15^{+0.09}_{-0.08}$
	BAT/FPMA	⋯	$1.02^{+0.19}_{-17}$	$1.05^{+0.19}_{-0.17}$	$1.05^{+0.19}_{-0.17}$	$0.89^{+0.17}_{-0.15}$
tbabs	N_H	10^{22} cm^{-2}	2.6 ± 0.4	5 ± 1	5 ± 1	$1.26^{+0.71}_{-0.69}$
pcfabs	N_H	10^{22} cm^{-2}	131^{+27}_{-26}	163^{+32}_{-29}	162^{+32}_{-29}	18^{+16}_{-6}
	Covering fraction	⋯	$0.65^{+0.04}_{-0.05}$	$0.63^{+0.05}_{-0.06}$	$0.63^{+0.05}_{-0.06}$	$0.61^{+0.13}_{-0.12}$
bbodyrad	kT	eV	⋯	⋯	122^{+22}_{-20}	⋯
	Norm[a]	10^5	⋯	⋯	$2.0^{+17}_{-1.8}$	⋯
Gaussian	E	keV	6.4[b]	6.4[b]	6.4[b]	6.4[b]
	σ	keV	$0.49^{+0.13}_{-0.11}$	$0.46^{+0.11}_{-0.10}$	$0.46^{+0.11}_{-0.10}$	0.36 ± 0.09
	N	10^{-5} ph cm^{-2} s^{-1}	$5.3^{+1.8}_{-1.4}$	$5.5^{+1.6}_{-1.3}$	$5.5^{+1.6}_{-1.3}$	2.2 ± 0.4
Equivalent width		eV	760^{+160}_{-170}	720^{+150}_{-160}	720^{+150}_{-140}	560 ± 130
reflect	$\Omega/2\pi$	⋯	⋯	⋯	⋯	1.0[b]
	A	⋯	⋯	⋯	⋯	1.0[b]
	A_{Fe}	⋯	⋯	⋯	⋯	1.0[b]
	$\cos i$	⋯	⋯	⋯	⋯	>0.75
bremss$_1$	kT	keV	42^{+16}_{-10}	37^{+13}_{-9}	37^{+13}_{-9}	58^{+21}_{-15}
	N	10^{-3}	$1.54^{+0.18}_{-0.14}$	1.7 ± 0.2	1.7 ± 0.2	$0.77^{+0.04}_{-0.03}$
bremss$_2$	kT	keV	⋯	$0.17^{+0.04}_{-0.03}$	⋯	⋯
	N	10^0	⋯	14^{+93}_{-12}	⋯	⋯
Observed flux	$0.5 - 100$ keV	10^{-11} erg cm^{-2} s^{-1}	1.6 ± 0.2	1.5 ± 0.1	1.5 ± 0.2	1.7 ± 0.2
χ^2/d.o.f.			$116/124$	$104/122$	$105/122$	$110/123$

Notes.
[a] Defined as R_{km}^2/D_{10}^2, where R_{km} is the source radius in km and D_{10} is the distance to the source in units of 10 kpc (see https://heasarc.gsfc.nasa.gov/xanadu/xspec/manual/node139.html.)
[b] Fixed value.

but, similar to the non-blackbody model, found that it does not dramatically improve the quality of the fit nor does it significantly reduce the Fe line widths, so we omit it.

3.2.2. Reflection Fits

While the spectral models discussed above adequately fit the broadband X-ray spectra of both J17528 and J20063, a few of the best-fit parameters have somewhat extreme values. For instance, the partial covering absorption derived from these models is much higher than typically observed from IPs (i.e., the values are usually a few $\times 10^{23}$ cm^{-2}; see, e.g., Evans & Hellier 2007; Bernardini et al. 2017). Additionally, the blackbody component in the spectral model of J20063 is on the hot end of the temperature distribution typically observed in IPs (Evans & Hellier 2007; Anzolin et al. 2008; Bernardini et al. 2017; de Martino et al. 2020). These issues motivated the use of a more complex spectral model that also accounts for the X-rays produced in the accretion column that are then reflected off of the WD's surface and have been observed in the X-ray spectra of several CVs (e.g., Mukai et al. 2015). To account for this component, we convolve the reflect model (Magdziarz & Zdziarski 1995) with the bremsstrahlung model. The reflect model has several parameters[13], including the reflection

amplitude ($\Omega/2\pi$), abundances of elements heavier than He relative to solar (A), abundance of Fe relative to A (A_{Fe}), and the cosine of the inclination angle ($\cos i$). It has been noted that the partial covering model and reflection are degenerate with one another (Yuasa et al. 2010; Hailey et al. 2016), thus including a reflection component can lower the hydrogen column density of the partial covering absorber. Additionally, the reflection component can also lower the temperature of the plasma component. For clarity, the reflection model used for both sources is const×tbabs×pcfabs×(reflect×(bremss)+Gauss), in XPSEC notation (hereafter referred to as Model 4), where the Gaussian is again centered at 6.4 keV. We keep the Gaussian component in this model because the reflect model does not account for fluorescent emission lines. Note, for J20063, we exclude the blackbody component when fitting the reflection model.

While setting up the model, we explored leaving various parameters in the reflect component free. For both sources, we found that, if the reflection amplitude is left free, the fit prefers values >1.0. However, this value is unphysical under the condition that we see all of the direct emission (Tomsick et al. 2016). Therefore, we fix this parameter to a value of 1 in the fits for both sources. We also freeze the abundances, both A and A_{Fe}, to 1 for both sources. For J17528, Model 3 provides a better fit to the data (i.e., $\chi^2/\nu = 241/247$ or $\Delta\chi^2$ of 11 for one fewer degree of freedom). The best-fit parameters provide a

---

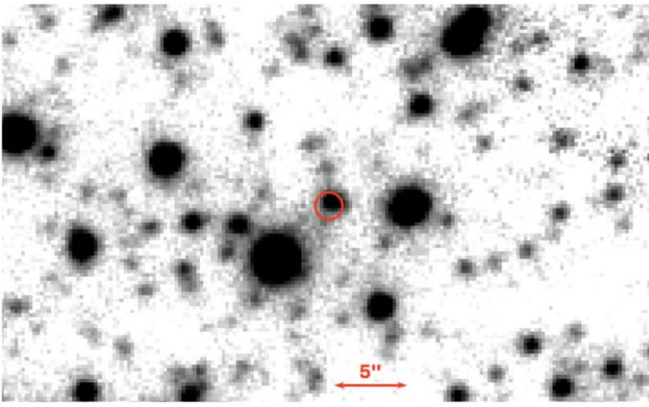[13] See https://heasarc.gsfc.nasa.gov/xanadu/xspec/manual/node292.html

Figure 6. Pan-STARRs y-band finding chart of the counterpart to J17528. The red circle, having a radius corresponding to the X-ray sources 2σ positional uncertainty, shows the Chandra position of J17528. Up is north and east is to the left.
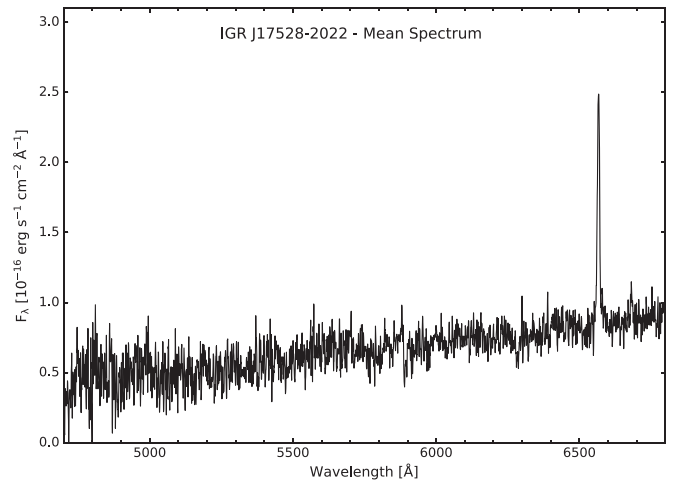

Figure 7. Mean MDM 2.4 m spectrum of J17528, from two 1000 s exposures. The spectrum has been smoothed with a three-point running average, and the flux calibration is derived from observations of spectrophotometric standard stars. Hα λ6563 emission is clearly visible, and there may be He I λ5876 and λ6678 emission, as well as interstellar Na I D absorption and diffuse interstellar bands.

lower lower bremsstrahlung temperature (see Table 1). The best-fit reflection spectra and the residuals are shown in Figure 4(a), (b).

For J20063, the reflection model provides a slightly worse fit to the data than Models 2 and 3, but has a more realistic value of the partial covering absorption column density (see Table 2). Additionally, the reflection model eliminates the systematic residuals at soft X-ray energies without the need of a relatively high-temperature blackbody component, which suggests that these residuals may be due to the lack of a reflection component in Model 1. Therefore, we favor the reflection models over the non-reflection models for both sources as they provide more reasonable physical values for the model parameters. The best-fit reflection spectral model for J20063 and the corresponding residuals are shown in Figure 5(a), (b).

3.3. Optical and NIR Data

3.3.1. IGR J17528−2022.

The Chandra observation of J17528 has allowed us to localize its position to an accuracy of about ∼1″, enabling us to identify its longer-wavelength counterpart. Only one Gaia optical counterpart (Gaia Collaboration et al. 2021) is located within the positional error radius of the X-ray source. The Pan-STARRS finding chart (Chambers et al. 2016; Flewelling et al. 2020) for this source is shown in Figure 6. Unfortunately, the Gaia counterpart has a negative parallax and a significant amount of astrometric excess noise ($\gtrsim$10.0; Gaia Collaboration et al. 2021). Therefore, its distance estimate of 5.8 kpc, inferred from the probabilistic method of Bailer-Jones et al. (2021), is likely unreliable.

We observed J17528 on 2019 July 2 UT, using the Ohio State Multi-Object Spectrograph (OSMOS; Martini et al. 2011) on the 2.4 m Hiltner telescope at MDM Observatory on Kitt Peak, Arizona. Two 1000 s spectra were obtained, covering 4200–6800 Å at 0.7 Å pixel^{-1} and ∼3 Å resolution. We also obtained three 20 s direct images through a Sloan g filter immediately prior to the spectra, as part of the target acquisition. We derived photometric zero-points from the Pan-STARRS 1 (PS1) g_{PSF} magnitudes of stars in the field, and using these we found $g = 20.5 \pm 0.3$ for J17528, basically identical to its PS1 magnitude $g_{PSF} = 20.48$ (Chambers et al. 2016; Flewelling et al. 2020).

Figure 7 shows our mean spectrum. The only clearly significant feature is emission at Hα, with an equivalent width of ∼16 Å and a FWHM of ∼9 Å. A hint of absorption may be seen near 6285 Å close to some diffuse interstellar bands (Jenniskens & Desert 1994) but also close to a telluric feature. There also may be some Na I D absorption (λ5889, λ5895) which, if present, would almost certainly be interstellar. The presence of the Hα and He I lines suggest that the optical emission is likely coming from the WD accretion column or disk.

In addition to using the archival multiwavelength photometry, we obtained an r-band time series of the source on 2019 June 3, using OSMOS in direct imaging mode to perform differential photometry. The duration of the observation was 3.4 hr at 64 s cadence (Figure 8). While J17528 did exhibit some variability, no strong periodic signal was detected, so we are unable to further constrain the spin and/or orbital period of the source.

3.3.2. IGR J20063+3641

The optical counterpart of J20063 was first identified by Halpern et al. (2018) who suggested that the source is a nova-like variable, or a mCV given that the He II λ4686 and Hβ lines were approximately the same strength. A photometric signal at 172 s was detected, the same as the X-ray period found here, but it was mistakenly attributed to a multiple of the 43 s sampling period. Halpern et al. (2018) could not find an unambiguous period from their Hα radial velocity measurements, but did find candidate periods of 0.421 ± 0.002 days and 0.733 ± 0.003 days.

We obtained 15 more spectra on 2018 September 28 and 29, using the MDM Hiltner telescope and modspec, configured as in Halpern et al. (2018); nine of these spectra gave usable radial velocities of the Hα emission. On 2019 July 4 and 5 we obtained another 11 Hα velocities with OSMOS (see Section 3.3.1). On these nights the acquisition images (calibrated against the Pan-STARRS g magnitudes as described earlier) showed the source at $g = 17.77$, with little variation from night to night, somewhat brighter than in Pan-STARRS. The top panel of Figure 9 shows
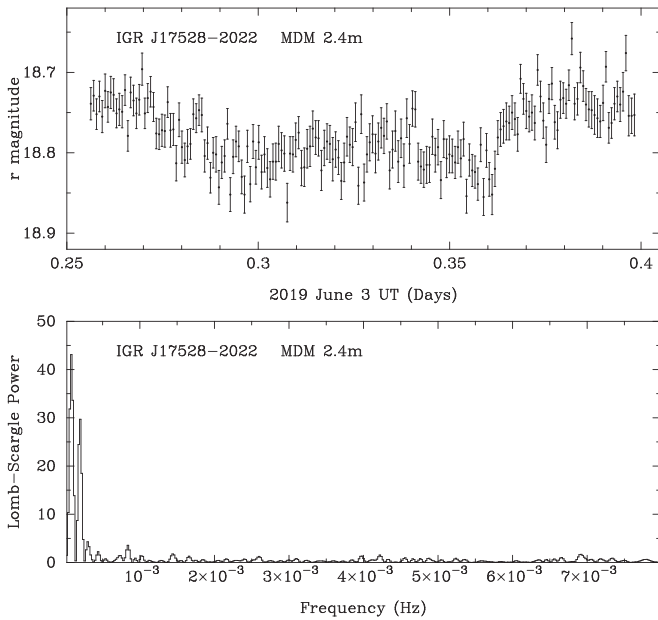
Figure 8. Top: MDM 2.4 m *r*-band time-series photometry of J17528 at 64 s cadence. The magnitude scale is referenced to Pan-STARRS photometry of a comparison star. Bottom: power spectrum of the time series. The light curve does exhibit variability, but no periodicity is detected, suggesting that any photometric period is >3 hr.

Figure 9. Top: mean spectrum of IGR J20063+3641 from 2019 July. Prominent emission lines and interstellar features are marked. Middle: periodogram of the Hα radial velocities, formed by fitting a full sinusoid at each trial frequency and inverting the squared residuals. Bottom: Hα radial velocities folded on the single best-fitting period; data are repeated over a second cycle for continuity. The 2018 September and 2019 July data are newly reported, while the earlier data are from Halpern et al. (2018).

the mean OSMOS spectrum. The new velocities resolve the period ambiguity firmly in favor of the 0.73 day alias; the middle panel of Figure 9 shows the periodogram. The number of cycles elapsed during the long intervals between observing runs is not determined, resulting in a cluster of fine-scale aliases and complicating the period uncertainty. Examining fits at different aliases leads to $P_{orb} = 0.731 \pm 0.015$ days as a conservative range. The lower panel of Figure 9 shows the radial velocities folded on the single best-fitting fine-scale period.

Halpern et al. 2018 also set an upper limit on the distance to the source of ∼4 kpc by using the extinction map of Green et al. (2015) and the typical unreddened absolute magnitudes of nova-like variables. The optical counterpart is detected by Gaia (Gaia Collaboration et al. 2021), which has measured its parallax, $\pi = 0.22 \pm 0.09$, and proper motion, $\mu_\alpha \cos\delta = -4.30 \pm 0.09$ mas yr^{-1}, $\mu_\delta = -5.3 \pm 0.1$ mas yr^{-1}, with an insignificant amount of astrometric excess noise. The measured parallax has a large relative uncertainty (∼40%), leading to a large uncertainty in the inferred distance, $d = 4.5^{+1.4}_{-1.1}$ kpc (Bailer-Jones et al. 2021). The optical counterpart of this source is also detected by Pan-STARRS (Flewelling et al. 2020; Chambers et al. 2016) at optical wavelengths, and by the UKIDSS survey (Lucas et al. 2008) at NIR wavelengths.

4. Discussion

4.1. IGR J17528−2022

J17528's X-ray spectrum is well described by a partially covered thermal bremsstrahlung model with a narrow neutral Fe line and a possible reflection component. This type of spectrum is most typically observed in CVs (e.g., Mukai et al. 2015; Tomsick et al. 2016). Furthermore, the source's optical spectrum shows a strong Hα emission line as well as weak He I lines, likely being produced by an accretion column or disk. The optical time-series photometry of J17528 shows flickering
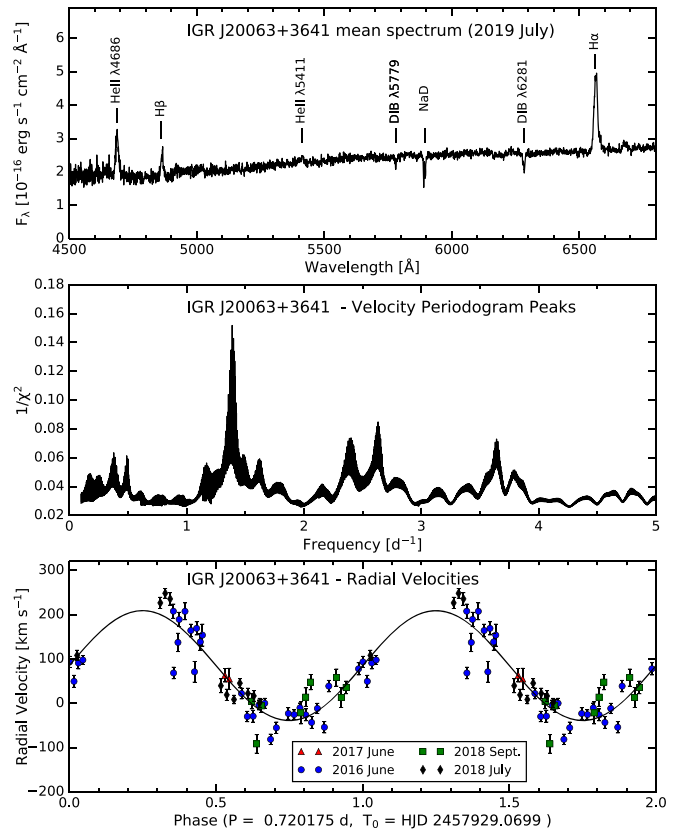
on minute-long timescales, which has also been observed in many CV systems (Halpern et al. 2018). All of these factors strongly suggest that J17528 is a CV.

Since J17528's optical emission is likely dominated by the accretion column/disk, it is difficult to place constraints on the source's distance or the spectral type of the companion star using the multiwavelength photometry. Converting the absorbing column density ($N_H = 3.2 \times 10^{22}$ cm^{-2}) from the best-fit X-ray spectrum to an optical absorption using the relation of Güver & Özel (2009) provides $A_V = 14.5$. The reddening map of Green et al. (2019) only extends to ∼2.5 kpc in the direction of J17528 and provides $A_V = 3.2$ at this distance. This suggests that J17528 is at a distance of at least a few kiloparsecs. Assuming a fiducial distance of 3 kpc to the source implies an observed X-ray luminosity of $L_X \approx 2 \times 10^{34}$ erg s^{-1} in the 0.5–79 keV energy range. Unfortunately, no spin or orbital period was detected in the optical or X-ray data, therefore we cannot make a firm conclusion on the type of CV (i.e., polar versus IP). We also mention that there is the possibility that this source could be a non-magnetic nova-like system, but we consider this possibility less likely as the majority of hard X-ray-detected CVs are mCVs (see, e.g., de Martino et al. 2020). Follow-up spectroscopy and photometry can help to better constrain the orbital/spin period of the system to help differentiate between the IP and polar scenario.

4.2. IGR J20063+3641

Prior to the analysis performed in this paper, Halpern et al. (2018) had already identified J20063 as a mCV based on its optical spectrum. The additional follow-up spectra of the source have confirmed that the orbital period of the system is $P_{orb} = 0.731 \pm 0.015$ days. Furthermore, the X-ray observations have also enabled a detection of the spin period of the WD at $P_{spin} = 172.46 \pm 0.01$ s, which is also detected in the optical observations (Halpern et al. 2018). Based on the detected orbital and spin periodicities, this system is likely an IP.

The estimated Gaia distance to the source, $d = 4.5^{+1.4}_{-1.1}$ kpc (Bailer-Jones et al. 2021), is a little larger than the rough upper-limit of $d \approx 4$ kpc placed by Halpern et al. (2018) (which was based on the optical spectrum and the Green et al. 2015 reddening map in the direction of the source), but are consistent within errors. Since we cannot place any additional constraints on the distance to the source, we assume a fiducial distance of 4 kpc. At this distance, the source has an observed X-ray luminosity $L_X \approx 3 \times 10^{34}$ erg s^{-1} in the 0.5–100 keV energy range, consistent with INTEGRAL-detected IP luminosities (de Martino et al. 2020). The IP V2731 Oph has the most similar X-ray luminosity ($L_X = 1.2 \times 10^{34}$ erg s^{-1} in the 0.1–100 keV energy range; Suleimanov et al. 2019), orbital period ($P_{orb} = 15.4$ hr; Gänsicke et al. 2005), and spin period ($P_{spin} = 128$ s; Gänsicke et al. 2005) of any confirmed IPs compared to J20063. The fact that J20063 is similar to V2731 Oph may suggest that it has an evolved donor star (see e.g., Goliasch & Nelson 2015; Lopes de Oliveira & Mukai 2019).

5. Summary

Through X-ray observations, we identified J17528 as a new strong mCV candidate. NuSTAR and Chandra X-ray spectra show strong neutral Fe Kα emission at 6.4 keV and are well fit by a partially covered bremsstrahlung model, with evidence for a reflection component. The Chandra observation has allowed for the optical counterpart of J17528 to be identified and followed-up with MDM optical spectroscopy and photometry. The optical spectrum shows strong Hα emission. No orbital or spin periodicity was detected in the X-ray data or in the optical time-series photometry. Assuming a distance of 3 kpc, the source's X-ray luminosity ($L_X \approx 10^{34}$ erg s^{-1}) is more consistent with those of IPs, but future X-ray and optical observations are needed to confirm this source as an IP by detecting the orbital and WD spin periods.

J20063 was confirmed as a CV system through optical spectroscopy by Halpern et al. (2018). The X-ray observations reported here have enabled us to measure the spectrum of this CV, which is well fit by a partially covered bremsstrahlung model and shows evidence of either having an additional blackbody or, more likely, a reflection component. The X-ray data also allowed for the detection of the WD spin period ($P_{spin} = 172.46 \pm 0.01$ s), while additional MDM optical spectroscopy has allowed for a clear determination of the orbital period at 0.731 ± 0.015 days. This has allowed us to further classify the source as an IP. Future NIR/IR spectroscopy could be used to further constrain the spectral type of the secondary star and to place tighter constraints on the source's distance.

ORCID iDs

Jeremy Hare ⓘ https://orcid.org/0000-0002-8548-482X
Jules P. Halpern ⓘ https://orcid.org/0000-0003-4814-2377
John A. Tomsick ⓘ https://orcid.org/0000-0001-5506-9855
John R. Thorstensen ⓘ https://orcid.org/0000-0002-4964-4144
Arash Bodaghee ⓘ https://orcid.org/0000-0002-7315-3732
Maïca Clavel ⓘ https://orcid.org/0000-0003-0724-2742
Roman Krivonos ⓘ https://orcid.org/0000-0003-2737-5673
Kaya Mori ⓘ https://orcid.org/0000-0002-9709-5389

References

Anzolin, G., de Martino, D., Bonnet-Bidaud, J.-M., et al. 2008, A&A, 489, 1243
Arnaud, K. A. 1996, in A.S.P. Conf. Series, 101, ed. G. H. Jacoby & J. Barnes, 17
Bachetti, M., Harrison, F. A., Cook, R., et al. 2015, ApJ, 800, 109
Bailer-Jones, C. A. L., Rybizki, J., Fouesneau, M., et al. 2021, AJ, 161, 147
Barlow, E. J., Knigge, C., Bird, A. J., et al. 2006, MNRAS, 372, 224
Baumgartner, W. H., Tueller, J., Markwardt, C. B., et al. 2013, ApJS, 207, 19

Bernardini, F., de Martino, D., Mukai, K., et al. 2017, MNRAS, 470, 4815
Bird, A. J., Bazzano, A., Malizia, A., et al. 2016, ApJS, 223, 15
Buccheri, R., Bennett, K., Bignami, G. F., et al. 1983, A&A, 128, 245
Burwitz, V., Reinsch, K., Beuermann, K., et al. 1997, A&A, 327, 183
Chambers, K. C., Magnier, E. A., Metcalfe, N., et al. 2016, arXiv:1612.05560
Chanmugam, G., Frank, J., King, A. R., et al. 1990, ApJL, 350, L13
Clavel, M., Tomsick, J. A., Bodaghee, A., et al. 2016, MNRAS, 461, 304
Clavel, M., Tomsick, J. A., Hare, J., et al. 2019, ApJ, 887, 32
Cusumano, G., Segreto, A., La Parola, V., et al. 2014, in Proceedings of Swift:
    10 Years of Discovery (SWIFT 10, 132)
de Martino, D., Bernardini, F., Mukai, K., et al. 2020, AdSpR, 66, 1209
Evans, P. A., & Hellier, C. 2007, ApJ, 663, 1277
Ezuka, H., & Ishida, M. 1999, ApJS, 120, 277
Ferrario, L., de Martino, D., & Gänsicke, B. T. 2015, SSRv, 191, 111
Flewelling, H. A., Magnier, E. A., Chambers, K. C., et al. 2020, ApJS, 251, 7
Fruscione, A., McDowell, J. C., Allen, G. E., et al. 2006, Proc. SPIE, 6270,
    62701V
Gaia Collaboration, Brown, A. G. A., Vallenari, A., et al. 2021, AAP, 649, A1
Gänsicke, B. T., Marsh, T. R., Edge, A., et al. 2005, MNRAS, 361, 141
Garmire, G. P., Bautz, M. W., Ford, P. G., et al. 2003, Proc. SPIE, 4851, 28
Goliasch, J., & Nelson, L. 2015, ApJ, 809, 80
Green, G. M., Schlafly, E., Zucker, C., et al. 2019, ApJ, 887, 93
Green, G. M., Schlafly, E. F., Finkbeiner, D. P., et al. 2015, ApJ, 810, 25
Güver, T., & Özel, F. 2009, MNRAS, 400, 2050
Hailey, C. J., Mori, K., Perez, K., et al. 2016, ApJ, 826, 160
Halpern, J. P., Thorstensen, J. R., Cho, P., et al. 2018, AJ, 155, 247
Hare, J., Halpern, J. P., Clavel, M., et al. 2019, ApJ, 878, 15
Harrison, F. A., Craig, W. W., Christensen, F. E., et al. 2013, ApJ, 770, 103
Hellier, C., & Mukai, K. 2004, MNRAS, 352, 1037
HI4PI Collaboration, Ben Bekhti, N., FlÖer, L., et al. 2016, A&A, 594, A116
Huppenkothen, D., Bachetti, M., Stevens, A. L., et al. 2019, ApJ, 881, 39
Jenniskens, P., & Desert, F.-X. 1994, A&AS, 106, 39
Kellogg, E., Baldwin, J. R., & Koch, D. 1975, ApJ, 199, 299
Kim, M., Kim, D.-W., Wilkes, B. J., et al. 2007, ApJS, 169, 401
Krivonos, R. A., Tsygankov, S. S., Mereminskiy, I. A., et al. 2017, MNRAS,
    470, 512
Lopes de Oliveira, R., & Mukai, K. 2019, ApJ, 880, 128
Lucas, P. W., Hoare, M. G., Longmore, A., et al. 2008, MNRAS, 391, 136
Lutovinov, A., Suleimanov, V., Luna, G. J. M., et al. 2020, NewAR, 91,
    101547
Madsen, K. K., Christensen, F. E., Craig, W. W., et al. 2017, JATIS, 3, 044003
Magdziarz, P., & Zdziarski, A. A. 1995, MNRAS, 273, 837
Martini, P., Stoll, R., Derwent, M. A., et al. 2011, PASP, 123, 187
Mukai, K. 2017, PASP, 129, 062001
Mukai, K., Rana, V., Bernardini, F., et al. 2015, ApJL, 807, L30
Oh, K., Koss, M., Markwardt, C. B., et al. 2018, ApJS, 235, 4
Suleimanov, V. F., Doroshenko, V., & Werner, K. 2019, MNRAS, 482, 3622
Tomsick, J. A., Rahoui, F., Krivonos, R., et al. 2016, MNRAS, 460, 513
Wilms, J., Allen, A., & McCray, R. 2000, ApJ, 542, 914
Winkler, C., Courvoisier, T. J.-L., Di Cocco, G., et al. 2003, A&A, 411, L1
Wu, K., Cropper, M., & Ramsay, G. 2001, MNRAS, 327, 208
Yuasa, T., Nakazawa, K., Makishima, K., et al. 2010, A&A, 520, A25

Using Chandra Localizations and Gaia Distances and Proper Motions to Classify Hard X-Ray Sources Discovered by INTEGRAL

John A. Tomsick[1] , Benjamin M. Coughenour[1], Jeremy Hare[2,11] , Roman Krivonos[3] , Arash Bodaghee[4] ,
Sylvain Chaty[5,6] , Maïca Clavel[7] , Francesca M. Fornasini[8] , Jerome Rodriguez[9] , and Aarran W. Shaw[10]

[1] Space Sciences Laboratory, 7 Gauss Way, University of California, Berkeley, CA 94720-7450, USA
[2] NASA Goddard Space Flight Center, Greenbelt, MD 20771, USA
[3] Space Research Institute, Russian Academy of Sciences, Profsoyuznaya 84/32, 117997 Moscow, Russia
[4] Georgia College & State University, CBX 82, Milledgeville, GA 31061, USA
[5] Université de Paris and Université Paris Saclay, CEA, CNRS, AIM, F-91190 Gif-sur-Yvette, France
[6] Université de Paris, CNRS, AstroParticule et Cosmologie, F-75013 Paris, France
[7] Univ. Grenoble Alpes, CNRS, IPAG, F-38000 Grenoble, France
[8] Stonehill College, 320 Washington Street, Easton, MA 02357, USA
[9] Dépt. of Astrophysics, lab AIM, CEA/IRFU, CNRS/INSU, Université Paris-Saclay, Université de Paris, Orme des Merisiers F-91191, Gif-sur-Yvette, France
[10] Department of Physics, University of Nevada, Reno, NV 89557, USA

Received 2021 March 30; revised 2021 April 18; accepted 2021 April 19; published 2021 June 15

Abstract

Here, we report on X-ray observations of ten 17–60 keV sources discovered by the International Gamma-Ray Astrophysics Laboratory satellite. The primary new information is sub-arcsecond positions obtained by the Chandra X-ray Observatory. In six cases (IGR J17040-4305, IGR J18017-3542, IGR J18112-2641, IGR J18434-0508, IGR J19504+3318, and IGR J20084+3221), a unique Chandra counterpart is identified with a high degree of certainty, and for five of these sources (all but J19504), Gaia distances or proper motions indicate that they are Galactic sources. For four of these, the most likely classifications are that the sources are magnetic cataclysmic variables (CVs). J20084 could be either a magnetic CV or a high-mass X-ray binary. We classify the sixth source (J19504) as a likely active galactic nucleus (AGN). In addition, we find likely Chandra counterparts to IGR J18010-3045 and IGR J19577+3339, and the latter is a bright radio source and probable AGN. The other two sources, IGR J12529-6351 and IGR J18013-3222, do not have likely Chandra counterparts, indicating that they are transient, highly variable, or highly absorbed.

Unified Astronomy Thesaurus concepts: High energy astrophysics (739); Surveys (1671); Astrometry (80)

1. Introduction

The International Gamma-Ray Astrophysics Laboratory (INTEGRAL; Winkler et al. 2003), which launched in 2002, has uncovered a large number of new or previously poorly studied sources by surveying the sky and Galaxy in the ~20–100 keV band. These are called *INTEGRAL Gamma-Ray* (IGR) sources. To produce emission in this energy band requires particles to be accelerated to high energies, and most of the IGR sources are places where extreme physics is taking place. In many cases, the extreme physics is related to accretion onto compact objects (black holes, neutron stars, or magnetic white dwarfs) or to highly magnetized neutron stars (pulsars or magnetars).

An INTEGRAL catalog based on 8 yr of observations includes 939 persistent and transient sources detected above the 4.5σ significance level in the 17–100 keV band (Bird et al. 2016). The largest groups of sources include 369 active galactic nuclei (AGNs), 129 low-mass X-ray binaries (LMXBs), 116 high-mass X-ray binaries (HMXBs), and 56 cataclysmic variables (CVs). Of the 939 sources, the source type was unknown for 219 at the time Bird et al. (2016) was written. The 939 sources include both previously known sources and 447 IGR sources. The main reasons that INTEGRAL has found new (IGR) sources are (1) the relatively large field of view has allowed for the full sky to be covered; (2) the high-energy bandpass is not affected by Galactic absorption; and (3) most

high-energy sources are transient or variable. While there are many notable sources among the IGR sources, INTEGRAL's capabilities have been especially good for finding new HMXBs, including a population of obscured HMXBs (Matt & Guainazzi 2003; Walter et al. 2006) and a population of Supergiant Fast X-ray Transients (Negueruela et al. 2006; Sguera et al. 2006; Romano et al. 2014).

While the Bird et al. (2016) analysis was carried out for INTEGRAL observations of the whole sky and included enhancements for finding transient sources, another INTEGRAL analysis effort has focused on sources within 17.5° of the Galactic plane (Krivonos et al. 2012). The Krivonos et al. (2012) 9 yr survey resulted in detections of 402 sources. While these included persistent and transient sources, the search focused on sources that were detected in the combined 9 yr of observations, which favors the detection of persistent sources. The most recent report on this survey used 14 yr of INTEGRAL data (Krivonos et al. 2017), and we selected sources from this catalog for the current work.

The current work is focused on making progress toward classifying IGR sources of currently unknown nature by observing a selection of them with the Chandra X-ray Observatory. INTEGRAL provides detections, high-energy spectra, and localization with 90% confidence uncertainties of $1'$–$5'$, depending on source strength. With such positional uncertainties, it is not usually possible to identify an optical or near-IR counterpart, especially in the Galactic plane. Thus, the most important information that Chandra can provide is a more precise source position. In addition, with its 0.3–10 keV

---

[11] NASA Postdoctoral Program Fellow.

Table 1
Source Information from the 2017 INTEGRAL Catalog

IGR Name	l[a] (deg)	b[b] (deg)	R.A.[c] (deg)	Decl.[c] (deg)	Flux[d] (17–60 keV)	Significance[e]
J20084+3221	70.04	−0.23	302.124	+32.350	0.68 ± 0.08	8.4
J18434-0508	27.45	−0.56	280.855	−5.138	0.52 ± 0.08	6.2
J12529-6351	303.10	−1.00	193.241	−63.868	0.49 ± 0.09	5.5
J17040-4305	343.61	−1.02	256.010	−43.080	0.44 ± 0.07	6.2
J19577+3339	69.95	+2.38	299.429	+33.658	0.46 ± 0.08	5.6
J19504+3318	68.87	+3.50	297.615	+33.311	0.63 ± 0.09	7.4
J18010-3045	0.12	−3.82	270.271	−30.764	0.37 ± 0.05	7.2
J18112-2641	4.78	−3.83	272.854	−26.707	0.48 ± 0.06	8.7
J18013-3222	358.74	−4.65	270.326	−32.371	0.34 ± 0.05	6.4
J18017-3542	355.90	−6.27	270.371	−35.638	0.42 ± 0.06	7.0

Notes.
[a] Galactic longitude converted from INTEGRAL position.
[b] Galactic latitude converted from INTEGRAL position.
[c] Source position measured by INTEGRAL and reported in Krivonos et al. (2017). Individual position uncertainties are not provided in Krivonos et al. (2007), but it is indicated that the typical 90% confidence INTEGRAL error radius for these sources is 3.6′.
[d] The flux measured by INTEGRAL in units of 10^{-11} erg cm^{-2} s^{-1}.
[e] The significance of the INTEGRAL detection in terms of signal to noise.

coverage, Chandra provides information about the soft X-ray energy spectrum. We have carried out similar studies in the past (e.g., Tomsick et al. 2012, 2016), and many of the analysis techniques that we employ in this work are the same as described in Tomsick et al. (2020).

1.1. Target Selection

We selected targets to observe with Chandra from the 72 new sources detected in the 17–60 keV band and reported in the 14 yr INTEGRAL catalog (Krivonos et al. 2017). This catalog includes only sources that were not detected in the previous catalog version (Krivonos et al. 2012). We eliminated sources with likely or definite classifications and with previous coverage with Chandra, XMM-Newton, or Swift. As our scientific focus is on Galactic sources, we also used Galactic latitude as a criterion, and $|b|$ is between 0.23° and 6.27° for the sources we study in this work. We obtained Chandra observations for eight sources in Chandra cycle 20 (observations carried out in 2019) and five sources during cycle 19. Results from three of the cycle 19 observations are reported in Hare et al. (2019) and Hare et al. (2021), providing classifications of one HMXB and two magnetic CVs. We report the results for the Chandra observations for the other two sources in this work.

In summary, we are reporting on short (∼5 ks) Chandra observations of the 10 IGR sources listed in Table 1. They are listed in order of how close they are to a Galactic latitude of $b = 0°$. In addition to the INTEGRAL source coordinates, we provide the flux and detection significance from Krivonos et al. (2017). We note that Krivonos et al. (2017) does not provide position uncertainties for individual sources but indicates that the 90% confidence INTEGRAL error radii are typically 3.6′. In Section 2, we describe the Chandra observations, analysis, and results, including searching for Chandra counterparts to the IGR sources, carrying out Chandra photometry, and providing X-ray localizations. Section 3 includes the results of fitting Chandra and INTEGRAL energy spectra. In Section 4, we search for multiwavelength counterparts using the accurate Chandra localizations. Sections 5 and 6 include a discussion of the results and conclusions, respectively.

Table 2
Chandra Observations

IGR Name	ObsID	Start Time (UT)	Exposure Time (s)
J18017-3542	20200	2018 Jul 15, 21.8 hr	4956
J12529-6351	20201	2018 Feb 20, 3.3 hr	4952
J20084+3221	21248	2019 Jan 9, 19.5 hr	4949
J18434-0508	21249	2019 Mar 5, 3.4 hr	4952
J17040-4305	21250	2019 May 29, 1.5 hr	4956
J19577+3339	21251	2018 Nov 30, 8.7 hr	4959
J19504+3318	21252	2019 Jan 12, 1.4 hr	4956
J18010-3045	21253	2019 May 14, 3.0 hr	4962
J18112-2641	21254	2019 Mar 6, 8.4 hr	4955
J18013-3222	21255	2019 May 13, 10.4 hr	5057

2. Chandra Observations, Analysis, and Results

Table 2 provides the basic information for the 10 Chandra observations, which occurred between 2018 February 20 and 2019 May 29. We used the ACIS-I instrument (Garmire et al. 2003) with exposure times of ∼5000 s, which is sufficient to expect >100 counts based on the INTEGRAL fluxes and extrapolation of a hard power law into the Chandra bandpass. The field of view of the four ACIS-I chips is 16.9′ × 16.9′, which easily contains the 90% confidence INTEGRAL error regions with one pointing per source. In each case, the pointing positions are the INTEGRAL positions given in Table 1.

We reduced the data using the Chandra Interactive Analysis of Observations (CIAO; Fruscione et al. 2006) version 4.13 software with the Calibration Database version 4.9.4, largely following instructions in the CIAO science threads.[12] We used `chandra_repro` for reprocessing the data, resulting in a photon list along with other instrument files.

We created exposure-corrected images in the 0.3–10 keV band for each of the 10 Chandra observations using `flux-image`. These images were then combed for sources by applying the wave detection algorithm `wavdetect`, using wavelets with scales of 1, 2, 4, 6, 8, 12, 16, 24, and 32, and

_____
[12] See http://asc.harvard.edu/ciao/threads/index.html.

Table 3
Source Detection and Shifts Based on Optical/IR Register Matches

IGR Name	ObsID	N_{Chandra}[a]	Survey	N_{matches}[b]	x_{shift}[c]	y_{shift}[c]	Avg. Residual[d]	Max. Residual[e]
J18017-3542	20200	19	Vista VVV	5	−0.08	−0.20	0.55	0.90
J12529-6351	20201	14	Gaia EDR3	5	0.20	−0.56	0.51	0.78
J20084+3221	21248	11	PanSTARRS	2	⋯	⋯	⋯	⋯
J18434-0508	21249	22	Gaia EDR3	6	0.13	−0.33	0.59	0.85
J17040-4305	21250	12	Gaia EDR3	2	⋯	⋯	⋯	⋯
J19577+3339	21251	11	Gaia EDR3	2	⋯	⋯	⋯	⋯
J19504+3318	21252	13	PanSTARRS	2	⋯	⋯	⋯	⋯
J18010-3045	21253	19	Gaia EDR3	8	−0.13	−0.14	0.45	0.84
J18112-2641	21254	18	Vista VVV	3	−0.59	−0.35	0.26	0.37
J18013-3222	21255	15	Gaia EDR3	7	−0.27	0.49	0.57	0.72

Notes.
[a] The number of Chandra sources detected on the four ACIS-I detector chips.
[b] The number of matches between the Chandra detections and the survey catalog.
[c] The shifts in the x and y detector coordinate directions in pixels. The conversion is 1 pixel = 0.492″.
[d] Average residual (in arcseconds) between the Chandra and O/IR sources.
[e] Maximum residual (in arcseconds) between the Chandra and O/IR sources.

with a detection threshold set to produce just one spurious source among the detection results. The number of sources detected for each observation is given in Table 3.

In order to account for any systematic uncertainty in our Chandra astrometry due to telescope pointing, we compared the detected source positions with several optical and near-IR catalogs using `wcs_match`, and shifted the source positions for each ObsID accordingly. The catalogs we used to match our detected Chandra sources include Gaia EDR3 (Gaia Collaboration 2020), the Variables in the Via Lactea (VVV) Survey by the Visual and Infrared Survey Telescope for Astronomy (VISTA; Minniti et al. 2010; McMahon et al. 2013; Minniti et al. 2017), the UKIRT Infrared Deep Sky Survey (UKIDSS; Lucas et al. 2008), and the Panoramic Survey Telescope and Rapid Response System (PanSTARRS; Chambers et al. 2016). For each observation we chose the survey that provided the most crossmatches with our Chandra sources, while ignoring the candidate IGR counterpart (when applicable, see Section 2.1 for details on counterpart selection), and these results are provided in Table 3. We also include the average and maximum residuals between the Chandra and optical/near-IR catalog positions, after translation of the Chandra coordinates. In observations where fewer than three crossmatches were found, as was the case for ObsIDs 21248, 21250, 21251, and 21252, we did not shift the Chandra positions.

We performed Chandra aperture photometry to determine the number of counts for all of the detected sources. We made a point-spread function (PSF) map using `mkpsfmap`[13] for an energy of 2.3 keV (the typical average photon energy for the full 0.3–10 keV Chandra bandpass), and determined the 95% encircled energy radius for each source. After defining background regions for each observation, we used `dmextract` to extract background-subtracted counts in the 0.3–2, 2–10, and 0.3–10 keV energy bands.

2.1. Selecting the Most Likely Counterparts

As in previous work (e.g., Tomsick et al. 2020), we calculated the probability that sources with the brightnesses we observe would be found in a search area with a radius of θ_{search} by chance. In cases where the source is within the

90% confidence INTEGRAL error radius (θ_{INTEGRAL}), $\theta_{\text{search}} = \theta_{\text{INTEGRAL}} = 3.6'$. If the source is outside the INTEGRAL error circle, then θ_{search} is equal to the angular distance from the best estimate of the INTEGRAL position. Another factor that is important in determining the probability that the Chandra/INTEGRAL association is spurious is the brightness of the source.

As in Tomsick et al. (2020), we determine the relative probabilities for all sources using

$$P_{\text{rel}} = 1 - e^{-\left(\frac{C_{2-10\,\text{keV}}}{C_0}\right)^{-1.0} \pi\, \theta_{\text{search}}^2} , \qquad (1)$$

where $C_{2-10\,\text{keV}}$ is the number of counts in the 2–10 keV band, C_0 is a normalization constant set to a value of 140 so that the brightest sources have P_{rel} values near 1%, and we use −1.0 as the slope of the $\log N - \log S$, which is intermediate between previously published profiles (Sugizaki et al. 2001; Fornasini et al. 2014). In our case, with all of the observations having the same exposure, it is valid to use counts (as opposed to count rates) for this calculation. The P_{rel} values for all the sources detected in the 10 Chandra observations are plotted in Figure 1. This results in the field sources clustering at low numbers of counts and high values of P_{rel}. For six of the IGR fields (IGR J17040-4305, IGR J18017-3542, IGR J18112-2641, IGR J18434-0508, IGR J19504+3318, and IGR J20084+3221), there are clear Chandra counterparts that are well separated from the field sources. There are also potential counterparts in the IGR J18010-3045 and the IGR J19577+3339 fields. The IGR J12529-6351 and IGR J18013-3222 fields do not appear to have likely counterparts.

The candidate Chandra source in the IGR J19577+3339 field has $P_{\text{rel}} = 16.4\%$, which is the highest spurious association probability of any of the eight candidates we consider, and Figure 1 shows that there are even some field sources with lower probabilities. However, searching in VizieR at this position finds a likely match with the radio source ICRF J195740.5+333827. The Chandra and radio Very Long Baseline Interferometry (VLBI) positions are consistent with a separation of 0.56″ ± 0.93″ (90% confidence). This is a bright radio source with a flux of 295 ± 9 mJy at 1.4 GHz that appears in a number of radio catalogs. The radio source is suspected to be an AGN, but no

---
[13] We later realized that `fluximage` can provide this same map.

Table 4
Chandra Candidate Counterparts to IGR Sources

IGR Name	CXOU Name	Chandra R.A. (J2000)	Chandra Decl. (J2000)	Uncertainty[a] (arcseconds)	θ[b]/$\theta_{INTEGRAL}$[c] (arcminutes)	ACIS Counts[d]	Hardness[e]
J17040	J170404.9-430537	$17^h04^m04.92^s$	$-43°05'37.9''$	0.81	0.95/3.6	583 ± 25	$+0.72 \pm 0.05$
J18010	J180100.6-303958	$18^h01^m00.61^s$	$-30°39'58.4''$	1.18	5.95/3.6	41 ± 8	$+0.48 \pm 0.21$
J18017	J180112.5-353912	$18^h01^m12.53^s$	$-35°39'12.1''$	0.89	3.48/3.6	55 ± 8	$+0.86 \pm 0.21$
J18112	J181058.4-264115	$18^h10^m58.41^s$	$-26°41'15.7''$	0.99	6.05/3.6	111 ± 12	$+0.43 \pm 0.12$
J18434	J184311.4-050545	$18^h43^m11.43^s$	$-05°05'45.2''$	0.83	4.26/3.6	450 ± 22	$+0.48 \pm 0.06$
J19504	J195019.7+331416	$19^h50^m19.73^s$	$+33°14'16.7''$	0.83	4.68/3.6	548 ± 24	$+0.19 \pm 0.05$
J19577	J195740.5+333828	$19^h57^m4059^s$	$+33°38'28.2''$	0.93	1.12/3.6	10 ± 4	$+0.80 \pm 0.60$
J20084	J200844.1+321818	$20^h08^m44.14^s$	$+32°18'18.3''$	0.83	4.06/3.6	313 ± 19	$+0.73 \pm 0.07$

Notes.
[a] 90% confidence.
[b] The angular distance between the center of the INTEGRAL error circle and the source.
[c] The size of the 90% confidence INTEGRAL error radius given in Krivonos et al. (2017).
[d] The number of counts, after background subtraction, measured by Chandra/ACIS-I in the 0.3–10 keV band.
[e] The hardness is given by $(C_2 - C_1)/(C_2 + C_1)$, where C_2 is the number of counts in the 2–10 keV band and C_1 is the number of counts in the 0.3–2 keV band.
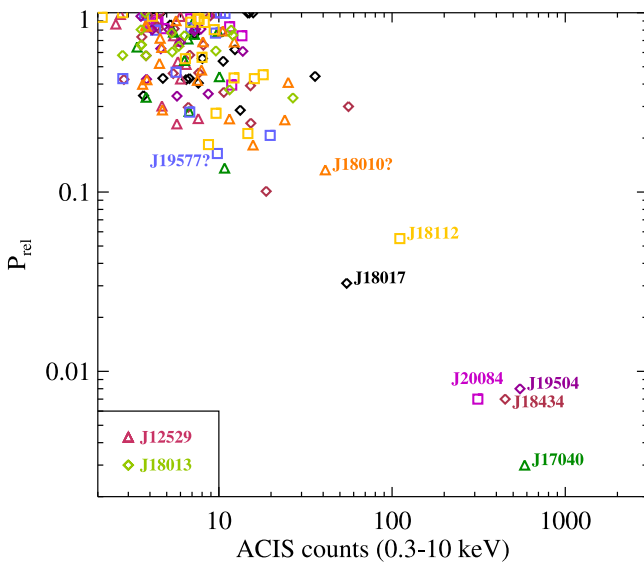

Figure 1. The relative probability of a chance detection (see Equation (1)) vs. the number of 0.3–10 keV ACIS-I counts for all Chandra sources detected in the 10 observations of IGR source fields. For the eight fields with candidate counterparts (although we note that J18010 and J19577 are questionable), the source that is least likely to be a spurious association is labeled with the IGR source name. The legend in the lower left corner of the plot lists the two IGR source fields without likely counterparts.

source. For the statistical uncertainty, we calculate the 90% confidence intervals following Equation (13) from Kim et al. (2007), which uses the number of counts as well as the angular distance of the source from the Chandra aimpoint. The Chandra counterpart to IGR J18112-2641 has the greatest separation from its INTEGRAL position, at 6.05′. We also include the potential counterpart to IGR J18010-3045 in Table 4 as well as in the rest of our analysis, although we cannot be as confident (with fewer counts and a separation of 5.95′) that the detected Chandra source is a true match.

In Section 3, we determine fluxes for the eight most likely counterpart candidates and use previously measured surface density ($\log N - \log S$) profiles (Sugizaki et al. 2001; Fornasini et al. 2014) to calculate absolute spurious probabilities for the Chandra/INTEGRAL associations.

3. Chandra Energy Spectra

For the eight candidate counterparts, we extracted Chandra energy spectra using `specextract`. We used the same source regions (circles with radii corresponding to 95% encircled energy) and background regions as for the photometry. We rebinned the spectra with the requirement of a detection in each bin at the 3σ–5σ level, depending on the total number of counts in the spectrum. The one exception is J19577, for which we binned to 1.5σ because the spectrum only includes 10 counts. We used XSPEC (Arnaud 1996) to fit the Chandra spectra with an absorbed power-law model, and the parameters are reported in Table 5. One of the bright sources, J17040, was also located close to the center of the field of view where the PSF is small. This resulted in significant photon pileup, and we included the XSPEC model `pileup` (Davis 2001) to account for this in the spectral fitting. Photon pileup does not impact the spectra of the other sources. We performed the fits by minimizing the C-statistic, and we give the C values and number of degrees of freedom (dof) in Table 5.

We use the C values and the variances in C (see Kaastra 2017) to assess the quality of the fits. The P_{reject} values in Table 5 indicate the probability that an absorbed power law does not provide a good description of the spectrum. The P_{reject} value is only meaningful if C is larger than the number of dof, and this is only the case for J17040 (41%), J19504 (41%), and

redshift has been measured. Although the X-ray source is faint, the combination of the hardness of its spectrum, the fact that it is only 1.12′ from the center of the INTEGRAL error circle, and the likely association with the bright radio source make it necessary for us to consider this candidate.

For the eight candidates, Table 4 gives the Chandra names and positions, the angular distance from the center of the INTEGRAL error circle (θ), the number of ACIS counts in the 0.3–10 keV band, and the hardness ratio. The uncertainties in the candidate positions include systematic and statistical contributions added in quadrature. We use the standard 0.8″ systematic uncertainty (at the 90% confidence level)[14] for each

---
[14] See http://cxc.cfa.harvard.edu/cal/ASPECT/celmon/.

Table 5
Chandra Spectral Parameters and Absolute Spurious Probabilities

IGR Name	N_H[a] $(\times 10^{22}\,\mathrm{cm}^{-2})$	$N_{H,Galactic}$[b] $(\times 10^{22}\,\mathrm{cm}^{-2})$	Γ	Absorbed Flux[c] (2–10 keV)	Unabsorbed Flux[d] (2–10 keV)	C/dof	P_{reject}[e]	Probability[f]
J17040	$0.5^{+0.7}_{-0.5}$	1.2	0.2 ± 0.4	7.45×10^{-12}	7.56×10^{-12}	23/19[g]	41%	0.19%–0.34%
J18010	$0.0^{+2.3}_{-0.0}$	0.3	$0.4^{+1.2}_{-0.4}$	3.57×10^{-13}	3.57×10^{-13}	1.2/2	⋯	10%–21%
J18017	5^{+12}_{-5}	0.2	$0.0^{+1.7}_{-1.3}$	7.05×10^{-13}	7.08×10^{-13}	2.2/3	⋯	2.2%–3.5%
J18112	$0.5^{+1.3}_{-0.5}$	0.3	$0.9^{+0.7}_{-0.5}$	7.50×10^{-13}	7.59×10^{-13}	3.5/4	⋯	5.8%–8.9%
J18434	$0.4^{+0.5}_{-0.4}$	1.4	0.7 ± 0.3	3.91×10^{-12}	3.96×10^{-12}	8/14	⋯	0.59%–0.80%
J19504	1.1 ± 0.4	0.5	1.8 ± 0.3	2.17×10^{-12}	2.24×10^{-12}	22/18	41%	1.4%–1.5%
J19577	$1.1^{+36}_{-1.1}$	0.9	$-0.6^{+4.5}_{-1.5}$	2.52×10^{-13}	2.57×10^{-13}	0.2/1	⋯	4.9%–12%
J20084	$1.0^{+1.0}_{-0.9}$	0.9	$0.1^{+0.4}_{-0.2}$	3.17×10^{-12}	3.24×10^{-12}	15/9[h]	77%	0.69%–0.86%

Notes.

[a] The errors on the parameters are 90% confidence. The column density is calculated assuming Wilms et al. (2000) abundances and Verner et al. (1996) cross sections.

[b] From the HI4PI survey (HI4PI Collaboration et al. 2016).

[c] In units of per square centimeter per second.

[d] Only corrected for Galactic absorption.

[e] The probability that an absorbed power law does not provide a good description of the spectrum based on a calculation of the variance of C according to the method described in Kaastra (2017).

[f] Absolute probability that a source of this brightness would be found by chance in the search region calculated using Equation (4). The range comes from using the two $\log N - \log S$ distributions in Equations (2) and (3).

[g] This includes a pileup correction. There is an improvement to C/dof = 11/17 if an iron emission line is added (see Section 3).

[h] There is an improvement to C/dof = 7/7 if an iron emission line is added (see Section 3).

J20084 (77%). For these three sources the largest residuals are single bins at 6.7 keV (3.6σ above the continuum), 1.7 keV (2.8σ above the continuum), and 6.5 keV (2.7σ above the continuum), respectively. While there is no immediate interpretation for the 1.7 keV residual, it is possible that J17040 and J20084 have iron Kα emission lines.

Adding a narrow line for J17040 improves the fit to C/dof = 11/17, and the parameters, with 90% confidence uncertainties, are $E_{line} = 6.7 \pm 0.1$ keV and $N_{line} = (6.4^{+19}_{-3.6}) \times 10^{-5}\,\mathrm{ph\,cm}^{-2}\,\mathrm{s}^{-1}$. The equivalent width is EW = $1.5^{+8.5}_{-1.5}$ keV, where the uncertainties come from simulations using the `eqwidth` command in XSPEC. Although the improvement in the fit and the fact that N_{line} is greater than zero at the 90% confidence level indicate that an iron line may be present, this is not a robust detection for at least three reasons: (1) The small value of C relative to the number of dof suggests that adding the emission line may be over-fitting the spectrum; (2) P_{reject} = 41% indicates that it is fairly likely (59%) that a power law provides a good description of the spectrum; and (3) the simulations for determining the EW indicate that the data are consistent with EW = 0 at 90% confidence.

For J20084, adding a narrow line improves the fit to C/dof = 7/7, and the parameters are $E_{line} = 6.7^{+0.1}_{-0.5}$ keV, $N_{line} = (3.1^{+2.9}_{-2.4}) \times 10^{-5}\,\mathrm{ph\,cm}^{-2}\,\mathrm{s}^{-1}$, and EW = $0.9^{+1.3}_{-0.8}$ keV. We estimate the significance of the emission line by determining the confidence level that makes the N_{line} error range consistent with zero, which is $\Delta C = 7.7$. This indicates a significance of approximately 99.2%, which corresponds to a 2.6σ detection.

We use the fluxes resulting from the spectral fits to determine the absolute spurious source probabilities for the eight Chandra candidates. As in Tomsick et al. (2020), we use

$$N(>F_{2-10\,\mathrm{keV,abs}}) = 9.2(F_{2-10\,\mathrm{keV,abs}}/10^{-13})^{-0.79}\,\mathrm{deg}^{-2}\ , \tag{2}$$

which is based on the $\log N - \log S$ curve for Galactic sources detected by the Advanced Satellite for Cosmology and Astrophysics (Sugizaki et al. 2001), and we also use

$$N(>F_{2-10\,\mathrm{keV,unabs}}) = 36(F_{2-10\,\mathrm{keV,unabs}}/10^{-13})^{-1.24}\,\mathrm{deg}^{-2}\ , \tag{3}$$

which is based on Chandra observations of the Norma region of the Galactic plane (Fornasini et al. 2014) and includes Galactic sources and AGN. In both cases, the 2–10 keV flux range is used, and while Sugizaki et al. (2001) simply use the absorbed fluxes, Fornasini et al. (2014) make a correction for Galactic absorption. Thus, from the power-law fits, we provide in Table 5 both the absorbed 2–10 keV fluxes as well as fluxes with an absorption correction. We correct for the best-fit value of N_H unless it is larger than the Galactic value from HI4PI Collaboration et al. (2016), in which case, we correct for $N_{H,Galactic}$ (also given in Table 5). The resulting absorption corrections are relatively small.

With these fluxes and the two $\log N - \log S$ curves, we use

$$P = 1 - e^{-N(>F_{2-10\,\mathrm{keV}})\,\pi\,\theta^2_{search}} \tag{4}$$

to calculate the absolute probability of finding a source in the search region (defined by θ_{search} as described in Section 2.1) as bright as the candidate sources by chance. The ranges of probabilities (from the two $\log N - \log S$ curves) for each source are given in Table 5. This shows that the candidate Chandra counterparts to J17040, J20084, and J18454 are very unlikely (<1%) to be detected in the search regions by chance. Also, the candidates to J19504 and J18017 are unlikely (one to a few percent) to be chance detections. The J18112, J19577, and J18010 candidates have somewhat higher spurious probabilities (5.8%–8.9%, 4.9%–12%, and 10%–21%, respectively), and although, in the following, we perform the same analyses for these three as for the other five, they may possibly be field sources rather than the actual counterpart to the IGR sources (although see Section 2.1 concerning the association of J19577 with a bright radio source).
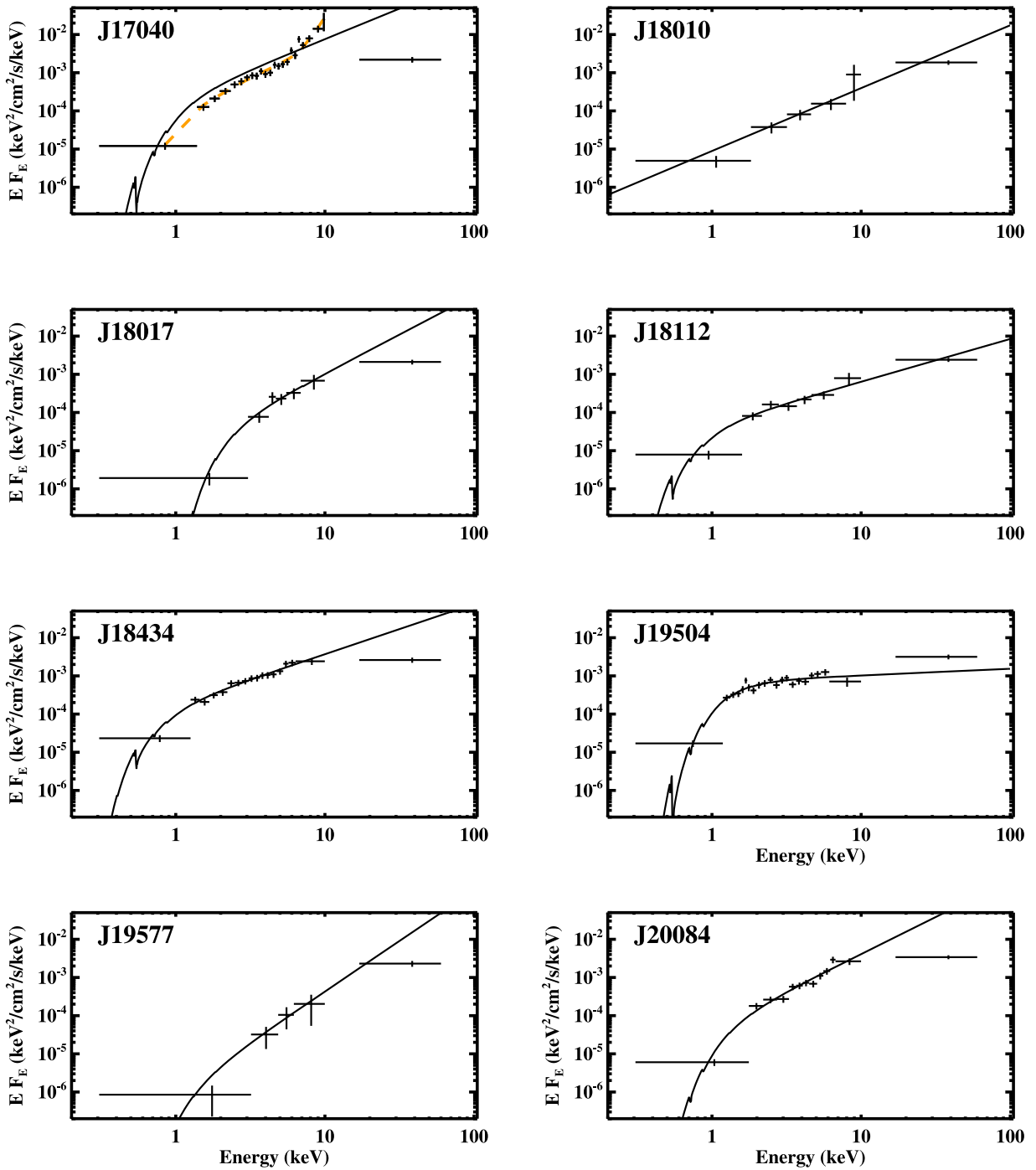
Figure 2. Chandra energy spectra for the eight candidate counterparts along with the 17–60 keV INTEGRAL flux point from Krivonos et al. (2017). The model shown is the best-fit absorbed power law to the Chandra data. The power law is extended to higher energies to compare the extrapolation to the INTEGRAL flux point. For J17040, the orange dashed curve shows the fit to the Chandra spectrum before the pileup correction.

Figure 2 shows the Chandra spectra with the absorbed power-law fits. As given in Table 5, the spectra have hard power-law photon indices with best-fit values between $\Gamma = -0.6$ and 1.8. In Figure 2, we have added a 17–60 keV point measured by INTEGRAL (Krivonos et al. 2017) for comparison to the extrapolation of the power law. In making this comparison, it is important to keep in mind that the INTEGRAL flux point is an average over 14 yr, while the Chandra spectra are a single observation. Thus, differences can be related to source variability or to a change in spectral slope between the Chandra band and the INTEGRAL band. The

17–60 keV flux point is lower than the extrapolation of the power law for J17040, J18010, J18017, J18434, J19577, and J20084, which makes it possible that the spectrum has a break or a cutoff above 10 keV. These are also the six sources with the hardest power-law indices (best-fit Γ values between -0.6 and 0.7). For J18112, the 17–60 keV point is consistent with the power-law extrapolation.

Although the softest source (J19504 with $\Gamma = 1.8 \pm 0.3$) has a 17–60 keV point that is higher than the power-law extrapolation, a reinspection of the INTEGRAL image shows significant noise in the part of the sky where J19504 lies due to

the proximity to the bright source Cygnus X-1. In fact, J19504 clearly sits on top of a positive noise artifact, indicating that the INTEGRAL flux reported in Krivonos et al. (2017) and shown in Figure 2 is an overestimation.

4. Optical/IR Identifications

We used the VizieR database to search for optical/IR counterparts to the eight Chandra sources. In Table 6, we provide details on the matches found using Gaia EDR3, including the G-, BP-, and RP-band magnitudes, the parallax, the astrometric noise, and the proper motion. For three of the sources, a reliable distance measurement is available, and we quote the geometric distances[15] calculated by Bailer-Jones et al. (2021). Those distances are 0.937 ± 0.046 kpc, 1.58 ± 0.13 kpc, and $3.0^{+1.2}_{-0.9}$ kpc, for J17040, J18017, and J18434, respectively. These three sources also have high proper motions as do J18112 (5.74 ± 0.09 mas yr^{-1}) and J20084 (4.77 ± 0.23 mas yr^{-1}). Thus, we conclude that all five of these sources are Galactic. J19504 has a proper motion of 0.12 ± 0.17 mas yr^{-1}, which is consistent with zero. The small proper motion does not distinguish between a Galactic or extragalactic nature for J19504, but it does allow for the possibility that the source is extragalactic. The Gaia counterpart to J18010 does not have parallax or proper motion measurements, presumably because it is too faint. J19577 does not have a Gaia counterpart. The closest Gaia source is 1.5″ away.

Although the Bailer-Jones et al. (2021) catalog provides distance estimates for J18112, J19504, and J20084, it also provides information about these estimates suggesting that they may not be reliable. For J18112 and J19504, the astrometric noise is larger than the value of the parallax (Table 6). For J20084, while there is no astrometric noise, the uncertainty on the parallax is almost twice that of the parallax value, and Figure 6 in Bailer-Jones et al. (2021) shows that, in such cases, the distance estimate is highly dependent on the prior distribution assumed.

We also used VizieR to search for All Wide-field Infrared Survey Explorer (AllWISE) (Cutri et al. 2021) IR counterparts to the eight Chandra sources. We found just two matches in the AllWISE catalog. These are for the Chandra counterparts to J19504 and J20084. Both AllWISE counterparts are consistent with being point sources according to the extended source parameter "ex," which has a value of zero in both cases. The J19504 counterpart is AllWISE J195019.73+331416.3, which has magnitudes of $W1 = 12.057 \pm 0.025$, $W2 = 11.209 \pm 0.020$, $W3 = 9.028 \pm 0.026$, and $W4 = 7.14 \pm 0.10$. The $W1$-$W2$ and $W2$-$W3$ colors place J19504 is a region of the near-IR color plot that is commonly populated by AGN (Mateos et al. 2012; Secrest et al. 2015). We have also checked the near-IR colors for J20084, but it does not fall in the AGN region. The positions of both of the AllWISE sources are consistent with the Gaia positions to within <0.3″.

In Table 7, we include the other identifications from the results of VizieR searches, focusing our results to the near-IR matches. These include those matches found in VISTA VVV (Minniti et al. 2010; McMahon et al. 2013; Minniti et al. 2017), the 2 Micron All-Sky Survey, (2MASS; Cutri et al. 2003), UKIDSS (Lucas et al. 2008), and PanSTARRS (Chambers et al. 2016).

Across these four survey catalogs, we have measurements of the source magnitudes in the Y, J, H, and K/K_s bands, except for J18010, which does not have a reliable Y-band measurement due to the source being too faint at those wavelengths. In all cases, the near-IR positions are consistent with the Gaia positions. In Figure 3 we provide the K/K_s images of the region in the sky covering each Chandra counterparts position, marked with a red circle in each image. Figure 4 provides the Y-band images for each of the eight Chandra counterparts as well. The images for J19577 show that there is no optical or near-IR counterpart in the Chandra error circle. Also, the VLBI radio position, which is inside the Chandra error circle, is marked.

In summary, by utilizing the Chandra counterpart positions and searching the VizieR database, we are able to find optical/IR counterparts for seven sources and a radio counterpart for J19577. From the Gaia EDR3 data, we established distances to three sources, while the proper motions of two of the remaining sources indicate that they are also Galactic in nature. For J19504, the fact that the AllWISE colors place it in a region populated by AGN suggest that J19504 is an AGN, and while the low proper motion in Gaia does not prove that the source is extragalactic, it is consistent with that interpretation. The near-IR counterpart information, including magnitudes, is provided in Table 7 and Figures 3 and 4.

The VizieR search also uncovered counterparts in the VST[16] Photometric Hα Survey of the Southern Galactic Plane and Bulge (VPHAS+ Data Release 2) for J17040 and J18434 (Drew et al. 2016). For J17040, the counterpart is VPHASDR2 J170405.0-430538.0 with magnitudes of 15.68 ± 0.01 for the Hα filter, $r = 16.10 \pm 0.01$, and $i = 15.47 \pm 0.01$. For J18434, the counterpart is VPHASDR2 J184311.4-050545.5 with magnitudes of 17.83 ± 0.02 (Hα), $r = 18.31 \pm 0.01$, and $i = 17.71 \pm 0.01$. These correspond to r–H$\alpha = 0.42 \pm 0.01$ and r–$i = 0.63 \pm 0.01$ for J17040 and r–H$\alpha = 0.48 \pm 0.02$ and r–$i = 0.60 \pm 0.01$ for J18434. Comparing to the field star distribution in Figure 17 of Drew et al. (2014), these measurements indicate that J17040 and J18434 have an excess at Hα, suggesting the presence of an emission line.

5. Sources Without Clear Chandra Counterparts to the IGR Sources

The Chandra observations for IGR J18013-3222 and IGR J12529-6351 did not lead to detections of clear counterparts, but here we consider the Chandra sources in each field with the lowest values of P_{rel}.

For J18013, the sources with the lowest values of P_{rel} have values of 37.2% and 33.5%, indicating that there is a high chance that they are spurious. In addition, the one with $P_{rel} = 33.5\%$, CXOU J180143.1-321540, is 8.4′ from the center of the INTEGRAL error circle, which is another reason to doubt that it is the correct counterpart. Within the 3.6′ INTEGRAL error circle, the brightest Chandra source only has four counts. We conclude that the upper limit on the 2–10 keV flux is $<1 \times 10^{-13}$ erg cm^{-2} s^{-1}.

For J12529, CXOU J125231.0-635021 is within the INTEGRAL error circle and has $P_{rel} = 24\%$ and 5.7 ± 3.6 detected ACIS counts. While this is a small number, they are all >2 keV, suggesting that it is a hard source. It is possible that this is the correct counterpart of the INTEGRAL source, but the evidence is not strong enough to consider it as a likely

---

[15] Although the Bailer-Jones et al. (2021) catalog includes both geometric and photogeometric distances, we use the geometric distances because the colors of the sources we are studying may deviate from the assumptions made for the photogeometric distances.

---

[16] Very Large Telescope (VLT) Survey Telescope.

Table 6
Gaia Identifications in EDR3

IGR Name	Gaia Number (in EDR3)	Separation[a] (arcsec)	G-magnitude	BP-magnitude	RP-magnitude	Parallax (mas)	Astrometric Noise (mas)	Distance[b] (kpc)	Proper Motion (mas yr^{-1})
J17040	5965412985207709184	0.470	16.312 ± 0.005	16.798 ± 0.014	15.627 ± 0.012	1.03 ± 0.06	0	0.937 ± 0.046	6.53 ± 0.07
J18010	4044148421630416256	0.784	20.133 ± 0.034	⋯	⋯	⋯	⋯	⋯	⋯
J18017	4038975665929542784	0.273	15.714 ± 0.008	15.827 ± 0.026	15.451 ± 0.020	0.61 ± 0.04	0	1.58 ± 0.13	6.89 ± 0.04
J18112	4064533126752366464	0.790	16.625 ± 0.003	16.991 ± 0.546	15.429 ± 0.015	0.37 ± 0.11	0.673	⋯	5.74 ± 0.09
J18434	4256616815760182528	0.366	18.248 ± 0.011	18.743 ± 0.043	17.625 ± 0.045	0.44 ± 0.15	0	$3.0^{+1.2}_{-0.9}$	3.98 ± 0.16
J19504	2034764091072416384	0.460	18.698 ± 0.012	⋯	⋯	-0.35 ± 0.16	0.338	⋯	0.12 ± 0.17
J20084	2054890685756667392	0.250	19.461 ± 0.006	20.893 ± 0.083	18.223 ± 0.021	0.15 ± 0.27	0	⋯	4.77 ± 0.23

Notes.
[a] The angular separation between the Chandra position and the Gaia catalog position.
[b] From Bailer-Jones et al. (2021).

Table 7
VISTA VVV, 2MASS, UKIDSS, and PanSTARRS Identifications

IGR Name	Catalog	Source (arcsec)	Separation[a]	Y	J	H	K/K_s	Class[b]
J17040	VISTA VVV	VVV J170404.96-430538.07	0.530	14.885 ± 0.003	14.627 ± 0.003	14.499 ± 0.006	K_s = 14.197 ± 0.001	−1
J18010	VISTA VVV	VVV J180100.64-303957.61	0.879	⋯	18.404 ± 0.487	16.681 ± 0.173	K_s = 15.640 ± 0.095	−1
J18017	VISTA VVV	VVV J180112.51-353912.10	0.191	15.288 ± 0.011	15.008 ± 0.008	14.945 ± 0.014	K_s = 14.821 ± 0.022	−1
J18112	VISTA VVV	VVV J181058.38-264114.93	0.839	14.467 ± 0.008	13.943 ± 0.008	13.290 ± 0.007	K_s = 13.024 ± 0.008	−1
J18112	PanSTARRS	75972727431145261	0.776	15.425 ± 0.002	⋯	⋯	⋯	52
J18434	UKIDSS	J184311.43-050545.6	0.403	⋯	18.932 ± 0.173	18.087 ± 0.206	16.883 ± 0.131	−1
J18434	PanSTARRS	101882807975695145	0.364	17.671 ± 0.027	⋯	⋯	⋯	52
J19504	2MASS	19501973+3314166	0.115	⋯	15.423 ± 0.060	14.542 ± 0.068	13.682 ± 0.049	⋯
J19504	PanSTARRS	1478829758214426046	0.166	17.136 ± 0.026	⋯	⋯	⋯	61
J20084	UKIDSS	J200844.16+321818.2	0.375	⋯	16.037 ± 0.007	15.306 ± 0.006	14.885 ± 0.011	−1
J20084	PanSTARRS	146763021840106679	0.279	17.652 ± 0.033	⋯	⋯	⋯	60

Notes.
[a] The angular separation between the Chandra position and the catalog position.
[b] For VISTA VVV and UKIDSS, the classification is based on the spatial profile, where −2 is a probable star, −1 is a star with probability ⩾90%, and 1 is a galaxy with probability ⩾90%. For PanSTARRS, quality flag 61 indicates that the source is extended, and flags 52 and 60 indicate that the criterion for the detection of source extension is not met.

counterpart. We conclude that the upper limit on the 2–10 keV flux is $<1 \times 10^{-13}$ erg cm^{-2} s^{-1}.

6. Discussion

From Chandra observations of 10 IGR sources, we have found definite or candidate soft X-ray counterparts in eight cases. The Chandra positions provide information about the multiwavelength properties of these sources, and we discuss the nature of the sources based on the X-ray and multi-wavelength information.

6.1. Galactic Sources with Distances

J17040, J18017, and J18434 are the three sources with distance constraints from Gaia (Table 6). Based on the X-ray fluxes measured by Chandra (Table 5) the 2–10 keV luminosities are $(7.9 \pm 0.8) \times 10^{32}$, $(2.1 \pm 0.4) \times 10^{32}$, and $(4.2^{+3.4}_{-2.6}) \times 10^{33}$ erg s^{-1}, respectively. Based on these X-ray luminosities and the hardness of the spectra, the emission is not from isolated stars (consistent with them being detected by INTEGRAL), and the most likely possibility would be that these are accreting binaries, such as CVs or X-ray binaries. For sources with X-ray spectra with power-law photon indices of $\Gamma < 1$, there are two types of binaries that are the most likely possibilities: magnetic CVs, such as intermediate polars, and HMXBs with highly magnetized neutron stars. The magnetic CVs typically have late-type donor stars, while the HMXBs have O or B type stars (by definition). In the following, we use the distances and near-IR magnitudes to consider the most likely classifications for J17040, J18017, and J18434.

Interpreting the near-IR magnitudes of these sources (Table 7) requires that we correct them for Galactic extinction, and we have used 3D dust maps to determine this. For J17040 and J18017, we use the mwdust code[17] (Bovy et al. 2016) to

obtain the $E(B - V)$ values shown in Table 8. The errors come from the $E(B - V)$ range for the Gaia distance range. For J18434, we use the Bayestar19 map from Green et al. (2019), accessing $E(g - r)$ values using a web interface[18] and multiplying by 0.94 to convert to $E(B - V)$.[19] In Table 8, $A_V = 3.1E(B - V)$, $A_J = 0.260A_V$, and $A_J - A_H = 0.090\ A_V$ (Fitzpatrick 1999). We correct the J and H magnitudes in Table 7 for extinction, obtaining J–H–$(A_J$-$A_H)$ values of $0.061^{+0.007}_{-0.008}$, $-0.030^{+0.016}_{-0.017}$, and 0.63 ± 0.27 for J17040, J18017, and J18434, respectively.

Using tables of stellar colors from Pecaut & Mamajek (2013), we find that the measured colors correspond to temperatures of $T_{\rm eff} = 7680 \pm 90$, 9600 ± 800, and 2200–5300 K for the three sources (Table 7). We also calculated the absolute J-band magnitudes, M_J, using the values of J and A_J, and the Gaia distances. Although we do not know if the near-IR emission is coming from a star or not, the values of M_J place limits on the main-sequence spectral types of a star in the system, and we determine these limits using tables of main-sequence stellar magnitudes and colors (Pecaut & Mamajek 2013). As shown in Table 8, the spectral type limits for J17040 and J18017 indicate temperatures of <5100 and <5770 K, respectively, which are less than the values derived from the colors. This suggests that the near-IR is dominated by hot emission from an accretion disk. On the other hand, for J18434, M_J indicates a temperature limit of <4400 K, which is consistent with the color temperature. Thus, based on this analysis, it is possible that the near-IR emission for J18434 comes from a cool star.

We repeated the color and magnitude analysis using the optical magnitudes from Gaia. In Table 8, $A_G = 0.90A_V$ and $A_{BP} - A_{RP} = 0.51\ A_V$ (Fitzpatrick 1999). For J17040 and J18017, the results are similar to the near-IR in that they show higher values of $T_{\rm eff}$ based on the colors than the temperature ($T_{\rm type}$) of a star of spectral type consistent with the observed

---

[17] See https://github.com/jobovy/mwdust.

[18] See http://argonaut.skymaps.info/query.
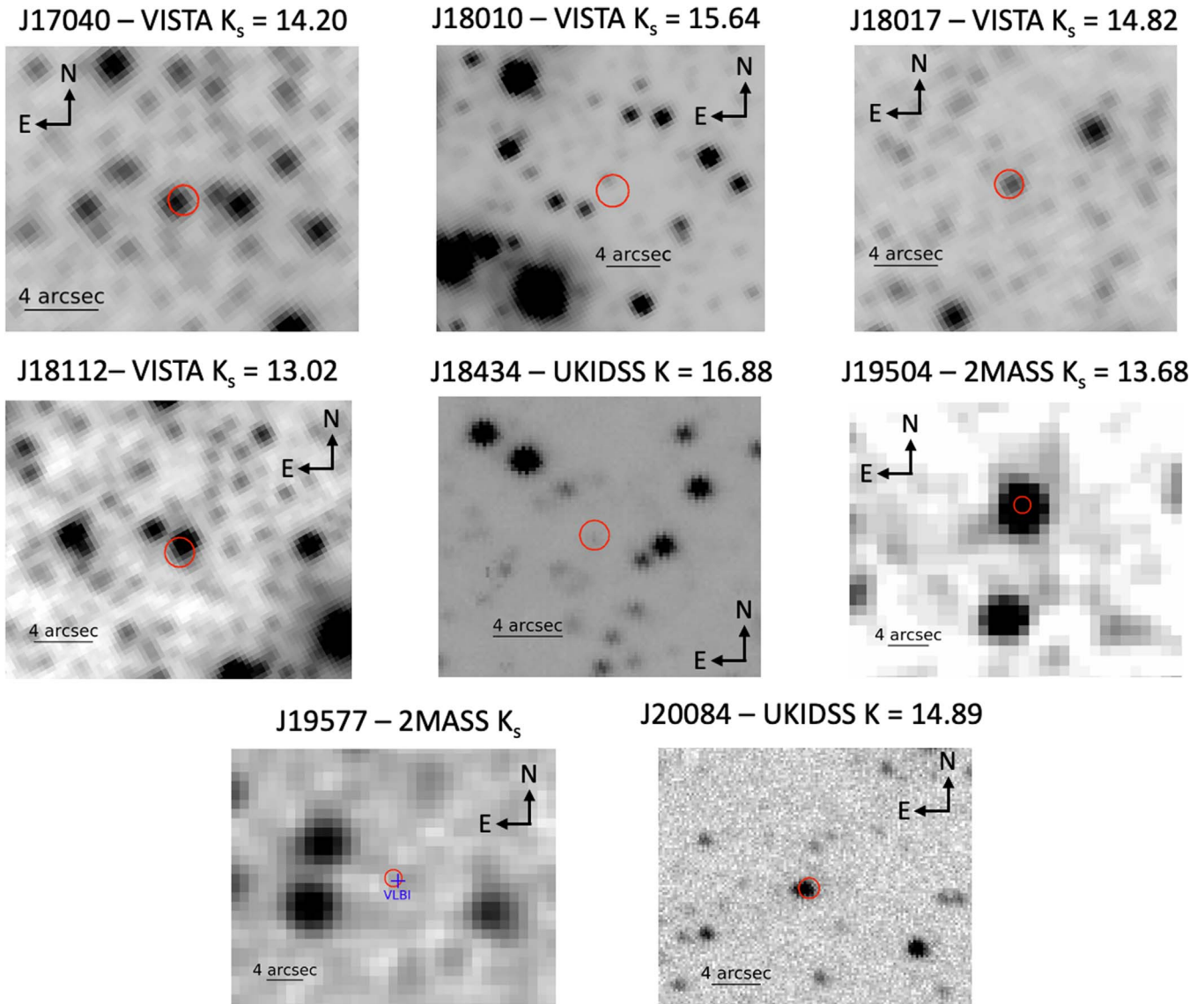[19] See http://argonaut.skymaps.info/usage.

Figure 3. K- or K_s-band images from the VISTA VVV, 2MASS, and UKIDSS surveys for the eight IGR sources with candidate Chandra counterparts. The red circles indicate the Chandra positions (90% confidence). For J19577, there is no 2MASS source consistent with the Chandra position, but there is a VLBI radio source (marked with a blue cross) in the Chandra error circle. Although J19504 appears to be a single source at 2MASS resolution, the PanSTARRS image in Figure 4 shows that it is blended.

absolute magnitude. Although the $T_{\rm eff}$ temperatures from the optical are not formally consistent with the near-IR, the measurements are still consistent with emission from an accretion disk, and the different temperatures may be caused by source variability. In addition, for J18434, $T_{\rm eff} > 7900$ K while $T_{\rm type}$ is constrained to be lower. Since the Gaia and near-IR measurements are made at different times, the likely interpretation is that J18434 also has emission from a variable accretion disk. A comparison of the VISTA and PanSTARRS magnitudes provides additional evidence that J18434 is variable in the optical and near-IR (Table 7). The evidence for Hα emission lines for J17040 and J18434 from the VPHAS + survey presented in Section 4 is consistent with emission from an accretion disk for these two sources.

Given the presence of hard X-ray emission, finding evidence for an accretion disk is expected. The presence of accretion, the evidence for late-type companions, and the very hard values of

the X-ray power-law index suggests a possible magnetic CV nature. For J17040, $\Gamma = 0.2 \pm 0.4$, which indicates that a magnetic CV nature is very likely. The power-law photon index is not as well constrained for J18017 ($\Gamma = 0.0^{+1.7}_{-1.3}$), but the source may also be a magnetic CV. At $\Gamma = 0.7 \pm 0.3$, J18434 is somewhat softer than J17040, but we still consider it to be a strong magnetic CV candidate.

6.2. Other Galactic Sources

J18112 and J20084 both have large Gaia-measured proper motions and are Galactic, but the source distances are not known. Both have hard spectra with $\Gamma = 0.9^{+0.7}_{-0.5}$ for J18112 and $0.1^{+0.4}_{-0.2}$ for J20084, suggesting that they may be magnetic CVs or HMXBs.

In the direction of J18112 ($l = 4.78°$, $b = -3.83°$, which is in the Galactic bulge), $E(B - V)$ increases from 0.14 at a distance
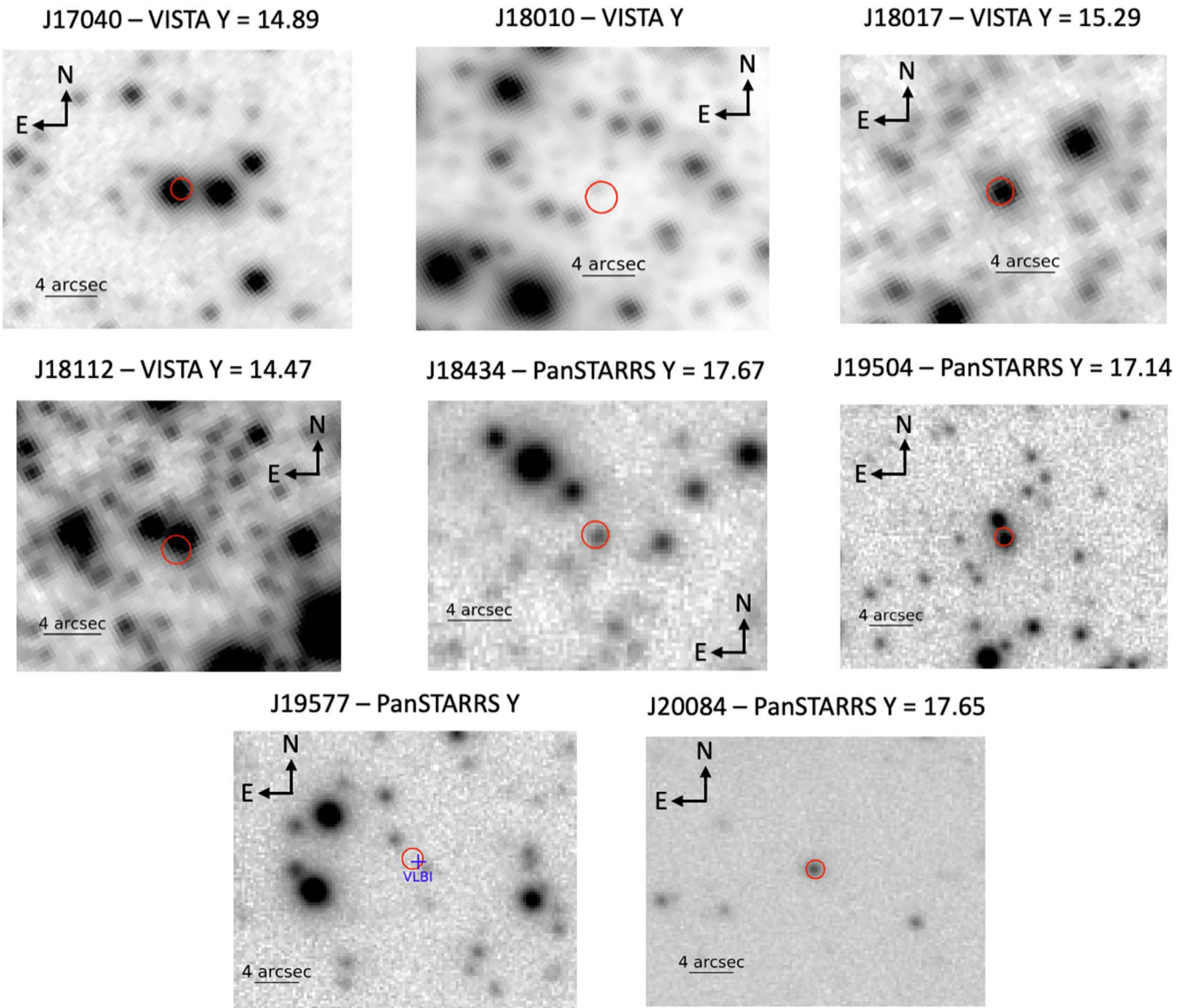
Figure 4. *Y*-band images from the VISTA VVV and PanSTARRS surveys for the eight IGR sources with candidate Chandra counterparts. The red circles indicate the Chandra positions (90% confidence). For J18010, although the near-IR counterpart is marginally visible, no *Y*-band magnitude is given in the VISTA VVV DR2 database.

(*d*) of 500 pc and reaches a maximum of 0.68 at $d = 4$ kpc (Bovy et al. 2016). At 500 pc and using the near-IR magnitudes in Table 7, $J–H–(A_J–A_H) = 0.615$, corresponding to $T_{eff} = 3660$ K, which is the temperature for an early M-type star. The absolute magnitude at 500 pc would be $M_J = 5.34$, corresponding to a late K-type main-sequence star. It is clear that the nearby distance scenario strongly disfavors the HMXB possibility. For distances >4 kpc, $J–H–(A_J–A_H) = 0.463 \pm 0.011$, corresponding to $T_{eff} = 4830–5100$ K (K2V-K3V). The absolute magnitude is $M_J < 0.39$ for $d > 4$ kpc. While the absolute magnitude at large distances allows for the presence of a high-mass companion star, the low temperature derived from the colors is inconsistent with this scenario. Thus, we conclude that a magnetic CV with a low-mass star is strongly favored. The brightness in the near-IR may indicate that the companion is an evolved giant star. However, there also may be a component of the emission from an accretion

disk based on the fact that J18112 is variable in the *Y* band (Table 7).

J20084 is essentially in the middle of the Galactic plane ($b = -0.23°$), and it has relatively high extinction. Using Green et al. (2019), we find $E(B − V) > 1.5$ if the distance is >1.8 kpc and $E(B − V) > 2.0$ if $d > 4.5$ kpc. Given the near-IR magnitudes (Table 7), $J–H–(A_J–A_H)$ is <0.30 at the lower distance and <0.16 for larger distances. These colors correspond to temperature limits of $T_{eff} > 5900$ K and >6700 K. Without a distance, M_J is highly uncertain. At a distance of 4.5 kpc and $A_J = 1.6$, $M_J = 1.2$, which would indicate an early-A spectral type if the stellar component dominates the near-IR emission. However, the distance could be larger, which would make the spectral type even earlier. Thus, we cannot rule out the possibility that J20084 is an HMXB.

Table 8
Galactic Sources with Distances

Parameter	J17040	J18017	J18434
L_x[a]	$(7.9 \pm 0.8) \times 10^{32}$	$(2.1 \pm 0.4) \times 10^{32}$	$(4.2^{+3.4}_{-2.6}) \times 10^{33}$
$E(B-V)$	$0.237^{+0.010}_{-0.012}$	$0.326^{+0.005}_{-0.016}$	$0.75^{+0.09}_{-0.17}$
A_V	$0.73^{+0.03}_{-0.04}$	$1.01^{+0.02}_{-0.05}$	$2.3^{+0.3}_{-0.5}$
		Near-IR analysis	
A_J	$0.190^{+0.008}_{-0.010}$	$0.262^{+0.005}_{-0.013}$	$0.60^{+0.08}_{-0.13}$
A_J–A_H	$0.066^{+0.003}_{-0.004}$	$0.091^{+0.002}_{-0.005}$	$0.21^{+0.03}_{-0.05}$
J–H–(A_J–A_H)	$0.062^{+0.008}_{-0.007}$	$-0.028^{+0.017}_{-0.016}$	0.64 ± 0.27
$T_{\rm eff}$ (K)	7680 ± 90	9600 ± 800	2200–5300
M_J	4.58 ± 0.11	3.75 ± 0.18	$5.9^{+0.9}_{-0.7}$
Limit on type[b]	K2V or later	G2V or later	K5V or later
$T_{\rm type}$ (K)	<5100	<5770	<4400
		Gaia analysis	
A_G	0.66 ± 0.03	$0.910^{+0.014}_{-0.045}$	$2.1^{+0.3}_{-0.5}$
A_{BP}–A_{RP}	0.37 ± 0.02	$0.516^{+0.008}_{-0.026}$	$1.17^{+0.15}_{-0.26}$
BP–RP–(A_{BP}–A_{RP})	0.79 ± 0.03	$-0.14^{+0.04}_{-0.03}$	$-0.05^{+0.27}_{-0.16}$
$T_{\rm eff}$ (K)	5880 ± 110	>11,000	>7900
M_G	5.79 ± 0.11	3.81 ± 0.18	$3.8^{+1.0}_{-0.8}$
Limit on type	K1V or later	F7.5V or later	F3V or later
$T_{\rm type}$ (K)	<5170	<6200	<6750

Notes.

[a] 2–10 keV luminosity in erg per second with 68% confidence errors.

[b] Spectral type if the J-band luminosity is dominated by emission from a star. If there is another contribution (from an accretion disk, for example), then any stellar component in the system would have a later spectral type.

6.3. Sources with Likely AGN Classifications

The evidence that J19504 is an AGN is primarily based on the fact that its Wide-field Infrared Survey Explorer (WISE) colors place it in the AGN region. Although it is marked as an extended source in PanSTARRS (Table 7), it is unclear whether it is truly extended or if the nearby and partially blended star (Figure 4) is the reason it is flagged as extended in the PanSTARRS processing. The Gaia measurements give a negative parallax and a proper motion consistent with zero (Table 6), which is consistent with but does not prove the AGN hypothesis. J19504 is also an outlier in it X-ray spectral parameters with a softer power-law slope ($\Gamma = 1.8 \pm 0.3$) and possible evidence for absorption greater than the Galactic value (Table 5). We conclude that IGR J19504+3318 is very likely to be an AGN, but more proof is needed.

For J19577, even though the flux of the Chandra counterpart allows for the possibility that it is unrelated to the INTEGRAL source, the fact that the source is actually more unusual in being a 295 mJy radio source increases the likelihood that it is related to IGR J19577+3339. The radio source does not have a redshift. We conclude that IGR J19577+3339 is likely to be an AGN.

6.4. Unclassified Sources

While three sources remain unclassified (J18010, J18013, and J12529), this study has provided useful information. For J18010, there is a candidate Chandra counterpart with a relatively hard spectrum that extrapolates to a flux in the INTEGRAL bandpass that is consistent with the flux measured by INTEGRAL (Figure 2). In addition, the Chandra position is consistent with an optical/near-IR source detected by Gaia (although it is too faint for a distance or proper motion

measurement) and VISTA. The K_s-band magnitude is 15.640 ± 0.095, which is bright enough to obtain a near-IR spectrum, which would greatly help in the classification of this source. We also note that the source is <4° from the center of the Galaxy, which increases the probability that it is Galactic.

Neither J18013 nor J12529 have likely Chandra counterparts. The flux upper limits are low enough compared to the flux measured by INTEGRAL that the source is likely to be variable or transient. However, since the Chandra and INTEGRAL bands do not overlap, we cannot rule out the possibility that Chandra does not detect the source due to a high column density.

7. Summary and Conclusions

The larger context for this work is the INTEGRAL Galactic plane surveys, which are providing new information about hard X-ray Galactic populations. Table 9 provides a summary of the results obtained using the 10 Chandra observations. In five cases, the Chandra localization identifies a Gaia source with a distance or high proper motion measurement, indicating that the sources are Galactic. They all have hard X-ray spectra, suggesting that they are either magnetic CVs or HMXBs. For the three sources with distance measurements (IGR J17040-4305, IGR J18017-3542, and IGR J18434-0508), we argue that the magnetic CV classification is the most likely one. For the other two Galactic sources, IGR J18112-2641 is also more likely to be a CV than an HMXB based on analysis of the near-IR magnitudes and the fact that the source shows variability by a magnitude in the Y band. IGR J20084+3221 could be a CV or an HMXB. IGR J19504+3318 and IGR J19577+3339 are candidate AGN. With the exception of J19577, the sources are bright enough for optical or near-IR spectroscopy, which will provide definitive classifications.

Table 9
Summary of Results

IGR Name	Chandra Counterpart or 2–10 keV flux limit	Galactic or Extragalactic	Source Type	Evidence
J12529-6351[a]	$<1 \times 10^{-13}$	…	…	…
J17040-4305	CXOU J170404.9-430537	Galactic	magnetic CV?	Gaia distance (0.937 ± 0.046 kpc)
J18010-3045	CXOU J180100.6-303958?	?	?	?
J18013-3222[a]	$<1 \times 10^{-13}$	…	…	…
J18017-3542	CXOU J180112.5-353912	Galactic	magnetic CV?	Gaia distance (1.58 ± 0.13 kpc)
J18112-2641	CXOU J181058.4-264115	Galactic	magnetic CV?	Gaia proper motion; variability in Y
J18434-0508	CXOU J184311.4-050545	Galactic	magnetic CV?	Gaia distance ($3.0^{+1.2}_{-0.9}$ kpc)
J19504+3318	CXOU J195019.7+331416	Extragalactic?	AGN?	WISE colors
J19577+3339	CXOU J195740.5+333828	Extragalactic?	AGN?	Bright radio source
J20084+3221	CXOU J200844.1+321818	Galactic	magnetic CV? or HMXB?	Gaia proper motion

Note.
[a] The Chandra limit indicates that the IGR source is transient, highly variable, or highly absorbed.

ORCID iDs

John A. Tomsick https://orcid.org/0000-0001-5506-9855
Jeremy Hare https://orcid.org/0000-0002-8548-482X
Roman Krivonos https://orcid.org/0000-0003-2737-5673
Arash Bodaghee https://orcid.org/0000-0002-7315-3732
Sylvain Chaty https://orcid.org/0000-0002-5769-8601
Maïca Clavel https://orcid.org/0000-0003-0724-2742
Francesca M. Fornasini https://orcid.org/0000-0002-9286-9963
Jerome Rodriguez https://orcid.org/0000-0002-4151-4468
Aarran W. Shaw https://orcid.org/0000-0002-8808-520X

References

Arnaud, K. A. 1996, in ASP Conf. Ser. 101, Astronomical Data Analysis Software and Systems V, ed. G. H. Jacoby & J. Barnes (San Francisco, CA: ASP), 17
Bailer-Jones, C. A. L., Rybizki, J., Fouesneau, M., Demleitner, M., & Andrae, R. 2021, AJ, 161, 147
Bird, A. J., Bazzano, A., Malizia, A., et al. 2016, ApJS, 223, 15
Bovy, J., Rix, H.-W., Green, G. M., Schlafly, E. F., & Finkbeiner, D. P. 2016, ApJ, 818, 130
Chambers, K. C., Magnier, E. A., Metcalfe, N., et al. 2016, arXiv:1612.05560
Cutri, R. M., Skrutskie, M. F., van Dyk, S., et al. 2003, 2MASS All-Sky Catalog of Point Sources yCAT, II/246
Cutri, R. M., Wright, E. L., Conrow, T., et al. 2021, AllWISE Data Release yCAT, II/328
Davis, J. E. 2001, ApJ, 562, 575
Drew, J. E., Gonzales-Solares, E., Greimel, R., et al. 2016, The VST Photometric Halpha Survey of the Southern Galactic Plane and Bulge (VPHAS+), Second VPHAS Data Release (DR2) yCAT, II/341
Drew, J. E., Gonzalez-Solares, E., Greimel, R., et al. 2014, MNRAS, 440, 2036
Fitzpatrick, E. L. 1999, PASP, 111, 63
Fornasini, F. M., Tomsick, J. A., Bodaghee, A., et al. 2014, ApJ, 796, 105
Fruscione, A., McDowell, J. C., Allen, G. E., et al. 2006, Proc. SPIE, 6270, 62701V

Gaia Collaboration 2020, yCAT, I/350

Garmire, G. P., Bautz, M. W., Ford, P. G., Nousek, J. A., & Ricker, G. R. 2003, Proc. SPIE, 4851, 28

Green, G. M., Schlafly, E., Zucker, C., Speagle, J. S., & Finkbeiner, D. 2019, ApJ, 887, 93

Hare, J., Halpern, J. P., Clavel, M., et al. 2019, ApJ, 878, 15

Hare, J., Halpern, J. P., Tomsick, J. A., et al. 2021, ApJ, in press (arXiv:2104.10503)

HI4PI Collaboration, Ben Bekhti, N., Flöer, L., et al. 2016, A&A, 594, A116

Kaastra, J. S. 2017, A&A, 605, A51

Kim, M., Kim, D.-W., Wilkes, B. J., et al. 2007, ApJS, 169, 401

Krivonos, R., Revnivtsev, M., Lutovinov, A., et al. 2007, A&A, 475, 775

Krivonos, R., Tsygankov, S., Lutovinov, A., et al. 2012, A&A, 545, A27

Krivonos, R. A., Tsygankov, S. S., Mereminskiy, I. A., et al. 2017, MNRAS, 470, 512

Lucas, P. W., Hoare, M. G., Longmore, A., et al. 2008, MNRAS, 391, 136

Mateos, S., Alonso-Herrero, A., Carrera, F. J., et al. 2012, MNRAS, 426, 3271

Matt, G., & Guainazzi, M. 2003, MNRAS, 341, L13

McMahon, R. G., Banerji, M., Gonzalez, E., et al. 2013, Msngr, 154, 35

Minniti, D., Lucas, P. & VVV Team 2017, VISTA Variables in the Via Lactea Survey DR2 - Gaia Collaboration 2020: Gaia Early Data Release 3 (EDR3) yCAT, II/348

Minniti, D., Lucas, P. W., Emerson, J. P., et al. 2010, NewA, 15, 433

Negueruela, I., Smith, D. M., Reig, P., Chaty, S., & Torrejón, J. M. 2006, in ESA SP-604: The X-ray Universe 2005, ed. A. Wilson (Noordwijk: ESA), 165

Pecaut, M. J., & Mamajek, E. E. 2013, ApJS, 208, 9

Romano, P., Krimm, H. A., Palmer, D. M., et al. 2014, A&A, 562, A2

Secrest, N. J., Dudik, R. P., Dorland, B. N., et al. 2015, ApJS, 221, 12

Sguera, V., Bazzano, A., Bird, A. J., et al. 2006, ApJ, 646, 452

Sugizaki, M., Mitsuda, K., Kaneda, H., et al. 2001, ApJS, 134, 77

Tomsick, J. A., Bodaghee, A., Chaty, S., et al. 2012, ApJ, 754, 145

Tomsick, J. A., Bodaghee, A., Chaty, S., et al. 2020, ApJ, 889, 53

Tomsick, J. A., Krivonos, R., Wang, Q., et al. 2016, ApJ, 816, 38

Verner, D. A., Ferland, G. J., Korista, K. T., & Yakovlev, D. G. 1996, ApJ, 465, 487

Walter, R., Zurita Heras, J., Bassani, L., et al. 2006, A&A, 453, 133

Wilms, J., Allen, A., & McCray, R. 2000, ApJ, 542, 914

Winkler, C., Courvoisier, T. J.-L., Di Cocco, G., et al. 2003, A&A, 411, L1

X-ray spectral and flux variability of the microquasar GRS 1758−258 on timescales from weeks to years

Maria Hirsch[1], Katja Pottschmidt[2,3], David M. Smith[4], Arash Bodaghee[5], Marion Cadolle Bel[6], Victoria Grinberg[7], Natalie Hell[8], Felicia Krauß[9,10], Ingo Kreykenbohm[1], Anne Lohfink[11], Michael A. Nowak[12], Bárbara H. Rodrigues[13], Roberto Soria[14,15], John A. Tomsick[16], and Jörn Wilms[1]

[1] Dr. Karl Remeis-Observatory & ECAP, Universität Erlangen-Nürnberg, Sternwartstr. 7, 96049 Bamberg, Germany
    e-mail: maria.hirsch@fau.de
[2] CRESST and NASA Goddard Space Flight Center, Greenbelt, MD 20771, USA
[3] Department of Physics and Center for Space Science and Technology, University of Maryland, Baltimore, MD 21250, USA
[4] Department of Physics and Santa Cruz Institute for Particle Physics, University of California, Santa Cruz, CA 95064, USA
[5] Department of Chemistry, Physics and Astronomy, Georgia College and State University, Milledgeville, GA 31061, USA
[6] Max Planck Computing and Data Facility, Gießenbachstr. 2, 85748 Garching, Germany
[7] Institut für Astronomie und Astrophysik, Universität Tübingen, Sand 1, 72076 Tübingen, Germany
[8] Lawrence Livermore National Laboratory, 7000 East Ave., Livermore, CA 94550, USA
[9] GRAPPA & Anton Pannekoek Institute for Astronomy, University of Amsterdam, Science Park 904, 1098 Amsterdam, The Netherlands
[10] Department of Astronomy and Astrophysics, Pennsylvania State University, University Park, PA 16802, USA
[11] Department of Physics, Montana State University, Bozeman, MT 59717-3840, USA
[12] Department of Physics, Washington University, CB 1058, One Brookings Drive, St. Louis, MO 63130-4899, USA
[13] Instituto Nacional de Pesquisas Espaciais, Avenida dos Astronautas, 1.758 São José dos Campos, Brazil
[14] National Astronomical Observatories, Chinese Academy of Sciences, Beijing 100012, PR China
[15] Sydney Institute for Astronomy, School of Physics A28, The University of Sydney, Sydney, NSW 2006, Australia
[16] Space Sciences Laboratory, 7 Gauss Way, University of California, Berkeley, CA 94720-7450, USA

ABSTRACT

We present the spectral and timing evolution of the persistent black hole X-ray binary GRS 1758−258 based on almost 12 years of observations using the *Rossi* X-ray Timing Explorer Proportional Counter Array. While the source was predominantly found in the hard state during this time, it entered the thermally dominated soft state seven times. In the soft state GRS 1758−258 shows a strong decline in flux above 3 keV rather than the pivoting flux around 10 keV more commonly shown by black hole transients. In its 3–20 keV hardness intensity diagram, GRS 1758−258 shows a hysteresis of hard and soft state fluxes typical for transient sources in outburst. The RXTE-PCA and RXTE-ASM long-term light curves do not show any orbital modulations in the range of 2–30 d. However, in the dynamic power spectra significant peaks drift between 18.47 and 18.04 d for the PCA data, while less significant signatures between 19 d and 20 d are seen for the ASM data as well as for the *Swift*/BAT data. We discuss different models for the hysteresis behavior during state transitions as well as possibilities for the origin of the long term variation in the context of a warped accretion disk.

Key words. X-rays: binaries – X-rays: individuals: GRS 1758−258

1. Introduction

GRS 1758−258 is a black hole binary discovered in 1990 during observations of the Galactic Center region by the Granat satellite (Mandrou 1990; Syunyaev et al. 1991, see Heindl & Smith 2002 for the determination of the source's position). As one of only three persistent, mostly hard state, black hole binaries in our Galaxy and the Magellanic Clouds (GRS 1758−258, 1E 1740.7−2942, and Cyg X-1)[1], GRS 1758−258 has since been observed in various energy ranges (e.g., Rodriguez et al. 1992; Cadolle Bel et al. 2006; Pottschmidt et al. 2008; Muñoz-Arjonilla et al. 2010; Soria et al. 2011; Luque-Escamilla et al. 2014, and references therein). As radio observations show a double-lobed

counterpart (Rodriguez et al. 1992) that shows similarities to winged radio galaxies (Martí et al. 2017), GRS 1758−258 is considered a microquasar.

The *Rossi* X-ray Timing Explorer (RXTE; Bradt et al. 1993) monitored GRS 1758−258 from 1996 to 2007 (see next section for a detailed description of these observations). Based on this program Smith et al. (2001) reported the transition to a soft state in 2001 during which the 3–25 keV flux declined by more than an order of magnitude. This episode lasted around a year. Using *XMM-Newton* observations Soria et al. (2011) showed that this transition still followed the canonical evolution through states but with the soft state showing increased flux only below ∼3 keV. The occurrence of a less extended soft state in 2003 was reported by Pottschmidt et al. (2006).

Using the 2.5–25 keV RXTE PCA monitoring light curve of GRS 1758−258 from 1997 to 2002, Smith et al. (2002a)

---

[1] Other persistent black hole binaries are the Galactic source 4U 1957+11, as well as LMC X-1 and LMC X-3, which are always or predominantly found in the soft state.

found a periodic signal of 18.45 ± 0.10 d. If this signal was due to a binary orbit and the companion is not a high-mass star (Martí et al. 1998), the companion would have to be a K giant star filling its Roche lobe (Rothstein et al. 2002). However, the identity of the companion star in the system was ambiguous for a long time (Smith 2010). After astrometric studies already hinted at the system being an intermediate-mass X-ray binary (Muñoz-Arjonilla et al. 2010; Luque-Escamilla et al. 2014), recent spectroscopy of the companion shows it is likely an A-type main sequence star (Martí et al. 2016). If true, the accretion process would still be Roche lobe overflow, which implies an orbital period in the range of 0.5–1.0 d (Martí et al. 2016), and, thus, significantly shorter than the signal at 18.45 ± 0.10 d found by Smith et al. (2002a).

In order to better understand this puzzling source we took a closer look at the RXTE monitoring obervations of GRS 1758−258 for the first time spanning the full time range from 1996 to 2007. The observations and the Proportional Counter Array (PCA; Jahoda et al. 2006) data reduction are described in Sect. 2. In Sect. 3, we present the spectral analysis of the RXTE-PCA data of GRS 1758−258, starting with a description of how Galactic ridge emission was taken into account in Sect. 3.1 before defining the source model and overall spectral modeling procedure in Sect. 3.2, and adding the hardness intensity diagram (HID) of the dataset as an additional diagnostic in Sect. 3.3. The evolution of the spectral parameters as well as the HID show seven soft states during this time. In Sect. 4, we report on the timing analysis of the long-term light curve of GRS 1758−258, presenting periodograms of the raw as well as of the detrended RXTE-PCA light curves in Sects. 4.1 and 4.2. Finally, we also looked at periodograms of RXTE's All Sky Monitor (ASM; Levine et al. 1996) light curve of GRS 1758−258 in Sect. 4.3. We find no coherent periodic signal that could be identified as an orbital period in the range of 2 d to 30 d, however, quasi-periodic oscillations are apparent in the period range around 18–20 d. In Sect. 5, we summarize and discuss the results and present our conclusions.

2. Observations and data reduction

RXTE monitored GRS 1758−258 with 1.0–1.5 ks long pointed snapshots starting in 1996 (Smith et al. 2001, 2002a). The exposures were performed in monthly intervals in 1996, weekly from 1997 through 2000, and twice a week from 2001 March to 2007 October. Each year there is a gap from November to January when the Sun was too close to the Galactic Center, that is the approximate pointing direction to GRS 1758−258.

The PCA consisted of five Proportional Counter Units (PCUs), each with a sensitivity between 2 keV and 90 keV with a field of view of ~1°. The Proportional Counter Unit 2 (PCU2) was the best calibrated one (Jahoda et al. 2006). Since the top layer had the highest signal-to-noise ratio (S/N), we only used data from this layer of PCU2. We reduced the data with our standard analysis pipelines (Wilms et al. 1999, 2006) applying the NASA HEASARC software package HEASOFT, version 6.8 for the RXTE spectra[2]. Data up to 15 min after passage through the South Atlantic Anomaly (SAA) were excluded (Fürst et al. 2009). We also required an electron ratio below 0.5 in order to

exclude time periods of high background. We obtained observed spectra as well as instrumental background spectra using the "faint source" background model.

Because of its location only 0°66 away from the very bright X-ray binary GX 5−1, GRS 1758−258 was a difficult source to observe with the collimated detectors onboard RXTE. The monitoring could therefore only be realized using offset pointings away from GX 5−1 (Smith et al. 2001, 2002a), that is using the triangular response of PCA's collimator to reduce the influence of GX 5−1. Response matrices were built taking the effect of the offset pointings into account.

The spectral analysis was performed using data taken in standard2f mode, which provides 129 energy channels. The spectra were rebinned to a minimum S/N of 5. We used data in the energy range of 3–20 keV. All spectral fitting was done using the Interactive Spectral Interpretation System (ISIS; Houck & Denicola 2000; Houck 2002; Noble & Nowak 2008).

The PCA timing analysis was performed starting from the 3–20 keV fluxes of GRS 1758−258 determined for each monitoring observation in the spectral analysis. The ASM timing analysis was performed using the 3–5 keV light curve[3] available in NASA's HEASARC database in a daily binning for the same time range as the PCA light curve. Empty bins were removed. The *Neil Gehrels Swift* Observatory BAT 15–50 keV daily light curve was obtained from the BAT Transient Monitor (Krimm et al. 2013)[4]. Both the ASM and the BAT light curve do not require further processing before the analysis. Due to the location of GRS 1758−258 near the GX 5−1, MAXI (Matsuoka et al. 2009) cannot observe the source.

3. Spectral evolution

3.1. Galactic ridge emission

Because GRS 1758−258 is faint and located close to the Galactic center in the Galactic Plane, all RXTE spectra of the source also contain a strong, diffuse background component caused by the Galactic ridge emission in the X-rays. This emission has long been known to exist (Worrall et al. 1982; Warwick et al. 1985; Koyama et al. 1986); its origin, however, is still under discussion (Ebisawa et al. 2008; Warwick 2014; Nobukawa et al. 2016, and references therein). To distinguish between source counts and Galactic ridge counts, background observations totalling 13 ks, 1°5 offset from GRS 1758−258, were performed by RXTE in 1999[5]. We were able to model this local Galactic ridge Emission with two bremsstrahlung components and an iron line complex (see Fig. 1). As RXTE cannot resolve the individual iron line components, the position of the three lines was fixed to 6.4 keV, 6.67 keV, and 7.0 keV, respectively, with equivalent widths that scale as 85:458:129 according to CCD *Suzaku* observations of the Galactic ridge (Ebisawa et al. 2007). The normalization of the whole complex was left free to vary in the fit. The fit parameters are summarized in Table 1. We assume that there is no local variation of the Galactic ridge emission, and then, keeping all spectral parameters fixed at their best-fit values, added this model to the spectral model of GRS 1758−258. Figure 2 illustrates the contribution of the ridge emission to the measured spectrum.
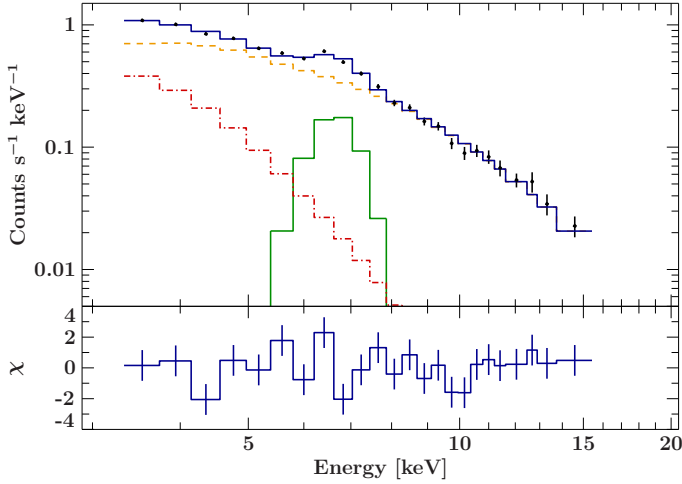
Fig. 1. Spectrum of the Galactic ridge emission as seen by RXTE. The data were fitted with two bremsstrahlung components (1: dashed line, 2: dash-dotted line) and an iron line complex as described in Ebisawa et al. (2007).
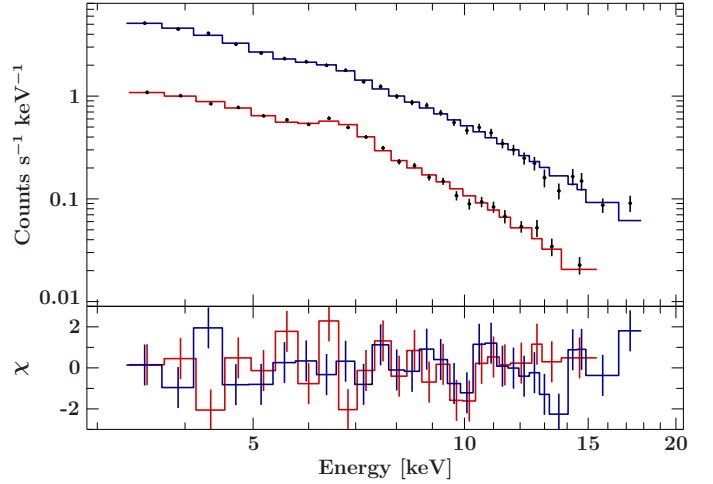
Fig. 2. RXTE-PCA spectrum of the total emission at the source position from the 2003 April observation. The total spectrum is modeled (blue histogram) as the sum of the source contribution and the Galactic ridge emission. The contribution of the Galactic ridge emission alone is also shown (red histogram).

Table 1. Galactic ridge model parameters.

$a_{\mathrm{brems,1}}$	0.011 ± 0.003	
kT_1	8^{+3}_{-1}	keV
$a_{\mathrm{brems,2}}$	$0.05^{+0.03}_{-0.01}$	
kT_2	$1.2^{+0.2}_{-0.1}$	keV
F_1	$\left(2.6^{+0.3}_{-0.4}\right) \times 10^{-5}$	ph s^{-1} cm^{-2}
σ_1	0.05	keV
E_1	6.4	keV
F_2	1.4×10^{-4}	ph s^{-1} cm^{-2}
σ_2	0.05	keV
E_2	6.67	keV
F_3	4×10^{-5}	ph s^{-1} cm^{-2}
σ_3	0.05	keV
E_3	7.0	keV

Notes. $a_{\mathrm{brems,1,2}}$: normalization of the bremsstrahlung components; $kT_{1,2}$: plasma temperature; $F_{1,2,3}$ is the total flux under a Gaussian centered at $E_{1,2,3}$ with a width $\sigma_{1,2,3}$. Values without uncertainties were kept fixed during the fit to the spectra from the background regions. Uncertainties are at the 90% confidence level.

3.2. Spectral modelling

Once the Galactic ridge background has been accounted for (see Sect. 3.1), all spectra were modeled using an empirical model consisting of an absorbed powerlaw (phabs × powerlaw). No high energy cutoff was needed as the cutoff energy is well above 20 keV (Pottschmidt et al. 2006), the upper limit of the energy range considered here. The column density due to interstellar absorption in the direction of GRS 1758−258 was kept fixed to the canonical value of $N_{\mathrm{H}} = 1.5 \times 10^{22}$ cm^{-2} (Mereghetti et al. 1997) using the abundances of Anders & Grevesse (1989). Although the Galactic ridge spectral component already contains an iron line complex, the residuals show that this component is insufficient to explain the data in the Fe Kα band. There are three potential explanations for such a deviation: the Galactic ridge emission could be spatially variable, there could be an intrinsic Fe Kα emission or a combination of both effects.

In order to characterize the deviation of the observed line from the assumed (non-spatially varying) ridge component, we add a line at a fixed energy of 6.4 keV to the model. We initially fixed the width of this line at 1 eV, well below the resolution of the PCA, and then fitted the flux of the line. In these fits a possible weak correlation between iron line flux and total source flux with a Spearman rank coefficient of 0.40 can be seen. A rough check of 100 000 permutations of the iron line flux against the total source flux gives a mean rank coefficient of 7.9×10^{-5} with individual values ranging between −0.15 and 0.15. If true, this variability would indicate that part of the line would be source intrinsic. We note, however, that a narrow line at 6.4 keV with a flux similar to that found in these fits would have been visible in the *XMM-Newton* observations discussed by Soria et al. (2011), but was not seen. RXTE's spectral resolution is so low, however, the width of the additional Fe Kα is not well constrained: Re-fitting the RXTE spectra with the iron line width left as a free parameter results in an average line width of about 800 eV. Simulating *XMM-Newton* EPIC pn spectra for some of our best fit models with such a broad line smears out the iron line beyond recognition. For this reason we cannot claim that the *XMM-Newton* data formally rule out that some of the broad line flux originates in GRS 1758−258, although we consider this an astrophysically unlikely interpretation of the RXTE result.

Some softer spectra also require an additional disk blackbody for improving the fit. To estimate the significance of this improvement, we performed Monte Carlo simulations of the best fit model without the disk by creating a set of 1000 fake spectra for each observation. These synthetic spectra were then fitted with both models and the respective improvement in χ^2_{red} was calculated. We only accepted the disk component in our best fit model if the improvement in χ^2_{red} of the real dataset was above at least 99% of the fake spectra improvements. There are four occasions where a disk is detected at a very high temperature and low normalization. All four can be modeled with a higher normalization and lower temperature, with only slight worsening in the reduced χ^2. These outliers thus are likely to be reflecting fit degeneracies and are not considered to be source intrinsic.

Fig. 3. Example of an instrument background subtracted spectrum taken by RXTE on 2009 April 08, containing the absorbed powerlaw component (dash-dotted line), the disk (dashed line), and the iron line (green solid line). For clarity the constant Galactic ridge model part is not shown.

Figure 3 shows an example of an instrument background subtracted spectrum and best fit model containing all the components.

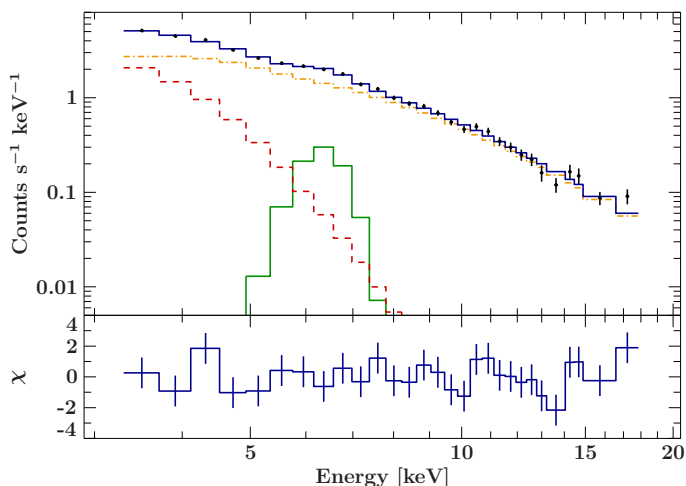To analyze the long term behavior of GRS 1758−258, for each spectrum, the source flux (i.e., with the Galactic ridge background subtracted but all other model components taken into account) was calculated integrating over the best fit model in the respective energy ranges for each observation. As apparent in Fig. 4, a change in flux is correlated with a change in the photon index: once the flux starts to decrease, the spectrum begins to soften. We classified as soft state all episodes that reach photon indices greater than two. The regions of interest were then defined to contain at least three data points before and after the peak, to fully catch the rise and decline. In some cases, this was not possible due to data gaps, which we do not want to cross for lack of information, for instance after the first soft state in 1999. Between 1997 and 2008, we found seven dim soft states, which are highlighted in Fig. 4. During the 2001 soft state, the source almost turned off completely with a remaining flux of only ~0.045 keV s^{-1} cm^{-2} in the 3–20 keV band. The blackbody disk emission appears only during these soft states where the low flux increases the uncertainties of the best fit parameters. Looking at the reduced χ^2 (see Fig. 4, bottom panel), we find the fits slightly overdetermined, both for the fits with the fixed (Fig. 4) and the free iron line width. A further reduction of free parameters, however, is not possible: the Galactic ridge background is added as a constant with no free parameters[6]. The iron line position is fixed, as is the absorption towards GRS 1758−258 ($N_H = 1.5 \times 10^{22}$ cm^{-2}, Mereghetti et al. 1997). The only free model parameters are the powerlaw normalization and photon index, the iron line flux, and the disk flux and temperature where a disk black body is needed. Furthermore, we did not add a systematic uncertainty to the data. We therefore conclude that we can not improve on the overdetermination of our fits.

---

[6] Variable ridge emission is in principle possible due to changes in roll angle and possible transient background sources, however, spectral modeling in which we kept the spectral shape of the ridge constant but let its flux vary does not lead to appreciable changes in the results presented in this paper compared to models where the ridge emission was kept fixed.

3.3. Hardness intensity diagram

As shown, for example, by Fender et al. (2004) or Belloni et al. (2005), it is typical for black hole transients to trace a q-shaped curve on their hardness intensity diagram (HID) during their outbursts. Pottschmidt et al. (2008) already found that GRS 1758−258 displays an unusual behavior in this respect: while persistent binaries usually occupy only a small area of the HID (see also Wilms et al. 2007), GRS 1758−258 shows a mixture of transient and persistent behavior. It moves anti-clockwise from the hard to the hard intermediate state, softens and then dims to the soft state, and finally hardens along the lower transitional branch back to the hard state. The 2001 extremely faint soft state directly follows an observational gap. Therefore, the transition from hard to soft state is not observed, leading to the atypical shape in the HID (Pottschmidt et al. 2008).

This behavior is confirmed here. Figure 5 shows the HID for the whole RXTE campaign. The soft states are highlighted using the same color scheme as in Fig. 4. It is obvious that GRS 1758−258 does not follow the usual q-shaped track but rather starts from the position of persistent sources on the upper right edge. Although the HID shows a clear hysteresis for hard and soft (absorbed) fluxes, there is no indication at all for a rise in the hard state from quiescence. No full return to the hard branch could be observed during the most extreme 2001 soft state: after the last soft state data point (MJD 52235.2961), there are no observations for almost two months. This mixed persistent/transient behavior of GRS 1758−258 was already observed by Smith et al. (2001), similar behavior has also been seen in 1E 1740.7−2942 (del Santo et al. 2005) and GX 339−4 (del Santo et al. 2008).

4. Time series analysis

For the time series analysis we used the complete flux light curve of GRS 1758−258, that is the sum of the flux band light curves shown in Fig. 4: as opposed to the count rate, flux values are independent of different detector responses to the respective spectral shape of GRS 1758−258. Due to many gaps and uneven spacing of the data points, we had to use the algorithm for generalized periodograms after Lomb (1976) and Scargle (1982).

4.1. Flux light curve and its periodogram

We now turn to the search for (quasi-)periodicities in the long-term light curve of the source, concentrating on the behavior of the 18.45 ± 0.10 d periodicity found by Smith et al. (2002a) in the 1997–2001 RXTE-monitoring. Applying the Lomb–Scargle algorithm to the whole unfiltered flux light curve led to a power spectrum without any prominent peaks, and neither does the power spectrum calculated for the 1997–2001 data contain significant peaks (Fig. 6). The large luminosity variations between hard and soft spectral states can decrease the significance of period measurements and therefore cause the lack of such peaks (Smith et al. 2002a). In a next step we therefore perform a period search on de-trended data under consideration of possible systematic effects.

4.2. Detrended flux light curve and its periodogram: a drifting 18 day period

Excluding all soft states from the time series analysis would lead to major gaps in the light curve. In order to avoid any influence of the very dim and soft states on our periodogram, we only used
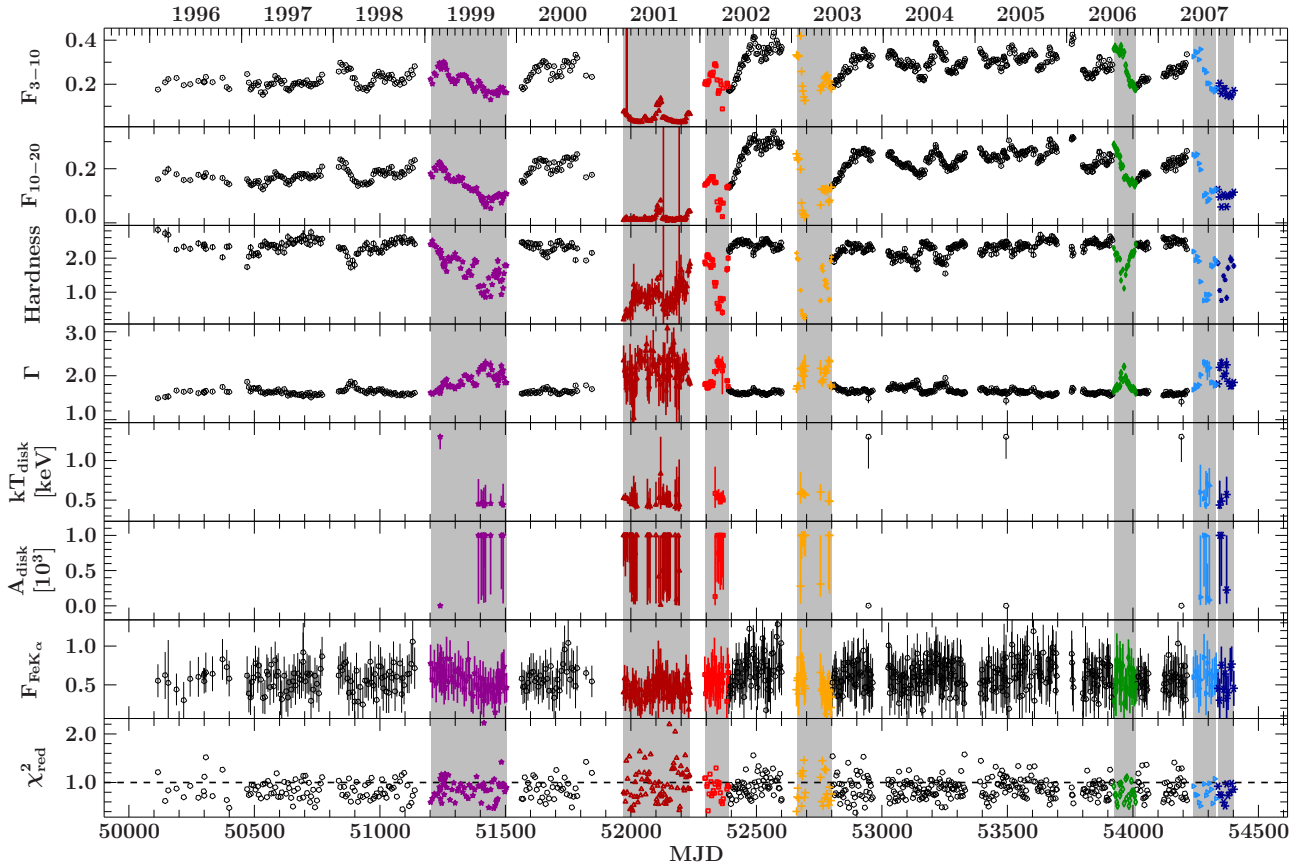
Fig. 4. Spectral parameters from RXTE monitoring observations of GRS1758−258: flux in keV s^{-1} cm^{-2} in the 3–10 keV and 10–20 keV bands, fitted to the spectra, spectral hardness (10–20 keV/3–5 keV) calculated with fluxes in keV s^{-1} cm^{-2}, photon index, temperature, and normalization of the disk component, total flux of the additional iron line in 10^{-3} ph s^{-1} cm^{-2} and the reduced χ^2. Soft states are highlighted for episodes reaching a photon index greater than 2.

data points with a photon index $\Gamma < 2$ (see Sect. 3). This step alone is not sufficient, however, to remove long term variations and consequently no signal is seen in these power spectra. To avoid lower significances of our measurements caused by large luminosity variations and to be able to compare our results to those of Smith et al. (2002a), a high pass filter was then applied to the data by subtracting a smoothed version of the light curve. The following analysis uses this long-term trend and the high frequency residuals.

To generate the smoothed light curve, for each data point we fitted a straight line to all data within the range of $n = 14$ d before and after. The subsequent analysis only used the high frequency residual, that is the difference between the data point and the value of the straight line to obtain a high pass-filtered light curve. This method was already applied by Smith et al. (2002a), who used a range of $n = 10$ d before and after the data point. We extended this range in order to get better statistics for the smoothing fit, although we emphasize that our results do not depend on the exact value of n chosen (Hirsch 2014). The smoothed long term trend and the residual flux light curve are shown in Fig. 7.

Using residual fluxes in the same time range as Smith et al. (2002a), that is 1997–2001, we are able to reproduce within the uncertainties the peak they found at 18.45 ± 0.10 d (Fig. 7): although we did not exclude the low energy flux where no modulations are expected, we find a peak at 18.475 ± 0.017 d[7].

When using the whole 11 years of data, however, this peak is shifted in period by 0.32 d (Fig. 8, left). Analyzing the data from 2002–2008, that is all data after the interval used by Smith et al. (2002a) and therefore statistically independent from their sample, this shift increases to 0.33 d (Fig. 8, right). This difference is reminiscent of changing superorbital modulations (see, e.g., Clarkson et al. 2003a,b). The figure also shows the maximum value of power spectra obtained when replacing the residual with Gaussian noise with the same mean and standard deviation. As discussed, for example, by Benlloch et al. (2001), these lines represent the "local significance" that the observed (quasi-) periodicity seen in the indicated 1 d broad period intervals is real. The Monte Carlo analysis automatically takes the trials factor into account. The power spectra therefore show significant peaks in the 18 d period band.

To study the evolution of the quasi periodic signal, we calculated a dynamic power spectrum (Fig. 9, see also Benlloch et al. 2001; Wilms et al. 2001): based on the 5 years interval of data originally used by Smith et al. (2002a), slices of the same length of 5 years were cut out of the light curve and analysed separately. Each time the starting time of the slice was shifted by 30 d, and each resulting power spectrum is shown as a color-coded line in Fig. 9. Note that the 83 individual slices are overlapping and thus not statistically independent. As expected, the first few lines of

---

[7] While Smith et al. (2002a) calculate their uncertainty using the FWHM of the peak in the PSD, we used 1000 sets of the long term

trend light curve plus Poisson-distributed random values for the respective light curve plus a sinusoid test signal at 16 d. The standard deviation of the distribution of the PSD peaks of this test signal was then taken as a measure for our period uncertainty.
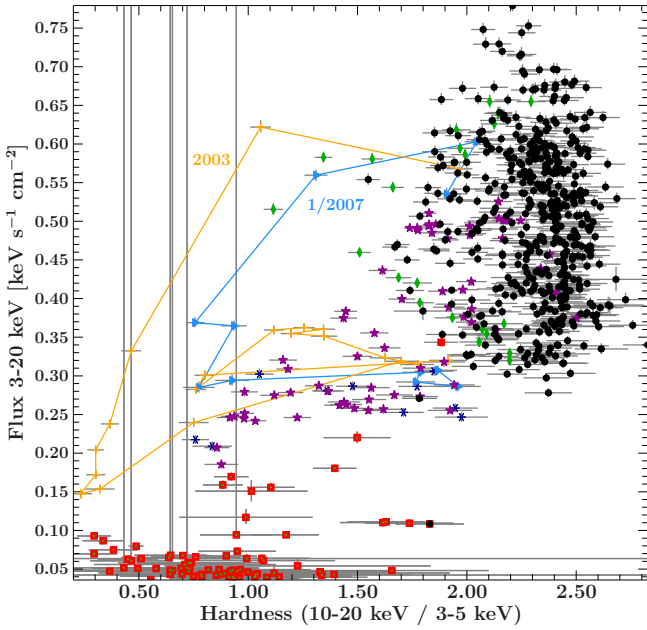
Fig. 5. Hardness intensity diagram (HID) from RXTE monitoring observations of GRS 1758−258 from 1997 until 2007. The seven dim soft states are highlighted as in Fig. 4. To show the "q"-shaped track of GRS 1758−258 in the HID, the data points of two soft state passages (2003 and 1/2007) are connected.
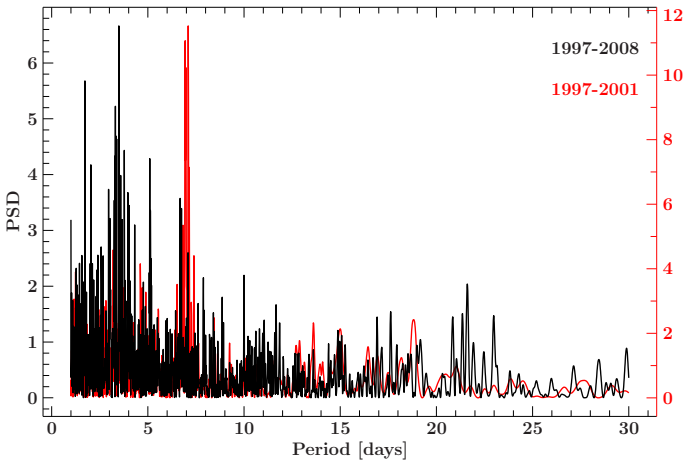
Fig. 6. Black: power spectrum of the full and unfiltered light curve, and red: power spectrum of the unfiltered 1997–2001 data already used by Smith et al. (2002a).

the dynamic periodogram show a peak at 18.475 ± 0.017 d. The maximum of this peak, however, is drifting with time, first to lower values to a minimum of 18.043 ± 0.005 d in 2003. Towards the end of the light curve, the period of the main peak is rising again. In addition, the period appears to fork into two peaks between 2000 and 2001. Figure 10 shows the modulation of the filtered light curve for the time range where the period in the dynamical power spectrum is stable (MJD 51769–53980).

Given the complexity of the data reduction, before we discuss the scientific implications of the peak we first discuss the significance of our measurements and explore how such a peak could be produced artificially.

We start by estimating the significance of the period. In order to do so we simulated 10 000 light curves consisting of a white noise component, that is Gaussian distributed random values

with the same standard deviation as that measured from the short term residuals obtained after detrending the original lightcurve. This approach therefore addresses both, the uncertainty of the individual flux measurements due to statistical effects as well as any excess noise that is due to intrinsic source variability. The residuals are consistent with Gaussian noise, such that more complex modeling, for example, using red noise residuals or applying a bootstrapping approach, is not necessary. For each simulated light curve, a dynamic power spectrum with 83 overlapping light curve slices was calculated in the same way as in Sect. 4.2. For each light curve slice, we then find the fraction of simulated white noise light curves that do not have their highest PSD peak in the range of the respective detected GRS 1758−258 period and its uncertainties. This fraction is a measure of the significance of the putative period of GRS 1758−258. We find significances for the drifting peak varying between 98.15% and 99.98%.

Although our high pass filter works well for detecting periodic signals in the data, it is not ideal. For example, the long term trend light curve, which is subtracted by the filter, still contains part of periodic signals in the range of 14–25 d. As the period found by Smith et al. (2002a) falls in this range, a closer look into the origin of this effect of the filter on the trend light curve is required.

To evaluate the range in which remnants of short-term periodic signals can be found in the long-term trend curve, we build an artificial light curve sampled at the same dates as those of the original light curve, containing Gaussian noise and a primary sinusoidal signal with a period in the range of 14–25 d. This light curve is then filtered to determine the long term trend. To test whether this trend still contains parts of the primary signal, we added an additional test signal at a different period, for example 12 d, filtered again and applied the Lomb–Scargle technique as in Sect. 4.2. The resulting periodogram shows a main peak at the period of the test signal and a second peak at the period of the primary sinusoidal period. Since the analysis is based on a noise light curve, the residual signal is not connected to the flux values in our GRS 1758−258 light curve. Neither changing the period of the test signal nor changing the length of the light curve section we use has any influence on this effect. Randomly selecting two thirds of the data points in the light curve lessens the effect, and at the same time also reduces the power seen in the test signal peak.

The distribution of time intervals between individual observations of GRS 1758−258, that is the time intervals between the data points in the GRS 1758−258 light curve, does not show an excess for intervals between 14 and 25 d. We can therefore exclude that the periodicity found in the long-term trend light curve is the result of the sampling of our GRS 1758−258 light curve. However, the range, in which the residual signal appears in the trend light curve, shifts according to the filter range n and is always located between n and $2n$. Thus we conclude that this residual signal is left because the filter is not an ideal high pass filter. But as we find a significant peak in the periodogram although the filter removes part of the signal together with the long term trend, the filtering approach effect does not impair the main results of our analysis.

We also tested whether the drifting peak in the GRS 1758−258 dynamic power spectrum could be caused by the filtering process. In order to do so, we consider a pure white noise light curve with the original sampling, apply the high pass filter, and then calculate a dynamic power spectrum of the short term residuals analogous to the GRS 1758−258 dynamic power spectrum shown in Fig. 9. As expected, none
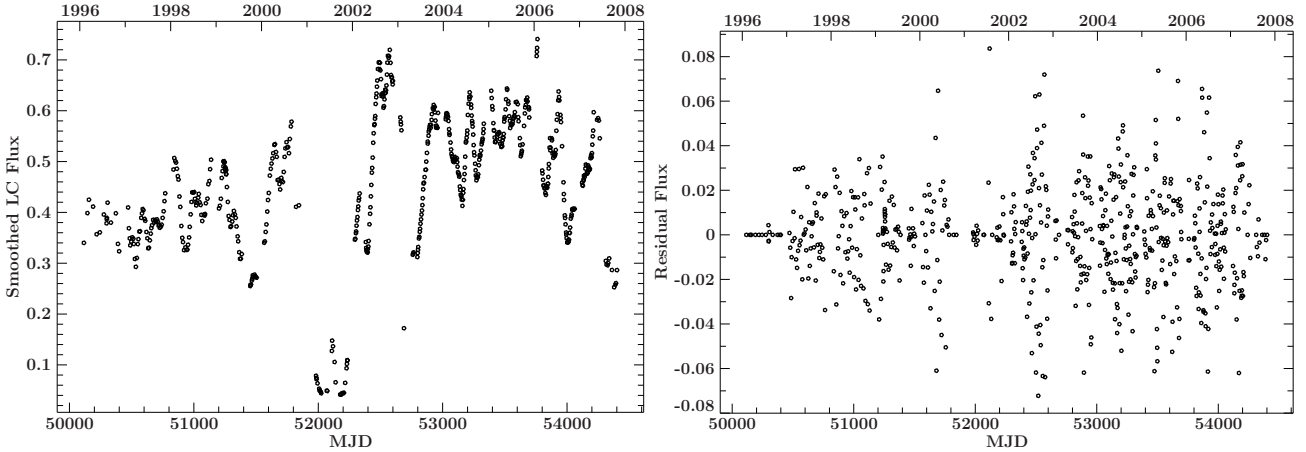
Fig. 7. Long term trend (*left*) and residual flux (*right*) light curves in keV s^{-1} cm^{-2} after application of the high pass filter.
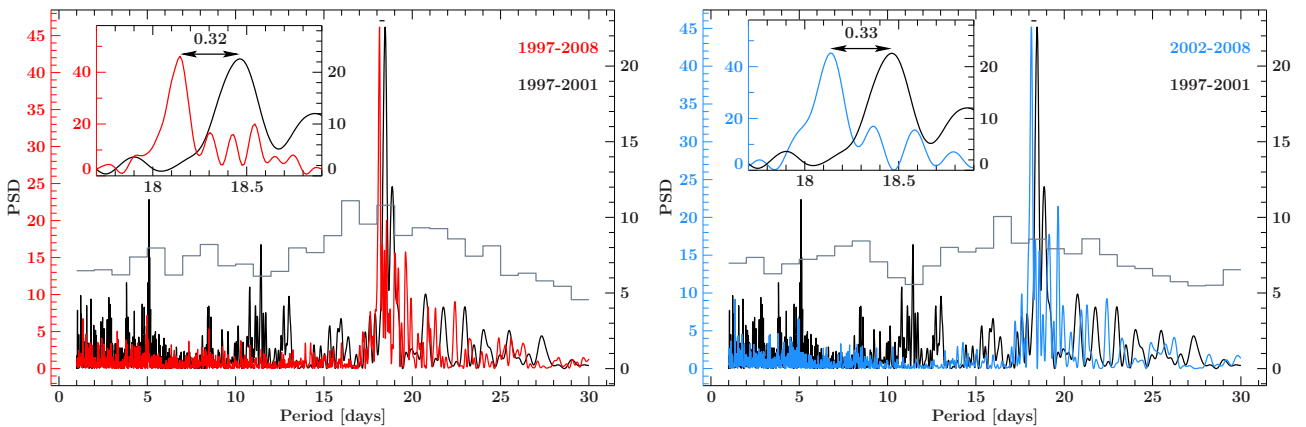
Fig. 8. Comparison of power spectra measured for the time interval 1997–2008 (red, *left*) and 2002–2008 (blue, *right*) to the power spectrum measured in the 1997–2001 data (black), i.e., the time interval used by Smith et al. (2002a). The peaks show a difference in period of 0.32 d and 0.33 d, respectively. Histograms show the peak PSD values for 10 000 realizations of a detrended light curve with residuals with a Gaussian distribution in the indicated period interval (see text for further explanation).

of the light curve slices, that is lines in the dynamic power spectrum, shows a prominent peak at periods between 1 d and 30 d in its periodogram. Thus, the period is not created by the filtering process.

Finally, in order to determine whether the shifting peak is real, we also tested whether the peak could be caused by the variability of the source being red noise. Red noise, used here to mean a stochastic process with a $f^{-\alpha}$ power spectrum, is notorious to exhibit quasi periodicities in its lightcurve when studying short light curve segments. We therefore used the algorithm of Timmer & Koenig (1995) to generate a red noise lightcurve with 100 000 data points (in order to avoid windowing effects caused by the simulation approach) with the same overall statistical properties as that of GRS 1758−258. We then selected a segment of that light curve to generate a red noise only lightcurve. This light curve was then analyzed in the same way as the real data, again using a high pass filter before applying the Lomb–Scargle algorithm. The resulting dynamic power spectrum does not show any peak at all in the period range we are interested in. We therefore can exclude a red noise origin for the drifting peak.

4.3. Comparison with Levine et al. (2011)

Smith et al. (2002a) were not the only ones reporting a periodicity for GRS 1758−258: Using ASM data in the 3–5 keV band and

a different filtering approach, Levine et al. (2011) found a signal at a frequency of 0.0527 cycles day^{-1}, corresponding to a period of 18.97 d. As this value is slightly different from what we obtain using the method of Smith et al. (2002a), we tried to reproduce their result, implementing the analysis method as described in Levine et al. (2011): we use the ASM light curve rebinned to a 2 d resolution and weighted according to the description in Levine et al. (2011), smooth it with a Gaussian kernel function with a full width at half maximum of 500 d, and then calculate the power spectrum via the classical Fourier transform. This power spectrum is then whitened to account for background power. Detailed descriptions of all these steps can be found in the appendix of Levine et al. (2011). The reason for using a different approach than for the data described in Sect. 4.2 is twofold: first, it allows us to see whether the results of Levine et al. (2011) hold also for the longer time interval considered here. Secondly, using a different methodology on the ASM data set avoids introducing the same potential systematic errors in the analysis and thus allows an independent confirmation of the results of the PCA analysis of Sect. 4.2.

Using this method, we are able to roughly reproduce their power spectrum of GRS 1758−258 (Levine et al. 2011, their Fig. 9, bottom). There is a deviation in the total power in the power spectrum which is due to differences in the normalization of the Fourier transformation routines (Fig. 11). We then
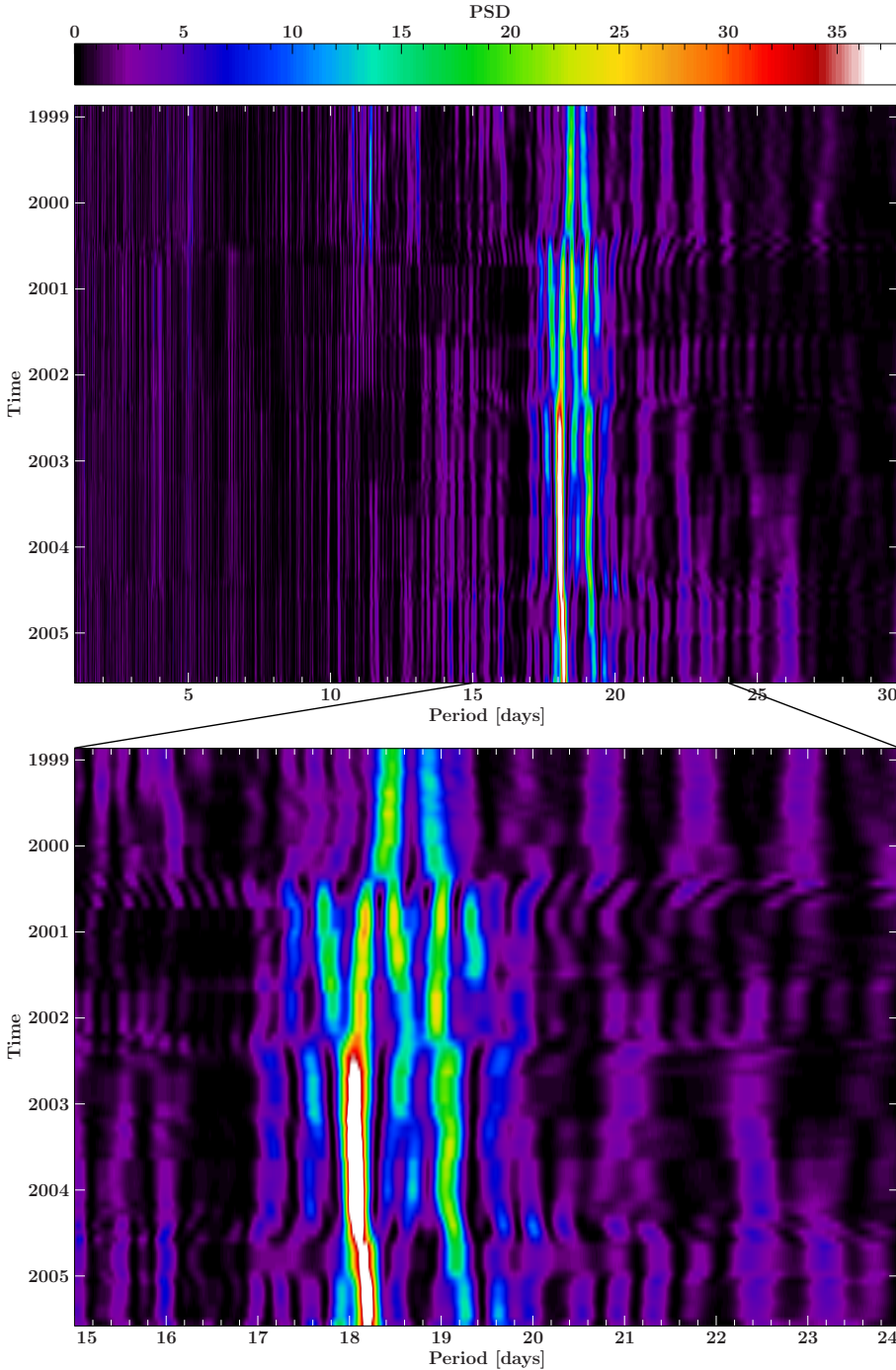
Fig. 9. Dynamical Lomb–Scargle periodogram for the entire 11 year 3–20 keV model flux light curve of GRS 1758−258. The periodogram is calculated in five year intervals (centered on the middle in the Time axis), stepped in intervals of 30 d.

calculated a dynamic power spectrum (Fig. 12) for the same light curve slices as above, using the ASM 3–5 keV light curve binned on a 2 d grid and the analysis method of Levine et al. (2011). As the ASM data are noisier than the PCA flux light curve (Fig. 9), there is no prominent peak as seen in the PCA data. However, there is a feature around 19 d as reported by Levine et al. (2011). This feature blends with a peak that starts at a period of nearly 20 d and then drifts first toward smaller periods with a minimum in 2003. As with the PCA data and analysis after Smith et al. (2002a), a side peak showing a similar behavior at longer periods is also present. However, in the ASM data the side peak is at a distance of ~2 d from the main peak, while in the PCA data the distance is only ~1 d. The region around mid-2000, where the main peak of the PCA data splits up into two peaks, is also

interesting in the ASM data: the main peak drifts towards a minor peak and broadens as the two periods are close to each other.

On the whole, however, apart from a systematic discrepancy in periods of about 1 d, the analysis of the ASM data using this different method confirms our first result of a drifting periodicity for GRS 1758−258: It is seen in different datasets, analyzed with different methods.

For another cross-check we analyzed the *Swift*/BAT light curve taken from the Transient Monitor (Krimm et al. 2013) following the algorithm of Smith et al. (2002a), using the same parameters for the high pass filter as in the analysis of the RXTE data. The resulting dynamic power spectrum is shown in Fig. 13. The energy band of 15–50 keV also shows a drifting
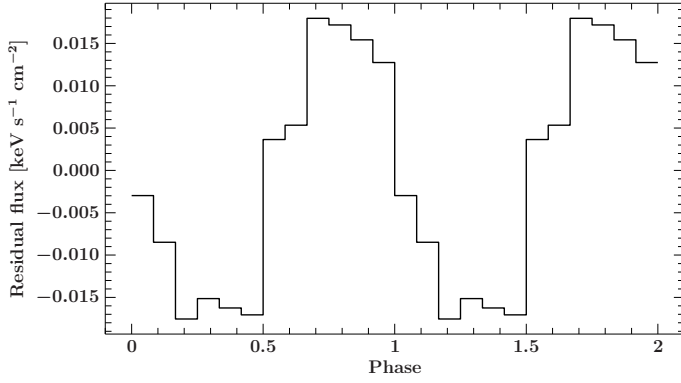
Fig. 10. Filtered 3–20 keV model flux light curve for the stable part of the dynamical power spectrum (MJD 51769–53980), folded on a period of 18.09 d.
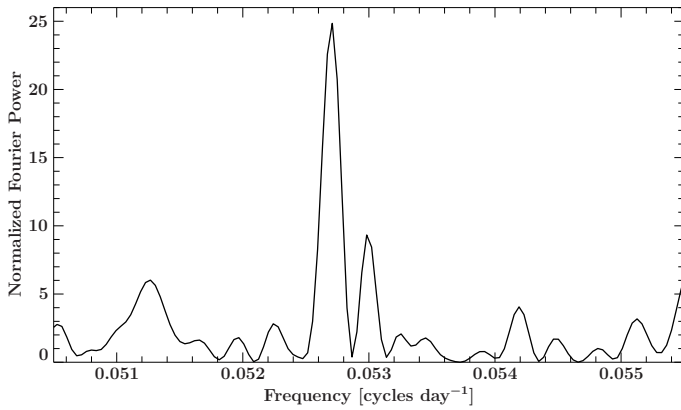
Fig. 11. Power spectrum of the 3–5 keV ASM light curve, using the method of Levine et al. (2011). We are able to reproduce their Fig. 9 (bottom).
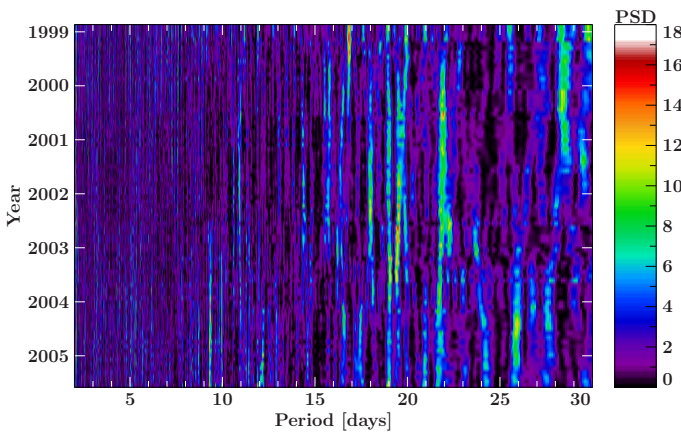
Fig. 12. Dynamic power spectrum of the 3–5 keV ASM light curve, using the method of Levine et al. (2011). A drifting peak is visible although much less prominent due to the poor signal to noise ratio of the ASM data.

periodicity between 18 d and 19 d. The signal is not as strong as in the PCA data, but the behavior is clearly the same in high as in low energies. Note that around the most recent, very dim 2016 soft state (Pottschmidt et al. 2016; Hirsch et al. 2016, and in prep.) a decrease in period is visible similar to the decrease in the PCA dynamic power spectrum around the very dim 2001 soft state. This additional observation of the drifting periodicity with another satellite than RXTE, at another time, in another
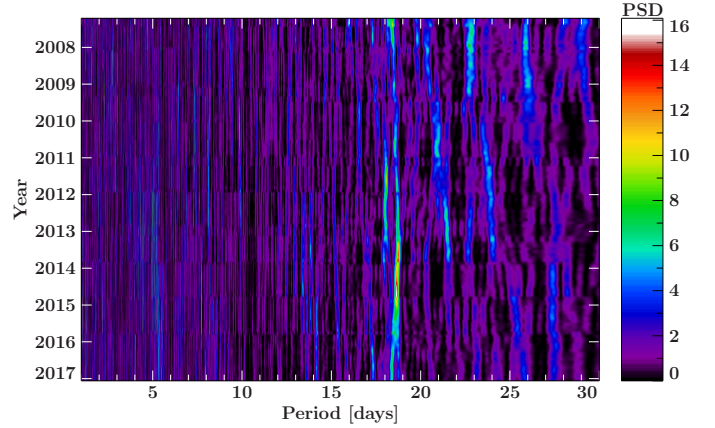
Fig. 13. Dynamic power spectrum of the 15–50 keV *Swift*/BAT light curve, using the method of Smith et al. (2002a). The high energy light curve also shows a drifting peak. A change in period is obvious in 2016, near the most recent soft state.

energy range, further increases the confidence that we are seeing a source-intrinsic signal.

5. Discussion

5.1. Spectral evolution and state transitions

Analyzing data of the eleven years long RXTE-PCA monitoring of GRS 1758−258 we find that the spectrum in the 3–20 keV range can always be described by an absorbed powerlaw (photon indices varying between 1.5 and 3) with a neutral Fe Kα line (which might be due to variations in the Galactic ridge emission) and, during the soft states with a photon index softer than 2, a disk-blackbody component. The Galactic ridge background emission was always accounted for. GRS 1758−258 entered a dim soft state for seven times between 1997 and 2008. During these soft states, the track of GRS 1758−258 in the hardness intensity diagram is similar to the q-shaped one of transient sources, however there is no rise from quiescence into the hard state. The high energy HID of GRS 1758−258 is comparable to that of Cyg X-1 (Obst et al. 2011).

The detection of an accretion disk in the soft state and its non-detection in the hard state are consistent with the *XMM-Newton* observations discussed by Soria et al. (2011), who also find a higher total X-ray luminosity in the 2001 XMM soft state data than in the 2008/2009 *Swift* XRT hard state observations. They conclude that luminosity cannot be the only driving force for a state transition in the GRS 1758−258 system.

There are several models that try to explain the evolution of X-ray binaries in the HID. One of the first attempts to explain the hysteresis is the picture of two accretion flows set up and applied to GRS 1758−258 by Smith et al. (2002b), and similar to models discussed by Meyer et al. (2000) and Meyer-Hofmeister et al. (2009): Based on Chakrabarti & Titarchuk (1995), they suggest a Keplerian accretion disk in combination with a hot, sub-Keplerian halo accreting proportional amounts of matter. A boost in accretion rate leads to the halo brightening at once (almost free fall timescale), while the brightening of the inner regions of the disk is delayed by the inspiral of matter (viscous timescale). Then the additional soft photons are cooling the halo and the spectrum softens. Similarly, a sudden drop in accretion rate would first affect the halo, its Comptonizing component declining rapidly. The Keplerian disk reacts only on the viscous timescale, causing the soft component to decay

slower (Smith et al. 2002b, 2007), which is the "dynamical soft state" observed in GRS 1758−258 and other black hole binaries, for instance, the transient source GX 339−4 (Debnath et al. 2015; Nagarkoti & Chakrabarti 2016) and many other transients (Gierliński & Newton 2006) as well as the persistent "twin source" of GRS 1758−258, 1E 1740.7−2942 (Smith et al. 2002b). Soria et al. (2011) refined this idea and suggest a magnetically powered coronal outflow as the source of the hard radiation. The accretion flow could then switch between the hard corona and the soft accretion disk because of changes in the poloidal magnetic field.

The interpretation of two accretion flows fits not only GRS 1758−258 but also other Galactic black hole binaries, With small changes, this picture can also be applied to high-mass X-ray binaries such as Cyg X-1 and LMC X-3 (Smith et al. 2002b, 2007): here, the mass input is no longer distributed proportionally between disk and halo. State changes are induced by the accretion flow switching between favouring the disk while starving the halo and favouring the halo while starving the disk. Thus, the bolometric luminosity should remain almost unchanged during state transitions in these systems. Recently, Ghosh & Chakrabarti (2018) have found further evidence for an advective and a Keplerian flow analyzing time lags in the spectral slope for different high mass X-ray binaries and low mass X-ray binaries. They use a more extensive dataset and a completely different method than Smith et al. (2002a), yet their results lead to the same conclusion.

We note, however, that other models are equally successful at describing state transitions, such as the hybrid model of an outer standard accretion disk and an inner, magnetized jet emitting disk of Petrucci et al. (2008, see also Ferreira et al. 2006; Marcel et al. 2018a,b), the explanation of the hysteretic cycle in black hole state transitions as a magnetic field effect put forward by Begelman & Armitage (2014), or the explanation of state transitions through severe disruptions of the accretion flow by Nixon & Salvesen (2014). Common to all of these analyses and also to the large number of other discussions in the literature is that they are biased by the few bright and well sampled black hole outbursts such as those from GX 339−4 or XTE J1550−564, and that the more complex hysteretic behavior seen here or in other persistent sources such as LMC X-3 or Cyg X-1 is typically not explained. We hope that the data presented here will stimulate further theoretical discussions that address the difference of GRS 1758−258 and other black hole binaries.

5.2. Timing behavior and long-term evolution

Analyzing the model flux light curve spanning 11 years of observations for timing analysis, we are unable to detect any orbital modulation in the dataset. However, after detrending the data we find that the dynamic power spectrum exhibits a peak which drifts at periods between 18.475 ± 0.017 and 18.043 ± 0.005 d and has a significance between 98.15% and 99.98%. This drifting behavior was confirmed using another data set and analysis method, however with a systematic deviation in periods of about 2 d.

Long-term periodicities in accreting systems are generally associated with periodic phenomena in the outer parts of the accretion disk, which are due to a combination of radiation pressure and orbital effects. The most prominent of such radiation driven periodicities are superhumps in cataclysmic variables (CVs). Such warps were first observed during superoutbursts of SU UMa systems (see Warner 2003, for a review and, e.g.,

Armstrong et al. 2013 for observations of superhumps in several CVs), where the superhumps are seen as periodic optical modulations caused by a 3:1 orbital resonance within the accretion disk, which causes the disk to be eccentric and to slowly precess. Here, irradiation of the accretion disk by the central source or inner part of the accretion disk results in a net torque on the disk which leads to a precessing, warped disk (Petterson 1977; Iping & Petterson 1990; Pringle 1996; Wijers & Pringle 1999; Maloney et al. 1996). The luminosity modulation is then caused by periodic variations of the efficiency of dissipative processes in the accretion disk (Whitehurst 1988; Whitehurst & King 1991; Lubow 1991a,b).

Masetti et al. (1996), Haswell et al. (2001), and Charles (2002) review observations of superhumps in soft X-ray transients and low mass X-ray binaries. Masetti et al. (1996) suggest an alternative origin for these modulations: with an elliptical disk shape, the accretion flow impacts the outer disk at varying distances from the central object and thus at different gravitational potentials, leading to modulations in the released energy. Other possible mechanisms include a variation in the uncovered area in the direction of the observer or varying absorption by a disk warp. Based on this idea, Clarkson et al. (2003b) suggest a similar mechanism to explain the superorbital period of the high mass X-ray binary SMC X-1 (Wojdowski et al. 1998), which consists of a neutron star and the B0 I optical companion Sk 160 (Reynolds et al. 1993). Clarkson et al. (2003b) found this period to be varying between 40 d and 60 d. These authors performed an analysis similar to ours, and also their dynamic power spectrum looks similar. They suggest the modulation being due to a bright spot at the intersection of accretion flow and accretion disk. This mechanism can support variations in the superorbital period (Clarkson et al. 2003b). In a follow-up paper, Clarkson et al. (2003a) present the analysis of a sample of other sources showing superorbital periods and put up a scheme, showing the evolution of disk warping with respect to the binary radius. With regard to the predictions of Ogilvie & Dubus (2001), Clarkson et al. due to irradiation of the disk is impossible for very close binaries. With increasing separation of the binary components one stable warp mode as seen, for example, in Her X-1 or LMC X-4. Above the boundary region, several strong periodicities interact, as seen, for example, in Cyg X-2. In the border region itself, stable warping is not possible, as is seen in SMC X-1, which shows sharp variations in the superorbital cycle length (Trowbridge et al. 2007). The underlying model, however, has to be more complex than described by Clarkson et al. (2003b), who expect a precessing warp and long periodicity for a source near this boundary, which is clearly inconsistent with the behavior reported by Trowbridge et al. (2007).

The result of Clarkson et al. (2003a,b) raises the question whether a similar mechanism is also applicable to GRS 1758−258. Both low mass X-ray binaries Her X-1 and LMC X-4 accrete via Roche lobe overflow, and the high mass X-ray binary SMC X-1, too, is best characterized by Roche lobe overflow properties (e.g., Li & van den Heuvel 1997; Içdem & Baykal 2011). Given that the companion of GRS 1758−258 is probably an A-type star (Martí et al. 2016), the system would probably be somewhere in between Her X-1 or LMC X-4 and SMC X-1, such that the observed behavior is not fully unlikely.

Beyond that, superorbital periods have also been observed in wind-accreting high mass X-ray binaries (e.g., Corbet & Krimm 2013). For such systems, different mechanisms have to be considered. Koenigsberger et al. (2006) suggest oscillations in the companion star driven by tidal interactions to be the source for the superorbital period, while Bozzo et al. (2017) propose

corotating interaction regions in the stellar wind to be responsible for the observed modulations.

There are many mechanisms that lead to an observable variability in the light curve for different kinds of binary systems, and many aspects that can influence the formation of warps in an accretion disk for a system like GRS 1758−258, so that we cannot finally conclude this special mechanism of a warped disk to be the origin of the variable periodicity in GRS 1758−258.

6. Conclusions

Overall, the RXTE monitoring data show that GRS 1758−258 fits into the general picture of X-ray binaries with a few source-characteristic features. The occasional very dim soft states as well as the striking timing behavior put a challenge to the current available physical models.

With the data currently available, it is neither possible to decide between the different models for the state transition in GRS 1758−258 nor between the mechanisms that lead to an observable variability in the light curve of a binary system. Further steps in theory and simulation have to be made to answer the open questions such as

- What physical model is behind the state transitions in GRS 1758−258 and other black hole binaries?
- Does the same model apply to low mass and high mass X-ray binaries, or do we need different mechanisms?
- Is there a model that can accomodate not only black hole binaries but also neutron star low-mass binaries, which display a similar behavior (Maccarone & Coppi 2003; Muñoz-Darias et al. 2014)?
- What factors influence the formation of warps in accretion disks in GRS 1758−258 and other sources and how do they influence it?
- Is it possible to explain both effects in one comprehensive picture?

Especially for the last two items, further observations of systems that are displaying superorbital periods are needed to have a statistical relevant sample of different behaviors and to be able to fit in the scheme sources as GRS 1758−258 where we do not know much about the distance, the companion or the binary separation and orbit.

References

Anders, E., & Grevesse, N. 1989, Geochim. Cosmochim. Acta, 53, 197
Armstrong, E., Patterson, J., Michelsen, E., et al. 2013, MNRAS, 435, 707
Begelman, M. C., & Armitage, P. J. 2014, ApJ, 782, L18
Belloni, T., Homan, J., Casella, P., et al. 2005, A&A, 440, 207
Benlloch, S., Wilms, J., Staubert, R., & Nowak, M. 2001, in Exploring the Gamma-Ray Universe, eds. A. Gimenez, V. Reglero, & C. Winkler (Noordwijk: ESA Publications Division), ESA Publ. Division, 459, 263
Bozzo, E., Oskinova, L., Lobel, A., & Hamann, W.-R. 2017, A&A, 606, L10
Bradt, H. V., Rothschild, R. E., & Swank, J. H. 1993, A&AS, 97, 355
Cadolle Bel, M., Goldwurm, A., & Sizun, P. 2006, in Populations of High Energy Sources in Galaxies, eds. E. J. A. Meurs, & G. Fabbiano (Cambridge: Cambridge University Press), IAU Symp., 230, 93
Chakrabarti, S., & Titarchuk, L. G. 1995, ApJ, 455, 623
Charles, P. A. 2002, in The Physics of Cataclysmic Variables and Related Objects, eds. B. T. Gänsicke, K. Beuermann, & K. Reinsch (San Francisco: ASP), ASP Conf. Ser., 261, 223
Clarkson, W. I., Charles, P. A., Coe, M. J., & Laycock, S. 2003a, MNRAS, 343, 1213
Clarkson, W. I., Charles, P. A., Coe, M. J., et al. 2003b, MNRAS, 339, 447
Corbet, R. H. D., & Krimm, H. A. 2013, ApJ, 778, 45
Debnath, D., Mondal, S., & Chakrabarti, S. K. 2015, MNRAS, 447, 1984
del Santo, M., Bazzano, A., Zdziarski, A. A., et al. 2005, A&A, 433, 613
del Santo, M., Malzac, J., Jourdain, E., Belloni, T., & Ubertini, P. 2008, MNRAS, 390, 227
Ebisawa, K., Yamauchi, S., Tanaka, Y., Koyama, K., & Suzaku Team 2007, Theor. Phys. Suppl., 169, 121
Ebisawa, K., Yamauchi, S., Tanaka, Y., et al. 2008, PASJ, 60, 223
Fender, R. P., Belloni, T. M., & Gallo, E. 2004, MNRAS, 355, 1105
Ferreira, J., Petrucci, P.-O., Henri, G., Saugé, L., & Pelletier, G. 2006, A&A, 447, 813
Fürst, F., Wilms, J., Rothschild, R. E., et al. 2009, Earth Planet. Sci. Lett., 281, 125
Ghosh, A., & Chakrabarti, S. K. 2018, MNRAS, 479, 1210
Gierliński, M., & Newton, J. 2006, MNRAS, 370, 837
Haswell, C. A., King, A. R., Murray, J. R., & Charles, P. A. 2001, MNRAS, 321, 475
Heindl, W. A., & Smith, D. M. 2002, ApJ, 578, L125
Hirsch, M. 2014, Master's Thesis, Remeis-Observatory, Friedrich-Alexander-Universität Erlangen-Nürnberg, Bamberg, Germany
Hirsch, M., Pottschmidt, K., Krauss, F., et al. 2016, ATel, 9890
Houck, J. C. 2002, in High Resolution X-ray Spectroscopy with XMM-Newton and Chandra, ed. G. Branduardi-Raymont, Proc. 2002 MSSL Workshop
Houck, J. C., & Denicola, L. A. 2000, in Astronomical Data Analysis Software and Systems IX, eds. N. Manset, C. Veillet, & D. Crabtree (San Francisco: ASP), ASP Conf. Ser., 216, 591
Içdem, B., & Baykal, A. 2011, A&A, 529, A7
Iping, R. C., & Petterson, J. A. 1990, A&A, 239, 221
Jahoda, K., Markwardt, C. B., Radeva, Y., et al. 2006, ApJS, 163, 401
Koenigsberger, G., Georgiev, L., Moreno, E., et al. 2006, A&A, 458, 513
Koyama, K., Makishima, K., Tanaka, Y., & Tsunemi, H. 1986, PASJ, 38, 121
Krimm, H. A., Holland, S. T., Corbet, R. H. D., et al. 2013, ApJS, 209, 14
Levine, A. M., Bradt, H., Cui, W., et al. 1996, ApJ, 469, L33
Levine, A. M., Bradt, H. V., Chakrabarty, D., Corbet, R. H. D., & Harris, R. J. 2011, ApJ, 196, 6
Li, X.-D., & van den Heuvel, E. P. J. 1997, A&A, 321, L25
Lomb, N. R. 1976, Ap&SS, 39, 447
Lubow, S. H. 1991a, ApJ, 381, 259
Lubow, S. H. 1991b, ApJ, 381, 268
Luque-Escamilla, P. L., Martí, J., & Muñoz-Arjonilla, Á. J. 2014, ApJ, 797, L1
Maccarone, T. J., & Coppi, P. S. 2003, MNRAS, 338, 189
Maloney, P. R., Begelman, M. C., & Pringle, J. E. 1996, ApJ, 472, 582
Mandrou, P. 1990, IAU Circ., 5032
Marcel, G., Ferreira, J., Petrucci, P.-O., et al. 2018a, A&A, 617, A46
Marcel, G., Ferreira, J., Petrucci, P. O., et al. 2018b, A&A, 615, A57
Martí, J., Mereghetti, S., Chaty, S., et al. 1998, A&A, 338, L95
Martí, J., Luque-Escamilla, P. L., & Muñoz-Arjonilla, Á. J. 2016, A&A, 596, 46
Martí, J., Luque-Escamilla, P. L., Bosch-Ramon, V., & Paredes, J. M. 2017, Nat. Commun., 8, 1757
Masetti, N., Bianchini, A., Bonibaker, J., della Valle, M., & Vio, R., 1996, A&A, 314, 123
Matsuoka, M., Kawasaki, K., Ueno, S., et al. 2009, PASJ, 61, 999
Mereghetti, S., Cremonesi, D. I., Haardt, F., et al. 1997, ApJ, 476, 829
Meyer, F., Liu, B. F., & Meyer-Hofmeister, E. 2000, A&A, 361, 175
Meyer-Hofmeister, E., Liu, B. F., & Meyer, F. 2009, A&A, 508, 329
Muñoz-Arjonilla, A. J., Martí, J., Luque-Escamilla, P. L., et al. 2010, A&A, 519, A15
Muñoz-Darias, T., Fender, R. P., Motta, S. E., & Belloni, T. M. 2014, MNRAS, 443, 3270
Nagarkoti, S., & Chakrabarti, S. K. 2016, MNRAS, 462, 850
Nixon, C., & Salvesen, G. 2014, MNRAS, 437, 3994

Noble, M. S., & Nowak, M. A. 2008, PASP, 120, 821

Nobukawa, M., Uchiyama, H., Nobukawa, K. K., Yamauchi, S., & Koyama, K. 2016, ApJ, 833, 268

Obst, M., Pottschmidt, K., Lohfink, A., et al. 2011, Acta Polytech., 51, 49

Ogilvie, G. I., & Dubus, G. 2001, MNRAS, 320, 485

Petrucci, P.-O., Ferreira, J., Henri, G., & Pelletier, G. 2008, MNRAS, 385, L88

Petterson, J. A. 1977, ApJ, 216, 827

Pottschmidt, K., Chernyakova, M., Zdziarski, A. A., et al. 2006, in The X-ray Universe 2005, ed. A. Wilson, ESA Spec. Publ., 604, 283

Pottschmidt, K., Chernyakova, M., Lubiński, P., et al. 2008, Proceedings of "An INTEGRAL view of compact objects" - 7th INTEGRAL Workshop (PoS[Integral08]), 67

Pottschmidt, K., Eikmann, W., Kreykenbohm, I., et al. 2016, ATel, 9625

Pringle, J. E. 1996, MNRAS, 281, 357

Reynolds, A. P., Hilditch, R. W., Bell, S. A., & Hill, G. 1993, MNRAS, 261, 337

Rodriguez, L. F., Mirabel, I. F., & Marti, J. 1992, ApJ, 401, L15

Rothstein, D. M., Eikenberry, S. S., Chatterjee, S., et al. 2002, ApJ, 580, L61

Scargle, J. D. 1982, ApJ, 263, 835

Smith, D. M., Heindl, W. A., Markwardt, C. B., & Swank, J. H. 2001, ApJ, 554, L41

Smith, D. M., Heindl, W. A., & Swank, J. H. 2002a, ApJ, 578, L129

Smith, D. M., Heindl, W. A., & Swank, J. H. 2002b, ApJ, 569, 362

Smith, D. M., Dawson, D. M., & Swank, J. H. 2007, ApJ, 669, 1138

Smith, I. A. 2010, in AAS/High Energy Astrophysics Division #11, Bull. Am. Astron. Soc., 42, 671

Soria, R., Broderick, J. W., Hao, J., et al. 2011, MNRAS, 415, 410

Syunyaev, R., Gilfanov, M., Churazov, E., et al. 1991, Sov. Astron. Lett., 17, 50

Timmer, J., & Koenig, M. 1995, A&A, 300, 707

Trowbridge, S., Nowak, M. A., & Wilms, J. 2007, ApJ, 670, 624

Warner, B. 2003, Cataclysmic Variable Stars (Cambridge: Cambridge University Press)

Warwick, R. S. 2014, MNRAS, 445, 66

Warwick, R. S., Turner, M. J. L., Watson, M. G., & Willingale, R. 1985, Nature, 317, 218

Whitehurst, R. 1988, MNRAS, 232, 35

Whitehurst, R., & King, A. 1991, MNRAS, 249, 25

Wijers, R. A. M. J., & Pringle, J. E. 1999, MNRAS, 308, 207

Wilms, J., Nowak, M. A., Dove, J. B., Fender, R. P., & Di Matteo, T. 1999, ApJ, 522, 460

Wilms, J., Nowak, M. A., Pottschmidt, K., et al. 2001, MNRAS, 320, 327

Wilms, J., Nowak, M. A., Pottschmidt, K., Pooley, G. G., & Fritz, S. 2006, A&A, 447, 245

Wilms, J., Pottschmidt, K., Pooley, G. G., et al. 2007, ApJ, 663, L97

Wojdowski, P., Clark, G. W., Levine, A. M., Woo, J. W., & Zhang, S. N. 1998, ApJ, 502, 253

Worrall, D. M., Marshall, F. E., Boldt, E. A., & Swank, J. H. 1982, ApJ, 255, 111

Evolution of MAXI J1631−479 during the January 2019 outburst observed by *INTEGRAL*/IBIS

M. Fiocchi,[1][*] F. Onori,[1] A. Bazzano,[1] A.J. Bird,[2] A. Bodaghee,[3] P. A. Charles,[2]
V. A. Lepingwell,[2] A. Malizia,[4] N. Masetti,[4,5] L. Natalucci,[1] P. Ubertini.[1]

[1]*Istituto di Astrofisica e Planetologia Spaziali (INAF), Via Fosso del Cavaliere 100, Roma, I-00133, Italy*
[2]*Department of Physics & Astronomy, University of Southampton, Highfield, Southampton, SO17 1BJ, UK*
[3]*DCPA Georgia College Milledgeville, USA*
[4]*INAF-Osservatorio di Astrofisica Spaziale e Scienza dello Spazio, via Gobetti 93/3, I-40129 Bologna, Italy*
[5]*Departamento de Ciencias Físicas, Universidad Andrés Bello, Fernández Concha 700, Las Condes, Santiago, Chile*

ABSTRACT

We report on a recent bright outburst from the new X-ray binary transient MAXI J1631−479, observed in January 2019. In particular, we present the 30-200 keV analysis of spectral transitions observed with *INTEGRAL*/IBIS during its Galactic Plane monitoring program. In the MAXI and BAT monitoring period, we observed two different spectral transitions between the high/soft and low/hard states. The *INTEGRAL* spectrum from data taken soon before the second transition, is best described by a Comptonised thermal component with a temperature of $kT_e \sim 30$ keV and a high luminosity value of $L_{2-200\,keV} \sim 3 \times 10^{38}$ erg s^{-1} (assuming a distance of 8 kpc). During the second transition, the source shows a hard, power-law spectrum. The lack of high energy cut-off indicates that the hard X-ray spectrum from MAXI J1631−479 is due to a non-thermal emission. Inverse Compton scattering of soft X-ray photons from a non-thermal or hybrid thermal/non-thermal electron distribution can explain the observed X-ray spectrum although a contribution to the hard X-ray emission from a jet cannot be determined at this stage. The outburst evolution in the hardness-intensity diagram, the spectral characteristics and the rise and decay times of the outburst are suggesting this system is a black hole candidate.

Key words: gamma rays: observations — radiation mechanisms: non-thermal — stars: individual: MAXI J1631−479— stars: black hole, neutron star — X-rays: binaries.

1 INTRODUCTION

In recent years, with the advent of new space and ground-based facilities, numerous efforts have been made to understand the X-ray emission in transient X-ray Binaries, containing either a neutron star (NS) or a black hole (BH). These systems are characterized by transitions between two main spectral states: the high/soft state, with the dominant soft X-ray emission originating from the accretion disc, and the low/hard state, where the dominant hard X-ray emission arises from the Inverse Compton scattering of soft thermal photons by hot electrons in the corona (Done et al. (2007)). The evolution of the spectral and timing properties are crucial to understand the accretion-ejection connection during an outburst for both BH and NS systems. The evolution of an outburst is well described in the hardness-

intensity diagram, which represents a useful tool to investigate on the phenomenological connections between the spectral-timing states and the outflows modes (Gardenier & Uttley (2018); Belloni (2018); Belloni & Motta (2016); Fender (2016); Fender & Belloni (2012); Done et al. (2007); Fender (2004); Fender et al. (2004), and references therein). Although the geometry of these systems is fairly well established, the jet contribution to the high energy emission in the hard state is still unclear.

A new outburst from MAXI J1631−479 was reported on 2018 December 21 by the *MAXI/GSC* nova alert system reporting a bright hard X-ray outburst in the Norma region (Kobayashi et al. 2018). The X-ray flux was $F_{4-10\,keV} = 209 \pm 27$ mCrab at the inferred position of R.A. (J2000)= 247.770 deg., DEC (J2000) = -47.920 deg., with a 90% confidence error radius of 10.2′. Confirmation of MAXI J1631−479 as a new X-ray transient source was provided by *NuSTAR* observations performed on 2018 December 28

---

[*] E-mail: mariateresa.fiocchi@inaf.it
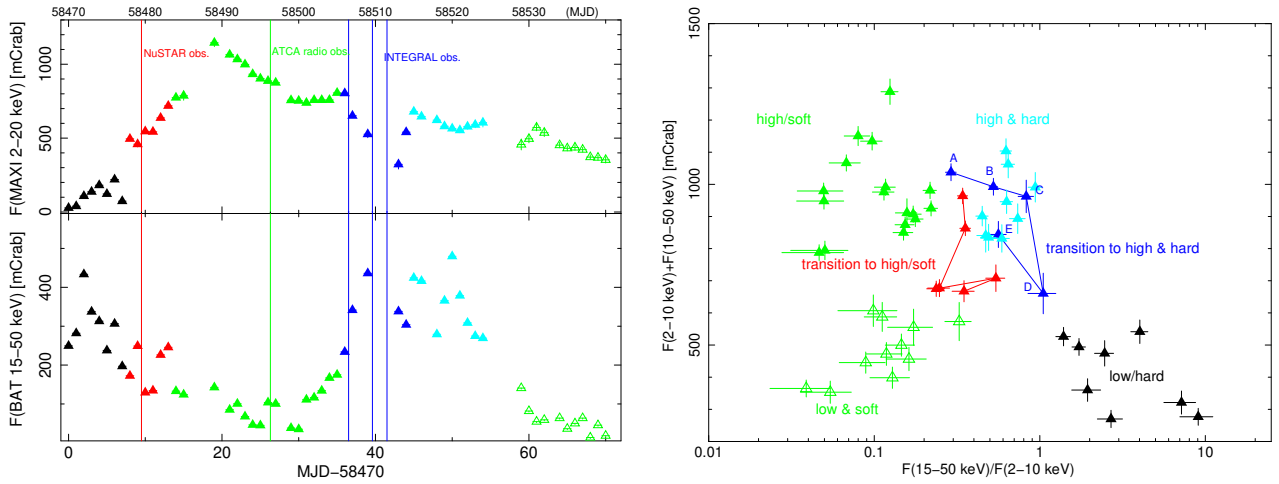
Figure 1. *Left panel*: the MAXI (upper) and Swift/BAT (lower) light curves of MAXI J1631−479, both with 1 day binning. Vertical lines indicate the time of the *NuSTAR*, ATCA and *INTEGRAL* observations. See text for details. *Right panel*: the hardness-intensity diagram with each point corresponding to 1 day: on the horizontal axis we show the ratio $F^{BAT}_{(15-50\,\text{keV})}/F^{MAXI}_{(2-10\,\text{keV})}$ and in the vertical axis the total flux $F^{BAT}_{(15-50\,\text{keV})} + F^{MAXI}_{(2-10\,\text{keV})}$. Colored points indicate the different time intervals. Capitals letters indicate the time evolution of the hardness-intensity data during this transition, with A being the starting of the transition and E the end.

at the refined position is R.A. (J2000) = 16:31:13.4, DEC (J2000) = -47:48:18 with an uncertainty of 15″.

On 2019 January 13 a radio counterpart for MAXI J1631−479 was detected by the Australia Telescope Compact Array (ATCA) observations at central frequencies of 5.5 and 9 GHz (Russell et al. 2019). A clear identification of an optical counterpart is missing, consistently with the high column density found in the *NuSTAR* observation. Indeed, the position of MAXI J1631−479 was observed with KMTNet telescopes (Kim et al. 2016), with the iTelescope.Net T17 and with the 1m telescope of the CHILESCOPE observatory (Kong 2019) and no new optical source was clear found at the position of the radio detection (Shin et al. 2019).

INTEGRAL started Norma region observations as part of the Galactic Plane Scan in revolution 2048 (2019 January 21- 23) and MAXI J1631−479 was clearly detected by *IBIS*/ISGRI (Onori et al. 2019). The position of the source in the 22–60 keV energy band was R.A. (J2000)=247.814 deg, DEC(J2000)=-47.800 deg with an error radius of 0.5′ and a flux $F_{22-60\,\text{keV}}$= 265.2±3.7 mCrab. Here, we report the results from our analysis of the *IBIS*/ISGRI data up to 200 keV.

2   OBSERVATIONS AND DATA ANALYSIS

MAXI J1631−479 has been monitored at high energies by *INTEGRAL* during three revolutions: 2048, 2049 and 2050, starting from 2019-01-21T13:30 UTC (58504.563 MJD), 2019-01-24T02:47 UTC (58507.117 MJD) and 2019-01-26T19:12 UTC (58509.801 MJD), respectively.
The *INTEGRAL*/IBIS (Ubertini et al. 2003) consolidated data for these observations were processed using the standard Off-line Scientific Analysis (`osa` v11.0) software, released by the *INTEGRAL* Science Data Centre (Courvoisier et al. 2003). This software was used to obtain both spectra and light curves of the source in different common time intervals and a systematic error of 2% was included. MAXI

J1631−479 was out of the JEM-X field of view and this precludes INTEGRAL detection at lower energies (¡30 keV).

The Neil Gehrels *Swift* observatory (Gehrels et al. 2004) collected data from this source in January 2019. We used the results from *BAT* (Krimm et al. 2013) observations, while the XRT (Burrows et al. 2004) data are not simultaneous with the INTEGRAL ones. In view of the strong variability of the source, a common INTEGRAL-Swift spectral study in a broad energy band is not possible.

MAXI J1631−479 was also observed by the Monitor of All-sky X–ray Image (Matsuoka et al. 2009), and their data have been used in our analysis.

We use `xspec` v12.10.1 (Arnaud 1996) in order to fit each spectral state in the 30-200 keV energy range.

3   SPECTRAL ANALYSIS RESULTS

In order to study the hard X-ray spectral properties of MAXI J1631−479, we analyze the *INTEGRAL*/IBIS data taken during the three *INTEGRAL* revolutions, over the energy range 30-200 keV.

The time evolution and the respective behavior of the different spectral states are shown in Figure 1, where the 1-day binned light curves from MAXI[1] and *Swift*/BAT[2] are reported. The variation of the source along the outbursts is clearly visible from these lightcurves. The epochs of the *NuSTAR* (red line), ATCA (green line) and *INTEGRAL* (blue line) observations are shown for comparison. The flux conversion into mCrab was obtained with the following factors: 1mCrab∼0.00022 ct cm^{-2} s^{-1} and 1Crab∼3.8 ph cm^{-2} s^{-1} for *Swift*/*BAT*[1] and *MAXI*/*GSC*[2], respectively.

Although the source is within the *BAT* confusion radius of another X-ray transient, namely AX J1631.9−4752,

---

[1] *http://MAXI/GSC.riken.jp/top/slist.html*
[2] *https://swift.gsfc.nasa.gov/results/transients*

the *MAXI/GSC* light curve is not contaminated significantly. Indeed, during the monitoring period, while MAXI J1631−479 is detected at high flux levels, AX J1631.9−4752 is continuously detected at low level by *Swift/BAT*. The lack of contamination is confirmed by the *INTEGRAL*/IBIS map, where the emission from AX J1631.9−4752 is lower than ∼10 mCrab (3σ upper limit) in the 30-50 keV energy range.

We performed an analysis for spectral variability by plotting the hardness versus total emission in two energy bands. Figure 1 (right panel) shows the hardness-intensity diagram for the *MAXI/GSC* and *Swift/BAT* observations. The hardness is derived using the ratio between the fluxes in these two X-ray bands $F^{BAT}_{(15-50\,\mathrm{keV})}/F^{MAXI}_{(2-10\,\mathrm{keV})}$ and is plotted versus the total flux $F^{BAT}_{(15-50\,\mathrm{keV})}+F^{MAXI}_{(2-10\,\mathrm{keV})}$. Each point corresponds to 1 day of time integration and only epochs for which both soft and hard X-ray data are available have been used.

The different colored points in the right panel of Figure 1 represent six regions we have selected from the temporal intervals. These regions correspond to the different spectral states identified in the *MAXI/GSC* and *Swift/BAT* light curves, as shown in the left panel of Figure 1:

- 1st *epoch*: from MJD 58470 to 58478, the source shows a low flux level at soft energy and a high flux level in the hard X-ray band. This is typical behavior for the low/hard state (black points).
- 2nd *epoch*: from MJD 58479 to 58485, the source shows an increasing soft flux and a decline in hard X-ray, indicating a transition from the low/hard state to a high/soft state (red points).
- 3rd *epoch*: from MJD 58486 to 58506, the source shows a high soft flux level and is low in hard X-rays, indicative of a standard high/soft state (green points).
- 4th *epoch*: from MJD 58507 to 58514, the source shows unusual variability during this period. A decline in the soft X-ray emission is observed for three days followed by a sudden increase lasting for two–three days. Unfortunately, no soft X-ray data are available for the two days in between this change in the emission. In the same period, the source experienced an increase in hard X-rays corresponding to a soft X-ray decline, followed by a slight drop in hard flux with a corresponding enhancement in soft X-rays. This behaviour suggests that during the first three days the source started a transition from the high/soft state to a low/hard state. Afterwards it suddenly reversed this trend towards a new state (blue points).
- 5th *epoch*: from MJD 58515 to 58522, the source shows a high flux level in both soft and hard bands. This suggests that in this epoch MAXI J1631−479 can be considered being in a intermediate state (light blue points), where the X-ray emission can be explained with hybrid (thermal and non-thermal) Comptonization models.
- 6th *epoch*: from MJD 58529 to 58540, the source transits towards a soft state at low luminosity level (green empty points).

The IBIS/*INTEGRAL* observations occurred during the 4th epoch and fall in the region of the blue points in the right panel of Figure 1 and marked as blue vertical lines in the left panel, for comparison. The IBIS observations carried out during revolution 2048 fall close in time to the first

MAXI/GSC blue point (point A in figure 1, right panel). No *MAXI/GSC* and *BAT* simultaneous data are available for the second and third IBIS/*INTEGRAL* observations.

The left panel of Figure 2 shows the 2–4 keV and 4–10 keV MAXI light curves (bin time 6h), together with the 30–60 keV IBIS light curve (bin time 2000 s). The variation in the source spectral state during the *INTEGRAL* observation is clearly visible. In particular, during the first *INTEGRAL*/IBIS observation (revolution 2048) the source is in a high/soft state, however during the subsequent observations (revolutions 2049 and 2050) the source flux increased by a factor ∼2 in the 30–60 keV energy range, indicating the occurrence of the transition to a low/hard state.

We performed spectral analysis for the three *INTEGRAL* revolutions separately.

First, we attempted to fit the spectra using a simple power law model. For the spectrum of revolution 2048 we obtain a spectral index of 3.1 ± 0.1 and a χ^2/d.o.f. of 34/20, with residuals at high energies. Then we modelled these data with a cut-off power-law, which resulted in a best-fit with χ^2/d.o.f.=25/19. In this case, we obtain a spectral index $\Gamma = 2.1^{+0.6}_{-0.5}$, $E_{\mathrm{cutoff}} = 62^{+20}_{-22}$ keV and a high energy flux of $F_{30-200\,\mathrm{keV}}=(2.8\pm0.1)\times10^{-9}$ erg cm^{-2} s^{-1} . However we remark that by using the latter model the fit improvement is only marginal. Indeed, applying the appropriate F-test statistics for model comparison (Press et al. 2007; see also Orlandini et al. 2012), we obtain an improvement probability of only about 28%.

In order to obtain the physical parameters of the source, we also fit this dataset using a model describing the Comptonization of soft photons in a hot plasma (`comptt` in `xspec`, Titarchuk 1994). The resulting Comptonized plasma has a temperature of ∼29 keV and optical depth $\tau \sim 0.7$, with the input soft photon Wien temperature fixed at the default value (0.1 keV), not affecting the high energy spectrum. The best fit parameters are listed in Table 1. In the right panel of Figure 2 the spectrum of revolution 2048, together with residuals with respect to the cut-off power-law model are shown (black filled triangles).

When fitting the IBIS data of revolutions 2049 and 2050 separately, we obtain similar results, both in flux and in spectral shape. This is also evident from Figure 1 (right panel), where IBIS observations fall in the same hardness region (between points C and D). Using a simple power law model, we obtain a spectral index of 3.0 ± 0.2, a flux of $F_{30-200\,\mathrm{keV}}=(5.9\pm0.2)\times10^{-9}$ erg cm^{-2} s^{-1} and a χ^2/d.o.f. of 20/20 for revolution 2049 and for revolution 2050 ($\Gamma = 3.0\pm0.2$, a flux of $F_{30-200\,\mathrm{keV}}=(5.9\pm0.2)\times10^{-9}$ erg cm^{-2} s^{-1} and a χ^2/d.o.f. of 20/20). No high energy cutoff is required for these data. Taking into account the spectral similarity, similar flux levels and hardness, data from revolutions 2049 and 2050 have been combined to improve the statistical quality of the spectra and to better constrain the physical parameters, as reported in Table 1. The resulting spectrum together with the residuals with respect to the power law model are shown in Figure 2 with red squares (right panel).

4   DISCUSSION

MAXI J1631−479 belongs to a class of transient systems showing spectral state transitions.
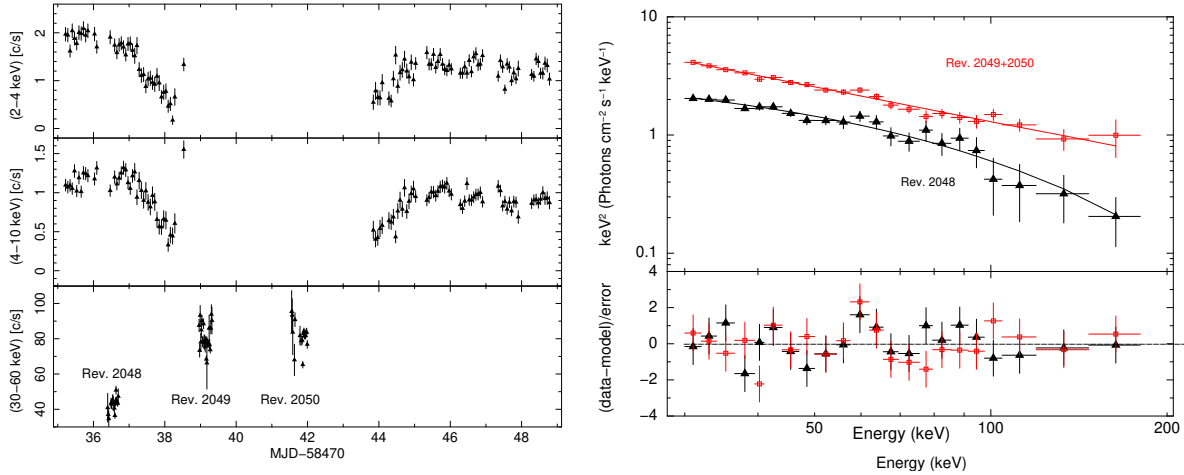
Figure 2. *Left panel*: Zoomed-in light curves during the *INTEGRAL* observation period, with the top (2-4 keV) and middle (4-10 keV) *MAXI/GSC* light curves (in 6h bins, data from *http://maxi.riken.jp/top/slist.html*) compared with the bottom (30-60 keV) IBIS light curve (in 2000 s bins) over the three *INTEGRAL* revolutions. *Right panel*: *INTEGRAL*/IBIS unfolded spectra and residuals in sigma during revolution 2048 (in black) and during revolutions 2049 and 2050 (in red). Model is a cut-off power-law for the first data set and a simple power-law for the second one.

Table 1. Spectral results of the IBIS/INTEGRAL observations.

Model	Parameter	Rev. 2048	Rev. 2049+2050
		IBIS Exposure	
		13 ks	36 ks
Power Law	Γ	3.1 ± 0.1	2.98 ± 0.04
	$F^a_{30-200\,\text{keV}}$	3.0 ± 0.1	5.9 ± 0.1
	χ^2/d.o.f.	34/20	20/20
Cutoff	Γ	$2.1^{+0.6}_{-0.5}$	...
Power law	E_{cutoff} (keV)	62^{+20}_{-22}	...
	$F^a_{30-200\,\text{keV}}$	2.8 ± 0.1	...
	χ^2/d.o.f.	25/19	...
Comptt	kT_e (keV)	29^{+43}_{-10}	...
	τ	0.7 ± 0.4	...
	$F^a_{30-200\,\text{keV}}$	2.9 ± 0.1	...
	χ^2/d.o.f.	25/19	...

^{a} Flux in units of 10^{-9} erg cm^{-2} s^{-1}

When it starts to transit towards a hard state (Negoro et al. 2019) the *INTEGRAL*/IBIS observation shows that the source had a high X-ray flux $F_{30-200\,\text{keV}} \sim 3\times10^{-9}$ erg cm^{-2} s^{-1} and a hard spectrum (blue lines of Figure 1, at ~ 58506 MJD) and it is dominated by a hard X-ray Comptonized component, arising from inverse Compton scattering of soft thermal photons in a hot corona with $kT_e \sim 29$ keV and $\tau \sim 0.7$.

This intermediate value of the electron temperature confirms that the source is not in a standard high/soft or low/hard state. Joinet et al. (2008) found a similar corona temperature (~ 30 keV) when the microquasar GRO J1655−40 transits from low/hard to hard/intermediate state. This temperature of the thermal population was also previously

observed in GX 339-4 (Motta et al. (2009)) before the source transits from low/hard to hard/intermediate state. In this case the high energy cutoff disappears near the hard/intermediate-soft/intermediate transition. This behavior is similar to the MAXI J1631−479 evolution: the high energy cutoff was not detected by *INTEGRAL*/IBIS when it moved towards a soft state at low luminosity. Indeed it is detected up to about 200 keV though the best fit is a simple power law ($\Gamma \sim 3$) suggesting a non-thermal origin for this X-ray emission. This behavior continued in later observations, as noted in Figure 1, where the light blue points show that the source moved towards an intermediate state at a high flux in both soft and hard bands.

Transitions from low/hard state to high/soft state and then towards an intermediate state with high flux at these energies has previously been observed in black hole systems (Done et al. 2007; Belloni 2018). The no-detection of a high energy cutoff using X-ray data up to 200 keV suggests that the hard X-ray emission may not be produced by thermal Comptonization. The observed spectrum in the intermediate state can be produced by Compton scattering on a non-thermal electron population (Gilfanov 2010) or by a mixture of thermal and non-thermal features (Coppi 1999; Del Santo et al. 2008). The shape of the hysteresis diagram of MAXI J1631−479 appears similar to the one of the black hole X-ray binary XTE J1550−564 (Russell et al. 2010). Moreover, MAXI J1631−479 showed radio emission at 5.5 and 9 GHz when it was in the high/soft state (Russell et al. 2019) and a similar behaviour was reported for XTE J1550−564. For that system, the authors were able to isolate the non-thermal emission from the jet and demonstrated that the synchrotron jet may dominate in hard X-ray when the source fades in the low/hard state, at very low luminosity level. In this case, the jet produces $\sim 100\%$ of the emission when the soft (3-10 keV) and hard (100-250 keV) fluxes are comparable.

In the case of MAXI J1631−479, Figure 2 shows that X-ray power-law component is observed when the soft and

hard fluxes are comparable, although the energy ranges are slightly different from those used for XTE J1550−564.

Unfortunately, for this source neither the distance nor the mass of the central object are known. In order to estimate the possible luminosity range of MAXI J1631−479 , we used the extreme values of distances and masses known so far for X-ray binaries. In particular, the distances span from 1 kpc (McClintock & Remillard 1986) to 27 kpc (Casares et al. 2004), while the black hole masses can assume values from 4 M$_\odot$ (Özel et al. 2010) to 15.65 M$_\odot$ (McClintock & Remillard 1986; Orosz et al. 2007). Using realistic values for a LMXB, the luminosity of MAXI J1631−479 during the intermediate state can vary from 5×10^{-1} L$_{Edd}$ (distance=20 kpc and mass=4 M$_\odot$) to 3.5×10^{-4} L$_{Edd}$ (distance=2 kpc and mass=15.65 M$_\odot$). Thus, as the emission of the jet in X-ray band can be dominant when the luminosity is between L$\sim2\times10^{-3}$ L$_{Edd}$ and L$\sim2\times10^{-4}$ L$_{Edd}$ (Russell et al. 2010), the wide range of possible values derived for the luminosity of MAXI J1631−479 do not allow us to exclude a contribute of the jet to the X-ray emission in MAXI J1631−479.

The lack of a high energy cut-off indicates that the X-ray emission from MAXI J1631−479 has a non-thermal origin that can be produced either by Comptonization of non-thermal electron population or by a hybrid thermal/non-thermal electron distribution.

The source outburst evolution and the typical times of the outburst suggest the BH nature of this source. Indeed, assuming the time spent to reach from 10% to 90% of the flux peak as the rise time and the reverse for the decay time, we obtained τ_{rise} ~15 days and τ_{decay} ≥50 days though it seems the outburst has not yet ended (see Fig 1, left panel). These values are compatible with decay and rise times for BH and incompatible with much faster evolution times for NS, reported in the statistical study of Yan and Yu (2015). This result is in agreement with previous studies performed at different energy bands during the same outburst. When MAXI J1631−479 transits from a low/hard to high/soft state (red line of Figure 1, ~58480 MJD) the *NuSTAR* 3–79 keV spectrum is well modelled by a disk-blackbody with a temperature of ~1.12 keV, a power-law with a photon index of ~2.39 and iron Kα emission line with an equivalent width of $\sim$ 90 eV (Miyasaka et al. 2018). Based on these spectral characteristics the authors suggested the system as a black hole binary in the high/soft state with most of the flux in the soft X-ray band (F$_{2-10\,keV}$=1.7×10^{-8} erg cm^{-2} s^{-1} and F$_{3-79\,keV}$=1.8×10^{-8} erg cm^{-2} s^{-1}). Russell et al. (2019) also report a similar conclusion on the source nature by using the radio observation performed on 2019 January 13 (green line of Figure 1, ~58496 MJD). A radio counterpart of MAXI J1631−479 was detected by Australia Telescope Compact Array (ATCA) with a flux density of F$_{5.5\,GHz}$=(630 ± 50) µJy and a radio luminosity L$_{5\,GHz}$=(9.5 ± 0.8)×10^{28} (d/5 kpc)^2 erg s^{-1}.

This radio emission could indicates the presence of a compact jet, as it was detected during the transition from high/soft to low/hard state, i.e. when synchroton jet emission could became dominant at X-ray wavelengths and at low luminosities.

REFERENCES

Arnaud K. A., 1996, in Jacoby G. H., Barnes J., eds, Astronomical Society of the Pacific Conference Series Vol. 101, Astronomical Data Analysis Software and Systems V. p. 17

Belloni T. M., 2018, arXiv e-prints, p. arXiv:1803.03641

Belloni T. M., Motta S. E., 2016, in Bambi C., ed., Astrophysics and Space Science Library Vol. 440, Astrophysics of Black Holes: From Fundamental Aspects to Latest Developments. p. 61 (arXiv:1603.07872), doi:10.1007/978-3-662-52859-4˙2

Burrows D. N., et al., 2004, in Flanagan K. A., Siegmund O. H. W., eds, Proc. SPIEVol. 5165, X-Ray and Gamma-Ray Instrumentation for Astronomy XIII. pp 201–216, doi:10.1117/12.504868

Casares J., Zurita C., Shahbaz T., Charles P. A., Fender R. P., 2004, ApJ, 613, L133

Coppi P. S., 1999, in Poutanen J., Svensson R., eds, Astronomical Society of the Pacific Conference Series Vol. 161, High Energy Processes in Accreting Black Holes. p. 375 (arXiv:astro-ph/9903158)

Courvoisier T. J.-L., et al., 2003, A&A, 411, L53

Del Santo M., Malzac J., Jourdain E., Belloni T., Ubertini P., 2008, MNRAS, 390, 227

Done C., Gierliński M., Kubota A., 2007, A&ARv, 15, 1

Fender R., 2004, New Astron. Rev., 48, 1399

Fender R., 2016, Astronomische Nachrichten, 337, 381

Fender R., Belloni T., 2012, Science, 337, 540

Fender R. P., Belloni T. M., Gallo E., 2004, MNRAS, 355, 1105

Gardenier D. W., Uttley P., 2018, MNRAS, 481, 3761

Gehrels N., et al., 2004, ApJ, 611, 1005

Gilfanov M., 2010, X-Ray Emission from Black-Hole Binaries. p. 17, doi:10.1007/978-3-540-76937-8˙2

Joinet A., Kalemci E., Senziani F., 2008, ApJ, 679, 655

Kim S.-L., et al., 2016, Journal of Korean Astronomical Society, 49, 37

Kobayashi K., et al., 2018, The Astronomer's Telegram, 12320

Kong A. K. H., 2019, The Astronomer's Telegram, 12504

Krimm H. A., et al., 2013, ApJS, 209, 14

Matsuoka M., et al., 2009, PASJ, 61, 999

McClintock J. E., Remillard R. A., 1986, ApJ, 308, 110

Miyasaka H., Tomsick J. A., Xu Y., Harrison F. A., 2018, The Astronomer's Telegram, 12340

Motta S., Belloni T., Homan J., 2009, MNRAS, 400, 1603

Negoro H., et al., 2019, The Astronomer's Telegram, 12421

Onori F., et al., 2019, The Astronomer's Telegram, 12418

Orosz J. A., et al., 2007, Nature, 449, 872

Özel F., Psaltis D., Narayan R., McClintock J. E., 2010, ApJ, 725, 1918

Russell D. M., Maitra D., Dunn R. J. H., Markoff S., 2010, MNRAS, 405, 1759

Russell T. D., van den Eijnden J., Degenaar N., 2019, The Astronomer's Telegram, 12396

Shin M.-S., Kim J.-W., Chang S.-W., Lee C.-U., Kim S.-L., 2019, The Astronomer's Telegram, 12438

Titarchuk L., 1994, ApJ, 434, 570

Ubertini P., et al., 2003, A&A, 411, L131

Astronomy & Astrophysics

The stellar and wind parameters of six prototypical HMXBs and their evolutionary status[*]

R. Hainich[1], L. M. Oskinova[1], J. M. Torrejón[2], F. Fuerst[3], A. Bodaghee[4], T. Shenar[1,5],
A. A. C. Sander[1,6], H. Todt[1], K. Spetzer[4], and W.-R. Hamann[1]

[1] Institut für Physik und Astronomie, Universität Potsdam, Karl-Liebknecht-Str. 24/25, 14476 Potsdam, Germany
e-mail: rhainich@astro.physik.uni-potsdam.de

[2] Instituto Universitario de Física Aplicada a las Ciencias y las Tecnologías, Universidad de Alicante, 03690 Alicante, Spain

[3] European Space Astronomy Centre (ESA/ESAC), Science Operations Department, Villanueva de la Cañada, Madrid, Spain

[4] Georgia College and State University, Department of Chemistry, Physics and Astronomy, 221 N. Wilkinson St., Milledgeville, GA 31061, USA

[5] Institute of astrophysics, KU Leuven, Celestijnlaan 200D, 3001 Leuven, Belgium

[6] Armagh Observatory and Planetarium, College Hill, Armagh, BT61 9DG, UK

ABSTRACT

Context. High-mass X-ray binaries (HMXBs) are exceptional astrophysical laboratories that offer a rare glimpse into the physical processes that govern accretion on compact objects, massive-star winds, and stellar evolution. In a subset of the HMXBs, the compact objects accrete matter solely from winds of massive donor stars. These so-called wind-fed HMXBs are divided in persistent (classical) HMXBs and supergiant fast X-ray transients (SFXTs) according to their X-ray properties. While it has been suggested that this dichotomy depends on the characteristics of stellar winds, they have been poorly studied.

Aims. With this investigation, we aim to remedy this situation by systematically analyzing donor stars of wind-fed HMXBs that are observable in the UV, concentrating on those with neutron star (NS) companions.

Methods. We obtained *Swift* X-ray data, HST UV spectra, and additional optical spectra for all our targets. The spectral analysis of our program stars was carried out with the Potsdam Wolf–Rayet model atmosphere code.

Results. Our multi-wavelength approach allows us to provide stellar and wind parameters for six donor stars (four wind-fed systems and two OBe X-ray binaries). The wind properties are in line with the predictions of the line-driven wind theory. Based on the abundances, three of the donor stars are in an advanced evolutionary stage, while for some of the stars, the abundance pattern indicates that processed material might have been accreted. When passing by the NS in its tight orbit, the donor star wind has not yet reached its terminal velocity but it is still significantly slower; its speed is comparable with the orbital velocity of the NS companion. There are no systematic differences between the two types of wind-fed HMXBs (persistent versus transients) with respect to the donor stars. For the SFXTs in our sample, the orbital eccentricity is decisive for their transient X-ray nature. The dichotomy of wind-fed HMXBs studied in this work is primarily a result of the orbital configuration, while in general it is likely that it reflects a complex interplay between the donor-star parameters, the orbital configuration, and the NS properties. Based on the orbital parameters and the further evolution of the donor stars, the investigated HMXBs will presumably form Thorne–Żytkow objects in the future.

Key words. X-rays: binaries – binaries: close – stars: early-type – stars: atmospheres – stars: winds, outflows – stars: mass-loss

1. Introduction

High-mass X-ray binaries (HMXBs) are binary systems consisting of a massive star, also denoted as the donor star, and a compact object, which is either a neutron star (NS) or a black hole (BH). These systems are characterized by high X-ray luminosities ($L_X \approx 10^{36}\,\mathrm{erg\,s^{-1}}$) emitted by stellar material accreted onto the compact object. Multi-wavelength studies of HMXBs offer the opportunity to contribute to a variety of physical and astrophysical research areas, including but not limited to accretion physics, stellar evolution, and the precursors of gravitational wave events.

The HMXB population encompasses different types of binary systems. Depending on the orbital configuration, the evolution state of the donor star, and how the matter is channeled to the compact object, one can distinguish between different types: in Roche–lobe overflow (RLOF) systems, the compact object directly accretes matter via the inner Lagrangian point (L1). In wind-fed HMXBs, the compact object accretes from the wind of the donor star. In OBe X-ray binary systems, the donor stars are usually OB-type dwarfs with a decretion disk. The compact object in these kind of systems either accretes matter from these disks or from the donor-star winds.

The wind-fed HMXBs are of particular interest (for recent reviews see Martínez-Núñez et al. 2017 and Sander 2019). Here the compact object is situated in and accretes solely from the wind of the massive star, usually a supergiant. Therefore, these objects are also denoted as SgXBs. Ostriker & Davidson (1973) realized that accretion from a stellar wind onto a compact object is sufficient to power the high X-ray luminosities observed for these objects. Depending on their X-ray properties, wind-fed HMXBs are distinguished into classical (or persistent) HMXBs

and the so-called Supergiant Fast X-ray Transients (SFXTs). While the former always exhibit an X-ray luminosity on the order of $L_X \approx 10^{36}\,\mathrm{erg\,s^{-1}}$, the latter are characterized by quiescent X-ray phases with $L_X \approx 10^{32} - 10^{34}\,\mathrm{erg\,s^{-1}}$, which are interrupted by sporadic X-ray flares ($L_X \geq 10^{36}\,\mathrm{erg\,s^{-1}}$). Although the origin of this dichotomy is hitherto not understood, it is assumed that the donor stars play an important role in this picture (e.g., in't Zand et al. 2007; Oskinova et al. 2012; Krtička et al. 2015; Giménez-García et al. 2016; Sidoli & Paizis 2018).

The Bondi–Hoyle–Lyttleton accretion mechanism (Hoyle & Lyttleton 1939; Bondi & Hoyle 1944) predicts that the X-ray luminosity (L_X) of a wind-fed HMXB is very sensitive to the mass-loss rate ($\dot{M}$) and the wind velocity (v_{wind}) of the donor star,

$$L_X \propto \dot{M}/v_{\mathrm{rel}}^4, \tag{1}$$

where $v_{\mathrm{rel}} = |v_{\mathrm{wind}} + v_{\mathrm{orb}}|$ is the relative velocity of the wind matter captured by the compact object. The orbital velocity (v_{orb}) is often neglected while evaluating Eq. (1), since stellar winds of OB-type stars have high terminal velocities, sometimes in excess of $2000\,\mathrm{km\,s^{-1}}$. However, most HMXBs are compact systems with orbital periods of a few days (Walter et al. 2015). This implies that the distance between the compact objects and the donor stars are relatively small, which means that donor star winds will not have reached their terminal velocities at the position of the compact objects. On the other hand, the v_{orb} can be quite high, especially during periastron in eccentric systems. Therefore, it is of high importance to reliably quantify the role of v_{wind} and v_{orb} in these kind of systems, especially because of the strong dependence of L_X on v_{rel}.

The X-rays emitted by the compact object can, in turn, have a significant impact on the donor star's atmosphere and wind. These X-rays strongly ionize a certain part of the donor star wind, which can lead to significant changes in the observed spectra of these sources. This is demonstrated by van Loon et al. (2001) for important UV wind-lines using phase resolved spectroscopy of several donor stars. The underlying mechanism is first discussed by Hatchett & McCray (1977), which is, therefore, also denoted as the Hatchett–McCray effect. Depending on the wind density, the orbital configuration, and the amount of X-rays emitted by the compact object, its influence on the donor wind can be quite diverse (e.g., Blondin et al. 1990; Blondin 1994).

For high X-ray luminosities, Krtička et al. (2015) and Sander et al. (2018) show that the donor wind velocity field in the direction of the compact object can be significantly altered. This is because the radiation of the compact object changes the ionization balance in the donor star wind, leading to a modification of the radiative acceleration of the wind matter. In extreme cases the donor star winds can be virtually stopped or even disrupted.

In this work, we concentrate on wind-fed HMXBs with NS companions and moderate X-ray luminosities, where the Hatchett–McCray effect is of modest importance and the winds are not significantly disturbed. However, even for those systems, the X-rays need to be accounted for during the spectral analysis, since they might have a noticeable effect on the ionization balance in the donor star wind and consequently on the spectra.

Despite the strong connection between the X-ray properties of wind-fed HMXBs and the properties of the donor stars, only a few of these stars have been studied so far. One reason for this deficiency is that most of the wind-fed HMXBs are highly obscured. Therefore, the most important wavelength range for the analysis of OB-star winds, the UV that provides essential wind diagnostics, is often not accessible. In this work,

we analyze four wind-fed HMXBs and two OBe X-ray binaries that are observable in the UV.

The paper is organized as follows: in Sect. 2, we introduce our sample, while the data used in this work are described in Sect. 3. The atmosphere models and the fitting process are outlined in Sect. 4. Our results are presented in Sect. 5, and discussed in Sects. 6 and 7. The summary and conclusions can be found in Sect. 9. Additional tables, comments on the individual objects, and the complete spectral fits are presented in Appendices A–C, respectively.

2. The sample

While about 30 wind-fed HMXBs are known in our Galaxy (see Martínez-Núñez et al. 2017 for a recent compilation), most of these objects are located in the Galactic plane (Chaty 2008). Therefore, they are often highly obscured and are not observable in the UV. However, ultraviolet resonance lines allow to characterize even the relatively weak winds of B-type stars (e.g., Prinja 1989; Oskinova et al. 2011). Since the determination of wind parameters is the main objective of this study, we restrict our sample to those wind-fed HMXBs that are observable in the UV.

In addition to Vela X-1, which has been analyzed previously by Giménez-García et al. (2016), only four more wind-fed HMXBs meet the above condition, namely HD 153919 (4U 1700-37), BD+60 73 (IGR J00370+6122), LM Vel (IGR J08408-4503), and HD 306414 (IGR J11215-5952). The latter two systems are SFXTs, while the first one is a persistent HMXB, and BD+60 73 (IGR J00370+6122) exhibits properties of both types. Our sample also includes the Be X-ray binary HD 100199 (IGR J11305-6256) and BD+53 2790 (4U 2206+54), which is classified as an Oe X-ray binary or as a persistent wind-fed binary with a non evolved donor. The latter classification is based on its X-ray properties, while the former is a result of the prominent hydrogen emission lines that are visible in optical spectra of this object. These lines are most likely formed in a decretion disk of the donor star. Thus, this systems might actually be intermediate between the classical wind-fed HMXB and the OBe X-ray binaries. The HMXB type, the spectral classification of the donor, and common alias names of the investigated systems are given in Table 1.

The orbital parameters of the investigated systems and the spin period of the neutron stars are compiled from the literature and listed in Table 2. The only exception is HD 100199 because neither the orbit nor the properties of its NS are known.

3. The data

3.1. Spectroscopy

For our UV survey of wind-fed HMXBs, we made use of the Space Telescope Imaging Spectrograph (STIS, Woodgate et al. 1998; Kimble et al. 1998) aboard the HST. These high resolution, high S/N spectra (Proposal ID: 13703, PI: L. M. Oskinova) cover important wind diagnostics in the range 1150–1700 Å. In this paper, we use the automatically reduced data that are provided by the HST archive. For three of our program stars, far UV data obtained with the Far Ultraviolet Spectroscopic Explorer (FUSE, Moos et al. 2000) were retrieved from the MAST archive.

These data are complemented by optical spectroscopy from different sources. For HD 100199, HD 306414, LM Vel, and HD 153919, we use data taken with the Fiber-fed Extended Range Optical Spectrograph (FEROS, Kaufer et al. 1999)

Table 1. Spectral classifications, distances, and common aliases.

Name	HMXB type	Spectral type of donor	Reference	Distance [a] (kpc)	Alias names
HD 153919	Persistent	O6 Iafpe	1	$1.7^{+0.3}_{-0.2}$	4U 1700-37, V* V884 Sco
BD+60 73	Intermediate	BN0.7 Ib	2	$3.4^{+0.3}_{-0.2}$	IGR J00370+6122
LM Vel	SFXT	O8.5 Ib-II(f)p	3	$2.2^{+0.2}_{-0.1}$	HD 74194, IGR J08408-4503
HD 306414	SFXT	B0.5 Ia	4	$6.5^{+1.4}_{-1.1}$	IGR J11215-5952
BD+53 2790	Persistent / Oe X-ray	O9.5 Vep	5	$3.3^{+0.4}_{-0.3}$	4U 2206+54
HD 100199	Be X-ray	B0 IIIne	6	$1.3^{+0.1}_{-0.1}$	IGR J11305-6256

Notes. [a]The distances are adopted from Bailer-Jones et al. (2018). These distances are based on the *Gaia* DR2 measurements (Gaia Collaboration 2018) and were calculated by means of a Bayesian approach assuming an exponentially decreasing space density with the distance.
References. (1) Sota et al. (2014); (2) González-Galán et al. (2014); (3) Sota et al. (2014); (4) Lorenzo et al. (2014); (5) Blay et al. (2006); (6) Garrison et al. (1977).

Table 2. Orbital parameters and the spin period of the neutron star.

Identifier	Orbital period (d)	Refs.	Eccentricity	Refs.	T_0 (MJD)	Ref.	Spin period (s)	Refs.
HD 153919	3.411660 ± 0.000004	1	$0.008 - 0.22$	1, 2	49149.412 ± 0.006	1	–	
BD+60 73	15.661 ± 0.0017	3	0.56 ± 0.07	3	55084.0 ± 0.4	3	346.0	4
LM Vel	9.5436 ± 0.0002	5	0.63 ± 0.03	5	54634.45 ± 0.04	5	–	
HD 306414	$\sim$164.6	6	$\sim$0.8 [a]	7	–		186.78	6, 8
BD+53 2790	$\sim$9.568	9, 10, 11, 12	0.30 ± 0.02	12	–		5750.0	13

Notes. [a]Uncertain.
References. (1) Islam & Paul (2016); (2) Hammerschlag-Hensberge et al. (2003); (3) González-Galán et al. (2014); (4) in't Zand et al. (2007); (5) Gamen et al. (2015); (6) Romano et al. (2009); (7) Lorenzo et al. (2014); (8) Swank et al. (2007); (9) Corbet & Peele (2001); (10) Ribó et al. (2006); (11) Reig et al. (2009); (12) Stoyanov et al. (2014); (13) Torrejón et al. (2018).

mounted at the 2.2 m telescope operated at the European Southern Observatory (ESO) in La Silla. These data sets were downloaded from the ESO archive. From the same repository, we also retrieved FOcal Reducer and low dispersion Spectrograph (FORS, Appenzeller et al. 1998) spectra for HD 153919. Optical spectra for BD+60 73 were kindly provided by A. González-Galán. These spectra were taken with the high-resolution FIbre-fed Echelle Spectrograph (FIES, Telting et al. 2014) mounted on the Nordic Optical Telescope (NOT) and published in González-Galán et al. (2014). For BD+53 2790, we downloaded a low resolution spectrum from the VizieR archive that was taken by Munari & Zwitter (2002) with a Boller & Chivens Spectrograph of the Asiago observatory. In addition, we obtained an optical spectrum of BD+53 2790 with a DADOS spectrograph in combination with two different SBIG cameras (SFT8300M & ST-8XME) mounted to the Overwhelmingly Small Telescope (OST) of the student observatory at the University of Potsdam. Default data reduction steps were performed for this data set using calibration data (dome flats, dark frames, Hg Ar-lamp spectrum) taken immediately after the science exposures. Finally Near-IR spectroscopy was obtained during the night of 2014 September 1, using the Near Infrared Camera and Spectrograph (NICS) mounted at the 3.5-m Telescopio Nazionale *Galileo* (TNG) telescope (La Palma island). Medium-resolution spectra (3.5 Å pixel^{-1}) were taken with the H and K_b grisms under good seeing conditions. Details on the reduction process can be seen in Rodes-Roca et al. (2018). The individual spectral exposures used in this work are listed in Table A.1. In this table, we also give the phase at which the observations were taken for those systems where ephemerides are available (see Table 2 and references therein).

3.2. Photometry

We compiled *UBVRI* photometry from various sources (Anderson & Francis 2012; Mermilliod 2006; Zacharias et al. 2004; Reig & Fabregat 2015; DENIS Consortium 2005) for all our program stars. *G*-band photometry was retrieved from the *Gaia* DR1 release (Gaia Collaboration 2016). Near-infrared photometry (J, H, K_S) was obtained from Cutri et al. (2003), while WISE photometry is available from Cutri et al. (2012) for all our targets. Moreover, we made use of MSX infrared photometry (Egan et al. 2003) for HD 153919. The complete list of photometric measurements used for the individual objects is compiled in Table A.2.

3.3. X-ray data

For all our HST observations, we obtained quasi-simultaneous X-ray data with the *Neil Gehrels Swift* Observatory (*Swift*, Gehrels et al. 2004). In addition, strictly simultaneous *Chandra* X-ray and HST UV observations were performed for HD 153919 (*Chandra* ObsID. 17630, exposure time 14.6 ks).

The data obtained with the X-ray telescope (XRT, Burrows et al. 2005) aboard *Swift* are reduced using the standard XRT

pipeline as part of HEASOFT v6.23. To extract the source spectra from data gathered while the XRT was in the photon counting (PC) mode, we used a circular region centered at its J2000 coordinates with a 25″ radius or 80″ radius depending on the source characteristics. Background counts were extracted from an annulus encompassing the source extraction region. When XRT was in the window timing mode (WT), the source extraction region consisted of a square with a width of 40 pixels while background counts were extracted from a similar-sized region situated away from the source.

The observed spectra were fitted using a suit of various X-ray spectral fitting software packages. For all objects, the photoionization cross-sections from Verner et al. (1996) and abundances from Wilms et al. (2000) were employed. The goal of X-ray spectral fitting was to provide the parameters describing the X-ray radiation field in the format required for the stellar atmosphere modeling (see Sect. 4.1). X-ray spectra of HMXBs are typically well represented by power law spectral models, which are not yet implemented in our stellar atmosphere model. Therefore, we decided to fit the observed spectra using a fiducial black body spectral model. The fitting returns a "temperature" parameter T_X, which is not-physical but is employed to describe the spectral hardness and X-ray photon flux.

The *Swift* XRT observation of HD 153919 was taken in the WT mode. We extracted 43 640 net source counts during 5270 s of exposure time. After rebinning the spectral data to contain a minimum of 20 net counts per bin, we fit an absorbed ($N_H = 15^{+4}_{-2} \times 10^{22}$ cm^{-2}) blackbody ($k_B T = 2.1 \pm 0.1$ keV) plus a power-law component ($\Gamma = 4 \pm 1$). The observed X-ray flux is $1.2^{+0.2}_{-0.1} \times 10^{-9}$ erg cm^{-2} s^{-1}. *Chandra* observations of HD 153919 are presented by Martinez-Chicharro et al. (2018). Towards the end of the observation which lasted about 4 h, the source experienced a flare with X-ray flux increasing by a factor of three. Our HST observations were partially obtained during the end of this flare.

Nineteen source (+background) counts were gathered during the XRT observation of BD+60 73 taken on the same day as the HST observation (ObsID 00032620025). Without rebinning the data, and assuming C-statistics (Cash 1979), we fit an absorbed blackbody model and obtained spectral parameters that were poorly constrained ($N_H = 4^{+28}_{-3} \times 10^{22}$ cm^{-2} and $k_B T \sim 1$ keV) with an observed flux of 6.2×10^{-14} erg cm^{-2} s^{-1}.

HD 306414 was not detected in any of the contemporaneous *Swift* observations, and therefore we could not measure its X-ray flux. HD 100199 was marginally detected with 12 ± 4 photons in an observation one day before the HST observation (ObsID 00035224007). We estimate a flux of $2.7^{+3.9}_{-1.8} \times 10^{-13}$ erg cm^{-2} s^{-1} from these data.

LM Vel was also very X-ray faint during the HST observation (ObsID 00037881107). We therefore use *Swift* data taken a few days earlier (ObsID 00037881103) to measure the spectral shape. We find that a thermal blackbody model describes the data well, and use this model to fit the simultaneous data. There we find a flux of 5.8×10^{-13} erg cm^{-2} s^{-1} between 3–10 keV.

For BD+53 2790 (4U 2206+543), we extracted 2511 net source counts during an 1106 s XRT observation in WT mode. The spectral data were arranged in order to contain at least 20 counts per bin, and were then fit with an absorbed blackbody model ($N_H \leq 8 \times 10^{21}$ cm^{-2} and $k_B T = 1.3 \pm 0.1$ keV). The model derived flux is $1.3 \pm 0.1 \times 10^{-11}$ erg cm^{-2} s^{-1}.

A compilation of the X-ray data used in this work can be found in Table A.3, while the derived X-ray luminosities are listed in Table 3.

Table 3. X-ray luminosities measured at times close to the HST observations (see text for details).

Identifier		$\log L_X$ [erg s^{-1}]
HD 153919	4U 1700-37	36.03
BD+60 73	IGR J00370+6122	31.90
LM Vel	IGR J08408-4503	32.50
HD 306414	IGR J11215-5952	–
BD+53 2790	4U 2206+54	34.24
HD 100199	IGR J11305-6256	–

Notes. The "–" indicates that the source was below the detection limit of *Swift* during the observations.

4. Spectral modeling

4.1. Stellar atmosphere models

The spectral analyses presented in this paper were carried out with the Potsdam Wolf–Rayet (PoWR) models. PoWR is a state-of-the-art code for expanding stellar atmospheres. The main assumption of this code is a spherically symmetric outflow. The code accounts for deviation from the local dynamical equilibrium (non-LTE), iron line blanketing, wind inhomogeneities, a consistent stratification in the quasi hydrostatic part, and optionally also for irradiation by X-rays. The rate equations for the statistical equilibrium are solved simultaneously with the radiative transfer in the comoving frame, while energy conservation is ensured. Details on the code can be found in Gräfener et al. (2002), Hamann & Gräfener (2003), Todt et al. (2015), and Sander et al. (2015).

The inner boundary of the models is set to a Rosseland continuum optical depth τ_{ross} of 20, defining the stellar radius R_*. The stellar temperature T_* is the effective temperature that corresponds to R_* via the Stefan–Boltzmann law,

$$L = 4\pi\sigma_{\mathrm{SB}}R_*^2 T_*^4, \tag{2}$$

with L being the luminosity. The outer boundary is set to $R_{\max} = 100 R_*$, which proved to be sufficient for our program stars.

In the subsonic part of the stellar atmosphere, the velocity field $v(r)$ is calculated consistently such that the quasi-hydrostatic density stratification is fulfilled. In the wind, corresponding to the supersonic part of the atmosphere, a β-law (Castor & Lamers 1979; Pauldrach et al. 1986) is assumed. A double-β law (Hillier & Miller 1999; Gräfener & Hamann 2005) in the form described by Todt et al. (2015) is used for those objects where β values larger than unity are required to achieve detailed fits. For the first exponent we always assume 0.8, while the second exponent is adjusted during the spectral fitting procedure. The gradient of such a double-β law is steeper at the bottom of the wind than for a single β-law with a large exponent.

In the main iteration, line broadening due to natural broadening, thermal broadening, pressure broadening, neglected multiplet splitting, and turbulence is approximately accounted for by assuming Gaussian line profiles with a Doppler width of 30 km s^{-1}. The turbulent pressure is accounted for in the quasi hydrostatic equation (see Sander et al. 2015 for details). In the formal integral, line broadening is treated in all detail. For the microturbulence we set $\xi = 10$ km s^{-1} in the photosphere, growing proportional with the wind velocity up to a value of $\xi(R_{\max}) = 0.1 v_\infty$. The only exceptions are the supergiants HD 306414 and BD+60 73 where higher ξ values are necessary

to reproduce the observation (see Appendix B for details). The atmospheric structures (e.g., the density and the velocity stratification) of the final models for the donor stars are listed in Tables A.6–A.11.

Wind inhomogeneities are accounted for in the "microclumping" approach that assumes optically thin clumps (Hillier 1991; Hamann & Koesterke 1998). The density contrast between the clumps of an inhomogeneous model and a homogeneous one (with the same mass-loss rate $\dot{M}$) is described by the clumping factor D. Since the interclump medium is assumed to be void, D is the inverse of the clump's volume filling factor $f_V = D^{-1}$. According to hydrodynamical simulations (e.g., Runacres & Owocki 2002; Sundqvist et al. 2018), a radial dependency is expected for the clumping factor. Here, we use the clumping prescription suggested by Martins et al. (2009). The clumping onset (parameterized by v_{cl}), where the clumping becomes significant, is set to $10\,\mathrm{km\,s^{-1}}$, since this results in the best fits for all objects where this property could be constrained. The clumping factor is adjusted for each individual object.

The PoWR code accounts for ionization due to X-rays. The X-ray emission is modeled as described by Baum et al. (1992), assuming that the only contribution to the X-ray flux is coming from free–free transitions. Since the current generation of PoWR models is limited to spherical symmetry, the X-rays are assumed to arise from an optically-thin spherical shell around the star. The X-ray emission is specified by three free parameters, which are the fiducial temperature of the X-ray emitting plasma T_X, the onset radius of the X-ray emission R_0 ($R_0 > R_*$), and a filling factor X_{fill}, describing the ratio of shocked to non-shocked plasma. For our HMXBs, the onset radius is set to the orbital distance between the donor star and the NS companion. The temperature of the X-ray emitting plasma are obtained from fits of the observed X-ray spectra (see Sect. 3.3). The X-ray filling factor is adjusted such that the wavelength integrated X-ray flux from the observations is reproduced by the model.

The effects of the X-ray field on the emergent spectra are illustrated in Fig. 1. While the photospheric absorption lines are not affected at all, certain wind lines change significantly. Whether the lines become stronger or weaker depends on the individual combination of the wind density at the position of the NS, the ionization balance in the wind, and the hardness and intensity of the X-rays injected. There is some parameter degeneracy as, for some models, nearly identical line profiles are obtained when reducing $\dot{M}$ and instead increasing the X-ray filling factor. Fortunately, this ambiguity can be avoided in the analysis of most of our targets because the X-ray field is constrained from observations (see Sect. 3.3). The injected X-ray radiation is often needed to reproduce the wind lines in the UV and, hence, to measure the terminal wind velocity and mass-loss rate.

Complex model atoms of H, He, C, N, O, Mg, Si, P, and S (see Table A.4 for details) are considered in the non-LTE calculations. The multitude of levels and line transitions inherent to the iron group elements (Sc, Ti, V, Cr, Mn, Fe, Co, and Ni) are treated in a superlevel approach (see Gräfener et al. 2002).

4.2. Applicability of the models

One of the main assumption of the PoWR models as well as all other stellar atmosphere codes, with the exception of the PHOENIX/3D code (Hauschildt & Baron 2014), is spherical symmetry. In HMXBs, however, the spherical symmetry is broken by the presence of the compact object. On the other hand, the X-ray luminosities are often quite modest in HMXBs with NS companions. This is also the case for the systems studied in this
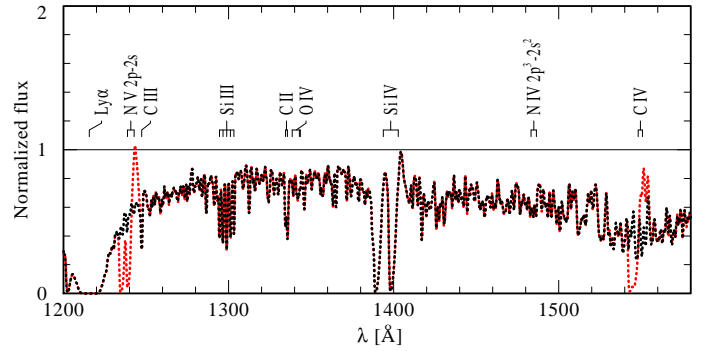
Fig. 1. Comparison between two model spectra calculated for BD+60 73 to illustrate the effect of the X-rays (red: with X-rays, black: without X-rays).

work, as illustrated by the values given in Table 3. For all but one sources, the X-ray luminosities are below $\log L_X = 35\,[\mathrm{erg\,s^{-1}}]$.

For those X-ray luminosities, we expect that the disruptive effect of the X-rays emitted by the NS on the donor star wind is relatively limited. The only exception might be HD 153919 (4U 1700-37) that exhibited an X-ray luminosity of $\log L_X = 36.03\,[\mathrm{erg\,s^{-1}}]$ during our HST observation. The HST spectrum of this source was taken during the end of an X-ray outburst described in Martinez-Chicharro et al. (2018). However, only minor variations are present in the HST spectrum compared to earlier observations with the *IUE* satellite. This is illustrated in Fig. 2, where we compare our HST spectrum with an averaged *IUE* spectrum constructed from observations in the high resolution mode that were taken between 1978 and 1989 with the large aperture. We used all available data sets with the exception of one exposure (Data ID: SWP36947) that exhibits a significantly lower flux compared to all other observations. The wind of HD 153919 does not show any sign of inhibition, suggesting that the volume significantly affected by the X-ray emission of the NS is rather small. This is consistent with the findings by van Loon et al. (2001).

This gives us confidence that the winds of the donor stars in the studied systems are not disrupted by the X-ray emission of the NSs and that the applied models are valid within their limitations. However, for the individual objects, observational time series are necessary to confirm this.

4.3. Spectral analysis

An in-depth spectral analysis of a massive star with non-LTE model spectra is an iterative process. Our goal is to achieve a overall best model fit to the observed data, while weighting the diagnostics according to their sensibility to the stellar parameters as described below. Starting from an estimate of the stellar parameters based on the spectral type of the target, a first stellar atmosphere model is calculated and its emergent spectrum is compared to the observations. This and the subsequent comparisons are performed "by eye" without any automatic minimization procedures. Based on the outcome of the initial comparison, the model parameters are adjusted, and a new atmosphere model is calculated. This procedure is repeated until satisfactory fits of the observations with the normalized line spectrum and the spectral energy distribution (SED) is achieved. As an example, the final fit of the normalized line spectrum of HD 306414 is presented in Fig. 3.

For those objects in our sample with $T_* > 30\,\mathrm{kK}$, the stellar temperature is primarily derived from the equivalent-width ratio
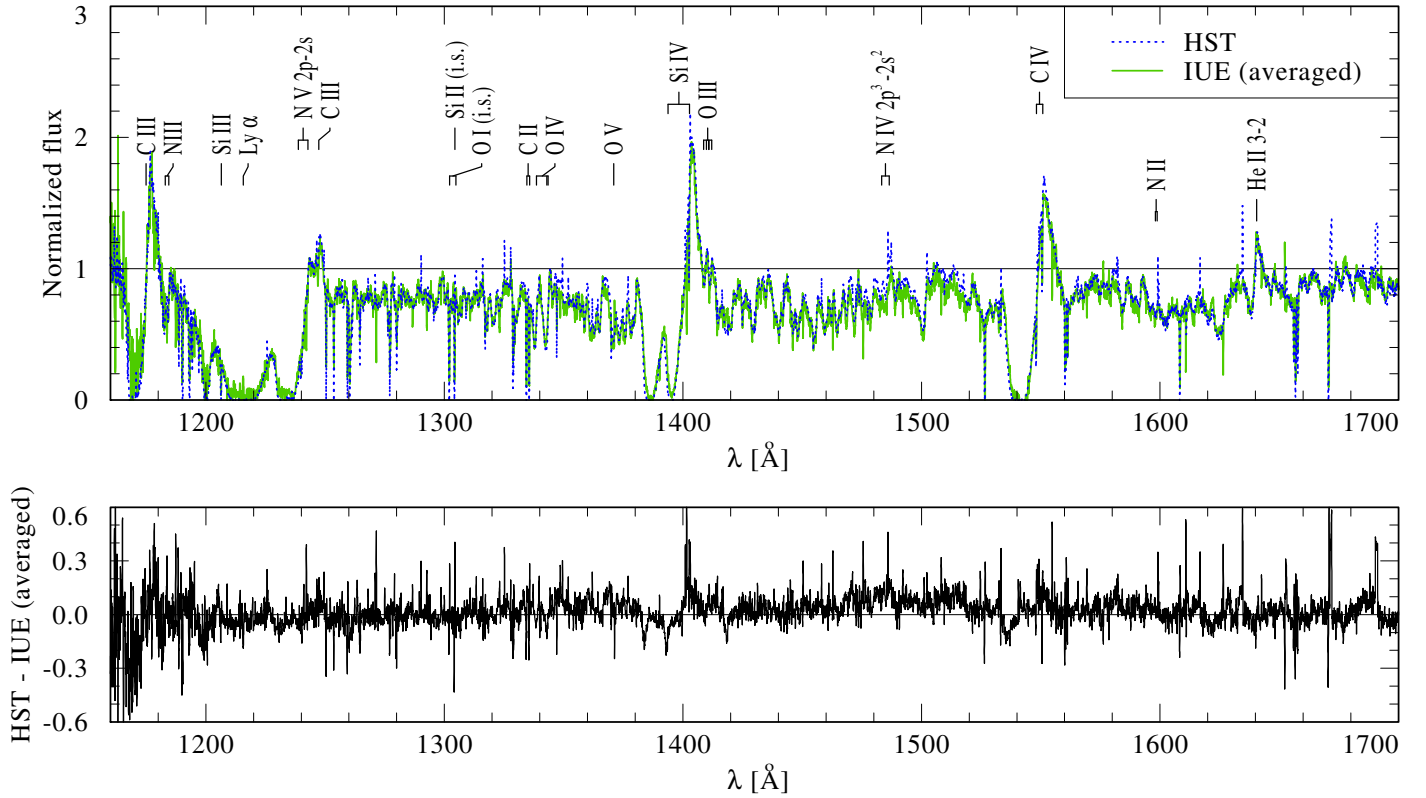
Fig. 2. HD 153919: comparison between our HST spectrum and an averaged *IUE* spectrum constructed from data taken between 1978 and 1989. *Upper panel*: HST spectrum (blue dotted line) and *IUE* spectrum (green continuous line); *lower panel*: difference between the HST spectrum and the averaged *IUE* spectrum.

between He I and He II lines, such as He I $\lambda\lambda$ 4026, 4144, 4388, 4713, 4922, 5015, 6678 and He II $\lambda\lambda$ 4200, 4542, 5412, 6683. For stars with lower stellar temperatures, we additionally used the line ratios of Si III to Si IV (Si III $\lambda\lambda$ 4553, 4568, 4575, 5740 and Si IV $\lambda\lambda$ 4089, 4116) and N II to N III (N II $\lambda\lambda$ 4237, 4242, 5667, 5676, 5680, 5686, and N III $\lambda\lambda$ 4035, 4097).

The surface gravity $\log g_{\rm grav}$ is derived from the pressure broadened wings of the Balmer lines, focusing on the Hγ and Hδ line, since Hβ and Hα are often affected by emission lines from the stellar wind.

The luminosities of all our targets together with the color excess E_{B-V} and the extinction-law parameter $R_{\rm V}$ for the individual lines of sight are obtained from a fit of the corresponding model SED to photometry and flux calibrated spectra. For this purpose, different reddening laws are applied to the synthetic SEDs. The finally adopted reddening prescriptions are given in Table 4. Moreover, the model flux is scaled to the distance of the corresponding star, using the values compiled in Table 1. For example, the SED fit of HD 306414 is shown in Fig. 4.

The projected rotational velocity and the microturbulence velocity in the photosphere are derived from the line profiles and the equivalent width of metal lines, such as Si IV $\lambda\lambda$ 4089, 4116; Si III $\lambda\lambda$ 4553, 4568, 4575; Mg II 4481 λ; and C IV $\lambda\lambda$ 5801, 5812. Macroturbulence is not considered in this approach, and thus the $v \sin i$ values reported in Table 4 must be considered as upper limits. With the `iacob-broad` tool (Simón-Díaz & Herrero 2014), which separately determines a possible macroturbulent contribution to the line broadening, we obtained similar $v \sin i$ values within their error margins. The terminal wind velocity and the radial dependence of the microturbulence velocity are simultaneously estimated from the extend and shape of the P Cygni

absorption troughs of the UV resonance lines. The β parameter of the velocity law is adjusted such that the synthetic spectrum can reproduce the profiles of the UV resonance lines and the full-width at half-maximum (FWHM) of the Hα emission. For the objects presented in this work, a double-β law with a second β exponent in the range of 1.2–3.0 result in slightly better spectral fits compared to the canonical β-law with $\beta = 0.8$ for O-type stars (Kudritzki et al. 1989; Puls et al. 1996). Note that the mass-loss rate derived from a spectral fit also slightly depend on the used β value.

The mass-loss rate and the clumping parameters are derived by fitting the wind lines in the UV and the optical. The main diagnostics for determining the mass-loss rates are the UV resonance lines exhibiting P Cygni line profiles, namely, C IV $\lambda\lambda$ 1548, 1551 and Si IV $\lambda\lambda$ 1394, 1403. The clumping factor and the onset of the clumping are adjusted such that a consistent fit of unsaturated UV lines and Hα could be achieved, utilizing the different dependency of those lines on density (linearly for the resonance lines and quadratic for recombination lines, such as Hα).

The abundances of the individual elements are adjusted such that the observed strength of the spectral lines belonging to the corresponding element are reproduced best by the model.

5. Stellar and wind parameters

The stellar and wind parameters of the investigated donor stars are listed in Table 4 together with the corresponding error margins. For those physical quantities that are directly obtained from the spectral fit ($T_*, \log g, \log L, v_\infty, \beta, \dot{M}, E_{B-V}, R_{\rm V}, v \sin i$, abundances), the corresponding errors are estimated by fixing
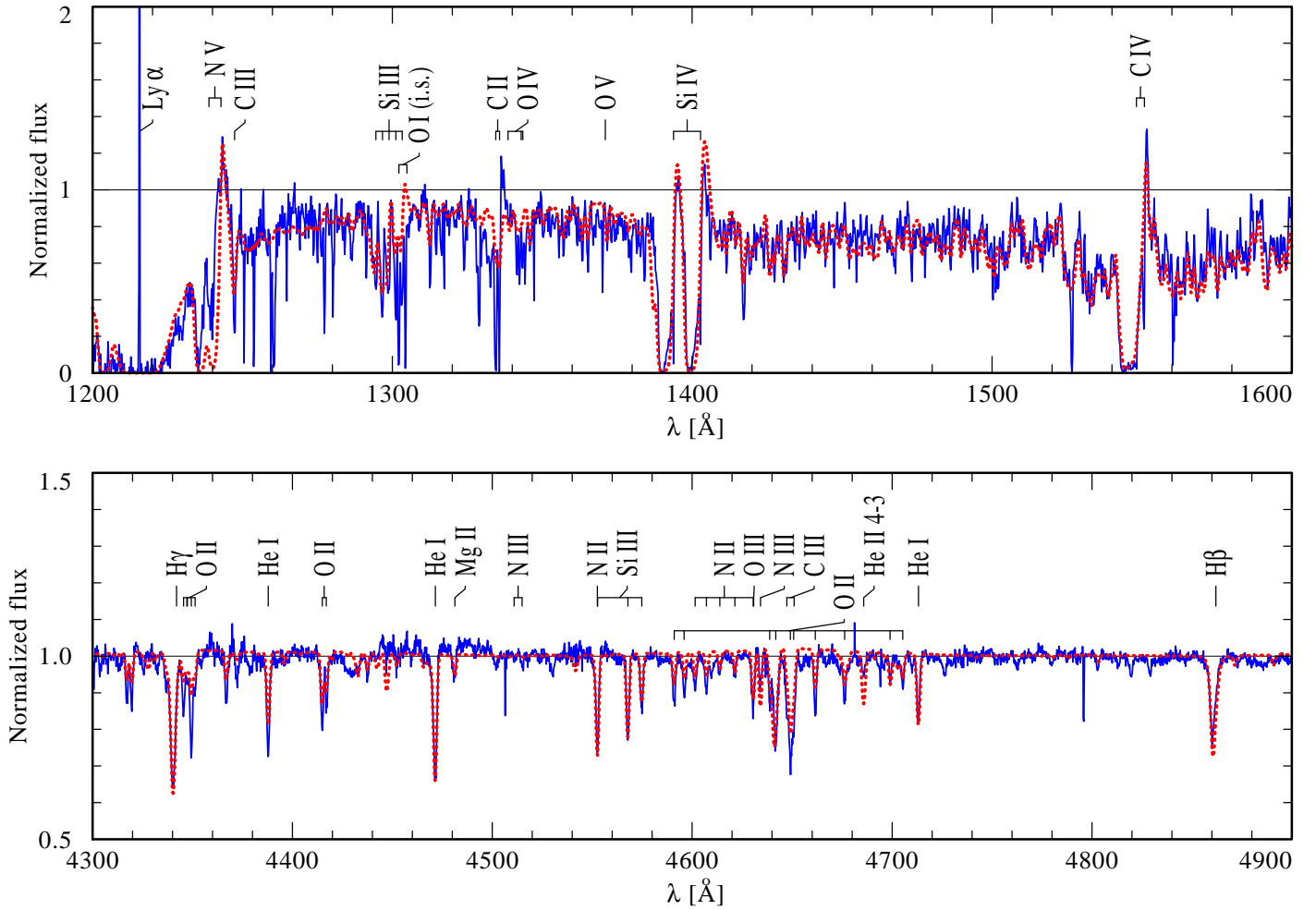
Fig. 3. Normalized line spectrum of HD 306414. The *upper panel* depicts a part of the UV spectrum, while the *lower panel* shows a section of the optical spectrum. The observation is shown in blue. The best fitting synthetic spectrum is overplotted by a dashed red line.

all parameters but one and varying this parameter until the fit becomes significantly worse. For those quantities that follow from the fit parameters, the errors are estimated by linear error propagation. We do not account for uncertainties in the orbital parameters, since they are often not known. Moreover, the quoted errors do not account for systematic uncertainties, e.g., because of the simplifying assumptions of the models such as spherical symmetry.

5.1. Comparison with single OB-type stars

The winds of massive stars are characterized by a number of quantities, such as $\dot{M}$, v_∞, or D. Since only a low number of donor-star winds have been analyzed by means of sophisticated atmosphere models, it is statistically unfavorable to pursue comparisons for individual wind parameters. Therefore, we use the so-called modified wind momentum D_{mom} to evaluate the winds of the donor stars. The modified wind momentum is defined as

$$D_{\mathrm{mom}} = \dot{M} v_\infty R_*^{1/2}. \tag{3}$$

In Fig. 5, we plot D_{mom} over the luminosity. A tight linear relation between the luminosity and the modified wind momentum is predicted by the line-driven wind theory (Kudritzki et al. 1995, 1999; Puls et al. 1996). This so-called wind-momentum luminosity relation (WLR) is observationally confirmed for a

variety of massive stars (e.g., Kudritzki et al. 1999; Kudritzki 2002; Massey et al. 2005; Mokiem et al. 2007). Exceptions are certain categories of objects such as the so-called weak-wind stars (Bouret et al. 2003; Martins et al. 2005; Marcolino et al. 2009; Shenar et al. 2017), where most of the wind mass-loss might be hidden from spectral analyses based on optical and UV data (see e.g., Oskinova et al. 2011; Huenemoerder et al. 2012). In addition to the stars analyzed in this work, we also plot in Fig. 5 the results obtained by Giménez-García et al. (2016) and Martínez-Núñez et al. (2015) for the donor stars in one SFXT (IGR J17544-2619) and two persistent HMXBs (Vela X-1 and U9 1909+07) as well as the values compiled by Mokiem et al. (2007) for Galactic O and B-type stars.

The donor stars in the investigated HMXBs fall in the same parameter regime as observed for other Galactic OB-type stars. Moreover, Fig. 5 shows that these donors also follow the same WLRs as other massive stars in the Galaxy, indicating that the fundamental wind properties of the donor stars in wind-fed HMXBs are well within the range of what is expected and observed for these kind of massive stars.

5.2. Wind parameters of SFXTs versus those of HMXBs

A comparison between the wind parameters of the donor stars in SFXTs with those in persistent HMXBs reveals that there is no general distinction (see Table 4). For example, HD 153919

Table 4. Inferred stellar and wind parameters.

HMXB type	Persistent	Intermediate	SFXT		Persistent/ Oe X-ray	Be X-ray
Name	HD 153919	BD+60 73	LM Vel	HD 306414	BD+53 2790	HD 100199
Spectral type	O6 Iafpe	BN0.7 Ib	O8.5 Ib-II(f)p	B0.5 Ia	O9.5 Vep	B0 IIIne
Alias name	4U 1700-37	IGR J00370+6122	IGR J08408-4503	IGR J11215-5952	4U 2206+54	IGR J11305-6256
T_* [kK]	35^{+2}_{-3}	24^{+1}_{-1}	30^{+3}_{-3}	25^{+1}_{-1}	30^{+3}_{-3}	30^{+2}_{-3}
$T_{2/3}$ [kK]	34	23	29	24	30	30
$\log g_*$ [cm s^{-2}]	$3.4^{+0.4}_{-0.4}$	$2.9^{+0.1}_{-0.1}$	$3.2^{+0.2}_{-0.2}$	$2.8^{+0.2}_{-0.2}$	$3.8^{+0.3}_{-0.5}$	$3.6^{+0.2}_{-0.2}$
$\log L$ [$L_\odot$]	$5.7^{+0.1}_{-0.1}$	$4.9^{+0.1}_{-0.1}$	$5.3^{+0.1}_{-0.1}$	$5.4^{+0.1}_{-0.1}$	$4.9^{+0.1}_{-0.1}$	$4.4^{+0.1}_{-0.1}$
$v_\infty/10^3$ [km s^{-1}]	$1.9^{+0.1}_{-0.1}$	$1.1^{+0.1}_{-0.2}$	$1.9^{+0.1}_{-0.1}$	$0.8^{+0.2}_{-0.1}$	$0.4^{+0.1}_{-0.1}$	$1.5^{+0.3}_{-0.3}$
β [a]	2^{+1}_{-1}	$1.2^{+0.6}_{-0.4}$	$1.4^{+0.4}_{-0.4}$	3^{+1}_{-1}	1.0	0.8
R_* [$R_\odot$]	19^{+5}_{-6}	17^{+4}_{-4}	17^{+6}_{-5}	28^{+6}_{-5}	11^{+4}_{-4}	6^{+2}_{-2}
$R_{2/3}$ [$R_\odot$]	20	18	17	31	11	6
D	20^{+50}_{-15}	20^{+50}_{-16}	20^{+10}_{-5}	20^{+10}_{-10}	10 [b]	10 [b]
$\log \dot{M}$ [$M_\odot$ yr^{-1}]	$-5.6^{+0.2}_{-0.3}$	$-7.5^{+0.1}_{-0.2}$	$-6.1^{+0.2}_{-0.2}$	$-6.5^{+0.2}_{-0.2}$	$-7.5^{+0.3}_{-0.3}$	$-8.5^{+0.5}_{-0.5}$
$v \sin i$ [km s^{-1}]	110^{+30}_{-50}	120^{+20}_{-20}	150^{+20}_{-20}	60^{+20}_{-20}	200^{+50}_{-50}	230^{+60}_{-60}
$M_{V,\mathrm{John}}$ [mag]	-6.4	-5.3	-5.8	-6.6	-4.7	-3.5
X_{H} [mass fr.] [c]	$0.65^{+0.1}_{-0.2}$	$0.45^{+0.1}_{-0.1}$	$0.5^{+0.1}_{-0.1}$	$0.6^{+0.13}_{-0.2}$	0.7375	0.7375
$X_{\mathrm{C}}/10^{-3}$ [mass fr.] [c]	2.5^{+2}_{-1}	$0.5^{+0.2}_{-0.2}$	$2.5^{+1.5}_{-1.0}$	$0.25^{+0.15}_{-0.10}$	2.37	2.37
$X_{\mathrm{N}}/10^{-3}$ [mass fr.] [c]	2.0^{+2}_{-1}	$2.5^{+1.5}_{-1.0}$	$2.0^{+1.0}_{-1.0}$	4.0^{+2}_{-2}	0.69	0.69
$X_{\mathrm{O}}/10^{-3}$ [mass fr.] [c]	3^{+2}_{-1}	3^{+1}_{-1}	6^{+2}_{-2}	$6^{+4.0}_{-2.5}$	5.73	5.73
$X_{\mathrm{Si}}/10^{-4}$ [mass fr.] [c]	3^{+3}_{-2}	4^{+1}_{-2}	6^{+3}_{-3}	10^{+5}_{-3}	6.65	6.65
$X_{\mathrm{Mg}}/10^{-4}$ [mass fr.] [c]	6.92	9^{+3}_{-3}	5^{+2}_{-2}	5^{+4}_{-2}	6.92	6.92
E_{B-V} [mag]	$0.50^{+0.01}_{-0.01}$	$0.85^{+0.01}_{-0.01}$	$0.44^{+0.01}_{-0.01}$	$0.83^{+0.01}_{-0.01}$	$0.595^{+0.015}_{-0.01}$	$0.34^{+0.01}_{-0.01}$
R_V (reddening law [d])	3.1 (Seaton)	$2.8^{+0.1}_{-0.1}$ (Cardelli)	3.1 (Seaton)	$3.0^{+0.1}_{-0.1}$ (Cardelli)	3.1 (Seaton)	3.1 (Seaton)
M_{spec} [$M_\odot$]	34^{+100}_{-28}	8^{+8}_{-4}	16^{+29}_{-11}	18^{+24}_{-11}	27^{+67}_{-23}	6^{+9}_{-4}
a_2 [R_*]	$1.6^{+1.5}_{-0.4}$	$2.9^{+3.2}_{-2.8}$	$2.9^{+1.6}_{-0.6}$	12^{+5}_{-3}	$5.4^{+4.3}_{-1}$	–
$v_{\mathrm{orb,apa}}$ [km s^{-1}]	500^{+900}_{-300}	90^{+50}_{-30}	120^{+200}_{-60}	30^{+30}_{-20}	200^{+400}_{-200}	–
$v_{\mathrm{orb,peri}}$ [km s^{-1}]	500^{+900}_{-300}	300^{+200}_{-90}	500^{+500}_{-200}	300^{+200}_{-100}	400^{+600}_{-200}	–
$v_{\mathrm{wind,apa}}$ [km s^{-1}]	400^{+600}_{-300}	850^{+50}_{-40}	1400^{+200}_{-200}	730^{+30}_{-20}	350^{+30}_{-30}	–
$v_{\mathrm{wind,peri}}$ [km s^{-1}]	400^{+600}_{-300}	200^{+200}_{-200}	30^{+600}_{-30}	220^{+200}_{-70}	300^{+50}_{-40}	–
$R_{\mathrm{rl,apa}}$ [R_*] [e]	$1.1^{+0.5}_{-0.2}$	$1.5^{+0.3}_{-0.2}$	$1.6^{+0.6}_{-0.3}$	$2.6^{+0.7}_{-0.3}$	$1.9^{+0.9}_{-0.3}$	–
$R_{\mathrm{rl,peri}}$ [R_*] [e]	$1.1^{+0.5}_{-0.2}$	$0.83^{+0.12}_{-0.07}$	$0.70^{+0.19}_{-0.08}$	$1.6^{+0.3}_{-0.2}$	$1.8^{+0.5}_{-0.2}$	–

Notes. [a] Values larger than unity refer to the second exponent in a double-β law (see Sect. 4.1 for details). [b] We were not able to determine the precise clumping factor (see Appendix B for details). [c] Entries without errors are fixed to solar abundances (Asplund et al. 2009). [d] Seaton (1979); Cardelli et al. (1989). [e] Calculated via the approximation presented by Sepinsky et al. (2007), assuming the orbital parameters given in Table 2.

and LM Vel both have winds with a high terminal velocity of 1900 km s^{-1}, but the former is a persistent HMXB, while the latter is a SFXT. Moreover, we find SFXTs with quite different wind properties: while LM Vel exhibits a fast stellar wind and a relatively high mass-loss rate, HD 306414 has a significantly slower wind ($v_\infty = 800$ km s^{-1}) and a low mass-loss rate. In fact, the parameters of HD 306414 are quite similar to those of Vela X-1 (Giménez-García et al. 2016), while Vela X-1 is a persistent source in contrast to HD 306414.

The wind properties are important for characterizing the donor stars. However, the accretion onto the compact object and, consequently, the X-ray properties of a system depend on the wind conditions at the position of the compact object. Based on the orbital parameters (Table 2), we determine the wind velocity at the apastron and periastron positions of the NS (see Table 4). As described in Sect. 4.1, we assume a double-β law (with the second β exponent given in Table 4) for the wind velocity in the supersonic regime. However, the double-β law as well as
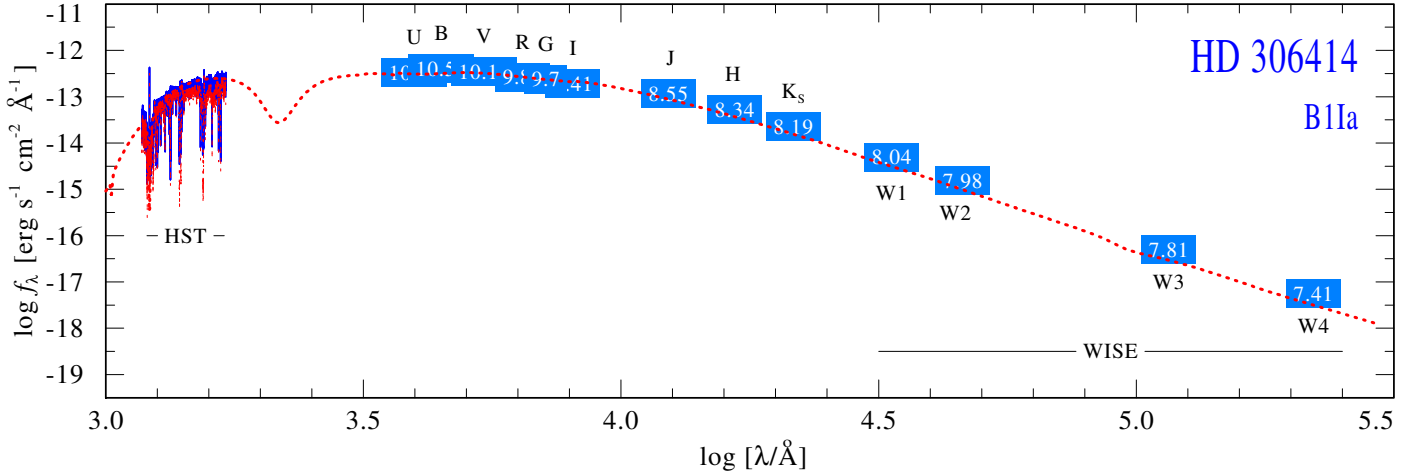
Fig. 4. Spectral energy distribution (SED) of HD 306414, composed of the flux calibrated HST spectrum (blue continuous line) and photometry (blue boxes, labeled with the corresponding magnitudes). The best fitting model SED is depicted by a dashed red line. The model flux is corrected for interstellar extinction and the geometric dilution according to the distance to HD 306414 (6.5 kpc).
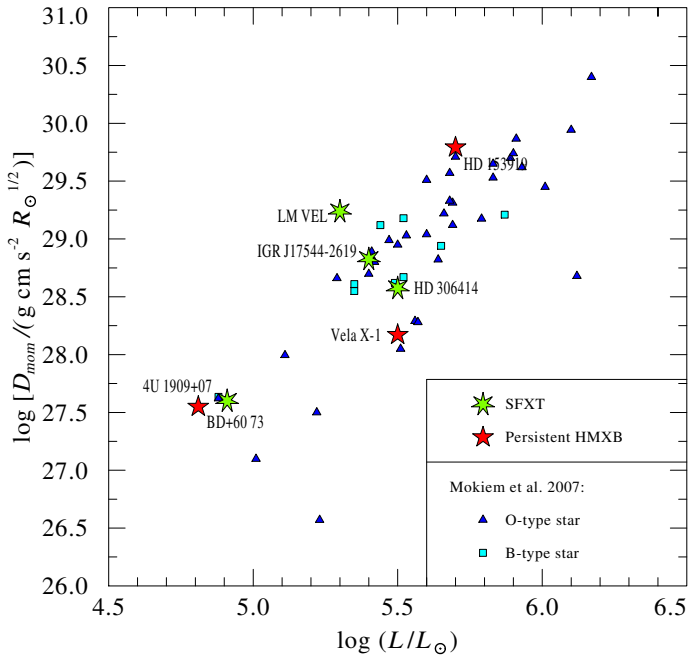
Fig. 5. Modified wind momentum over the luminosity. The SFXTs and the persistent HMXBs are shown by green and red asterisks, respectively. In addition to the objects investigated in this work, we also show the results obtained by Martínez-Núñez et al. (2015) and Giménez-García et al. (2016). The dark blue triangles and light blue squares depict the analyses compiled by Mokiem et al. (2007) for O and B-type stars, respectively.

the single β-law might not be a perfect representation of the wind structure in some HMXBs (Sander et al. 2018). Moreover, the wind velocity in the direction to the NS might be reduced because of the influence of the X-rays on the wind structure (Krtička et al. 2015; Sander et al. 2018). Thus, the real wind velocity could be slightly lower than what we constrain here. However, we do not expect that this effect is significant for the objects in our sample because of the relatively low X-ray luminosities of the NSs (see Table 3). A more detailed investigation will be presented in a forthcoming publication using hydrodynamic atmosphere models.

From Table 4, we clearly see that the velocities of the donor star winds at the position of the NSs ($v_{\mathrm{wind,peri}}$ & $v_{\mathrm{wind,apa}}$) are significantly lower than the corresponding terminal wind velocities (v_∞). We note that the value of the β velocity-law derived in this work defines the wind structure and as such has an influence on the wind velocity determined for the position of the NS. Low β values result in higher velocities compared to high β values. For the extreme case of HD 304614, the uncertainty from the spectral fit is ± 1 for the second exponent of the double-β law. This uncertainty results in an error of less than 5% for the wind velocity at the position of the NS during apastron, while it is about 30% during periastron. These errors are significantly smaller than the those resulting from the orbital configuration, which are the main source for the errors quoted in Table 4.

The wind velocities at the position of the NSs are modulated with the orbital configurations of the systems. An intriguing example is LM Vel: while the wind velocity at apastron is $1400\,\mathrm{km\,s^{-1}}$, it is as low as $30\,\mathrm{km\,s^{-1}}$ at periastron. In contrast, the system harboring HD 153919 (4U 1700-37), the only truly persistent source in our sample, exhibits a negligible eccentricity and, therefore, a stable wind velocity at the position of the NS. This velocity is about 20% of its terminal value, while the wind velocity at apastron in the SFXTs is >70% of v_∞. In general, it seems that in SFXTs, the velocity of the donor star winds at the periastron position of the NSs is lower than in the persistent sources. During apastron passage this situation appears to be reversed. Hence, we can conclude that the wind velocities at the position of the NS are significantly modulated by the orbital configuration in the SFXTs. This suggests that the orbits might play an important role in the dichotomy of wind-fed HMXBs as already proposed by Negueruela et al. (2006). In general, this dichotomy likely reflects a complex interplay between the donor-star parameters, the orbital configuration, and the NS properties.

5.3. Relative velocities and constraints on the formation of temporary accretion disks

Another interesting discovery is that the donor star wind velocity at periastron in all studied systems is within the uncertainties statistically indiscernible from the NSs orbital velocity. According to Wang (1981) these conditions are favorable for the formation

of an accretion disk around the NS. Such a disk would act as a reservoir and might allow for X-ray outbursts peaking after periastron passage, and should also modify the X-ray light curve (see e.g., Motch et al. 1991). The formation of accretion disks regularly during periastron could potentially also influence the evolution of the spin period of the neutron star.

To check whether an accretion disk can form, we adopt the prescription from Wang (1981) in the formulation given by Waters et al. (1989). According to these studies, an accretion disk can form if

$$v_{\text{rel}} \leq 304\,\eta^{1/4} \left(\frac{P_{\text{orb}}}{10\,\text{d}}\right)^{-1/4} \left(\frac{M_{\text{NS}}}{M_\odot}\right)^{5/14} \left(\frac{R_{\text{NS}}}{10^6\,\text{cm}}\right)^{-5/28}$$

$$\times \left(\frac{B_0}{10^{12}\,\text{G}}\right)^{-1/14} \left(\frac{L_{\text{X}}}{10^{36}\,\text{erg\,s}^{-1}}\right)^{1/28}\,\text{km\,s}^{-1}, \tag{4}$$

where P_{orb} is the orbital period in days and η describes the efficiency of the angular momentum capture. The NS properties enter with the magnetic flux density B_0, the X-ray luminosity L_{X}, the NS mass M_{NS}, and radius R_{NS}.

With the help of Eq. (4), we can thus estimate whether an accretion disk around the NSs in our target systems would form. For R_{NS}, we assume 1.1×10^6 cm based on the estimates by Özel & Freire (2016). We assume a magnetic flux density of $B_0 = 10^{12}$ G for all NSs in our sample. The only exception is BD+53 2790, where Torrejón et al. (2018) constrain the magnetic field of the NS to $B_0 > 2 \times 10^{13}$ G. We also assume the canonical NS mass $M_{\text{NS}} = 1.4\,M_\odot$ (Thorsett & Chakrabarty 1999). The only exception is the NS companion of HD 153919, for which Falanga et al. (2015) derive a mass of $1.96\,M_\odot$. Moreover, we set the efficiency factor to $\eta = 1$, as expected in the presence of an accretion disk (Waters et al. 1989). Based on these assumptions, we find that no disks are predicted to form in any of our target systems. Note that Eq. (4) is strictly valid only for circular systems. Moreover, if the X-ray luminosity of the SFXTs is higher during an outburst than during our *Swift* observations, we might obtain a different result. However, even for $L_{\text{X}} = 10^{38}$ erg s^{-1} no accretion disks are predicted to form.

Recent detailed studies of wind dynamics in the vicinity of an accreting NS have been performed by El Mellah et al. (2019a). Their 3D simulations show that when orbital effects are dynamically important, the wind dramatically departs from a radial outflow in the NS vicinity and the net angular momentum of the accreted flow could be sufficient to form a persistent disk-like structure. On the other hand, the 3D hydrodynamic models by Xu & Stone (2019) show that in flows that are prone to instability, such as stellar winds, the disks are not likely to form. In support of this, observations do not indicate presence of stable accretion disks in HMXBs with NS components (e.g., Bozzo et al. 2008). Thus, the question of persistent disk formation remains open. Our spectral models, which rely on spherical symmetry, are capable of reproducing the line shapes formed in the stellar wind (e.g., lines with P Cygni profiles); this argues in the favor of the models where the wind flow is strongly bent only in a limited volume close to the NS.

We highlight that the orbital velocity cannot be neglected, since it is comparable to the wind velocity at the position of the NS. Thus, it needs to be accounted for when estimating the mass accretion rate from the donor-star wind according to the Bondi-Hoyle-Lyttleton mechanism. Consequently, the orbital velocity is important for predicting the X-ray luminosity (see also Sects. 1 and 7).

5.4. Abundances

In Table 4, we also list the chemical abundances for our program stars. Abundances that are derived from the spectral fits are given with the estimated errors. For those elements where only insufficient diagnostics are available, the abundances are fixed to the solar values, and the corresponding entries in Table 4 are given without errors.

Two thirds of our sample (HD 153919, BD+60 73, HD 306414, and LM Vel) shows a significant depletion of hydrogen compared to the primordial abundance. For BD+53 2790 and HD 100199 no deviation from this value could be detected. Nitrogen is enriched with respect to the solar value (Asplund et al. 2009) in all investigated wind-fed HMXBs. HD 153919 and LM Vel exhibit a carbon abundance that is approximately solar, while carbon is subsolar in all other objects. The same applies to oxygen, which is depleted in all investigated objects with the exception of HD 306414 and LM Vel, which shows an oxygen abundance of about $X_{\text{O}} = X_{\text{O},\odot}$ and $1.1\,X_{\text{O},\odot}$, respectively.

Crowther et al. (2006) determine CNO abundances for 25 Galactic OB-type supergiants. They constrain mean [N/C], [N/O], and [C/O] logarithmic number ratios (relative to solar) of +1.10, +0.79, and −0.31, respectively. Only BD+60 73 appears to be fully consistent with these results, while the other objects in our sample exhibit conspicuous abundance patterns. The [C/O] ratio of HD 153919 and LM Vel (0.31 and 0.01) is significantly higher than the average values derived by Crowther et al. (2006), while it is substantially lower for HD 306414 ([C/O] = −1.0).

In general, silicon and magnesium seems to be depleted in our program stars, with the exception of HD 306414 and BD+60 73. The former shows a supersolar silicon abundance, while the latter exhibits a slightly supersolar magnesium abundance. However, we note that the uncertainties for these abundance measurements are quite high. Hence, the results have to be interpreted with caution. In the next section, we will discuss these abundance patterns in an evolutionary context.

6. Stellar evolutionary status

The detailed investigation of HMXBs offers the possibility to constrain open questions of massive star evolution, SN kicks, and common envelope (CE) phases.

6.1. Common envelope evolution and NS natal kicks

The formation of a HMXB is a complex process. In the standard scenario, a massive binary system initiates RLOF from the primary to the secondary. This mass transfer becomes dynamically unstable, if the secondary cannot accrete all of the material. This often results in a CE phase that either leads to a merger or to the ejection of the primary's envelope, entailing a significant shrinkage of the binary orbit (e.g., Paczyński 1967; Taam & Sandquist 2000; Taam & Ricker 2010; Ivanova et al. 2013, and references therein). In the latter case, the stripped primary will undergo a core collapse forming a compact object, which can accrete matter from the rejuvenated secondary. These systems then emerge as HMXB.

If the mass transfer is stable, or in the case of large initial orbital separations, a CE phase can be avoided. To form a HMXB, however, this evolutionary path requires fortuitous SN kicks to reduce the orbital separation to the small values observed for the majority of these systems (Walter et al. 2015).

With the exception of HD 306414, all investigated wind-fed HMXBs have tight orbits with periods of less than 16 d

and semi-major axes of less than $64\,R_\odot$. These separations are significantly smaller than the maximum extension of the NS progenitor. Therefore, each of these systems could indeed have already passed through a CE phase. Alternatively, the core collapse that leads to the formation of the NS was asymmetric and imparted a natal kick on the new-born NS. This reduced the orbital separations and hardened the system. A third possibility, in principle, is that the binary was in a close configuration from the beginning, and this has not changed because the components evolved quasi-homogeneously (e.g., Maeder 1987; Langer 1992; Heger & Langer 2000; Yoon & Langer 2005; Woosley & Heger 2006). This prevents a significant expansion of the stars, so that the system never entered a CE phase. However, there is no reason to suspect quasi homogeneous evolution (QHE) in our studied donor stars.

No significant eccentricity is expected for post CE systems, which is in strong contrast to most HMXBs in our sample. Yet, the current eccentricity of these systems might be a result of the core-collapse event, suggesting that relatively large natal kicks are associated with the formation of NSs. This appears to be consistent with the results presented by Tauris et al. (2017), who find evidence that the kicks of the first SN in binaries evolving towards double neutron stars (DNSs) are on average larger than those of the second SN. In our sample, only HD 153919 does not show any substantial eccentricity. This is either a result of tidal circularization after the first SN, which appears plausible considering the advanced evolutionary status of HD 153919, or of a CE phase, which however implies that the SN kick was negligible in this case. Although the presence of a NS in this system is strongly favored (Martinez-Chicharro et al. 2018), a BH cannot be excluded. Thus, a third possibility exists for HD 153919. Since the formation of a BH is not necessary associated with a SN and a corresponding kick, the virtual circular orbit of HD 153919 might be a result of a CE phase.

6.2. Abundance pattern

The atmospheric abundance pattern of evolved massive stars, such as OB-type supergiants, is often affected by CNO burning products. Those are mixed to the surface due to processes, such as rotational induced mixing (Heger & Langer 2000). Accordingly, it is expected that the oxygen and carbon abundance decrease in favor of the nitrogen abundance in the course of the evolution. As stated in Sect. 5, most of our program stars are not compatible with this scenario. On the one hand, HD 153919, LM Vel, HD 306414, and BD+60 73 show hydrogen depletion and nitrogen enrichment, which point to an advanced evolution state. On the other hand, HD 153919 and LM Vel have about solar carbon abundance, and HD 306414 has a supersolar oxygen abundance. Only for BD+60 73 the hydrogen and the CNO abundances are consistent with an advanced evolution state according to single-star evolution.

For HD 153919, Clark et al. (2002) point out that its carbon overabundance has to be a result of accretion from the NS progenitor during its Wolf-Rayet (WR) stage, more precisely during the carbon sequence WR (WC) phase. This can also serve as an explanation for the high carbon and oxygen abundances of LM Vel and HD 306414, respectively. In the latter case, the NS progenitor had to reach the oxygen rich WR (WO) phase before exploding as SN. For this scenario to work, the masses of the corresponding WC and WO stars had to be below a certain limit to form NSs at the end. Woosley (2019) estimate that most stars with final masses up to $6\,M_\odot$, corresponding to $9\,M_\odot$ helium core masses or $30\,M_\odot$ on the ZAMS, will leave neutron

star remnants. This constraint is compatible with a few Galactic WC stars (Sander et al. 2019). If this scenario is true, it proves that the low mass WC/WO stars indeed explode as Type Ibc SN, instead of directly collapsing to a BH.

Alternatively, the high carbon and oxygen abundances might be explained by pollution of material ejected during the SN explosion. In this case, significant enrichment by other elements such as silicon and magnesium is expected as well, based on calculation of nucleosynthesis yields from core-collapse SNe (e.g., Rauscher et al. 2002; Nomoto et al. 2006, 2013; Woosley & Heger 2007). This is in contradiction to what is derived in our spectral analyses such as the low silicon abundances in the atmospheres of HD 153919 as well as the slightly subsolar magnesium abundance in LM Vel and HD 306414. However, we note the supersolar magnesium abundance of HD 306414 and BD+60 73.

6.3. Angular momentum transfer and projected rotational velocities

Interacting binary stars do not only exchange mass but also angular momentum. Mass transfer due to RLOF often spins up the accreting star until this mass gainer rotates nearly critical (Packet 1981; de Mink et al. 2013). As mentioned earlier, the orbital parameters of all objects in our sample suggest that mass transfer has occurred in these systems in the past. However, in subsequent phases (especially the presented HMXB stage) the remaining OB-type star could loose angular momentum by its wind. It is therefore interesting to check if the donor stars exhibit rapid rotation.

We derive projected rotational velocities in the range from 60 to $230\,\mathrm{km\,s^{-1}}$. Interestingly, the smallest $v\sin i$ is found for HD 306414, which might has avoided strong binary interactions in the past. The two OBe stars in our sample exhibit the larges projected rotational velocities (200 and $230\,\mathrm{km\,s^{-1}}$). Nonetheless, we can rule out very rapid rotation for all donor stars in our sample. Using a rough approximation for the critical velocity $v_{\mathrm{crit}} = \sqrt{GM_*R_*^{-1}}$ (neglecting for example effects due to oblateness) and adopting the mean statistical inclination of $57°$, all donor stars are found to rotate far below critical.

The $v\sin i$ distribution of Galactic OB-type stars has been investigated in many studies (e.g., Dufton et al. 2006; Fraser et al. 2010; Bragança et al. 2012; Simón-Díaz 2010; Simón-Díaz & Herrero 2014; Garmany et al. 2015). These studies often find evidence of a bimodal distribution, showing a low $v\sin i$ peak and a group of fast rotators that extends to very high $v\sin i$ (e.g., Ramírez-Agudelo et al. 2013; Simón-Díaz & Herrero 2014; Garmany et al. 2015). A similar result is obtained by Ramachandran et al. (2018) for >200 OB-type stars in the Large Magellanic Cloud (LMC). de Mink et al. (2013) predict that the high $v\sin i$ peak predominantly results from massive stars that were spun up because of binary interactions, while the low-velocity peak consists of single stars and binary systems that have not interacted yet.

Based on a study of about 200 northern Galactic OB-type stars, which also accounts for the effects of macroturbulence and microturbulence, Simón-Díaz & Herrero (2014) find that the $v\sin i$ distribution for O and B-type supergiants peaks at 70 and $50\,\mathrm{km\,s^{-1}}$, respectively. Comparing this with the projected rotational velocities of our sample, it appears that our program stars rotate on average more rapidly than single OB-type stars. This is in accordance with mass accretion in the past. The only exception might be HD 306414.

For the O-type components in six Galactic WR + O binaries, Shara et al. (2017) derive rotational velocities. Those are expected to be nearly critical, since the O-type stars are spun up by RLOF from the WR progenitor. However, Shara et al. (2017) find that these stars spin with a mean rotational velocity of $350\,\mathrm{km\,s^{-1}}$, which is about 65% of their critical value. They argue that a significant spin-down even on the short timescales of the WR-phase (a few hundred thousand years) must have taken place. The rotational velocities derived for our donor stars are substantially lower than those of the O-type components in the WR binaries. Compared to these objects, the evolution time scales of our stars are significantly larger (a few million years). Thus, our donor stars might had more time to spin down, which would be consistent with their lower rotational velocities. In this picture, our results and those by Shara et al. (2017) coincide nicely.

6.4. Mass-luminosity relation

In binary systems it is expected that the mass gainer is internally mixed because of angular momentum transfer. Therefore, the mass gainer should be overluminous compared to single stars of the same mass (e.g., Vanbeveren & De Loore 1994). To investigate whether this is the case for our program stars, we compare the spectroscopic masses constrained in this work with masses from stellar-evolution tracks. The latter are obtained with the BONNSAI Bayesian statistics tool (Schneider et al. 2014). Using stellar and wind parameters ($T_*, \log L, \log g, v\sin i, X_{\mathrm{H}}, \dot{M}$) and their corresponding errors as input, the BONNSAI tool interpolates between evolutionary tracks calculated by Brott et al. (2011). Based on this set of single star evolution tracks, the tool predicts the current mass that an object with these parameters would have, if it has evolved like a single star. The correlated parameters are listed and compared in Table A.5.

For BD+60 73 and HD 306414, evolution masses could not be derived in this way, since the parameters of these stars are not reproduced by any of the underlying stellar evolution models. BD+53 2790 exhibits a spectroscopic mass that is 35% larger than its evolution mass. HD 153919 and LM Vel seem to be overluminous for their current mass.

6.5. Future evolution

Unfortunately, binary evolution tracks that would be applicable to the HMXBs investigated in this work are not available. Nevertheless, the future evolution of our targets can be discussed based on their current orbital configuration and the stellar properties of the donor stars. All investigated systems are compact enough that the donor stars, in the course of their further evolution, will expand sufficiently to eventually fill their Roche lobe, initiating direct mass transfer to their NS companions. Whether or not this mass transfer is stable will significantly influence the further evolution and the final fate of these HMXBs.

The stability of the mass-transfer in such systems has recently received increased attention. van den Heuvel et al. (2017) study whether this mass-transfer would lead to a (second) CE phase and whether this would result in a merger. They conclude that the mass-transfer is indeed unstable for a broad parameter range, and that the vast majority of the known HMXBs, consisting of supergiants with NS companions (>95%) would not survive the spiral-in within a CE phase. Applying their findings to our results, and assuming a NS mass of $1.4\,M_\odot$, suggests that also all systems investigated in this work will enter a CE phase that leads to a merger. The same can be concluded from a comparison of the stellar and orbital parameters of our

HMXBs with the CE-ejection solutions calculated by Kruckow et al. (2016) for massive binary systems. For all our objects, the minimal orbital separation is significantly lower than $100\,R_\odot$, while the spectroscopic masses are higher than $8\,M_\odot$. Comparing these constraints with the solutions presented by Kruckow et al. (2016, see their Fig. 2) suggests that the systems studied in this work are not able to eject the CE in the upcoming CE phase. These findings are consistent with conclusions by previous studies (e.g., Podsiadlowski 1994; van den Heuvel et al. 2017; Tauris et al. 2017).

If the systems studied in this work merge, they will form so-called Thorne–Żytkow objects (TŻO, Thorne & Zytkow 1975, 1977). Cannon et al. (1992) already discuss HMXBs as a potential source of TŻOs, identifying this as one of two possible channels. Podsiadlowski et al. (1995) estimate the number of TŻOs in the Galaxy to be 20–200. Thorne–Żytkow objects will likely appear as red supergiants (RSGs) (Biehle 1991; Cannon 1993), which are only distinguishable from normal RSGs by means of specific abundance patterns. These abundances are a result of the extremely hot non-equilibrium burning processes, that allow for interrupted rapid proton addition (Thorne & Zytkow 1977; Cannon 1993). The first promising candidate for a TŻO is identified by Levesque et al. (2014). According to Tauris et al. (2017), a few to ten percent of the luminous red supergiants ($L \geq 10^5\,L_\odot$) in the Galaxy are expected to harbor a NS in their core.

Alternatively, TŻOs might appear as WN8 stars. This is suggested by Foellmi & Moffat (2002) because of the peculiar properties of these class of objects, such as the low binary fraction, strong variability, and the high percentage of runaways. Recently, this has been proposed to be a valid scenario for WR 124 (Toalá et al. 2018). Based on population synthesis models, already De Donder et al. (1997) have proposed that WR stars with compact objects at their center should exist. They denote these objects as "weird" WR stars. In view of the above results, we are inclined to conclude that the binaries examined in this work will presumably form some kind of TŻOs in the future.

However, a certain fraction of the HMXB population obviously survives, since we see compact DNS systems. If the HMXBs can avoid a merger in the imminent CE phase, they will likely undergo an additional phase of mass transfer according to the Case BB scenario (Tauris et al. 2015, 2017). This will lead to an ultra stripped star, which will explode as a Type Ib/Ic SN, leaving a NS. Since the associated kick will likely be small (Tauris et al. 2017), the binary system will presumably stay intact, forming a DNS.

Independent of the future evolution of the HMXBs investigated in this study, we highlight that HMXBs and their properties offer the possibility to falsify stellar evolution scenarios and population synthesis models predicting event rates of double degenerate mergers. These simulations often also include some kind of HMXB evolution phase. Thus, the properties of the HMXB population can be used to constrain these models. Therefore, further studies analyzing a large fraction of the HMXB population are imperative.

7. Efficiency of the accretion mechanism

The X-ray luminosity L_{X} of the accreting NS in our HMXBs is related to the accretion rate S_{accr} via the accretion efficiency parameter ϵ:

$$L_{\mathrm{X}} = \epsilon S_{\mathrm{accr}} c^2. \tag{5}$$

The actual value of the accretion efficiency depends on the detailed physics of the accretion mechanism. Comparing the

X-ray luminosities measured with *Swift* during our HST observation (see Table 3) with theoretical expectations, we are able to put observational constraints on ϵ in some of the systems in our sample.

In the Bondi–Hoyle–Lyttleton formalism (e.g., Davidson & Ostriker 1973; Martínez-Núñez et al. 2017), the stellar wind accretion rate, S_{accr}, can be estimated as

$$S_{\mathrm{accr}} \approx 1.5 \times 10^7 \left(\frac{\dot{M}}{M_\odot \, \mathrm{yr}^{-1}} \right) \left(\frac{v_{\mathrm{rel}}}{10^8 \mathrm{cm \, s}^{-1}} \right)^{-4}$$
$$\times \left(\frac{M_{\mathrm{NS}}}{M_\odot} \right) \left(\frac{d_{\mathrm{NS}}}{R_\odot} \right)^{-2} S_{\mathrm{Edd}}, \tag{6}$$

where d_{NS} is the orbital separation and S_{Edd} is the Eddington accretion rate, which is defined as

$$S_{\mathrm{Edd}} = \frac{L_{\mathrm{Edd}}}{c^2}, \tag{7}$$

with L_{Edd} being the Eddington luminosity. For a fully ionized plasma that only consists of helium and hydrogen, L_{Edd} can be approximated as

$$L_{\mathrm{Edd}} \approx 2.55 \times 10^{38} \frac{M_{\mathrm{NS}}/M_\odot}{1 + X_{\mathrm{H}}} \, \mathrm{erg \, s}^{-1}. \tag{8}$$

The hydrogen mass fraction X_{H} of the accreted material is obtained from our spectral analyses. The orbital separation between the donor star and the NS as well as the relative velocity of the matter passing by the NS are phase dependent. To allow for a meaningful comparison between the observed and the predicted X-ray flux, these parameters need to be calculated for the specific phase of our simultaneous HST and *Swift* observation. This is possible for only two systems in our sample (BD+60 73 and LM Vel) because an estimate of the inclination i is prerequisite for these calculations. To derive i, we make use of the mass function

$$f(M) = \frac{M_{\mathrm{NS}}^3 \sin^3 i}{(M_{\mathrm{spec}} + M_{\mathrm{NS}})^2}. \tag{9}$$

For BD+60 73 a mass function of $f(M) = 0.0069 \, M_\odot$ is derived by González-Galán et al. (2014), while Gamen et al. (2015) determine $f(M) = 0.004 \, M_\odot$ for LM Vel. Using the spectroscopic mass of the donor stars as derived from our spectral analyses, we are able to estimate the inclination to about 38° and 50° for BD+60 73 and LM Vel, respectively.

With the inclination at hand and the orbital period as well as the eccentricity from Table 2, we solve the Kepler equation numerically. This allows us to derive the phase dependent distance between the NS and the donor star d_{NS}. The wind velocity at the position of the NSs during our HST and *Swift* observations can then be derived from the atmosphere models.

With these properties, we are able to derive the accretion efficiencies using Eqs. (5)–(8). For BD+60 73, we obtain $\epsilon = 1.1 \times 10^{-3}$, while it is approximately a factor of two higher for LM Vel ($\epsilon = 2.1 \times 10^{-3}$). Although all stellar and wind parameters of the donor stars are constrained well, these results must be treated with some caution because of the discrepancies of the spectral fits described in Appendix B. Shakura et al. (2014) suggest that at low-luminosity states, SFXTs can be at the stage of quasi-spherical settling accretion when the accretion rate on to the NS is suppressed by a factor of ∼30 relative to the Bondi–Hoyle–Lyttleton value. This might be sufficient to explain the low accretion efficiency deduced for LM Vel and BD+60 73. Alternatively, Grebenev & Sunyaev (2007) and Bozzo et al. (2008) suggest that a magnetic gating or a propeller mechanism could strongly inhibit the accretion in SFXTs.

8. Wind accretion vs. Roche–lobe overflow

All HMXBs in our sample are thought to accrete matter only from the donor star wind or from its decretion disk. This perception is called into question by our analyses. For a subset of our sample RLOF during periastron passage seems plausible.

The Roche–lobe radii of the donor stars in our sample are estimated using a generalization of the fitting formula by Eggleton (1983) for nonsynchronous, eccentric binary systems provided by Sepinsky et al. (2007). For BD+60 73 and LM Vel, the Roche–lobe radius at periastron, $R_{\mathrm{rl,peri}}$, is smaller than the stellar radius (see in Table 4). During this orbital phase, matter can be directly transferred to the NS via the inner Lagrangian point. We note that this finding has no influence on the estimates performed in the previous section since the HST and corresponding *Swift* observations of these sources were performed during a quiescent X-ray phase.

Interestingly, both of these sources are classified as X-ray transients. For BD+60 73, the X-ray light curve folded with the orbital phase peaks around $\phi \approx 0.2$, corresponding to 3–4 d after periastron (González-Galán et al. 2014). This behavior is usually attributed to an increased wind accretion-rate during periastron passage because of the lower wind velocity and higher wind density during this phase. However, for BD+60 73, the reason could be direct overflow of matter, which follows the gravitational potential. The delay between periastron passage and outburst might be due to inhibition of direct accretion onto the NS because of magnetic and centrifugal gating mechanisms (Illarionov & Sunyaev 1975; Grebenev & Sunyaev 2007; Bozzo et al. 2008).

For LM Vel, the X-ray outbursts cluster around periastron as well (Gamen et al. 2015). In contrast to BD+60 73, however, the outbursts are also observed prior to periastron passage ($\phi = 0.84 - 0.07$), suggesting that in this case a combination of donor-wind capture and RLOF might feed the accretion.

For these two systems, the amount of mass transfer via RLOF needs to be relatively limited, since otherwise these systems are expected to quickly enter a CE phase. Moreover, we note that our estimates of the Roche-lobe radius should be treated with caution, since some of the orbital parameters of our binary systems, such as the inclination, are not well constrained.

Hydrodynamical simulations (Mohamed & Podsiadlowski 2007) suggest that a further mode of mass transfer plays a role in certain binary systems. This so-called wind Roche-lobe overflow (WRLOF) invokes a focusing of the primary stellar-wind towards the secondary. Recently, El Mellah et al. (2019b) have suggested that this mechanism is chiefly responsible for the formation of so-called ultra-luminous X-ray sources (ULXs), and that it also plays a role in certain HMXBs. Wind Roche-lobe overflow gets important when the radius were the wind is accelerated beyond the escape velocity is comparable to the Roche-lobe radius (Mohamed & Podsiadlowski 2007; Abate et al. 2013). This condition is fulfilled for all wind-fed HMXBs in our sample (HD 153919, HD 306414, BD+60 73, and LM Vel). However, the detailed calculations by El Mellah et al. (2019b) suggest that this might be a too crude criterion. Their scenario for NSs is roughly applicable to HD 306414. For this object, their model predicts WRLOF for periastron, but not for apastron.

WRLOF seems to be a possible mass-transfer mechanism in wind-fed HMXBs, but presumably not during all orbital phases. Mass-transfer in these systems can be significantly higher compared to the classical Bondi–Hoyle–Lyttleton mechanism (Podsiadlowski & Mohamed 2007). However, this is not directly reflected in the X-ray luminosities of these objects, which are

moderate (see e.g., Table 3). So, an effective gating mechanism seems to be at work in these systems that hampers the accretion of the transferred material (see also discussion in El Mellah et al. 2019b on Vela X-1).

9. Summary and conclusions

For this study, we observed six HMXBs with the HST STIS and secured high S/N, high resolution UV spectra. Simultaneously to these HST observations, we obtained *Swift* X-ray data to characterize the X-ray emission of the NSs. These data sets were used to determine the wind and stellar parameters of the donor stars in these HMXBs by means of state of the art model atmospheres, accounting for the influence of the X-rays on the donor-star atmosphere. The wind parameters of these objects were deduced for the first time. Based on these analyses, we draw the following conclusions:

– The donor stars occupy the same parameter space as the putatively single OB-type stars from the Galaxy. Thus, the winds of these stars do not appear to be peculiar, in contrast to earlier suggestions.

– There is no systematic difference between the wind parameters of the donor stars in SFXTs compared to persistent HMXBs.

– All SFXTs in our sample are characterized by high orbital eccentricities. Thus, the wind velocities at the position of the NS and, consequently, the accretion rates are strongly phase dependent. This leads us to conclude that the orbital eccentricity is decisive for the distinction between SFXTs and persistent HMXBs.

– In all investigated systems, the orbital velocities of the NSs are comparable to the wind velocity at their position. Therefore, the orbital velocity is important and can not be neglected in modeling the accretion or in estimating the accretion rate.

– Since all systems in our study have very tight orbits, the donor-star wind has not yet reached its terminal velocity when passing the position of the NS. While this has been reported earlier, it is in strong contrast to what is often implicitly assumed in the wider literature.

– For BD+60 73 and LM Vel, RLOF potentially occurs during periastron passage. Moreover, WRLOF seems plausible in a variety of HMXBs.

– The donor stars of HD 153919, BD+60 73, and LM Vel are in advanced evolutionary stages, as indicated by their abundance patterns. They are on the way to become red supergiants and will thus engulf their NS companion soon.

– The carbon and oxygen abundances of HD 153919, LM Vel, and HD 306414 suggest that their atmospheres were polluted by material accreted from the wind of the NS progenitor or SN ejecta.

– The donor star of HD 153919 and LM Vel are overluminous for their current mass.

– Statistically, the donor stars in our sample rotate faster than single OB-type stars typically do, suggesting mass accretion because of RLOF in the past. This is consistent with the orbital parameters of these systems.

– Most likely, the donor stars and the NSs of the HMXBs studied in this work will merge in an upcoming CE phase, forming some kind of Thorne–Żytkow objects.

– The accretion efficiency parameters ϵ of the NS in our sample are quite low, suggesting that either spherical settling accretion or a gated accretion mechanism was at work during our observations.

Note added in proof. In a recently published study, Ducci et al. (2019) analyze the LM Vel system (IGR J08408-4503) using archival and newly acquired X-ray data. The authors discuss in detail the possibility of RLOF and the formation of an accretion disc around the NS, leading to conclusions that are similar to ours.

References

Abate, C., Pols, O. R., Izzard, R. G., Mohamed, S. S., & de Mink S. E. 2013, A&A, 552, A26
Anderson, E., & Francis, C. 2012, Astron. Lett., 38, 331
Appenzeller, I., Fricke, K., Fürtig, W., et al. 1998, The Messenger, 94, 1
Asplund, M., Grevesse, N., Sauval, A. J., & Scott, P. 2009, ARA&A, 47, 481
Bailer-Jones, C. A. L., Rybizki, J., Fouesneau, M., Mantelet, G., & Andrae, R. 2018, AJ, 156, 58
Baum, E., Hamann, W.-R., Koesterke, L., & Wessolowski, U. 1992, A&A, 266, 402
Biehle, G. T. 1991, ApJ, 380, 167
Blay, P., Negueruela, I., Reig, P., et al. 2006, A&A, 446, 1095
Blondin, J. M. 1994, ApJ, 435, 756
Blondin, J. M., Kallman, T. R., Fryxell, B. A., & Taam, R. E. 1990, ApJ, 356, 591
Bondi, H., & Hoyle, F. 1944, MNRAS, 104, 273
Bouret, J.-C., Lanz, T., Hillier, D. J., et al. 2003, ApJ, 595, 1182
Bozzo, E., Falanga, M., & Stella, L. 2008, ApJ, 683, 1031
Bragança, G. A., Daflon, S., Cunha, K., et al. 2012, AJ, 144, 130
Brott, I., de Mink, S. E., Cantiello, M., et al. 2011, A&A, 530, A115
Burrows, D. N., Hill, J. E., Nousek, J. A., et al. 2005, Space Sci. Rev., 120, 165
Cannon, R. C. 1993, MNRAS, 263, 817
Cannon, R. C., Eggleton, P. P., Zytkow, A. N., & Podsiadlowski, P. 1992, ApJ, 386, 206
Cardelli, J. A., Clayton, G. C., & Mathis, J. S. 1989, ApJ, 345, 245
Cash, W. 1979, ApJ, 228, 939
Castor, J. I., & Lamers, H. J. G. L. M. 1979, ApJS, 39, 481
Chaty, S. 2008, Chin. J. Astron.d Astrophys. Suppl., 8, 197
Clark, J. S., Goodwin, S. P., Crowther, P. A., et al. 2002, A&A, 392, 909
Corbet, R. H. D., & Peele, A. G. 2001, ApJ, 562, 936
Crowther, P. A., Lennon, D. J., & Walborn, N. R. 2006, A&A, 446, 279
Cutri, R. M., Skrutskie, M. F., van Dyk, S., et al. 2003, VizieR Online Data Catalog: II/246
Cutri, R. M., Wright, E. L., Conrow, T., et al. 2012, VizieR Online Data Catalog: II/311
Davidson, K., & Ostriker, J. P. 1973, ApJ, 179, 585
De Donder, E., Vanbeveren, D., & van Bever, J. 1997, A&A, 318, 812
de Mink, S. E., Langer, N., Izzard, R. G., Sana, H., & de Koter, A. 2013, ApJ, 764, 166
DENIS Consortium 2005, VizieR Online Data Catalog: II/263
Ducci L., Ramano P., Ji L., Santangelo A. 2019, A&A, 631, A135
Dufton, P. L., Smartt, S. J., Lee, J. K., et al. 2006, A&A, 457, 265
Egan, M. P., Price, S. D., Kraemer, K. E., et al. 2003, VizieR Online Data Catalog: V/114
Eggleton, P. P. 1983, ApJ, 268, 368
El Mellah, I., Sander, A. A. C., Sundqvist, J. O., & Keppens, R. 2019a, A&A, 622, A189
El Mellah, I., Sundqvist, J. O., & Keppens, R. 2019b, A&A, 622, L3

Falanga, M., Bozzo, E., Lutovinov, A., et al. 2015, A&A, 577, A130
Feldmeier, A., Puls, J., & Pauldrach, A. W. A. 1997, A&A, 322, 878
Foellmi, C., & Moffat, A. F. J. 2002, ASP Conf. Ser., 263, 123
Fraser, M., Dufton, P. L., Hunter, I., & Ryans, R. S. I. 2010, MNRAS, 404, 1306
Gaia Collaboration 2016, VizieR Online Data Catalog: I/337
Gaia Collaboration (Brown, A. G. A., et al.) 2018, A&A, 616, A1
Gamen, R., Barbà, R. H., Walborn, N. R., et al. 2015, A&A, 583, L4
Garmany, C. D., Glaspey, J. W., Braganca, G. A., et al. 2015, AJ, 150, 41
Garrison, R. F., Hiltner, W. A., & Schild, R. E. 1977, ApJS, 35, 111
Gehrels, N., Chincarini, G., Giommi, P., et al. 2004, ApJ, 611, 1005
Giménez-García, A., Shenar, T., Torrejón, J. M., et al. 2016, A&A, 591, A26
González-Galán, A., Negueruela, I., Castro, N., et al. 2014, A&A, 566, A131
Gräfener, G., & Hamann, W.-R. 2005, A&A, 432, 633
Gräfener, G., Koesterke, L., & Hamann, W.-R. 2002, A&A, 387, 244
Grebenev, S. A., & Sunyaev, R. A. 2007, Astron. Lett., 33, 149
Hainich, R., Rühling, U., Todt, H., et al. 2014, A&A, 565, A27
Hamann, W.-R., & Gräfener, G. 2003, A&A, 410, 993
Hamann, W.-R., & Koesterke, L. 1998, A&A, 335, 1003
Hammerschlag-Hensberge, G., van Kerkwijk, M. H., & Kaper, L. 2003, A&A, 407, 685
Hatchett, S., & McCray, R. 1977, ApJ, 211, 552
Hauschildt, P. H., & Baron, E. 2014, A&A, 566, A89
Heger, A., & Langer, N. 2000, ApJ, 544, 1016
Hillier, D. J. 1991, A&A, 247, 455
Hillier, D. J., & Miller, D. L. 1999, ApJ, 519, 354
Hoyle, F., & Lyttleton, R. A. 1939, Proc. Camb. Philos. Soc., 35, 405
Huenemoerder, D. P., Oskinova, L. M., Ignace, R., et al. 2012, ApJ, 756, L34
Illarionov, A. F., & Sunyaev, R. A. 1975, A&A, 39, 185
in 't Zand, J. J. M., Kuiper, L., den Hartog, P. R., Hermsen, W., & Corbet, R. H. D. 2007, A&A, 469, 1063
Islam, N., & Paul, B. 2016, MNRAS, 461, 816
Ivanova, N., Justham, S., Chen, X., et al. 2013, A&ARv, 21, 59
Kaufer, A., Stahl, O., Tubbesing, S., et al. 1999, The Messenger, 95, 8
Kimble, R. A., Woodgate, B. E., Bowers, C. W., et al. 1998, ApJ, 492, L83
Krtička, J., Kubát, J., & Krtičková, I. 2015, A&A, 579, A111
Kruckow, M. U., Tauris, T. M., Langer, N., et al. 2016, A&A, 596, A58
Kudritzki, R. P. 2002, ApJ, 577, 389
Kudritzki, R. P., Pauldrach, A., Puls, J., & Abbott, D. C. 1989, A&A, 219, 205
Kudritzki, R.-P., Lennon, D. J., & Puls, J. 1995, in Science with the VLT, eds. J. R. Walsh, & I. J. Danziger (Heidelberg: Springer), 246
Kudritzki, R. P., Puls, J., Lennon, D. J., et al. 1999, A&A, 350, 970
Langer, N. 1992, A&A, 265, L17
Levesque, E. M., Massey, P., Żytkow, A. N., & Morrell, N. 2014, MNRAS, 443, L94
Lorenzo, J., Negueruela, I., Castro, N., et al. 2014, A&A, 562, A18
Lucy, L. B., & Solomon, P. M. 1970, ApJ, 159, 879
Maeder, A. 1987, A&A, 178, 159
Marcolino, W. L. F., Bouret, J.-C., Martins, F., et al. 2009, A&A, 498, 837
Martinez-Chicharro, M., Torrejón, J. M., Oskinova, L., et al. 2018, MNRAS, 473, L74
Martínez-Núñez, S., Sander, A., Gímenez-García, A., et al. 2015, A&A, 578, A107
Martínez-Núñez, S., Kretschmar, P., Bozzo, E., et al. 2017, Space Sci. Rev., 212, 59
Martins, F., Schaerer, D., Hillier, D. J., et al. 2005, A&A, 441, 735
Martins, F., Hillier, D. J., Bouret, J. C., et al. 2009, A&A, 495, 257
Massey, P., Puls, J., Pauldrach, A. W. A., et al. 2005, ApJ, 627, 477
Mermilliod, J. C. 2006, VizieR Online Data Catalog: II/168
Mohamed, S., & Podsiadlowski, P. 2007, ASP Conf. Ser., 372, 397
Mokiem, M. R., de Koter, A., Vink, J. S., et al. 2007, A&A, 473, 603
Monet, D. G., Levine, S. E., Canzian, B., et al. 2003, AJ, 125, 984
Moos, H. W., Cash, W. C., Cowie, L. L., et al. 2000, ApJ, 538, L1
Morel, M., & Magnenat, P. 1978, A&AS, 34, 477
Motch, C., Stella, L., Janot-Pacheco, E., & Mouchet, M. 1991, ApJ, 369, 490
Munari, U., & Zwitter, T. 2002, A&A, 383, 188
Negueruela, I., & Reig, P. 2001, A&A, 371, 1056
Negueruela, I., Smith, D. M., Reig, P., Chaty, S., & Torrejón, J. M. 2006, ESA SP, 604, 165
Nomoto, K., Tominaga, N., Umeda, H., Kobayashi, C., & Maeda, K. 2006, Nucl. Phys. A, 777, 424
Nomoto, K., Kobayashi, C., & Tominaga, N. 2013, ARA&A, 51, 457
Oskinova, L. M., Hamann, W.-R., & Feldmeier, A. 2007, A&A, 476, 1331
Oskinova, L. M., Todt, H., Ignace, R., et al. 2011, MNRAS, 416, 1456

Oskinova, L. M., Feldmeier, A., & Kretschmar, P. 2012, MNRAS, 421, 2820
Ostriker, J. P., & Davidson, K. 1973, IAU Symp., 55, 143
Özel, F., & Freire, P. 2016, ARA&A, 54, 401
Packet, W. 1981, A&A, 102, 17
Paczyński, B. 1967, Acta Astron., 17, 355
Pallavicini, R., Golub, L., Rosner, R., et al. 1981, ApJ, 248, 279
Pauldrach, A., Puls, J., & Kudritzki, R. P. 1986, A&A, 164, 86
Podsiadlowski, P. 1994, Mem. Soc. Astron. It., 65, 359
Podsiadlowski, P., & Mohamed, S. 2007, Balt. Astron., 16, 26
Podsiadlowski, P., Cannon, R. C., & Rees, M. J. 1995, MNRAS, 274, 485
Prinja, R. K. 1989, MNRAS, 241, 721
Puls, J., Kudritzki, R.-P., Herrero, A., et al. 1996, A&A, 305, 171
Ramachandran, V., Hamann, W.-R., Hainich, R., et al. 2018, A&A, 615, A40
Ramírez-Agudelo, O. H., Simón-Díaz, S., Sana, H., et al. 2013, A&A, 560, A29
Rauscher, T., Heger, A., Hoffman, R. D., & Woosley, S. E. 2002, ApJ, 576, 323
Reig, P., & Fabregat, J. 2015, A&A, 574, A33
Reig, P., Torrejón, J. M., Negueruela, I., et al. 2009, A&A, 494, 1073
Ribó, M., Negueruela, I., Blay, P., Torrejón, J. M., & Reig, P. 2006, A&A, 449, 687
Rodes-Roca, J. J., Bernabeu, G., Magazzù, A., Torrejón, J. M., & Solano, E. 2018, MNRAS, 476, 2110
Romano, P., Sidoli, L., Cusumano, G., et al. 2009, ApJ, 696, 2068
Runacres, M. C., & Owocki, S. P. 2002, A&A, 381, 1015
Sander, A. A. C. 2019, IAU Symp., 346, 17
Sander, A., Shenar, T., Hainich, R., et al. 2015, A&A, 577, A13
Sander, A. A. C., Fürst, F., Kretschmar, P., et al. 2018, A&A, 610, A60
Sander, A. A. C., Hamann, W.-R., Todt, H., et al. 2019, A&A, 621, A92
Schneider, F. R. N., Langer, N., de Koter, A., et al. 2014, A&A, 570, A66
Seaton, M. J. 1979, MNRAS, 187, 73P
Sepinsky, J. F., Willems, B., & Kalogera, V. 2007, ApJ, 660, 1624
Shakura, N., Postnov, K., Sidoli, L., & Paizis, A. 2014, MNRAS, 442, 2325
Shara, M. M., Crawford, S. M., Vanbeveren, D., et al. 2017, MNRAS, 464, 2066
Shenar, T., Oskinova, L. M., Järvinen, S. P., et al. 2017, A&A, 606, A91
Sidoli, L., & Paizis, A. 2018, MNRAS, 481, 2779
Simón-Díaz, S. 2010, A&A, 510, A22
Simón-Díaz, S., & Herrero, A. 2014, A&A, 562, A135
Sota, A., Maíz Apellániz, J., Morrell, N. I., et al. 2014, ApJS, 211, 10
Stoyanov, K. A., Zamanov, R. K., Latev, G. Y., Abedin, A. Y., & Tomov, N. A. 2014, Astron. Nachr., 335, 1060
Sundqvist, J. O., Owocki, S. P., & Puls, J. 2018, A&A, 611, A17
Swank, J. H., Smith, D. M., & Markwardt, C. B. 2007, ATel, 999
Taam, R. E., & Ricker, P. M. 2010, New Astron. Rev., 54, 65
Taam, R. E., & Sandquist, E. L. 2000, ARA&A, 38, 113
Tauris, T. M., Langer, N., & Podsiadlowski, P. 2015, MNRAS, 451, 2123
Tauris, T. M., Kramer, M., Freire, P. C. C., et al. 2017, ApJ, 846, 170
Telting, J. H., Avila, G., Buchhave, L., et al. 2014, Astron. Nachr., 335, 41
Thorne, K. S., & Zytkow, A. N. 1975, ApJ, 199, L19
Thorne, K. S., & Zytkow, A. N. 1977, ApJ, 212, 832
Thorsett, S. E., & Chakrabarty, D. 1999, ApJ, 512, 288
Toalá, J. A., Oskinova, L. M., Hamann, W.-R., et al. 2018, ApJ, 869, L11
Todt, H., Sander, A., Hainich, R., et al. 2015, A&A, 579, A75
Torrejón, J. M., Reig, P., Fürst, F., et al. 2018, MNRAS, 479, 3366
Vanbeveren, D., & De Loore, C. 1994, A&A, 290, 129
van den Heuvel, E. P. J., Portegies Zwart, S. F., & de Mink, S. E. 2017, MNRAS, 471, 4256
van Loon, J. T., Kaper, L., & Hammerschlag-Hensberge, G. 2001, A&A, 375, 498
Verner, D. A., Ferland, G. J., Korista, K. T., & Yakovlev, D. G. 1996, ApJ, 465, 487
Walter, R., Lutovinov, A. A., Bozzo, E., & Tsygankov, S. S. 2015, A&ARv, 23, 2
Wang, Y.-M. 1981, A&A, 102, 36
Waters, L. B. F. M., de Martino, D., Habets, G. M. H. J., & Taylor, A. R. 1989, A&A, 223, 207
Wilms, J., Allen, A., & McCray, R. 2000, ApJ, 542, 914
Woodgate, B. E., Kimble, R. A., Bowers, C. W., et al. 1998, PASP, 110, 1183
Woosley, S. E. 2019, ApJ, 878, 49
Woosley, S. E., & Heger, A. 2006, ApJ, 637, 914
Woosley, S. E., & Heger, A. 2007, Phys. Rep., 442, 269
Xu, W., & Stone, J. M. 2019, MNRAS, 488, 5162
Yoon, S.-C., & Langer, N. 2005, A&A, 443, 643
Zacharias, N., Monet, D. G., Levine, S. E., et al. 2004, BAAS, 36, 1418

Appendix A: Additional tables

Table A.1. Spectroscopic data.

Identifier	Wavelength (Å)	Instrument	Resolving power	Observation date	MJD (d)	Phase
HD 153919	905–1187	FUSE	20 000	2003-07-30	52 850.918 969 91	0.945
	905–1187	FUSE	20 000	2003-07-31	52 851.763 298 61	0.193
	905–1187	FUSE	20 000	2003-04-07	52 736.607 476 85	0.439
	905–1187	FUSE	20 000	2003-08-02	52 853.352 546 3	0.658
	1150–1700	STIS/HST	45 800	2015-02-22	57 075.260 507 76	0.138
	3630–7170	FEROS/ESO-2.2m	48 000	2005-06-25	53 546.318 821 76	0.773
	3630–7170	FEROS/ESO-2.2m	48 000	2009-05-03	54 954.273 102 96	0.457
	3630–7170	FEROS/ESO-2.2m	48 000	2011-05-18	55 699.248 950 24	0.816
BD+60 73	1150–1700	STIS/HST	45 800	2015-01-01	57 023.491 883 41	0.841
	3630–7170	FIES/NOT	25 000	2013-01-29	56 321.839 447 92	0.038
LM Vel	905–1187	FUSE	20000	1999-12-26	51 538.837 581 02	0.366
	1150–1700	STIS/HST	45 800	2015-07-16	57 219.381 830 42	0.855
	1150–1980	SWP/IUE	10 000	1994-12-09	49 607.753 564 81	0.709
	1150–1980	SWP/IUE	10 000	1994-12-09	49 607.881 655 09	0.695
	1150–1980	SWP/IUE	10 000	1994-12-09	49 607.991 550 93	0.684
	1850–3350	LWP/IUE	15 000	1994-12-09	49 607.840 416 67	0.7
	1850–3350	LWP/IUE	15 000	1994-12-09	49 607.952 280 09	0.688
	3630–7170	FEROS/ESO-2.2m	48 000	2006-01-04	53 739.209 607 84	0.806
	3630–7170	FEROS/ESO-2.2m	48 000	2007-04-18	54 208.999 846 17	0.58
HD 306414	1150–1700	STIS/HST	45 800	2015-08-16	57 250.785 858 94	–
	3630–7170	FEROS/ESO-2.2m	48 000	2007-01-17	54 117.146 425 24	–
	3630–7170	FEROS/ESO-2.2m	48 000	2007-02-13	54 144.068 183 66	–
BD+53 2790	1150–1700	STIS/HST	45 800	2015-08-15	57 249.562 247 83	–
	3230–7530	B&C/Asiago	150–400	–	–	–
	3950–5780	DADOS/OST	3500	2016-04-20	57 498.944 537 04	–
	5290–7140	DADOS/OST	3500	2016-03-04	57 451.024 027 78	–
	14800–17800	NICS/TNG	1150	2014-09-01	56 901	–
	19500–23400	NICS/TNG	1250	2014-09-01	56 901	–
HD 100199	905–1187	FUSE	20 000	2000-03-24	51 627.242 361 11	–
	1150–1700	STIS/HST	45 800	2015-01-16	57 038.999 233 04	–
	3630–7170	FEROS/ESO-2.2m	48 000	2007-06-27	54 278.001 558 06	–
	3630–7170	FEROS/ESO-2.2m	48 000	2007-06-29	54 280.965 128 31	–

Table A.2. Photometry.

	HD 153919	BD+60 73	LM Vel	HD 306414	BD+53 2790	HD 100199
U (mag)	6.06 [a]	9.79 [b]	7.053 [c]	10.12 [c]	9.42 [c]	7.351 [c]
B (mag)	6.724 [d]	10.21 [b]	7.722 [d]	10.52 [d]	10.11 [e]	8.19 [c]
V (mag)	6.543 [d]	9.64 [b]	7.558 [d]	10.11 [d]	9.84 [e]	8.187 [c]
R (mag)	6.43 [d]	9.31 [d]	7.47 [d]	9.84 [d]	9.64 [e]	8.18 [f]
G (mag) [g]	6.38	9.4	7.449	9.703	9.726	8.176
I (mag)	5.93 [a]	9.072 [b]	–	9.41 [h]	9.43 [e]	8.22 [f]
J (mag) [i]	5.744	8.389	6.935	8.548	9.218	8.048
H (mag) [i]	5.639	8.265	6.887	8.340	9.116	8.067
K_S (mag) [i]	5.496	8.166	6.808	8.185	9.038	8.009
$W1$ (mag) [j]	5.36	8.104	6.756	8.043	8.7	8.063
$W2$ (mag) [j]	5.109	8.085	6.687	7.982	8.562	8.012
$W3$ (mag) [j]	4.927	7.994	6.585	7.807	8.191	7.625
$W4$ (mag) [j]	4.273	7.521	6.207	7.412	7.9	7.041
MSX6C A (Jy)	0.6344 [k]	–	–	–	–	–

References. [a]Morel & Magnenat (1978), [b]Anderson & Francis (2012), [c]Mermilliod (2006), [d]Zacharias et al. (2004), [e]Reig & Fabregat (2015), [f]Monet et al. (2003), [g]Gaia Collaboration (2016), [h]DENIS Consortium (2005), [i]Cutri et al. (2003), [j]Cutri et al. (2012), [k]Egan et al. (2003).

Table A.3. X-ray measurements at times close to the UV observations.

Identifier	ObsIDs	Observation mode	Observation date	MJD (d)	Phase
HD 153919	00033631008	WT	2015-02-22	57 075.178 724 58	0.141
BD+60 73	00032620025	PC	2015-01-01	57 023.680 822 04	0.853
LM Vel	00037881103	PC	2015-07-08	57 211.149 012 27	0.008
	00037881107	PC	2015-07-16	57 219.123 576 39	0.901
HD 306414	00030881043	PC	2015-08-16	57 250.846 361 96	–
BD+53 2790	00033914003	WT	2015-08-15	57 249.215 370 77	–
HD 100199	00035224007	PC	2015-01-15	57 037.818 252 68	–

Table A.4. Atomic model used in the stellar atmosphere calculations.

Ion	Number of levels	Number of transitions	Ion	Number of levels	Number of transitions
H I	22	231	Mg III	43	903
H II	1	0	Mg IV	17	136
He I	35	595	Mg V	0	0
He II	26	325	Mg VII	0	0
He III	1	0	Si II	1	0
N II	38	703	Si III	24	276
N III	36	630	Si IV	23	253
N IV	38	703	Si V	1	0
N V	20	190	P IV	12	66
N VI	14	91	P V	11	55
C II	32	496	P VI	1	0
C III	40	780	G II [a]	1	0
C IV	25	300	G III [a]	13	40
C V	29	406	G IV [a]	18	77
C VI	15	105	G V [a]	22	107
O II	37	666	G VI [a]	29	194
O III	33	528	G VII [a]	19	87
O IV	29	406	G VIII [a]	14	49
O V	36	630	G IX [a]	15	56
O VI	16	120	G X [a]	1	0
O VII	0	0	G XI [a]	0	0
O VIII	0	0	G XII [a]	0	0
S III	23	253	G XIII [a]	0	0
S IV	11	55	G XIV [a]	0	0
S V	10	45	G XV [a]	0	0
S VI	1	0	G XVI [a]	0	0
Mg I	1	0	G XVII [a]	0	0
Mg II	32	496			

Notes. [a] G denotes a generic atom which incorporates the following iron group elements Fe, Sc, Ti, Cr, Mn, Co, and Ni. The corresponding ions are treated by means of a superlevel approach (for details see Gräfener et al. 2002).

Table A.5. Empirical stellar parameters, compared to the best-fitting single-star evolution model as interpolated with the BONNSAI tool.

	HD 153919		LM Vel		BD+53 2790 [a]	
	This study	BONNSAI	This study	BONNSAI	This study	BONNSAI
T_* [kK]	35^{+2}_{-3}	35^{+3}_{-3}	30^{+3}_{-3}	29^{+3}_{-3}	30^{+3}_{-3}	31^{+3}_{-3}
$\log L$ [$L_\odot$]	$5.7^{+0.1}_{-0.1}$	$5.68^{+0.09}_{-0.08}$	$5.3^{+0.1}_{-0.1}$	$5.34^{+0.09}_{-0.09}$	$4.9^{+0.1}_{-0.1}$	$4.9^{+0.1}_{-0.1}$
$\log g_*$ [cm s^{-2}]	$3.4^{+0.4}_{-0.4}$	$3.5^{+0.2}_{-0.2}$	$3.2^{+0.2}_{-0.2}$	$3.3^{+0.2}_{-0.3}$	$3.8^{+0.3}_{-0.5}$	$3.8^{+0.2}_{-0.3}$
$v \sin i$ [km s^{-1}]	110^{+30}_{-50}	100^{+40}_{-40}	150^{+20}_{-20}	150^{+20}_{-20}	200^{+50}_{-50}	200^{+45}_{-57}
X_H [mass fr.]	$0.65^{+0.1}_{-0.2}$	$0.72^{+0.00}_{-0.01}$	$0.5^{+0.1}_{-0.1}$	$0.72^{+0.00}_{-0.2}$		
$\log \dot{M}$ [$M_\odot$yr^{-1}]	$-5.6^{+0.2}_{-0.3}$	$-5.7^{+0.2}_{-0.2}$	$-6.1^{+0.2}_{-0.2}$	$-6.2^{+0.2}_{-0.2}$		
M [$M_\odot$] [b]	34^{+100}_{-28}	43^{+5}_{-6}	16^{+29}_{-11}	24^{+6}_{-2}	27^{+67}_{-23}	20^{+2}_{-2}

Notes. [a] X_H and $\log \dot{M}$ not used as input for the BONNSAI tool. [b] Parameter not used as input for the BONNSAI tool.

Table A.6. Atmospheric structure of the model used to fit HD 153919.

Depth index	$r-1$ [R_*]	T_e [K]	$\log N$ [Atoms cm^{-3}]	$\log N_e$ [Electrons cm^{-3}]	τ_{Ross}	v [km s^{-1}]	$\partial v/\partial r$ $\left[\frac{\text{km s}^{-1}}{R_*}\right]$	D
1	99.0	16849	6.200	6.202	0.000000	1900	0.51	20.00
2	78.6	16568	6.400	6.402	0.000044	1891	0.51	20.00
3	65.0	16181	6.564	6.566	0.000087	1883	0.76	20.00
4	54.5	15711	6.718	6.720	0.000136	1873	1.10	20.00
5	45.1	15333	6.882	6.883	0.000199	1861	1.61	20.00
6	36.6	15117	7.064	7.065	0.000284	1844	2.43	20.00
7	28.7	15107	7.271	7.273	0.000407	1821	3.70	20.00
8	22.9	15175	7.469	7.471	0.000555	1794	5.48	20.00
9	19.2	15467	7.619	7.621	0.000691	1769	7.79	20.00
10	16.6	16009	7.747	7.748	0.000827	1745	10.54	20.00
11	14.2	16773	7.878	7.880	0.000990	1716	13.92	20.00
12	12.2	17643	8.013	8.015	0.001188	1683	18.44	20.00
13	10.4	18457	8.151	8.153	0.001427	1645	24.48	20.00
14	8.81	19083	8.291	8.294	0.001714	1601	32.50	20.00
15	7.45	19465	8.434	8.436	0.002060	1550	43.06	20.00
16	6.29	19980	8.579	8.582	0.002475	1492	56.84	20.00
17	5.30	20661	8.726	8.728	0.002976	1427	74.61	20.00
18	4.45	21644	8.874	8.877	0.003578	1355	95.49	20.00
19	3.82	22689	9.003	9.006	0.004195	1287	117.89	20.00
20	3.42	23515	9.098	9.101	0.004713	1233	142.12	20.00
21	3.05	24297	9.194	9.197	0.005305	1176	167.15	20.00
22	2.67	25122	9.305	9.308	0.006077	1108	193.42	20.00
23	2.38	26042	9.401	9.405	0.006839	1047	222.16	20.00
24	2.16	26966	9.481	9.485	0.007544	995.4	249.83	20.00
25	1.98	27963	9.554	9.559	0.008261	947.0	276.22	20.00
26	1.81	29049	9.627	9.632	0.009044	898.6	303.88	20.00
27	1.64	30313	9.707	9.713	0.009993	845.4	332.64	20.00
28	1.49	31661	9.788	9.794	0.011065	791.6	362.37	20.00
29	1.36	32934	9.862	9.870	0.012162	742.6	392.66	20.00
30	1.24	34109	9.936	9.945	0.013371	694.5	423.02	20.00
31	1.12	35304	10.016	10.028	0.014850	642.9	456.27	20.00
32	0.994	36696	10.115	10.132	0.016931	581.3	492.35	20.00
33	0.862	38300	10.228	10.251	0.019733	513.7	527.73	20.00
34	0.760	39712	10.327	10.356	0.022600	457.8	562.79	20.00
35	0.669	41002	10.426	10.460	0.025938	405.0	595.39	20.00

Notes. The columns depict the index of the radius grid, the radius (r), the electron temperature (T_e), the particle density (N), the electron density (N_e), the Rosseland optical depth (τ_{Ross}), the velocity (v), the velocity gradient ($\partial v/\partial r$), and the clumping factor (D).

Table A.6. continued.

Depth index	$r - 1$ [R_*]	T_e [K]	$\log N$ [Atoms cm^{-3}]	$\log N_e$ [Electrons cm^{-3}]	τ_{Ross}	v [km s^{-1}]	$\partial v / \partial r$ $\left[\frac{\mathrm{km\,s}^{-1}}{R_*}\right]$	D
36	0.561	42161	10.561	10.599	0.031308	339.6	623.69	20.00
37	0.456	42264	10.718	10.757	0.039027	272.1	647.10	20.00
38	0.368	41181	10.876	10.916	0.048496	214.3	661.02	19.99
39	0.295	39459	11.035	11.075	0.059908	165.8	663.77	19.90
40	0.234	37646	11.196	11.235	0.073615	125.8	657.89	19.32
41	0.185	36045	11.360	11.399	0.089940	93.53	647.26	16.99
42	0.145	34786	11.530	11.569	0.109027	67.79	636.99	12.19
43	0.113	33915	11.708	11.749	0.130726	47.61	632.82	7.25
44	0.910E-01	33440	11.875	11.917	0.151891	33.72	638.17	4.43
45	0.779E-01	33216	12.011	12.054	0.169234	25.26	655.41	3.14
46	0.678E-01	33244	12.153	12.197	0.187398	18.55	683.78	2.35
47	0.598E-01	33712	12.318	12.362	0.208329	12.88	722.27	1.82
48	0.549E-01	34493	12.468	12.512	0.226873	9.201	771.17	1.54
49	0.522E-01	35113	12.589	12.632	0.241223	7.014	827.48	1.39
50	0.502E-01	35403	12.713	12.757	0.255687	5.288	863.94	1.28
51	0.485E-01	35173	12.854	12.898	0.272694	3.832	782.85	1.20
52	0.470E-01	34479	12.992	13.034	0.294653	2.799	589.33	1.14
53	0.455E-01	33462	13.127	13.168	0.325997	2.057	398.93	1.10
54	0.438E-01	32606	13.258	13.297	0.375705	1.526	241.83	1.08
55	0.417E-01	32468	13.380	13.419	0.459618	1.156	134.45	1.06
56	0.390E-01	33724	13.500	13.542	0.614719	0.8811	80.66	1.04
57	0.353E-01	35909	13.642	13.686	0.901224	0.6406	56.54	1.03
58	0.314E-01	38217	13.794	13.840	1.341922	0.4549	40.76	1.02
59	0.275E-01	40824	13.951	13.998	1.989510	0.3195	29.16	1.02
60	0.234E-01	43946	14.113	14.161	2.931172	0.2215	21.02	1.01
61	0.196E-01	47337	14.273	14.321	4.197718	0.1546	14.89	1.01
62	0.158E-01	51294	14.435	14.483	6.019716	0.1071	10.38	1.01
63	0.118E-01	55869	14.597	14.645	8.649841	0.7438E-01	7.05	1.00
64	0.800E-02	60945	14.752	14.801	12.284350	0.5239E-01	4.92	1.00
65	0.451E-02	65974	14.892	14.940	16.803763	0.3826E-01	3.63	1.00
66	0.197E-02	69898	14.992	15.041	21.052537	0.3052E-01	2.92	1.00
67	0.985E-03	71482	15.031	15.080	22.968391	0.2797E-01	2.54	1.00
68	0.492E-03	72328	15.051	15.099	23.991583	0.2677E-01	2.42	1.00
69	0.246E-03	72775	15.060	15.109	24.520859	0.2619E-01	2.41	1.00
70	0.00	73172	15.071	15.119	25.062930	0.2559E-01	2.41	1.00

Table A.7. Same as Table A.6, but for BD+60 73.

Depth index	$r - 1$ [R_*]	T_e [K]	$\log N$ [Atoms cm^{-3}]	$\log N_e$ [Electrons cm^{-3}]	τ_{Ross}	v [km s^{-1}]	$\partial v / \partial r$ $\left[\frac{\mathrm{km\,s}^{-1}}{R_*}\right]$	D
1	99.0	10780	4.589	4.673	0.0000000	1100	0.21	20.00
2	77.0	11061	4.807	4.891	0.0000011	1096	0.21	20.00
3	62.4	11307	4.988	5.072	0.0000022	1092	0.33	20.00
4	50.3	11610	5.175	5.259	0.0000036	1087	0.51	20.00
5	40.0	11869	5.372	5.456	0.0000054	1081	0.77	20.00
6	32.7	12085	5.544	5.629	0.0000074	1074	1.18	20.00
7	26.6	12370	5.720	5.805	0.0000099	1065	1.76	20.00
8	21.5	12672	5.904	5.989	0.0000131	1054	2.56	20.00
9	17.8	12882	6.062	6.147	0.0000165	1042	3.75	20.00
10	14.8	13067	6.220	6.305	0.0000205	1029	5.54	20.00
11	11.8	13271	6.413	6.499	0.0000265	1009	8.26	20.00
12	9.21	13475	6.620	6.705	0.0000347	982.6	12.44	20.00
13	7.39	13637	6.803	6.889	0.0000437	954.2	18.99	20.00
14	5.88	13879	6.993	7.078	0.0000553	919.2	28.41	20.00

Table A.7. continued.

Depth index	$r-1$ [R_*]	T_e [K]	$\log N$ [Atoms cm^{-3}]	$\log N_e$ [Electrons cm^{-3}]	τ_{Ross}	v [km s^{-1}]	$\partial v/\partial r$ $\left[\frac{\mathrm{km\,s}^{-1}}{R_*}\right]$	D
15	4.59	14181	7.194	7.280	0.0000708	874.6	41.37	20.00
16	3.68	14465	7.372	7.458	0.0000877	828.2	59.70	20.00
17	2.98	14811	7.540	7.624	0.0001069	778.5	81.88	20.00
18	2.46	15188	7.690	7.773	0.0001276	728.5	106.43	20.00
19	2.12	15415	7.806	7.874	0.0001457	686.8	132.78	20.00
20	1.87	15526	7.903	7.945	0.0001624	649.8	158.02	20.00
21	1.66	15676	7.991	8.014	0.0001785	614.8	183.80	20.00
22	1.48	15866	8.079	8.091	0.0001958	578.9	212.54	20.00
23	1.30	16163	8.177	8.184	0.0002170	537.6	244.27	20.00
24	1.13	16511	8.278	8.282	0.0002412	494.5	278.98	20.00
25	1.00	16803	8.369	8.371	0.0002653	455.3	316.33	20.00
26	0.889	17088	8.459	8.461	0.0002917	416.6	355.69	20.00
27	0.773	17456	8.561	8.562	0.0003248	373.3	396.57	20.00
28	0.670	17787	8.667	8.668	0.0003629	329.9	438.45	20.00
29	0.589	18003	8.762	8.763	0.0004006	292.5	480.21	20.00
30	0.519	18164	8.857	8.857	0.0004415	257.5	520.41	20.00
31	0.449	18330	8.966	8.967	0.0004938	219.8	561.22	20.00
32	0.377	18579	9.103	9.103	0.0005667	177.8	601.70	20.00
33	0.311	18795	9.260	9.261	0.0006620	136.6	636.86	20.00
34	0.262	18783	9.408	9.408	0.0007627	104.8	663.89	19.99
35	0.223	18557	9.561	9.561	0.0008787	78.47	678.39	19.85
36	0.190	18140	9.736	9.736	0.0010278	55.43	681.30	18.62
37	0.166	17723	9.905	9.905	0.0011855	39.15	673.31	14.51
38	0.147	17410	10.081	10.082	0.0013636	26.92	655.43	8.75
39	0.133	17258	10.279	10.280	0.0015789	17.51	630.71	4.65
40	0.123	17255	10.470	10.471	0.0018024	11.48	598.74	2.85
41	0.116	17309	10.673	10.674	0.0020619	7.283	563.73	1.97
42	0.110	17376	10.894	10.895	0.0023756	4.421	520.47	1.51
43	0.107	17430	11.093	11.094	0.0026989	2.812	426.00	1.30
44	0.104	17478	11.271	11.271	0.0031069	1.878	289.33	1.19
45	0.102	17525	11.443	11.443	0.0037374	1.269	190.02	1.13
46	0.991E-01	17569	11.602	11.602	0.0046423	0.8847	128.33	1.09
47	0.968E-01	17610	11.740	11.740	0.0058162	0.6466	89.33	1.06
48	0.947E-01	17659	11.867	11.867	0.0073703	0.4844	64.20	1.05
49	0.924E-01	17722	11.992	11.992	0.0095380	0.3645	46.32	1.04
50	0.900E-01	17821	12.128	12.128	0.0129282	0.2677	32.39	1.03
51	0.868E-01	18002	12.295	12.296	0.0193523	0.1832	21.86	1.02
52	0.832E-01	18287	12.484	12.485	0.0313790	0.1194	14.25	1.01
53	0.795E-01	18617	12.668	12.669	0.0512036	0.7867E-01	9.09	1.01
54	0.758E-01	18909	12.852	12.853	0.0843564	0.5185E-01	5.85	1.00
55	0.719E-01	19386	13.037	13.037	0.1400030	0.3417E-01	3.79	1.00
56	0.682E-01	20123	13.212	13.213	0.2275228	0.2298E-01	2.44	1.00
57	0.642E-01	21329	13.388	13.389	0.3732539	0.1543E-01	1.55	1.00
58	0.601E-01	23023	13.562	13.562	0.6152817	0.1043E-01	0.97	1.00
59	0.558E-01	25021	13.723	13.724	1.0052881	0.7259E-02	0.58	1.00
60	0.510E-01	27525	13.871	13.873	1.6851150	0.5203E-02	0.32	1.00
61	0.454E-01	30726	13.994	14.008	2.9320173	0.3965E-02	0.15	1.00
62	0.388E-01	34591	14.078	14.131	5.0927269	0.3309E-02	0.08	1.00
63	0.306E-01	38867	14.163	14.243	8.4239990	0.2761E-02	0.07	1.00
64	0.210E-01	43101	14.292	14.379	13.2000894	0.2094E-02	0.07	1.00
65	0.119E-01	46971	14.440	14.530	19.0187288	0.1513E-02	0.06	1.00
66	0.532E-02	49918	14.560	14.650	24.5025477	0.1165E-02	0.05	1.00
67	0.266E-02	51158	14.609	14.700	27.0975069	0.1045E-02	0.04	1.00
68	0.133E-02	51802	14.634	14.724	28.4967969	0.9904E-03	0.04	1.00
69	0.665E-03	52142	14.646	14.736	29.2234434	0.9644E-03	0.04	1.00
70	0.00	52405	14.658	14.749	29.9683734	0.9390E-03	0.04	1.00

Table A.8. Same as Table A.6, LM Vel.

Depth index	$r-1$ [R_*]	T_e [K]	$\log N$ [Atoms cm^{-3}]	$\log N_e$ [Electrons cm^{-3}]	τ_{Ross}	v [km s^{-1}]	$\partial v/\partial r$ $\left[\frac{\mathrm{km\,s^{-1}}}{R_*}\right]$	D
1	99.0	12244	5.776	5.777	0.000000	1900	0.36	20.00
2	81.3	12377	5.947	5.947	0.000011	1895	0.36	20.00
3	66.8	12551	6.117	6.117	0.000024	1888	0.52	20.00
4	56.5	12679	6.261	6.261	0.000037	1882	0.74	20.00
5	48.0	12817	6.401	6.402	0.000053	1874	1.06	20.00
6	39.5	12960	6.570	6.570	0.000075	1864	1.55	20.00
7	31.3	13147	6.769	6.770	0.000108	1849	2.41	20.00
8	24.1	13368	6.993	6.994	0.000156	1827	3.80	20.00
9	18.9	13604	7.202	7.203	0.000213	1801	5.82	20.00
10	15.7	13805	7.359	7.360	0.000266	1778	8.49	20.00
11	13.4	14001	7.492	7.492	0.000319	1755	11.70	20.00
12	11.4	14222	7.628	7.628	0.000383	1728	15.69	20.00
13	9.70	14466	7.767	7.767	0.000459	1696	21.13	20.00
14	8.19	14722	7.908	7.909	0.000552	1660	28.50	20.00
15	6.89	14971	8.052	8.052	0.000663	1616	38.46	20.00
16	5.78	15196	8.197	8.198	0.000797	1567	51.82	20.00
17	4.83	15390	8.345	8.346	0.000959	1509	69.62	20.00
18	4.02	15549	8.494	8.495	0.001154	1444	93.06	20.00
19	3.33	15731	8.644	8.645	0.001388	1370	121.24	20.00
20	2.83	15952	8.775	8.776	0.001627	1300	152.43	20.00
21	2.50	16149	8.871	8.872	0.001828	1244	186.93	20.00
22	2.21	16414	8.969	8.970	0.002057	1184	222.80	20.00
23	1.91	16712	9.082	9.082	0.002355	1111	261.55	20.00
24	1.68	16970	9.180	9.181	0.002649	1045	305.24	20.00
25	1.51	17213	9.262	9.263	0.002921	988.6	347.98	20.00
26	1.36	17459	9.337	9.338	0.003194	935.4	389.43	20.00
27	1.23	17685	9.412	9.413	0.003491	881.9	433.54	20.00
28	1.10	17894	9.495	9.495	0.003848	822.5	480.18	20.00
29	0.982	18129	9.579	9.579	0.004249	762.0	529.60	20.00
30	0.883	18393	9.656	9.656	0.004650	706.9	580.95	20.00
31	0.794	18681	9.732	9.733	0.005086	652.9	633.15	20.00
32	0.705	18987	9.817	9.818	0.005615	594.2	690.93	20.00
33	0.608	19312	9.922	9.923	0.006342	524.4	754.71	20.00
34	0.512	19689	10.044	10.045	0.007291	448.7	819.36	20.00
35	0.439	20102	10.152	10.154	0.008248	385.8	884.82	20.00
36	0.375	20625	10.263	10.264	0.009332	327.6	945.90	20.00
37	0.303	21340	10.413	10.415	0.011037	257.8	1000.06	20.00
38	0.236	22101	10.596	10.598	0.013495	188.3	1046.78	20.00
39	0.183	22892	10.787	10.789	0.016552	132.2	1077.15	20.00
40	0.144	23705	10.988	10.990	0.020378	89.05	1087.19	19.95
41	0.118	24287	11.176	11.177	0.024497	60.57	1083.67	19.18
42	0.102	24608	11.323	11.325	0.028054	44.31	1073.03	16.32
43	0.908E-01	24844	11.476	11.477	0.031960	31.87	1061.83	11.25
44	0.813E-01	25025	11.647	11.649	0.036511	21.86	1051.91	6.38
45	0.748E-01	25140	11.813	11.816	0.040987	15.09	1044.61	3.84
46	0.700E-01	25233	11.992	11.994	0.045888	10.10	1042.53	2.52
47	0.665E-01	25296	12.195	12.197	0.051621	6.370	1032.38	1.81
48	0.642E-01	25204	12.393	12.395	0.057535	4.056	878.32	1.46
49	0.623E-01	25229	12.569	12.572	0.065284	2.708	502.37	1.29
50	0.603E-01	27320	12.684	12.688	0.077380	2.090	293.09	1.22
51	0.583E-01	28131	12.816	12.822	0.093865	1.546	274.98	1.16
52	0.567E-01	27241	12.965	12.969	0.114059	1.101	223.44	1.11
53	0.548E-01	26588	13.128	13.131	0.147806	0.7595	140.38	1.07
54	0.523E-01	26431	13.321	13.324	0.220182	0.4888	79.17	1.05
55	0.495E-01	27674	13.484	13.489	0.354247	0.3375	39.43	1.03
56	0.464E-01	29787	13.605	13.620	0.573287	0.2571	20.56	1.02
57	0.431E-01	31828	13.703	13.737	0.909476	0.2066	12.59	1.02
58	0.393E-01	33907	13.797	13.852	1.417588	0.1675	9.16	1.02

Table A.8. continued.

Depth index	$r-1$ [R_*]	T_e [K]	$\log N$ [Atoms cm^{-3}]	$\log N_e$ [Electrons cm^{-3}]	τ_{Ross}	v [km s^{-1}]	$\partial v/\partial r$ $\left[\frac{\text{km s}^{-1}}{R_*}\right]$	D
59	0.350E-01	36272	13.903	13.972	2.164155	0.1323	7.45	1.01
60	0.304E-01	38936	14.024	14.099	3.202444	0.1011	6.11	1.01
61	0.256E-01	41928	14.159	14.236	4.646333	0.7472E-01	4.83	1.01
62	0.206E-01	45302	14.308	14.386	6.665918	0.5354E-01	3.68	1.01
63	0.155E-01	49061	14.467	14.545	9.486130	0.3753E-01	2.68	1.00
64	0.103E-01	53284	14.629	14.708	13.487831	0.2608E-01	1.91	1.00
65	0.577E-02	57568	14.771	14.849	18.354869	0.1901E-01	1.40	1.00
66	0.255E-02	60902	14.870	14.949	22.796765	0.1522E-01	1.12	1.00
67	0.127E-02	62339	14.909	14.988	24.826495	0.1394E-01	0.98	1.00
68	0.637E-03	63111	14.929	15.008	25.908347	0.1334E-01	0.93	1.00
69	0.319E-03	63510	14.939	15.018	26.467092	0.1305E-01	0.89	1.00
70	0.00	63874	14.949	15.027	27.038266	0.1277E-01	0.89	1.00

Table A.9. Same as Table A.6, HD 306414.

Depth index	$r-1$ [R_*]	T_e [K]	$\log N$ [Atoms cm^{-3}]	$\log N_e$ [Electrons cm^{-3}]	τ_{Ross}	v [km s^{-1}]	$\partial v/\partial r$ $\left[\frac{\text{km s}^{-1}}{R_*}\right]$	D
1	99.0	11408	5.354	5.358	0.0000000	800.0	0.33	20.00
2	77.9	11693	5.563	5.568	0.0000086	794.5	0.33	20.00
3	61.0	12069	5.777	5.782	0.0000120	787.3	0.52	20.00
4	49.0	12371	5.968	5.973	0.0000328	779.4	0.79	20.00
5	40.5	12609	6.135	6.140	0.0000465	771.1	1.15	20.00
6	34.4	12800	6.276	6.282	0.0000603	762.7	1.59	20.00
7	29.5	12977	6.413	6.419	0.0000760	753.5	2.21	20.00
8	24.5	13177	6.576	6.582	0.0000984	740.7	3.15	20.00
9	19.6	13408	6.770	6.775	0.0001316	722.6	4.68	20.00
10	15.3	13654	6.988	6.994	0.0001797	697.9	7.00	20.00
11	12.2	13857	7.190	7.196	0.0002360	670.6	10.08	20.00
12	10.3	13995	7.337	7.343	0.0002860	647.6	13.79	20.00
13	9.01	14091	7.459	7.461	0.0003339	626.6	17.77	20.00
14	7.85	14166	7.583	7.584	0.0003899	603.5	22.19	20.00
15	6.83	14228	7.708	7.708	0.0004555	578.2	27.57	20.00
16	5.94	14280	7.834	7.835	0.0005323	550.8	34.03	20.00
17	5.16	14332	7.961	7.962	0.0006223	521.3	41.12	20.00
18	4.57	14390	8.072	8.072	0.0007122	494.5	48.26	20.00
19	4.18	14441	8.153	8.154	0.0007858	474.1	55.55	20.00
20	3.82	14500	8.235	8.236	0.0008681	452.9	62.68	20.00
21	3.45	14582	8.330	8.331	0.0009738	428.1	69.81	20.00
22	3.15	14674	8.412	8.412	0.0010752	406.3	77.99	20.00
23	2.88	14784	8.494	8.495	0.0011885	384.2	86.43	20.00
24	2.60	14935	8.590	8.590	0.0013344	358.7	94.57	20.00
25	2.38	15085	8.672	8.672	0.0014748	336.8	103.56	20.00
26	2.18	15253	8.754	8.755	0.0016315	315.0	112.41	20.00
27	1.97	15461	8.849	8.850	0.0018336	290.3	120.56	20.00
28	1.80	15645	8.931	8.932	0.0020283	269.6	129.12	20.00
29	1.65	15833	9.013	9.014	0.0022456	249.4	137.71	20.00
30	1.47	16091	9.125	9.125	0.0025817	223.1	146.09	20.00
31	1.28	16393	9.253	9.254	0.0030365	194.7	154.38	20.00
32	1.11	16691	9.380	9.381	0.0035735	168.7	161.37	20.00
33	0.970	16976	9.507	9.507	0.0042083	145.1	166.07	20.00
34	0.845	17237	9.632	9.632	0.0049592	124.1	168.57	20.00
35	0.710	17526	9.785	9.786	0.0060918	101.4	168.34	19.99
36	0.555	17870	9.997	9.998	0.0081641	75.29	165.97	19.80
37	0.428	18156	10.211	10.212	0.0109919	54.51	163.50	18.49
38	0.353	18344	10.368	10.368	0.0135395	42.36	164.01	15.69

Table A.9. continued.

Depth index	$r-1$ $[R_*]$	T_e [K]	$\log N$ [Atoms cm^{-3}]	$\log N_e$ [Electrons cm^{-3}]	τ_{Ross}	v [km s^{-1}]	$\partial v/\partial r$ $\left[\frac{\mathrm{km\,s^{-1}}}{R_*}\right]$	D
39	0.303	18503	10.496	10.497	0.0159196	33.98	169.30	12.23
40	0.260	18682	10.634	10.634	0.0186632	26.50	179.14	8.54
41	0.224	18856	10.784	10.785	0.0217985	19.84	194.86	5.54
42	0.196	18997	10.956	10.956	0.0253665	14.01	217.61	3.52
43	0.175	19018	11.159	11.160	0.0294662	9.089	246.53	2.31
44	0.162	19012	11.373	11.373	0.0334954	5.678	280.01	1.70
45	0.155	19000	11.566	11.567	0.0368697	3.679	286.92	1.41
46	0.150	18988	11.772	11.773	0.0411500	2.309	215.92	1.24
47	0.145	18985	11.957	11.957	0.0476307	1.524	127.86	1.16
48	0.140	19025	12.135	12.136	0.0586751	1.019	75.69	1.10
49	0.134	19183	12.329	12.329	0.0795186	0.6597	46.75	1.06
50	0.128	19445	12.511	12.511	0.1134129	0.4388	29.38	1.04
51	0.122	19829	12.672	12.672	0.1619540	0.3061	19.20	1.03
52	0.116	20581	12.816	12.817	0.2300313	0.2216	12.96	1.02
53	0.111	21773	12.948	12.949	0.3242194	0.1650	9.23	1.02
54	0.106	22843	13.082	13.082	0.4568929	0.1227	7.09	1.01
55	0.100	23741	13.226	13.227	0.6513269	0.8879E-01	5.15	1.01
56	0.946E-01	25314	13.358	13.359	0.9437404	0.6615E-01	3.04	1.01
57	0.886E-01	27456	13.453	13.456	1.3805658	0.5374E-01	1.55	1.01
58	0.819E-01	29203	13.521	13.531	2.0163611	0.4653E-01	0.86	1.00
59	0.741E-01	31253	13.581	13.605	2.9201390	0.4118E-01	0.62	1.00
60	0.649E-01	33713	13.647	13.690	4.1636413	0.3593E-01	0.59	1.00
61	0.547E-01	36162	13.739	13.791	5.8232465	0.2968E-01	0.60	1.00
62	0.437E-01	38800	13.857	13.912	8.0412546	0.2309E-01	0.56	1.00
63	0.325E-01	41730	13.991	14.047	11.0154549	0.1733E-01	0.47	1.00
64	0.214E-01	44925	14.135	14.192	14.9653989	0.1269E-01	0.38	1.00
65	0.119E-01	47999	14.268	14.325	19.4763247	0.9537E-02	0.31	1.00
66	0.525E-02	50430	14.363	14.421	23.4784414	0.7752E-02	0.26	1.00
67	0.263E-02	51496	14.402	14.459	25.3068721	0.7128E-02	0.23	1.00
68	0.131E-02	52157	14.422	14.479	26.2823676	0.6828E-02	0.23	1.00
69	0.657E-03	52558	14.432	14.490	26.7874630	0.6675E-02	0.22	1.00
70	0.00	52821	14.442	14.499	27.3050162	0.6539E-02	0.22	1.00

Table A.10. Same as Table A.6, BD+53 2790.

Depth index	$r-1$ $[R_*]$	T_e [K]	$\log N$ [Atoms cm^{-3}]	$\log N_e$ [Electrons cm^{-3}]	τ_{Ross}	v [km s^{-1}]	$\partial v/\partial r$ $\left[\frac{\mathrm{km\,s^{-1}}}{R_*}\right]$	D
1	99.0	11737	5.542	5.569	0.0000000	400.0	0.06	8.58
2	78.1	12020	5.746	5.775	0.0000050	398.9	0.06	8.57
3	61.3	12482	5.955	5.984	0.0000116	397.6	0.10	8.55
4	49.4	12842	6.141	6.170	0.0000189	396.0	0.16	8.54
5	39.5	13227	6.333	6.363	0.0000283	394.1	0.25	8.51
6	31.1	13612	6.538	6.568	0.0000410	391.4	0.38	8.48
7	25.2	13934	6.720	6.749	0.0000549	388.6	0.60	8.44
8	20.1	14242	6.912	6.942	0.0000733	384.8	0.96	8.39
9	15.1	14566	7.153	7.183	0.0001033	378.9	1.61	8.31
10	10.9	14834	7.422	7.452	0.0001489	370.2	2.75	8.18
11	8.16	15004	7.664	7.694	0.0002034	359.9	4.49	8.02
12	6.57	15097	7.841	7.871	0.0002531	350.6	6.84	7.87
13	5.48	15168	7.987	8.016	0.0003023	341.6	9.65	7.72
14	4.55	15250	8.135	8.151	0.0003614	331.1	13.15	7.53
15	3.76	15352	8.284	8.290	0.0004325	319.0	17.87	7.30
16	3.10	15494	8.435	8.438	0.0005177	305.1	24.19	7.01
17	2.53	15693	8.587	8.589	0.0006200	289.2	31.92	6.67

Table A.10. continued.

Depth index	$r - 1$ $[R_*]$	T_e [K]	$\log N$ [Atoms cm^{-3}]	$\log N_\mathrm{e}$ [Electrons cm^{-3}]	τ_Ross	v [km s^{-1}]	$\partial v/\partial r$ $\left[\frac{\mathrm{km\,s}^{-1}}{R_*}\right]$	D
18	2.12	15914	8.719	8.720	0.0007243	273.8	40.44	6.32
19	1.85	16109	8.816	8.818	0.0008116	261.6	50.04	6.03
20	1.61	16337	8.916	8.917	0.0009110	248.4	60.57	5.71
21	1.37	16635	9.030	9.030	0.0010397	232.3	71.91	5.31
22	1.18	16948	9.129	9.130	0.0011664	217.5	84.64	4.95
23	1.04	17239	9.213	9.214	0.0012832	204.8	97.45	4.63
24	0.926	17525	9.290	9.290	0.0013999	192.8	110.14	4.33
25	0.822	17828	9.366	9.367	0.0015259	180.6	123.98	4.03
26	0.718	18199	9.451	9.452	0.0016782	167.0	138.90	3.71
27	0.624	18620	9.538	9.539	0.0018480	153.0	154.71	3.39
28	0.546	19045	9.618	9.619	0.0020161	140.4	171.44	3.11
29	0.477	19498	9.698	9.699	0.0021970	127.9	189.02	2.85
30	0.409	20034	9.789	9.790	0.0024180	114.3	209.03	2.58
31	0.335	20718	9.901	9.902	0.0027177	98.18	231.89	2.29
32	0.264	21505	10.032	10.034	0.0031026	80.89	255.53	2.00
33	0.211	22153	10.155	10.156	0.0034926	66.54	280.07	1.78
34	0.167	22699	10.281	10.282	0.0039266	53.61	305.02	1.60
35	0.120	23135	10.456	10.458	0.0045845	38.86	329.03	1.41
36	0.796E-01	23368	10.682	10.684	0.0055233	24.84	350.98	1.25
37	0.546E-01	23238	10.901	10.903	0.0064921	15.72	368.94	1.15
38	0.413E-01	23058	11.080	11.081	0.0073063	10.69	381.45	1.10
39	0.316E-01	22896	11.274	11.275	0.0082285	6.962	389.12	1.06
40	0.248E-01	22903	11.489	11.490	0.0092919	4.302	394.24	1.04
41	0.211E-01	23030	11.674	11.674	0.0102258	2.834	397.71	1.03
42	0.191E-01	23198	11.824	11.825	0.0110017	2.013	399.74	1.02
43	0.178E-01	23346	11.957	11.958	0.0117054	1.485	400.84	1.01
44	0.171E-01	23441	12.049	12.050	0.0121967	1.204	401.57	1.01
45	0.166E-01	23525	12.129	12.129	0.0126296	1.003	402.93	1.01
46	0.160E-01	23685	12.247	12.248	0.0132922	0.7642	402.06	1.01
47	0.154E-01	23935	12.394	12.394	0.0141543	0.5461	373.50	1.00
48	0.149E-01	24560	12.581	12.581	0.0155132	0.3552	278.56	1.00
49	0.142E-01	25103	12.810	12.811	0.0183749	0.2098	176.84	1.00
50	0.136E-01	24958	13.041	13.042	0.0236009	0.1234	108.99	1.00
51	0.130E-01	24668	13.231	13.231	0.0310055	0.7983E-01	67.98	1.00
52	0.125E-01	24440	13.400	13.401	0.0416734	0.5406E-01	43.60	1.00
53	0.121E-01	24575	13.555	13.556	0.0583258	0.3788E-01	28.98	1.00
54	0.117E-01	24851	13.684	13.684	0.0794263	0.2821E-01	21.09	1.00
55	0.114E-01	25006	13.771	13.772	0.0996977	0.2307E-01	15.74	1.00
56	0.111E-01	25151	13.856	13.857	0.1260902	0.1898E-01	12.06	1.00
57	0.106E-01	25657	13.977	13.977	0.1776913	0.1439E-01	8.45	1.00
58	0.100E-01	27571	14.124	14.125	0.2902426	0.1027E-01	5.20	1.00
59	0.917E-02	30432	14.309	14.314	0.5734276	0.6722E-02	2.94	1.00
60	0.792E-02	34785	14.528	14.547	1.3708623	0.4071E-02	1.55	1.00
61	0.640E-02	40349	14.756	14.787	3.1923999	0.2411E-02	0.86	1.00
62	0.494E-02	45722	14.957	14.990	6.0455958	0.1523E-02	0.50	1.00
63	0.368E-02	50537	15.122	15.155	9.6362444	0.1044E-02	0.32	1.00
64	0.248E-02	55262	15.273	15.307	14.2824528	0.7391E-03	0.22	1.00
65	0.141E-02	59572	15.402	15.436	19.6519884	0.5505E-03	0.16	1.00
66	0.629E-03	62774	15.492	15.526	24.4564486	0.4479E-03	0.13	1.00
67	0.314E-03	64099	15.528	15.562	26.6464869	0.4128E-03	0.11	1.00
68	0.157E-03	64779	15.546	15.579	27.7999200	0.3965E-03	0.10	1.00
69	0.786E-04	65124	15.554	15.588	28.3915125	0.3887E-03	0.10	1.00
70	0.00	65456	15.563	15.597	28.9935364	0.3808E-03	0.10	1.00

Table A.11. Same as Table A.6, HD 100199.

Depth index	$r - 1$ [R_*]	T_e [K]	$\log N$ [Atoms cm^{-3}]	$\log N_e$ [Electrons cm^{-3}]	τ_{Ross}	v [km s^{-1}]	$\partial v/\partial r$ $\left[\frac{\text{km s}^{-1}}{R_*}\right]$	D
1	99.0	12487	4.448	4.479	0.00000000	1500	0.19	10.00
2	76.4	12519	4.672	4.703	0.00000026	1496	0.19	10.00
3	61.5	12556	4.859	4.890	0.00000054	1493	0.31	10.00
4	49.0	12603	5.054	5.085	0.00000089	1488	0.49	10.00
5	38.4	12660	5.261	5.293	0.00000138	1481	0.76	10.00
6	31.0	12720	5.446	5.477	0.00000191	1474	1.20	10.00
7	24.8	12783	5.636	5.668	0.00000260	1465	1.97	10.00
8	18.5	12868	5.884	5.915	0.00000376	1449	3.36	10.00
9	13.2	12963	6.164	6.195	0.00000557	1426	6.06	10.00
10	9.51	13055	6.436	6.467	0.00000799	1395	11.16	10.00
11	6.88	13134	6.699	6.730	0.00001114	1355	20.00	8.81
12	5.02	13227	6.949	6.981	0.00001516	1305	34.65	6.27
13	3.71	13397	7.184	7.216	0.00002010	1245	57.55	4.21
14	2.77	13678	7.400	7.433	0.00002595	1176	91.19	2.89
15	2.11	14059	7.596	7.629	0.00003259	1100	137.03	2.11
16	1.65	14530	7.770	7.803	0.00003975	1021	194.85	1.67
17	1.31	15232	7.921	7.954	0.00004709	944.1	262.27	1.42
18	1.08	15991	8.048	8.081	0.00005426	872.4	339.99	1.28
19	0.885	16737	8.171	8.204	0.00006209	798.4	427.44	1.18
20	0.718	17555	8.297	8.330	0.00007112	718.8	521.63	1.12
21	0.600	18374	8.403	8.436	0.00007950	649.7	632.56	1.08
22	0.498	19121	8.510	8.543	0.00008868	579.6	751.84	1.05
23	0.402	19844	8.630	8.663	0.00009998	501.4	878.47	1.03
24	0.331	20454	8.740	8.773	0.00011097	432.7	1029.13	1.02
25	0.270	21186	8.853	8.886	0.00012301	365.6	1206.04	1.01
26	0.205	22268	9.014	9.047	0.00014111	280.9	1423.71	1.01
27	0.147	23069	9.226	9.259	0.00016613	190.2	1688.63	1.00
28	0.112	22896	9.438	9.471	0.00019099	124.0	1995.87	1.00
29	0.936E-01	22088	9.626	9.659	0.00021166	83.23	2340.38	1.00
30	0.807E-01	21169	9.851	9.884	0.00023493	50.73	2698.73	1.00
31	0.728E-01	20773	10.127	10.160	0.00026105	27.26	2941.03	1.00
32	0.686E-01	20823	10.391	10.424	0.00028707	14.98	2536.14	1.00
33	0.656E-01	20904	10.614	10.647	0.00031901	9.003	1798.04	1.00
34	0.635E-01	20951	10.808	10.840	0.00035636	5.788	1342.38	1.00
35	0.618E-01	20916	10.978	11.009	0.00040018	3.922	1000.32	1.00
36	0.604E-01	20733	11.146	11.173	0.00045871	2.677	761.16	1.00
37	0.591E-01	20472	11.311	11.334	0.00053449	1.833	574.53	1.00
38	0.579E-01	20085	11.470	11.485	0.00063570	1.274	400.57	1.00
39	0.565E-01	19677	11.666	11.672	0.00081875	0.8130	264.20	1.00
40	0.548E-01	19315	11.915	11.916	0.00120685	0.4600	167.89	1.00
41	0.534E-01	19082	12.129	12.129	0.00178802	0.2818	105.31	1.00
42	0.525E-01	18976	12.254	12.255	0.00231811	0.2117	69.67	1.00
43	0.517E-01	18907	12.363	12.363	0.00294110	0.1649	50.66	1.00
44	0.506E-01	18845	12.514	12.514	0.00416281	0.1168	35.31	1.00
45	0.491E-01	18823	12.718	12.719	0.00691978	0.7311E-01	22.89	1.00
46	0.475E-01	19210	12.917	12.917	0.01180975	0.4646E-01	14.35	1.00
47	0.464E-01	19883	13.041	13.041	0.01701427	0.3498E-01	9.08	1.00
48	0.455E-01	20597	13.144	13.144	0.02335890	0.2765E-01	6.26	1.00
49	0.441E-01	21577	13.278	13.278	0.03569885	0.2035E-01	4.41	1.00
50	0.424E-01	22734	13.432	13.433	0.05860181	0.1431E-01	3.00	1.00
51	0.408E-01	23911	13.567	13.568	0.09165617	0.1052E-01	2.02	1.00
52	0.394E-01	24958	13.680	13.681	0.13427244	0.8136E-02	1.40	1.00
53	0.376E-01	26078	13.809	13.810	0.20751901	0.6068E-02	0.97	1.00
54	0.356E-01	27569	13.940	13.941	0.33324300	0.4508E-02	0.65	1.00
55	0.337E-01	29239	14.048	14.051	0.50845771	0.3522E-02	0.44	1.00
56	0.316E-01	31237	14.160	14.166	0.78475584	0.2735E-02	0.31	1.00
57	0.292E-01	33585	14.272	14.285	1.22862146	0.2124E-02	0.22	1.00
58	0.266E-01	36028	14.380	14.402	1.85941849	0.1665E-02	0.16	1.00

Table A.11. continued.

Depth index	$r-1$ $[R_*]$	T_e [K]	$\log N$ [Atoms cm^{-3}]	$\log N_e$ [Electrons cm^{-3}]	τ_{Ross}	v [km s^{-1}]	$\frac{\partial v/\partial r}{\left[\frac{\mathrm{km\,s}^{-1}}{R_*}\right]}$	D
59	0.239E-01	38665	14.491	14.519	2.76197651	0.1295E-02	0.12	1.00
60	0.210E-01	41573	14.608	14.639	4.04300390	0.9963E-03	0.09	1.00
61	0.179E-01	44755	14.727	14.759	5.81888400	0.7616E-03	0.07	1.00
62	0.146E-01	48214	14.849	14.882	8.22337369	0.5793E-03	0.05	1.00
63	0.112E-01	51953	14.974	15.008	11.45581654	0.4366E-03	0.04	1.00
64	0.764E-02	56039	15.105	15.138	15.82692333	0.3258E-03	0.03	1.00
65	0.433E-02	60001	15.222	15.256	20.97503222	0.2501E-03	0.02	1.00
66	0.191E-02	63068	15.306	15.340	25.59129956	0.2070E-03	0.02	1.00
67	0.954E-03	64320	15.339	15.373	27.63159559	0.1924E-03	0.02	1.00
68	0.477E-03	64962	15.355	15.389	28.70379599	0.1855E-03	0.01	1.00
69	0.238E-03	65305	15.363	15.397	29.25308606	0.1823E-03	0.01	1.00
70	0.00	65609	15.371	15.404	29.81117931	0.1792E-03	0.01	1.00

Appendix B: Comments on the individual stars

HD 153919 (4U 1700-37). The donor star in this persistent HMXB has the earliest spectral-type in our sample, exhibiting prominent emission lines in its spectrum. Based on our spectra and our spectral analysis we would classify this donor star as O6 If/WN9, in contrast to the O6 Iafpe classification assigned by Sota et al. (2014). We would assign this different spectral type, since from our perspective this object is actually evolving from an Of to a WN star, in contrast to what is discussed by Sota et al. (2014) for the O6 Iafpe classification. In this sense, the O6 If/WN9 category would be an extension of the Of/WN class to cooler temperatures in reminiscence of the old "cool slash" category. From our perspective, an O6 If/WN9 classification would be more suitable also in representation of the wind parameters of this object, which point to an object that is on its way to the WR stage. The derived mass-loss rate is compatible with that of other Of/WN stars (Hainich et al. 2014).

The basic stellar parameters derived in this work are in good agreement with the previous results obtained by Clark et al. (2002). The mass-loss rate derived by means of our models accounting for wind inhomogeneities is almost a factor of four lower than the value obtained by Clark et al. (2002) with unclumped models. The latter authors already have noted that moderate wind clumping would reduce their derived mass-loss rate. Taking into account the uncertainties of the individual studies, this brings the two works into agreement. We note that the terminal velocity determined from our HST spectrum is slightly higher (by 150 km s^{-1}) than obtained by Clark et al. (2002).

Interestingly, the hydrogen abundance deduced from our spectral fit coincides (within the uncertainties) with the value assumed by Clark et al. (2002). While we also derived a super-solar nitrogen abundance, it is a factor of three lower compared to the value determined by Clark et al. (2002). The carbon and oxygen abundances are in a better agreement. Like Clark et al. (2002), we determine a solar carbon abundance and a oxygen abundance of about 0.5 $X_{\mathrm{O},\odot}$.

BD+60 73 (IGR J00370+6122). According to González-Galán et al. (2014), this system is intermediate between a persistent HMXB and an "intermediate" SFXT because of its exceptional X-ray properties. In contrast to almost all other donor stars in our sample, a micro turbulence velocity of $\xi = 17^{+2}_{-2}$ km s^{-1} is required to achieve a satisfying fit. Most of the

stellar parameters we deduce for BD+60 73 agree very well with the results by González-Galán et al. (2014). While these authors assume a wind-strength Q-parameter of $\log Q = -13.0$, our detailed wind analysis results in a value that almost a factor of three higher. Also the derived abundances partly differ. The carbon and nitrogen abundances are a factor of about 1.5 higher in our study than the results presented by González-Galán et al. (2014), while our oxygen abundance is lower by the same factor. The deviation is the highest for the magnesium abundances, which is twice as high in our study compared to their value. The derived silicon abundances are approximately compatible. The same holds for the hydrogen abundance, which is only a few percent lower in this work.

In the fit shown in Fig. C.2, the model obviously falls short to reproduce the resonance doublets of N v $\lambda\lambda$ 1239, 1243 and C IV $\lambda\lambda$ 5801, 5812 with the observed strength. This model has been calculated with an X-ray irradiation that is consistent with the *Swift* observation. However, if we adopt an approximately 70 times higher X-ray irradiation, those resonance doublets perfectly match the observation, as demonstrated in Fig. C.3. Obviously, the stronger X-ray field causes sufficient photo- and Auger ionization to populate the N v and C IV ground states.

At this point, we have to realize that the X-ray measurement with *Swift* was not strictly simultaneous to our HST exposure, but was taken 4.5 h later for technical reasons. Thus, given the X-ray variability of this target, we conclude that at the exact time of the HST observation the X-ray irradiation was somewhat enhanced due to some kind of flare.

LM Vel (IGR J08408-4503). To our knowledge, the spectral analysis presented here is the first one for LM Vel. Although the overall spectral fit represents the observed spectrum very well, we are not able to achieve a satisfactory fit of the C III line at 1245 Å, which is stronger in the model compared to the observation. This might be a result of the neglection of macro clumping in our analysis, which in turn might imply an underestimation of the mass-loss rate (Oskinova et al. 2007).

Similar to BD+60 73, the model that has been calculated with an X-ray irradiation, which is consistent with the *Swift* data, falls short to reproduce the N v $\lambda\lambda$ 1239, 1243 doublet (see Fig. C.4). Those models that are able to reproduce this doublet to a satisfactory level (see Fig. C.5) require an X-ray flux that is roughly 300 times higher than measured by the *Swift* observations. For

technical reasons, the *Swift* data was taken 6.2 h earlier than the HST data. Thus, this X-ray transient might experienced an X-ray outburst during our HST observations.

As for HD 153919, we find that this donor star is hydrogen and oxygen depleted, while the carbon abundance is solar and the nitrogen abundance is supersolar.

BD+53 2790 (4U 2206+54). Unfortunately, we only have low resolution optical spectra with a low S/N at hand for this object, which is one reason for the relatively large error margins for some of the stellar parameters listed in Table 4. Nevertheless, these spectra clearly show a double peaked Hα emission line, as typical for the decretion disks of Be- and Oe-type stars. The same spectral characteristic is posed by the hydrogen lines in the *H*- and *K*-band spectra shown in Fig. C.7. However, Blay et al. (2006, see also Negueruela & Reig 2001) argue that this star does not fulfill all criteria of a classical Be-type star, but is rather a peculiar O9.5 V star. While the donor star in this system is analyzed in this work, it is not considered in the discussion section of this paper because of its unclear HMXB type.

Since our atmosphere models are restricted to spherical symmetry, we cannot account for asymmetries caused by the high rotational velocities of Be- and Oe-type stars, such as oblateness or decretion disks. Nevertheless, an adequate spectral fit can be achieved for most parts of the observed spectrum, with the exception of the hydrogen lines that are filled by the emission from the decretion disks. We also note that the width of the emission peaks of the resonance lines of C IV and N V in the UV cannot be reproduced completely by our model, most likely because of asymmetries in the wind of this star. Since the Hα line is dominated by emission from the decretion disk, this line cannot be used to constrain the clumping within the donor star atmosphere and wind. Therefore, we assume a clumping factor of $D = 10$.

HD 306414 (IGR J11215-5952). This system is one of the SFXTs in our sample. Since it was not detected in our *Swift* observations, we had to assume a certain X-ray flux to proceed with the atmosphere model fits.

Massive stars are inherent X-ray sources because of their winds that exhibit an intrinsic instability. This so-called line-driven wind instability (Lucy & Solomon 1970) gives rise to wind inhomogeneities as well as shocks that can produce X-rays (e.g., Feldmeier et al. 1997; Runacres & Owocki 2002). The intrinsic X-ray flux of massive stars is proportional to their stellar luminosity with $L_X / L \approx 10^{-7}$ (Pallavicini et al. 1981).

In the atmosphere model for this source, we therefore approximated the X-ray flux by two components. For the first one, we used a relatively soft X-ray continuum corresponding to an X-ray temperature of $T_X = 3 \times 10^6$ K. This component was inserted at a radius of $1.5\,R_*$, while the corresponding filling factor was adjusted such that $L_X \approx 10^{-7}\,L$ is produced. To model the contribution of the NS to the X-ray emission, a second X-ray continuum with an X-ray temperature of $T_X = 3 \times 10^7$ K was injected at the position of the NS. The filling factor for this component was chosen such that the UV observations are reproduced best by the model, while ensuring that the total X-ray flux is below the detection limit of *Swift*.

The donor star has previously been analyzed by Lorenzo et al. (2014). While we obtain a slightly higher stellar temperature and surface gravity as the latter authors, the luminosity derived in our analysis is 0.2 dex lower even after accounting for the difference in the assumed distance. The reason for this discrepancy might be the different reddening estimates. While in our case the reddening is derived from an SED fit spanning from UV to infrared data, the estimate conducted by Lorenzo et al. (2014) is solely based on optical and IR photometry, leading to a significantly higher R_V value of 4.2 and a slightly lower $E_{B-V} = 0.7$. Assuming these values for our model SED does not result in a satisfactory fit, providing confidence to our solution. The lower luminosity obtained from our analysis in comparison to that derived by Lorenzo et al. (2014) also entails a spectroscopic mass that is about 30% lower.

Our spectral analysis based on UV and optical data also results in a significantly lower mass-loss rate than determined by Lorenzo et al. (2014) solely on the basis of optical spectra. This discrepancy in the derived mass-loss rate can be in large part attributed to the neglect of wind inhomogeneities in the spectral analysis by Lorenzo et al. (2014). If we scale the mass-loss rate determined by Lorenzo et al. (2014) according to the clumping factor ($D = 20$) derived in this work, the discrepancy nearly vanishes.

The hydrogen, oxygen, and magnesium abundances determine by our analysis agree very well with the ones obtained by Lorenzo et al. (2014). The carbon abundances coincide on a 20% level, while the nitrogen and silicon abundance are higher by 30 and 40%, respectively, in our study compared to those derived by Lorenzo et al. (2014). These deviations might be a result of different micro turbulence velocities assumed in the spectral analyses. Unfortunately, Lorenzo et al. (2014) do not specify the micro turbulence velocity they assume. However, a value slightly different to the $\xi = 20^{+5}_{-5}$ km s^{-1} required by our analysis might explain the differences in the abundance measurements.

HD 100199 (IGR J11305-6256). In this work we present the first spectral analysis of this Be X-ray binary. The same restrictions as outlined for BD+53 2790 apply to the spectral modeling of HD 100199. Overall, an excellent fit quality could be achieved with the exception of the line cores of the hydrogen lines in the optical. As for BD+53 2790, we are not able to constrain the clumping and assume $D = 10$.
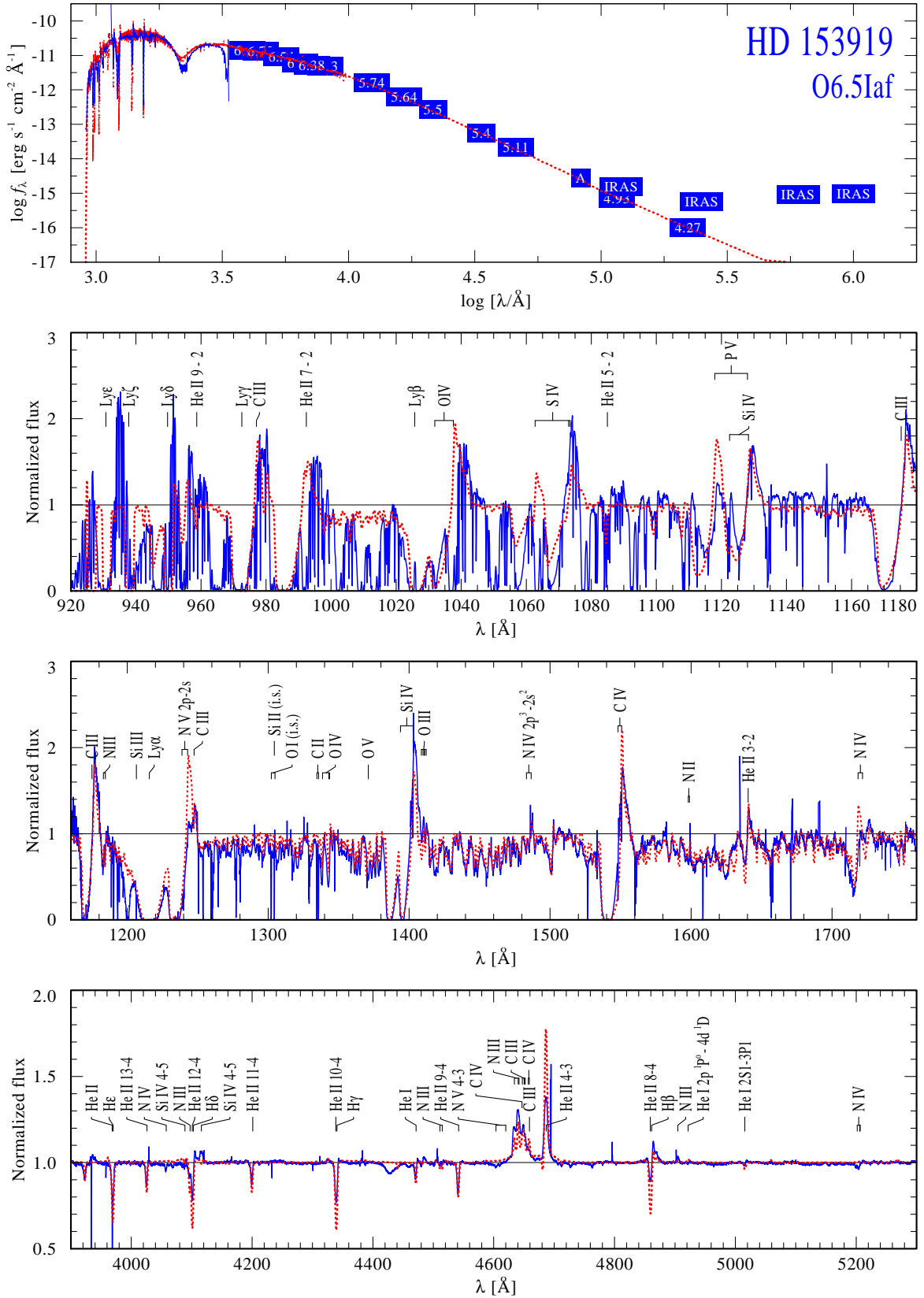
Appendix C: Spectral fits

Fig. C.1. Spectral fit of HD 153919. The observations are shown as blue continuous lines (spectra) and blue boxes (photometry). The best fitting model is overplotted by a dashed red line. Note that the observed far UV spectrum (FUSE) is heavily contaminated by interstellar abortion lines, mostly originating from H_2.
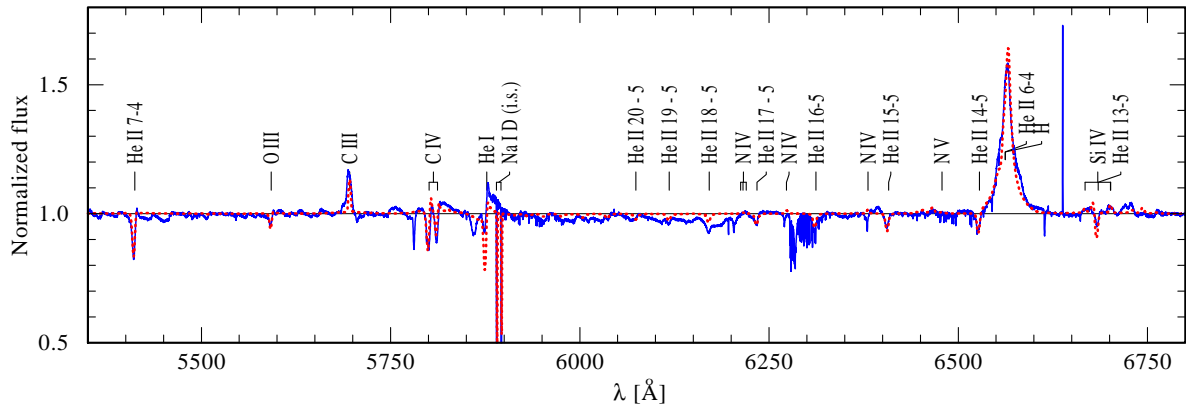
Fig. C.1. continued.
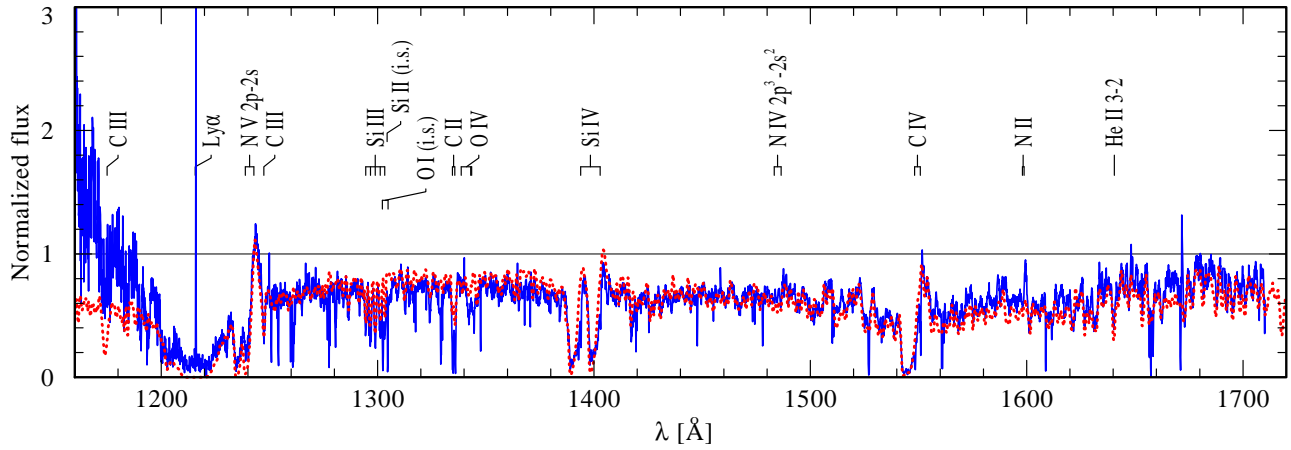
Fig. C.2. Same as Fig. C.1, but for BD+60 73.

Fig. C.3. BD+60 73: alternative UV-line fit (cf. Fig. C.2, second panel). For the model shown here, an approximately 70 times higher X-ray irradiation has been adopted, which brings the resonance doublets of N V $\lambda\lambda$ 1239, 1243 and C IV $\lambda\lambda$ 5801, 5812 to the observed strength (see text in Appendix B).
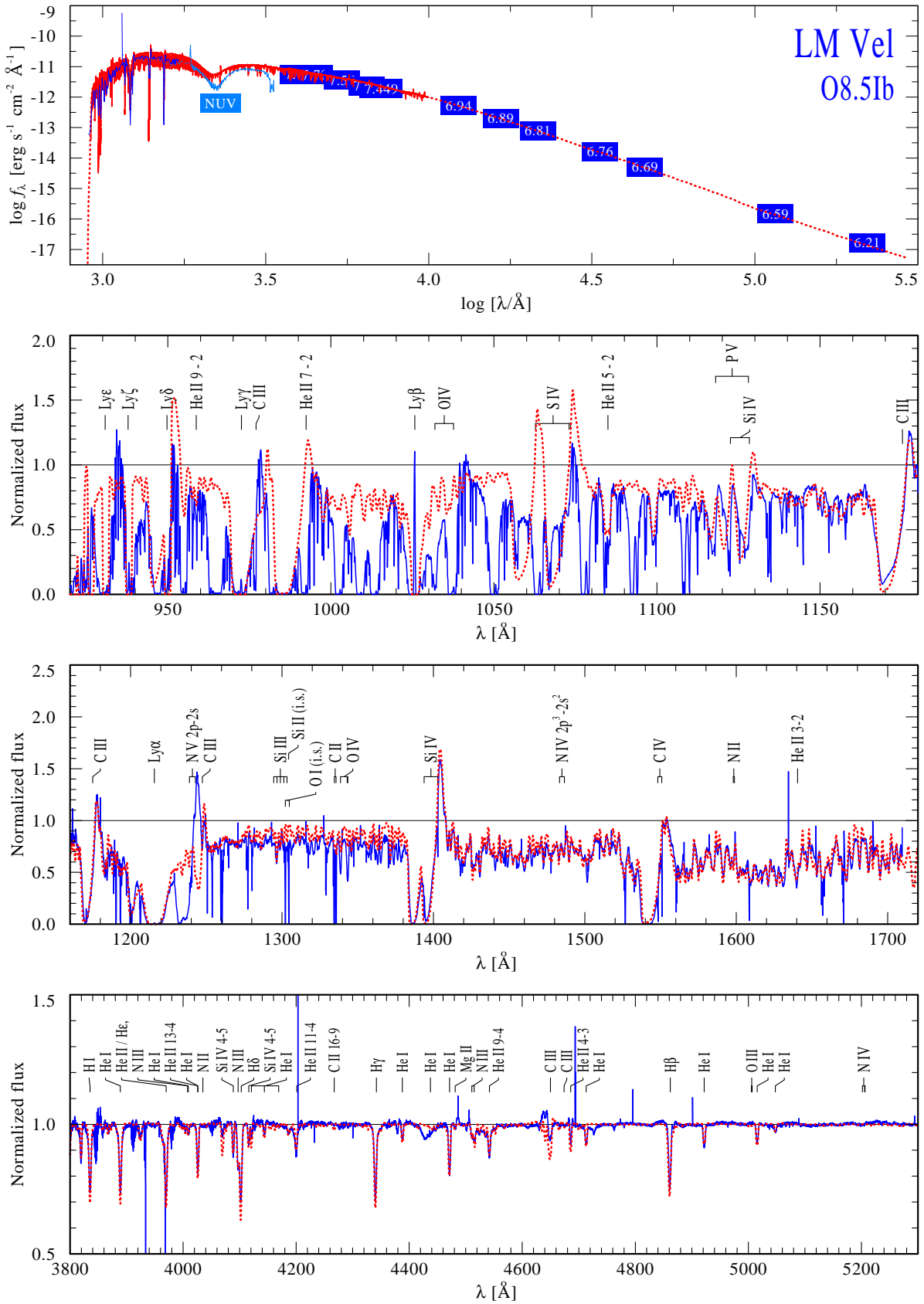
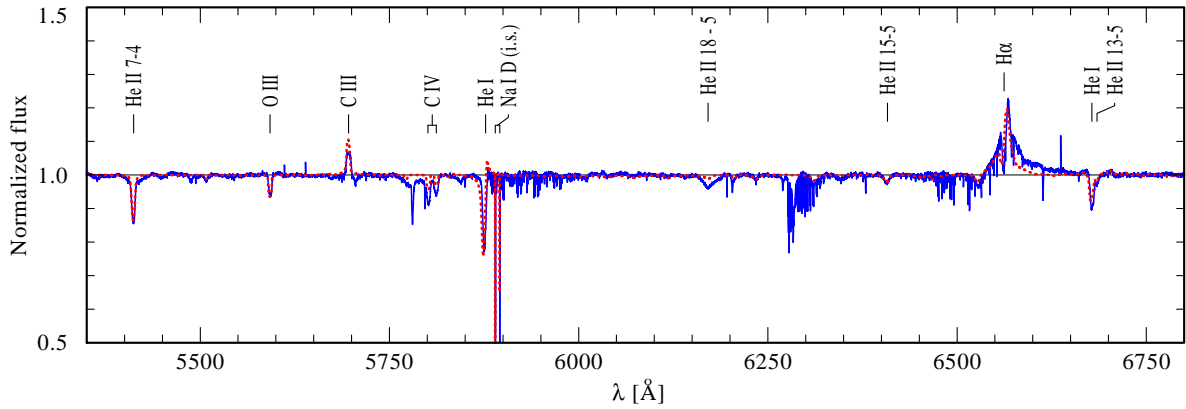**Fig. C.4.** Same as Fig. C.1, but for LM Vel.
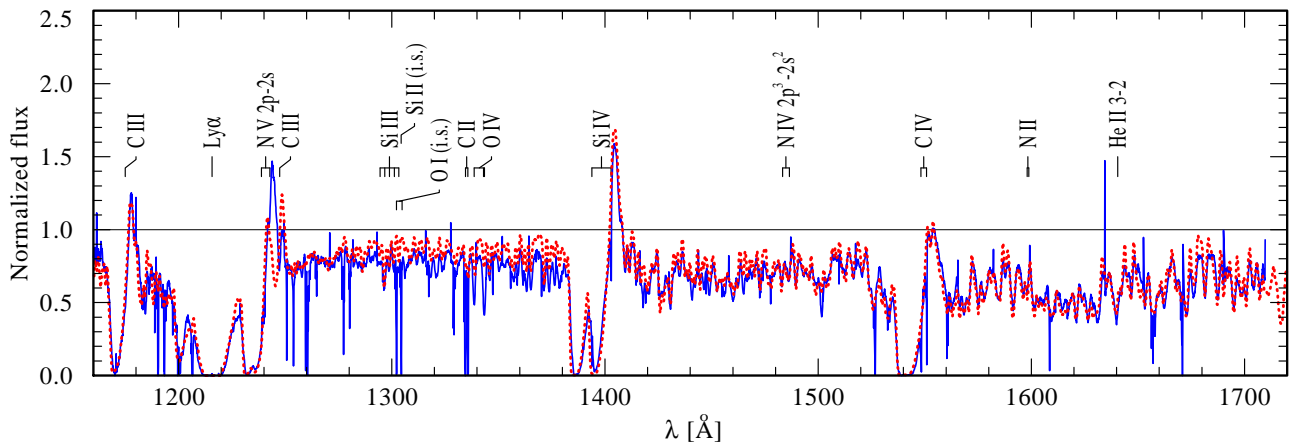
Fig. C.4. continued.

Fig. C.5. LM Vel: alternative UV-line fit (cf. Fig. C.4, second panel). For the model shown here, a roughly 300 times higher X-ray irradiation has been adopted, which brings the resonance doublet of N V $\lambda\lambda$ 1239, 1243 almost to the observed strength (see text in Appendix B). The remaining discrepancy is because of the C III line at 1245 Å (see Appendix B for details).

Fig. C.6. Same as Fig. C.1, but for HD 306414.

Fig. C.7. Same as Fig. C.1, but for BD+53 2790. The IR spectrum is clearly dominated by emission from the decretion disk.

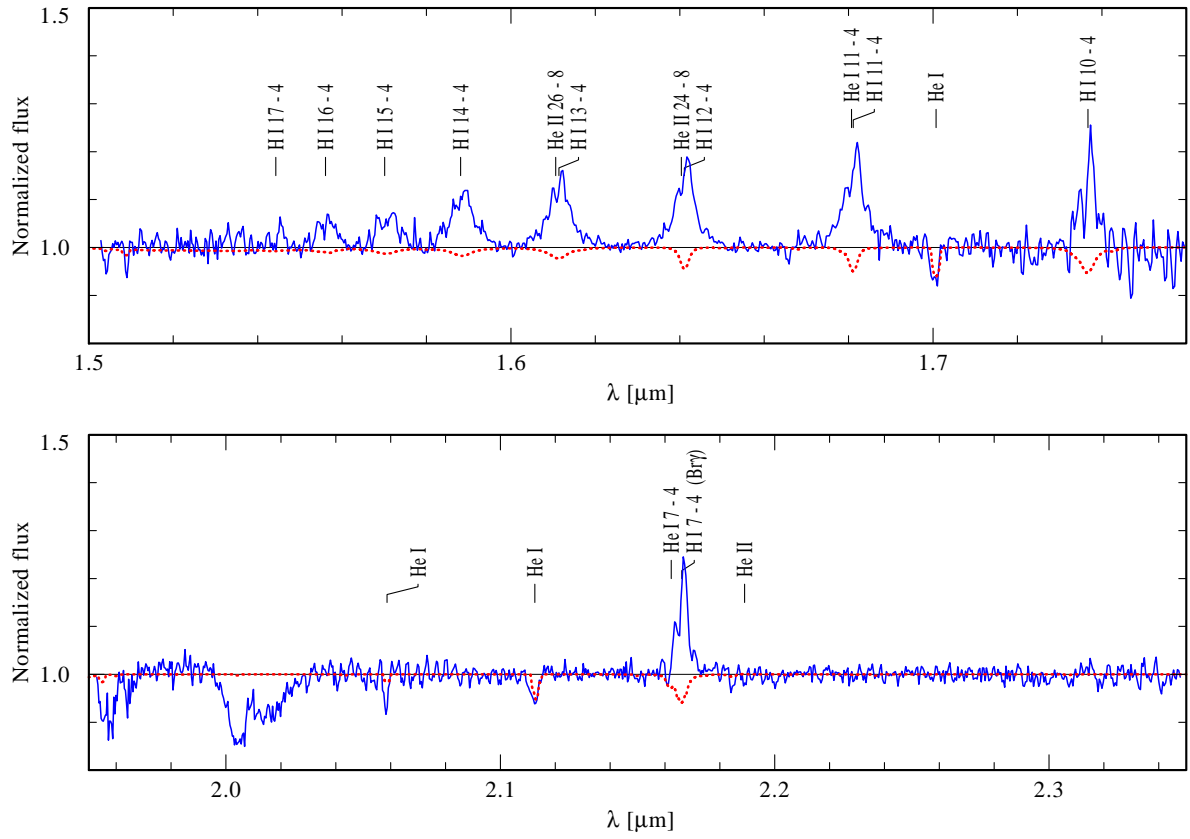**Fig. C.7.** continued.

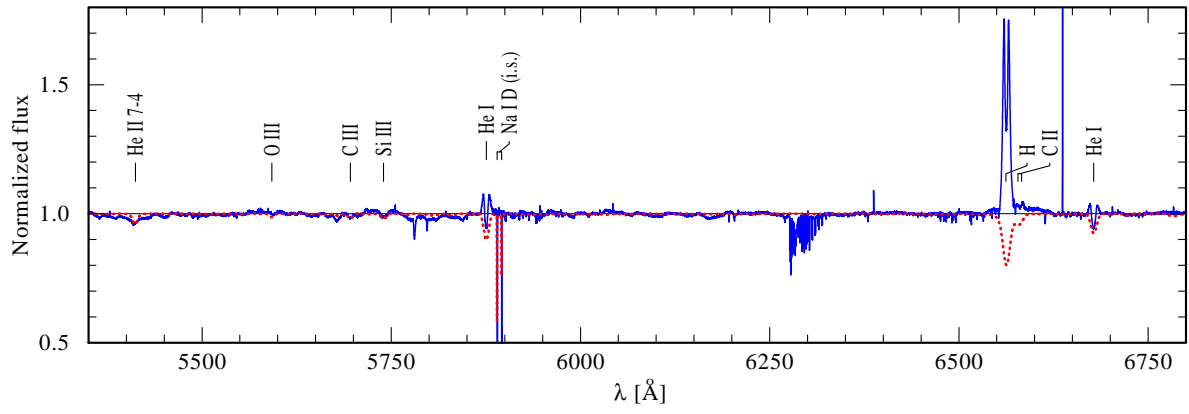**Fig. C.8.** Same as Fig. C.1, but for HD 100199.

Fig. C.8. continued.

Chandra Observations of High-energy X-Ray Sources Discovered by *INTEGRAL*

John A. Tomsick[1] , Arash Bodaghee[2] , Sylvain Chaty[3,4], Maïca Clavel[5] , Francesca M. Fornasini[6] , Jeremy Hare[1,7,10] ,
Roman Krivonos[8] , Farid Rahoui[9] , and Jerome Rodriguez[3]

[1] Space Sciences Laboratory, 7 Gauss Way, University of California, Berkeley, CA 94720-7450, USA
[2] Georgia College & State University, CBX 82, Milledgeville, GA 31061, USA
[3] AIM, CEA, CNRS, Université Paris-Saclay, Université Paris Diderot, Sorbonne Paris Cité, F-91191 Gif-sur-Yvette, France
[4] APC, Université Paris Diderot, CNRS/IN2P3, CEA/IRFU, Observatoire de Paris, Sorbonne Paris Cité, Paris 75205, France
[5] Univ. Grenoble Alpes, CNRS, IPAG, F-38000 Grenoble, France
[6] Harvard-Smithsonian Center for Astrophysics, 60 Garden Street, Cambridge, MA 02138, USA
[7] NASA Goddard Space Flight Center, Greenbelt, MD 20771, USA
[8] Space Research Institute, Russian Academy of Sciences, Profsoyuznaya 84/32, 117997 Moscow, Russia
[9] Independent, France

Abstract

The *International Gamma-Ray Astrophysics Laboratory* (*INTEGRAL*) satellite has detected in excess of 1000 sources in the ∼20–100 keV band during its surveys of the sky over the past 17 years. We obtained 5 ks observations of 15 unclassified *INTEGRAL* Gamma-Ray (IGR) sources with the *Chandra X-ray Observatory* in order to localize them, to identify optical/IR counterparts, to measure their soft X-ray spectra, and to classify them. For 10 of the IGR sources, we detect *Chandra* sources that are likely (or in some cases certain) to be the counterparts. IGR J18007−4146 and IGR J15038−6021 both have *Gaia* parallax distances, placing them at $2.5^{+0.5}_{-0.4}$ and $1.1^{+1.5}_{-0.4}$ kpc, respectively. We tentatively classify both of them as intermediate polar-type cataclysmic variables. Also, IGR J17508−3219 is likely to be a Galactic source, but it is unclear if it is a Dwarf Nova or another type of transient. For IGR J17118−3155, we provide a *Chandra* localization, but it is unclear if the source is Galactic or extragalactic. Based on either near-IR/IR colors or the presence of extended near-IR emission, we classify four sources as active galactic nuclei (AGNs; IGR J16181−5407, IGR J16246−4556, IGR J17096−2527, and IGR J19294+1327), and IGR J20310+3835 and IGR J15541−5613 are AGN candidates. In addition, we identified an AGN in the *INTEGRAL* error circle of IGR J16120−3543 that is a possible counterpart.

Unified Astronomy Thesaurus concepts: X-ray sources (1822); Cataclysmic variable stars (203); High mass X-ray binary stars (733); Active galactic nuclei (16); Galaxy stellar content (621)

1. Introduction

Since 2002, the *International Gamma-Ray Astrophysics Laboratory* (*INTEGRAL*) satellite has been carrying out observations with its large field of view coded aperture mask instruments (Winkler et al. 2003). In particular, as the exposure time in the ∼20–100 keV band across the sky and especially in the Galactic plane has increased, more new or previously poorly studied "*INTEGRAL* Gamma-Ray" (IGR) sources have been found. *INTEGRAL* has now detected in excess of 1000 sources (Bird et al. 2016; Krivonos et al. 2017) with the majority being new sources.

The hard X-ray bandpass of *INTEGRAL* provides a way to select sources where extreme physics is occurring. The high-energy emission can be produced by accretion onto a compact object (magnetic white dwarf, neutron star, or black hole) or when particle acceleration leads to nonthermal emission. The Bird et al. (2016) *INTEGRAL* source catalog includes 939 sources. Over the whole sky, active galactic nuclei (AGNs) dominate and account for 369 of the sources. The Galactic population is dominated by 129 low mass X-ray binaries, 116 high mass X-ray binaries (HMXBs), and 56 cataclysmic variables (CVs). Pulsar wind nebulae (PWNe), supernova remnants, and galaxy clusters are also among the IGR sources. Thus, *INTEGRAL* is providing a much more complete picture of the populations of hard X-ray sources, and making discoveries about Galactic sources, including two new classes of

HMXBs: obscured HMXBs (Matt & Guainazzi 2003; Walter et al. 2006) and Supergiant Fast X-ray Transients (Negueruela et al. 2006; Sguera et al. 2006; Romano et al. 2014); larger numbers of hard X-ray emitting intermediate polars (IPs; Bonnet-Bidaud et al. 2007; Landi et al. 2009; Tomsick et al. 2016b); and highly energetic PWNe (Tomsick et al. 2012b; Pavan et al. 2014).

While *INTEGRAL* excels at detecting sources in the 20–100 keV band, it only localizes the sources to 1′–5′, which is not adequate for finding optical/IR counterparts. Thus, in most cases, sources are not classified until higher angular resolution X-ray observations are obtained, providing an image to identify extended sources or to improve the source localization, allowing for multiwavelength counterparts to be found. Large X-ray follow-up programs include the use of the *Neil Gehrels Swift Observatory* X-ray Telescope (*Swift*/XRT; Landi et al. 2017, and references therein) and the *Chandra X-ray Observatory* (e.g., Tomsick et al. 2006, 2008, 2016a). The X-ray localizations enable optical and near-IR spectroscopy (e.g., Chaty et al. 2008; Coleiro et al. 2013; Masetti et al. 2013; Fortin et al. 2018), at which point confident source classifications are nearly always obtained.

1.1. Target Selection

When the Bird et al. (2016) catalog was released, there were 219 unidentified sources in the catalog, and we selected sources to observe with *Chandra* based on the following criteria:

Table 1
Source Information from the 2016 *INTEGRAL* Catalog

IGR Name	l[a] (deg)	b[b] (deg)	R.A.[c] (deg)	Decl.[c] (deg)	Uncertainty[d] (arcmin)	Flux[e] (20–40 keV)	Flux[e] (40–100 keV)	Variability[f]	Significance[g]
J20310+3835	77.77	−0.49	307.755	+38.576	4.54	0.6 ± 0.1	<0.3	⋯	5.5
J15038−6021	318.60	−1.57	225.941	−60.357	3.95	0.5 ± 0.1	0.4 ± 0.2	⋯	6.4
J03599+5043	150.58	−1.74	59.973	+50.728	4.01	0.7 ± 0.2	1.2 ± 0.3	Y	6.3
J15541−5613	326.38	−1.90	238.527	−56.216	4.32	<0.2	0.8 ± 0.2	Y	5.8
J19294+1327	49.22	−2.12	292.374	+13.451	3.43	0.5 ± 0.1	0.5 ± 0.1	⋯	7.5
J16246−4556	336.83	+2.46	246.091	−45.923	4.61	0.4 ± 0.1	<0.3	Y	5.4
J16181−5407	330.35	−2.62	244.533	−54.103	4.61	0.5 ± 0.1	0.4 ± 0.1	⋯	5.4
J17508−3219	357.68	−2.72	267.721	−32.330	2.31	0.6 ± 0.1	0.9 ± 0.1	⋯	11.6
J17118−3155	353.48	+4.41	257.959	−31.927	2.84	0.3 ± 0.1	<0.2	Y	9.2
J20413+3210	73.96	−6.02	310.384	+32.219	3.42	<0.3	<0.4	Y	7.5
J07202+0009	216.12	+6.47	110.063	+0.127	4.25	<0.4	<0.7	Y	5.9
J17096−2527	358.47	+8.56	257.432	−25.470	2.73	0.8 ± 0.1	0.8 ± 0.1	⋯	9.6
J18007−4146	350.38	−9.12	270.202	−41.802	3.19	0.9 ± 0.1	0.5 ± 0.2	⋯	8.1
J16482−2959	351.94	+9.52	252.145	−30.019	4.25	0.3 ± 0.1	0.6 ± 0.2	Y	5.9
J16120−3543	342.36	+11.35	242.974	−35.754	4.69	0.4 ± 0.2	0.6 ± 0.3	Y	5.3

Notes.
[a] Galactic longitude converted from *INTEGRAL* position.
[b] Galactic latitude converted from *INTEGRAL* position.
[c] Source position measured by *INTEGRAL* and reported in Bird et al. (2016).
[d] 90% confidence *INTEGRAL* error radius.
[e] The flux measured by *INTEGRAL* in units of mCrab.
[f] As described in Bird et al. (2016), "Y" indicates that the source's detection significance in the *INTEGRAL* data is variable at a level of between 10% and 400%.
[g] The significance of the *INTEGRAL* detection in terms of signal-to-noise.

1. the selected sources have IGR names, indicating discovery in the hard X-rays by *INTEGRAL*;
2. the nature is completely unknown for the selected sources (i.e., the type is listed as "?");
3. the sources are "new" in that they did not appear in the Bird et al. (2010) catalog, implying that there has been little opportunity for follow-up observations; and
4. they are within 15° of the Galactic plane, increasing the chances that they are Galactic (we note that the highest Galactic latitude in our final list is $b = 11°.35$).

After applying these four criteria, 56 sources remained, but we reduced the list further based on available information about performed or planned observations with *Chandra*, the *X-ray Multi-Mirror Mission* (*XMM-Newton*), and *Swift*. For example, when we selected targets, 20 of the 56 sources had planned *Swift* observations, and these were removed from our list (although we kept some sources that already had *Swift* observations after confirming that the *Swift* localization did not identify a unique optical or near-IR counterpart). We also found that some of the sources show evidence for being variable or strongly variable in the hard X-rays based on the analysis of Bird et al. (2016). Strong variability (changes in *INTEGRAL* detection significance over time by >400%) could indicate that the source is truly transient, which means that it could be too faint to be detected in a short *Chandra* observation, and so none of the sources in our final list are in the strongly variable category. However, most Galactic sources (and certainly X-ray binaries) are variable, so we kept the sources in the variable category (changes in *INTEGRAL* detection significance over time by between 10% and 400%), and these are indicated in Table 1.

After the above considerations, the list of 15 IGR sources in Table 1 remained. They were observed with *Chandra*, and we describe the observations in Section 2. In Section 3, we describe the analysis of the data and present the results. The primary goal is to obtain X-ray positions of the IGR sources with subarcsecond accuracy, but this also includes assessing which is the most likely *Chandra* counterpart for each IGR source. For this, we follow methods that are similar to those we have developed in earlier works (Tomsick et al. 2009, 2012a). We discuss the results in Section 4 and summarize our conclusions in Section 5.

2. *Chandra* Observations

The list of IGR targets and information about the *Chandra* observations is provided in Table 2. For all 15 observations, the target was observed with the ACIS-I instrument (Garmire et al. 2003), which has a bandpass of 0.3–10 keV. IGR sources are typically relatively bright, with X-ray fluxes of $\sim 10^{-12}\,\mathrm{erg\,cm^{-2}\,s^{-1}}$. At these flux levels, exposure times of ~ 5 ks are sufficient to detect tens or hundreds of counts, depending on spectral shape and variability. Although some highly absorbed or highly variable IGR sources could have significantly lower X-ray flux levels, longer exposure times would not necessarily lead to the identification of the *Chandra* counterpart. With the 90% confidence *INTEGRAL* error circles having radii between 2′.31 and 4′.69, we would expect the sky density of field sources to make it difficult to select the true counterpart if it had a significantly lower X-ray flux level than expected.

Table 2 also provides the pointing positions used for each IGR source. In 11 cases, we simply used the *INTEGRAL* position reported in the Bird et al. (2016) catalog. However, for four sources (IGR J19294+1327, IGR J16181−5407, IGR J20310 +3835, and IGR J18007−4146), *Swift*/XRT observations identified a possible counterpart, and we used the XRT position for the *Chandra* pointing. However, in each case, the full *INTEGRAL* error circle was included in the ACIS-I field of

Table 2
Chandra Observations

IGR Name	ObsID	Start Time (UT)	Exposure Time (s)	R.A. (deg)	Decl. (deg)	Reference
J20310+3835	18969	2017 Feb 26, 19.2 hr	4880	307.73052	+38.56095	our analysis[a]
J15038–6021	18970	2017 Apr 26, 13.5 hr	4899	225.941	−60.357	Bird et al. (2016)
J03599+5043	18971	2017 Mar 20, 1.8 hr	5056	59.973	+50.728	Bird et al. (2016)
J15541–5613	18972	2017 May 22, 5.3 hr	4995	238.527	−56.216	Bird et al. (2016)
J19294+1327	18973	2017 Feb 24, 5.9 hr	4880	292.37417	+13.45151	Pavan et al. (2011)
J16246–4556	18974	2017 May 3, 12.6 hr	4886	246.091	−45.923	Bird et al. (2016)
J16181–5407	18975	2017 May 20, 14.1 hr	5019	244.53342	−54.10272	Landi et al. (2012)
J17508–3219	18976	2017 May 8, 22.6 hr	5013	267.721	−32.330	Bird et al. (2016)
J17118–3155	18977	2017 Jan 27, 16.8 hr	4883	257.959	−31.927	Bird et al. (2016)
J20413+3210	18978	2017 Feb 24, 7.8 hr	4730	310.384	+32.219	Bird et al. (2016)
J07202+0009	18979	2017 Sep 9, 18.1 hr	4899	110.063	+0.127	Bird et al. (2016)
J17096–2527	18980	2017 Jan 25, 11.0 hr	4845	257.432	−25.470	Bird et al. (2016)
J18007–4146	18981	2017 Aug 22, 5.2 hr	4994	270.17792	−41.78028	our analysis[a]
J16482–2959	18982	2017 Jun 20, 15.6 hr	4979	252.145	−30.019	Bird et al. (2016)
J16120–3543	18983	2017 Mar 31, 16.8 hr	4880	242.974	−35.754	Bird et al. (2016)

Note.

[a] We determined this position via analysis of *Swift*/XRT data. The XRT position is now published in Landi et al. (2017).

view, and in searching for the IGR source, we considered our search region to be the *INTEGRAL* error circle.

3. Analysis and Results

3.1. Chandra *Source Detection, Localization, and Photometry*

We reduced the data using the *Chandra* Interactive Analysis of Observations (CIAO; Fruscione et al. 2006) version 4.11 software along with the Calibration Database version 4.8.4.1. We used chandra_repro to reprocess the data, which results in an event list along with several other files with information about the spacecraft aspect, bad detector pixels, etc. After reprocessing, the steps in our analysis are to search for sources on the four ACIS-I detector chips, cross-correlate with the *Gaia* Data Release 2 (DR2) optical source catalog (Prusti et al. 2016; Gaia Collaboration et al. 2018) to register the images and reduce the contribution of the systematic pointing uncertainty to the source localization uncertainties, and perform aperture photometry to determine the number of counts for each detected source. We generally follow the instructions in the CIAO science threads.[11]

For each of the 15 observations, we used fluximage to produce an exposure-corrected image in the 0.3–10 keV energy band, and applied the wavdetect source detection algorithm to this image with wavelet scales of 1, 2, 4, 6, 8, 12, 16, 24, and 32 and the detection threshold set at a level to produce a list of sources for which only one spurious source is expected. Table 3 shows that between 6 and 28 *Chandra* sources were detected per ObsID. We used the imaging program SAOImage (ds9) to search the *Gaia* DR2 catalog for optical sources in the ACIS-I field and cross-correlated the *Chandra* and *Gaia* source lists using CIAO's wcs_match. For 11 of the ObsIDs, between 3 and 7 matches were found, allowing for a position shift to be calculated to register the *Chandra* image to the *Gaia* reference frame. The shifts are listed in Table 3 along with the average residuals between the *Chandra* and *Gaia* positions, which are between 0″.32 and 0″.63. We take these values to be the systematic pointing uncertainty. The four remaining

ObsIDs have zero or one match, and we do not perform any position shifts for these. Thus, the systematic pointing uncertainty in these four cases is 0″.8 (90% confidence).[12]

We carried out the *Chandra* aperture photometry to determine the number of counts for all of the detected sources. We made a point-spread function (PSF) map using mkpsfmap for an energy of 2.3 keV (the typical average photon energy for the full 0.3–10 keV *Chandra* bandpass), and determined the 95% encircled energy radius for each source. After defining large (typically ∼15 arcmin^2) source-free background regions for each observation, we used dmextract to extract background-subtracted counts in the 0.3–2 keV, 2–10 keV, and 0.3–10 keV energy bands. Based on our previous work (e.g., Tomsick et al. 2012a), for each source we calculated the probability that the source would be detected in a search area with a radius of θ_{search}. In cases where the source is within the 90% confidence *INTEGRAL* error radius ($\theta_{INTEGRAL}$), $\theta_{search} = \theta_{INTEGRAL}$. If the source is outside the *INTEGRAL* error radius then θ_{search} is equal to the angular distance from the best estimate of the *INTEGRAL* position.

The predicted surface density of sources is the other factor that is important for determining the spurious source probability. In Tomsick et al. (2012a), we used

$$N(>F_{2-10\,keV}) = 9.2(F_{2-10\,keV}/10^{-13})^{-0.79}\,\mathrm{deg}^{-2}, \quad (1)$$

which is based on the $\log N$-$\log S$ curve from the *Advanced Satellite for Cosmology and Astrophysics* (Sugizaki et al. 2001). However, this work only included the Galactic sources, so we also consider a more recent determination of the $\log N$-$\log S$ in the Norma Region of the Galactic Plane

$$N(>F_{2-10\,keV}) = 36(F_{2-10\,keV}/10^{-13})^{-1.24}\,\mathrm{deg}^{-2}, \quad (2)$$

which also includes AGNs (Fornasini et al. 2014). In addition, the Norma Region is centered on the Galactic plane, covering $-0°.4 < b < 0°.4$, likely representing an upper bound on the source density. While we use these exact equations in Section 3.2 to determine the absolute spurious source

---

[11] See http://asc.harvard.edu/ciao/threads/index.html.

[12] See http://cxc.cfa.harvard.edu/cal/ASPECT/celmon/.

Table 3
Source Detection and Shifts Based on *Gaia* DR2 Matches

IGR Name	ObsID	$N_{Chandra}$ [a]	$N_{matches}$ [b]	x_{shift} [c]	y_{shift} [c]	Residual [d]
J20310+3835	18969	11	5	−0.46	0.75	0.34
J15038−6021	18970	12	3	0.59	0.21	0.42
J03599+5043	18971	10	0	…	…	…
J15541−5613	18972	21	5	−0.11	−0.20	0.63
J19294+1327	18973	17	3	−1.20	0.77	0.32
J16246−4556	18974	27	5	0.09	−0.41	0.43
J16181−5407	18975	14	4	−0.02	−0.41	0.49
J17508−3219	18976	28	7	−0.49	0.18	0.41
J17118−3155	18977	25	4	0.54	−0.21	0.62
J20413+3210	18978	6	0	…	…	…
J07202+0009	18979	26	3	−0.70	0.10	0.35
J17096−2527	18980	23	7	0.20	0.69	0.38
J18007−4146	18981	22	4	0.65	−0.45	0.50
J16482−2959	18982	13	0	…	…	…
J16120−3543	18983	17	1	…	…	…

Notes.
[a] The number of *Chandra* sources detected on the four ACIS-I detector chips.
[b] The number of matches between the *Chandra* detections and the *Gaia* DR2 catalog.
[c] The shifts in the *x* and *y* detector coordinate directions in pixels. The conversion is 1 pixel = $0''.492$.
[d] Average residual (in arcseconds) between the *Chandra* and Gaia DR2 sources.

probabilities for *Chandra* sources that are likely candidates to be associated with the IGR sources, we first determine the relative probabilities for all sources using

$$P_{rel} = 1 - e^{-\left(\frac{C_{2-10\,keV}}{C_0}\right)^{-1.0} \pi\, \theta_{search}^2} \quad , \qquad (3)$$

where $C_{2-10\,keV}$ is the number of counts in the 2–10 keV band, C_0 is an arbitrary normalization constant set so that the brightest sources have P_{rel} values near 1%, and we use −1.0 as the slope of the $\log N - \log S$ since this is the midpoint between the Sugizaki et al. (2001) and Fornasini et al. (2014) values.

Using Equation (3), with $C_0 = 140$, we calculate P_{rel} for all the sources detected in the 15 *Chandra* observations, and these are plotted in Figure 1. This parameter space leads to a large cluster of low count/high P_{rel} field sources and relatively clear separation between this cluster and the *Chandra* sources that are candidates to be counterparts to the IGR sources. For ten of the IGR fields, the most likely counterpart is labeled in Figure 1, and there are two fields with two potential counterparts.

For these 12 sources, Table 4 gives the *Chandra* names and positions, the angular distance from the center of the *INTEGRAL* error circle (θ), the number of ACIS counts in the 0.3–10 keV band, and the hardness ratio. The uncertainties in the positions include systematic and statistical contributions added in quadrature. The determination of the systematic uncertainty is described above (see Table 3). For the statistical contribution, we use Equation (13) from Kim et al. (2007), which uses the number of counts and the angular distance of the source from the *Chandra* aimpoint. The information in Table 4 provides additional information about the likelihood that the *Chandra* sources are the true counterparts to the IGR sources. In particular, J16246a is a questionable counterpart because it is one of the softer sources in the list, and it is well outside the *INTEGRAL* error circle ($\theta = 7'.92$ compared to the error circle radius of $4'.61$). Also, J17508a is questionable since

it is a very soft source, and it is outside the *INTEGRAL* error circle.

3.2. Chandra *and* INTEGRAL *Energy Spectra*

For the 12 candidate counterparts, we extracted *Chandra* energy spectra using specextract. For the source extraction region, we used a circle with a radius corresponding to 95% encircled energy, which we determined from the PSF map. However, we also checked each source for photon pile-up by making an image for energies greater than 10 keV. For the three sources with evidence for pile-up (J16181, J18007, and J20310), we used an annular source extraction region with an inner radius of 1 pixel to cut out the core of the PSF. We also extracted a background spectrum using the same region used for the photometry. The spectra were rebinned to require a detection in each bin at the 3σ level unless this resulted in fewer than five bins, in which case a 2σ requirement was used.

Using XSPEC (Arnaud 1996), we fit the *Chandra* spectra with an absorbed power-law model, and the parameters are reported in Table 5. We performed the fits by minimizing the C-statistic, and we give the C values and number of degrees of freedom (dof) in Table 5. We use these values along with the variances in C, calculated according to Equations (20)–(22) in Kaastra (2017), to quantify the quality of the fits. The P_{reject} values in Table 5 indicate the probability that an absorbed power law does not provide a good description of the spectrum. The most significant deviations from an absorbed power law are for J16246a, J18007, and J17508a, which have P_{reject} values of 99.7%, 88%, and 84%, respectively. While an absorbed power-law fit is not a formally acceptable model in these cases, the residuals do not show clear evidence for spectral features such as emission lines.

The measured N_H values exceed the Galactic column density (see Table 5 for both) for J16181 ($N_H = (9 \pm 7) \times 10^{22}\,cm^{-2}$; 90% confidence errors are given) and J19294 ($N_H = (2.8^{+3.8}_{-2.4}) \times 10^{23}\,cm^{-2}$). Several other sources have upper limits on N_H that are higher than the Galactic N_H (HI4PI Collaboration et al. 2016), but we note that there may be spatial variations in

Table 4
Chandra Candidate Counterparts to IGR Sources

| IGR Name	CXOU Name	*Chandra* R.A. (J2000)	*Chandra* Decl. (J2000)	Uncertainty[a] (arcsec)	θ[b]$/\theta_{INTEGRAL}$[c] (arcmin)	ACIS Counts[e]	Hardness[d]
J15038	J150415.7−602123	$15^h04^m15^s.70$	$-60°21'23''.0$	0.46	3.69/3.95	259 ± 17	$+0.65 \pm 0.08$
J15541	J155413.0−560932	$15^h54^m13^s.09$	$-56°09'32''.6$	0.75	3.54/4.32	44 ± 8	$+0.60 \pm 0.21$
J16181	J161807.7−540612	$16^h18^m07^s.74$	$-54°06'12''.5$	0.50	0.04/4.61	253 ± 17	$+0.94 \pm 0.09$
J16246a	J162425.2−460316	$16^h24^m25^s.20$	$-46°03'16''.5$	0.67	7.92/4.61	660 ± 27	$+0.14 \pm 0.04$
J16246b	J162430.7−455514	$16^h24^m30^s.77$	$-45°55'14''.1$	0.46	1.56/4.61	125 ± 12	$+0.62 \pm 0.12$
J17096	J170950.2−252934	$17^h09^m50^s.27$	$-25°29'34''.4$	0.55	2.02/2.73	34 ± 7	$+0.12 \pm 0.22$
J17118	J171135.8−315504	$17^h11^m35^s.89$	$-31°55'04''.5$	0.81	3.08/2.84	23 ± 6	$+0.30 \pm 0.29$
J17508a	J175106.8−321827	$17^h51^m06^s.85$	$-32°18'27''.9$	0.44	3.21/2.31	713 ± 28	-0.55 ± 0.04
J17508b	J175108.7−322122	$17^h51^m08^s.78$	$-32°21'22''.2$	0.48	3.68/2.31	169 ± 14	$+0.03 \pm 0.09$
J18007	J180042.6−414650	$18^h00^m42^s.69$	$-41°46'50''.0$	0.51	1.68/3.19	441 ± 22	$+0.27 \pm 0.05$
J19294	J192930.1+132705	$19^h29^m30^s.14$	$+13°27'05''.7$	0.39	0.10/3.43	39 ± 7	$+1.00 \pm 0.27$
J20310	J203055.2+383347	$20^h30^m55^s.28$	$+38°33'47''.1$	0.35	1.39/4.54	266 ± 17	$+0.86 \pm 0.09$

Notes.
[a] 90% confidence.
[b] The angular distance between the center of the *INTEGRAL* error circle and the source.
[c] The size of the 90% confidence *INTEGRAL* error radius given in Bird et al. (2016).
[d] The hardness is given by $(C_2 - C_1)/(C_2 + C_1)$, where C_2 is the number of counts in the 2–10 keV band and C_1 is the number of counts in the 0.3–2 keV band.
[e] The number of counts, after background subtraction, measured by *Chandra*/ACIS-I in the 0.3–10 keV band.
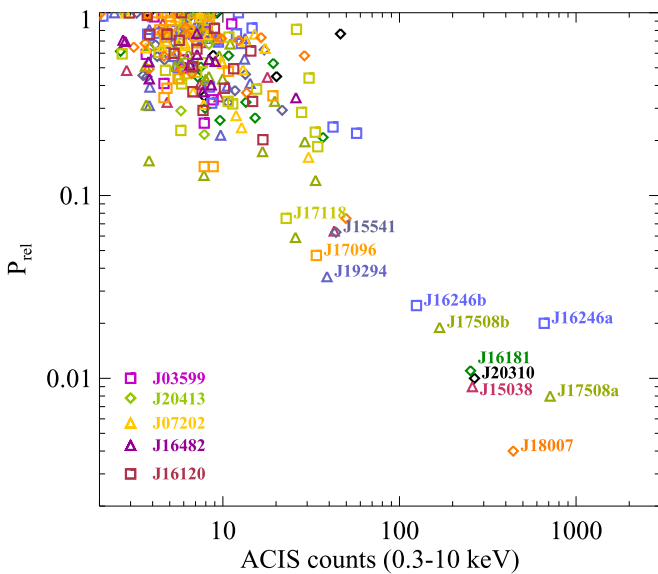
Figure 1. Relative probability of a chance detection (see Equation (3)) vs. the number of ACIS-I counts in the 0.3–10 keV bandpass for all *Chandra* sources detected in the 15 observations of IGR source fields. For the ten fields with candidate counterparts, the source that is least likely to be spurious is labeled with the IGR source name. In two fields (J16246 and J17508), there are two sources that are potential counterparts. The legend in the lower left corner of the plot only includes the five IGR source fields without likely counterparts.

N_H on scales smaller than the angular resolution of the survey. The measured Γ values show that most of the spectra are intrinsically hard. Nine of the sources have photon indices with best-fit values less than or equal to 1.5. J17058a is the softest source with $\Gamma = 3.0 \pm 0.2$. While J17096 and J17508b have $\Gamma = 1.9 \pm 1.3$ and 1.8 ± 0.5, respectively, the errors are relatively large. We use these fits to determine the fluxes in the 2–10 keV band. The "unabsorbed" fluxes are only corrected for the interstellar (Galactic) column density. With

these fluxes, we use

$$P = 1 - e^{-N(>F_{2-10\,keV})\,\pi\,\theta_{search}^2} \qquad (4)$$

to assess the absolute probability of finding a source in the search region (defined by θ_{search}) as bright as the candidate sources. We find $N(>F_{2-10\,keV})$ using the unabsorbed fluxes in Table 5 and Equations (1) and (2), which provides a range of probabilities depending on whether we use the Sugizaki et al. (2001) or the Fornasini et al. (2014) expression. The range of probabilities for each source is given in Table 5. The least likely sources to be chance coincidences are J15038 (0.97%–1.03%), J18007 (1.3%–1.7%), and J20310 (1.5%–1.6%), and the sources that are most likely to be chance coincidences are J15541 (5.4%–10.7%) and J17096 (4.7%–13.7%).

While these are the formal probabilities, we can also obtain information by exploring how the *Chandra* spectra extrapolate into the *INTEGRAL* band. To accomplish this comparison, we produced 2-bin *INTEGRAL* spectra using the fluxes in the Bird et al. (2016) catalog, and refit the *Chandra* spectra jointly with these two higher-energy points. An important caveat is that the *INTEGRAL* fluxes are averages over 7–8 years (up to 2010) while the *Chandra* spectrum is from a single observation in 2017. While the source flux (and possibly spectral shape) may be different for *Chandra* and *INTEGRAL*, we carry out fits without allowing for an offset between the two. Thus, a mismatch between *Chandra* and *INTEGRAL* could be caused by variability or it could indicate that the *Chandra* counterpart is incorrect. Also, for many of the *INTEGRAL* spectra, the flux is dropping between the 20–40 and 40–100 keV energy bands, indicating that the spectrum must change slope between *Chandra* and *INTEGRAL*. For this reason, we use a power law with an exponential cutoff, and fit each spectrum with the XSPEC model tbabs*cutoffpl.

Figure 2 shows the *Chandra*+*INTEGRAL* spectra, and the parameters are given in Table 6. We also used XSPEC for these fits, but we minimized χ^2 instead of C because the *INTEGRAL* points are based on fluxes rather than Poissonian counts. In

Table 5
Chandra Spectral Parameters and Absolute Spurious Probabilities

IGR Name	N_H[a] $(\times 10^{22}$ cm$^{-2})$	$N_{H,Galactic}$[b] $(\times 10^{22}$ cm$^{-2})$	Γ	Absorbed Flux[c] (2–10 keV)	Unabsorbed Flux[d] (2–10 keV)	C/dof	P_{reject}[e]	Probability[f]
J15038	<1.0	1.3	0.0 ± 0.3	2.34×10^{-12}	2.35×10^{-12}	25/23	21%	0.97%–1.03%
J15541	<4.3	0.8	1.1 ± 1.1	3.54×10^{-13}	3.78×10^{-13}	5.8/6	⋯	5.4%–10.7%
J16181	9 ± 7	0.5	0.8 ± 1.1	1.27×10^{-12}	1.29×10^{-12}	5.0/7	⋯	2.3%–2.8%
J16246a	0.4 ± 0.3	0.8	1.5 ± 0.2	2.82×10^{-12}	2.89×10^{-12}	90/57	99.7%	3.0%–3.5%
J16246b	2.5 ± 1.6	0.8	1.3 ± 0.7	9.27×10^{-13}	1.04×10^{-12}	16/10	75%	2.9%–3.5%
J17096	<3.6	0.2	1.9 ± 1.3	1.33×10^{-13}	1.45×10^{-13}	5.6/4	31%	4.7%–13.7%
J17118	<4.2	0.3	$1.2^{+1.7}_{-1.1}$	3.22×10^{-13}	3.37×10^{-13}	2.8/2	19%	3.9%–6.4%
J17508a	0.2 ± 0.1	0.5	3.0 ± 0.2	6.22×10^{-13}	6.33×10^{-13}	75/59	84%	1.9%–3.2%
J17508b	0.5 ± 0.5	0.5	1.8 ± 0.5	4.87×10^{-13}	5.00×10^{-13}	17/13	51%	3.1%–5.6%
J18007	<0.14	0.12	0.8 ± 0.2	1.06×10^{-12}	1.06×10^{-12}	23/14	88%	1.3%–1.7%
J19294	28^{+38}_{-24}	0.8	$0.6^{+2.7}_{-2.2}$	5.84×10^{-13}	5.91×10^{-13}	2.1/5	⋯	2.3%–4.0%
J20310	<5.6	1.5	-0.2 ± 0.9	1.95×10^{-12}	2.04×10^{-12}	9.2/9	3%	1.5%–1.6%

Notes.
[a] The errors on the parameters are 90% confidence. The column density is calculated assuming Wilms et al. (2000) abundances and Verner et al. (1996) cross sections.
[b] From the HI4PI survey (HI4PI Collaboration et al. 2016).
[c] In units of erg cm^{-2} s^{-1}.
[d] Only corrected for Galactic absorption.
[e] The probability that an absorbed power law does not provide a good description of the spectrum based on a calculation of the variance of C according to the method described in Kaastra (2017).
[f] Absolute probability that a source of this brightness would be found by chance in the search region.

nearly all cases, the `tbabs*cutoffpl` model provides a reasonably good description of the spectra. One notable exception is J17508a, for which the power-law index is well-constrained by the *Chandra* spectrum to be soft, and the extrapolation into the *INTEGRAL* bandpass is below the *INTEGRAL* fluxes by orders of magnitude. Although this might indicate that J17508b is the correct counterpart, the model does not fit the *Chandra*+*INTEGRAL* spectrum very well for J17508b either ($\chi^2/\nu = 43/14$), and we discuss the case of IGR J17508–3219 further in Section 4.1. J17096 is another case where the `tbabs*cutoffpl` model does not provide a very good fit, but it is clear that a better spectrum is required to understand the cause of the residuals. It is possible that J17096 and J18007 both require an extra spectral component at low energies.

3.3. Optical/IR Identifications

We used the VizieR database to search for optical/IR counterparts to the 12 *Chandra* sources. In seven cases, a *Gaia* DR2 optical source with a position consistent with the *Chandra* position was found, and these are listed in Table 7. Parallax measurements are available for six of the sources. They are negative in two cases, but for the four sources with positive parallaxes, the distance estimates from Bailer-Jones et al. (2018) are $1.1^{+1.5}_{-0.4}$, $2.20^{+0.28}_{-0.22}$, $0.135^{+0.002}_{-0.001}$, and $2.5^{+0.5}_{-0.4}$ kpc for J15038, J16246a, J17508a, and J18007, respectively. Thus, all four sources are Galactic, but it is doubtful that J17508a[13] is the correct counterpart to the IGR source, and J16246a is a questionable counterpart. However, IGR J15038–6021 is a Galactic source at a distance of $1.1^{+1.5}_{-0.4}$ kpc, and IGR J18007–4146 is a Galactic source at a distance of $2.5^{+0.5}_{-0.4}$ kpc.

Six of the twelve *Chandra* sources are present in the AllWISE IR catalog (Cutri et al. 2014), and the *Wide-field Infrared Survey Explorer* (*WISE*) magnitudes at 3.4 μm (*W1*),

4.6 μm (*W2*), 12 μm (*W3*), and 22 μm (*W4*) are given in Table 8. The *WISE* colors *W3-W2* and *W2-W1* have been used to identify AGN and blazars (e.g., Massaro et al. 2012; Secrest et al. 2015; Massaro & D'Abrusco 2016), and we plot these colors for the six sources in Figure 3. It has already been reported by Ursini et al. (2018) that IGR J16181–5407 (and the *Chandra* source J16181) is likely to be an AGN based on its *WISE* colors, and Figure 3 shows that the same criterion leads to IGR J17096–2527 (J17096) being a likely AGN. Figure 3 also shows that the two Galactic sources (based on *Gaia* as discussed above) are far away from the AGN region. J16246b and J19294 are the other two sources in the AllWISE catalog, but we cannot conclude on their nature based on their location in the *WISE* color–color diagram. However, we note that all four AGN candidates (J16181, J17096, J16246b, and J19294) are listed in AllWISE as having spatial profiles that are inconsistent with a point source in at least one photometric band, and the two Galactic sources (J16246a and J17508a) do not show evidence for extension (see Table 8).

In addition to *Gaia* and *WISE*, we found many more optical/IR counterparts to the 12 *Chandra* sources in the VizieR database. Here, we focus on the near-IR information from the Visible and Infrared Survey Telescope for Astronomy (VISTA; Minniti et al. 2010; McMahon et al. 2013; Minniti et al. 2017), the UKIRT Infrared Deep Sky Survey (UKIDSS; Lucas et al. 2008), and the 2 Micron All-Sky Survey (2MASS; Cutri et al. 2003), providing the *J*, *H*, and *K*/*K_s* magnitudes in Table 9 and the *K*/*K_s* images in Figure 4. In the *K*/*K_s* bands, the sources range in brightness with the faintest sources being J17118 ($K_s = 16.97 \pm 0.20$) and J20310 ($K = 16.54 \pm 0.04$) and the brightest sources being J17508a ($K_s = 7.45 \pm 0.03$) and J16246a ($K_s = 11.49 \pm 0.02$). Although J15541 does not appear in the catalogs, Figure 4 shows that it has a faint K_s-band counterpart that is very close to a bright star. In addition, the *K*-band images for J16246b, J19294, and probably J16181 confirm that these sources are extended, making it very likely that they are AGN. It is unclear from the VISTA image

---

[13] Catalog searches also uncovered that this source is the star HD 162186.
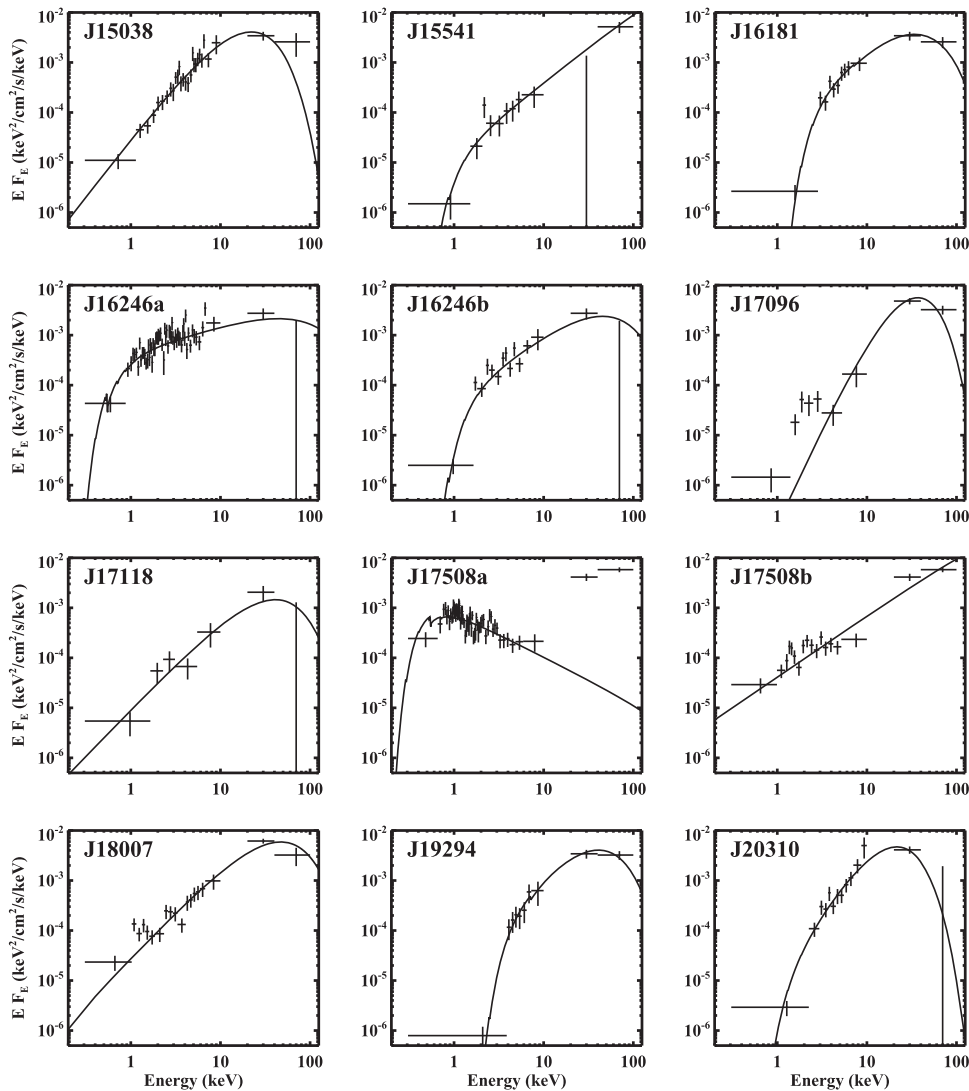
Figure 2. *Chandra* and *INTEGRAL* energy spectra for the 12 candidate counterparts. The two highest energy data points are derived from the fluxes reported in Bird et al. (2016). The best-fit absorbed power law with an exponential high-energy cutoff model (`tbabs*cutoffpl`) is shown. We note that the *INTEGRAL* measurements were made during 2002–2010 while the *Chandra* spectra were obtained in 2017. Thus, it is possible for source variability to cause poor fits in some cases.

whether J17096 is extended, and it is also classified as being a star in the VISTA catalog (see Table 9); however, we still consider it to be likely that J17096 is an AGN based on the *WISE* information. For J20310, the *K*-band image from UKIDSS may show some extension, and the source is classified as being a galaxy in the UKIDSS catalog.

In summary, the parallax measurements for J15038, J16246a, J17058a, and J18007 show that these four *Chandra* sources are Galactic, and the K/K_s images (Figure 4) are consistent with this in that they do not show evidence that these sources are extended. Based on the sources being extended and/or the *WISE* colors, J16181, J16246b, J17096, and J19294 are AGN, and J20310 is an AGN candidate based on the UKIDSS information. We discuss the nature of the remaining three sources (J15541, J17118, and J17058b) below.

4. Discussion

The main goal of this work is to determine the nature of the 15 IGR sources (see Table 2) by determining the most likely *Chandra* counterparts and then using the *Chandra* localizations along with information in online catalogs and databases to classify the sources. There are two IGR sources with two possible *Chandra* counterparts: IGR J16246−4556 and IGR J17508−3219; and we discuss those cases first. Then, we consider the two sources definitively classified as being Galactic: IGR J18007−4146 and IGR J15038−6021. After that, we discuss the unclassified sources with *Chandra* counterparts: IGR J15541−5613 and IGR J17118−3155 and then the cases without likely *Chandra* counterparts.

4.1. IGR Sources with Two Candidate Chandra Counterparts

For IGR J16246−4556, the two candidate *Chandra* counterparts that we are considering are J16246a (3.0%–3.5%) and J16246b (2.9%–3.5%). Both of them have hard spectra ($\Gamma = 1.5 \pm 0.2$ and 1.3 ± 0.7, respectively, from the *Chandra*-only fits) that are consistent with the *INTEGRAL* fluxes (see Figure 2), and their spurious probabilities are the same because J16246a is about three times brighter, while J16246b is only $1\rlap{.}'56$ from the center of the *INTEGRAL* error circle, while $\theta = 7\rlap{.}'92$ for J16246a. Given that the 90% confidence *INTEGRAL* radius is $4\rlap{.}'61$, an

Table 6
Chandra+INTEGRAL Spectral Parameters

IGR Name	$N_{\rm H}$[a] $(\times 10^{22}\,{\rm cm}^{-2})$	Γ	$E_{\rm fold}$ (keV)	Unabsorbed Flux[b] (0.3–100 keV)	$\chi^2/{\rm dof}$[c]
J15038	<1.0	$-0.3^{+0.6}_{-0.3}$	10^{+8}_{-2}	1.11×10^{-11}	22/24
J15541	<2.4	$0.6^{+0.2}_{-0.6}$	>36	1.07×10^{-11}	5/7
J16181	8 ± 5	0.3 ± 0.7	20^{+33}_{-8}	1.10×10^{-11}	5/8
J16246a	0.3 ± 0.3	1.4 ± 0.3	>22	1.01×10^{-11}	86/58
J16246b	1.4 ± 1.3	0.6 ± 0.7	>12	7.6×10^{-12}	18/11
J17096[c]	0.0	-2.0	9	1.15×10^{-11}	21/5
J17118	<1.4	$0.2^{+1.1}_{-0.7}$	>8	4.2×10^{-12}	6/3
J17508a[c]	0.15	2.9	500	2.2×10^{-12}[d]	192/60
J17508b	<0.8	0.8 ± 0.1	>179	1.35×10^{-11}	43/14
J18007	<0.12	0.1 ± 0.3	25^{+13}_{-8}	1.67×10^{-11}	43/15
J19294	24^{+21}_{-14}	-0.1 ± 0.9	20^{+42}_{-8}	1.08×10^{-11}	2/6
J20310	<4.6	-0.9 ± 1.1	7^{+10}_{-3}	1.14×10^{-11}	9/10

Notes.
[a] The errors on the parameters are 90% confidence. The column density is calculated assuming Wilms et al. (2000) abundances and Verner et al. (1996) cross sections.
[b] In units of erg cm^{-2} s^{-1}, and corrected for Galactic absorption.
[c] The quality of the fit does not allow for errors to be calculated. The `tbabs*cutoffpl` does not provide a good description of the spectrum.
[d] This is the flux for the model shown in Figure 2, which is well below the *INTEGRAL* measurements.

Table 7
Gaia Identifications

IGR Name	*Gaia* Number (in DR2)	Separation[a] (arcsec)	G-magnitude	Parallax (milliarcsecond)	Distance[b] (kpc)
J15038	5876459780108921216	0.072	19.055 ± 0.006	1.09 ± 0.37	$1.08^{+1.53}_{-0.42}$
J15541	5836092447721411584	0.245	20.392 ± 0.019	-6.92 ± 1.87	⋯
J16246a	5942431027538084608	0.463	15.494 ± 0.003	0.43 ± 0.05	$2.20^{+0.28}_{-0.22}$
J17096	4112378173142821248	0.049	19.360 ± 0.006	-0.52 ± 0.43	⋯
J17508a	4043524762244704000	0.240	9.027 ± 0.001	7.33 ± 0.04	$0.135^{+0.002}_{-0.001}$
J17508b	4043518508770139648	0.383	18.884 ± 0.018	⋯	⋯
J18007	6725376279628784384	0.331	16.009 ± 0.006	0.38 ± 0.06	$2.49^{+0.49}_{-0.36}$

Notes.
[a] The angular separation between the *Chandra* position and the *Gaia* catalog position.
[b] From Bailer-Jones et al. (2018).

Table 8
WISE Identifications

IGR Name	AllWISE Name	Separation[a] (arcsec)	$W1$	$W2$	$W3$	$W4$	ex[b]
J16181	J161807.75–540612.3	0.21	11.29 ± 0.04	10.12 ± 0.02	7.55 ± 0.02	4.97 ± 0.04	1
J16246a	J162425.20–460316.7	0.28	11.35 ± 0.03	11.37 ± 0.02	11.88 ± 0.38	⋯	0
J16246b	J162430.78–455514.4	0.35	10.70 ± 0.02	10.52 ± 0.02	8.74 ± 0.04	6.58 ± 0.07	1
J17096	J170950.25–252934.7	0.41	13.61 ± 0.04	12.54 ± 0.03	9.40 ± 0.06	6.78 ± 0.14	1
J17508a	J175106.84–321827.8	0.11	7.41 ± 0.03	7.48 ± 0.02	7.29 ± 0.02	6.52 ± 0.09	0
J19294	J192930.14+132705.9	0.32	12.56 ± 0.03	12.28 ± 0.03	9.71 ± 0.05	7.38 ± 0.12	1

Notes.
[a] The angular separation between the *Chandra* position and the AllWISE catalog position.
[b] A "0" indicates that the source is consistent with being a point source, and a "1" indicates that the profile is not well-described as a point source in at least one photometric band.

offset of 7′.92 corresponds to the 3σ error radius; thus, it is unlikely that the source would be offset by this much, and we note that none of the other *Chandra* counterparts have values of θ that are more than 3′.7 (see Table 4). While J16246a may be an interesting source and worthy of attention, we identify J16246b

with IGR J16246–4556, making this IGR source an AGN. The fact that J16246b is a galaxy is confirmed by the VizieR search, which shows a detection of the source in the Parkes HI zone of avoidance survey (Staveley-Smith et al. 2016). It is the galaxy HIZOA J1624-45B, which has a distance of 78.7 Mpc.

Table 9
VISTA, 2MASS, and UKIDSS Identifications

IGR Name	Catalog	Source (arcsec)	Separation[a]	J	H	K/K_s	Class[b]
J15038	VISTA	VVV J150415.72–602122.87	0.230	16.13 ± 0.02	15.48 ± 0.02	K_s = 15.03 ± 0.02	−1
J15541	⋯	⋯	⋯	⋯	⋯	See Figure 4.	⋯
J16181	2MASS	2MASS J16180771–5406122	0.365	⋯	14.09 ± 0.04	K_s = 12.85 ± 0.06	⋯
J16246a	2MASS	2MASS J16242520–4603169	0.409	12.61 ± 0.02	11.78 ± 0.02	K_s = 11.49 ± 0.02	⋯
J16246b	2MASS	2MASS J16243080–4555144	0.519	14.31 ± 0.10	12.98 ± 0.11	K_s = 12.19 ± 0.08	⋯
J17096	VISTA	VHS 472814537075	0.135	17.06	⋯	K_s = 15.81	−1
J17118	VISTA	VVV J171135.91–315503.61	0.929	18.64 ± 0.28	18.00 ± 0.33	K_s = 16.97 ± 0.20	−2
J17508a	2MASS	2MASS J17510684–3218276	0.054	7.89 ± 0.02	7.59 ± 0.04	K_s = 7.45 ± 0.03	⋯
J17508b	VISTA	VVV J175108.76–322122.39	0.306	14.73 ± 0.02	13.63 ± 0.02	K_s = 13.17 ± 0.01	−1
J18007	VISTA	VVV J180042.71–414650.23	0.339	15.60 ± 0.01	15.34 ± 0.01	K_s = 15.31 ± 0.03	−1
J19294	UKIDSS	UGPS J192930.11+132705.7	0.372	16.30 ± 0.01	15.09 ± 0.01	K = 14.32 ± 0.01	1
J20310	UKIDSS	UGPS J203055.29+383347.1	0.180	18.83 ± 0.05	17.30 ± 0.02	K = 16.54 ± 0.04	1

Notes.
[a] The angular separation between the *Chandra* position and the catalog position.
[b] The classification based on the spatial profile, where −2 is a probable star, −1 is a star with probability ⩾90%, and 1 is a galaxy with probability ⩾90%.
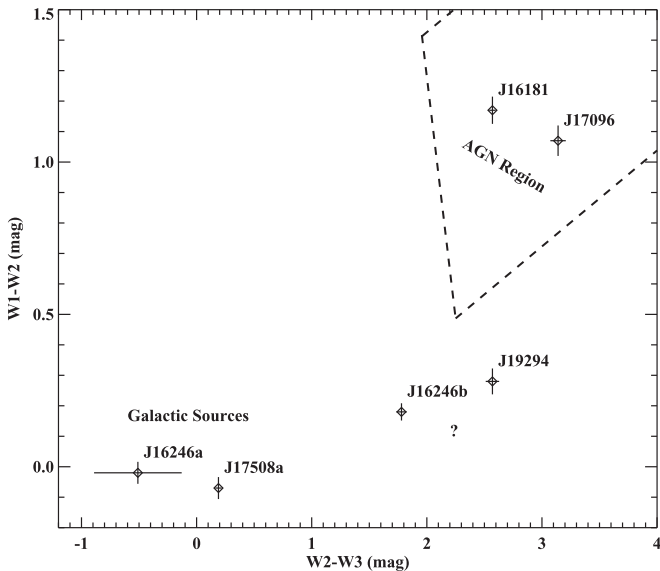
Figure 3. Near-IR colors measured for six of the IGR sources by *WISE*. $W1$, $W2$, and $W3$ are 3.4 μm, 4.6 μm, and 12 μm, respectively. Based on *Gaia* distances, J16246a and J17508a are Galactic sources (this work). J16181 and J17096 are in a region commonly populated by AGN (Secrest et al. 2015; Ursini et al. 2018). The region originally defined by Mateos et al. (2012) is indicated by the dashed lines.

Based on the *Chandra* and *INTEGRAL* spectrum, the unabsorbed 0.3–100 keV flux is 7.7×10^{-12} erg cm^{-2} s^{-1}, making the luminosity 5.7×10^{42} erg s^{-1}.

IGR J17508–3219 has the two candidate *Chandra* counterparts J17508a and J17508b. Both are outside the $2\rlap{.}'31$ (90% confidence) *INTEGRAL* error circle with $\theta = 3\rlap{.}'21$ and $3\rlap{.}'68$ for J17508a and J17508b, respectively. As mentioned earlier, J17508a is a soft source ($\Gamma = 3.0 \pm 0.2$) and is inconsistent with the *INTEGRAL* fluxes (see Figure 2); thus, we rule out J17508a as the counterpart. For J17508b, the VizieR search shows that it is coincident with the source OGLE-BLG-DN-0184, which is a dwarf nova (DN) non-magnetic CV with a few optical outbursts per year. The typical outburst duration for OGLE-BLG-DN-0184 is 13.1 days where the optical brightness increases from $I = 17.5$ to 15.7 (Mróz et al. 2015). Although 56 CVs appear in the Bird et al. (2016) catalog,

nearly all of the CVs that have been classified are IPs or polars, which have highly magnetized white dwarfs. However, some non-magnetic DNe can produce hard X-ray emission above at least 14 keV (Mukai 2017), and J17508b has a relatively hard spectrum with $\Gamma = 1.8 \pm 0.5$. Although we consider J17508b to be a possible counterpart, we also note that Landi et al. (2017) reported on a *Swift*/XRT observation where a third source (#1 in the work of Landi) was detected within the *INTEGRAL* error circle with a 2–10 keV flux of 8×10^{-13} erg cm^{-2} s^{-1} and $\Gamma = 0.6 \pm 0.8$. Landi source #1 is not detected in the *Chandra* observation, and the upper limit on the 2–10 keV flux is approximately an order of magnitude lower than the flux detected by *Swift*. If Landi source #1 is the true counterpart of IGR J17508–3219, this level of variability is surprising given that it is noted to be a persistent source in Bird et al. (2016). Given that Landi source #1 is a hard source within the *INTEGRAL* error circle, it must be considered as a strong candidate, but we also cannot rule out the possibility that J17508b also contributes to the flux seen by *INTEGRAL*.

4.2. Galactic Source IGR J18007–4146

IGR J18007–4146 is associated with an *XMM-Newton* slew source XMMSL1 J180042.8–414651, and the source was also detected by *Swift*/XRT (Landi et al. 2017). Multiple optical/IR sources are consistent with the *XMM* and *Swift* localizations (Landi et al. 2017), but the *Chandra* position for CXOU J180042.6–414650 that we report allows for a unique identification in multiple optical/IR surveys, including VISTA and *Gaia*. It is the VISTA source VVV J180042.71–414650.23, and the *Gaia* counterpart has a parallax distance measurement of $2.5^{+0.5}_{-0.4}$ kpc. The *Chandra* energy spectrum is a very hard power law ($\Gamma < 1$), and combining it with the *INTEGRAL* fluxes indicates that the spectrum turns over at around 25 keV. The 0.3–100 keV flux is $(1.67 \pm 0.35) \times 10^{-11}$ erg cm^{-2} s^{-1}, and this corresponds to a luminosity of $(1.2 \pm 0.5) \times 10^{34}$ erg s^{-1}. Known Galactic source types that may match these properties are CV/IPs or accreting pulsars, which are most often found in HMXBs.

The origin of the optical/IR emission is unclear. If the source is a CV/IP, the emission would be a combination of an accretion disk and a star. Most CV/IPs have late-type stars, and the accretion disk dominates. If the source is an HMXB, then the
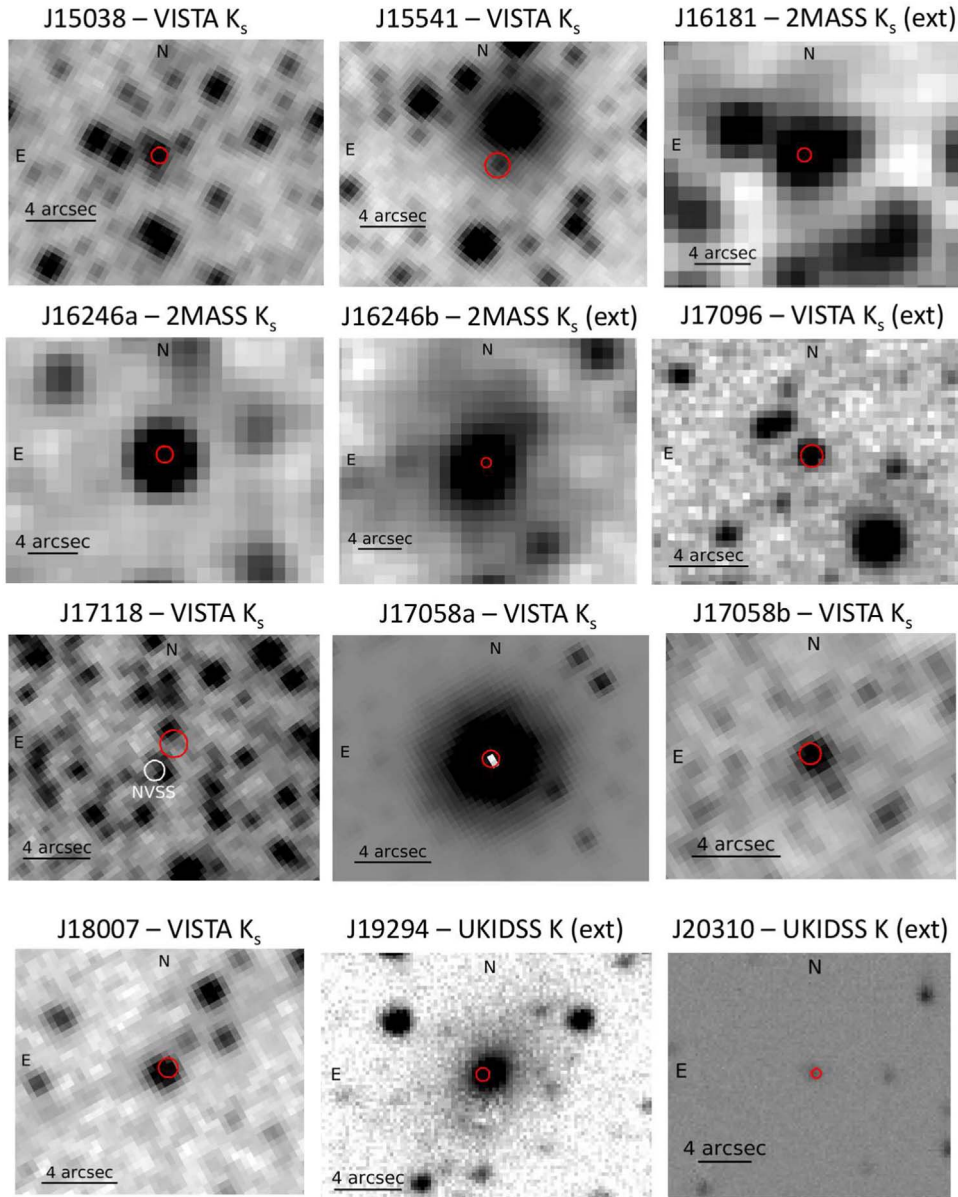
Figure 4. K or K_s band images from the VISTA, 2MASS, and UKIDSS surveys for the 12 candidate counterparts. The red circles indicate the *Chandra* positions (90% confidence). The sources that are extended (i.e., with spatial distributions that are not point-like; see Table 9) are J16181, J16246b, J17096, J19294, and J20310 and are indicated with "(ext)" in the titles above the images.

high-mass star (O- or B-type) would dominate. In either case, the emission is thermal, and we can estimate the temperature using the near-IR colors. The X-ray spectrum does not show evidence for any absorption, with a 90% confidence upper limit of $N_H < 1.2 \times 10^{21}$ cm^{-2}, corresponding to $A_V < 0.54$ (Güver & Özel 2009). Using the VISTA near-IR magnitudes and the Cardelli et al. (1989) extinction law, the dereddened magnitudes are $J = 15.45$–15.60 and $H = 15.34$–15.24. Thus, J–H is between 0.21 and 0.26, which corresponds to a temperature of ~ 6500 K. If this was a stellar temperature, it would correspond to an F5V spectral type, which has $M_J = 2.7$. For IGR J18007–4146, if the extinction is zero, then $M_J = 3.6 \pm 0.4$, and if the extinction is at the maximum value ($A_J = 0.15$), it would be $M_J = 3.5 \pm 0.4$, and these values correspond to a spectral type of G2V. To accommodate a F5V star, the source distance would need to be ~ 3.5 kpc, which is higher than the Bailer-Jones et al. (2018) value at the 2σ level. Regardless of whether the distance could be as high

as 3.5 kpc, these calculations show that IGR J18007–4146 does not harbor a high-mass O- or B-type star. In fact, if there is a significant contribution to the optical/IR emission from an accretion disk, it is possible that the source is a binary with a late-type star. Given the possible classifications mentioned above (a CV/IP or an HMXB), a CV/IP is strongly favored. However, follow-up optical spectroscopy is needed for confirmation.

4.3. Galactic Source IGR J15038–6021

IGR J15038–6021 was also previously reported as a *Swift*/ XRT source by Landi et al. (2017), but the X-ray localization was not adequate to identify a unique optical/IR counterpart. The detection of this source by *Chandra* as CXOU J150415.7–602123 provides the unique optical/IR identification with the VISTA source VVV 150415.72–602122.87 as well as a *Gaia* source, which provides a parallax distance of $1.1^{+1.5}_{-0.4}$ kpc. The X-ray energy spectrum is slightly harder than IGR J18007–4146, and

the 0.3–100 keV flux is $(1.11 \pm 0.28) \times 10^{-11}$ erg cm^{-2} s^{-1}, corresponding to a luminosity of $(1.6^{+4.4}_{-1.2}) \times 10^{33}$ erg s^{-1}. This suggests the same possibilities for classifications mentioned above: HMXB or CV/IP.

We carry out a similar calculation as for IGR J18007–4146 using the J and H magnitudes along with the *Gaia* distance. Even though IGR J15038–6021 is closer than IGR J18007–4146, it is in the Galactic plane ($b = -1°57$ compared to $b = -9°12$ for IGR J18007–4146), and although the best-fit value for N_H is zero for both sources, the upper limit for IGR J15038–6021 is higher ($N_H < 1.0 \times 10^{22}$ cm^{-2}). This limit on the column density corresponds to $A_V < 4.52$ (Güver & Özel 2009), and we calculate dereddened magnitudes of $J = 14.86$–16.13 and $H = 14.62$–15.48, giving a range of J–H values between 0.24 and 0.65 and a range of temperatures between 4000 and 6500 K. This allows for a range of stellar spectral types between K5V and F5V.

Turning to the measurement of the absolute magnitude, assuming the *Gaia* distance ($1.1^{+1.5}_{-0.4}$ kpc), if there is no extinction, then $M_J = 5.9^{+0.8}_{-3.0}$, and if the extinction is maximal ($A_J = 1.27$), then $M_J = 4.7^{+0.8}_{-3.0}$. If the errors are included, these absolute magnitudes correspond to spectral types between K5V and A5V. Although this is a large range, it does not cover O and B stars. However, in this case, we must treat the *Gaia* distance with some caution because the *Gaia* DR2 catalog indicates that the astrometric noise for this source is significant. Thus, we performed an additional calculation and found that the distance would need to be 10 kpc to move the absolute magnitude of IGR J15038–6021 into the late B-type range. Thus, based on both the temperatures derived above and the fact that it is very unlikely for the true distance to be larger than the *Gaia* measurement by 6σ, we conclude that IGR J15038–6021 is likely to be a CV/IP.

4.4. Unclassified Sources with Chandra Counterparts

Although our candidate *Chandra* counterpart to IGR J15541–5613, CXOU J155413.0–560932, has a relatively high spurious probability of 5.4%–10.7%, Figure 2 shows that the spectrum rises throughout the *Chandra* band with $\Gamma = 1.1 \pm 1.1$, and the source is also unusual for a Galactic source in having a higher flux in the 40–100 keV band than in the 20–40 keV band. This suggests that IGR J15541–5613 is more likely to be an AGN than a Galactic source. It is conceivable that the high point in the *Chandra* spectrum at ∼2 keV is a redshifted iron line, but the statistical significance of the putative line is low. Also, the implied redshift is $z \sim 2$, and this would indicate a very luminous and rare AGN. Figure 4 shows that, with the bright nearby source, obtaining an optical or near-IR spectrum of IGR J15541–5613 will be challenging, but it may be possible.

For our candidate *Chandra* counterpart to IGR J17118–3155, CXOU J171135.8–315504, a search of the SIMBAD database shows a possible Very Large Array radio counterpart, NVSS J171135–315506. This radio source is quite bright, and is seen in several radio surveys (Douglas et al. 1996; Condon et al. 1998; Murphy et al. 2007; Intema et al. 2017): the Giant Metrewave Radio Telescope/GMRT (1496 mJy at 150 MHz); the Texas Survey/TXS (606 mJy at 365 MHz); the Molonglo Galactic Plane Survey/MGPS-2 (225 mJy at 843 MHz); and the NRAO VLA Sky Survey/NVSS (165 mJy at 1420 MHz). However, considering the best estimates for the radio positions, only the TXS position is within the *Chandra* error circle with the other sources being $2″3 \pm 2″0$ (GMRT), $1″5 \pm 1″6$ (MGPS-2), and $2″0 \pm 0″6$ (NVSS) away from the center of the *Chandra*

error circle. The NVSS error circle is shown on the VISTA K_s image (Figure 4), and it is clear that the error region does not overlap with *Chandra*. We also plotted the NVSS error circle on the *Chandra*/ACIS image, and none of the 23 ACIS counts fall within the NVSS error circle. We repeated this analysis without the $0″3$ position registration shift (see Table 3), and there are still no ACIS counts in the NVSS error circle. While it would be a somewhat surprising coincidence for these two relatively unusual sources to be as close to each other as they are and not be associated, our analysis does not support an association between the two.

4.5. IGR Sources without Likely Chandra Counterparts

Although *Chandra* sources were detected in the *INTEGRAL* error circles for all 15 IGR sources included in this work, there were five cases (IGR J03599+5043, IGR J07202+0009, IGR J16482–2959, IGR J16120–3543, and IGR J20413+3210) where the *Chandra* sources all had relatively high probability of being chance detections of field sources. The *Chandra* sources in *INTEGRAL* error circles of these five IGR sources with the lowest values of P_{rel} are 24.9%, 27.9%, 37.0%, 20.2%, and 21.6%, respectively. We searched the VizieR database to check whether any of the *Chandra* sources have a classified counterpart, and the source with $P_{rel} = 20.2\%$ (CXOU J161147.0–354634)[14] is a *WISE* source (AllWISE J161147.06–354635.0) that has been classified as an AGN based on its *WISE* colors (Secrest et al. 2015). The 2–10 keV X-ray flux is $(9.9^{+6.5}_{-7.1}) \times 10^{-14}$ erg cm^{-2} s^{-1}. While this may still be a spurious identification, we consider the CXOU/AllWISE source to be a candidate counterpart.

Within the *INTEGRAL* error circles of the other four IGR sources (IGR J03599+5043, IGR J07202+0009, IGR J16482–2959, and IGR J20413+3210), the *Chandra* sources with the lowest P_{rel} values have between five and seven counts in the 2–10 keV band. Taking seven counts (0.0014 c s^{-1}) as the upper limit, we can use PIMMS[15] to determine the approximate flux upper limit. If we assume $\Gamma > 0$ and $N_H = 10^{22}$ cm^{-2}, we find a flux limit of $<7 \times 10^{-14}$ erg cm^{-2} s^{-1} in the 2–10 keV energy band. There are several possible interpretations for these IGR sources. When similar results have previously been obtained for other IGR sources, Tomsick et al. (2016a) consider that those IGR sources may be variable or may have hard spectra (either due to high column densities or hard power-law slopes). It is notable that IGR J03599+5043, IGR J07202+0009, IGR J16482–2959, and IGR J20413+3210 are marked as being variable in Bird et al. (2016; see Table 1). Another possibility is that these IGR sources are spurious, but the *INTEGRAL* signal-to-noise values are between 5.9 and 7.5 (Table 1).

5. Summary and Conclusions

Our final results for each of the 15 IGR sources are summarized in Table 10, including the name of the *Chandra* counterpart or upper limit on the X-ray flux, our conclusion about the source type, and the main evidence we use to come to our conclusion. IGR J15038–6021 and IGR J18007–4146 are strong CV/IP candidates, and this could be confirmed in the future with optical or near-IR spectroscopy. We definitively

---

[14] The *Chandra* position is R.A. = $16^h11^m47^s04$, decl. = $-35°46'34″9$, equinox 2000.0 with a 90% confidence position uncertainty of $0″90$.
[15] See https://asc.harvard.edu/toolkit/pimms.jsp.

Table 10
Summary of Results

IGR Name	*Chandra* Counterpart or 2–10 keV Flux Limit	Source Type	Evidence
J03599+5043	$<1.5 \times 10^{-13}$	…	…
J07202+0009	$<1.4 \times 10^{-13}$	…	…
J15038−6021	CXOU J150415.7−602123	CV/IP?	*Gaia* distance, near-IR magnitudes, X-ray spectrum
J15541−5613	CXOU J155413.0−560932	AGN?	X-ray spectrum
J16120−3543	CXOU J161147.0−354634?	AGN?	*WISE* colors
J16181−5407	CXOU J161807.7−540612	AGN	*WISE* colors and extended in near-IR
J16246−4556	CXOU J162430.7−455514	AGN	Extended in near-IR
J16482−2959	$<1.5 \times 10^{-13}$	…	…
J17096−2527	CXOU J170950.2−252934	AGN	*WISE* colors and extended in near-IR
J17118−3155	CXOU J171135.8−315504	?	?
J17508−3219	CXOU J175108.7−322122?	?[a]	?
J18007−4146	CXOU J180042.6−414650	CV/IP?	*Gaia* distance, near-IR magnitudes, X-ray spectrum
J19294+1327	CXOU J192930.1+132705	AGN	Extended in near-IR
J20310+3835	CXOU J203055.2+383347	AGN?	Likely extended in near-IR
J20413+3210	$<1.5 \times 10^{-13}$	…	…

Note.
[a] While CXOU J175108.7−322122 is classified as a Dwarf Nova and may be the counterpart, source #1 detected in the field by *Swift* (Landi et al. 2017) is a variable source that is another possible counterpart.

classify four IGR sources as AGN and three as AGN candidates. This relatively high fraction of AGN may not be too surprising as the new IGR sources found recently are, on average, fainter than the IGR sources found earlier in the mission. We also note that the plot of near-IR colors measured by *WISE* (Figure 3), which has been used to identify AGN, may be a useful tool for identifying Galactic sources as well. Finally, although we detected likely *Chandra* counterparts to IGR J17508−3219 and IGR J17118−3155, the classifications are unclear. Additional X-ray observations of IGR J17508−3219 may be useful to determine if the true counterpart is CXOU J175108.7−322122 or the Landi et al. (2017) *Swift* source. For IGR J17118−3155, the uncertainty on the X-ray position could be reduced with a longer *Chandra* observation with the source on-axis.

ORCID iDs

John A. Tomsick ⓘ https://orcid.org/0000-0001-5506-9855
Arash Bodaghee ⓘ https://orcid.org/0000-0002-7315-3732
Maïca Clavel ⓘ https://orcid.org/0000-0003-0724-2742
Francesca M. Fornasini ⓘ https://orcid.org/0000-0002-9286-9963
Jeremy Hare ⓘ https://orcid.org/0000-0002-8548-482X
Roman Krivonos ⓘ https://orcid.org/0000-0003-2737-5673
Farid Rahoui ⓘ https://orcid.org/0000-0001-7655-4120
Jerome Rodriguez ⓘ https://orcid.org/0000-0002-4151-4468

References

Arnaud, K. A. 1996, in ASP Conf. Ser. 101, Astronomical Data Analysis Software and Systems V, ed. G. H. Jacoby & J. Barnes (San Francisco, CA: ASP), 17
Bailer-Jones, C. A. L., Rybizki, J., Fouesneau, M., Mantelet, G., & Andrae, R. 2018, AJ, 156, 58
Bird, A. J., Bazzano, A., Bassani, L., et al. 2010, ApJS, 186, 1
Bird, A. J., Bazzano, A., Malizia, A., et al. 2016, ApJS, 223, 15
Bonnet-Bidaud, J. M., de Martino, D., Falanga, M., Mouchet, M., & Masetti, N. 2007, A&A, 473, 185
Cardelli, J. A., Clayton, G. C., & Mathis, J. S. 1989, ApJ, 345, 245
Chaty, S., Rahoui, F., Foellmi, C., et al. 2008, A&A, 484, 783
Coleiro, A., Chaty, S., Zurita Heras, J. A., Rahoui, F., & Tomsick, J. A. 2013, A&A, 560, A108
Condon, J. J., Cotton, W. D., Greisen, E. W., et al. 1998, AJ, 115, 1693
Cutri, R. M., Skrutskie, M. F., van Dyk, S., et al. 2003, 2MASS All Sky Catalog of Point Sources, NASA/IPAC Infrared Science Archive, http://irsa.ipac.caltech.edu/applications/Gator/
Cutri, R. M., et al. 2014, yCat, 2328, 0
Douglas, J. N., Bash, F. N., Bozyan, F. A., Torrence, G. W., & Wolfe, C. 1996, AJ, 111, 1945
Fornasini, F. M., Tomsick, J. A., Bodaghee, A., et al. 2014, ApJ, 796, 105

Fortin, F., Chaty, S., Coleiro, A., Tomsick, J. A., & Nitschelm, C. H. R. 2018, A&A, 618, A150

Fruscione, A., McDowell, J. C., Allen, G. E., et al. 2006, Proc. SPIE, 6270, 62701V

Gaia Collaboration, Brown, A. G. A., Vallenari, A., et al. 2018, A&A, 616, A1

Garmire, G. P., Bautz, M. W., Ford, P. G., Nousek, J. A., & Ricker, G. R. 2003, Proc. SPIE, 4851, 28

Güver, T., & Özel, F. 2009, MNRAS, 400, 2050

HI4PI Collaboration, Ben Bekhti, N., Flöer, L., et al. 2016, A&A, 594, A116

Intema, H. T., Jagannathan, P., Mooley, K. P., & Frail, D. A. 2017, A&A, 598, A78

Kaastra, J. S. 2017, A&A, 605, A51

Kim, M., Kim, D.-W., Wilkes, B. J., et al. 2007, ApJS, 169, 401

Krivonos, R. A., Tsygankov, S. S., Mereminskiy, I. A., et al. 2017, MNRAS, 470, 512

Landi, R., Bassani, L., Bazzano, A., et al. 2017, MNRAS, 470, 1107

Landi, R., Bassani, L., Dean, A. J., et al. 2009, MNRAS, 392, 630

Landi, R., Bassani, L., Masetti, N., et al. 2012, ATel, 4233

Lucas, P. W., Hoare, M. G., Longmore, A., et al. 2008, MNRAS, 391, 136

Masetti, N., Parisi, P., Palazzi, E., et al. 2013, A&A, 556, A120

Massaro, F., & D'Abrusco, R. 2016, ApJ, 827, 67

Massaro, F., Paggi, A., D'Abrusco, R., & Tosti, G. 2012, ApJ, 750, L35

Mateos, S., Alonso-Herrero, A., Carrera, F. J., et al. 2012, MNRAS, 426, 3271

Matt, G., & Guainazzi, M. 2003, MNRAS, 341, L13

McMahon, R. G., Banerji, M., Gonzalez, E., et al. 2013, Msngr, 154, 35

Minniti, D., Lucas, P. & VVV Team 2017, yCat, 2348, 0

Minniti, D., Lucas, P. W., Emerson, J. P., et al. 2010, NewA, 15, 433

Mróz, P., Udalski, A., Poleski, R., et al. 2015, AcA, 65, 313

Mukai, K. 2017, PASP, 129, 062001

Murphy, T., Mauch, T., Green, A., et al. 2007, MNRAS, 382, 382

Negueruela, I., Smith, D. M., Reig, P., Chaty, S., & Torrejón, J. M. 2006, in ESA SP-604: The X-ray Universe 2005, ed. A. Wilson (Noordwijk: ESA), 165

Pavan, L., Bordas, P., Puehlhofer, G., et al. 2014, A&A, 562, A122

Pavan, L., Bozzo, E., Pühlhofer, G., et al. 2011, A&A, 533, A74

Prusti, T., de Bruijne, J. H. J., Brown, A. G. A., et al. 2016, A&A, 595, A1

Romano, P., Krimm, H. A., Palmer, D. M., et al. 2014, A&A, 562, A2

Secrest, N. J., Dudik, R. P., Dorland, B. N., et al. 2015, ApJS, 221, 12

Sguera, V., Bazzano, A., Bird, A. J., et al. 2006, ApJ, 646, 452

Staveley-Smith, L., Kraan-Korteweg, R. C., Schröder, A. C., et al. 2016, AJ, 151, 52

Sugizaki, M., Mitsuda, K., Kaneda, H., et al. 2001, ApJS, 134, 77

Tomsick, J. A., Bodaghee, A., Chaty, S., et al. 2012a, ApJ, 754, 145

Tomsick, J. A., Bodaghee, A., Rodriguez, J., et al. 2012b, ApJL, 750, L39

Tomsick, J. A., Chaty, S., Rodriguez, J., et al. 2006, ApJ, 647, 1309

Tomsick, J. A., Chaty, S., Rodriguez, J., Walter, R., & Kaaret, P. 2009, ApJ, 701, 811

Tomsick, J. A., Kalemci, E., Kaaret, P., et al. 2008, ApJ, 680, 593

Tomsick, J. A., Krivonos, R., Wang, Q., et al. 2016a, ApJ, 816, 38

Tomsick, J. A., Rahoui, F., Krivonos, R., et al. 2016b, MNRAS, 460, 513

Ursini, F., Bassani, L., Malizia, A., et al. 2018, ATel, 11890, 1

Verner, D. A., Ferland, G. J., Korista, K. T., & Yakovlev, D. G. 1996, ApJ, 465, 487

Walter, R., Zurita Heras, J., Bassani, L., et al. 2006, A&A, 453, 133

Wilms, J., Allen, A., & McCray, R. 2000, ApJ, 542, 914

Winkler, C., Courvoisier, T. J.-L., Di Cocco, G., et al. 2003, A&A, 411, L1